

TABLE OF CONTENTS
VENUS-MARS CAPSULE STUDY

- I. Introduction
- II. Summary
- III. Analysis
 - 1.0 Trajectory Analysis
 - 2.0 Instrumentation
 - 3.0 Communications
 - 4.0 Power Supply
 - 5.0 Theoretical Vehicle-Environment Interactions
 - 6.0 Experimental Vehicle-Environment Interactions
 - 7.0 Capsule Parametric Analysis
 - 8.0 Sterilization
- IV. Recommended Research and Development Program

I INTRODUCTION

I. INTRODUCTION

As part of the overall plan for space exploration, Mariner spacecraft are to be launched so as to fly by the planets Mars and Venus. Besides obtaining data as to the nature of interplanetary space, the spacecraft will attempt to secure answers to many questions that still remain as to the characteristics of these planets. Since the Mariner spacecraft is only designed to fly by the planets, it would be difficult to obtain much additional data as to the nature of the planetary atmospheres if one were to rely wholly upon this spacecraft.

The ideal means for measuring the characteristics of the Martian and Venusian atmospheres will be to utilize a vehicle that would survive the atmospheric entry and measure and transmit back to earth the data during the descent to the surface of the planet. Since the entry vehicles will only have to be of a modest size, it could be carried by the Mariner spacecraft and ejected at some point during transit to follow a ballistic path until entry into the planetary atmospheres. The point at which the entry vehicle would be released from the spacecraft is a function of the energy available for ejection and the guidance accuracy of the spacecraft.

The design of an entry vehicle for Mars was presented in reference 1 where it was shown that a Martian entry vehicle will be characterized by 1) a low ballistic coefficient 30-50 lbs/ft², 2) a supersonic retardation system (parachute) to ensure that the vehicle decelerates to subsonic speeds high in the atmosphere so as to maximize the time for sampling the atmosphere and 3) modest heat shield requirements because of the relatively low entry velocity 25,000 ft/sec. and the nature of the Martian atmosphere.

In the case of Venus our knowledge of its atmosphere is much more uncertain than that of Mars. However, there does appear to be certain marked differences between the two planetary atmospheres which will require different design features for the entry vehicle. The more important differences are 1) higher Venusian entry velocity, 40,000 ft/sec vs. 25,000 ft/sec. 2) higher CO₂ content of the Venusian atmosphere 25 per cent vs. 7 per cent which increases

the heat transfer, 3) higher surface temperature and pressure on Venusian, 700°K and 54 atms. vs. 260°K and 0.1 atms., 4) a much more rapid decrease in density with increasing altitude on Venus than Mars which will cause a higher deceleration rate and heating for Venusian entry and 5) a factor of two to four (depending on launch date) reduction in communication distance for Venus from that required for Mars.

Therefore, since there appears to be a marked difference between the problems associated with entry into Venusian and Mars this study has as its purpose to:

1. Determine the feasibility of sending capsules on impact trajectories to Venus and have them transmit to the earth information about the thermodynamic variation of the planet atmosphere.
2. Investigate and establish the primary controlling parameters as they affect the performance and capability of a capsule design.
3. Relate the capsule requirements and capabilities to:
 - a. Future capsule mission to Venus
 - b. Capsule mission to Mars

1.0 ASSUMPTIONS

The assumptions used for this study are given in JPL Documents EPD-33 Revision I and EPD-33 Ditto entitled "Requirements for a Venus-Mars Capsule Study." The more important assumptions are listed in this section for completeness.

1.1 VENUSIAN ATMOSPHERE

The model atmospheres used as the basis of this study are given in Tables I-1 to I-4. The range of possible compositions given in Table I-1 was considered to be independent of the thermodynamic properties given in Table I-2 to I-4 for the purpose of determining the effect of atmospheric constituents on the heat transfer.

Since the atmospheric data in EPD-33 Ditto was given in terms of temperature and pressure, it was necessary to calculate the density. This quantity was calculated from the gas law

$$\rho = \frac{pm}{RT}$$

The units of density are given in earth lbs/cu. ft. The density of the Venusian atmosphere is given by

$$0.87 \times \rho \times \left(\frac{6161 + Z}{6161} \right)^2 = \text{lbs/cu ft}$$

where Z is the altitude in kilometers.

The ratio of specific heats was calculated as follows:

The weighted mean of the molecular weight of all dissociated monatomic molecules was taken as 14.3, and for diatomic molecules as 29.6. Then given the mean molecular weight for any given altitude, and allowing x to be the fraction of monatomic molecules, we have

$$14.3 x + 29.6 (1 - x) = \overline{\text{m.w.}}$$

from which x is obtained. The specific heat C_p/R of monatomic molecules is 2.5. For diatomic molecules $(C_p/R)_2$ was taken from reference 2 where for the temperatures considered the specific heats of CO, NO and N_2 are very similar.

$$\text{Then } \gamma = \bar{C}_p / \bar{C}_v = \frac{2.5 x + (C_p/R)_2 (1 - x)}{2.5 x + (C_p/R)_2 (1 - x) - 1}$$

The sonic velocity is given by

$$a = (g \gamma RT/m)^{1/2}$$

where m is the molecular weight in earth lbs/cu ft. and g is the acceleration of gravity at the surface of the earth.

The density as a function of altitude is given in Figure I-1, for the three model atmospheres considered. The models used in this study are based upon EPD-33 Ditto. Later models were given in EPD-33 Revision I but were received

too late to be factored into the study. These values are given as dotted lines in Figure I-1. A qualitative discussion of what effect the newer models will have on the results of the study is given in Section II of this report.

1.2 PLANETARY AND TRAJECTORY DATA

The assumptions as to the physical and orbital characteristics of the planets are given in Table I-5 while the characteristics of the transit trajectories of interest in this study are given in Table I-6.

1.3 SPACECRAFT RESTRICTIONS

For the purpose of capsule configuration studies the design of the Mariner B spacecraft was taken into consideration so that time would not be wasted on unrealistic capsule configurations. The maximum capsule envelope that was considered is given in Figure I-2.

2.0 METHOD OF APPROACH

Because of the breadth of the study and the time allotted an optimum system design was not attempted. Rather, the purpose was to investigate and establish the primary controlling parameters as they affect the performance and capability of a capsule design. In order to accomplish this, it was necessary to study in some detail the various critical areas. Some of the more important ones are:

1. Communications
2. Power Supply
3. Instrumentation
4. Thermal control
5. Effect of sterilization requirements
6. Effect of entry conditions on capsule design
7. Effect of atmospheric model on capsule design
8. Effect of capability to control entry conditions on capsule design

9. Effect of changes in spacecraft capability on capsule mission reliability and capability
10. Equipment survival and reliability to meet the environment

After each of these areas were studied in detail, the interplay of such variables as:

- Transfer trajectory
- Entry conditions
- Model atmosphere
- Capsule weight
- Capsule size
- Capsule shape
- Ballistic coefficient
- Type of communication system
- Type of instrumentation
- Type of power supply

on the overall capability of a Venusian entry capsule was considered.

Since this is perhaps one of the first broad studies of the problems involved in designing a Venusian entry system, certainly one of the more important outputs should be an outline of the research and development program necessary to deliver such a system. This Program Plan is given in Section IV.

REFERENCES

1. "Suitability of the Discoverer and Nerv Entry Vehicles for Mars Atmospheric Entry." GE-MSVD Report 30 April 1962.
2. Browne, W. G. "Thermodynamic Properties of Some Diatomic and Linear Polyatomic Molecules." Engineering Physics Technical Memo No. 3, GE-MSVD.

Table I-1. Composition of Venusian Atmosphere

<u>I ('best')</u>	<u>II</u>	<u>III</u>
90% N ₂	96% N ₂	74% N ₂
9% CO ₂	3% CO ₂	25% CO ₂
1% A	1% A	1% A
$\bar{m} = 29.6$	$\bar{m} = 28.6$	$\bar{m} = 32.1$
$\bar{\delta} = 1.39$	$\bar{\delta} = 1.40$	$\bar{\delta} = 1.38$
$\frac{\bar{\delta}}{\bar{\delta} - 1} = 3.56$	$\frac{\bar{\delta}}{\bar{\delta} - 1} = 3.50$	$\frac{\bar{\delta}}{\bar{\delta} - 1} = 3.63$
$\Gamma = -8.5^{\circ}\text{K/km}$	$\Gamma = -8.4^{\circ}\text{K/km}$	$\Gamma = -8.9^{\circ}\text{K/km}$

\bar{m} = mean molecular mass

$\bar{\delta}$ = mean ratio of specific heats*

Γ = dry adiabatic lapse rate*

*These quantities are given for STP. At the temperatures and pressures which appear to be present near the surface of Venus they are badly in error.

Table I-2. Venusian Atmosphere Best Model

Altitude KM	Pressure ATM	Density Earth lbs./ft. ³	Temp. °K	Molecular Wt.	Sp. Ht. Ratio	Speed of Sound ft./sec.
0	16.6	.6244	600	29.6	1.363	1565
18.8	5.5	.2816	440	29.6	1.39	1367
42.9	0.59	.0565	235	29.6	1.40	1003
110.0	2.76×10^{-6}	3.1111×10^{-7}	200	29.6	1.40	925
122.0	5.72×10^{-7}	0.5605×10^{-7}	230	29.6	1.40	993
133.0	1.68×10^{-7}	1.4555×10^{-8}	260	29.6	1.40	1054
144.0	5.92×10^{-8}	4.3555×10^{-9}	300	29.0	1.405	1149
178.0	4.94×10^{-9}	2.4277×10^{-10}	450	29.0	1.393	1400
235.0	4.94×10^{-10}	1.4555×10^{-11}	700	27.1	1.38	1797
292.0	8.88×10^{-11}	1.6277×10^{-12}	800	19.3	1.506	2379
349.0	3.95×10^{-11}	0.5816×10^{-12}	900	17.4	1.555	2700

Table I-3. Venusian Atmosphere Extreme Model I

Altitude KM	Pressure ATM	Density Earth lbs./ft. ³	Temp. °K	Molecular Wt.	Sp. Ht. Ratio	Speed of Sound ft/sec.
0	54	1.6277	750	29.6	1.347	1732
36.5	8	0.41	440	29.6	1.389	1367
60.5	.86	8.27×10^{-2}	235	29.6	1.4	1003
110.0	5.92×10^{-6}	5.1277×10^{-7}	260	29.6	1.4	1058
122.0	1.58×10^{-6}	1.1444×10^{-7}	310	29.6	1.4	1144
133.0	6.02×10^{-7}	3.6666×10^{-8}	370	29.6	1.396	1256
144.0	2.37×10^{-7}	1.1611×10^{-8}	450	29.0	1.392	1394
178.0	4.25×10^{-8}	1.25×10^{-9}	750	29.0	1.352	1777
235.0	8.29×10^{-9}	1.3722×10^{-10}	1250	27.1	1.340	2368
292.0	3.16×10^{-9}	3.1944×10^{-11}	1450	19.3	1.476	3162
349.0	1.58×10^{-9}	1.2611×10^{-11}	1650	17.4	1.532	3691

Table I-4. Venusian Atmosphere Extreme Model II

Altitude KM	Pressure ATM	Density Earth lbs./ft. ³	Temp. °K	Molecular Wt.	Sp. Ht. Ratio	Speed of Sound ft/sec.
0	6.3	.285	500	29.6	1.381	1447
7.1	4.0	.206	440	29.6	1.39	1367
31.2	0.42	.0404	235	29.6	1.40	1003
41.2	8.38×10^{-2}	1.264×10^{-2}	150	29.6	1.40	796
60.0	1.865×10^{-3}	2.72×10^{-4}	150	29.6	1.40	796
80.0	3.06×10^{-5}	4.61×10^{-6}	150	29.6	1.40	796
100.0	5.13×10^{-7}	7.72×10^{-8}	150	29.6	1.40	796
150.0	1.875×10^{-11}	2.82×10^{-11}	150	29.6	1.40	796
200.0	7.1×10^{-16}	1.07×10^{-16}	150	29.6	1.40	796
250.0	2.66×10^{-20}	4.01×10^{-21}	150	29.6	1.40	796
300.0	9.65×10^{-25}	1.457×10^{-25}	150	29.6	1.40	796

Table I-5. Planetary Dynamic Data — Venus and Mars

	<u>Venus</u>	<u>Mars</u>
Radius	$0.97 \pm 0.01 R_E$ $6200 \pm 100 \text{ Km}$	$0.52 R_E$ $3400 \pm 50 \text{ Km}$
Mass	$0.82 \pm 0.01 \text{ Mg}$ $4.90 \times 10^{24} \text{ Kg}$	0.107 Mg $6.40 \times 10^{23} \text{ Kg}$
Density	$5.0 \pm 0.3 \text{ gm/cc}$	$4.0 \pm 1 \text{ gm/cc}$
Oblateness	1%	1/192
Surface Gravity	$0.88 \pm 0.03 \text{ g}$ $860 \pm 30 \text{ cm/sec}^2$	$390 \pm 10 \text{ cm/sec}^2$ 0.39 g
<u>Orbit Details</u>		
Mean distance to Sun	$108.1 \times 10^6 \text{ Km}$	$227.8 \times 10^6 \text{ Km}$
Maximum distance to Sun	$109.4 \times 10^6 \text{ Km}$	$248 \times 10^6 \text{ Km}$
Minimum distance to Sun	$106.5 \times 10^6 \text{ Km}$	$206 \times 10^6 \text{ Km}$
Eccentricity of Orbit	0.007	0.093
Inclination of orbit to plane of ecliptic	$3^\circ 24'$	$1^\circ 51'$
Minimum distance to Earth	$42 \times 10^6 \text{ Km}$	$1^\circ 51'$
Maximum distance to Earth	$257 \times 10^6 \text{ Km}$	
Sidereal period	225 days	687 days
Synodic period	584 days	780 days
Mean orbit velocity	35.0 Km/sec	24.2 Km/sec
Semi-major axis	$108.21 \times 10^6 \text{ Km}$	$227.9 \times 10^6 \text{ Km}$
period of rotation	undetermined	24 hrs 37 min
escape velocity	10.4 Km/sec	5.0 Km/sec
inclination of Equator to orbital plane	undetermined	$25^\circ 12'$
Satellites	none detected	2

Table I-6. Preliminary Trajectory Characteristics for the Mariner Missions
to Venus and Mars During the Years 1964 - 1967

Mission	28-Day Launch Period	Flight Time Range (Days)	Earth-Probe Communication Distance at Planet Encounter (10^6 km)	Hyperbolic Excess Speed with Respect to Planet at Encounter (km/sec)	Angle Between Hyperbolic Excess Velocity Vector and Earth Planet Vector at Encounter (deg)	Arrival Dates
Venus 1964	3/15 - 4/11	123 - 96	55 - 60	7.0 - 5.5	30 - 60	7/15-7/20, 1964
Mars 1964	11/13 - 12/10	243 - 217	215 - 220	4.5 - 4.0	5 - 15	7/15-7/20, 1965
Venus 1965	10/29 - 11/25	117 - 90	55 - 60	6.0 - 4.5	15 - 55	2/22-2/28, 1966
Mars 1966	12/22 - 1/18	205 - 178	150 - 155	6.5 - 5.5	10 - 30	7/15-7/20, 1967
Venus 1967	6/1 - 6/28	131 - 104	60 - 70	4.5 - 3.5	15 - 55	10/5-10/10, 1967

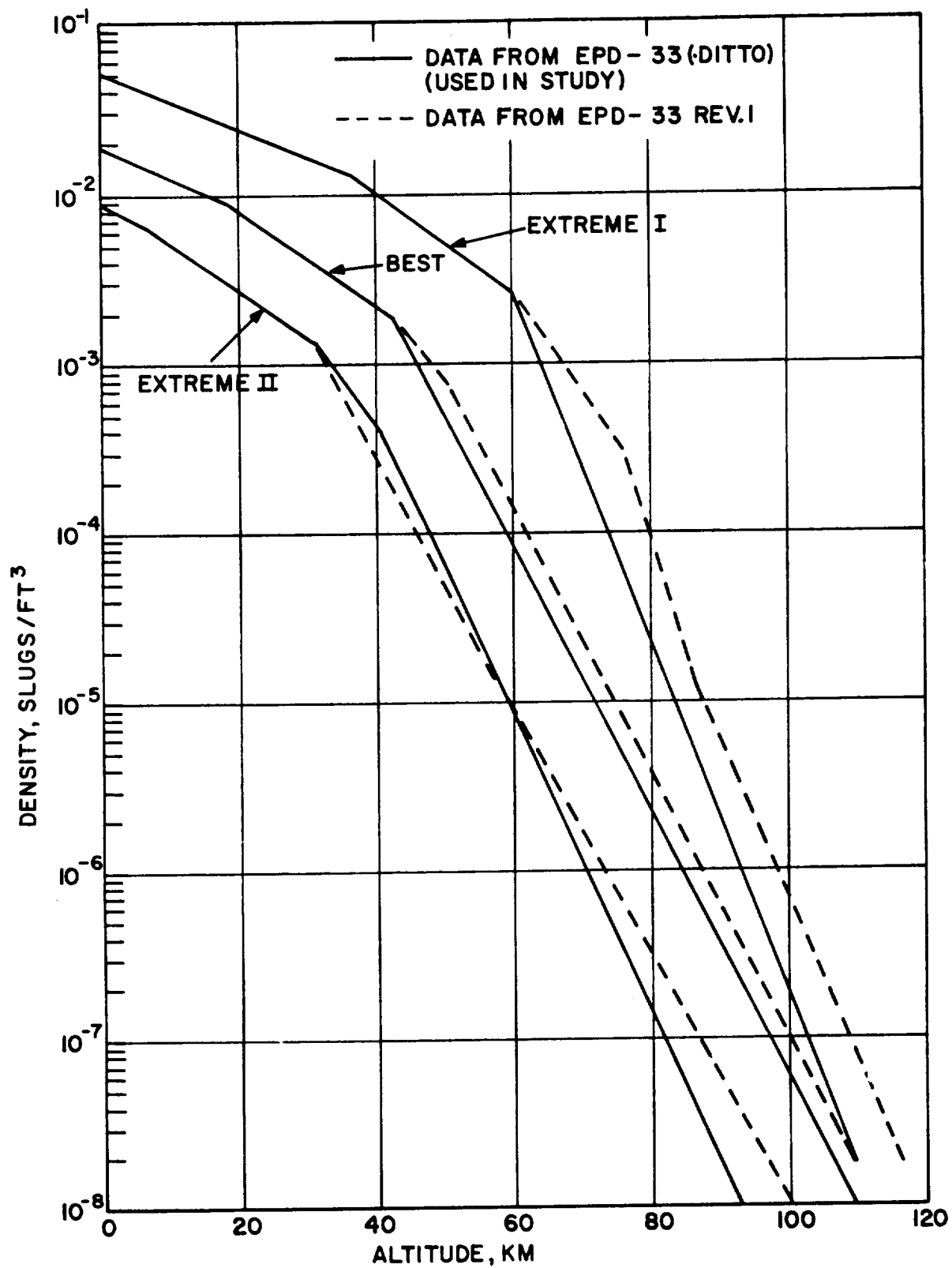


Figure I-1. Venusian Model Atmospheres

II SUMMARY

II. SUMMARY AND CONCLUSIONS

The results of this study indicate that it is feasible to design a capsule that will survive entry and collect and transmit to the Earth data as to the characteristics of the Venusian atmosphere. The feasibility of performing the Mars entry mission has already been proven*.

The differences in the design of an entry capsule for Mars and Venus can be indicated in a gross sense by comparing the differences in weight distribution between two typical capsules. Referring to Table II-1 it can be seen that the heat shield may be twice as heavy for the Venus capsule as the one for Mars. (There is more conservatism in the Venus heat shield than in the Mars design which may reduce this difference.) While the Venus entry capsule will experience much higher deceleration loads, the difference in structure weight is not significant since the Mars capsule requires an inner capsule for the parachute descent phase which is not required in the case of Venus. This points up perhaps the most significant difference between the two entry vehicles: namely the Mars capsule will require a parachute retardation system in order to obtain adequate subsonic descent times while the Venus capsule obtains roughly the same descent times without one. These differences in the two capsules tend to balance out on a weight bases yielding capsules with roughly the same payload capability for the same total weight. An interesting point is that if one considers the complexity of the retardation system required for the Mars capsule with the greater communication distances to Mars than to Venus (they differ by a factor of three to four) and balance this against the more difficult heat shield design for Venus, it is not immediately evident which entry capsule should be considered the more difficult to develop from an overall system viewpoint.

The two capsules in Table II-1 were designed around the Discoverer shape. While the results of the study indicate that this shape may not be too far off optimum, better payload capability could probably be obtained by considering (for the Venus capsule) sphere-cone shapes with increasing bluntness ratios and

* "Suitability of the Discoverer and Nerv Entry Vehicle for Mars Atmosphere Entry" GE-MSVD Report, JPL Contract No. 950226

TABLE II-1

Planetary Entry Vehicles

<u>Weight</u>	<u>Mars*</u>	<u>Venus</u>
Heat Shield, lbs.	27.5	57
Structure	60.4	62
Retardation System	31.4	--
Timer	----	2
Thermal Control	<u>15.7**</u>	<u>10</u>
	135.0	131
Total Weight	<u>197.5</u>	<u>197.5</u>
Payload lbs.	62.5	66.5
Vehicle Diameter, inches	33	29

*Reference 1

**Less Efficient System

cone angles which result in lower ballistic coefficients. This optimization of the capsule design is more important in the case of a Venus capsule than one for Mars because of the much heavier heat shield required for the former. In addition the uncertainty in the heat shield weights (approximately 35 per cent) for the Venus capsule, indicate that the payoff is large in terms of payload by reducing this uncertainty through experimental and theoretical research.

If one considers the following payload package:

Telemetry (including antenna)	29 lbs.
Instrumentation	6
Radar altimeter	14
Power Supply	6
Supporting Structure	<u>14</u>
	69 Lbs.

the results of the study indicate that with a capsule total weight of between 160 and 200 pounds (depending upon heat shield weight) it is possible to measure and transmit the following information during a Venus entry mission:

- Ambient temperature
- Ambient pressure
- Density
- CO₂ density
- Velocity
- Altitude of Clouds
- Peak deceleration
- Ablation
- Peak internal temperature

A brief description of the more attractive subsystem and the factors considered in the analysis is given in the following paragraphs.

A recommended program for the development of a Venus entry capsule is given in Section IV.

II-1 INSTRUMENTATION

The instrumentation systems pertinent to a capsule designed for meteorological investigations of the planet Venus have been examined. Primary attention was given to the principal variables of atmospheric pressure, density and temperature. Secondary parameters for which instrumentation was considered included carbon dioxide density, and the presence and type of clouds that might be encountered. Techniques for measuring altitude and velocity - or elapsed distance - were investigated from the viewpoint of relating measurements performed as a function of time into data as a function of altitude above the planets surface. All the meteorological parameter measurements were considered primarily during that portion of the trajectory when the capsule was traveling at subsonic velocities since no feasible techniques were found for investigating the undisturbed properties of the atmosphere from a vehicle traveling at hypersonic speeds without seriously compromising the survival of the capsule. It was shown from capsule parameter and trajectory analysis that in all cases it would be possible to carry-on subsonic measurements at altitudes corresponding to pressures of 0.7 atm. (40 km. for the "best" atmosphere model) and that for a low entry angle trajectory measurements could begin as high as 0.015 atmospheres (65 km. altitude for the "best" atmosphere model).

During the course of the study, a typical instrumentation system (Table II-2) was evolved which is based on a capsule design that permits measurements to begin at a pressure of about 0.01 atmospheres (corresponding to 200,000 feet for the "best" atmosphere and hence is designed to permit measurement of phenomena (low pressure, clouds) expected to occur at those altitudes. For designs which a priori exclude measurements until pressures of 0.1 atmosphere have been reached, the Mode I operation is superfluous.

The instrumentation system operates in three modes:

- Mode I: Initial until velocity is down to about 200 ft/sec.
- Mode II: Retransmission of stored hypersonic data.
- Mode III: Steady state mode.

In Mode I only data concerning temperature, pressure and velocity is transmitted but sampled every two seconds, with five-bit accuracy. In addition the cloud sensor (a small light source) is operated on one-bit accuracy.

The thermistor type temperature sensors are used. For pressure measurement (using the potentiometer transducer type) the 0-2 psi full scale sensors is used at four-bit accuracy switching to the 0-10 psi sensor as the upper end of the scale is reached. The fifth bit of information is used to indicate which sensor is activated.

The "propeller" velocity meter is used to determine velocity as a digital basis, and also to activate Mode II. The velocity is measured over a 0-800 ft./sec. scale accurated to ± 12 feet per second (five-bit resolution).

Mode II is activated when the velocity drops to 200 feet per second with a backup timer activation, in case of "speedometer" failure.

In Mode II the stored data from the hypersonic measurements (ablation rate, peak "g's") is transmitted sequentially, the transmission being repeated once. The total information amounts to 24 bits, requiring six seconds for duplicate transmission at eight bits per second.

Mode III begins immediately after the hypersonic information has been transmitted. Information from all active sensors is sampled at the rate of once every 1000 feet in altitude - to be compatible with an eight bit per second telemetry system.

Two ranges of carbon dioxide density (using infrared absorption measurements) and total density (using gamma backscattering) are sampled alternately, that is, each range is sampled every 12 seconds (about 2000 feet). The total number of revolutions is telemetered from the velocity meter, every telemetry cycle (six seconds), to determine relative altitude.

Additional information is given by the cloud sensor, cloud moisture indicator, and thermistors monitoring the temperature of sensitive components (photomultiplier tubes, solid state devices).

TABLE II-2
INSTRUMENTATION PACKAGE

A. Temperature Sensors

T1: Resistance thermometer 150°K to $800^{\circ}\text{K} \pm 10^{\circ}\text{K}$

T2: Resistance thermometer 300°K to $700^{\circ}\text{K} \pm 6^{\circ}\text{K}$ (2 units)

T3: Thermistor 200°K to $320^{\circ}\text{K} \pm 2^{\circ}\text{K}$ (2 units)

B. Pressure Sensors

P1: 0 - 2 psi (two units)

P2: 0 - 10 psi (two units)

P3: 0 - 100 psi (two units)

P4: 0 - 1000 psi (one unit)

C. Total Density Sensors

D1 Range: 10^{18} - 5×10^{19} particles/cm³

D2 Range: 3×10^{19} - 10^{21} particles/cm³

D. Carbon Dioxide Density Sensors

C1 Range: 10^{17} - 5×10^{18} particles/cm³

C2 Range: 3×10^{18} - 1×10^{20} particles/cm³

E. Velocity - Elapsed Distance Sensor

F. Cloud Detector

G. Peak g - Sensors

G1: 0-1000 g, located along velocity vector axis.

G2 and G3: 0-500 g, located along the other two orthogonal axes of the vehicle.

H. Ablation Sensors

I. Peak Temperature Sensors

The total weight and power requirements for this typical instrumentation system is six pounds and 20 watts, respectively.

In addition, the feasibility of performing line-of-sight measurements by observing the sun from the vehicle and studying carbon dioxide absorption and molecular scattering as a function of altitude was considered. This study was discontinued as impractical due to low probability of seeing the sun, possibility of cloud obscuration effects and excessive weight penalties.

Each technique was examined from the aspects of measurement accuracy, reliability, compatibility with vehicle environment (particularly g-forces and ambient temperature), and minimum power and weight requirements.

Consideration was given to the effects of individual sensor failure on interpretation of data from other sensors, and redundancy/reliability was maximized for those sensors whose measurements were deemed most essential.

A brief section was included considering the relative importance of measurements of different types of parameters from a meteorological viewpoint, as a basis for trade-offs if telemetry, power or weight limitations did not permit performing all measurements from a single capsule.

A cursory look was taken at the interaction telemetry capacity and quantity and accuracy of measurement data obtained. In view of the fact that it appears that bit rates as high as eight per second can be obtained without additional power requirements on the transmitter system beyond what is required for the carrier, and in view of the fact that this data transmittal rate appears to give adequate sensor information, it appears that additional telemetry capacity would simply be used for additional redundancy, possible parallel rather than sequential sampling of redundant sensors, and possible a higher sampling rate for all sensors.

Additional telemetry would also be required if weight considerations would permit using the radar altimeter. Using this more satisfactory technique of measuring altitude would result in an instrumentation system weight of 20 pounds and a power requirement of 40 watts.

II-2 COMMUNICATIONS

This section contains a summary of the problem areas and trade-offs occurring in the capsule telemetry system. Both a relay link to the Mariner spacecraft and a direct link to a DSIF ground station have been considered.

The data rate has been taken as a variable in the analyses. The typical instrumentation system presented in Section III-2.0 of this report requires a rate of eight bits per second.

Data rates in the vicinity of 25 bits per second or more appear feasible on the relay link with a 25-watt transmitter, using any one of several modulation techniques, (PCM/PS, PCM/PS/PM or PCM/FSK/PM).

For the direct link the carrier-tracking power alone (with an 85-foot paraboloid) requires about 33 watts of transmitter output power. Using a 50-watt transmitter, a PCM/PS system offers a communication capacity of about six bits per second, while a PCM/PS/PM system offers about two bits per second. A summary of a typical elementary system is given in Table II-3.

TABLE II-3
Typical Telemetry System

	<u>Direct Link</u>	<u>Relay Link</u>
Frequency	2295 MC	100 MC
Bits/sec	2 8 16	8 25
Antenna Size, Ft.	85 210 210	—————
Output Power, W	50 25 50	2.2 6.5
Type Modulation	PCM/PS/PM	PCM/PS/PM
Weight, Lbs.	30 28 30	35
Spacecraft Receiving Equipment	None	6 lbs. 15 watts

Numerical results such as the above in a broad analysis of this type are more valid on a comparative basis than on a definite basis. Time did not permit the optimization of all parameters nor the precise evaluation of gain and attenuation estimates. Before starting the system design, a rigorous analysis of the

selected system must be made. By that time the mission parameters should also be better defined.

The broad analyses showed further that a non-coherent relay link, using PPM/AM or PCM/FM does not appear feasible unless the frequency uncertainty region (due primarily to doppler effect and long-term oscillator instability) can be made very small.

Periodic checkouts of the transmission equipment during the transit time between capsule separation and entry appear possible by using a small solar-cell-battery power supply system. If adequate power is available in the spacecraft, it would be better to operate the spacecraft receiver continuously and to program only the capsule transmitter on for a period of perhaps one to two minutes every other day. This would avoid the long power-consuming transmitting periods which timing inaccuracies would require if the receiver were programmed, too.

The requirement for isotropic antenna pattern coverage for this checkout function will be determined by the maximum rate of capsule tumble and the acquisition time of the receiver. Tumbling rates as high as six RPM might be permissible without losing lock.

It might also be desirable to check out the capsule transmitter prior to separation from the spacecraft. It does not seem necessary nor desirable to do this more than once. Such a check might range from a simple monitoring of the DC voltage test points (requiring an umbilical connection) to actually taking a calibrated RF wattmeter reading near the capsule antenna. If the latter is done, extreme care must be taken in the design to prevent damaging the transmitter through impedance mismatch due to the proximity of the spacecraft to the capsule antenna.

If weight alone were the sole criteria, these results would indicate that 500 mc is the optimum carrier frequency (Figure II-1). However, weight alone is not an adequate criterion. Other factors which must be considered are thermal dissipation, reliability, design simplicity, availability of qualified components,

past experience, etc. These considerations generally point toward the 100-mc equipment. This is particularly attractive because of the possibility of a completely solid-state transmitter. Since such a transmitter would not require any warm-up time, it could be activated by a "g" switch upon entry and perhaps eliminate the need for an accurate timer.

Therefore, on the basis of these considerations, a 100-mc solid-state transmitter appears the most attractive.

Signal Acquisition and Tracking

The results of the tracking and acquisition analysis indicated that for the relay link a few watts of carrier power will give quite good performance for ranges in the order of 20,000 to 30,000 km., if the carrier frequency is in the lower portion of the 100-500 mc band. This lower frequency will also place less stringent requirements on the stability of the oscillators.

The results of the direct link analysis are more difficult to evaluate, since two major problem areas require further resolution: oscillator stability and pre-detection recording. There appears to be no oscillator presently available which has been qualified to survive such an entry and still maintain adequate stability to operate in a 3-cps receiver loop bandwidth. If such an oscillator is developed, there still remains the problem of real-time acquisition by the DSIF. This might be obviated by the use of pre-detection recording, allowing the use of optimum filtering techniques for post-flight signal processing. The problems involved here require further, more specific investigation.

Propagation Effects

The propagation effects investigated in this study include Venus ionospheric attenuation, multipath effect, and communication during entry.

Calculations using the JPL model atmospheres showed the maximum ionospheric attenuation to be 1.35 db in the Extreme II atmosphere. The attenuation was found to be less than one db with the other atmospheric models as well as at higher frequencies. Calculations showed that the multipath problem (from

the surface of Venus) for the relay link could be obviated by adequate suppression of forward gain of the capsule antenna radiation pattern.

Calculation of the entry plasma characteristics showed that radio frequency blackout will occur upon entry for the blunt capsule both at Venus and at Mars. The only possibility found for entry communication is to use a flared-cone configuration, and even then, an unseparated flow field condition would have to exist at least in the neighborhood of the antenna.

Error-Correction Coding

A brief study was made regarding the weight and effectiveness of a single-bit parity encoder and its corresponding decoder. It was found that for a seven-bit word, the use of such a Wagner code would reduce the required transmitter power by about 2.5 db for 10^{-3} and 10^{-4} bit-error rates.

The encoding equipment in the capsule would weigh about five pounds and draw about five watts of power. The corresponding decoding equipment on the spacecraft (for a relay link) would weigh about ten pounds and draw about ten watts of power. (Of course these decoder requirements would not be a significant factor in the direct link.)

Since the capsule's transmitting equipment and battery power supply are quite lightweight, it appears that, for the low data rates presently anticipated, the reduction offered in transmitter power does not justify the additional weight and complexity of the error-correction equipment. However, for higher data rates requiring higher transmitter powers, the reduction in transmitter complexity (through lowering the required power output) might make error-correction coding appear attractive, even though it would not reduce the payload weight significantly.

Relay Equipment for the Spacecraft

In comparing the relay link to the direct link, due account must be taken of the receiving equipment required in the Mariner spacecraft. In this study this has been considered as only a secondary factor and in the binary form, "too heavy" or "not too heavy."

four and one-half pounds. This assumes that the capsule will have attained an internal temperature of $+80^{\circ}\text{F}$ just prior to entry into the Venus atmosphere. The temperature must always be maintained above -65°F to prevent the electrolyte from freezing.

For the auxiliary power supply, a small nickel-cadmium battery with a recharging solar array is recommended. Silver-cadmium batteries are not recommended, since the slight weight saving attributed to sil-cads would be more than off-set by the higher reliability of the nickel-cadmium batteries. A nickel-cadmium battery-solar cell system capable of providing 200 watts of power for one and one-half minutes once every 24 to 48 hours would weigh only about five pounds. At the 100-watt level the system would weigh about three pounds.

II-3 CAPSULE PARAMETRIC ANALYSIS

The results of the capsule parametric analysis indicate that it is feasible to design a capsule capable of fulfilling the mission of Venusian atmosphere penetration and investigation and of transmitting sufficient data back to earth.

Aerodynamic studies investigated the effects of ballistic coefficients from 20-100, vehicle shape factors expressed as a bluntness ratio ($\frac{r_{\text{nose}}}{r_{\text{base}}}$), various defined atmospheres, and entry trajectories. These studies point out that maximum payload weight to total weight ratio is strongly influenced by $W/C_D A$ with lower ballistic coefficients being desirable. Entry path angle is an extremely strong parameter on maximum loads with steep trajectories giving larger "g" loads. Drag modulation investigations produced evidence that argued against employment of such devices since adequate subsonic time before impact is available for accomplishment of the mission and reduction of the extremely high "g" loads is of minor relative magnitude.

The majority of the study work was conducted on a Discoverer type vehicle since it was shown early in the study that a sphere-cone configuration with a modest nose radius was close to optimum. However, since the heat shield is a

It was readily found that the receiving equipment did not appear to be too heavy. A typical receiver (to produce a demodulated digital output) would weigh about five pounds, require about 15 watts, and be about 4 X 4 X 7 inches in size. It could be completely solid-state with low-noise Germanium transistor front ends, and would thus have a very high reliability.

A crossed-dipole receiving antenna mounted either on the planet horizontal platform (PHP) or on the favored side of the vehicle (i.e., the side predicted to be toward Venus, based on ephemeris data of the Sun and ⁿCaropus), and having about a hemisphere of coverage appears to be satisfactory. This would weigh only about one to two pounds, including its matcher and cabling.

Power Supply

The capsule power supply is required to provide all electrical power (at 28 VDC \pm 10 per cent) for the operation of the instrumentation and communication equipment. It must withstand the prelaunch sterilization procedure and must operate under the severe environment to be encountered after entering the Venusian atmosphere.

For this mission two separate power supplies are recommended, due to the differing requirements and environments to be encountered in the two phases of the mission. The primary power supply will provide all electrical power after atmosphere entry. The auxiliary power supply will be used for equipment check-outs and/or for providing filament-heating power prior to entry, if either of these is required.

Based on the results of the power supply studies presented in this section, the following paragraphs summarize the most promising method found for meeting the probable requirements of this mission.

For the primary power supply, sealed silver-zinc batteries are recommended. They can be designed with additional capacity to allow for losses during inactive transportation and still be relatively light-weight. For instance, a battery capable of delivering 235 watts for 30 minutes would weigh only about ?

II-4 THE INFLUENCE OF MODEL ATMOSPHERE CHARACTERISTICS ON ENTRY VEHICLE DESIGN

After having conducted a design analysis of entry vehicles for Venus, it is worth while to consider what portion or characteristics of the different model atmospheres influenced the design. This is of importance to those most interested in refining model atmospheres so as to indicate regions or characteristics that one should concentrate on in order to aid the vehicle designer.

From the results of the entry trajectory analysis, it is possible to indicate where in the atmosphere the following three significant events take place: the beginning of deceleration (~ 0.1 g), peak deceleration and the point at which the vehicle's velocity becomes subsonic. Since these events are a function of entry angle and ballistic coefficient in addition to model atmosphere, they will fall within a certain band for the variables considered in the present study. These bands or regions are indicated in Figure II-2. The lower region of each band is for a 15° entry angle while the upper limit is for a 90° entry angle.

These regimes indicate that the regions of most interest to the entry vehicle designer are altitudes of from 30 KM to 110 KM for densities of 10^{-8} to 10^{-3} slugs/ft³. It is interesting to note that the models for the upper atmospheres furnished in EPD 33 have no effect on the entry vehicle design.

The characteristics of a model atmosphere that determine the level of maximum deceleration is the rate of change in density with altitude. For a given decrease in altitude, the model atmosphere that has the greater increase in density will yield the highest peak deceleration. Therefore, from Figure II-2 Extreme I atmosphere should yield the highest maximum deceleration with Extreme II atmosphere somewhat lower and the "best" atmosphere the lowest. This is indeed in agreement with the results presented in Section III-1.0.

Because of time limitations, the model atmospheres presented in EPD 33 Rev 1 could not be considered in the present study. However, the effect of these changes can be discussed on a qualitative bases (Figure II-2). Using the reasoning given in the preceding paragraph, the following trends can be noted:

- 1) The new Extreme I atmosphere will yield slightly higher peak deceleration loads than what was obtained in this study.

good percentage of the total weight, the payoff realized through shape optimization appears to be significant. Therefore, future work should be aimed at such an optimization. The present study shows that the shape trend should be to higher bluntness ratios and higher cone angles (lower ballistic coefficients).

The results indicate that some increase in payload is possible if the entry angle is held to a value in the region of 30° for vehicles up to a diameter of 36 inches. Above this size the angle for maximum payload approaches 15° . At large entry angles both the structure and heat shield weight increase resulting in a lighter payload. However, the increase in payload realized by controlling entry angle is so small (except when the vehicle size and weight approach 40 inches and 400 pounds) in relation to the complexity involved that it appears to be more desirable to design the capsule for all entry angles from 15° to 90° .

Of all the various techniques investigated for temperature control of the capsule during transit, the system involving a radioisotope of the size of SNAP 3 appears to be the most promising on the basis of weight and complexity. In the period of the capsule descent to the surface through the Extreme I model atmosphere, two conditions were studied in ascertaining the insulation required:

- 1) ejecting the heat shield when the capsule reaches Mach one and
- 2) retaining the heat shield to impact.

The analysis indicates that the insulation weight required is less for the case when the heat shield is ejected. However, the difference in insulation for the two cases is of the order of a few pounds and almost equal to the required ejection system. Therefore, from the standpoint of reliability, it appears desirable to eliminate the ejection system and retain the heat shield to impact.

In addition to optimizing the capsule shape, it appears to be desirable to reduce the uncertainty in the heat shield analysis since this uncertainty represents a high percentage of the total payload.

- 2) The new Best atmosphere should yield the same peak deceleration loads.
- 3) The new Extreme II atmosphere will yield lower peak deceleration loads than what was calculated in the present study. In fact they will be below the peak loads estimated for the Best model atmosphere.

The effect of the changes in the model atmospheres on the heat shield requirements is difficult to determine on a qualitative basis. However, it is believed that the changes would be within the order of uncertainty in the present analysis.

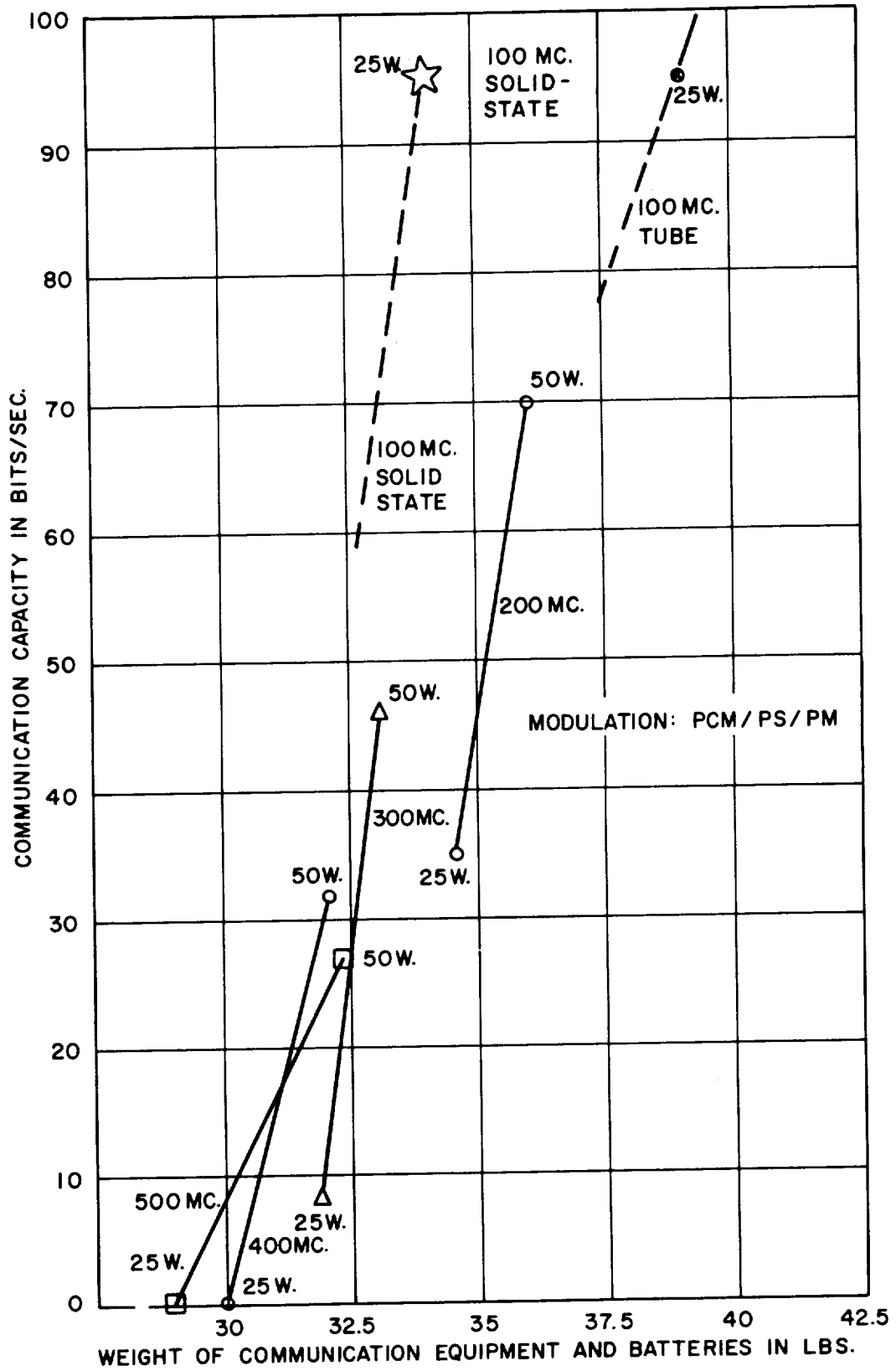


Figure II-1 Communication Capacity vs. Weight (Relay Link)

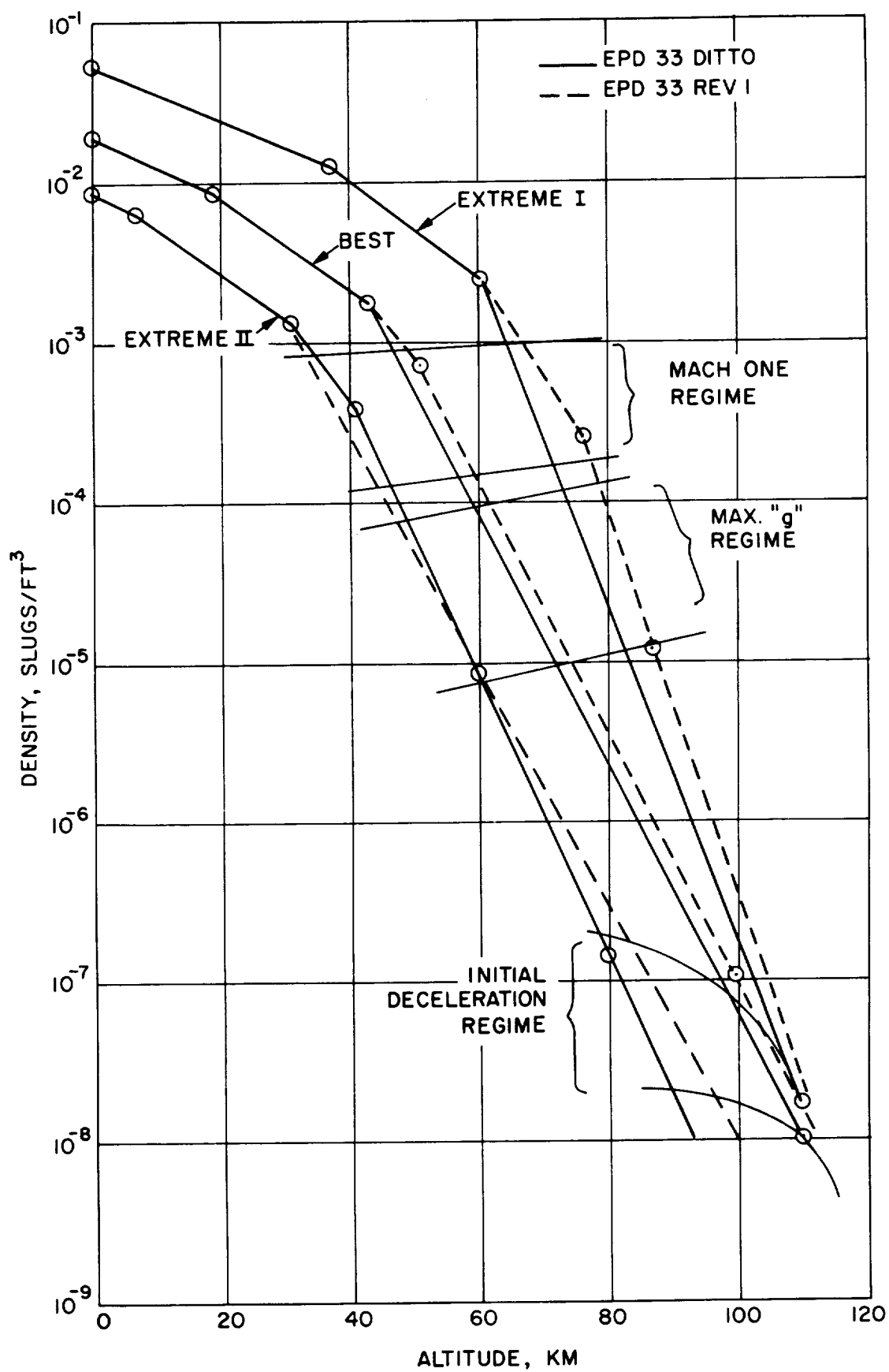


Figure II-2. Venusian Model Atmospheres

III ANALYSIS

1. TRAJECTORY ANALYSIS

1.1 POINT MASS ENTRY TRAJECTORIES

Entry trajectories have been computed on an IBM 7090 computer, using a three degrees-of-freedom, in translation, point mass program (1). This program contained the following assumptions:

1. a non-rotating spherical planet with a 1.9924541×10^7 feet radius
2. $27.886171 \text{ ft/sec}^2$ surface gravity
3. no winds
4. speed of sound and drag coefficient vary linearly between tabulated values
5. logarithmically variation in density between tabulated values.

The three Venus atmospheric models which were considered were those given in Section I. Drag coefficient values were obtained as functions of both Mach Number and altitude as shown in Figures 3-1.6 and 3-1.7 of Reference 2.

Entry altitude was defined as 350 km since the density at this altitude corresponds to Earth density at 400,000 feet, the accepted re-entry altitude. Variables which were considered, included entry angle (capture to 90° down from horz.), entry velocity (11 to 14 km/sec.) and $W/C_D A$ (20 to 300 earth lb/ft^2). A trajectory run log is presented in Table 1.1 and shows that most trajectories utilized Extreme I atmosphere since it produced the highest axial loads. This is demonstrated in Figure 1.1 which shows maximum deceleration and altitude at maximum deceleration, as functions of entry angle for the three model atmospheres.

Peak deceleration versus entry angle is presented in Figures 1.2 and 1.3 for the Extreme I and "Best" atmospheres respectively for entry velocities of 11, 12, 13, and 14 km/sec. This information is cross-plotted in Figure 1.4 and 1.5 to obtain the angular entry corridor between the peak deceleration limits of 100, 200, 300, and 400 earth g's and a skip limit which is defined as the minimum entry angle for capture during the initial entry.

Figure 1.6 presents range and time from entry to impact versus entry angle. The influence of $W/C_D A$ on time from Mach 1 to impact and altitude for peak deceleration and Mach 1 is in Figure 1.7a. $W/C_D A$ has negligible effect on peak deceleration magnitude. Figure 1.7b indicates the observation time available in subsonic flow conditions. Note that the extreme II atmosphere gives the shortest time of eight minutes. The observation time is not strongly dependant on the entry angle. Entry time histories showing altitude, dynamic pressure, velocity, and axial g's have been selected for representative trajectories (corresponding to log numbers 2, 6, 7, 10, 11, 12, 13, 17, 19, and 21) and are presented in Figures 1.8 to 1.27 respectively.

1.2 THREE DEGREE OF FREEDOM TRAJECTORIES

The trajectory program utilized for the three degree of freedom analysis (two degrees in translation and pitch rotation) is described in detail in Reference 3. The same planetary constants used in the point mass trajectories were employed. All computations are done in a trajectory fixed system (i.e., components of position and velocity are given along the flight path and normal to it in the trajectory plane).

Initial conditions for these trajectories were taken from the point mass trajectories at a dynamic pressure of one pound per ft². This permitted the angle of attack to be specified just before peak dynamic pressure and resulted in obtaining approximate worst case loading. Initial angle of attack was selected as large as possible without resulting in a backwardly stable trajectory. Gas-dynamic coefficients were assumed to vary with both altitude and Mach No.

Capsule physical characteristics assumed for the two configurations considered are shown in Table 1.2. The majority of trajectories were run for configuration "B," which corresponds to a Discover-type vehicle. The remaining trajectories used an Apollo-type vehicle denoted by configuration "A." A trajectory run log is presented in Table 1.3 and shows that all trajectories used the Extreme I (maximum loads) atmospheric model and a 12 km/sec entry velocity.

Data obtained from these trajectories include: 1) pitch frequency in cycles per second, 2) angle of attack envelopes, 3) normal and axial loads, and 4) normal and axial loads per foot. Loadings per foot are due to the angular acceleration and are therefore related to distance from the c.g.

Figures 1.28 and 1.29 present data on configuration "B" entering vertically. Comparison of peak axial load from this trajectory with that of the corresponding point mass trajectory shows a 15 per cent reduction in the former case. Note that the maximum normal load is approximately 80 per cent of the axial load. The pitch frequency which reaches 13.3 cycles per sec is high compared to a nominal Mars entry (9 cycles/sec) and compares with a re-entering nosecone (9 to 15 cycles/sec maximum). Although the capsule tumbles initially, the angle of attack envelope shows a convergence to a ± 12 degree limit cycle oscillation.

The effect of moving the c.g. is shown in Figures 1.30 through 1.33. These figures show that moving the c.g. forward increases the frequency and loading but has little influence on angle of attack envelope.

Figures 1.34 and 1.35 show that reducing the entry flight path angle reduces the loading and frequency as expected (axial values 15 per cent less than point mass value). The angle of attack still converges to about ± 11 degrees. Peak normal load exceeds the peak axial load by 10 per cent.

The effect of initial pitch rate on peak conditions is presented in Figure 1.36. Values are almost symmetrical about zero pitch rate. As initial pitch rate increases, frequency and axial loading increase while the normal loading and loading per foot decrease, however the maximum normal loads are of most interest for design purposes.

Entry data for capsule configuration "A" is shown in Figures 1.37 and 1.40. The initial angle of attack was reduced from 179 degrees (for configuration "B") to 90 degrees in an attempt to prevent backward stability. This was successful for the shallow entry trajectory (Figure 1.37) but not for the vertical entry trajectory (Figure 1.39), which shows a backward diverging angle of attack envelope. For the shallow entry, the angle of attack, although converging, oscillated ± 42 degrees after passing through peak loading conditions. For this case, the axial load was almost twice the normal load and the pitch frequency reached eight cycles per second versus 4.4 cycles per second for the "B" configuration.

1.3 GENERAL ENTRY AND APPROACH DATA

The relationship between hyperbolic excess velocity (V_{∞}) and local velocity is presented in Figure 1.41 and should prove helpful in interpreting the results in the following sections. Flight path angle is presented in Figure 1.42 versus hyperbolic excess velocity and distance from Venus. The angle subtended by Venus and time before perifocus is shown in Figures 1.43 and 1.44 as a function of distance from Venus.

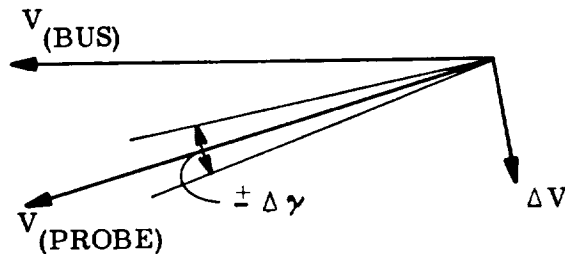
Entry angular corridors have previously been determined from point mass trajectories. The entry conditions of velocity and flight path angle have been taken from these data and used to determine corresponding vacuum perifocus values. Vacuum perifocus was calculated for the Extreme I and Best atmospheres and the results presented in Figure 1.45. Using the Extreme II atmosphere produces results which are bounded by the other two atmospheres.

Data from Figure 1.45 was cross-plotted in Figures 1.46 and 1.47 for a hyperbolic excess velocity of 5.0 km/sec. which is typical for a 1965 Venus mission. Figure 1.46 presents the linear corridor for entry between the skip limit and the noted peak axial deceleration. Figure 1.47 presents similar information, but here the minimum entry angle is defined by the 100 g's trajectory rather than the skip limit, since a high integrated heating value may necessitate a steeper entry than the skip limit. Figures 1.45 and 1.46 show that with the Extreme I atmosphere, an accuracy of ± 300 km will result in peak loads of 200 g's and 226 g's when using the skip limit and the 100 g limit, respectively, to define minimum entry angle.

Approach guidance accuracy ($\pm \Delta \gamma$), as used herein and seen in Sketch 1.0.0, defines the maximum allowable flight path angle tolerance of the capsule as it is ejected from the bus. Accuracy requirements have been calculated as a function of entry corridor, entry velocity, Venus atmosphere, and distance from Venus for a typical capsule configuration. Figures 1.48 and 1.49 present data for the Extreme I and Best Venus atmospheres respectively. Extreme II atmosphere accuracy requirements are between these two.

It is possible that minimum path angle must be increased beyond the present skip limit because of heating considerations. If, for example, the minimum entry path angle should be 100 earth g's, then the accuracy requirements can be obtained from the figures by subtracting the $\pm \Delta \gamma$ value for 100 g's from the $\pm \Delta \gamma$ value for peak deceleration, but current information indicates that the above effect is less important than the atmosphere model selected, which can change the accuracy requirements by a factor of 2.

An example of the manner in which the figures can be used is described below. Assume that the peak deceleration is limited to 300 earth g's and the entry velocity is 12 km/sec. Then, for a guidance accuracy of ± 0.25 degrees, the approach guidance must be made closer to Venus than 19 radii assuming Extreme I atmosphere or 36 radii assuming the "Best" model atmosphere.



SKETCH 1.0.0. EJECTION CONDITIONS

1.4 RETRO-ROCKET CONSIDERATIONS

The present Venus probe concept requires that the main vehicle (bus) approach the surface of Venus as close as 12,000 km. At some yet to be determined time before bus perifocus, the entry capsule will separate from the bus. A retro rocket will fire, causing the resultant velocity vector of the capsule to rotate such that acceptable planetary entry will occur, while the bus continues on its original trajectory. Figures 1.50, 1.51, and 1.52 show retro-rocket velocity increments required for the capsule to enter the center of the 300 g corridor for various bus perifoci, as a function of steering distance from Venus (r_s) and hyperbolic excess velocity. The retro-rocket was assumed to fire impulsively and perpendicular to the resultant probe velocity to obtain maximum turn angle.

The purpose of the following area of study was to determine the sensitivity of the capsule to retro-rocket velocity error. Sensitivity as used herein denotes the change in capsule virtual (vacuum) perifocus (r_p) per unit error in retro-rocket velocity ($\partial r_p / \partial \Delta V$).

Linear corridors have previously been determined (Section 1.3) for various peak axial decelerations. Both 300 and 400 Earth g's corridors have been considered since the final corridor, which depends on heating limits, instrumentation loading and weight trade-offs, has not yet been determined. The 300 g corridor is reproduced in Figure 1.53 and shows the corridor centerline which corresponds to the nominal entry case.

The effect of the magnitude of retro-rocket velocity error on virtual perifocus was investigated and it was shown that for the area of interest, a linear variation is an adequate representation. This is demonstrated in Figure 1.54 which shows nearly constant slope for typical conditions.

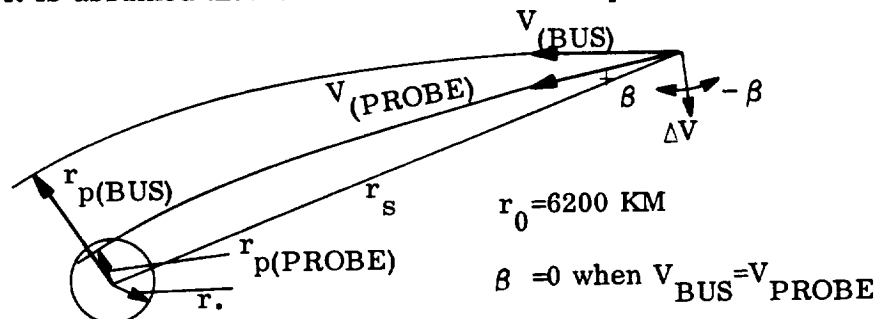
Sensitivity is presented in Figure 1.55 as a function of distance from Venus where bus and capsule separate (r_s/r_o) and hyperbolic excess velocity. The data presented in the above figures were obtained by solving the exact equations. Appendix A presents the perturbation method of solving for sensitivity and shows excellent agreement with the exact value.

Retro-rocket accuracy required for entry within the 300 and 400 g's corridors is shown in Figure 1.56 as a function of bus perifocus ($r_{p(bus)}$) and hyperbolic excess velocity. Calculations show that accuracy requirements are essentially independent of distance from Venus at separation. Figure shows that the greater the bus perifocus, the more stringent the retro-rocket velocity accuracy requirements. For example, for a hyperbolic excess velocity of 6 km/sec and assuming a 300 g corridor, the retro-rocket velocity error can be 14 per cent for a bus perifocus of 10,000 km but only two per cent for a bus perifocus of 37,800 km.

Results of the previous paragraph show the effect of retro-rocket magnitude error on probe virtual perigee. The purpose of this section is to show the effect of retro-rocket alignment error ($\Delta \gamma$) on probe virtual perifocus. The nomenclature used in this study is defined in Sketch 1.0.1.

The results shown in the following figures were obtained by solving the exact equations. Figure 1.57 shows that increasing the steering distance reduces the effect of alignment error on virtual perigee. Figures 1.58, 1.59, and 1.60 show that although the influence of alignment error is reduced as hyperbolic excess velocity is increased, this is more than compensated for by the change in linear corridor. In all cases, virtual perifocus is more affected by a positive error in β than a negative error. This is easily understood since any alignment error causes the flight path angle to become more horizontal, which results in an increased virtual perifocus; but a negative β also reduces the velocity of the probe and somewhat compensates for the flight path change.

For the case of determining the combined effect of both magnitude and alignment error it is assumed that the RMS method should provide a close approximation.



SKETCH 1.0.1

1.5 APPROACH GEOMETRY DATA

It is the purpose of this section of the study to determine if the maximum probe to bus communication time after probe entry is sufficient to permit the bus to be used as an information relay link.

The bus is assumed to approach the surface of Venus as close as two Venus radii. If terminal guidance is required, then, at some yet to be determined time before bus perifocus, a retrorocket will be fired causing the velocity vector of the probe to be rotated such that planetary entry will occur, while the bus continues on its original trajectory. Since the probe has a smaller virtual perifocus than the bus, its average velocity will be greater and will result in the probe arriving at Venus first.

Communication time was assumed to start when the probe was 1 radius from the center of Venus and to end when "line of sight" limits from the surface of Venus were reached. In Section 3.0, it was determined that ionosphere reflection will not limit communication for probable transmission frequencies. In the calculations, two items were considered compensatory and were neglected. They were (1) atmospheric refraction and (2) atmospheric effect on entry range.

Data is presented showing the maximum probe to bus communication time during entry as a function of bus perifocus ratio $(r_p/r_o)_B$, probe perifocus ratio $(r_p/r_o)_p$, hyperbolic excess velocity, and distance from Venus at capsule ejection (r_s/r_o) . Partial results of this study are presented in Figure 1.61, which shows communication time versus hyperbolic excess velocity for a bus perifocus ratio of 2.0 radii and for steering ratios and probe perifocus ratios between 10-100 Venus radii and 0.1-0.8 Venus radii respectively. Figure 1.62 shows similar data for a bus perifocus ratio of 3.0 radii.

For each set of bus and probe conditions where only r_s/r_o is varied, there is a minimum communication time which corresponds to increasing r_s/r_o values for increasing bus perifocus ratios. This can be explained best by examining the effect of r_s/r_o on the beginning and end limits of communication time. As r_s/r_o is decreased, the probe will lead the bus less at the start of communications.

But also as r_g/r_o is decreased, the impact point moves such that the terminal line of sight limit increases communication time until infinite communication time is achieved. These opposing trends combine to produce a minimum value.

It can be seen from Figures 1.61 and 1.62 that very little communication time is gained by increasing the steering ratio beyond 50 radii. But, communication time is extended considerably by increasing the probe perifocus ratio (i.e., entry angle becomes less steep). It is therefore evident that communication time is limited by the steep entry trajectory even though actual entry time (obtained from point mass trajectories) is greater for the shallow entry. Entry trajectories have indicated that probe perifocus ratio must be greater than 0.8 for the peak deceleration to be less than 400 g's. Figure 1.16 shows that entry time for a 30° entry path angle attains a limit of approximately 30 minutes for low $W/C_D A$. It is, therefore, obvious that adequate communication time is available for bus perifocus ratios equal to or greater than 3.0 Venus radii. For smaller bus perifocus ratio or smaller probe perifocus ratio, communication time is obtained by cross-plotting the data of Figures 1.61 and 1.62.

REFERENCES

1. Blecher, R. L., "Equations of Motion for the Unpowered Trajectory of a Ballistic Missile," GE TIS R58-SD201, January 8, 1958.
2. "Suitability of the Discoverer and Nery Entry Vehicles for Mars Atmospheric Entry," Vol. I, GE-MSVD, April 30, 1962.
3. Denninson, A. J., "A Method in Three Degrees of Freedom for Determining the Trajectory, Loads and Stability for an Arbitrary Aerodynamic Configuration," GE TIS R59-SD354, May 5, 1959.

TABLE 1.1
POINT MASS TRAJECTORIES

Trajectory No.	Atmosphere*	Entry Velocity V_E (Kilometers/Sec)	$W/C_D A$ (PSF)	Entry Angle (Degrees Down from Local Horizontal) γ_E
1	II	12	60.8	90
2	II	12	60.8	30
3	II	12	60.8	15
4	II	12	60.8	12
5	I	12	60.8	12
6	B	12	60.8	90
7	B	12	60.8	30
8	B	12	60.8	15
9	B	12	60.8	12
10	I	12	60.8	90
11	I	12	60.8	30
12	I	12	60.8	15
13	I	12	20	30
14	I	12	40	30
15	I	12	100	30
16	I	12	200	30
17	I	12	300	30
18	I	11	60.8	30
19	I	13	60.8	30
20	I	12	60.8	14.5
21	I	12	60.8	13.25
22	I	11	60.8	90
23	I	13	60.8	90
24	B	11	60.8	90
25	B	14	60.8	90
26	B	13	60.8	90
27	I	12	100	15
28	I	12	100	90
29	I	12	20	15
30	I	12	20	90

* I = Extreme Model I
 II = Extreme Model II
 B = Best Model

TABLE 1.2
CONFIGURATION CHARACTERISTICS

Config.	W/C_D^A	Static Margin	I_{Pitch} (slug-ft ²)	I_{Yaw} (slug-ft ²)	I_{xy}^2 (slug-ft ²)
A	20	.1d	1.6	1.6	0
B	60	.1d	5.2	5.2	0

TABLE 1.3
THREE DEGREE OF FREEDOM TRAJECTORIES

Trajectory No.	Configuration	Entry Path Angle	Initial Pitch Rate	c.g. Position
		deg. (DFH)	(deg/sec)	(ft from nose)
101	B	90	0	1.11
102	B	90	0	1.06
103	B	90	0	1.17
104	B	15	0	1.11
105	B	15	10	1.11
106	B	15	20	1.11
107	B	15	-20	1.11
108	B	15	0	1.09
109	A	90	0	.69
110	A	15	0	.69

NOTES:

All trajectories used Extreme I atmosphere. Entry velocity was always 12 Km/sec. Initial angle of attack of 179 deg for Configuration A and -90 deg for Configuration B.

APPENDIX A

Retro-rocket sensitivity by Perturbation Method. From basic hyperbola equations:

$$r_p = \frac{r^2 \cos^2 \gamma v^2}{K (1 + e)}$$

and

$$v^2 = \frac{2K}{r} + v_\infty^2$$

Therefore

$$r_p = \frac{r \cos^2 \gamma (2K + v_\infty^2 r)}{2K + r_p v_\infty^2}$$

Differentiating with respect to flight path angle γ_1 and assuming ∂v is small such that

Give: $\partial \gamma = \frac{\partial \Delta V}{V}$

$$\frac{\partial r_p}{\partial \Delta V} = \frac{(2K + v_\infty^2 r) r \sin 2 \theta}{(2K + 2 v_\infty^2 r_p) v}$$

Example:

$$\begin{aligned} K &= 3.3 \times 10^5 \text{ Km}^3/\text{sec}^2 \\ v_\infty &= 6 \text{ Km/sec} \\ r &= 186,000 \text{ Km } (r/r_o = 30) \\ r_p &= 5720 \text{ Km } (\approx 300 \text{ g corridor}) \\ \gamma &= 86.5^\circ \text{ (DFH)} \end{aligned}$$

Solving the above equation gives

$$\frac{\partial r_p}{\partial \Delta V} = -24400 \text{ km/(km/sec)}$$

And this compares with -24100 obtained from the exact equations and presented in Figure 1.55.

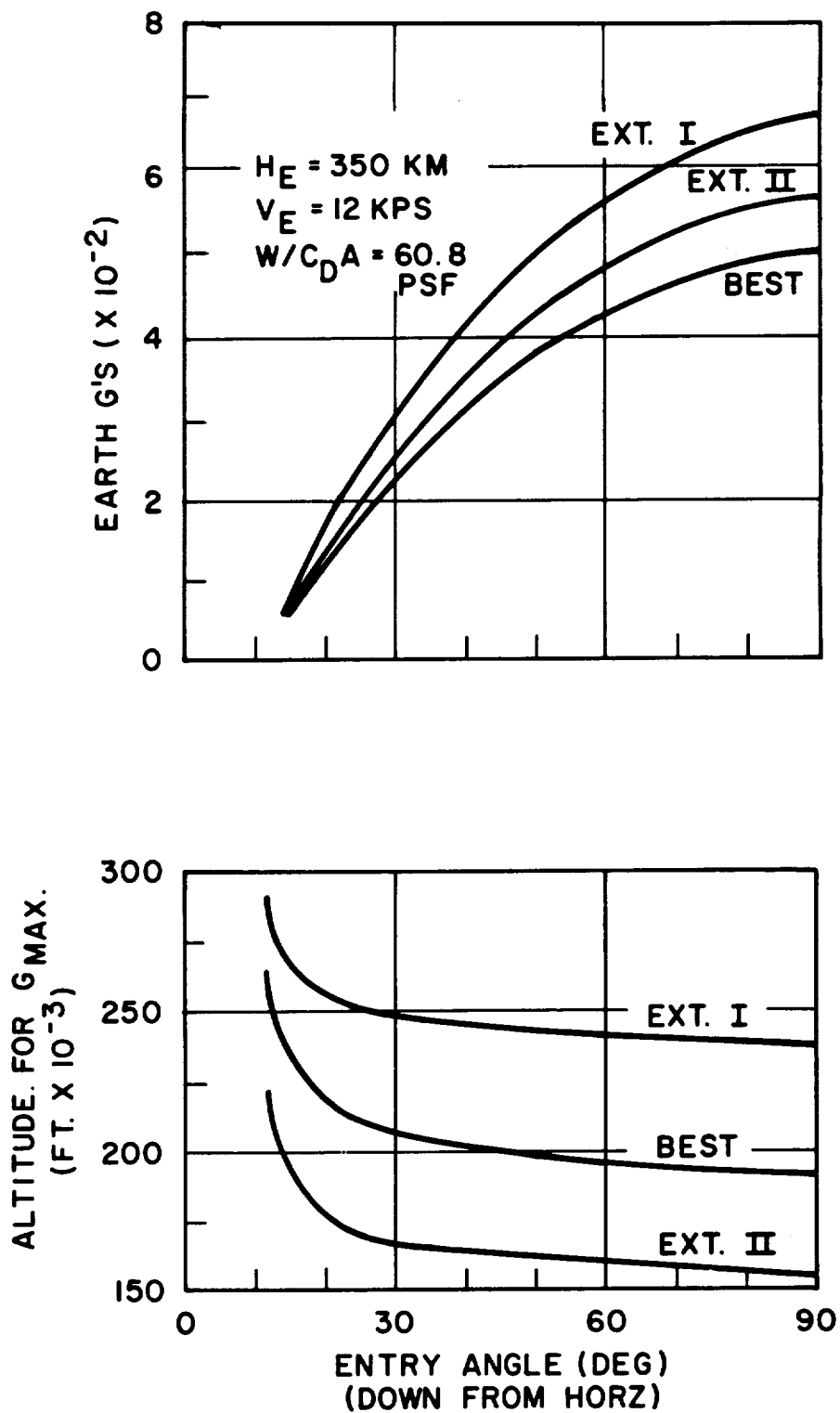


Figure 1.1. Peak Axial Loads and Corresponding Altitude for $V_E = 12 \text{ km/sec}$

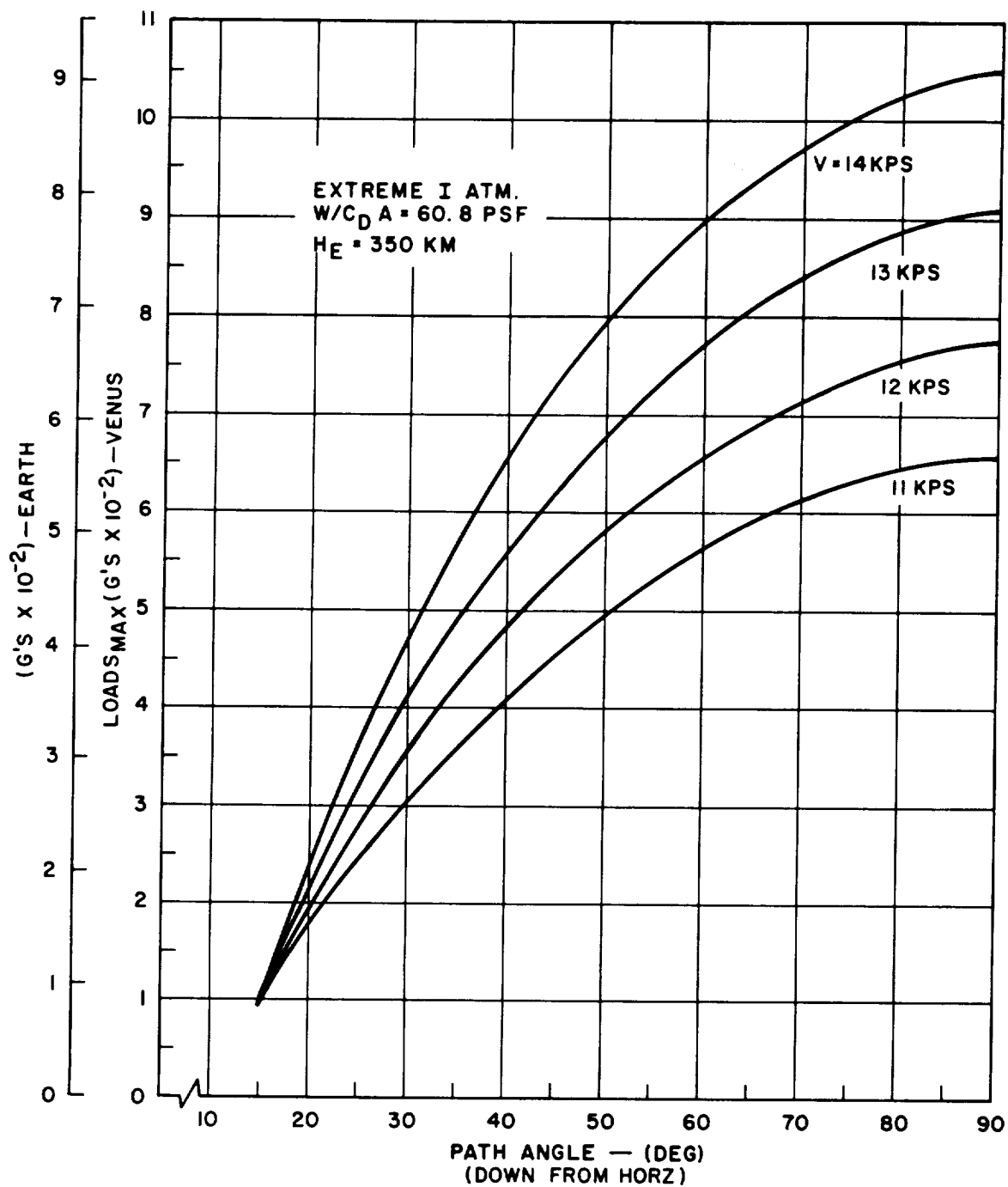


Figure 1.2. Peak Axial Loads for Extreme I Atmosphere, $W/C_D A = 60.8 \text{ lb/ft}^2$

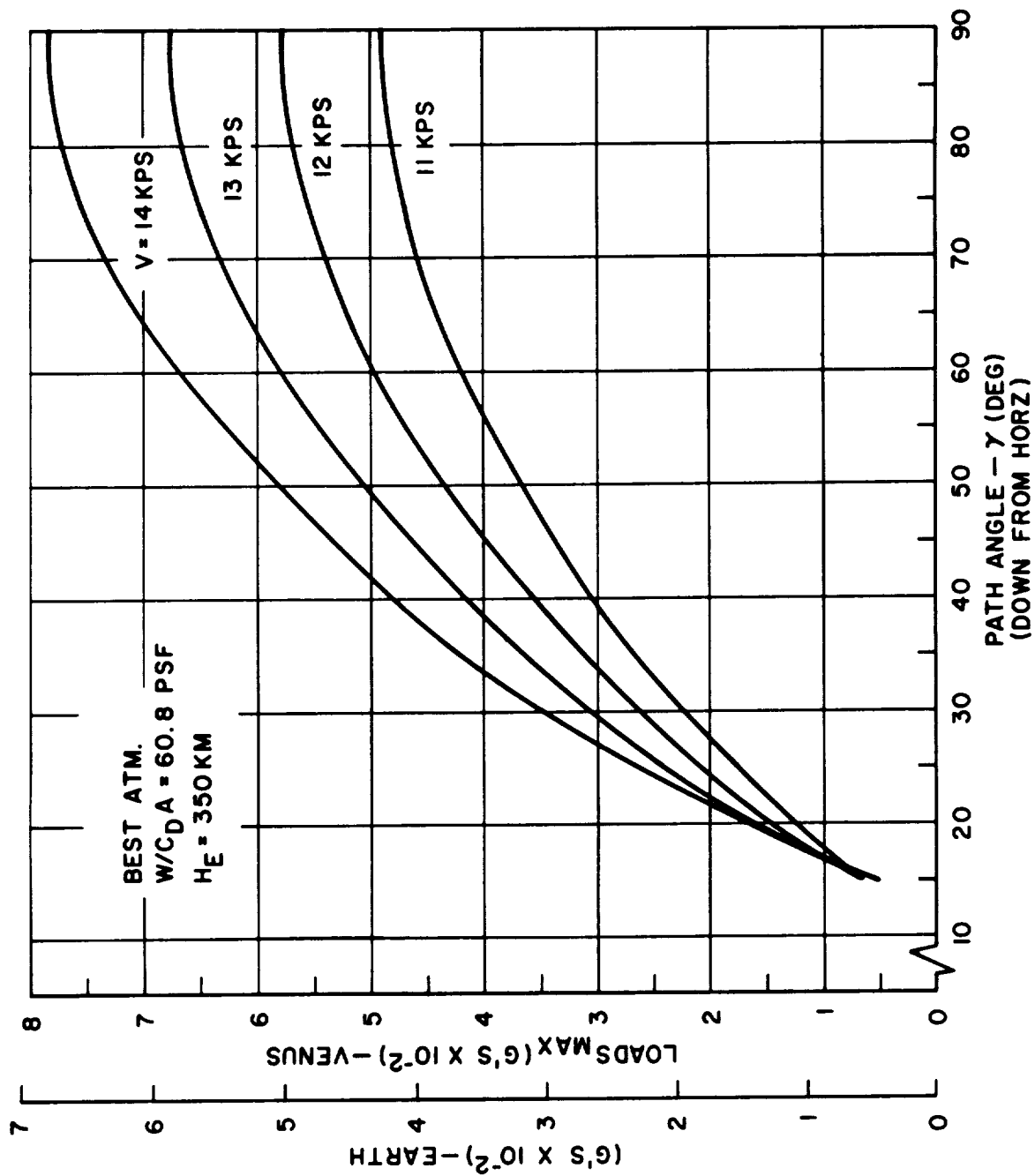


Figure 1.3. Peak Axial Loads for Best Atmosphere, $W/C_D A = 60.8 \text{ lb/ft}^2$

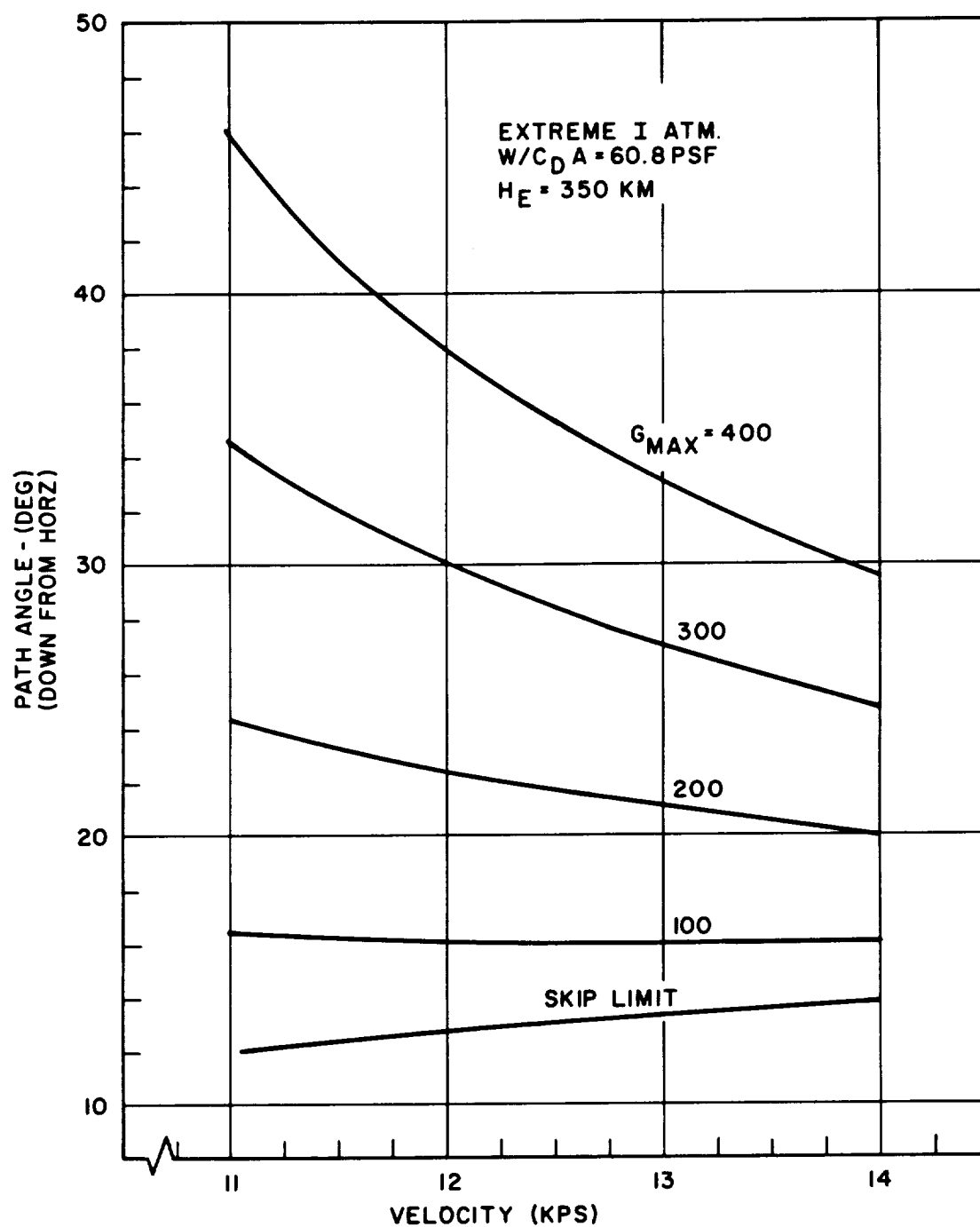


Figure 1.4. Venus Corridor, Extreme I Atmosphere

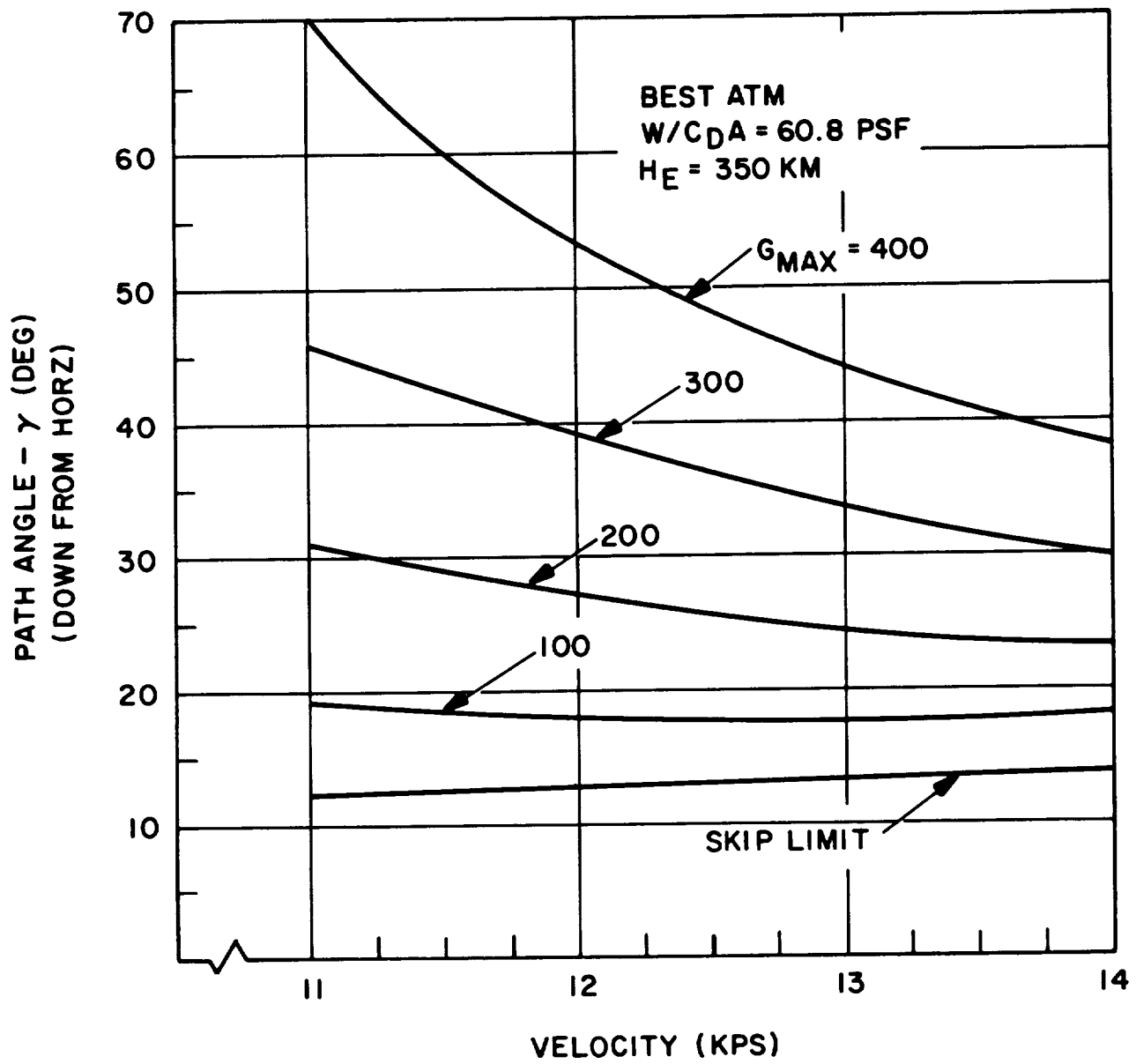


Figure 1.5. Venus Corridor, Best Atmosphere

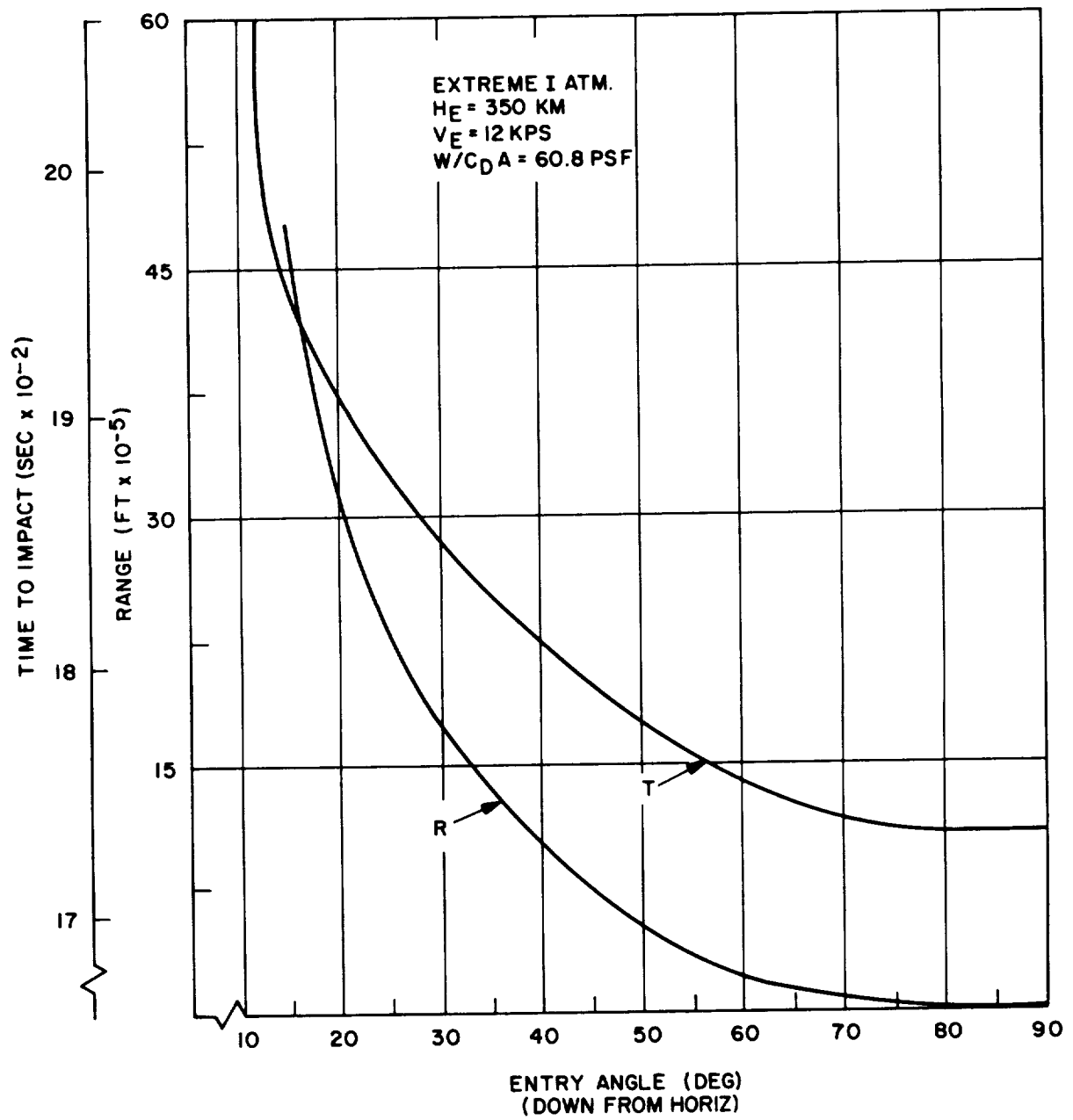


Figure 1.6. Time From Entry to Impact

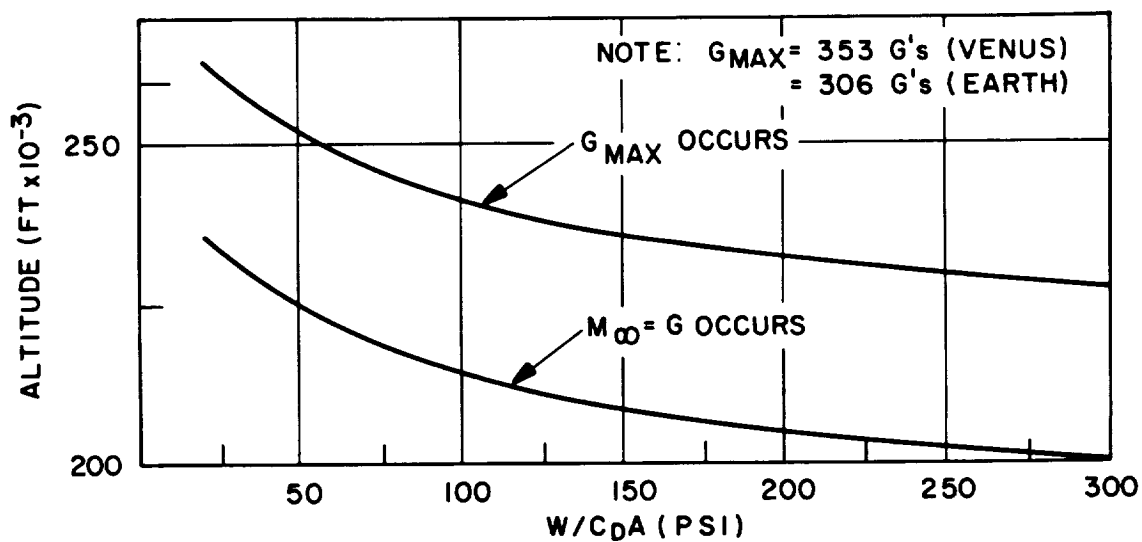
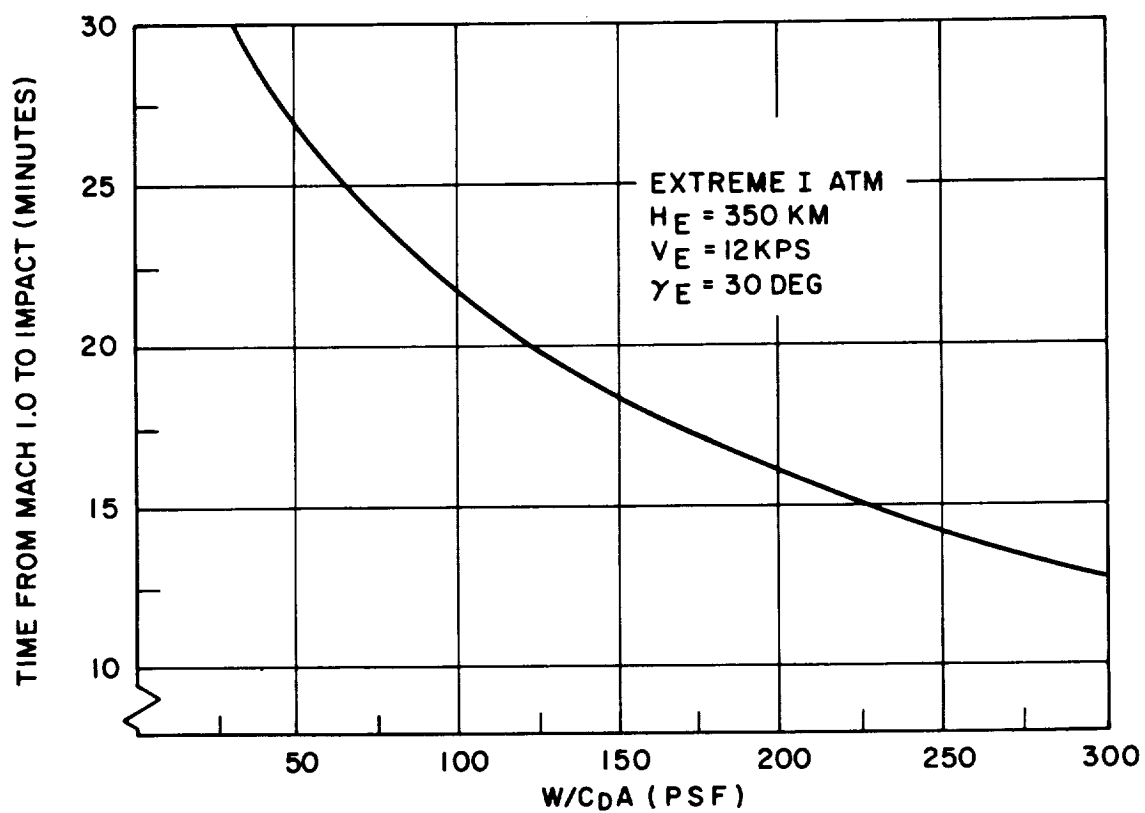


Figure 1.7a. Time from Mach Number 1.0 to Impact and Corresponding Altitude, $\gamma_E = 30 \text{ deg}$

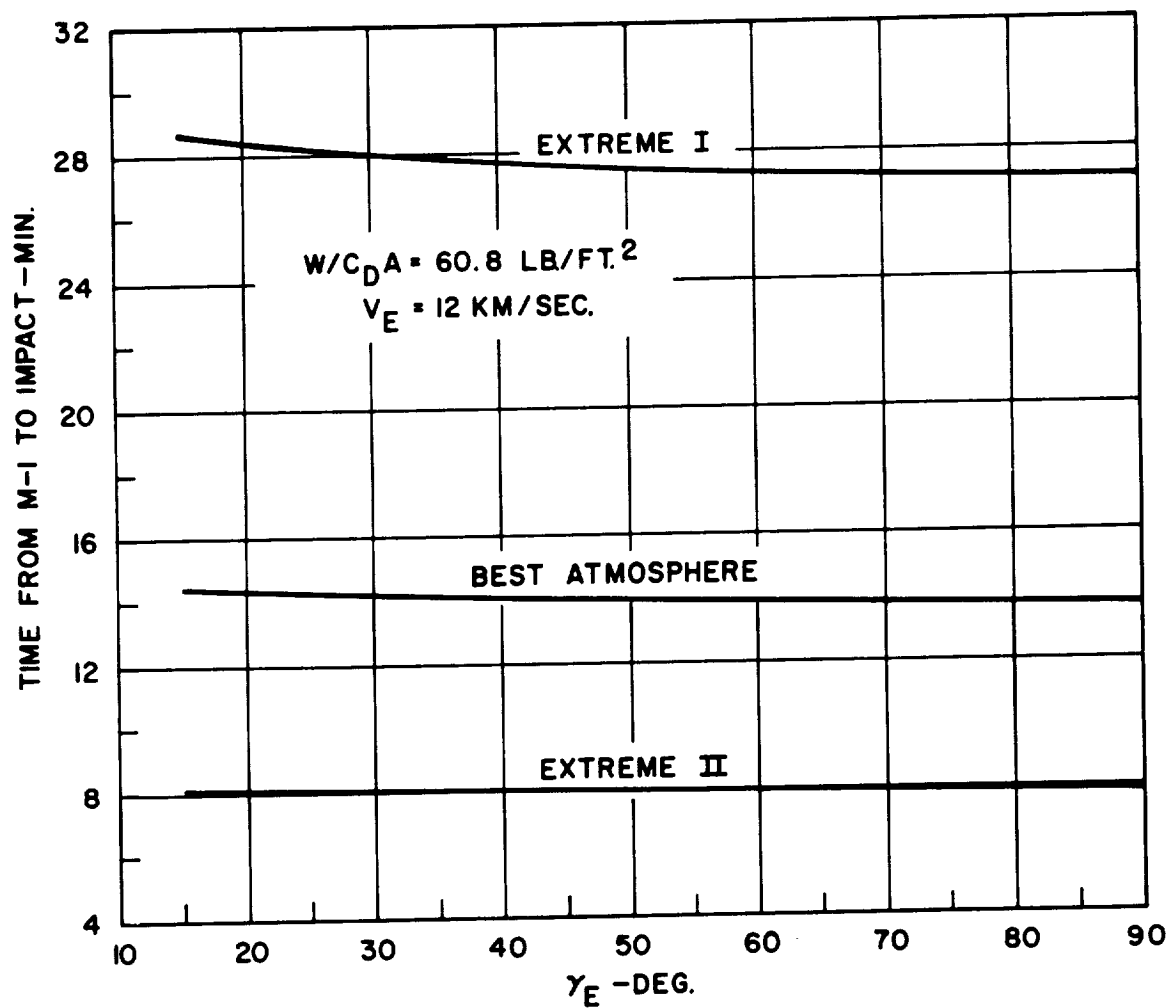


Figure 1.7b. Time from Mach Number 1.0 to Impact,
 $W/C_D A = 60.8 \text{ lb/ft}^2$

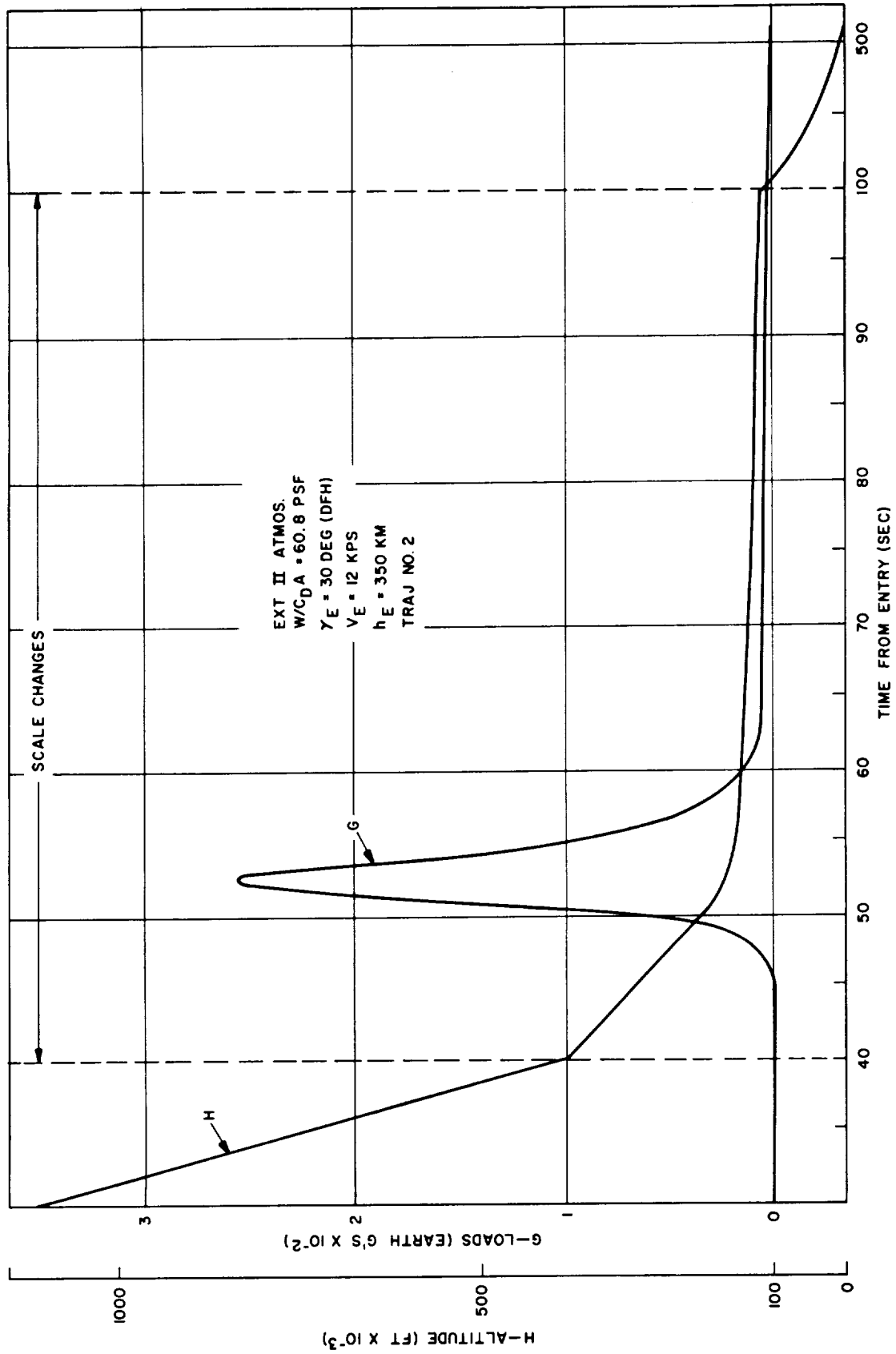


Figure 1.8. Time History of Point Mass Entry Traj. #2

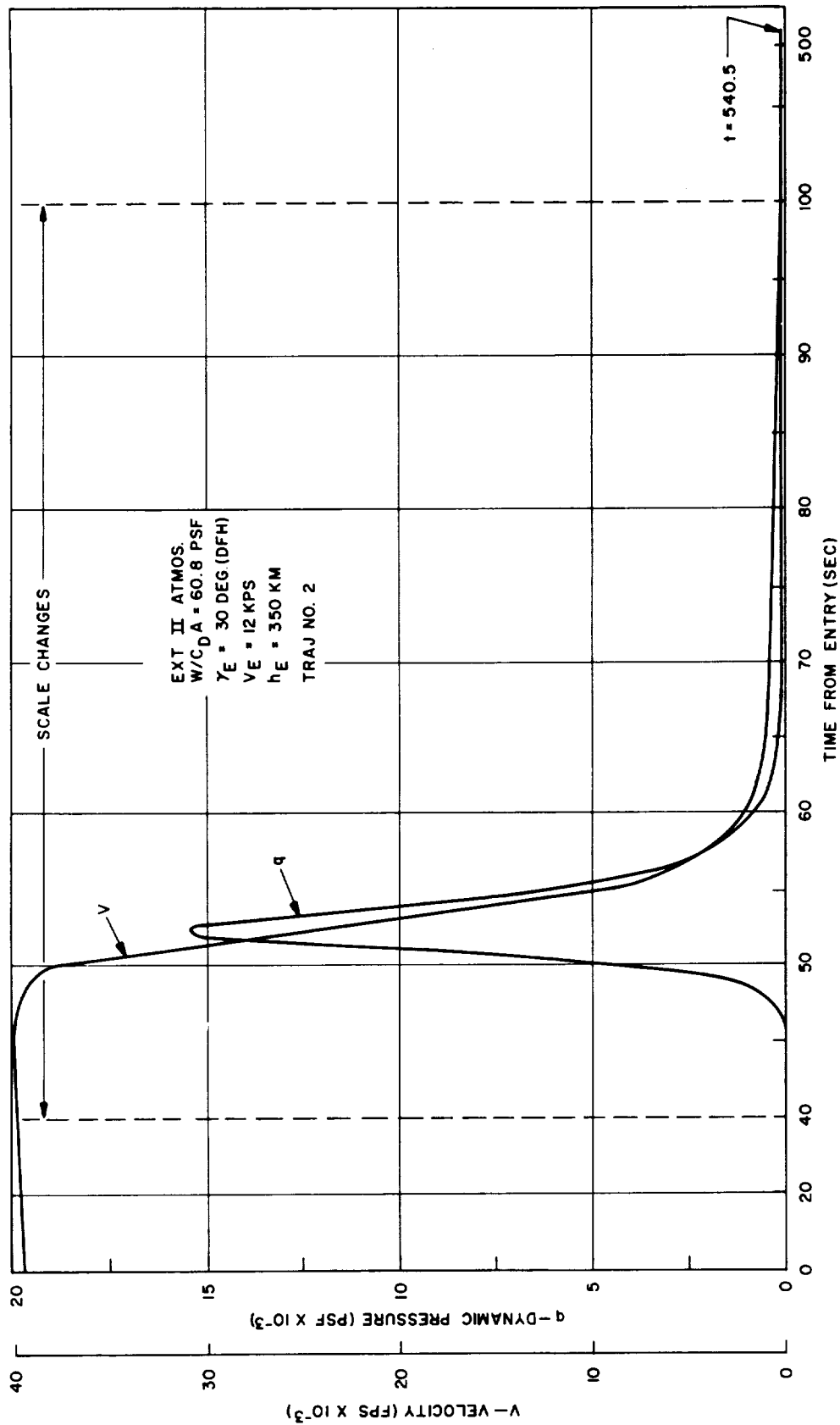


Figure 1.9. Time History of Point Mass Entry Traj. #2 (Concluded)

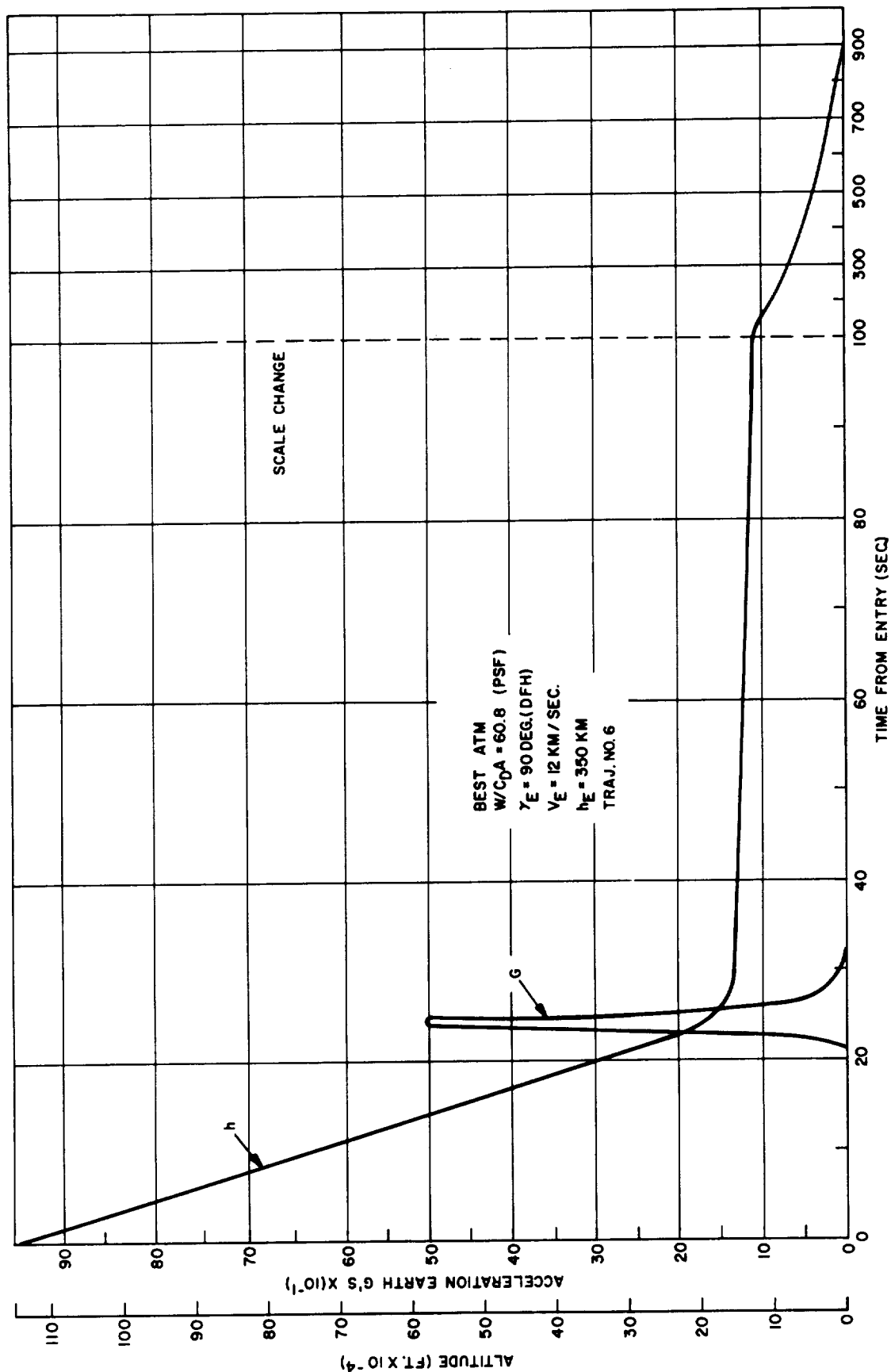


Figure 1.10. Time History of Point Mass Entry Traj. #6

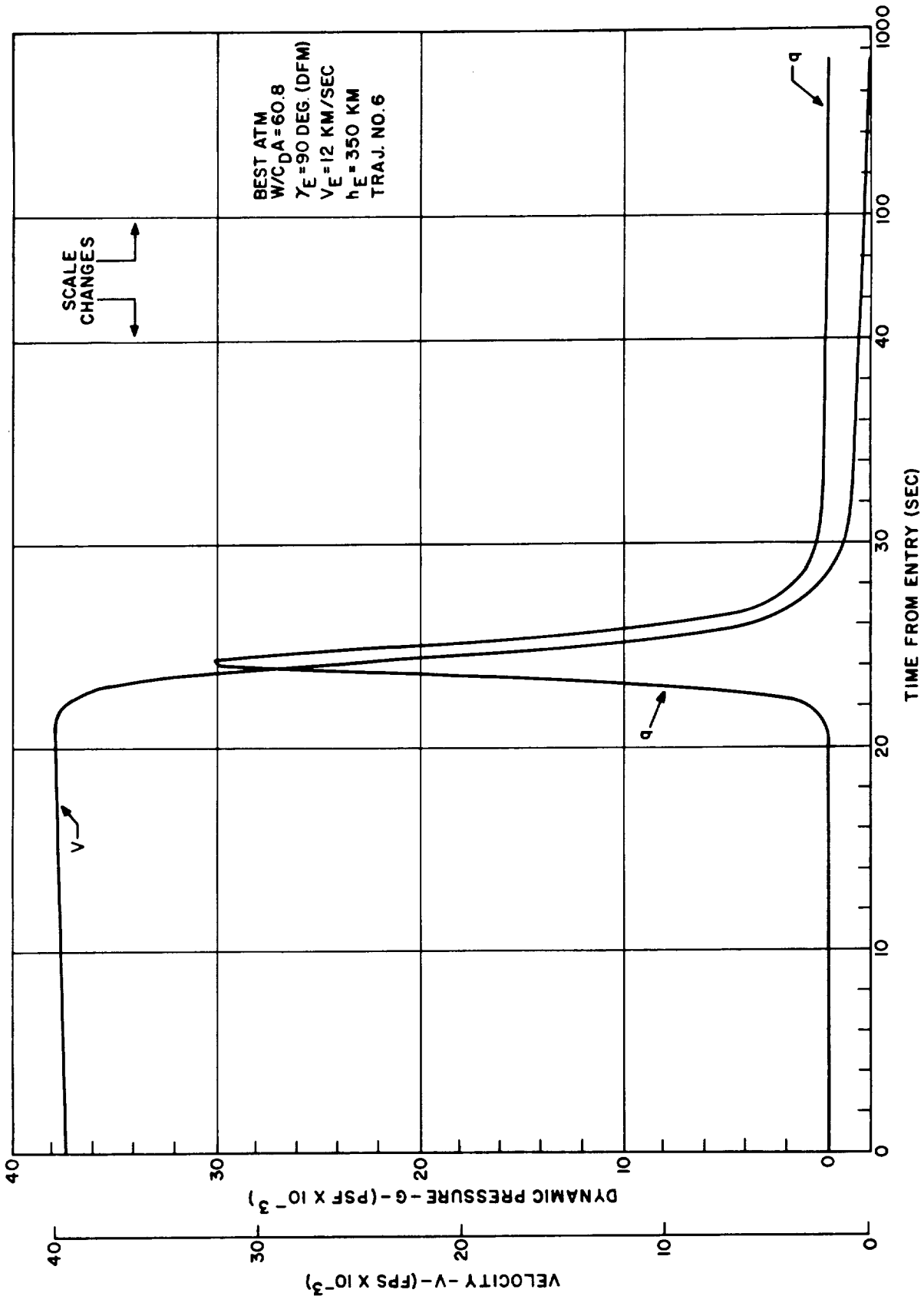


Figure 1.11. Time History of Point Mass Entry Traj. #6 (Concluded)

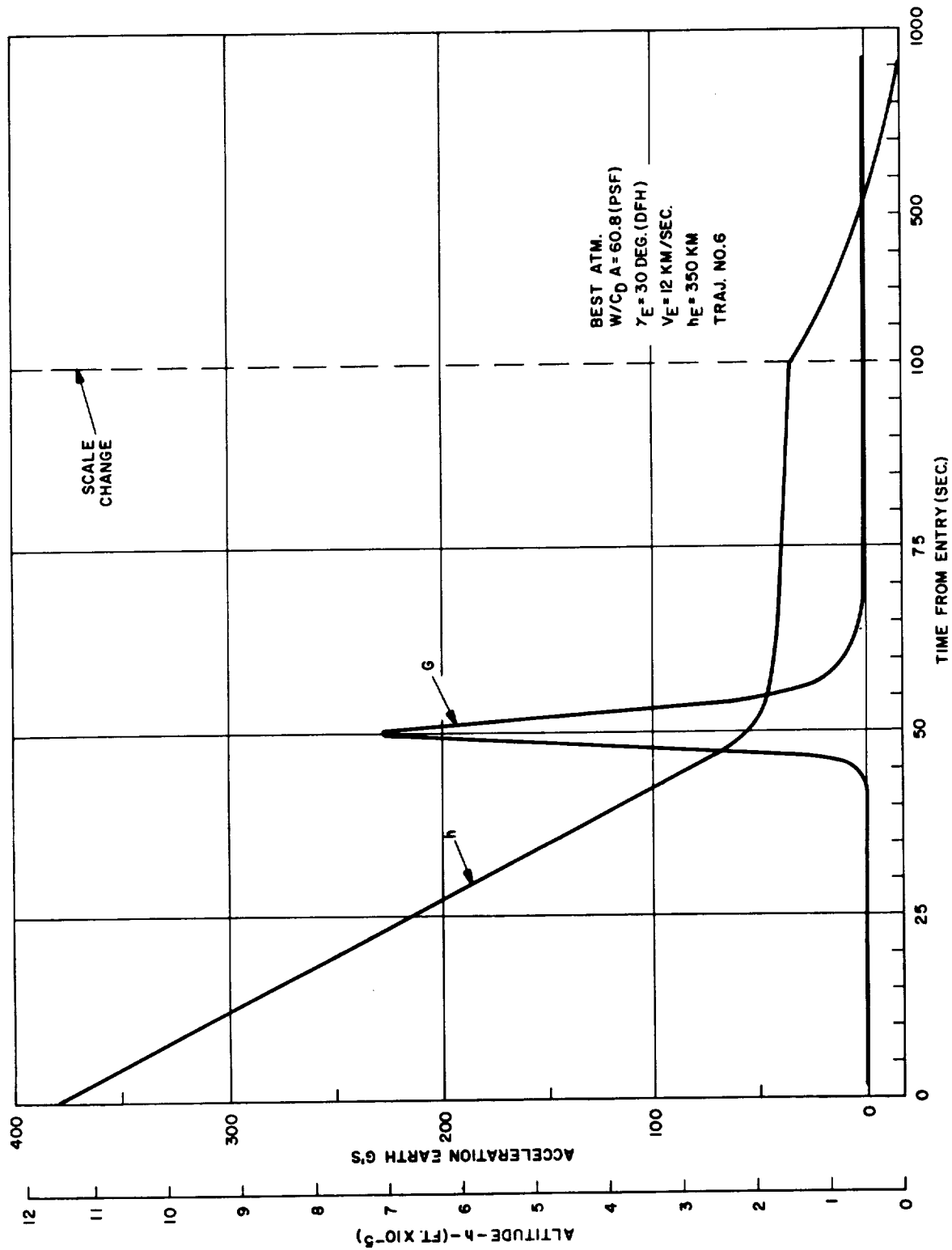


Figure 1.12. Time History of Point Mass Entry Traj. #7

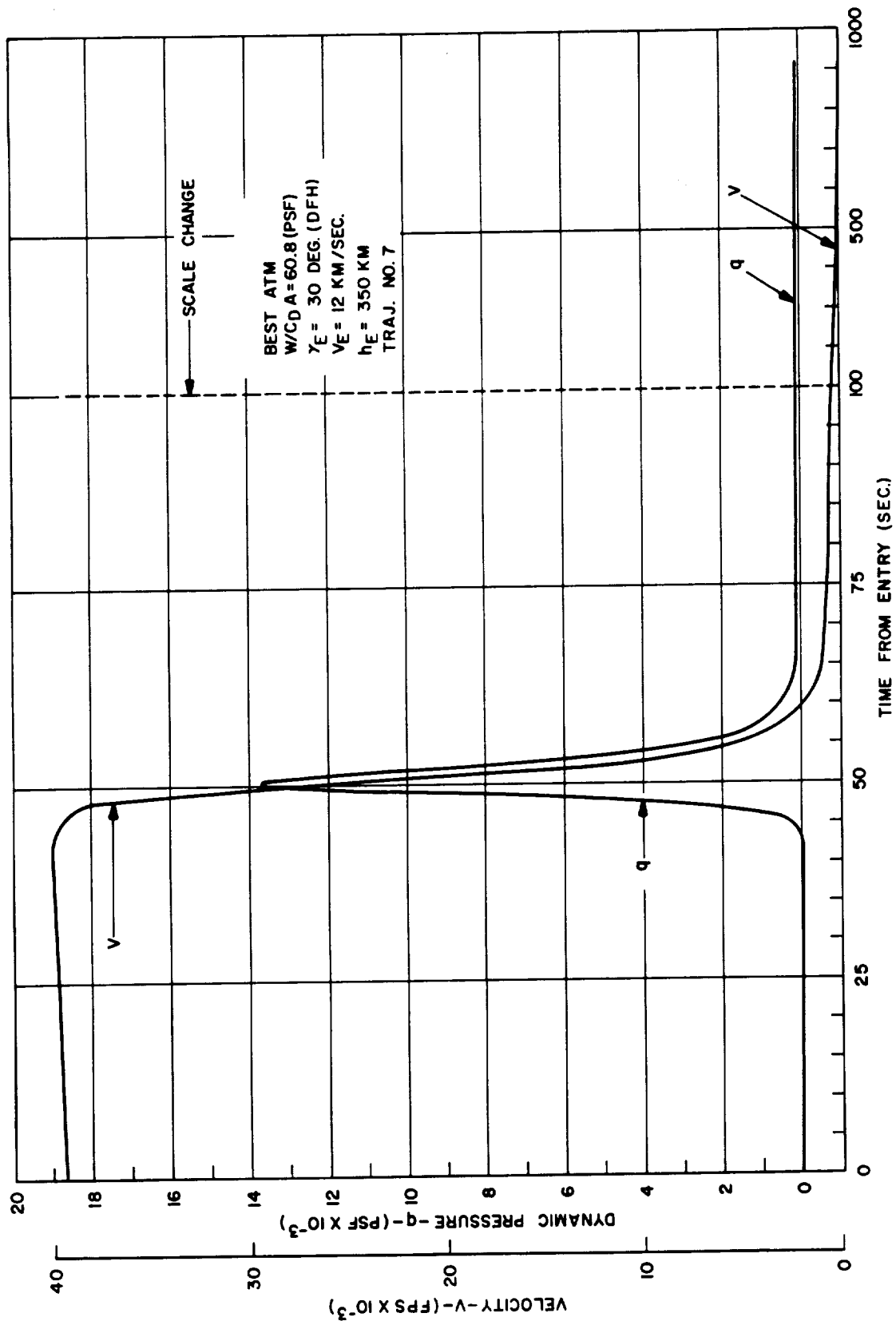


Figure 1.13. Time History of Point Mass Entry Traj. #7 (Concluded)

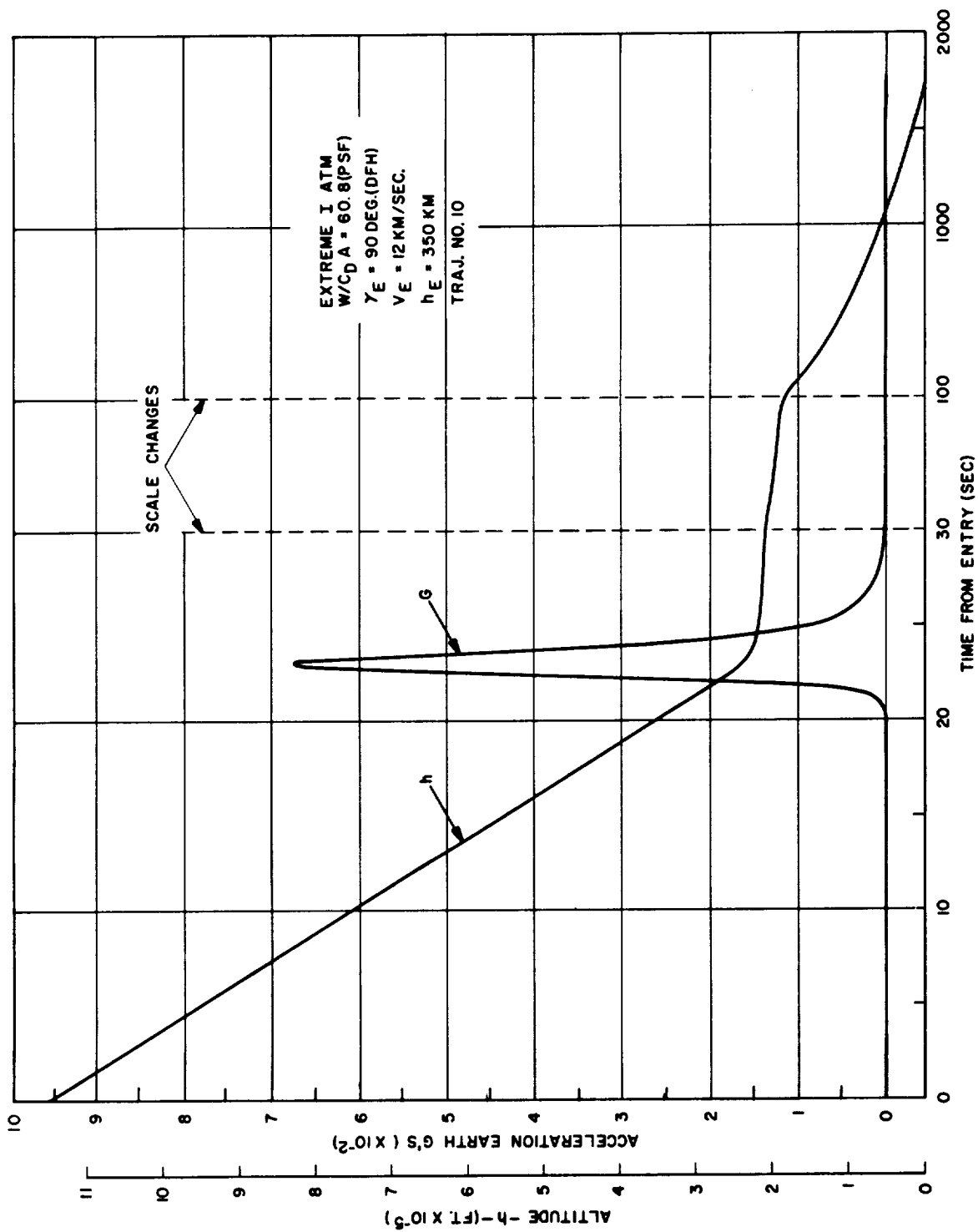


Figure 1.14. Time History of Point Mass Entry Traj. #10

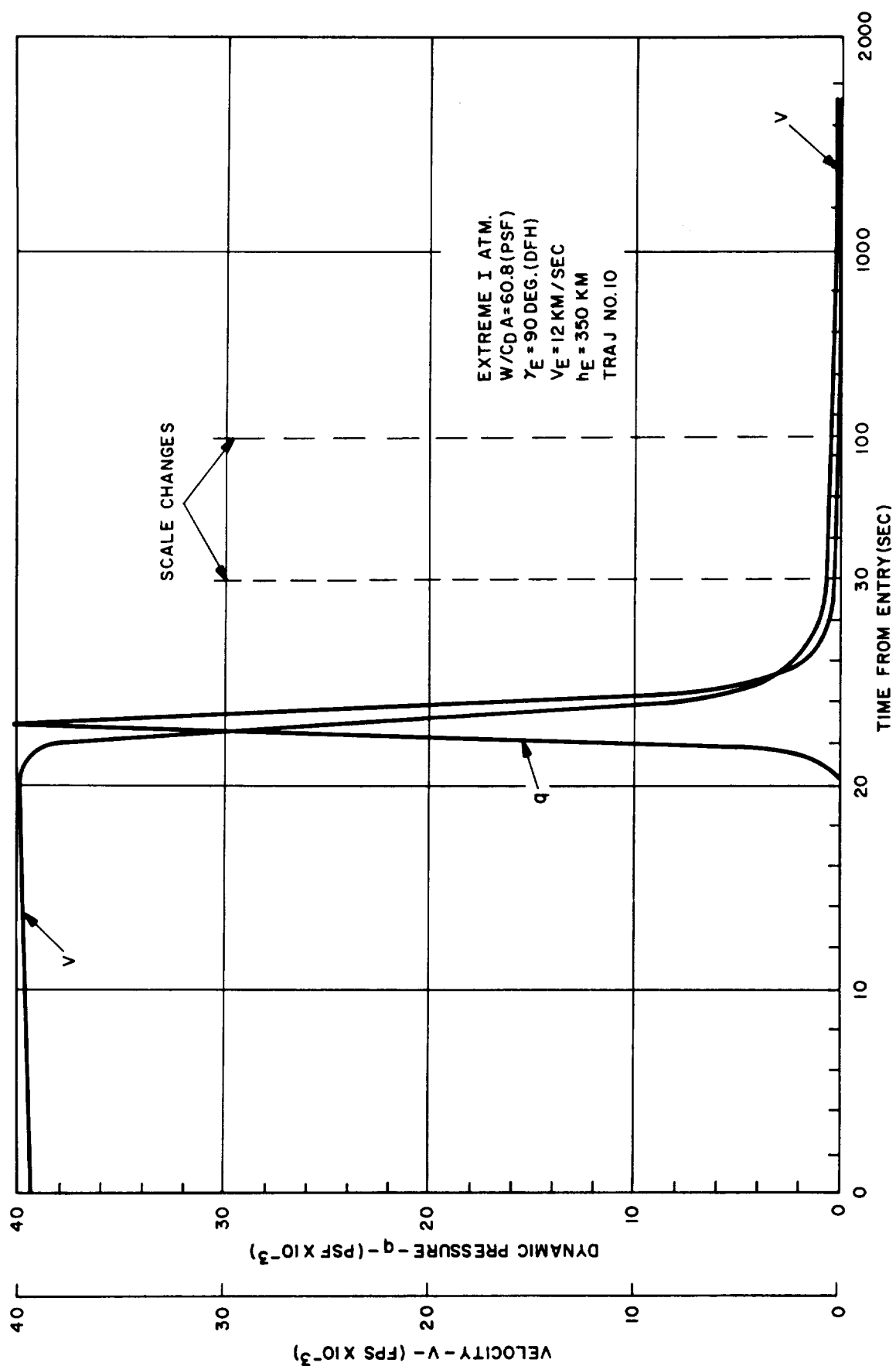


Figure 1.15. Time History of Point Mass Entry Traj. #10 (Concluded)

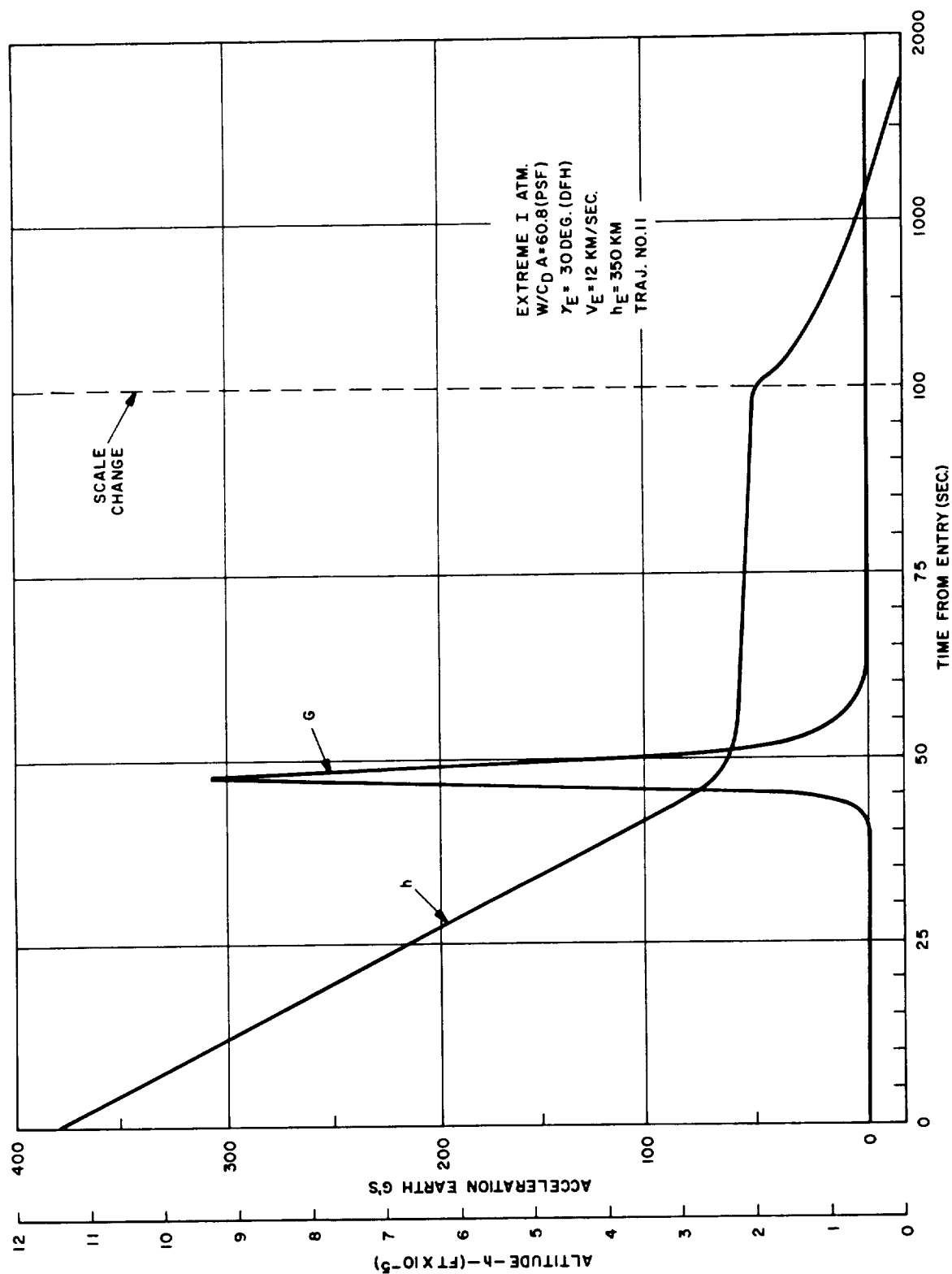


Figure 1.16. Time History of Point Mass Entry Traj. #11

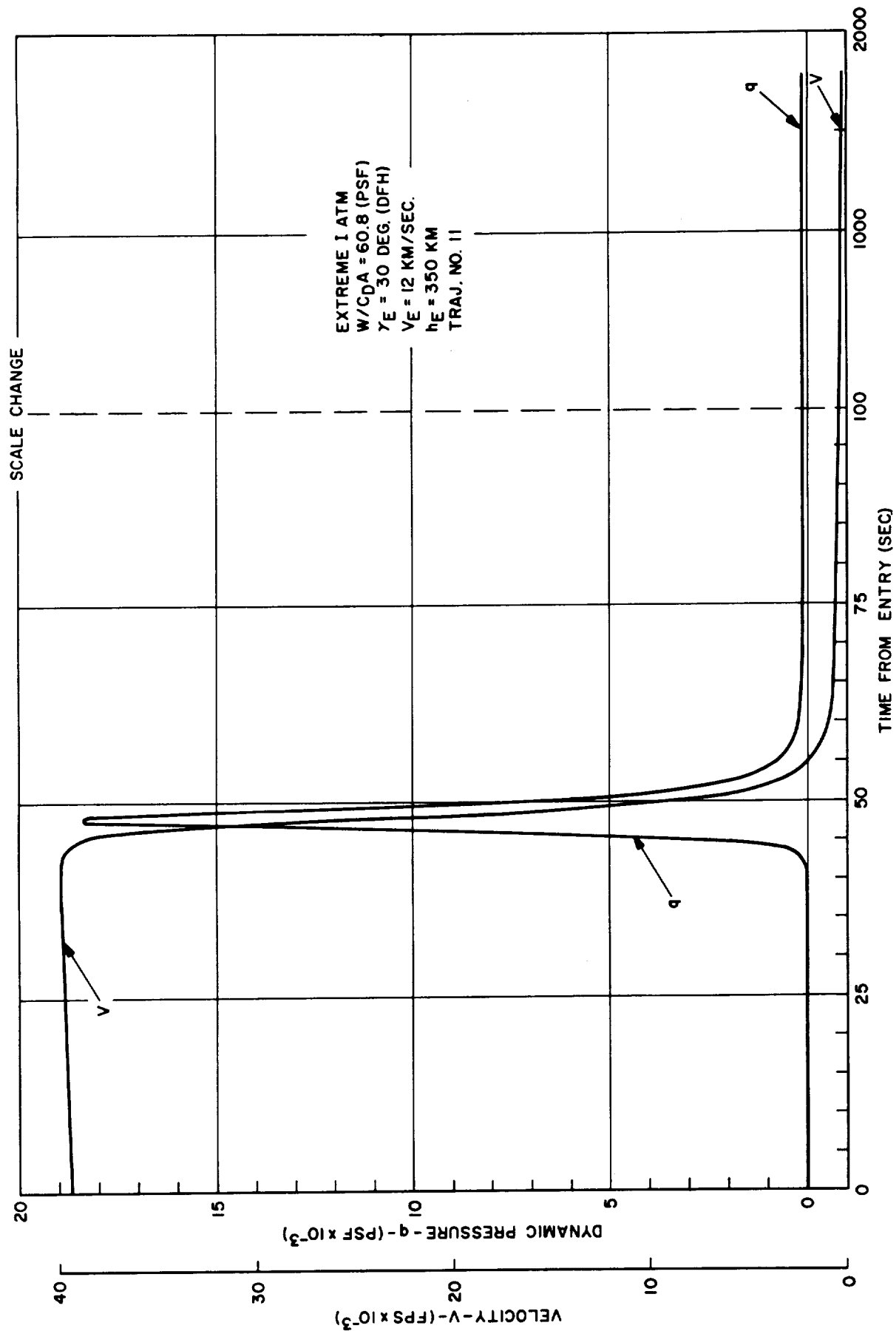


Figure 1.17. Time History of Point Mass Entry Traj. #11 (Concluded)

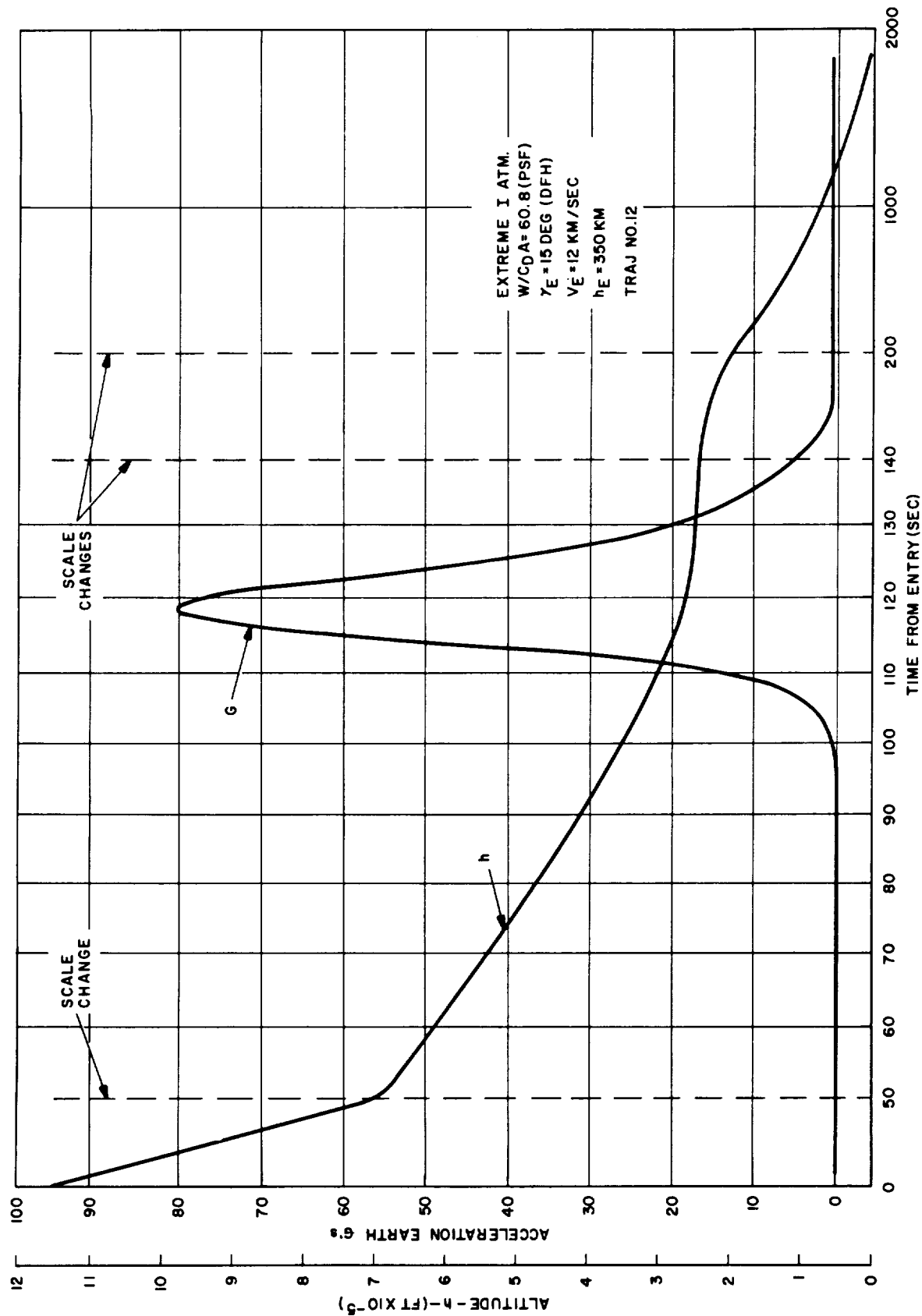


Figure 1.18. Time History of Point Mass Entry Traj. #12

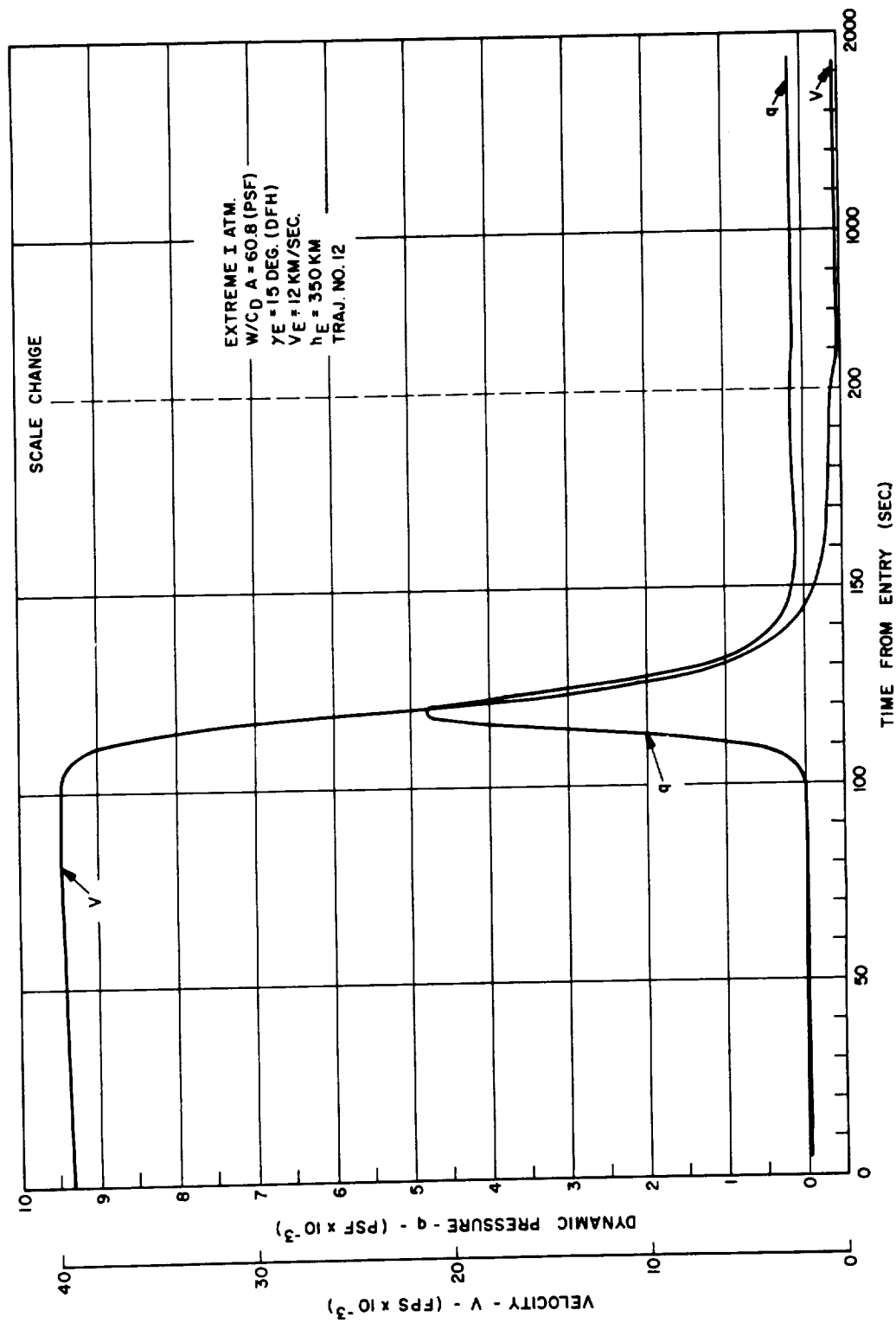


Figure 1.19. Time History of Point Mass Entry Traj. #12 (Concluded)

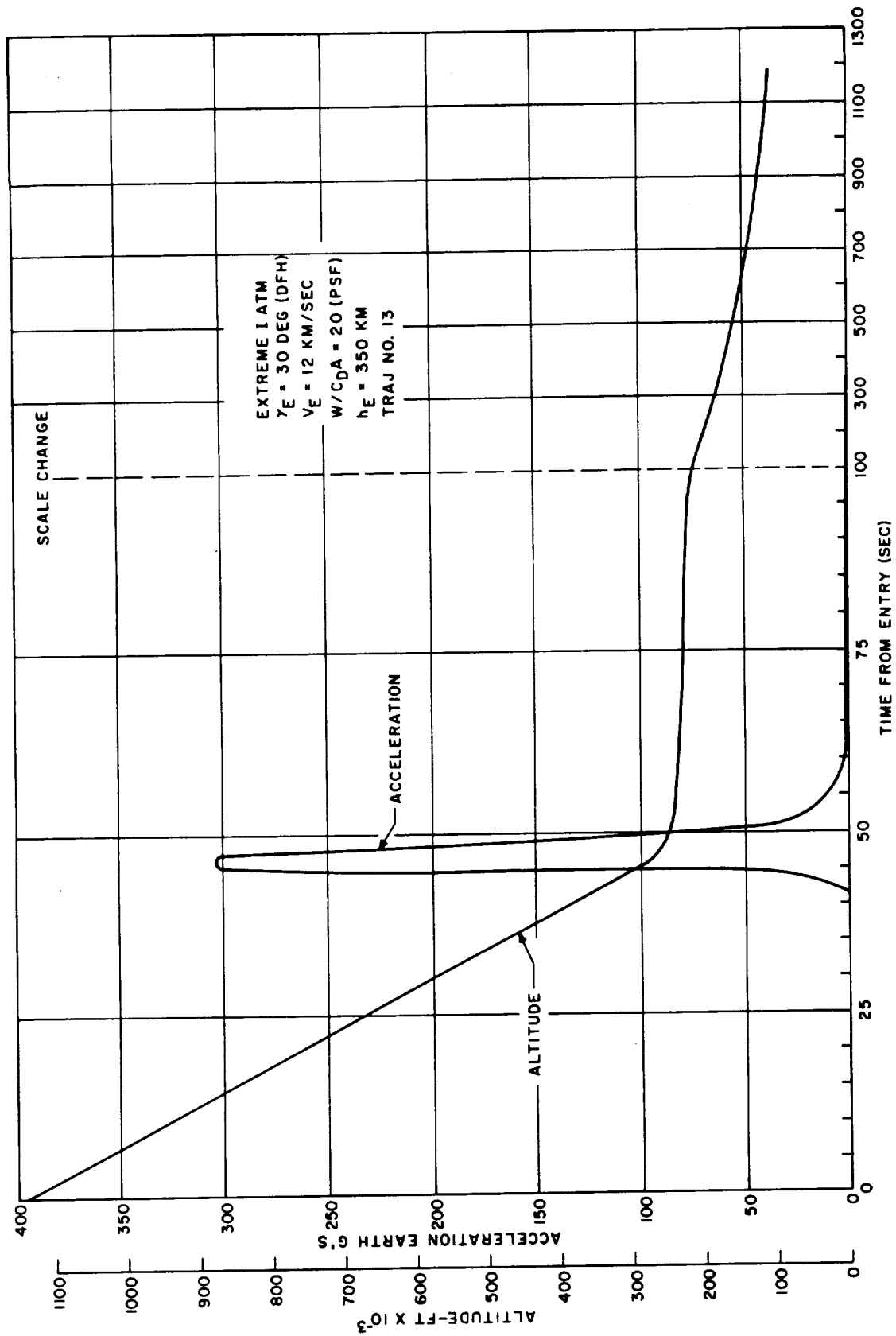


Figure 1.20. Time History of Point Mass Entry Traj. #13

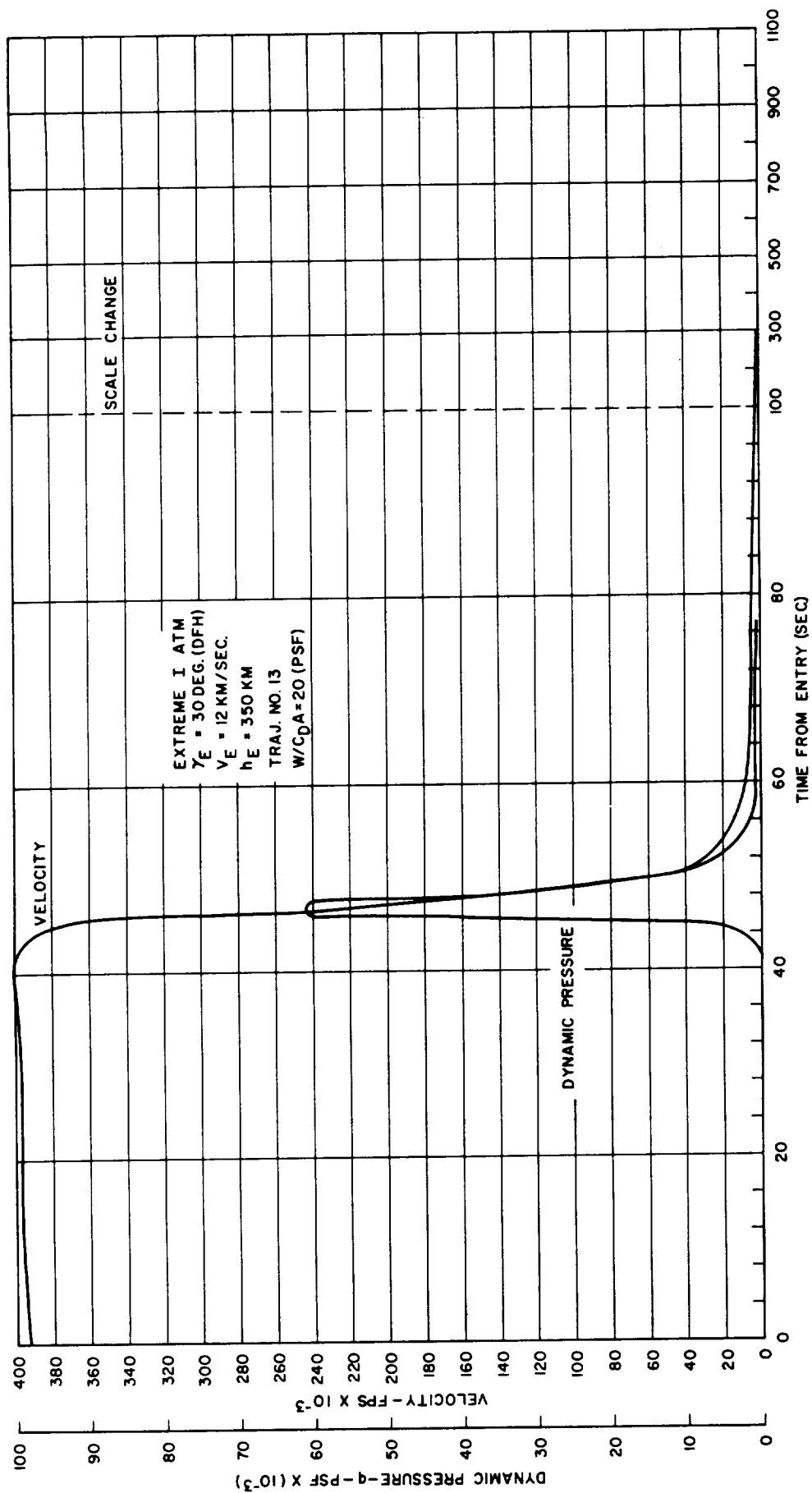


Figure 1.21. Time History of Point Mass Entry Traj. #13 (Concluded)

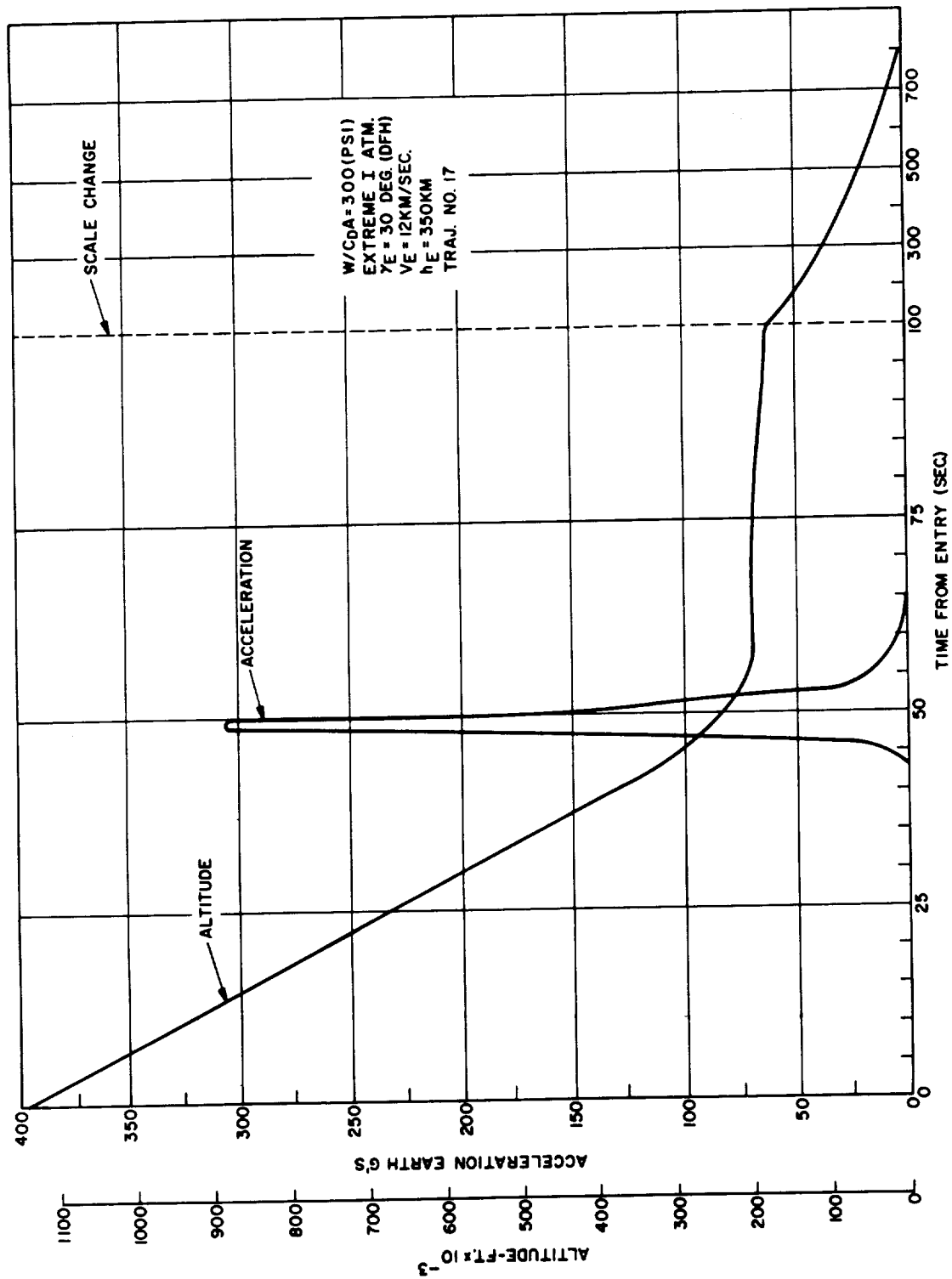


Figure 1.22. Time History of Point Mass Entry Traj. #17

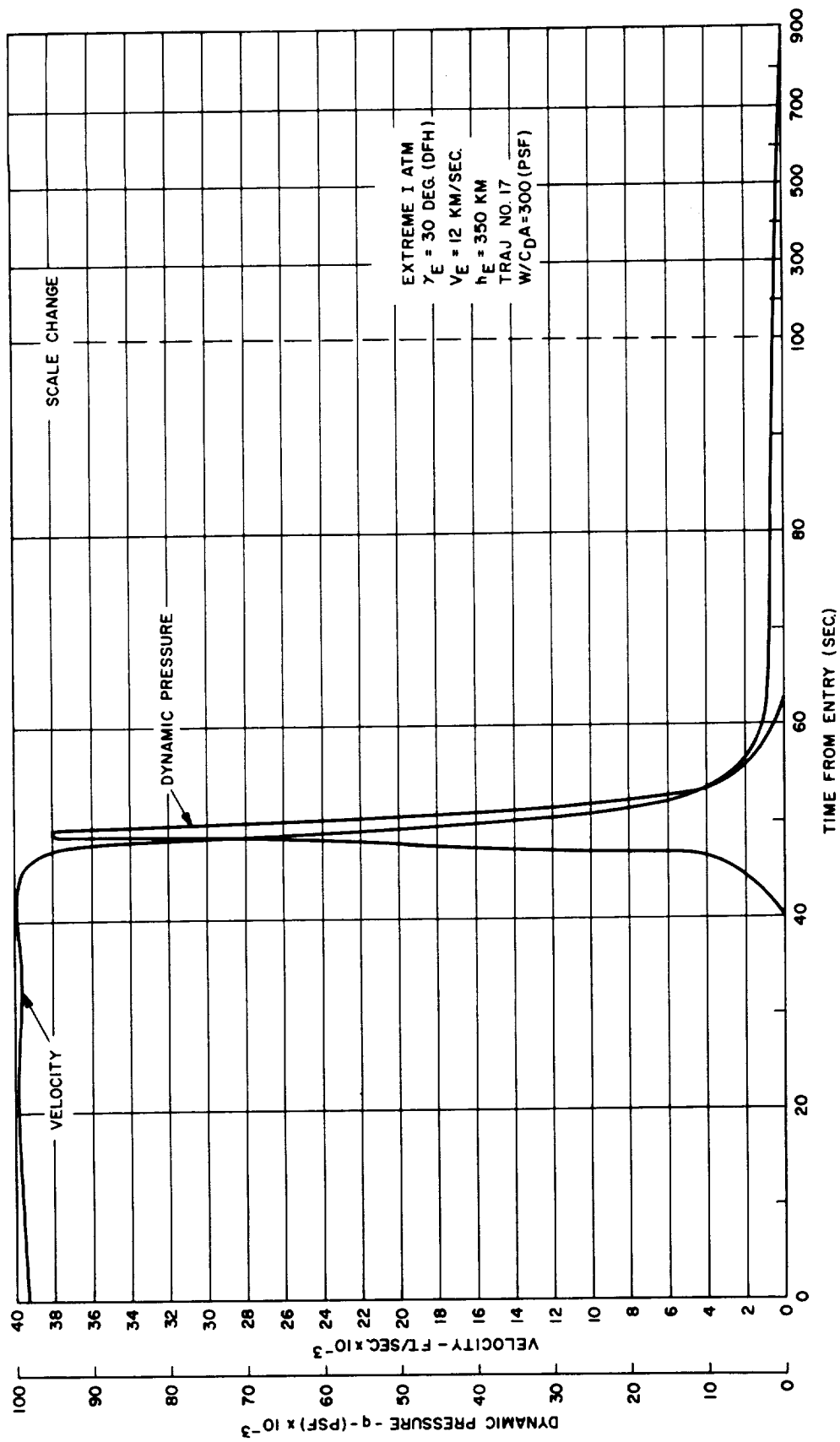


Figure 1.23. Time History of Point Mass Entry Traj. #17 (Concluded)

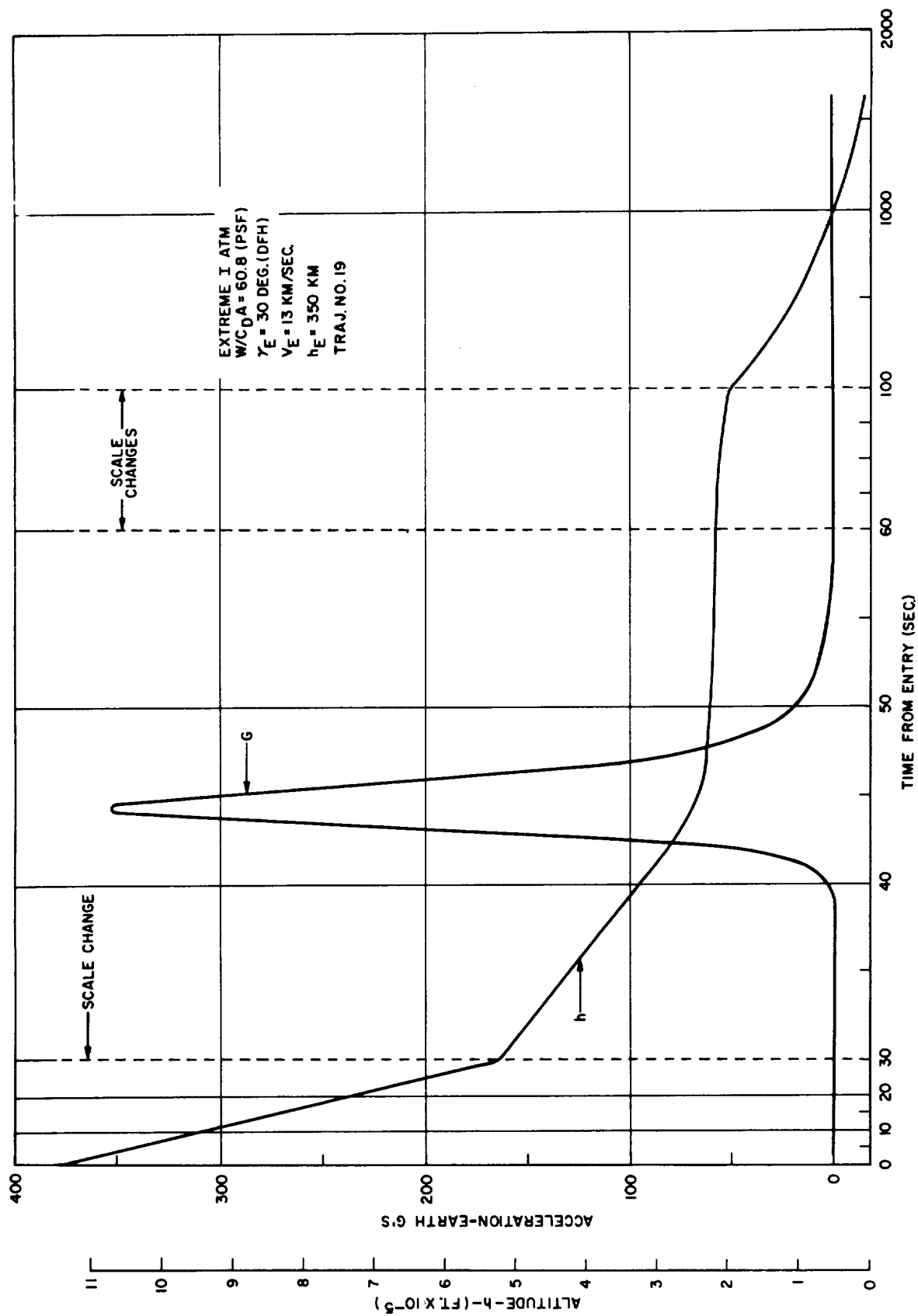


Figure 1.24. Time History of Point Mass Entry Traj. #19

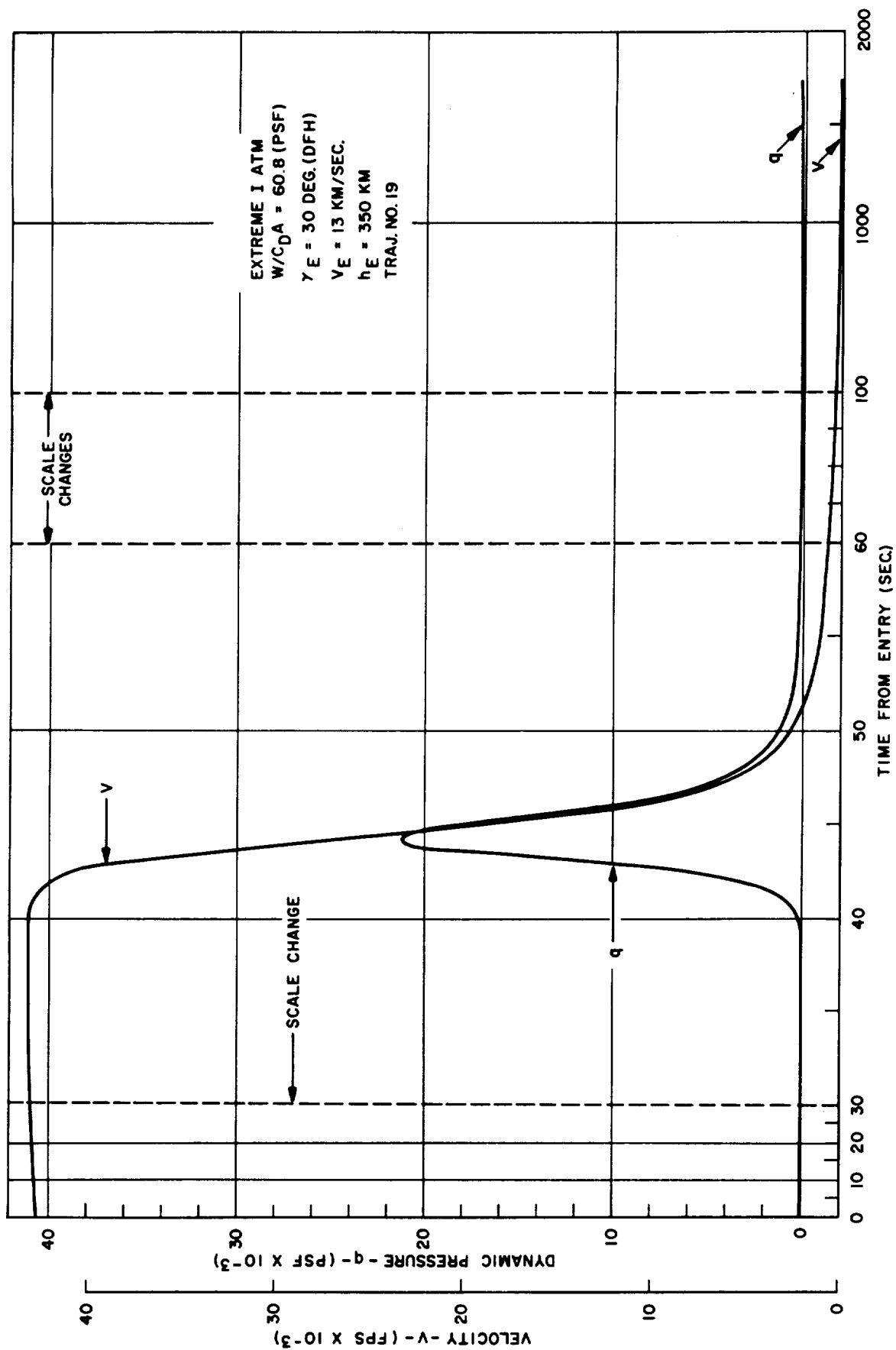


Figure 1.25. Time History of Point Mass Entry Traj. #19 (Concluded)

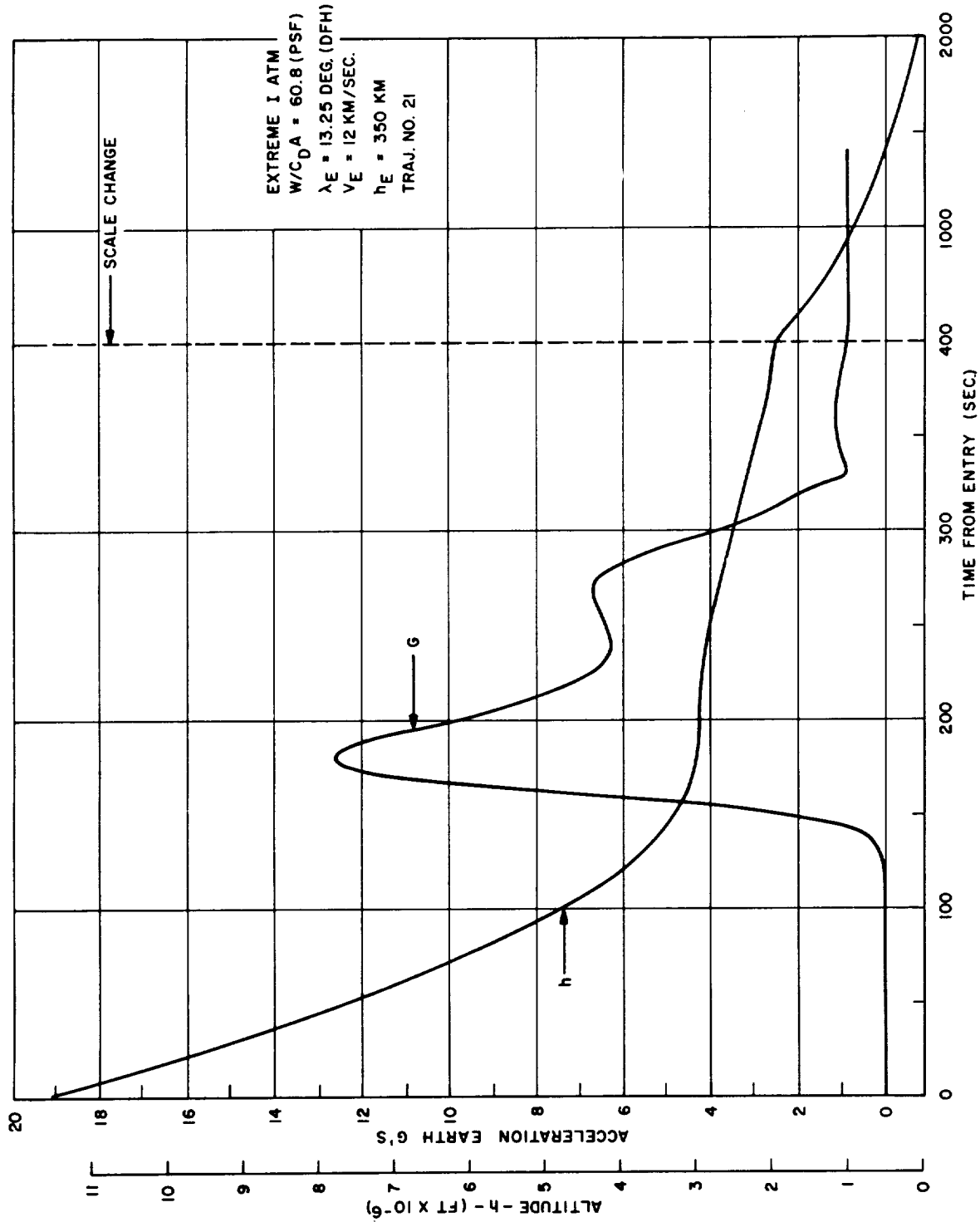


Figure 1.26. Time History of Point Mass Entry Traj. #21

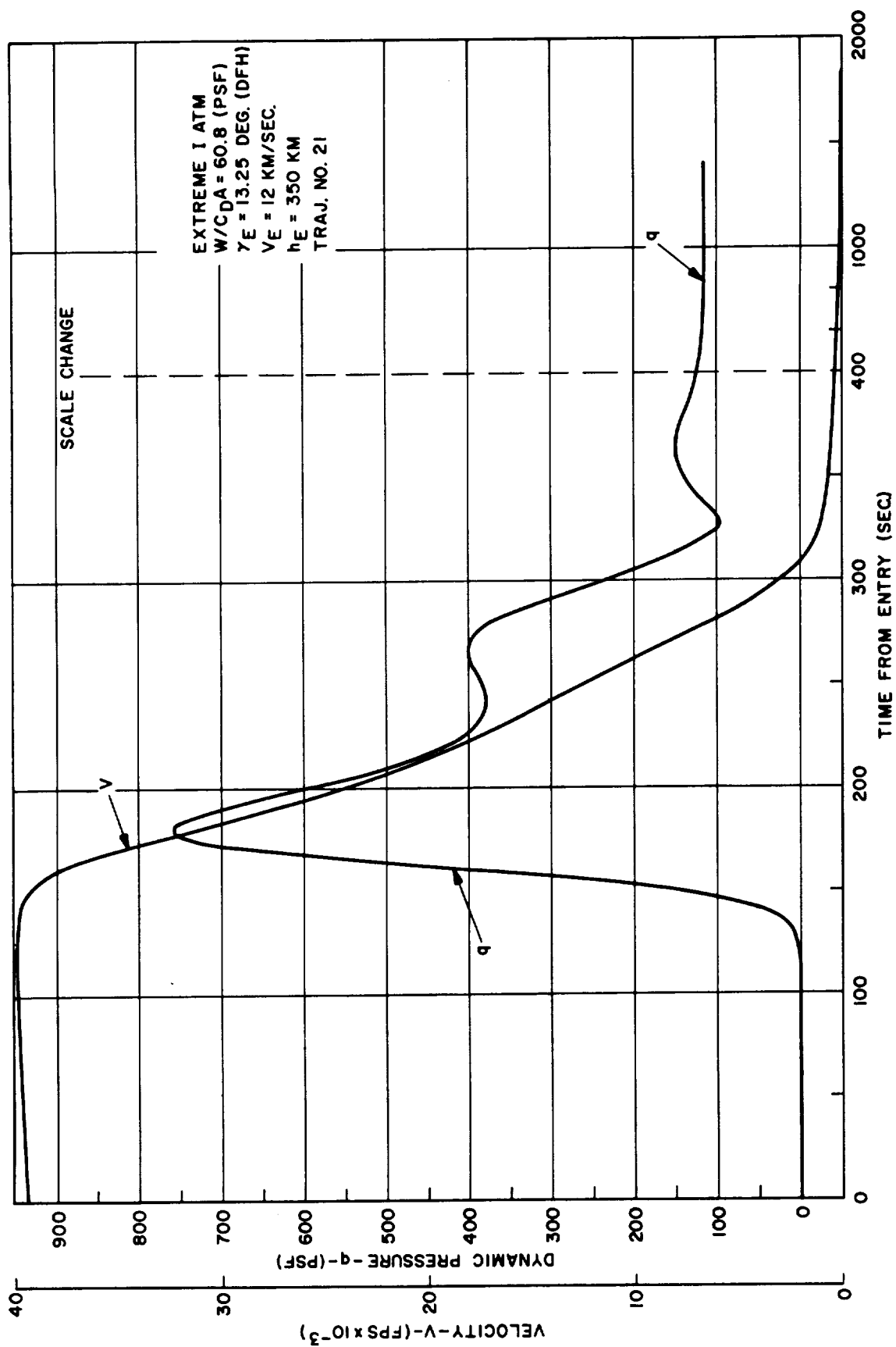


Figure 1.27. Time History of Point Mass Entry Traj. #21 (Concluded)

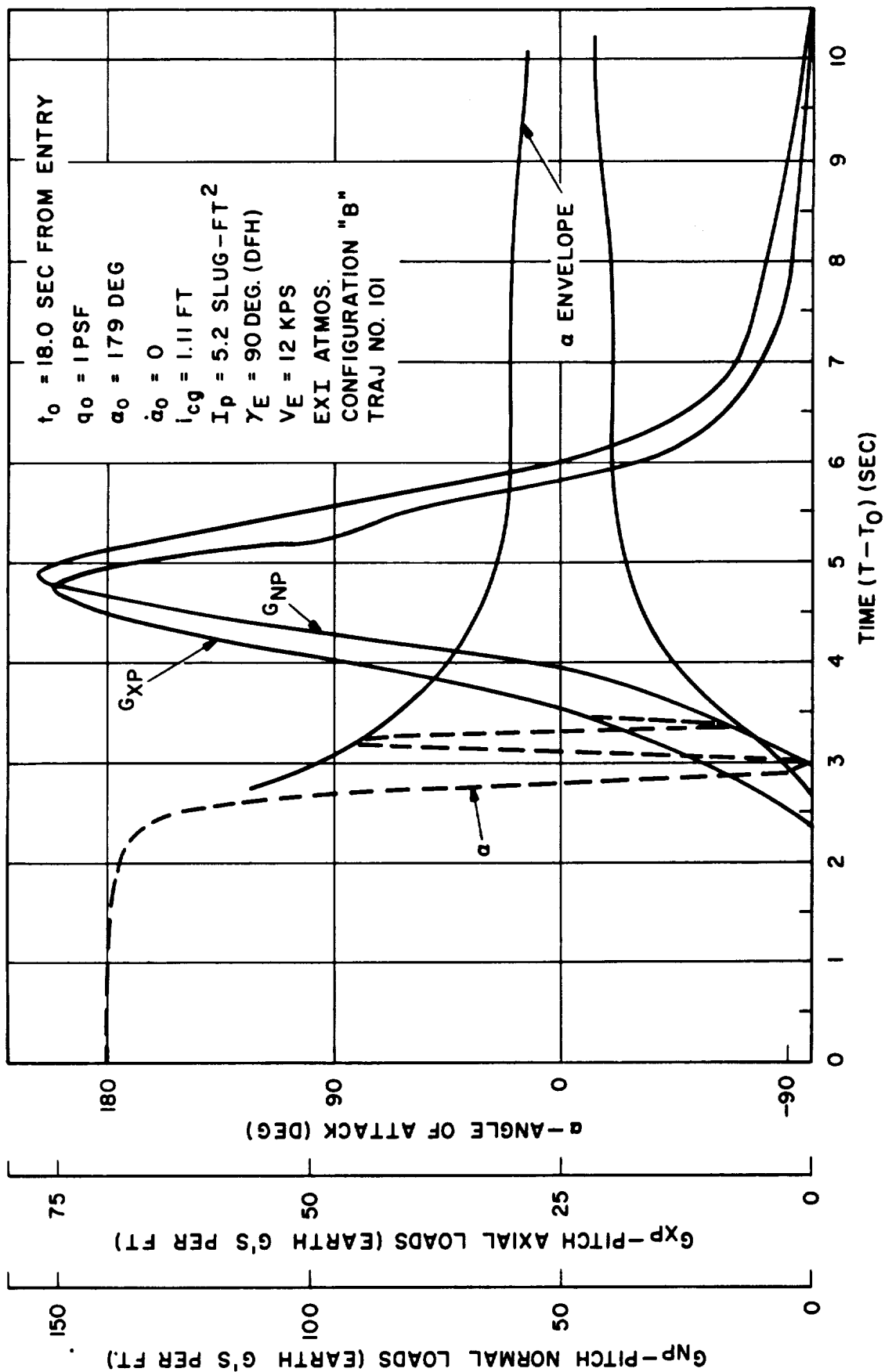


Figure 1.28. Time History of 3° Entry Traj. #101

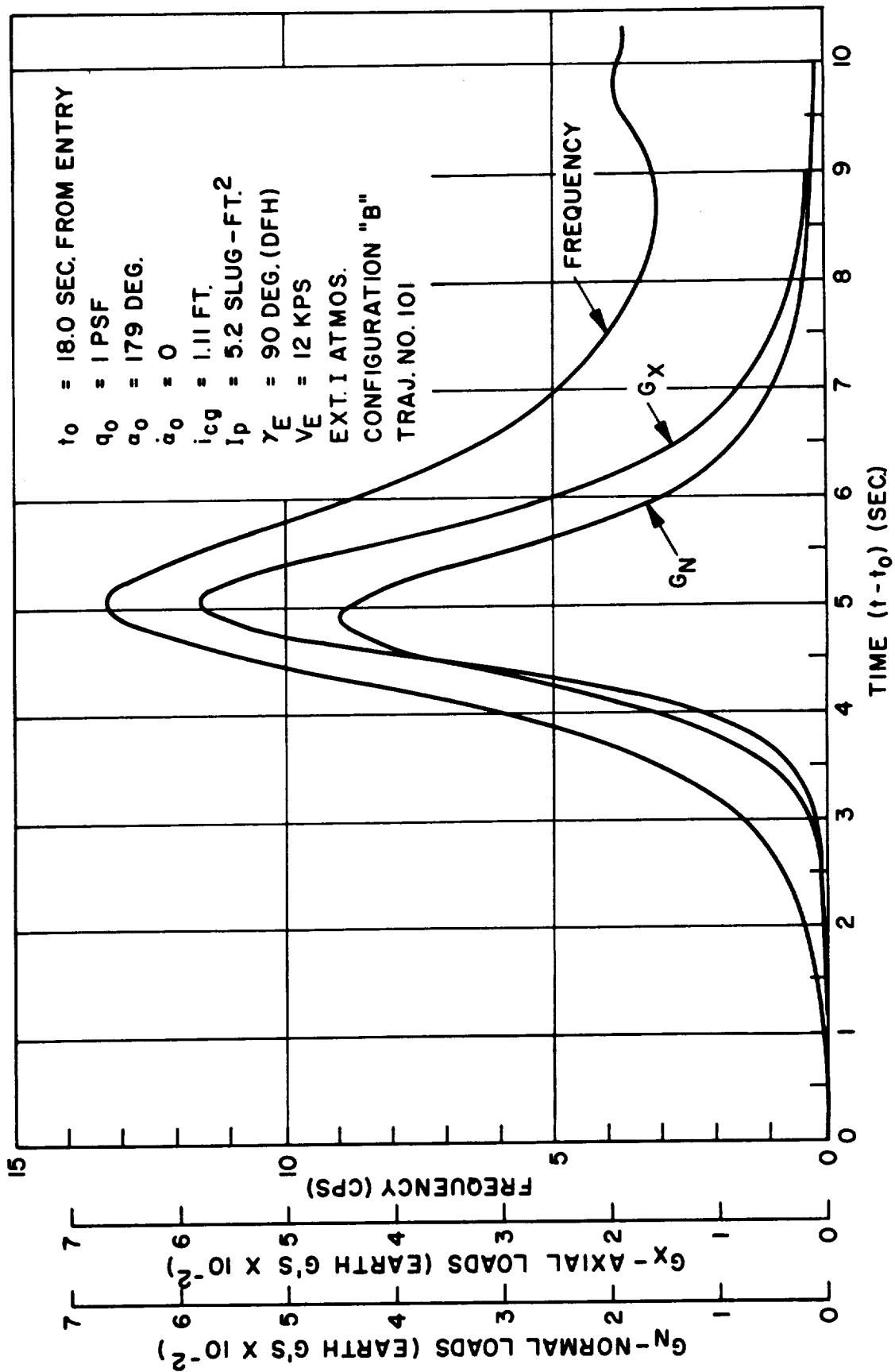


Figure 1.29. Time History of 3° Entry Traj. #101 (Concluded)

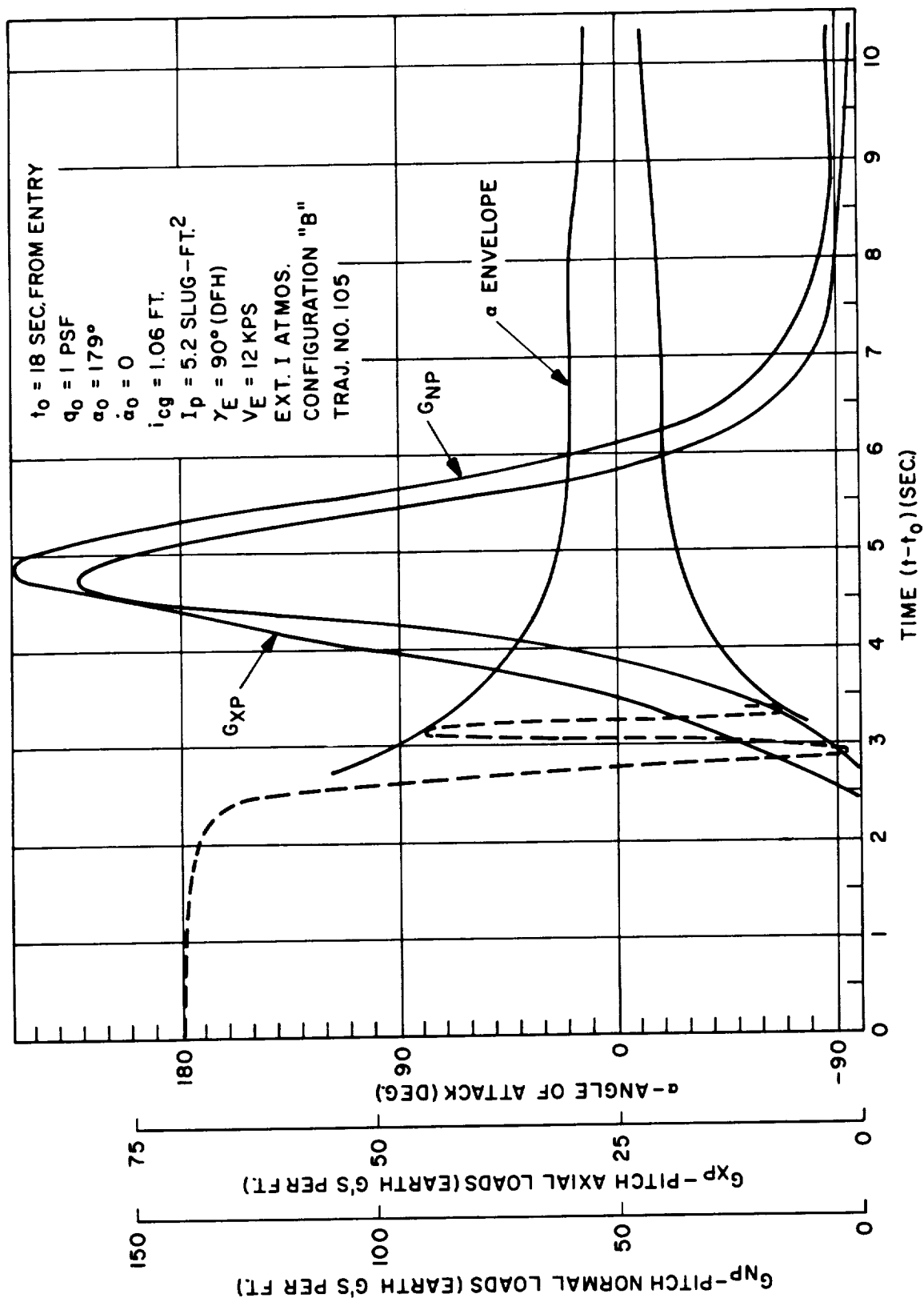


Figure 1.30. Time History of 3° Entry Traj. #102

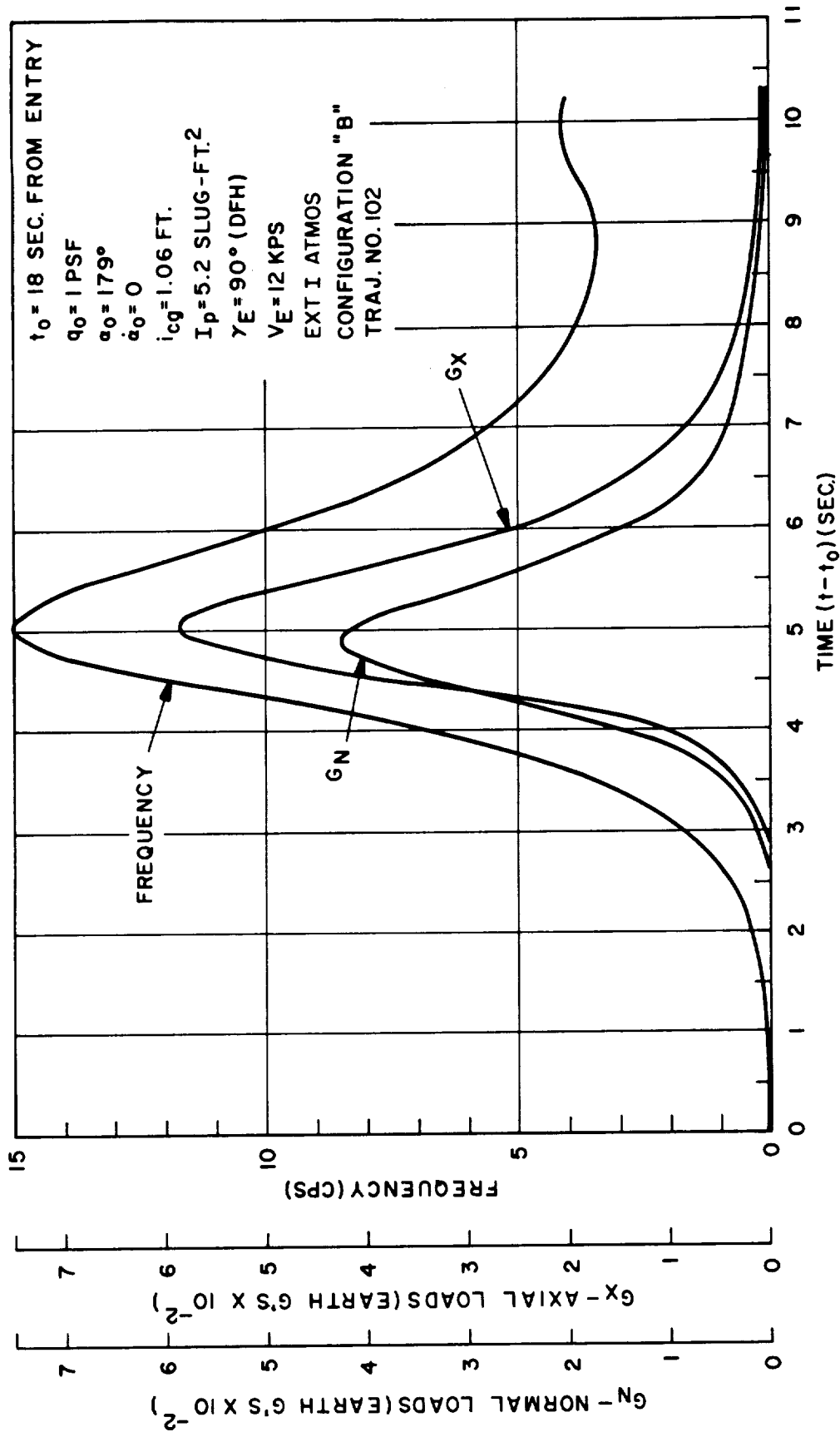


Figure 1.31. Time History of 3° Entry Traj. #102 (Concluded)

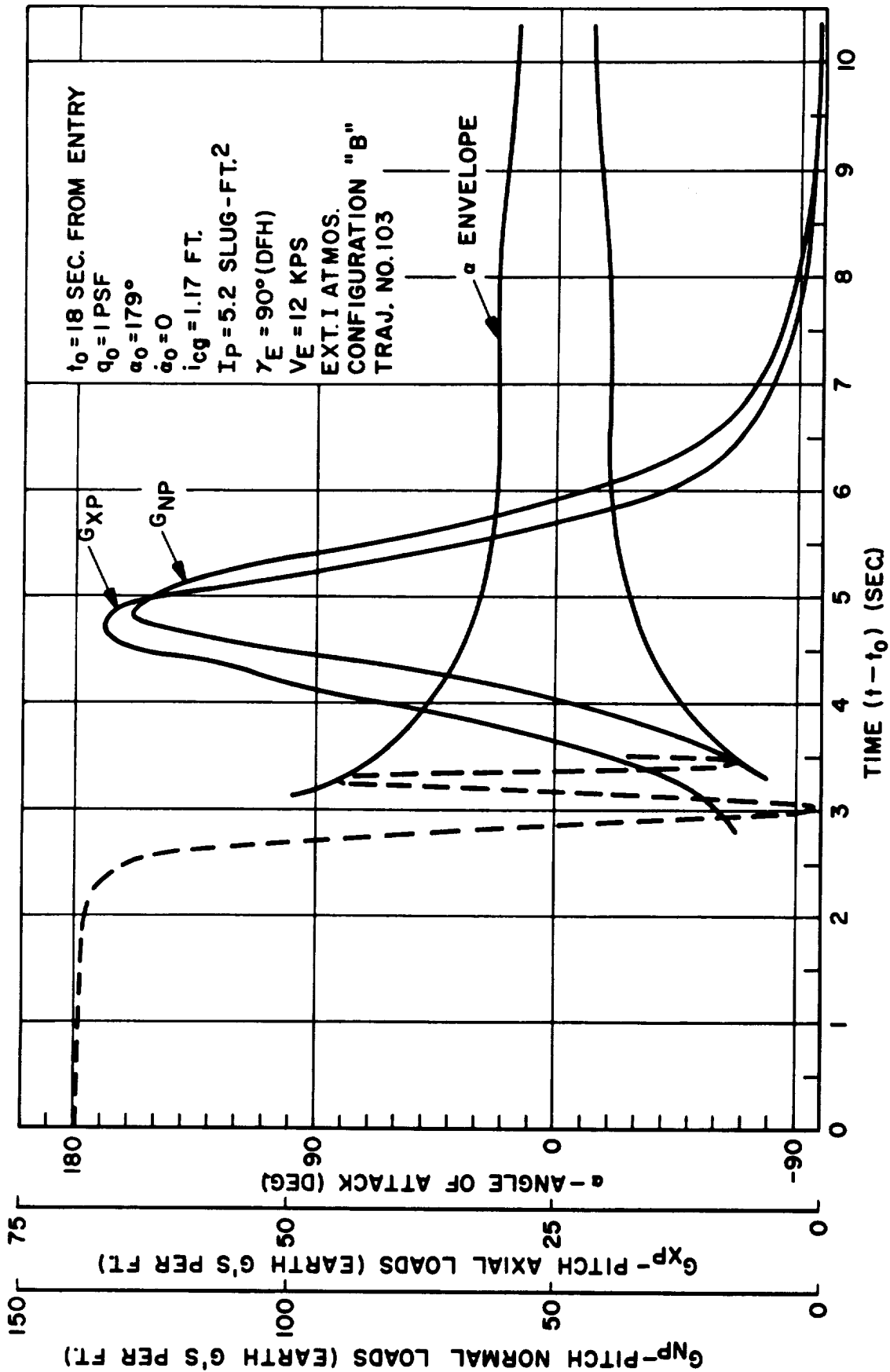


Figure 1.32. Time History of 3° Entry Traj. #103

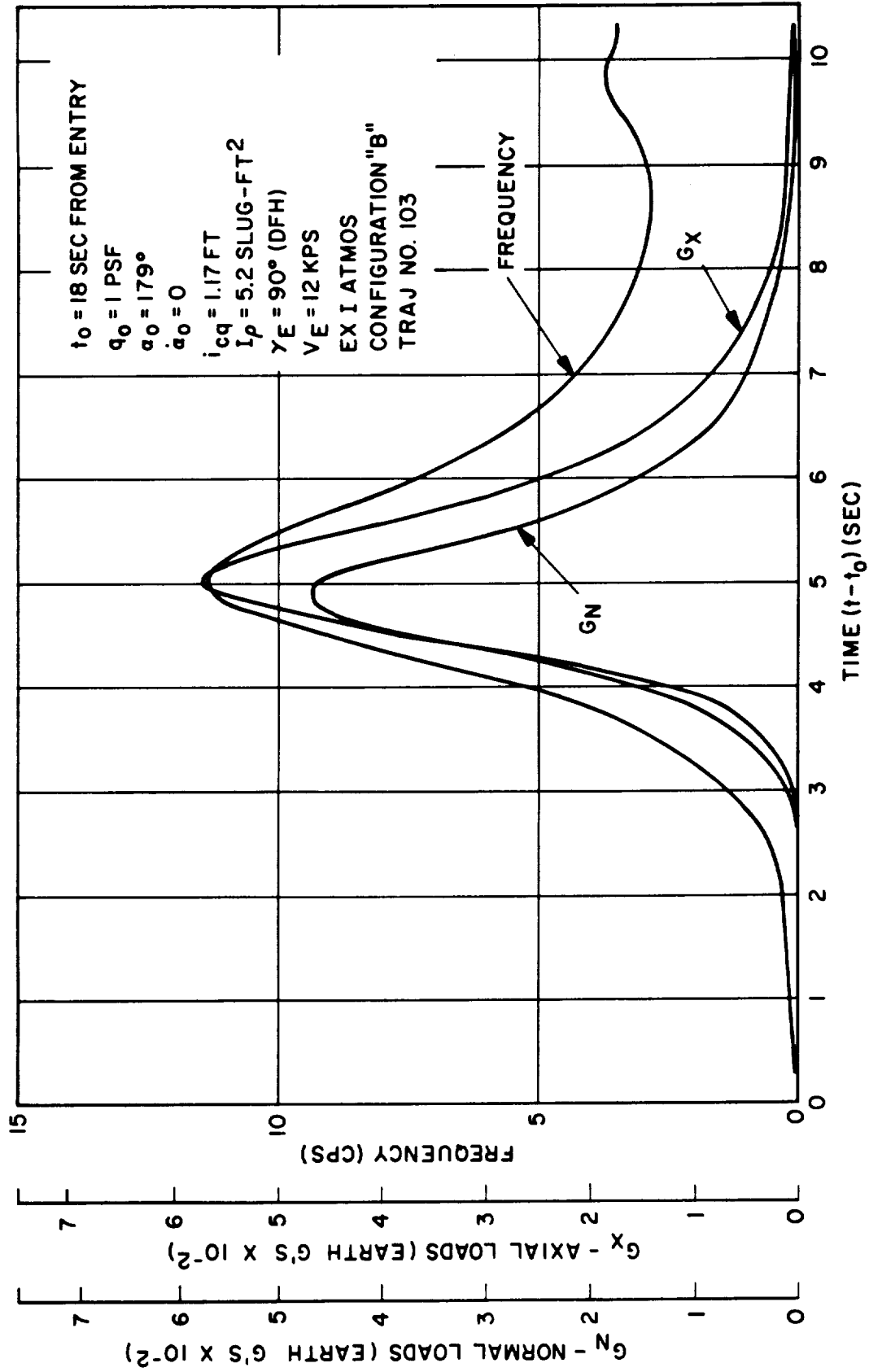


Figure 1.33. Time History of 3° Entry Traj. #103 (Concluded)

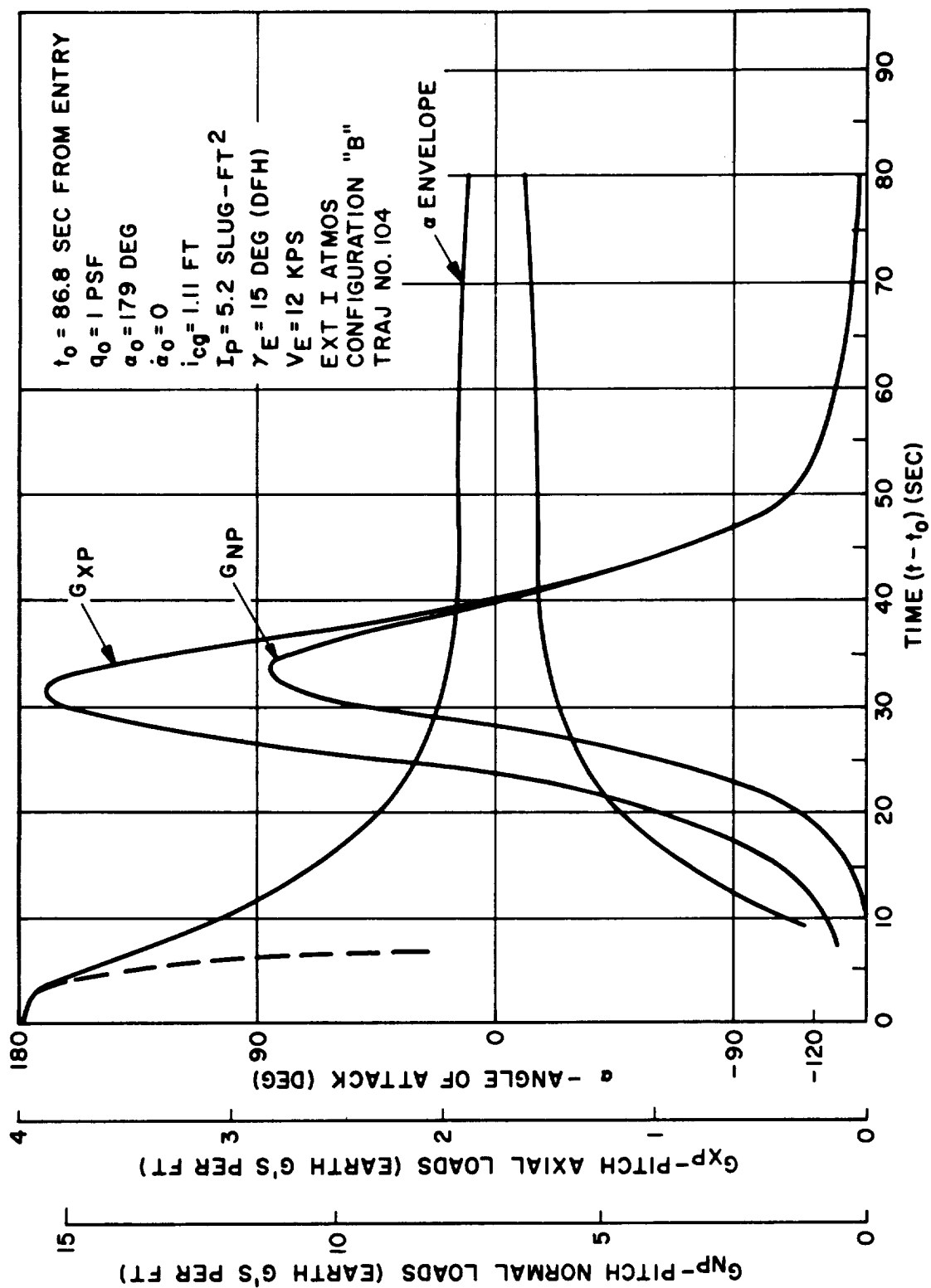


Figure 1.34. Time History of 3° Entry Traj. #104

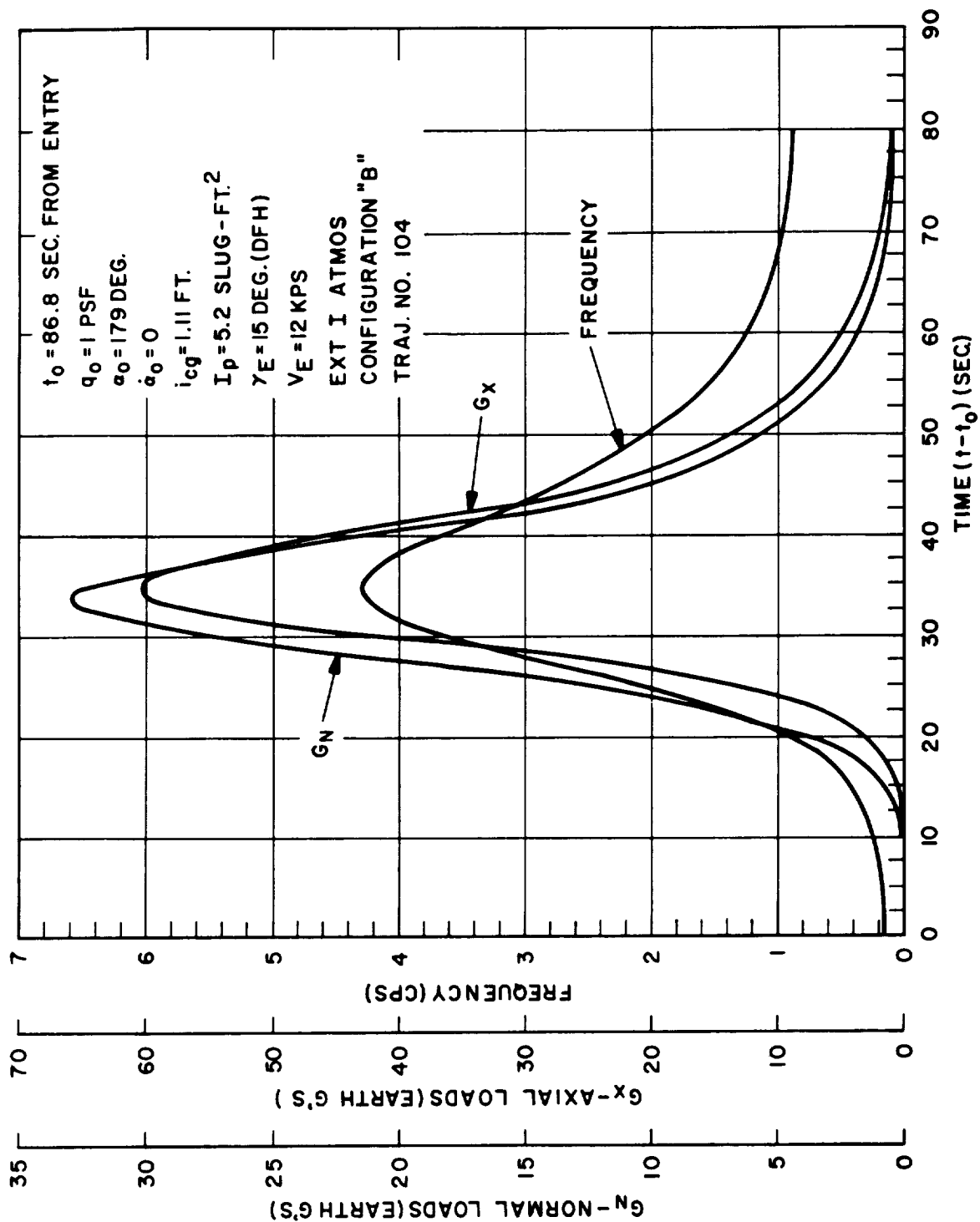


Figure 1.35. Time History of 3° Entry Traj. #104 (Concluded)

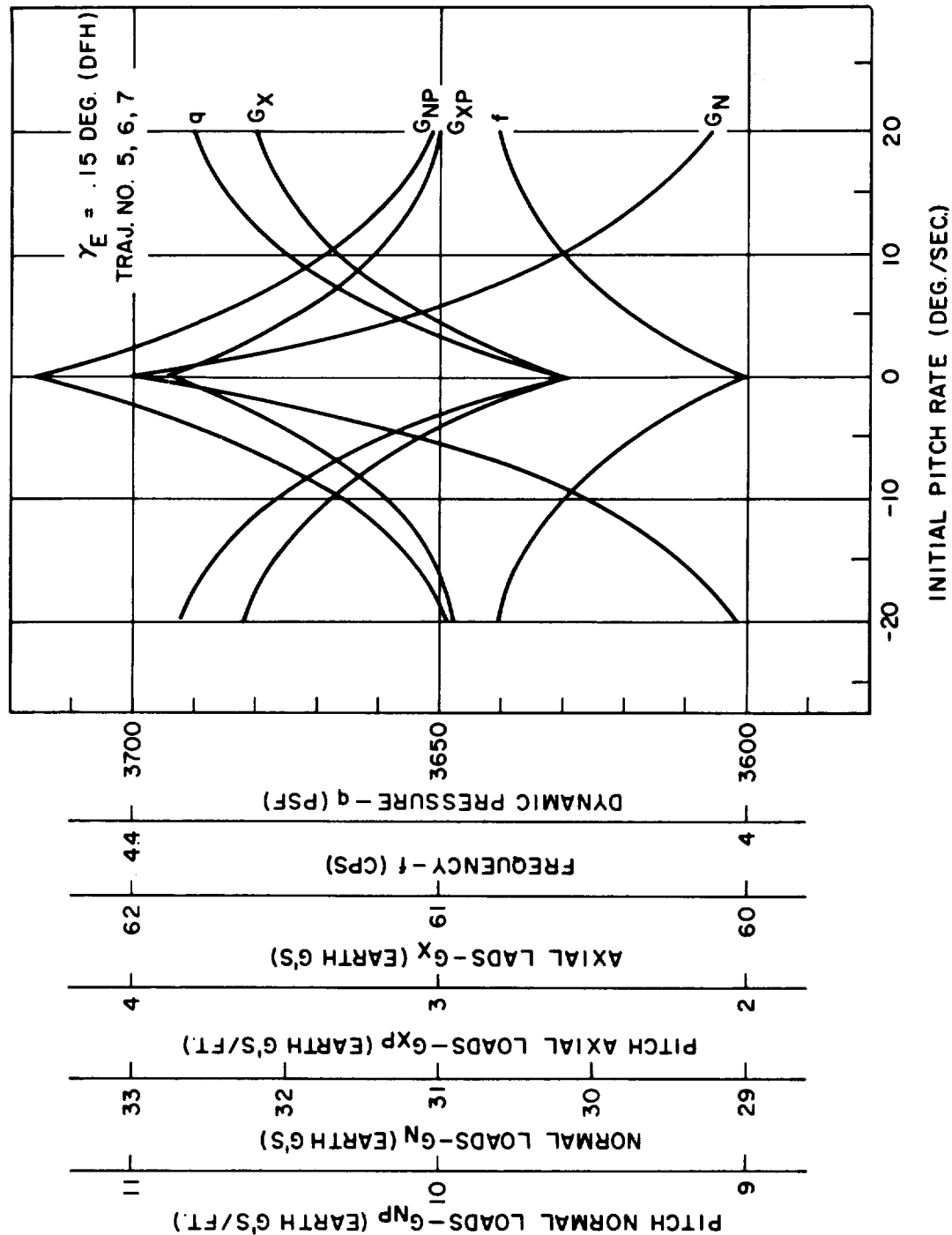


Figure 1.36. Peak Conditions as Functions of Initial Pitch Rate

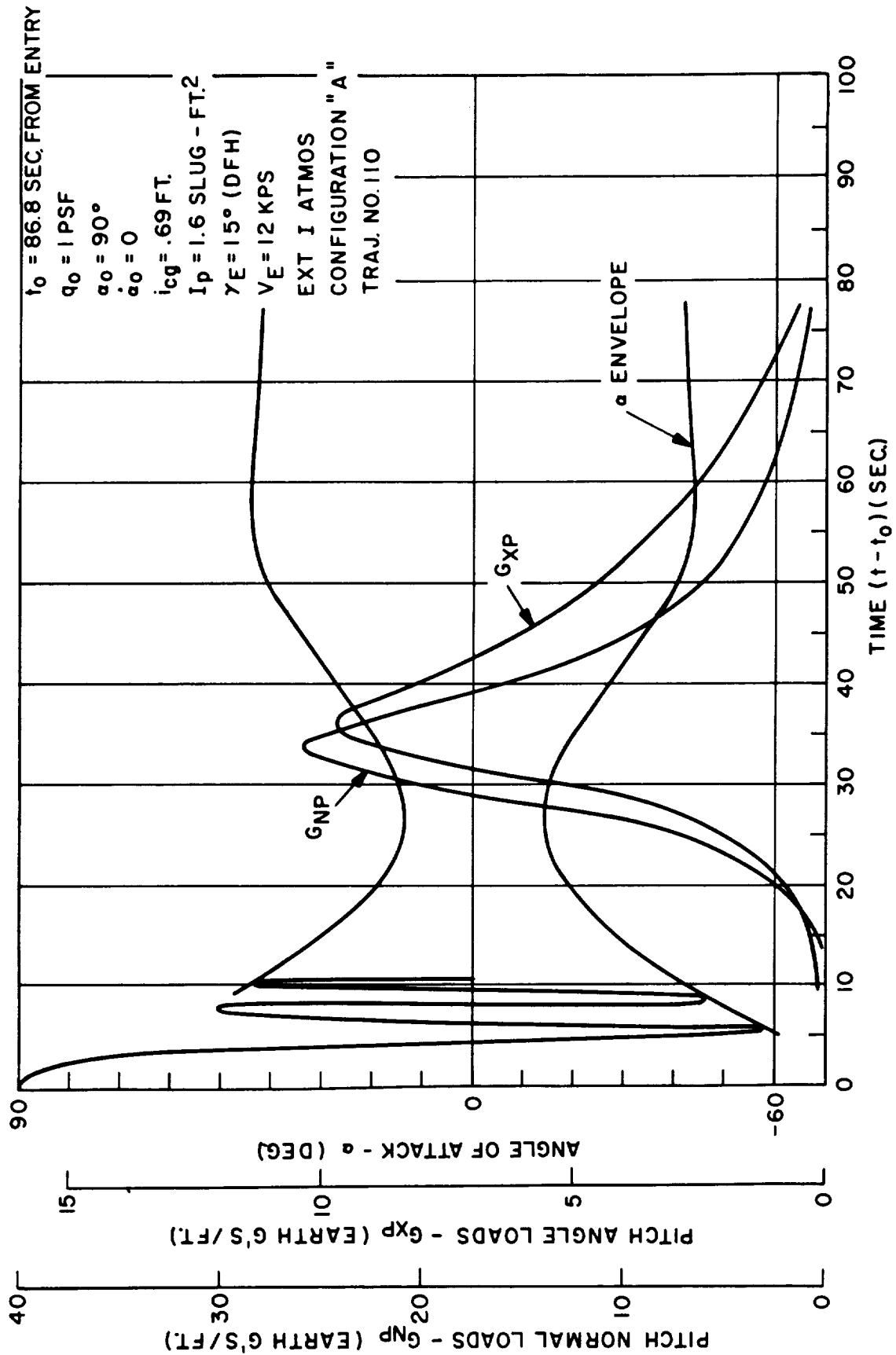


Figure 1.37. Time History of 3° Entry Traj. #110

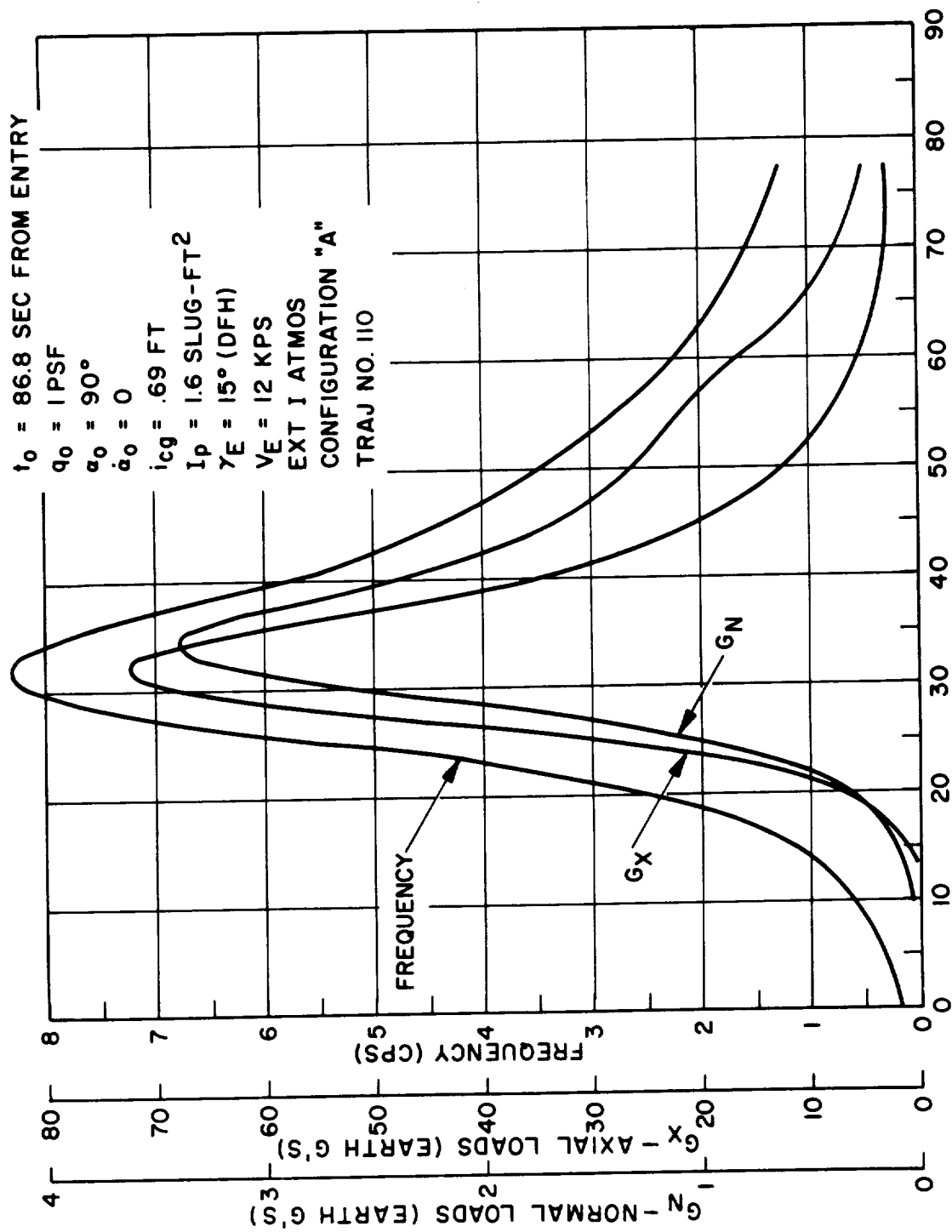


Figure 1.38. Time History of 3° Entry Traj. #110 (Concluded)

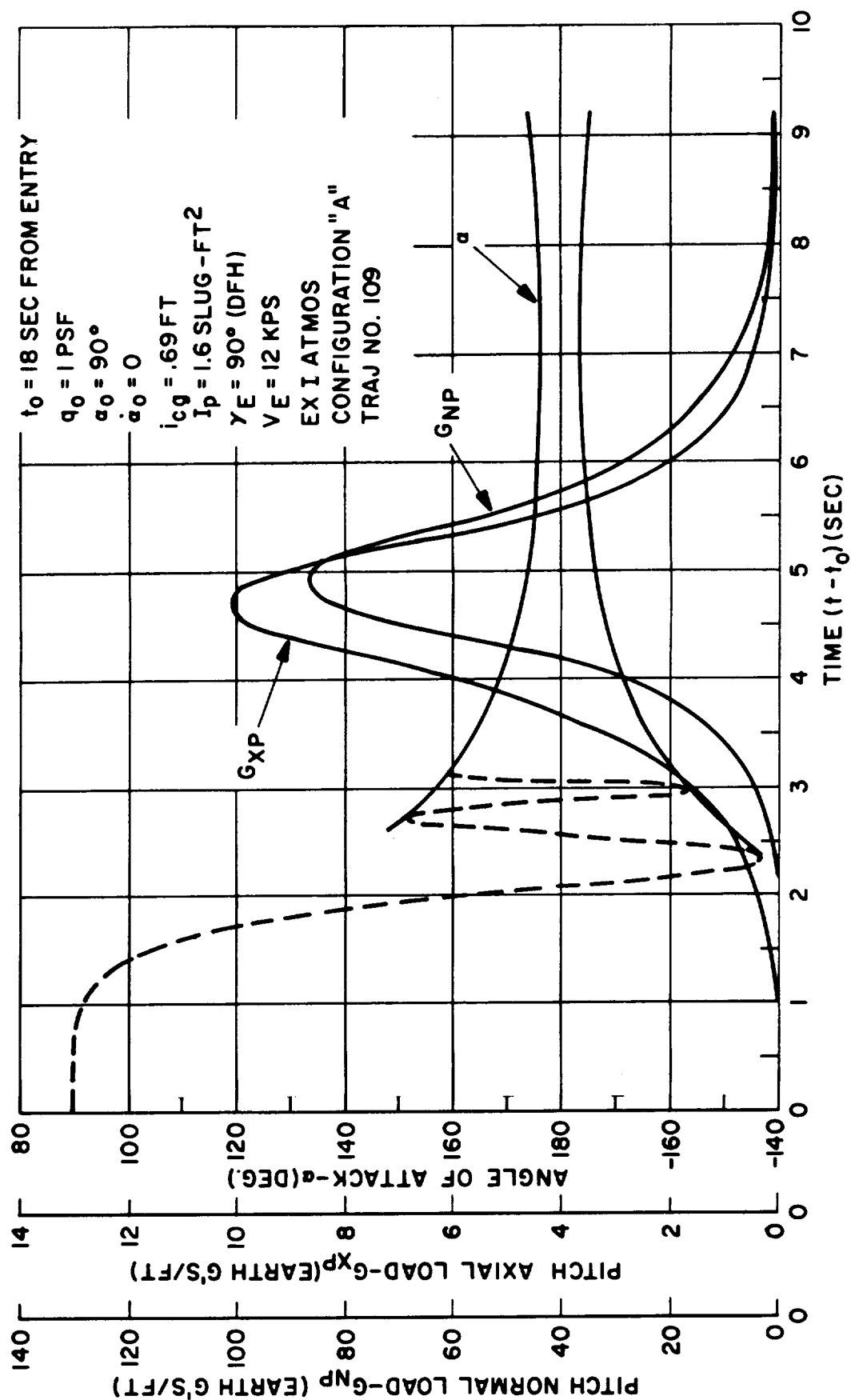


Figure 1.39. Time History of 3° Entry Traj. #109

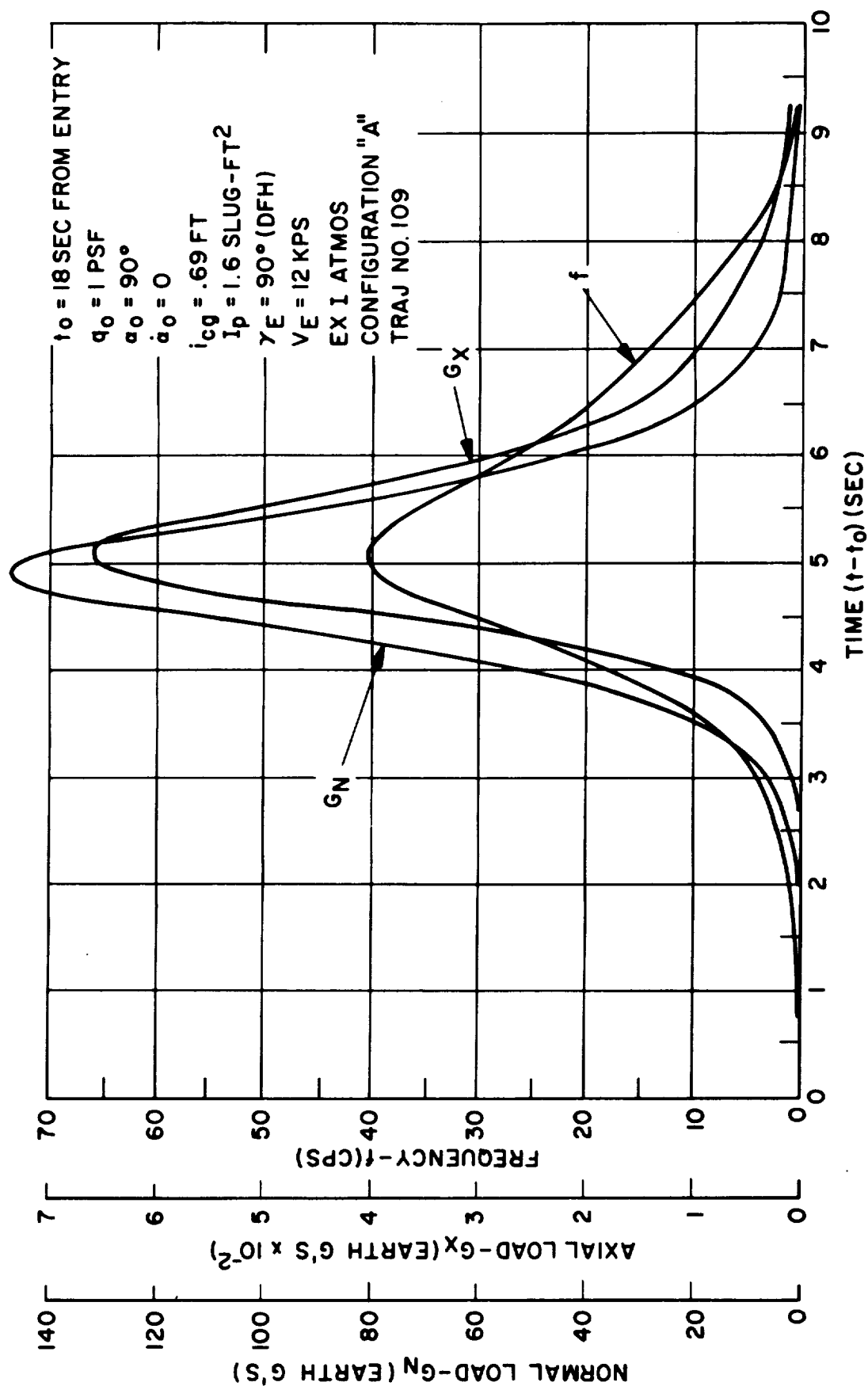


Figure 1.40. Time History of 3° Entry Traj. #109 (Concluded)

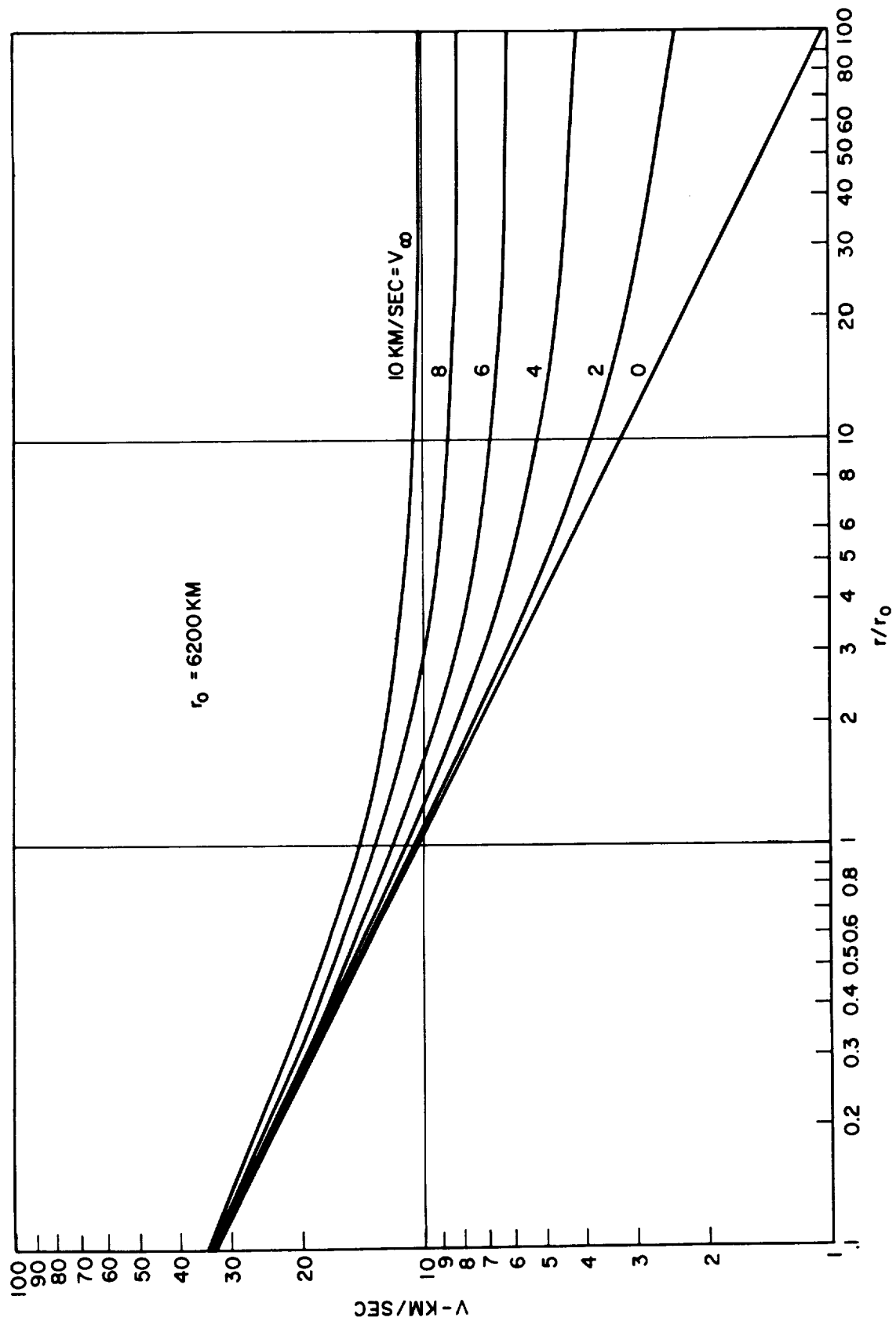


Figure 1.41. Approach Velocity

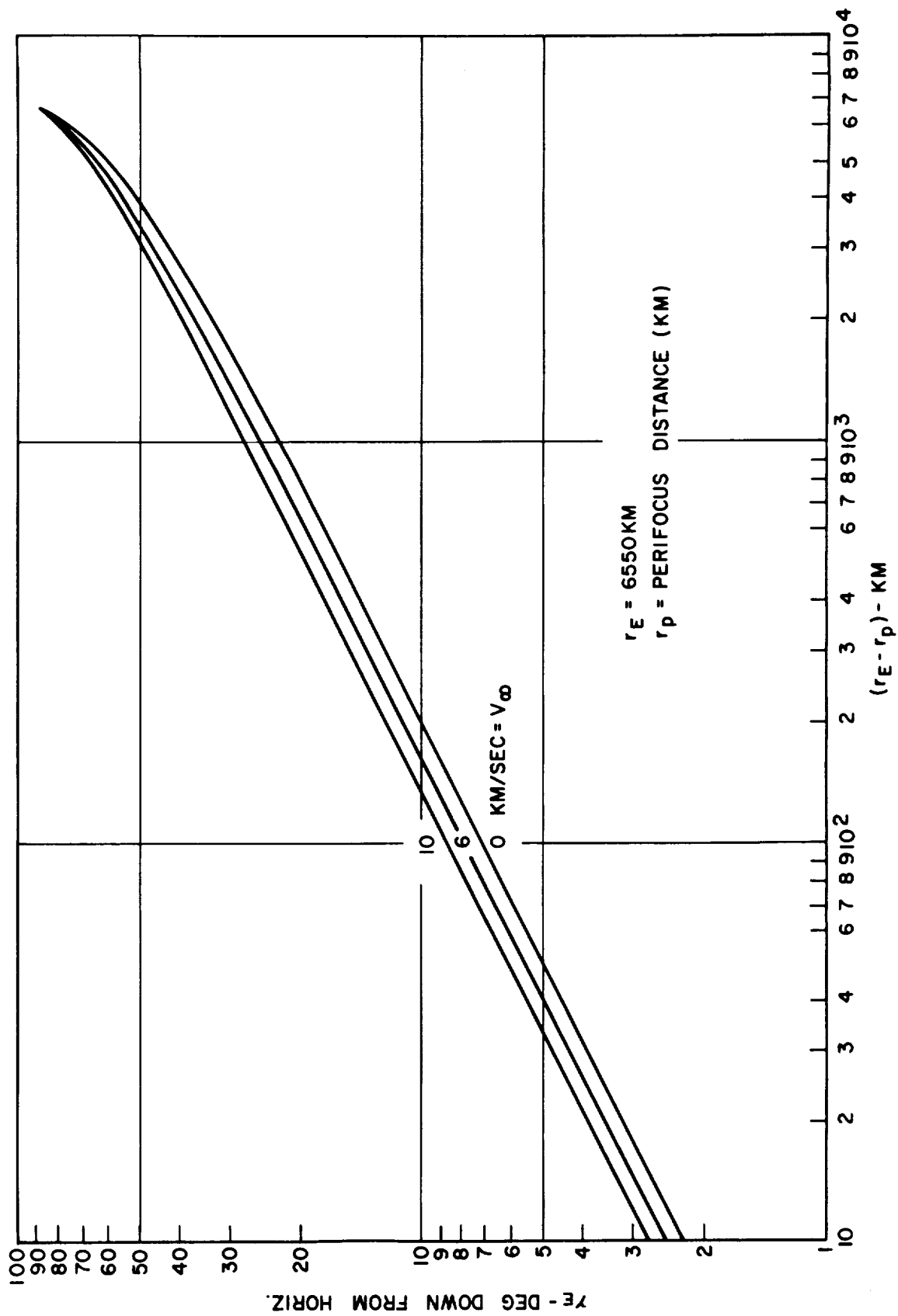


Figure 1.42. Entry Path Angle versus Vacuum Perifocus

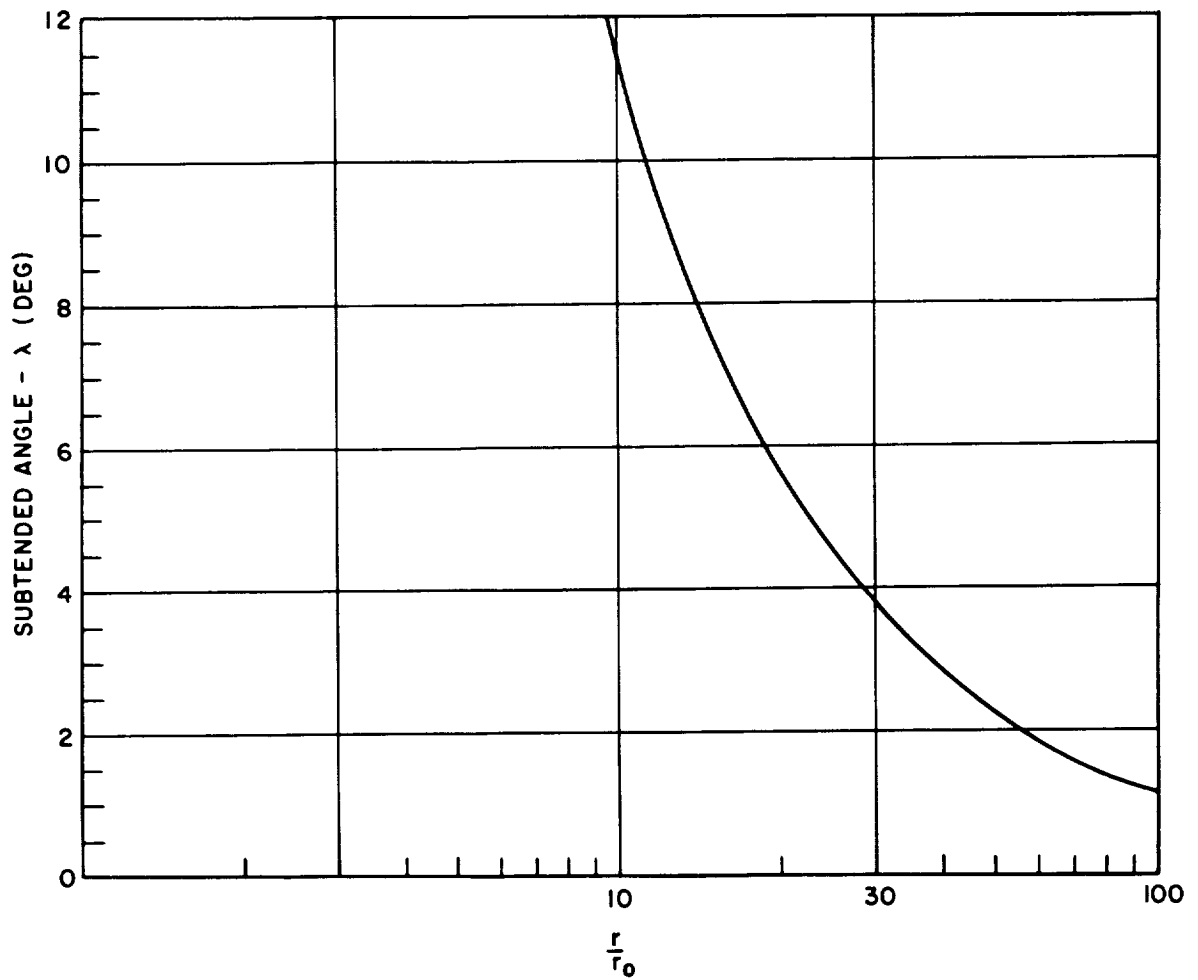
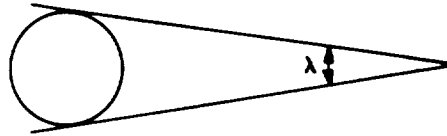


Figure 1.43. Angle Subtended by Venus

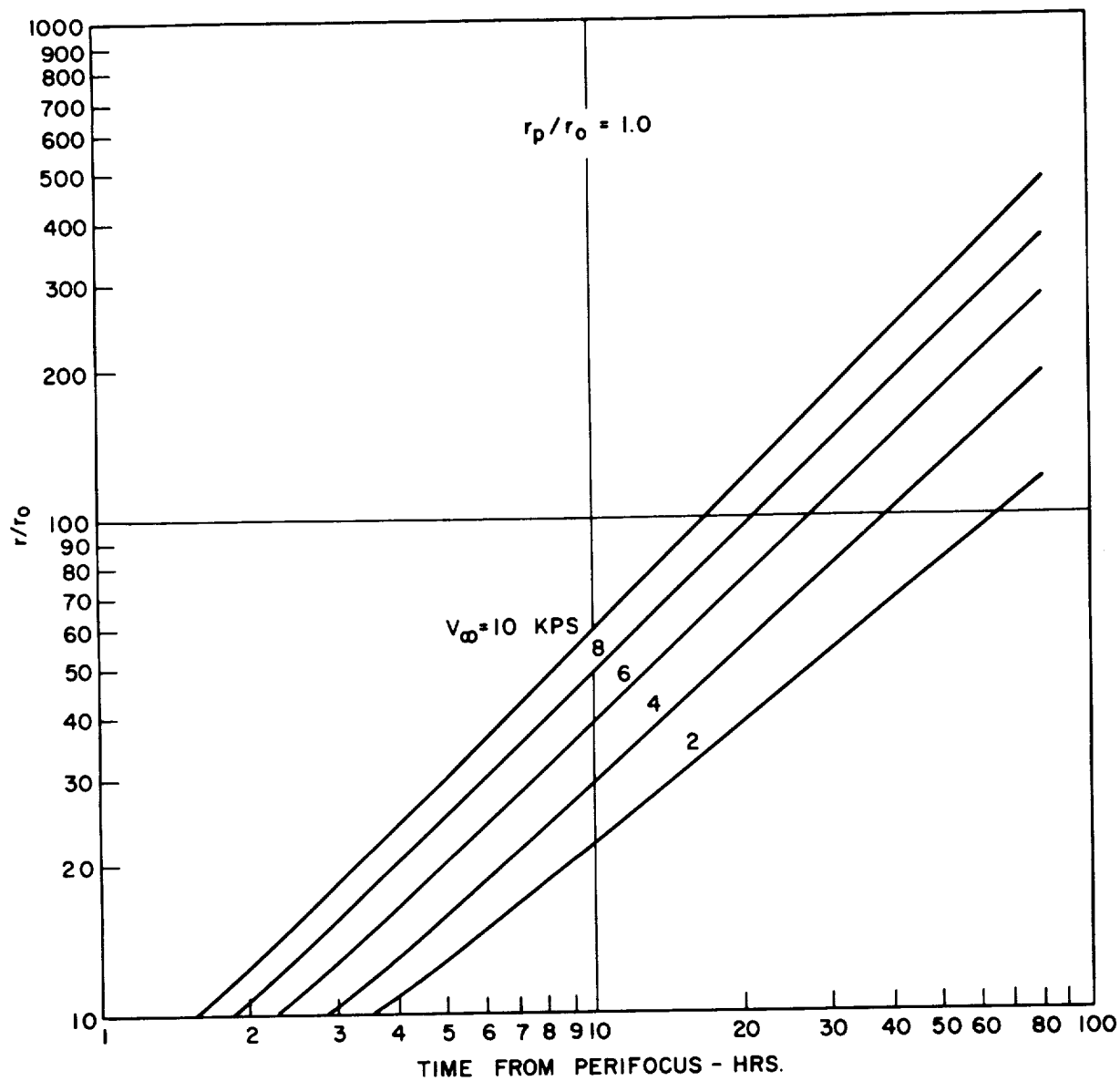


Figure 1.44. Time to Perifocus

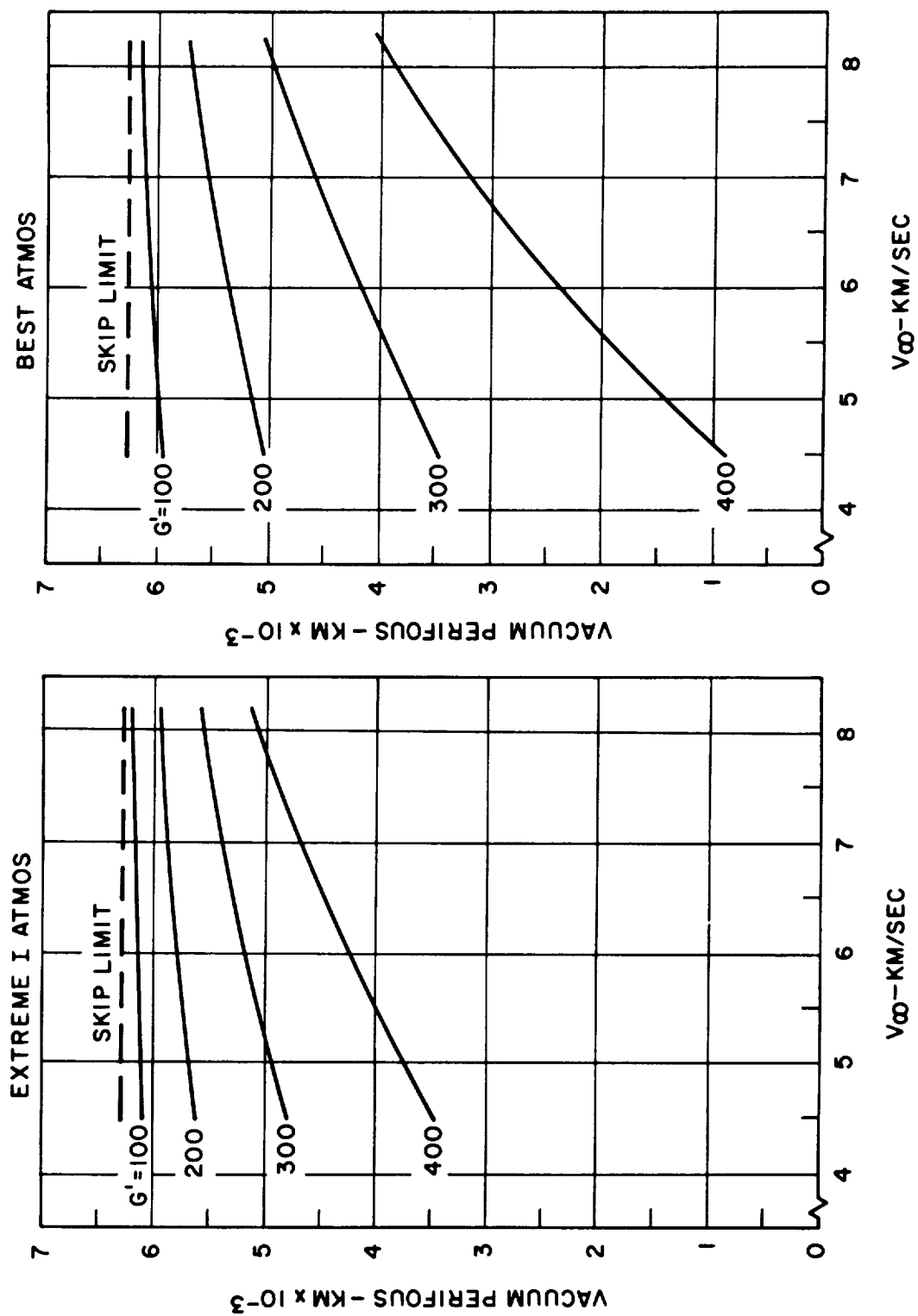


Figure 1.45. Linear Corridor

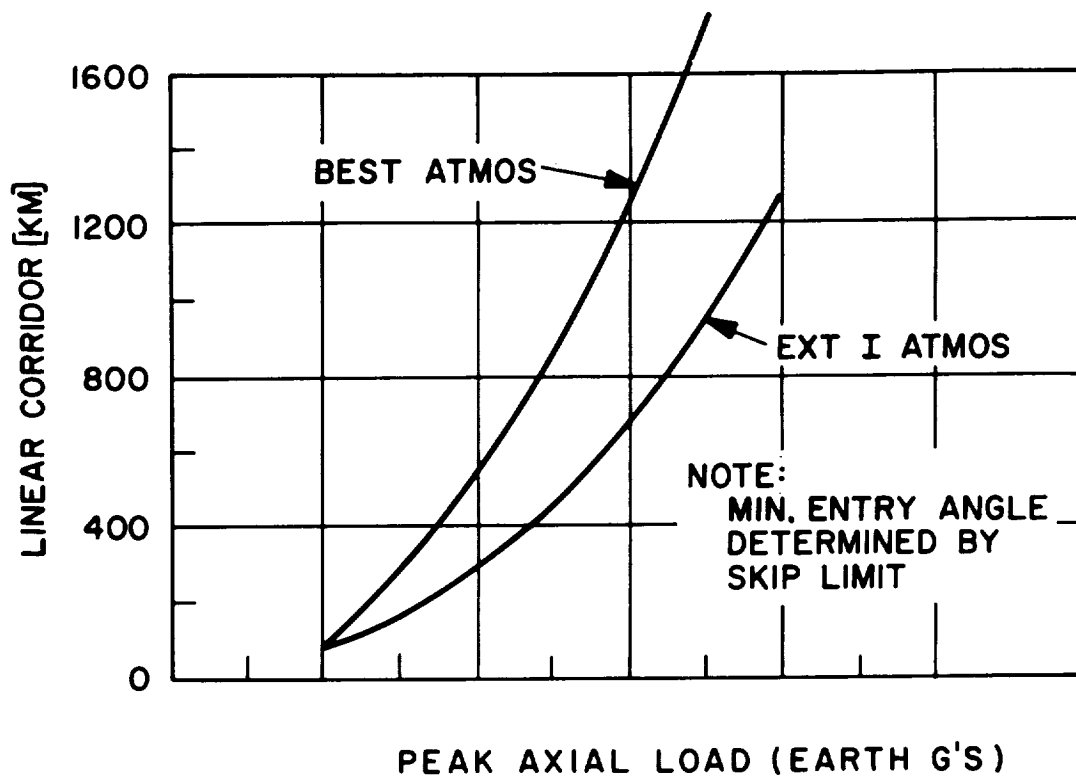


Figure 1.46. Linear Corridor, Skip Limit & $V_{\infty} = 5$ km/sec

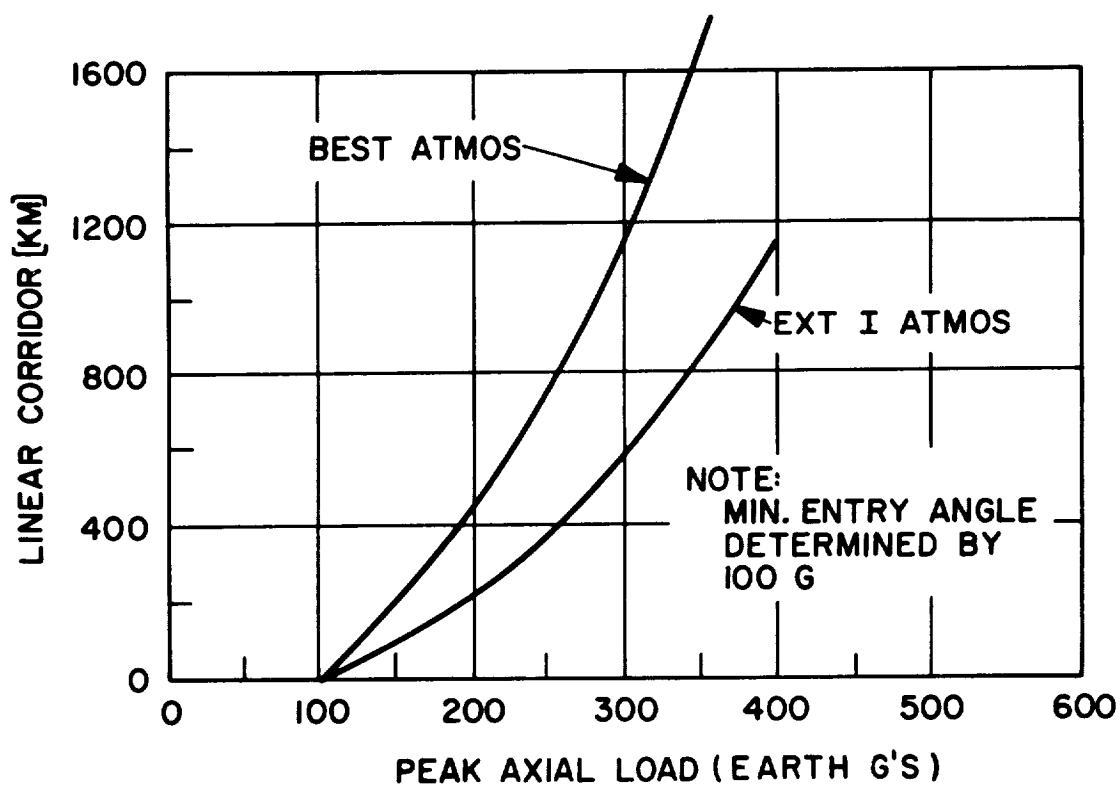


Figure 1.47. Linear Corridor, 100g Limit & $V_{\infty} = 5$ km/sec

$h_E = 350 \text{ KM}$
 $r_0 = 6200 \text{ KM}$

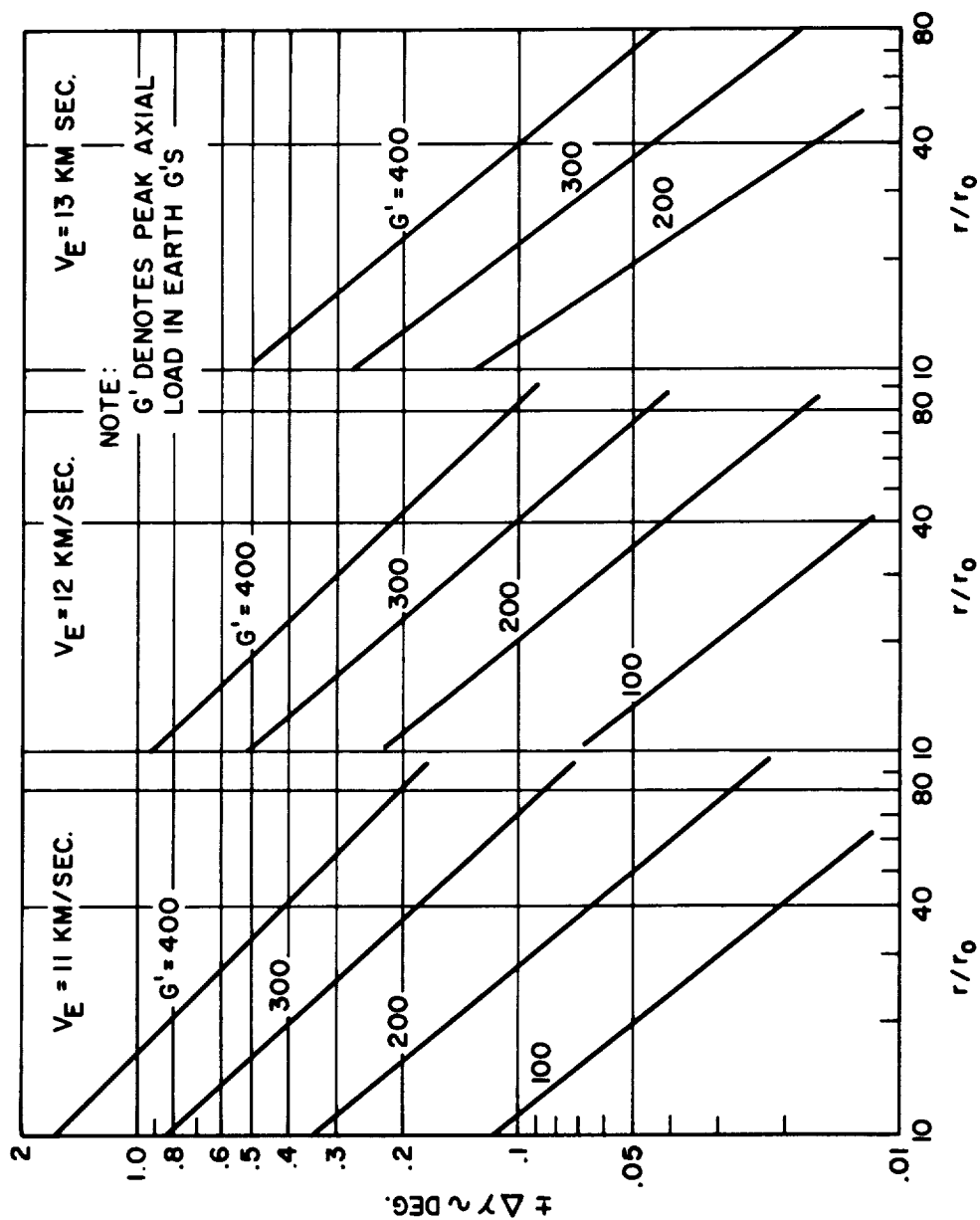


Figure 1.48. Venus Approach Guidance Accuracy, Extreme I Atmosphere

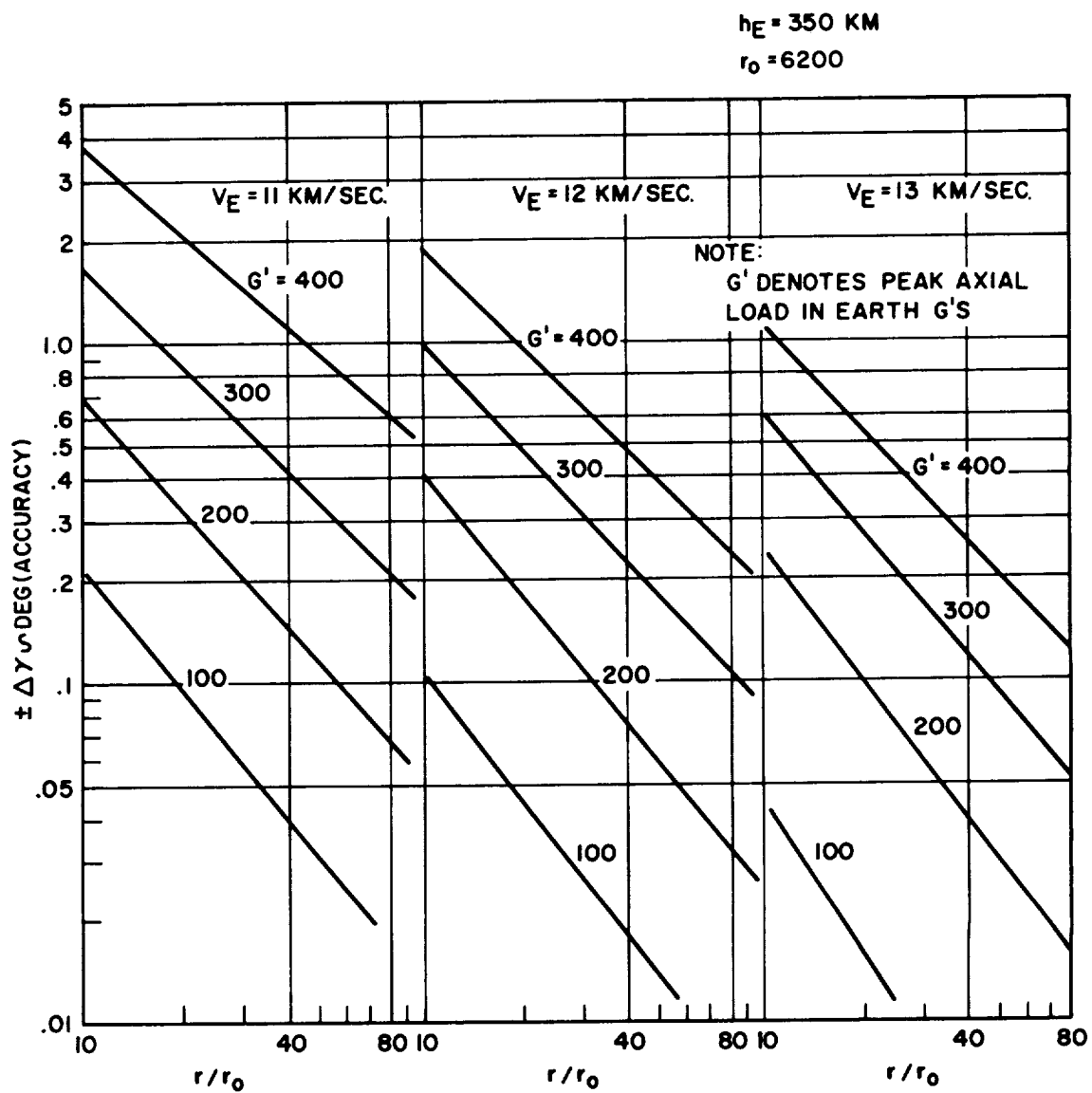


Figure 1.49. Venus Approach Guidance Accuracy, Best Atmosphere

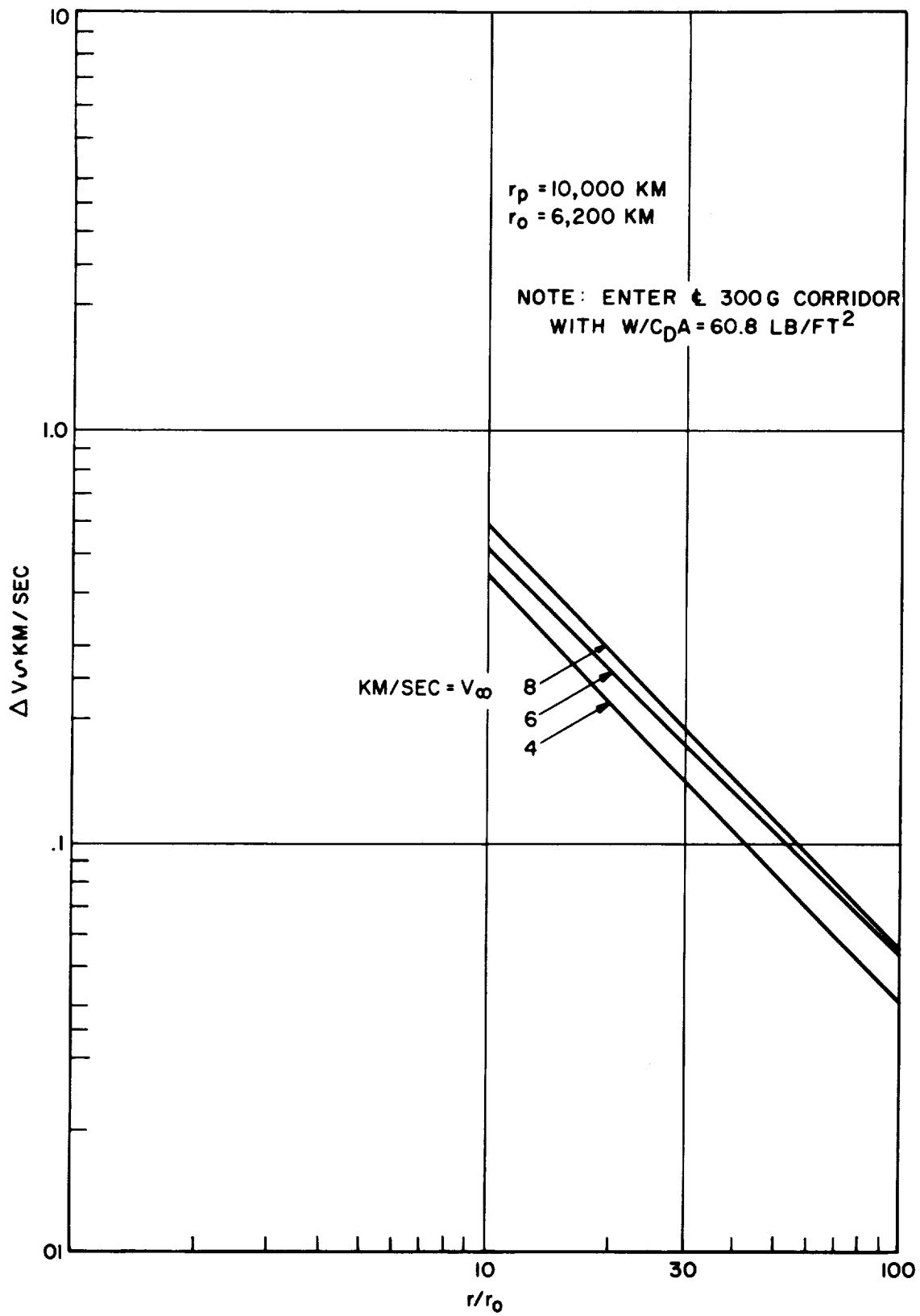


Figure 1.50. Retro-Rocket Requirements, Bus $r_p = 10,000 \text{ Km}$

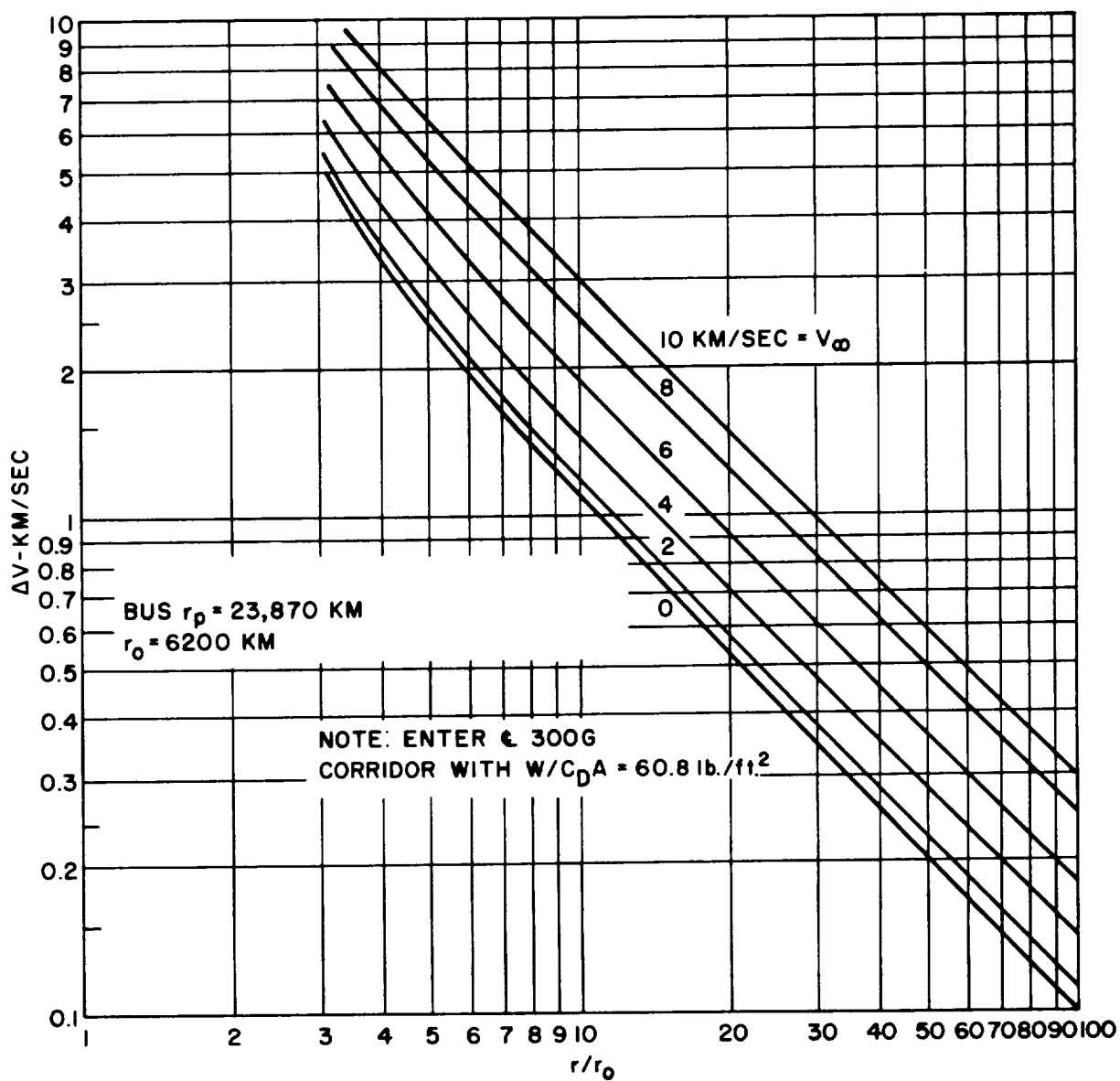


Figure 1.51. Retro-Rocket Requirements, Bus $r_p = 23,870$ Km

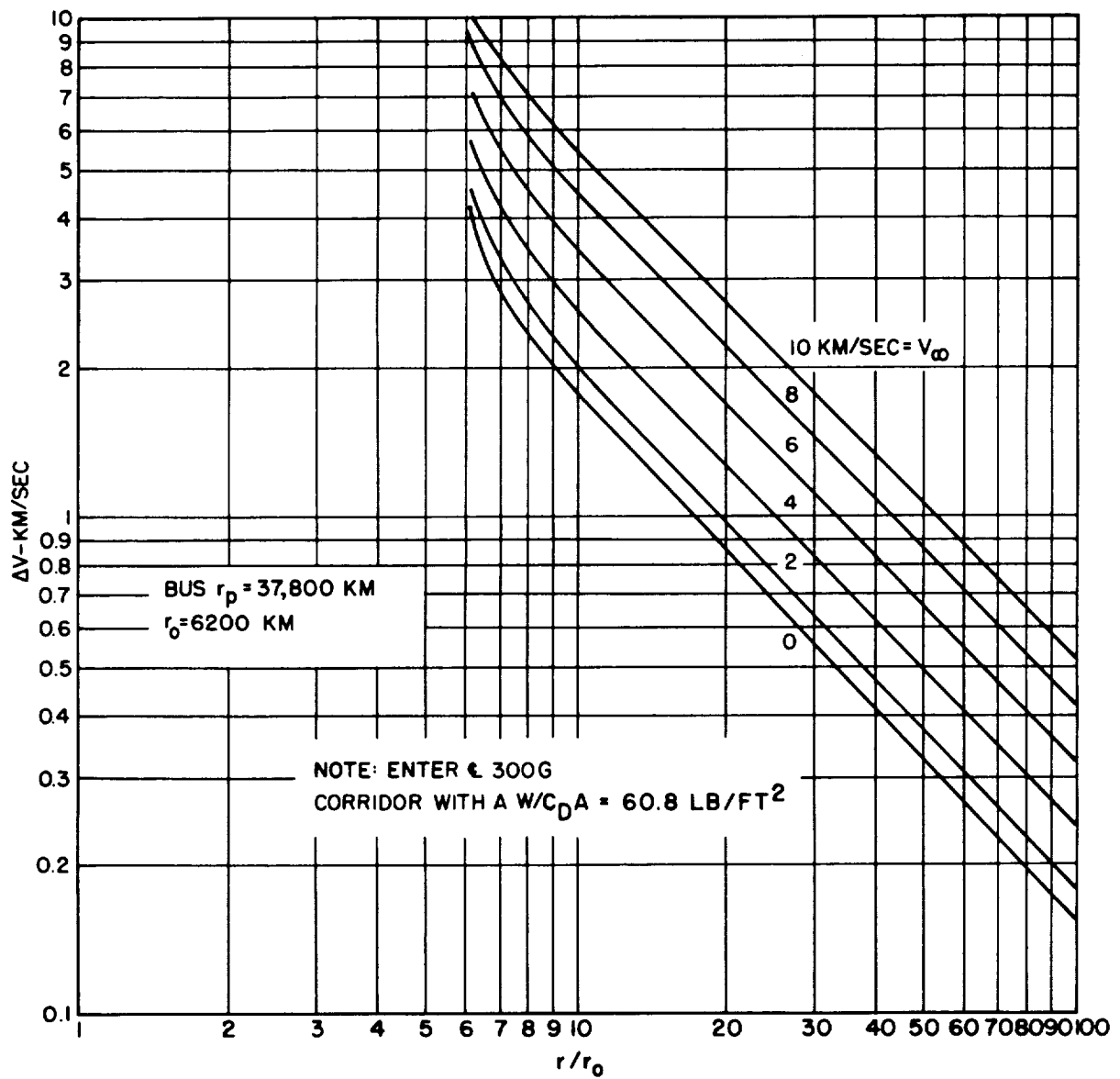


Figure 1.52. Retro-Rocket Requirements, Bus $r_p = 37,800 \text{ Km}$

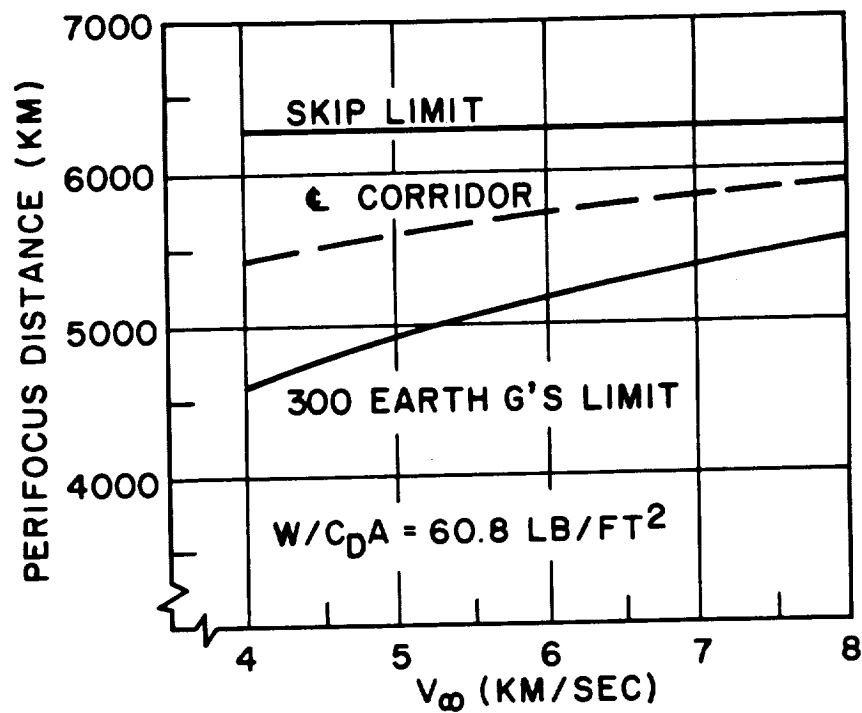


Figure 1.53. 300g Linear Corridor

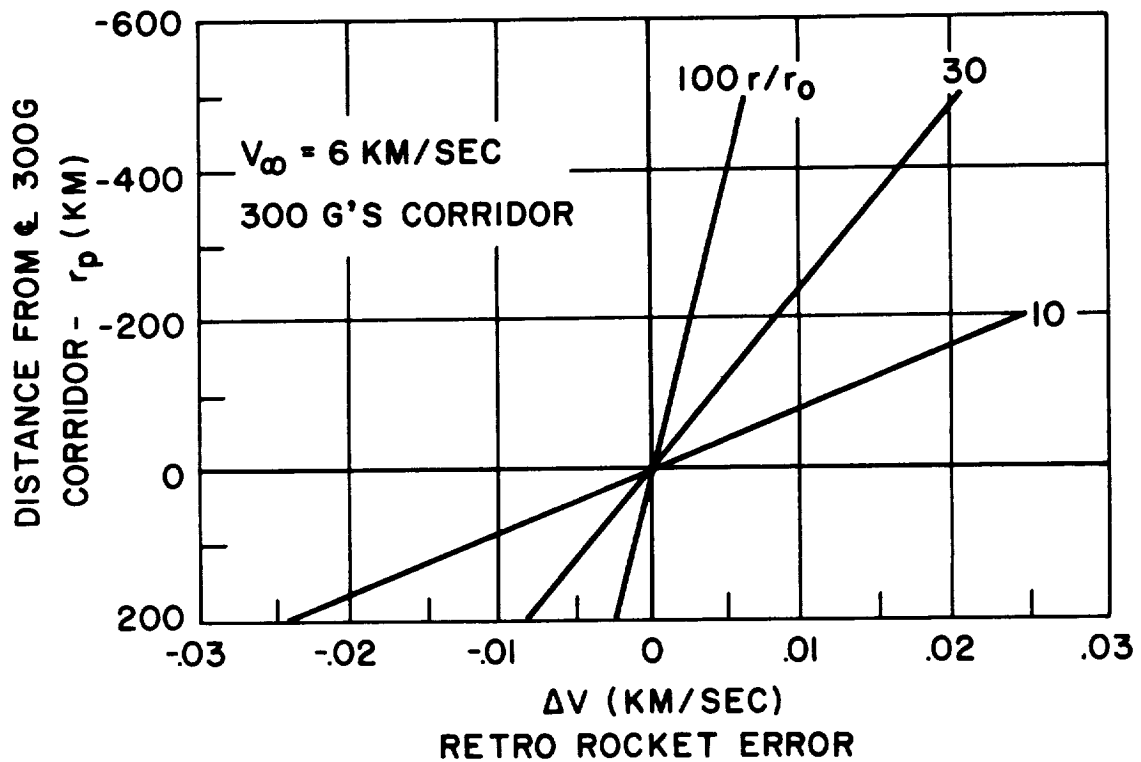


Figure 1.54. Perifocus Error versus Retro-Rocket Error

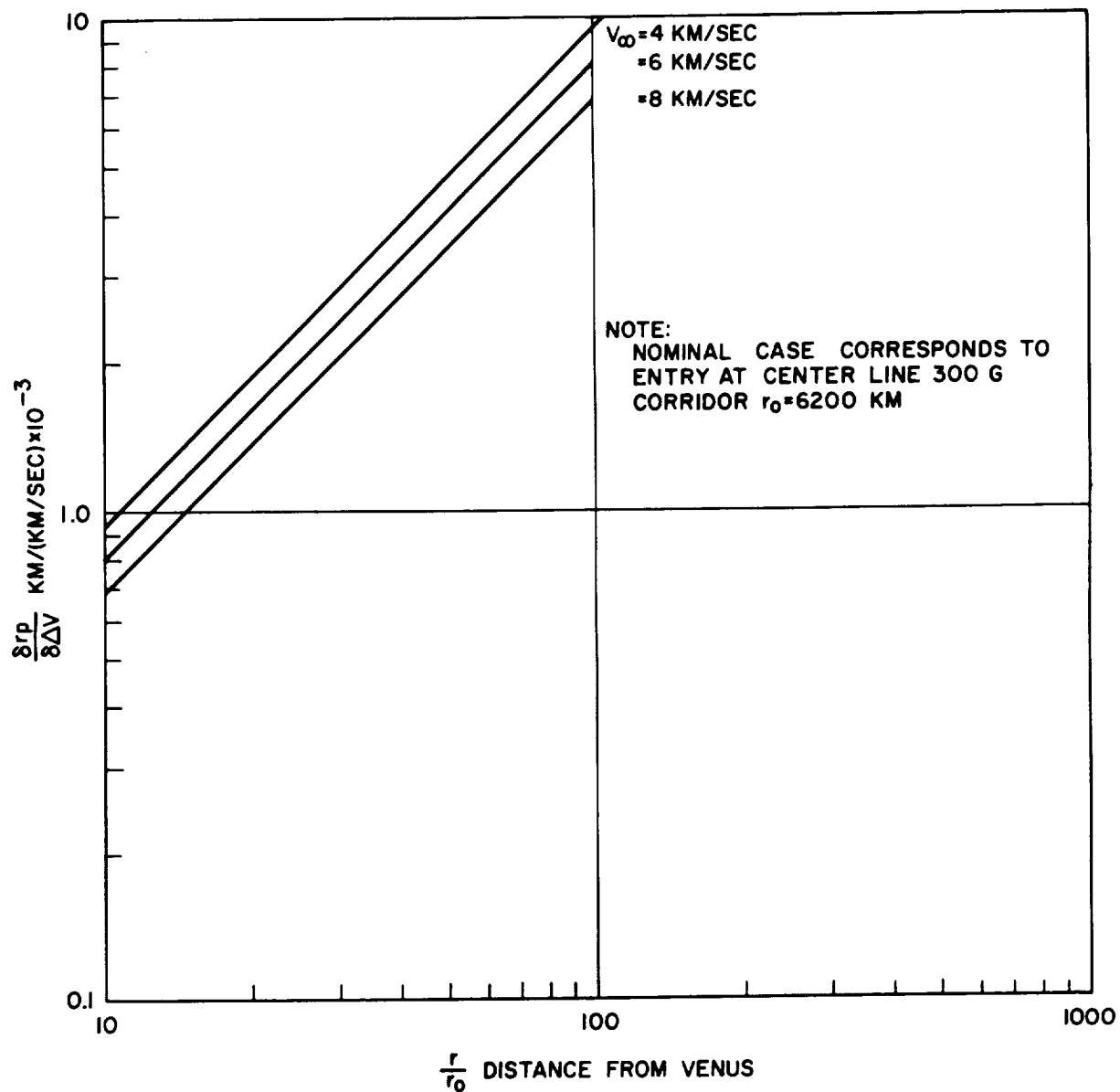


Figure 1.55. Perifocus Sensitivity to Retro-Rocket Velocity Error

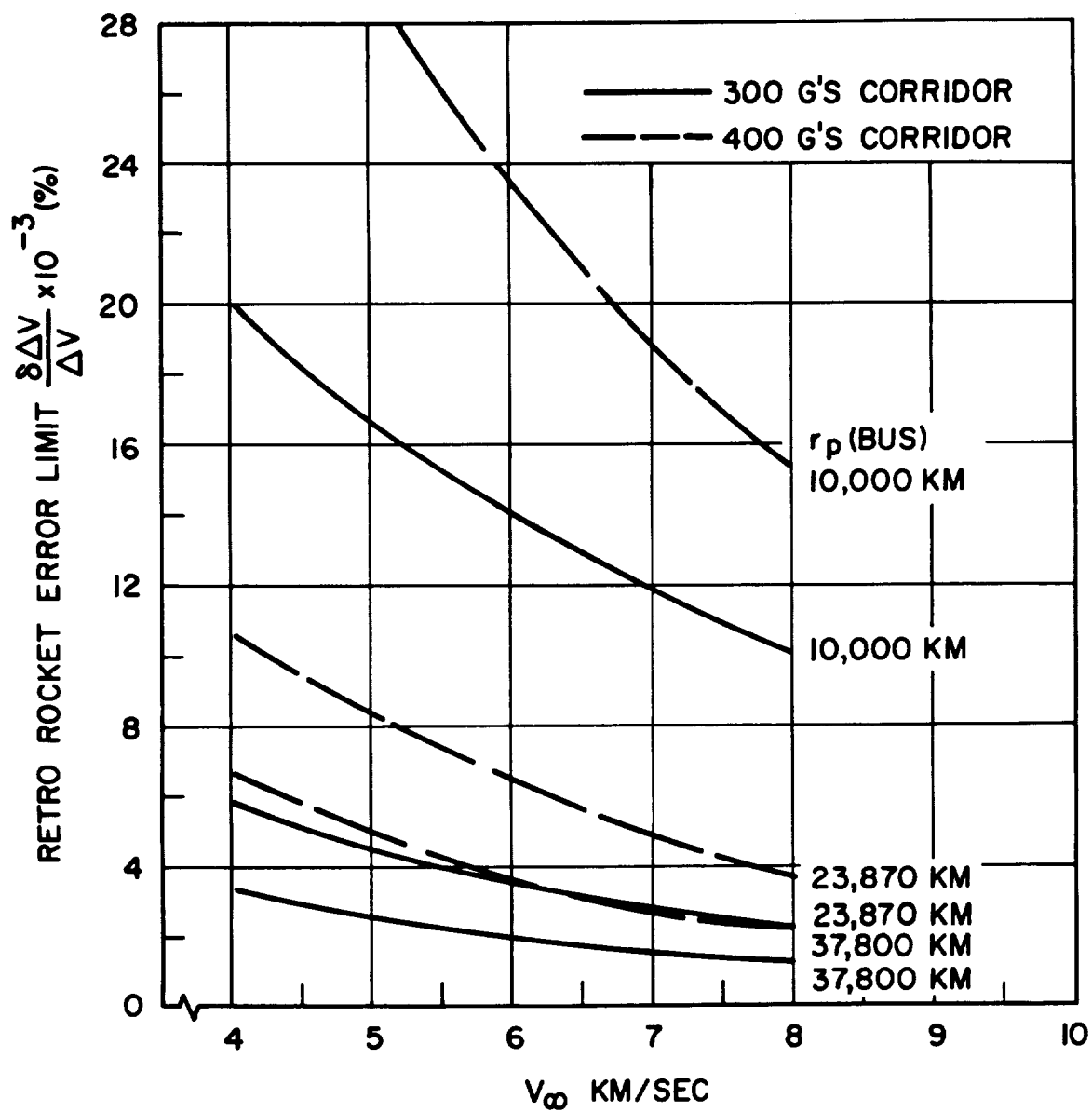


Figure 1.56. Retro-Rocket Accuracy Required

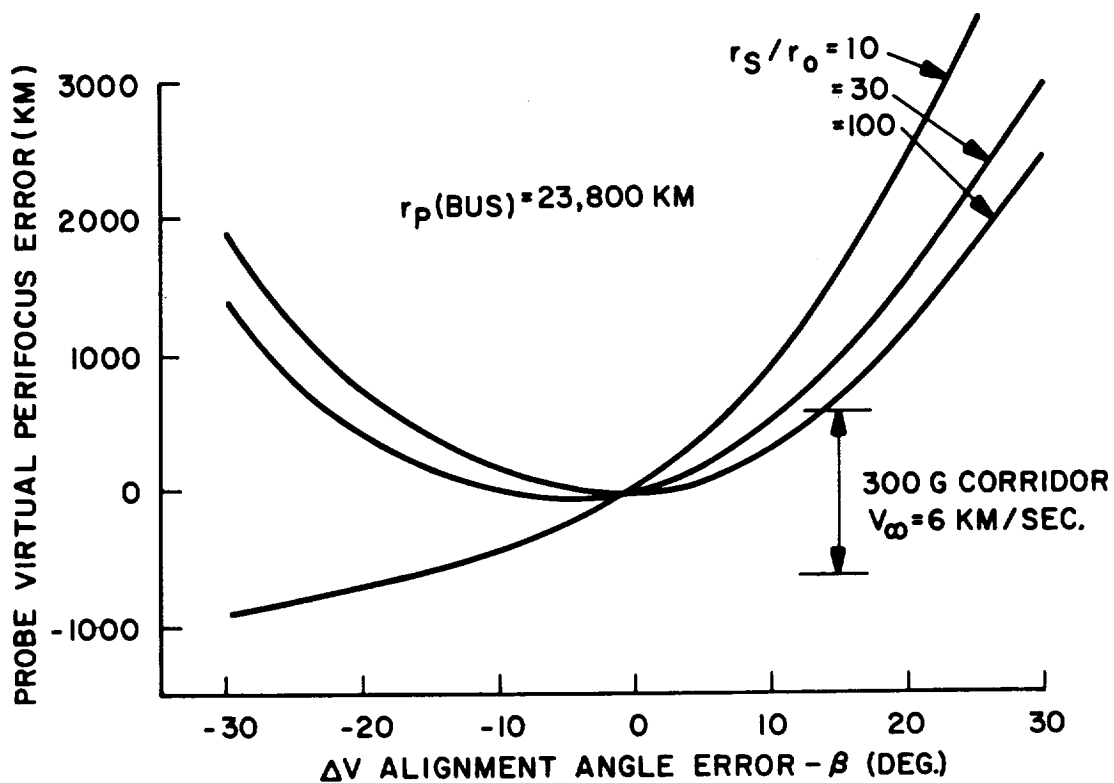


Figure 1.57. Perifocus Sensitivity to Retro-Rocket Alignment Error,
Bus $r_p = 23,800 \text{ km}$

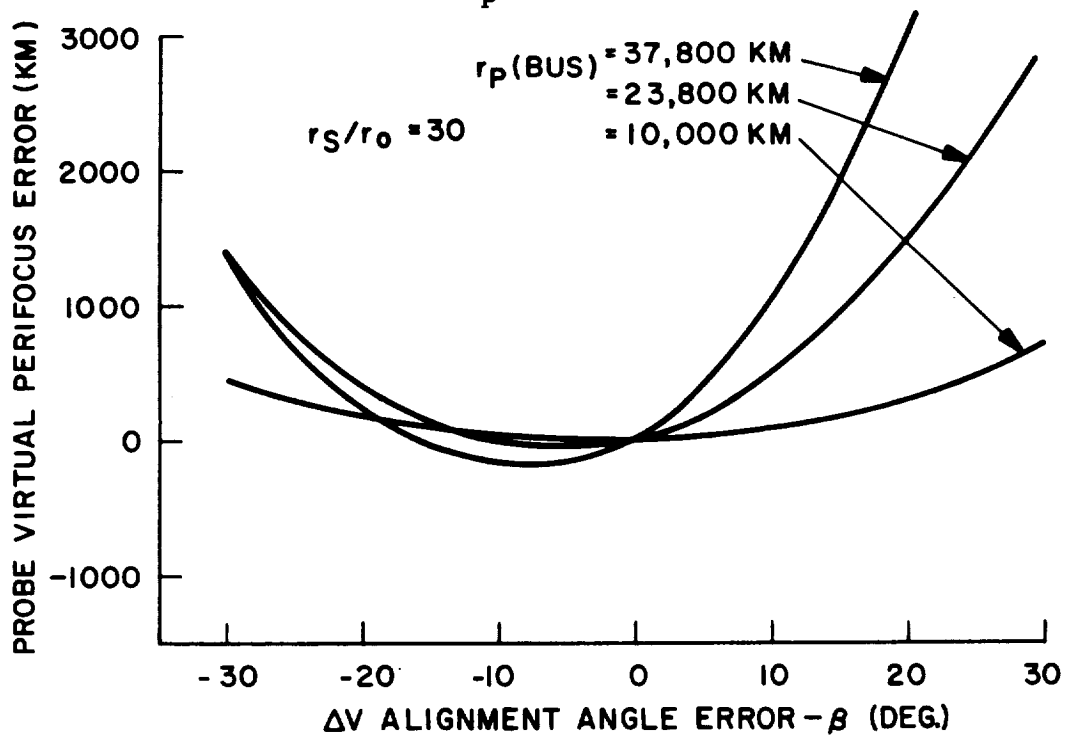


Figure 1.58. Perifocus Sensitivity to Retro-Rocket Alignment Error $V_\infty = 6 \text{ km/sec}$

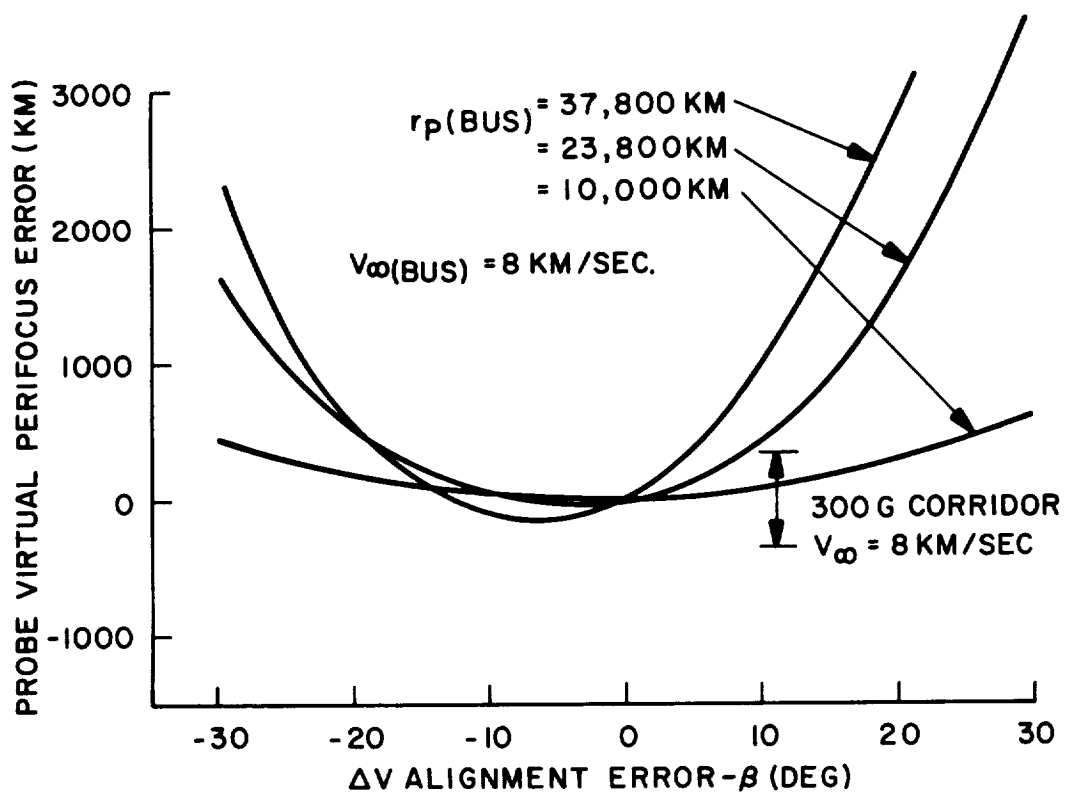


Figure 1.59. Perifocus Sensitivity to Retro-Rocket Alignment Error, $V_{\infty} = 8$ km/sec

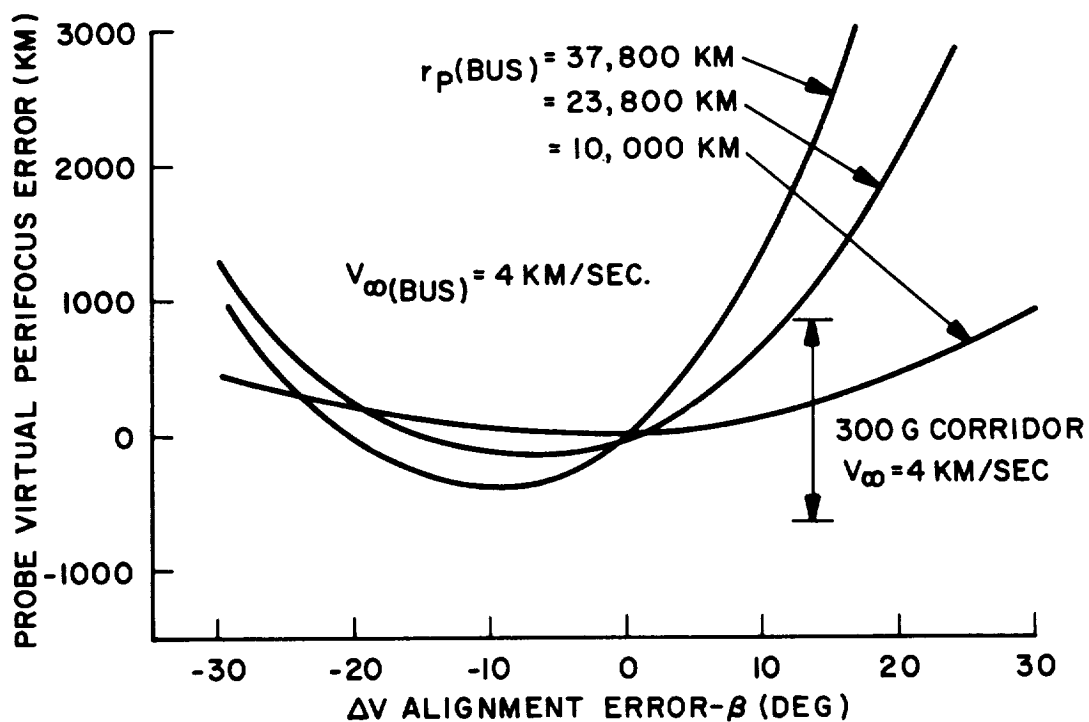


Figure 1.60. Perifocus Sensitivity to Retro-Rocket Alignment Error, $V_{\infty} = 4$ km/sec

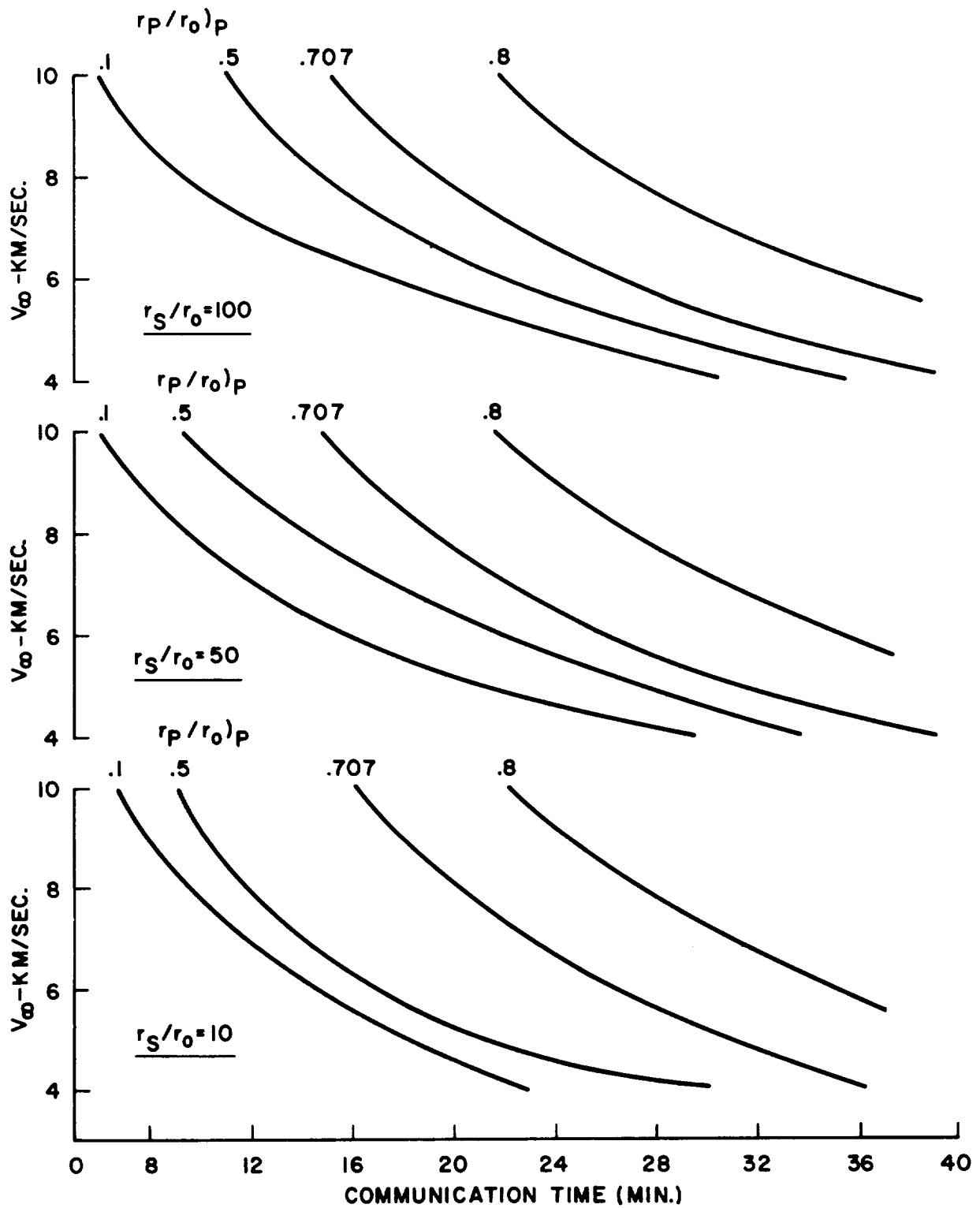


Figure 1.61. Probe to Bus Communication Time, Bus $r_P/r_0 = 2.0$

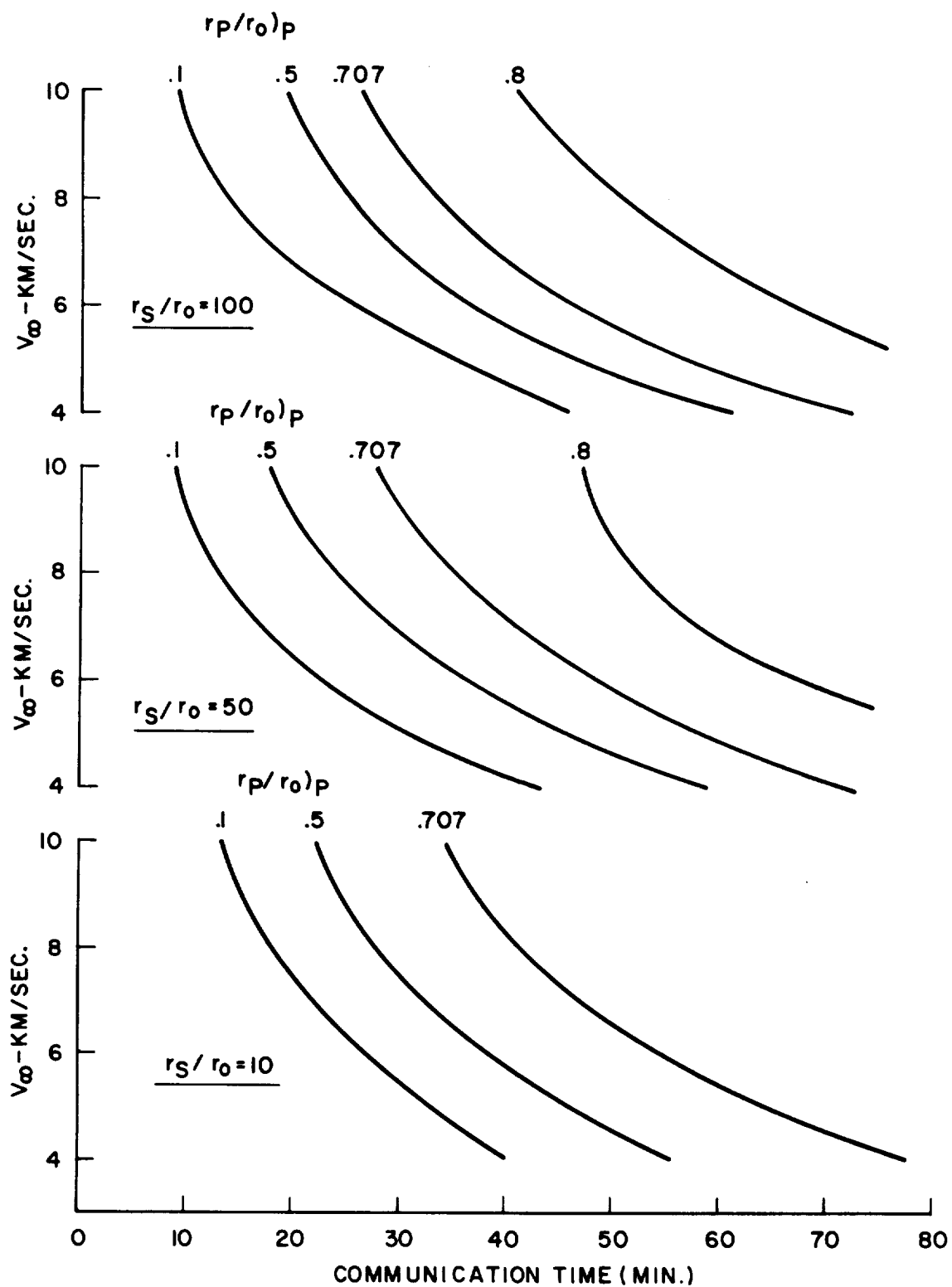


Figure 1.62. Probe to Bus Communication Time, Bus $r_p/r_o = 3.0$

2.1 INTRODUCTION

The primary objective of a Venus-Mars Entry Capsule is to gain knowledge about the planet's atmospheric environment. For this reason it is of particular significance to consider what means will be used to gain knowledge about the planetary atmosphere and to examine both the requirements placed on the capsule design by the measurement techniques and the type of information that can be expected to be obtained.

The purpose of the instrumentation section of this study is to examine techniques for measuring the primary meteorological unknowns, namely pressure, temperature and density as a function of altitude and to insure compatibility between capsule design and likely measurement techniques. It is not the objective of the instrumentation study to select the method by which the above cited parameters, as well as several auxiliary parameters, are to be measured, but rather it is its purpose to consider various techniques and to cite their merits and disadvantages.

The study was specifically required to consider techniques for measuring pressure, temperature and density under that altitude range during which the capsule is travelling at subsonic velocities. In addition, it was considered desirable to consider techniques for measuring the percentage of carbon dioxide in the Venus atmosphere, on the assumption that this and nitrogen were the major constituents present. Since the data is primarily measured as a function of time, while interpretation requires measurements as a function of altitude, it appeared necessary to consider techniques for establishing the altitude that the capsule is above the surface as a function of time. The most direct approach for this later purpose involves the use of a radar type altimeter and hence, a preliminary system design for such a device was carried out. In addition, since weight and power restrictions may preclude the use of an altimeter, techniques were investigated for determining altitude by indirect means, particularly by integrating velocity measurements. The indirect methods for establishing altitude requires a reference point which could either be the time of impact at the planet's surface - if the instrumentation and communication subsystems survive -

or (less desirably) the time at which a cloud layer is encountered. The altitude of cloud layers is of course, also of direct interest in the study of the meteorology of the planet and hence, some thought was given to a simple scheme for detecting the presence of clouds.

Ultimately, the output of this investigation will be utilized in conducting parametric analysis which will culminate in the selection of an appropriate instrumentation system and hence, it is necessary to list certain specific information with respect to the techniques for determining each unknown.

Specifically in the following sections we have considered for each unknown (1) types of measurement techniques available (2) choice of components available for each technique (3) measurement range and accuracy requirements (4) effects of environment: temperature, deceleration, vacuum (5) calibration and data correction requirements as a function of instrument reliabilities and system redundancy (6) auxiliary measurements required, such as supply voltages, sensor temperatures (7) vehicle interactions: holes or windows required, thermal control and stabilization and (8) basic instrument parameters: weight, volume and power requirements.

The results of the study are listed in summary form in the following section.

Succeeding sections consider measurement requirements, a typical instrument subsystem, details of pressure, temperature, density, carbon dioxide measurements, molecular scattering, velocity measurements, a radar altimeter and cloud detection.

A final section considers some hypersonic regime measurements that could be performed to aid in the design of future entry capsules.

2.2 SUMMARY

The instrumentation systems pertinent to a capsule designed for meteorological investigations of the planet Venus have been examined. Primary attention was given to the principal variables of atmospheric pressure, density and temperature. Secondary parameters for which instrumentation was considered included carbon dioxide density, and the presence and type of clouds that might be encountered. Techniques for measuring altitude and velocity - or elapsed distance - were investigated from the viewpoint of relating measurements performed as a function of time into data as a function of altitude above the planet's surface. All the meteorological parameter measurements were considered primarily during that portion of the trajectory when the capsule was travelling at subsonic velocities since no feasible techniques were found for investigating the undisturbed properties of the atmosphere from a vehicle travelling at hypersonic speeds without seriously compromising the survival of the capsule. It was shown from capsule parameter and trajectory analysis that in all cases it would be possible to carry-on subsonic measurements at altitudes corresponding to pressures of 0.7 atm. (40 km. for the "best" atmosphere model) and that for a low ballistic parameter capsule on a grazing entry trajectory measurements could begin as high as 0.015 atmospheres (65 km. altitude, for the "best" atmosphere model).

Hypersonic measurements were included to the extent required for capsule design and performance evaluation.

The following techniques were investigated in some detail:

Pressure sensors: Bourdon tube and diaphragm types, with various kinds of transducers (potentiometer, strain gage and reluctance type).

Density sensors: Attenuation and backscattering of alpha and beta particles and of gamma rays.

Temperature sensors: Thermistors and resistance thermometers, using open ports and also using "vortex tubes" or other devices for eliminating velocity effects.

Carbon dioxide density: Infrared absorption and thermal conductivity.

Altitude and Velocity: Radar altimeter, velocity revolution and/or revolution per minute indicator, differential static temperature - total temperature measurements, differential static-pressure-pitot pressure measurements.

In addition, the feasibility of performing line-of-sight measurements by observing the sun from the vehicle and studying carbon dioxide absorption and molecular scattering as a function of altitude was considered. This study was discontinued as impractical due to low probability of seeing the sun, possibility of cloud obscuration effects and excessive weight penalties.

Each technique was examined from the aspects of measurement accuracy, reliability, compatibility with vehicle environment (particularly g-forces and ambient temperature), and minimum power and weight requirements.

Consideration was given to the effects of individual sensor failure on interpretation of data from other sensors, and redundancy/reliability was maximized for those sensors whose measurements were deemed most essential.

A brief section was included considering the relative importance of measurements of different types of parameters from a meteorological viewpoint, as a basis for trade-offs if telemetry, power or weight limitations did not permit performing all measurements from a single capsule. A cursory look was taken at the interaction of telemetry capacity and quantity and accuracy of measurement data obtained. In view of the fact that it appears that bit rates as high as 8/second can be obtained without additional power requirements on the transmitter system beyond what is required for the carrier, and in view of the fact that this data transmittal rate appears to give adequate sensor information, it appears that additional telemetry capacity would simply be used for additional redundancy, parallel rather than sequential sampling of redundant sensors, or a higher sampling rate for all sensors.

Additional telemetry would also be required if weight considerations would permit using the radar altimeter, and instrumentation to measure other parameters than those considered in this study.

A typical instrumentation system approach is given as illustration of the capabilities of the instrumentation system and the overall weight, power and telemetry requirements. The system considered has a weight of about six pounds, requires about 20 watts of power and an eight bit/second telemetry system.

Using the more satisfactory technique of measuring altitude by means of the radar altimeter would result in an instrumentation system weight of 20 pounds and a power requirement of 40 watts.

It should be noted that to obtain absolute altitude from elapsed distance (velocity) measurements requires time of impact as a fixed reference point. This requirement does not exist if an altimeter is employed.

2.3 TYPICAL INSTRUMENTATION PACKAGE

The instrumentation concepts evaluated during the course of this study have been assembled into a typical system in order to better illustrate over-all capabilities, as well as weight, power and telemetry requirements:

A) Temperature Sensors

T1: Resistance thermometer 150°K to $800^{\circ}\text{K} \pm 10^{\circ}\text{K}$

Weight: 0.1 lb. Power 2 watts

Telemetry: 5 bit resolution

T2: Resistance thermometer 300°K to $700^{\circ}\text{K} \pm 6^{\circ}\text{K}$

(2 units) Weight: 0.2 lbs. Power 4 watts

Telemetry: 5 bit resolution, two units sampled alternately

T3: Thermistor 220°K to $320^{\circ}\text{K} \pm 2^{\circ}\text{K}$

(2 units) Weight: 0.1 lb. Power 1 watt

Telemetry: 5 bit resolution, two units sampled alternately

B) Pressure Sensors

P1: 0 - 2 psi (two units) total weight: 0.1 lb.

P2: 0 - 10 psi (two units) total weight: 0.1 lb.

P3: 0 - 100 psi (two units) total weight: 0.1 lb.

P4: 0 - 1000 psi (one unit) total weight: 0.5 lbs.

All pressure sensors are of the potentiometer transducer type and accurate to \pm three per cent (4 bit resolution). Total power required \sim 1 watt

C) Total Density Sensors

D1 Range: 10^{18} - 5×10^{19} particles/cm³

D2 Range: 3×10^{19} - 10^{21} particles/cm³

Gamma backscattering using scintillation crystals and photomultiplier tubes as detectors could be used for density measurement. The different ranges are obtained by different degrees of detector collimation. The output of the photomultiplier is in pulse rate (digital) form and will be telemetered to 5 bit (\pm 1.5 per cent) resolution. The temperature of the detectors will be controlled and monitored.

Total Weight ~ 2 pounds

Total Power ~ 6 watts

D) Carbon Dioxide Density Sensors

C1 Range: $10^{17} - 5 \times 10^{18}$ particles/cm³

C2 Range: $3 \times 10^{18} - 1 \times 10^{20}$ particles/cm³

Infrared absorption measurements in the 15 micron spectral region will be used, the two ranges being obtained by different source detector distances. The signals will be telemetered to 5 bit resolution, to give adequate sensitivity at the low end of the scale. Since the thermistor radiation detector is likely to fail if operated at temperature above 50°C, it will be thermally insulated, its temperature will be monitored, and the bias current will be removed if safe temperature limits are exceeded.

It is planned to provide thermoelectric cooling to this detector if detail studies indicated that the 50°C limit will be exceeded before the capsule has descended to ten kilometer altitude.

Total Weight: 0.5 pound, Power: 2 watts

E) Velocity - Elapsed Distance Sensor

A propeller type sensor could be used, duplicate units being provided. The revolutions are recorded (digitally) by a magnetic pickoff and transmitted as r.p.s. (velocity) at velocities above 200 feet per second. In addition, the total number of revolutions is accumulated, and transmitted as "relative height" once the velocity has dropped to below 200 feet per second. Allowing for a maximum elapsed distance of 200,000 feet the data will be transmitted digitally to $\pm 1\frac{1}{2}$ per cent. The counter will start reading from zero again for larger elapsed distances.

Total Weight: 1 pound

Total Power: 4 watts

for 2 units

F) Cloud Detector

This device is simply envisioned as a small light source, filtered to around 6000A and a solid state light detector, located so that the "atmosphere" passes between them. A screen coated with material that becomes conducting in the presence of moisture is included to aid in the identification of possible water in clouds. It should be noted that indication of very dense clouds will also be given by the carbon dioxide density monitoring system, and that correlation of this with the device operating around 6000A would give some indication of cloud particle size.

Total Weight: 0.2 pounds

Total Power: 1 watt

G) Peak g - Sensors

G1: 0-800 g, located along velocity vector axis

5 bit resolution, will record peak g value

G2 and G3: 0-800 g located along the other two orthoganal axes of the vehicle.

Total Weight: 0.3 pounds

Total Power: 0.1 watts

Data will be stored and telemetered after end of blackout (mode 2).

Total information: 13 bits.

H) Ablation Sensors

Two locations are envisioned: One near stagnation point, and one along the 45° axis. Sensors will be located at eight depths, at each station. The associated electronics indicate the last sensor broken. Data will be stored and telemetered after end of blackout (Mode 2). Total information: 6 bits

Power Requirements: 10 watts for about 20 seconds.

I) Peak Temperature Sensors

Thermistors will be located at several critical points inside the capsule to indicate the peak temperature reached during entry.

Weight and Power: Negligible

Information will be stored and telemetered after blackout (Mode 2). Total information: 4 - 6 bits.

Over-All Requirements

Total Weight: ~ 6 pounds

Total Power: ~20 watts

All instrumentation is in the interior of the capsule, with the exception of the density sensor which is located near the surface.

The instrumentation system is based on a capsule design that permits measurements to begin at a pressure of about 0.01 atmospheres (corresponding to 200,000 feet for the "best" atmosphere), and hence, is designed to permit measurement of phenomena (low pressure, clouds) expected to occur at those altitudes. For designs which a priori exclude measurements until pressures of 0.1 atmospheres have been reached the Mode I operation is superfluous (see Section 24.3).

In addition, it is assumed that ten seconds after the vehicle has reached Mach 1, measurements can begin, that is that the required ports have been opened by that time.

The instrumentation system operates in three modes:

Mode 1: Initial until velocity is down to about 200 feet per second.

Mode 2: Retransmission of stored, hypersonic data.

Mode 3: Steady state mode.

In Mode I only data concerning temperature, pressure and velocity will be transmitted, but sampled every two seconds, with 5 bit accuracy. In addition the cloud sensor will operate at one bit accuracy.

The thermistor temperature sensors will be used. For pressure the 0-2 psi full scale sensors will be used at four bit accuracy switching to the 0-10 psi sensor as the upper end of the scale is reached. The fifth bit of information will be used to indicate which sensor is activated.

The "propeller" velocity meter will be used to determine velocity as a digital basis, and also to activate Mode 2. The velocity will be measured over a 0-800 feet per second scale, accurate to ± 12 feet per second. (five bit resolution.)

Mode II will be activated when the velocity drops to 200 feet per second with a backup timer activation, in case of "speedometer" failure.

In Mode II the stored data from the hypersonic measurements will be transmitted sequentially, the transmission being repeated once. The total information amounts to 24 bits, requiring six seconds for duplicate transmission at eight bits per second.

Mode III begins immediately after the hypersonic information has been transmitted. Information from all active sensors will be sampled at the rate of once every 1000 feet in altitude - to be compatible with an eight-bit per second telemetry system.

The pressure sensors P1, P2, P4 and the temperature sensors T2 and T3 will sequence as they reach full scale readings.

Temperature sensor T1 and pressure sensor P3 will be on continuously. The two ranges of carbon dioxide density and total density will be sampled alternately, that is, each range will be sampled every 12 seconds (about 2000 feet). The total number of revolutions will be telemetered from the velocity meter, every telemetry cycle (six seconds), to determine relative altitude.

Additional information will be given by the cloud sensor, cloud moisture indicator, and thermistors monitoring the temperature of sensitive components (photomultiplier tubes, solid state devices).

2.4 MEASUREMENT REQUIREMENTS

2.4.1 Meteorological Requirements

The vertical pressure distribution in an atmosphere in hydrostatic equilibrium is given by the relation

$$dP = -g \rho dz, \quad (1)$$

where P is pressure, g is acceleration of gravity, ρ is density, and z is height. For practical purposes g is constant for altitude ranges of interest here, in which case integration of Equation (1) from a reference altitude z_0 at which $P = P_0$ gives

$$\int_{P_0}^P dP = -g \int_{z_0}^z \rho dz. \quad (2)$$

From the equation of state of the gaseous mixture, the density is

$$\rho = \frac{PM}{R^*T}, \quad (3)$$

T being temperature, R^* the universal gas constant, and M the effective molecular weight of the mixture. On substitution of Equation (3) into Equation (1), one obtains

$$dP = -g \frac{PM}{R^*T} dz, \quad (4)$$

which gives, an integration

$$P = P_0 e^{-\frac{gM}{R^*T}(z - z_0)} \quad (5)$$

Equation (5) shows that if temperature and molecular weight are known it is possible to build up a pressure - height curve for the atmosphere. Conversely

from pressure measurements as a function of altitude, one can deduce what the temperature structure for a given composition must be. Measurements of both pressure and temperature as a function of altitude provide the possibility of determining an effective molecular weight of the gas. Data on pressure, temperature, and molecular weight entered into the equation of state gives density values which can be plotted as a density-height curve.

Present thinking indicates that no altimeter will be included on the Venus capsule under discussion, but that the temperature, pressure, density, and atmospheric composition will be measured. From these data altitude changes can be determined by Equation (4). Then if some reference altitude can be established, an entire profile of the atmosphere above that reference can be constructed. Hopefully the reference level can be the planetary surface.

Accuracies required for various measurements during the descent of a capsule through the Venus atmosphere depend on the uses for which the information is desired. As a working philosophy it seems more important to obtain relatively rough measurements of several quantities than to strive for high accuracy for particular quantities. It is likely that there will be large variations of temperature, density, etc., with time and position on the planet, and knowledge of the variations is still lacking. Great accuracy of measurement at one or a few locations and times is unwarranted in such conditions.

On the other hand it is desirable that the system contain as much redundancy as feasible and that the instruments be able to cover great dynamic ranges. For instance, the low temperatures in the upper atmosphere of Venus are supplanted by high temperatures at the surface. The instruments must not only withstand these large temperature changes, but they must be capable of providing meaningful data throughout the range likely to exist and still have range to spare for unexpected contingencies.

The following is a preliminary analysis of the accuracy and dynamic range requirements for measurements of the different physical parameters.

Temperature

The temperature range expected in the Venus atmosphere is estimated by J. P. L. to range from 200°K to 600°K . Temperatures to 750°K are included in the "extreme model," but these high values are not based on direct evidence. Measurements of $600^{\circ} \pm 65^{\circ}\text{K}$ at 10.3 cm wavelength are reported by Mayer, McCullough, and Sloanaker of the Naval Research Laboratory. There is still a possibility that there are no such high temperatures on Venus, the microwave signals being emitted by the Venus ionosphere, but this hypothesis is not generally accepted at the present time. Consequently, it is very desirable that the instrumentation system have the capability of not only being undamaged by temperatures up to 750°K but also being able to provide reasonably accurate measurements at these elevated temperatures.

One can advantageously use a comparison with measurements in the Earth's atmosphere to establish accuracy criteria for similar measurements on Venus. Typically, surface temperatures are read to 0.1°F by the U.S. Weather Bureau observers, but it is questionable if this high accuracy has any practical significance. Thermometers with low time constants show short-period fluctuations of 1° or 2° or more in natural settings with normal atmospheric turbulence. This would seem to set the degree of accuracy desirable for surface temperature measurements on Earth. In the free atmosphere the short period fluctuations are not so pronounced but the data obtained by radiosondes and similar instruments are accurate to at best 1°C or 2°C under flight conditions. Comparisons of data taken with radiosonde instruments manufactured in different countries show an order of magnitude more uncertainty than this. These data are currently in use by the various weather services and apparently are of adequate accuracy for useful results.

In order to show how errors in temperature measurement will affect the density-height profile of the atmosphere, computations were made for the various J. P. L. model atmospheres of Venus under the assumption that the thermometer was subject to given constant errors. Errors of $\pm 0.1^{\circ}\text{K}$, $\pm 1.0^{\circ}\text{K}$, $\pm 10.0^{\circ}\text{K}$, and $\pm 20^{\circ}\text{K}$ were assumed. The results are shown by the density versus altitude

plots for the "best" and first "extreme" atmospheric models of JPL in Figure 2.3.1 and Figure 2.3.2, respectively. Curves for errors of $\pm 0.1^{\circ}\text{K}$ and $\pm 1.0^{\circ}\text{K}$ are not included because they are in the main too close to the middle curve for showing on this scale.

It is seen that positive temperature errors will indicate too low densities at the surface, and vice versa. However, the change of pressure with increasing altitude is too great for negative temperature errors and too small for positive temperature errors, resulting in a reversal of the sign of density error at some altitude. This occurs in the 18-22 km range for the "best" model and about 24 to 28 km for the "extreme" model. Above these altitudes positive temperature errors cause positive density errors, and vice versa, the percentage error increasing monotonically with increasing altitude. For the "best" model the density error at 50 km is about one percent for each 1°K temperature error. This increases to about ten percent density error per 1°K temperature error at 200 km.

Of perhaps more importance for temperature measurements are the non-consistent errors, i.e., the random or short-period errors, as they affect lapse rate determinations. The lapse rate, in turn, is useful in deducing atmospheric stability, atmospheric circulations, and atmospheric radiative properties. The limiting value is the adiabatic lapse rate in which case there is neutral stability of the atmosphere. Complete vertical mixing of the atmosphere would produce an adiabatic lapse rate in the absence of non-adiabatic processes such as radiative energy transfers or changes of state. Lapse rates appreciably greater than adiabatic are unlikely to exist for either very long times or through very deep layers, as the smallest perturbation in such a layer will amplify with time and produce violent vertical motions, thereby reverting to the adiabatic profile. The net result is that super-adiabatic lapse rates are a rare phenomenon, except very near a heated surface, in the Earth's atmosphere. Presumably the same would apply to the Venus atmosphere.

The temperature errors necessary to indicate super-adiabatic lapse rates are, of course, dependent on the value of the lapse rate itself and on the altitude

intervals at which the measurements are made. The lapse rate in the Earth's atmosphere is in general roughly one half the (dry) adiabatic value of 9.8°C per 1000 meters, so measurements made at say kilometer intervals can contain considerable error and still not indicate super-adiabatic conditions. However, it is likely, because of high surface temperatures on Venus, that approximately adiabatic conditions exist through deep layers. Thus relatively small but variable temperature errors may make the difference between indications of static stability and instability. The adiabatic lapse rate for Venus depends on the atmospheric composition assumed but is nominally 8.5°K/km to 9.0°K/km . Obviously if adiabatic conditions exist, small temperature measurement errors may cause indications of either stability or instability. Conversely, if the lapse rate is much less than adiabatic, then errors of temperature measurement amounting to even several degrees per kilometer will not give false impressions of absolute instability, although such gross errors may well bring about unrealistic deductions of the important atmospheric processes.

The pressure errors which result from large and consistent temperature error errors can be judged from the curves of Figure 2.3.3. The middle curve of the figure is the pressure computed for the "best" Venus model. The upper curve is for a constant $+20^{\circ}\text{K}$ temperature error and the bottom curve is for a -20°K constant error. It is seen that the fractional errors in pressures resulting from applying these errors to the whole atmosphere, beginning at the surface, increase with height and reach a factor of five or so at the 120 km level. In the 40-50 kilometer range the errors in pressure are only 10 percent to 20 percent.

Pressure

Before assessing the significance in pressure errors, it is well to see the purposes to which pressure measurements will be put. In meteorological work on Earth the pressure is included as a primary measurement in standard weather observations. Here, however, no particular use is made of the individual measurement in ordinary applications. It is of use for providing altimeter settings for aircraft, but mainly it is combined with similar observations taken at other

locations to obtain a horizontal pressure distribution or pressure surface contours from which atmospheric circulations can be deduced. This deduction is not possible from a single pressure measurement at one location.

A time history of pressure at a given location is of value on the Earth in determining the movement or passage of weather systems. In meteorology this measurement is called pressure tendency and is included in standard weather observations. The time period over which the pressure tendency is taken is normally three hours, and the pressure change during that time is of the order of a few tenths of millibars, although in disturbed conditions it may be several millibars.

Obviously neither of these applications of pressure measurement is contemplated for the Venus entry capsule. It appears, then, that unless the pressure has some effect on operation of the vehicle itself, the pressure measurement is of value only as it contributes to the definition of other parameters.

Pressure enters both the equation of state -- Equation (3) -- and the hydrostatic equation -- Equation (1). The equation of state is a linear relation between pressure, temperature, density, and molecular weight. Thus, the error in the determination of any of the other three variables from a pressure measurement is directly proportional to the error of the pressure measurement itself. The hydrostatic equation can be written as

$$\frac{dP}{P} = d(\ln P) = -\frac{gM}{R^*T} dz. \quad (6)$$

Here it is seen that if the other variables are constant, dz is linearly dependent on the logarithm of the pressure, or on the fractional change of pressure. Thus the sensitivity of z to errors of pressure change measurements is small at high pressures and large at low pressures.

Density

If the equation of state is differentiated and substituted into the hydrostatic equation, the result can be expressed in the form

$$\frac{d\rho}{\rho} = d(\ln \rho) = -\frac{dT}{T} + \frac{dM}{M} - \frac{gM}{R^*T} dz. \quad (7)$$

It is seen that for constant temperature and molecular weight the change of altitude is proportional to the fractional change of density by the relation

$$\frac{d\rho}{\rho} = d(\ln \rho) = -\frac{gM}{R^*T} dz. \quad (8)$$

The dependence of altitude on density is a logarithmic function of density, just as it was seen to be a logarithmic function of pressure by Equation (6). This means that to determine altitude changes accurately one has to have very accurate density measurements at high levels but larger errors are tolerable at low levels, i.e., in dense portions of the atmosphere.

At a given altitude the fractional change of density is equal to the fractional change of temperature, as can be seen from either Equation (7) or from the equation of state. The same can be said for the pressure-density relation in an isothermal atmosphere of constant composition.

Composition

There are two aspects to the determination of composition which should be considered. First, it would be ideal to measure directly the absolute amounts of materials which compose the atmosphere. This measurement should be continuous during the capsule's descent, as there are apt to be variations of composition with altitude. In the high altitudes diffusive separation of the gases may exist, while at low altitudes there may be variable amounts of gases, because of non-uniform distribution of sources or because of the circulation of the atmosphere. An example of such low-level-variability is that of water vapor in the Earth's atmosphere.

This direct measurement of composition is particularly valuable in detecting trace gases. Each of the various forms of oxygen, nitrogen, carbon, hydrogen, etc., plays its own role in processes within the Earth's atmosphere. Presumably the same statement would apply to Venus, although the effects may well be different. As an example of the importance of trace gases on Earth, the very small amount of ozone which exists in the upper atmosphere, only two or three cm at STP, absorbs high-energy ultraviolet radiation and thereby permits life as we know it to exist on Earth. Perhaps a more cogent reason to measure trace gases on Venus is to study the processes which are responsible for the trace gas.

The second aspect of interest is the gross atmospheric composition. Until comparatively recently it was thought that the Venus atmosphere is predominantly CO_2 . Later evidence, or a reinterpretation of evidence, indicates only five percent to 25 percent CO_2 . Presumably the remainder is nitrogen, although this has not been established.

These gross proportions could be obtained by a determination of molecular weight of the mixture. If ρ_1 , M_1 , ρ_2 , M_2 are, respectively, the density and molecular weight of CO_2 and N_2 , then the molecular weight of the mixture is given by

$$M = M_1 \frac{\rho_1}{\rho} + M_2 \frac{\rho_2}{\rho} , \quad (9)$$

and

$$\rho = \rho_1 + \rho_2 . \quad (10)$$

On substituting Equation (10) into Equation (9) and solving for ρ_1 and ρ_2 , one obtains

$$\left. \begin{aligned} \rho_1 &= \rho \left(\frac{M - M_2}{M_1 - M_2} \right) \\ \rho_2 &= \rho \left(\frac{M - M_1}{M_2 - M_1} \right) \end{aligned} \right\} \quad (11)$$

M_1 and M_2 are known constants. From measurements of ρ , P , and T and use of the equation of state, the molecular weight M of the mixture can be determined. Then ρ_1 and ρ_2 are readily computed from Equation (11).

The ratio of densities of the two gases, i.e.,

$$\frac{\rho_1}{\rho_2} = \frac{M - M_2}{M - M_1} \quad (12)$$

can be determined to the accuracy to which M is known. From the equation of state,

$$M = \frac{R^* \rho T}{P} \quad (13)$$

it is seen that M is linearly dependent on ρ , P , and T . If each of these quantities is measured to \pm three percent during entry, M , and therefore ρ_1/ρ_2 , is determined \pm nine percent. This is adequate for the major constituents, but would not furnish any information about the minor constituents of the atmosphere.

2.4.2 System Requirements

The variables to be measured place certain requirements on the overall instrumentation. These were discussed in the previous section. In addition, there are certain requirements which are due to the type of mission that is being considered of entry capsule under consideration, the space and entry environment, as well as weight, power and telemetry capacity limitations, and these are discussed here in a general manner. Specific limits intrinsic in a given instrument or component are discussed in the sections discussing each measurement techniques.

One of the primary considerations in the overall instrumentation system is the tremendous range of the principal parameters that have to be measured: in general pressure, density and carbon dioxide density all vary about a factor of one thousand between initial measurements in the subsonic region, and measurements very close to the surface of the planet. Should it be desired to maintain

constant (or at least approximately constant) relative error in the measurements over this entire 1000:1 range, and if this measurement uncertainty were set at ± 50 per cent of the measured value one would require 10 binary steps (i.e a 10 bit resolution). Similarly, if each value were to be measured to ± 20 per cent, 20 bit resolution would be required. (It should be noted that in the mid term report a measurement range of 10,000:1 was considered, the number of bits required there are 14 for 50 per cent accuracy and 27 for 20 per cent accuracy.) In contrast with the requirements for this precision, telemetry encoders usually resolve five bits per variable, and six bit codes can be used. (Seven bit encoders are marginal at the present state of the art.) Quite apart from this, the transducers themselves are usually good to about three per cent of full scale (this applies particularly to pressure transducers), equivalent to a four bit resolution, significantly less than what would be required to cover the entire parameter range with one sensor and constant measurement uncertainty of even 50 per cent. (It should be noted that the telemetry bit rate reflects step size and hence uncertainty in any given measurement point. If the sampling rate is fast compared to the time that a given parameter takes to vary by one measurement step, and if continuous data reception is assumed, statistical uncertainties in the measured parameter are far less. Unfortunately this type of approach does not apply to the transducer itself, though even there one can use non-linear devices.)

One obvious approach is to divide the measurement range for a given parameter into several smaller ranges, using several transducers. The ranges for the transducers could again be selected to hold the relative error approximately constant, or, preferably, should be tailored so that maximum precision is available in the region where the data is of particular meteorological significance. Thus, for example, the overall pressure range can be covered by three transducers respectively 10, 100 and 1000 psi full scale, each one of them good to three per cent of their full scale value. Conversely, if one is particularly interested in the pressure altitude of possible clouds, which are expected to occur at pressures somewhere between 20 and 100 mB (Circa 0.3 to 1.5 psi), one would provide a transducer covering about 0 to 2 psi, and use either a total of four pressure ranges, or sacrifice accuracy in some other range.

A different problem which also influences the design of the instrumentation system, is the data sampling rate considered. In general, one can set an upper limit on the desired sampling rate by requesting data every 1000 ft in altitude. Assuming that one requires data to this specification only after the vehicle is travelling at less than 500 ft/sec (an event which occurs only a few seconds after leaving the hypersonic regime) this would imply sampling each sensor every two seconds. A much more reasonable requirement would be requesting the data every 10,000 ft initially, corresponding to sampling the data every 20 seconds. By the time the vehicle has slowed down to 100 feet/sec., that is, a few seconds later, this would correspond to data points every 2000 feet in altitude and for the terminal velocity in the neighborhood of 50 feet per second (for a vehicle with a ballistic coefficient of about 60) expected at the lower altitudes (higher densities) data will be obtained every 1,000 feet.

Another aspect to be considered is the reliability of the various instruments as contrasted with the possibility of providing either redundant measurement or redundant information from the cross-correlation of various types of measurements. Most of the sensors considered in the instrumentation system are simple and reliable. Most likely, the critical items will be the communication system and the altimeter. Both of these units will be relatively heavy and consume a large amount of power and hence, duplicate systems are not feasible. Most of the sensors themselves are small enough that it is feasible to duplicate the entire unit and telemeter the output of redundant identical sensors sequentially. This approach is particularly applicable to the pressure and temperature sensors. For other units it may be more practical to provide duplicates only for the most critical portions of the given instrument. Thus, for example, in the CO₂ density measurement by infrared absorption, it would be practical to provide a single source, since this could be simply a piece of one millimeter diameter resistance wire heated to well below failure temperature, but provide two or more radiation detectors (e.g., thermistors). By spacing the thermistors at various distances from the source, one could combine redundancy with expansion of the measurement range. Similarly in the density gage one could use one radioactive source and several scintillator-light sensor combinations.

The effects of the environment are of course critical in the design of the instrumentation and the selection of the individual components. While the interactions by the sensor and environment are considered separately for each device in the appropriate sections, some overall aspects are discussed at this point. Four specific effects were considered in all cases and these were effects of space vacuum, effects of atmosphere temperature at subsonic portion of field, effects of sterilization and g-loading during deceleration. Of these, the most serious item appears to be the high ambient temperature during the final portion of the mission. Several of the instrument sensors will not perform properly with the temperature above 100 or possibly 150°C. In the non-operative condition all the components will tolerate at least 150°C, and hence, no problems are expected during the sterilization procedure. Several of the sensors (photo multiplier tubes, thermistors, pressure gages) and temperature dependent output even within their operating region and hence, the temperature of these sensors will have to be monitored to permit corrections to be applied to the telemetered data. The most critical element in this respect is the thermistor detector used in the determination of carbon dioxide density by infrared absorption. This device can operate only at temperatures between 0 and 50°C under conditions of constant voltage bias and can tolerate only slightly higher temperature variations if operated under constant current bias (but this later type of operations requires somewhat more power) and its temperature should be monitored to better than five degrees. There is also some possibility that residues of chemicals (for example, ethylene oxide) used in sterilization, may interfere with measurements and hence, the instrument designer will have to have accurate knowledge of the exact components used. There may even be a requirement for inert gas purge, to remove residual chemicals.

The effect of g-loading does not appear as serious as originally envisioned since solid state detectors are planned for many of the devices. The most critical element will be the photo-multiplier tube and hence, serious thought is being given to replacing this with a solid state light detector. This later device is smaller, sturdier and requires less power, but on the other hand, is less sensitive and more temperature dependent than the photo-multiplier. The effect of

being exposed to the vacuum of space for an extended period of time appears to be particularly significant in the design of the bearing for the propellor suggested for velocity measurements. This problem has, however, been studied in conjunction with investigations on long-life space vehicles and does not appear to be insurmountable.

Particular thought has been given to the interactions of the results from the various types of measurements proposed for the capsule. The problem was examined from the viewpoint of being able to interpret the data from the other sensors if a particular type of measurement produced no results. Also, thought was given to the relative importance of the various types of measurements if weight restrictions should make it impossible to accommodate all instruments.

The most critical measurement is the ambient temperature since in the extreme case meteorologists can gain some knowledge of the atmosphere from just the variation of this parameter along the descent trajectory. Fortunately, this parameter can easily be measured to the accuracy required for this purpose (see previous section) and the sensors are rugged and reliable. In spite of this, one should consider a minimum of four temperature sensors, two of which cover the temperature region which occurs over the greatest part of the altitude regime of interest (200 to 300°K) while the others cover the entire expected range of temperatures.

The measurement which meteorologically appears to have the next highest priority is the determination of the presence or absence of clouds since this will permit typing the data to those based on bus measurements.

The third priority is the measurement of either density or pressure. The measurement of density is slightly more useful but if the range of compositions suggested as input for this study (that is, if the atmosphere is between 75% and 97% nitrogen with most of the residue being carbon dioxide) the pressure measurement would have the advantage of using a simpler and lighter sensor.

The last most critical item is some technique for determining altitude as a function of time since, without this, continuous measurements of temperature

and density would be required through to impact to obtain an altitude reference point. The most desirable technique would be to directly measure altitude with a radar altimeter. Since this device is, however, quite heavy, the integration of velocity as determined, for example, by propeller, would accomplish the same purpose. Obviously, this would again require that both velocity meter and communication system survive to impact.

Next in importance is the measurement of carbon dioxide density since this fixes composition and thermodynamic properties for the two component modes considered for the atmosphere.

Lowest priority would be given to the pressure (or density, whichever was not used previously) measurement, since to a certain degree there is redundancy between measurements of temperature, density, composition and pressure. This should not be taken as a suggestion that the measurement should not be performed since redundancy in a system of this nature is extremely desirable.

2.4.3 Capsule Design Limitations

There are of course obvious interactions between the design of the entry capsule, and its chief payload, namely the instrumentation system. The capsule design is therefore tailored to its only mission: that of carrying instruments and communication systems through hypersonic entry and then to impact, permitting accomplishment of the mission. Since most of the measurements will be carried out during the subsonic portion of entry, the instrumentation places no direct limit on the capsule heat shield. After that portion of the capsule has accomplished its purpose it will either be discarded, or suitable ports will be opened in it. Similarly, the two types of hypersonic measurements proposed - accelerometers and ablation sensors - are also compatible with any heat shield design.

There are two capsule system parameters which have a strong effect on the range over which useful meteorological measurements can be carried out, namely the capsule ballistic coefficient, and the initial entry angle.

As an example, below are tabulated some parameters for capsules of two different ballistic coefficients (20 and 60 pounds/square foot, and a variety of entry angles: (All for the "best" atmosphere and $V_e = 12$ KM/sec.)

γ	$W/C_D A = 20$			$W/C_D A = 60$		
	-15°	-30°	-90°	-15°	-30°	-90°
t_1 Deceleration = 5 g	~153	62	31	156	61	31
t_2 Velocity = 1000 ft/sec	175	69	32	185	66	32
$\Delta t = t_2 - t_1$	~ 22	~7	1	29	5	1
Altitude at t_2 (ft)	205,000	190,000	173,000	180,000	170,000	155,000
Pressure at t_2 (atm)	.01	.05	.13	.07	.14	.3
$t_3 = t_2 + \Delta t (15^\circ) + 10$	185	101	64	195	100	70
Altitude at t_3	~200,000	~165,000	160,000	175,000	150,000	135,000
Pressure at t_3	.02	.17	.2	.1	.4	.7

It can be seen from the table that if we want to commence measurements at the upper limit of where the clouds are expected - 20 millibars or 0.02 atmospheres - one would have to begin at about 200,000 feet altitude. This in turn requires a capsule with a low ballistic coefficient travelling on a grazing trajectory, with an entry angle of 15° . Even if one assumes the highest pressure at which the clouds are expected - 0.1 atmospheres - one must still begin measurements before one reaches 175,000 feet. There is, of course, no absolute requirement that measurements begin at cloud level (and in addition there is no assurance that clouds will be found on the path taken by the capsule) but no bus measurements can penetrate through the cloud layer, and correlation between the two sets of data would be more difficult if the capsule measurements began much lower.

Therefore, the above indicates that a low ballistic coefficient is desirable if the cloud altitude is to be determined.

In addition, it is impractical to require a grazing entry, but the desire to begin measurements as high as possible suggests the desirability of approach guidance, and entry angles between 15° and 30° . Any uncertainty in the entry angle is doubly deleterious insofar as the desire for high altitude measurements is concerned: first of all the steeper the angle, the lower the altitude at which sonic speed is reached; second, the heat shield cannot be removed (or the measurement ports cannot be opened) until one is sure that the vehicle has reached sonic speed. If one times this, for example, by a time delay from the time deceleration has decreased to 5 g (t_1 in the table), the time delay must be set for the flattest trajectory, since that is where the interval between the time of 5 g and sonic speed is greatest. Using this time delay, plus an additional ten seconds as safety margin and to accomplish the shedding of the shield, the measurements (for a ballistic coefficient of 20) could begin at 210,000 feet for a 15° entry angle, but only at 170,000 feet for a 30° entry angle. In the first case one would begin about five seconds after reaching sonic speed, while in the second case it would be 20,000 feet later, if the shield removal were activated by a g-sensor. This implies that considerable thought should be given

to devising a technique that would insure capsule survival, but would still activate measurement systems at a preset velocity, regardless of error in trajectory. This is mainly important if cloud altitude is of high interest.

It should be emphasized that while the altitudes discussed in this section all referred to the "best atmosphere," the pressures for all these events would be about the same for the other two atmospheres, though the altitudes would, of course, be quite different.

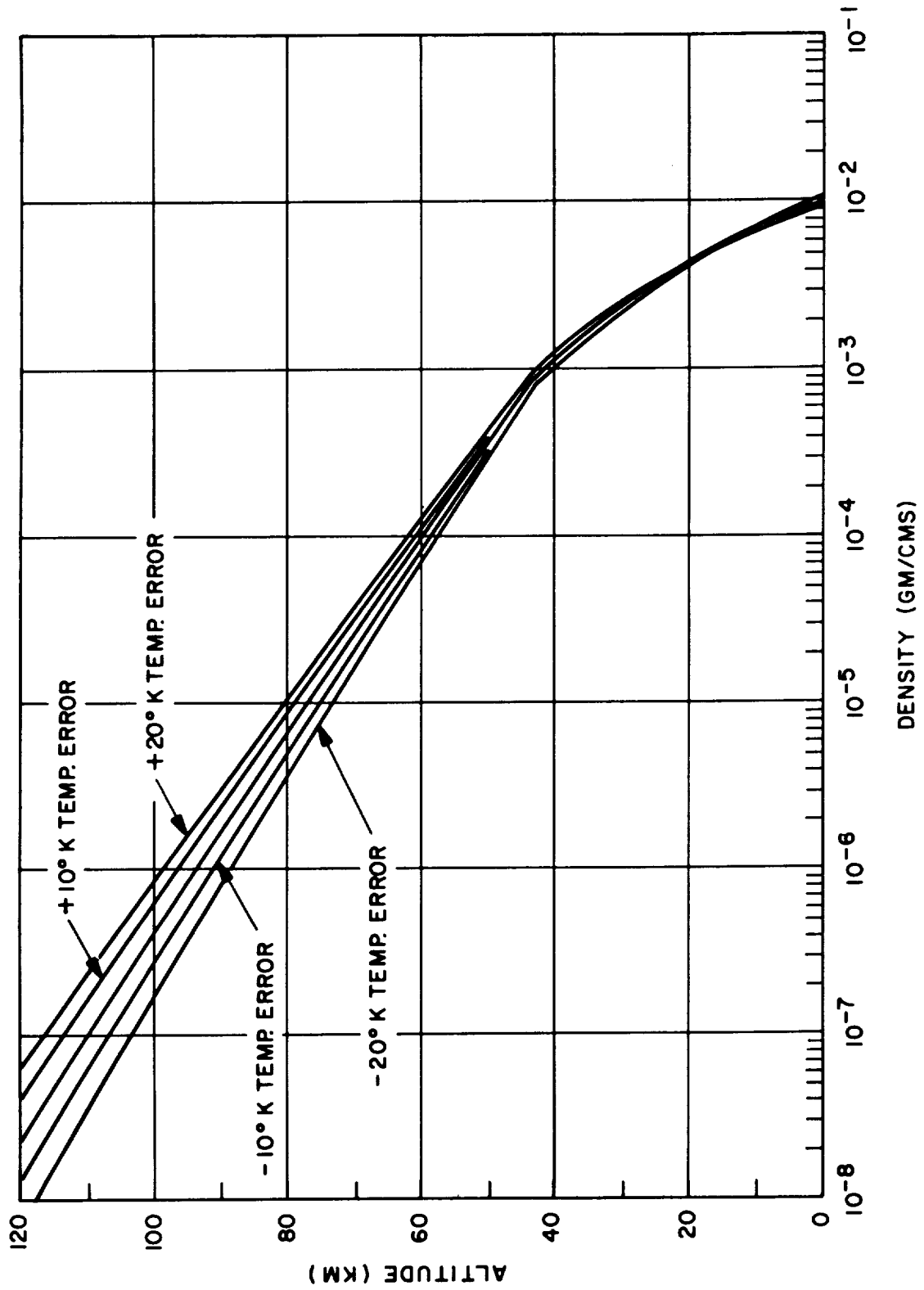


Figure 2.4.1. Vertical Density Profiles for the Venus Best Atmospheric Model (Middle Curve) and for Models in Which the Temperature is $\pm 10^{\circ}\text{K}$ and $\pm 20^{\circ}\text{K}$ Different from that of the "Best" Model

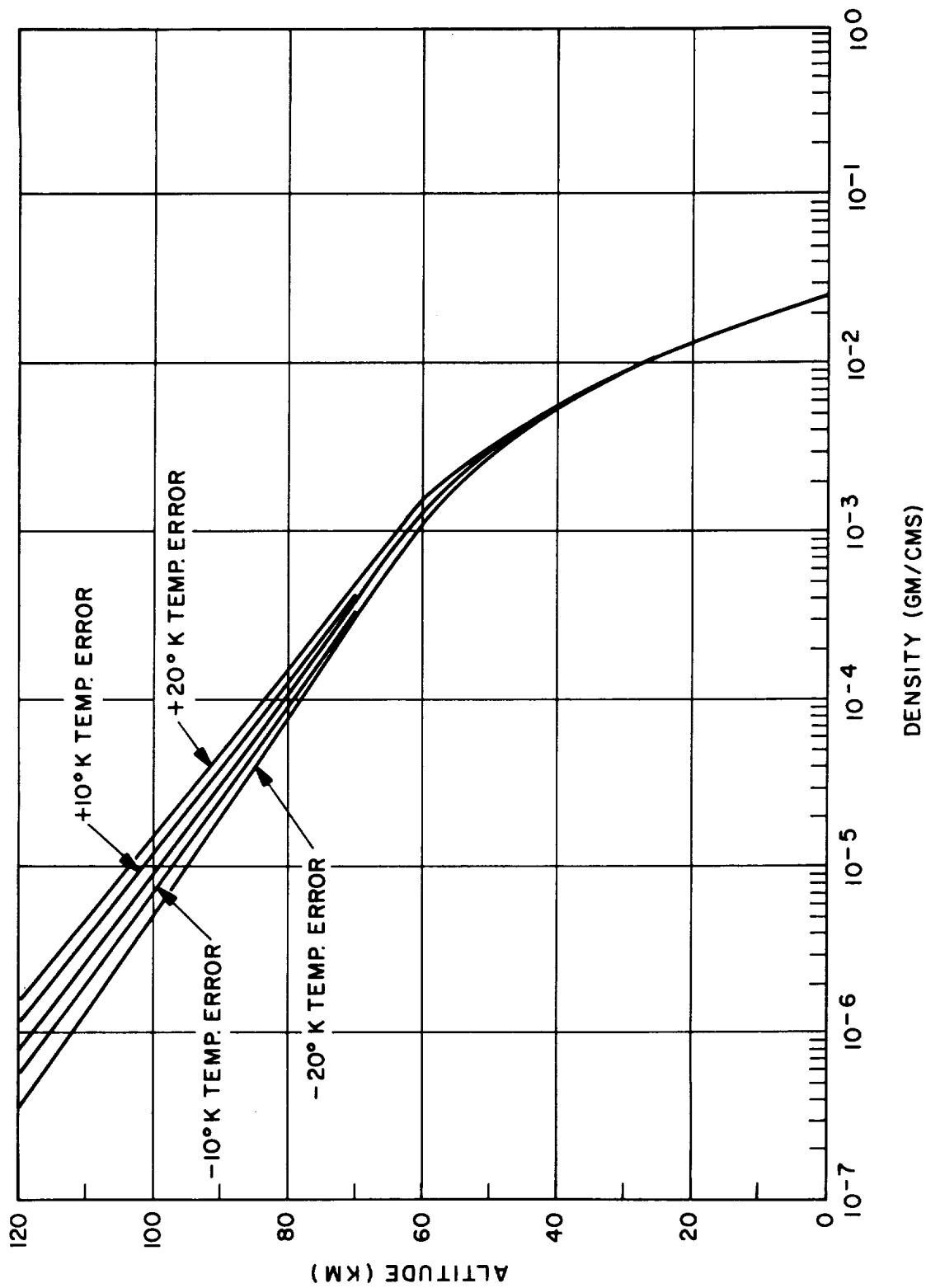


Figure 2.4.2. Vertical Density Profiles for the Venus "Extreme" Atmospheric Model (Middle Curve) and for Models in Which the Temperature is $\pm 10^{\circ}\text{K}$ and $\pm 20^{\circ}\text{K}$ Different from that of the "Extreme" Model

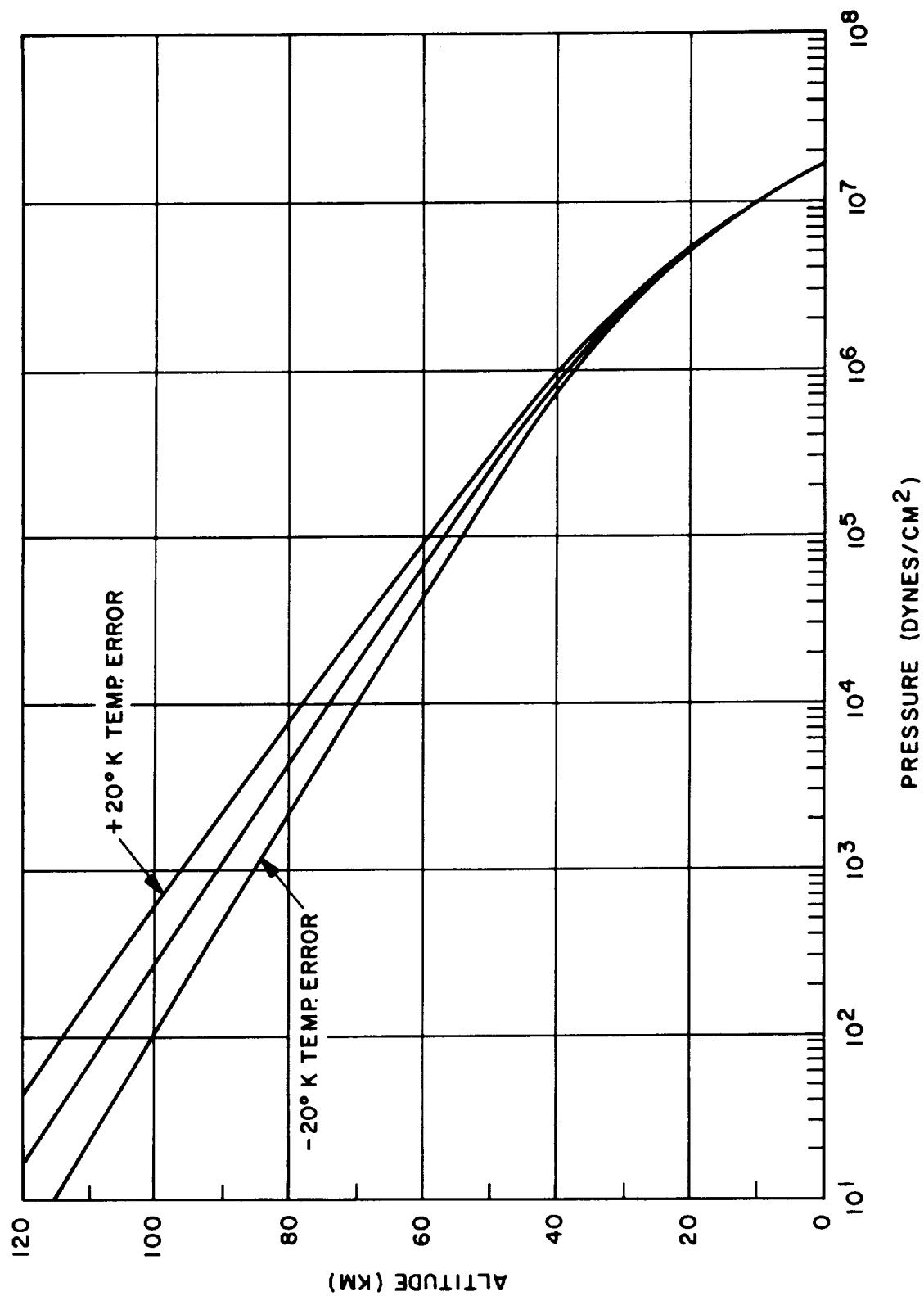


Figure 2.4.3. Pressure-Height Curves for the Venus "Best" Atmospheric Model (Middle Curve) and for Models in which the Temperature is $\pm 20^\circ \text{K}$ Different from that of the "Best" Model

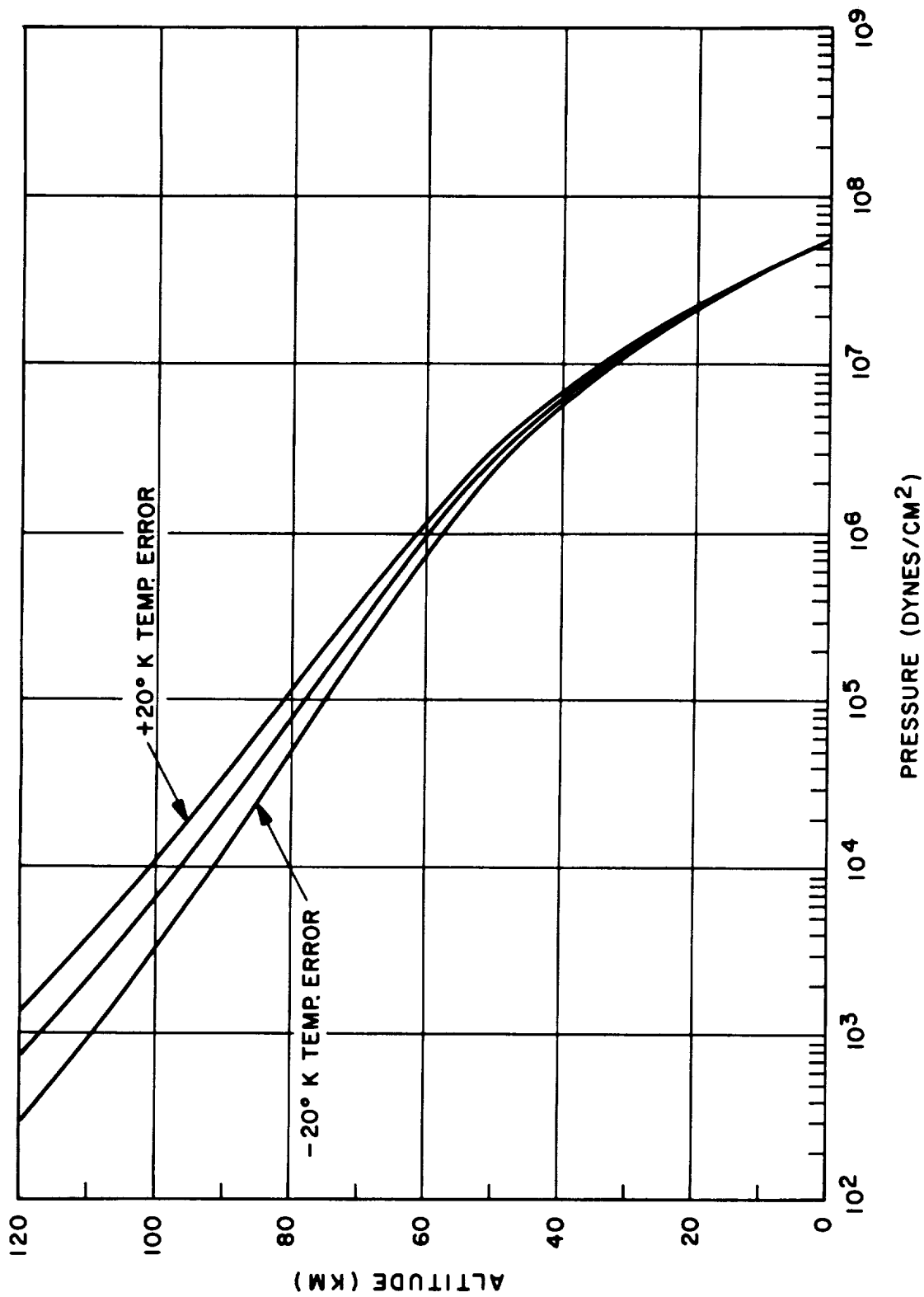


Figure 2.4.4. Pressure-Height Curves for the Venus "Extreme" Atmospheric Model (Middle Curve) and for Models in which the Temperature is $\pm 20^\circ \text{K}$ Different from that of the "Extreme" Model

2.5 PRESSURE MEASUREMENTS

One of the flight objectives is to determine the variation of the static pressure of the atmosphere with altitude. Included in the problems of making this measurement are the effects of velocity and angle of attack on the pressure at the port, the determination of the optimum type of probe or port and its location, the type of transducer to be used, considering sensitivity to the entry decelerations, temperature, and reliability, and the ranges of transducers necessary to cover the predicted range of pressures with adequate accuracy. Each of these problems is considered in detail in the following sections.

2.5.1 Velocity Effects

Measurement of the static pressure of a gas with the instrumentation mounted on a moving vehicle is complicated by the pressure disturbances due to the motion of the vehicle through the fluid. The pressures adjacent to the vehicle are increased in front of the vehicle and decreased behind it. The magnitude of the pressure increase depends on the velocity of the vehicle and the density of the medium through which it moves, while the distribution of pressures around the vehicle depends on the orientation of the vehicle with respect to its velocity vector, i. e., its angle of attack.

As given by Dean*, if a stream is reversibly and adiabatically decelerated without shaft work to zero velocity, the resultant stagnation pressure P_o is given by:

$$\frac{k}{k-1} p_s \left[\left(\frac{p_o}{p_s} \right)^{\frac{k-1}{k}} - 1 \right] = \frac{\rho_s V^2}{2 g_o} \quad (1)$$

where k = ratio of specific heats
 p_s = static pressure
 p_o = stagnation pressure

*Dean, Robert C., Jr. Aerodynamic Measurements, Massachusetts Institute of Technology, Gas Turbine Laboratory - 1953

ρ_s = density

V = velocity

g_o = dimensional proportionally constant to Newton's Law

Although derived and expressed for the case of a moving gas decelerated to zero velocity, the process is reversible and, therefore, the expression can also be used for a gas accelerated with respect to its initial environment and then brought to zero velocity with respect to the vehicle containing the pressure-measuring equipment.

Introducing Mach number M and rewriting, Equation (1) becomes

$$\Delta p = p_o - p_s = \frac{\rho V^2}{2 g_o} \left[1 + \frac{M^2}{2 \cdot 2!} + \frac{2-k}{2^2 \cdot 3!} M^4 + \dots \right] \quad (2)$$

This equation includes the effects of compressibility. If the terms involving Mach number are not included, Equation (2) reduces to

$$\Delta p = \frac{\rho V^2}{2 g_o} \quad (3)$$

which is the relationship applicable to incompressible flow conditions. Comparison of the two equations show that Equation (3) may be used to a Mach number of about 0.5 without exceeding an error of five percent. At $M = 0.8$, the error introduced by ignoring compressibility effects is about 15 percent, so that, even at this velocity, an appreciable error in Mach number estimation would cause only a small error in the velocity correction.

The effect of velocity on changing the pressure from the static value is also a function of the position of the pressure port and the angle between the pressure port and the velocity vector. Goldstein* shows that, for any point P on the surface of a cylinder with a gas flowing past the cylinder,

$$p - p_s = \frac{1}{2} \rho V^2 (1 - 4 \sin^2 \theta) \quad (4)$$

where: p = local pressure

θ = angle subtended by the arc
from the stagnation point to

*Goldstein, S. Modern Developments in Fluid Mechanics, Oxford University Press - 1938

Experimental results verify the validity of this equation for values of θ of up to 30° , where the indicated port pressure is approximately equal to the static pressure. (In Equation (4), if $\theta = 30^\circ$, $p = p_s$. Also, if $\theta = 0$, $p = p_s + \frac{1}{2} \rho V^2 = p_o$.) Experimental results of the pressure distribution on spheres in a moving gas stream are also given by Goldstein. The curves are of the same general shape, with the local pressure equal to the static pressure at an angle of about 40° from the stagnation point. As discussed above, positions can be found on cylinders and spheres where the pressure on the port will be equal to the static pressure in the stream. This is also true for other shapes. Newell* cites reports made on the V2 rocket tests indicating that pressure ports, properly located, gave indicated pressures equal to the static pressure with an error not exceeding two percent of the impact pressure head. These results covered a range of Mach numbers from 0.14 to 0.84, and showed that the velocity did not change the results by more than \pm two percent over this range. Similar information on the Mar's vehicle can be obtained by wind tunnel testing, if needed. If the heat shield is not dropped, changes in shape may increase the uncertainty to port location and changes in velocity. The maximum error is estimated to be less than \pm ten percent in this event. The effect of angle of attack will vary approximately as the cosine of the angle. The angle of attack for the more stable shapes, such as the Discover, converge rapidly toward zero. If it is assumed that the amplitude of the angle of attack envelope has decreased to $\pm 15^\circ$ when Mach 1 has been reached, the maximum pressure increase over static will be about four percent of the impact head. The average will, of course, be less.

To evaluate the magnitude of the velocity effect on the pressure measurements, impact pressures were calculated at various altitudes for the best and extreme I atmospheres, for entry angles of 90° and 15° , starting at about Mach 1 and continuing to impact. The results, as plotted in Figure 2.5.1, show that the maximum total impact pressure head is less than one psi at terminal velocity, which is reached soon after entry. The impact pressure is less than five percent of static below 37KM for the best atmosphere and below 55KM for the

*Newell, Homer E. "High Altitude Rocket Research" Academic Press
New York - 1953

extreme 1 atmosphere. Adding the uncertainty due to shape changes on the velocity and port location errors to the angle of attack error gives a maximum uncertainty of ± 14 percent. With a total pressure head of 0.8 psi, the error would be less than ± 0.12 psi. At ambient pressures of 12 psi or greater, this would be an error of less than one percent. As shown in Figure 2.5.1, this would cover the major portion of the trajectory. Thus, the velocity effect on the pressure indication can be neglected for the majority of the flight. No information is needed on angle of attack, and the location of the pressure ports is not critical. The length of time spent at high velocities is such a short part of the trajectory that it does not seem worthwhile to provide special pressure instrumentation for this period.

There are three basic methods which could be used to sample the ambient gas pressure. Pressure ports could be located in the side of the vehicle, a sample of gas could be caused to flow down a tube through the center of the vehicle, or a boom with pressure ports in it could be erected after entry.

The least complex method would be to simply provide pressure ports in the side of the vehicle with tubing leading to transducers inside the vehicle. Such ports have been used and pressure measurements made even during the peak ablating conditions on re-entry vehicles. Thus, this method could be used regardless of whether or not the heat shield was dropped after entry. If the shield were not dropped, the ports could extend through the shield. If it were dropped, the ports in the liner would be protected by the heat shield until it is dropped.

The methods used to provide pressure ports in the heat shields of re-entry vehicles has varied with the shield material being used. For some materials, a stack of thin graphite disks with a hole through the center was placed in the shield. As the shield material ablated, successive disks flaked off, thus preventing clogging of the pressure port and also keeping the edges of the port square and otherwise maintaining its shape. Such a technique could serve to maintain the shape of the port through the ablating period. Due to the high (of the order of 200 or more psi) peak dynamic pressures, however, the transducers

would have to be protected during the entry period by suitable valving to cut off the pressure lines during this period. The pressure lines would be opened only after the pressure had dropped to a low level after entry into the atmosphere. One system would be to have the pressure lines sealed off by a solenoid-actuated valve. Power to the solenoid circuit would be made available when the transmitter is actuated by the g-switch, and power would be applied when a pressure switch indicated that the pressure had dropped to a safe level. If the heat shield is dropped, the shield could cover ports in the liner during entry, and expose the ports only after the shield is removed.

If a passage is provided through the center of the vehicle or booms erected to hold other instrumentation, pressure ports could be installed in these locations rather than in the vehicle's surface. Satisfactory measurements can be made with ports in the surface, however, and the additional complexity of the alternate methods is not justified by the pressure measurement requirements.

Since the impact pressure is a function of velocity, it is natural to consider measuring the velocity by measuring the impact pressure. Such a measurement could serve as a back-up to the radar altimeter, if available, or, by integration, could give altitude information if the impact time is known. Impact pressures can be converted to velocity only if density is known. With known density, the terminal velocity can be calculated without pressure information, since the gravitational constant of Venus is known and the drag coefficient of the capsule can be determined. A combination of wind-tunnel and drop tests would give the drag coefficient of the capsule under all conditions, and would provide sufficient information to convert density measurements to velocity, without using the pressure information. It should be noted that obtaining the necessary information would require an additional gage to measure the differential pressure, since the pressure difference is much too small to be obtained by taking the differences of other gages.

2.5.2 Type of Transducers

The most severe environmental limitation governing the selection of a type of transducer is the deceleration experienced upon entry into the atmosphere of Venus. The internal temperature rise will be the second most critical factor. The ability to withstand other conditions, such as vibration on take-off, has been demonstrated by a number of commercially available transducers.

For flight vehicles, the choice of transducer is generally limited (in the pressure ranges under consideration) to the mechanical types, where the applied pressure deflects a sensitive member, such as a capsule, a diaphragm, or a conventional or a twisted Bourdon tube. The choice between the capsule or diaphragm and the Bourdon tube types is generally made by the manufacturer on the basis of range, with gages of a few hundred psi a full scale or less generally being of the capsule type, and the higher ranges being of the Bourdon tube type.

In order to make a pressure measurement, the deflection of the sensitive member must be determined. Pick-offs for this determination may be resistive (potentiometer), resistive strain bridge (bonded or unbonded), capacitive, or magnetic, including variable reluctance, differential transformer, etc.

Table 2.5.1 below gives a brief, order-of-magnitude, comparison of average values of size, weight, and power for the various types of transducers.

TABLE 2.5.1

Type gage	Potentiometer	Potentiometer	Strain	Inductive
Range (psia)	up to 0-250	0-1000	all	all
Size (in ⁻³)	2	4	6	20
Weight (oz)	1	8	8	16
Power (watts)	.03	.03	2	5
Ruggedness (relative)	worst	worst	intermediate	best

Note: All gages to have 5 volt output. Figures include weight of amplifiers when required.

The values given for relative ruggedness are arbitrary and based on such considerations as the fact that the variable reluctance types usually have the stiffest sensing element and therefore the smallest deflection, and would be affected the least by the entry decelerations. Applications of this type sensor to flight applications in the past has been limited by the need for a separate carrier supply and demodulator-amplifier. These are now supplied as an integral part of the sensor, and have an output suitable for telemetry systems. Strain gage types would also be rugged for this application, but their low output would require amplification before use.

Table 2.5.1 shows the potentiometer type to be best for all considerations except relative ruggedness. This relatively lower rating is based on the fact that the actuating element must move farther in the potentiometer type than in the others, in order to move the wiper a detectable amount over the potentiometer. These larger motions make the potentiometer more sensitive to the effects of acceleration. However, since the gage need not operate during the peak deceleration, suitable stops and supports could be provided to damage to the gage.

Another potential source of difficulty with the potentiometer type is their need for bearings to support the moving members. During prolonged exposure to vacuum, any lubrication in such bearings would be evaporated. This difficulty may not be serious, since jeweled bearings are used by many vendors. Other vendors, using flexure pivots in their gages, would not be troubled by exposure to vacuum. The flexure pivot type would also be less susceptible to damage during deceleration.

Another type of gage now reaching the market is the semi-conductor strain type. The development of this gage is in too early a stage for evaluation, but the advantages of the semi-conductor type in small size, high output, low power consumption, and probable ruggedness means that this type should be carefully evaluated at the time the capsule is designed.

A check was made on General Electric Company experience with gages subjected to high accelerations. Extensive testing had been done on potentiometer

type gages operating at 100 g's for re-entry vehicles. An application was found where a Wiancko gage had been tested and calibrated at 240 g's. Since the present application requires only survival of the high g loading, with measurements made at low g levels after entry, this data looks promising.

To check further, the engineering departments of the three well-known vendors (Pace Eng., Edcliff Instruments, and Giannini Controls) were contacted and asked to express an opinion on the magnitude of the problem of designing a transducer to withstand 800 g's and then operate. All three indicated that such a design was feasible and within the present state of the art.

Two well-known manufacturers of variable reluctance type are Pace Engineering Co., North Hollywood, California, and Daystron-Wiancko Engineering Co., Pasadena, California. Strain types are made by Statham Instruments, Inc., Los Angeles, California and by Consolidated Electrodynamics Corp., Monrovia, California. Potentiometer types are made by Giannini Controls, Inc., Duarte, California.

A more complete listing of vendors and types of gages manufactured can be found in the "Telemetry Transducer Handbook" Vol. II, compiled by the Research Division of Radiation Incorporated, Orlando, Florida under Contract AF 33(616)-7466.

2.5.3 Transducer Ranges

The maximum predicted ambient pressure at zero altitude is less than 900 psia for the extreme I atmosphere. Since the impact velocity pressure is less than one psia, the maximum range to be instrumented is effectively 900 psia. The minimum range can be set by referring to Figure 2.5.1. It can be seen that, for both the best and extreme I atmospheres, the impact pressure head is decreasing rapidly toward its terminal velocity value when the ambient pressure is in the neighborhood of three psia. At higher altitudes, the measurement of ambient pressures would have large errors due to velocity effects. It would seem reasonable, therefore, to have a gage with a range of 0 to 10 psia as the

most sensitive gage. The entire range could then be covered by three gages, 0 to 10 psia, 0 to 100 psia, and 0 to 1000 psia. If greater accuracy is required at some particular pressure point, additional gages could be included to increase the sensitivity at the points of interest.

In order to estimate the time response required of the sensor, it is necessary to know the rate of change of pressure with time. At 30 KM, the pressure changes about 0.001 psia/ft at an ambient pressure of 30 psia. At a velocity of 300 ft/second, the pressure is then changing at the rate of one percent per second. A transducer with a response time of one second or less would be sufficiently fast to follow this rate of change.

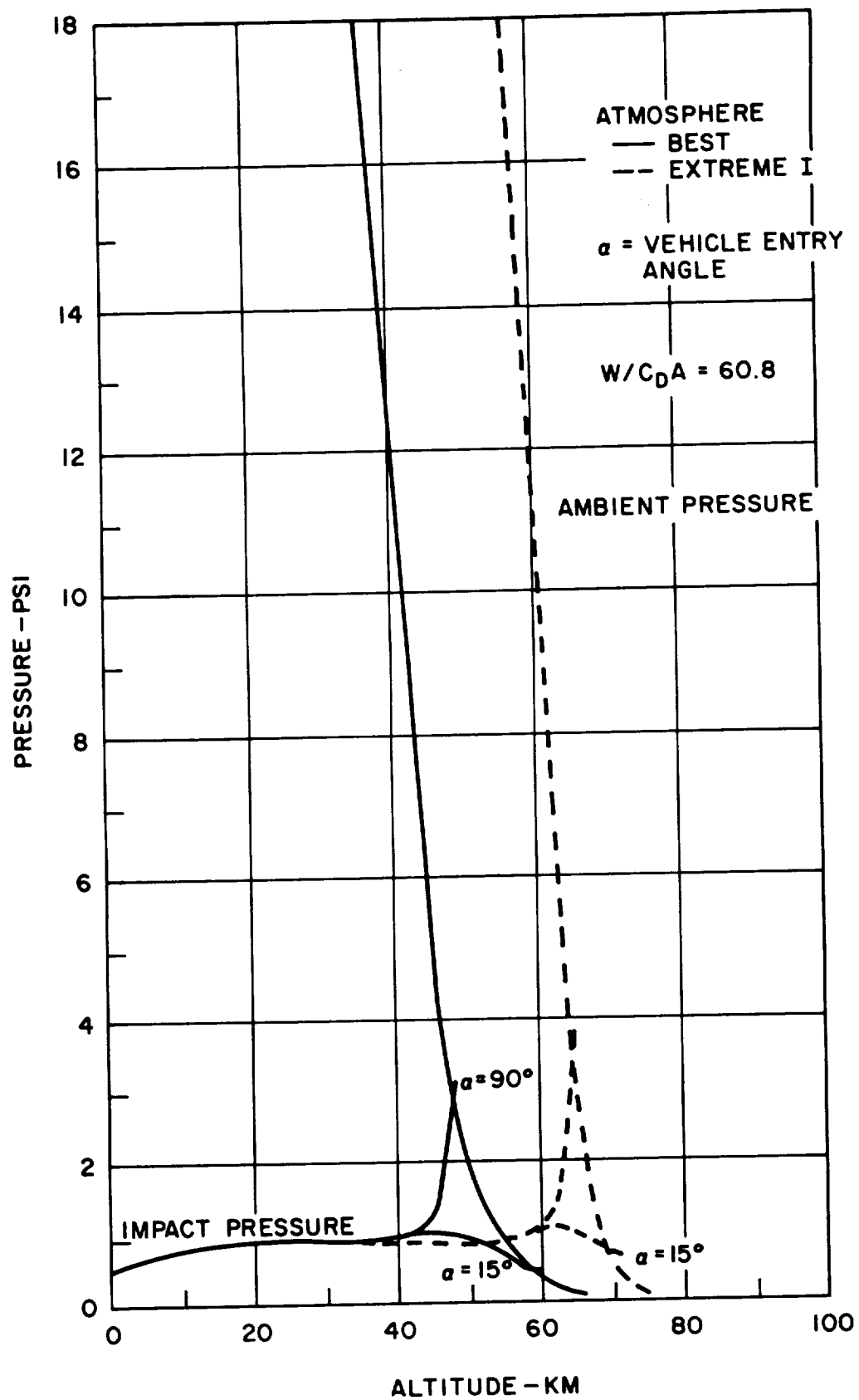


Figure 2.5.1. Subsonic Impact Pressures

2.6 TEMPERATURE MEASUREMENTS

Another flight objective is to determine the variation of the ambient temperature of the atmosphere with altitude. The problems associated with this measurement include the effects of velocity on the indicated temperature, the determination of the optimum type of probe and its location, and the ranges of transducers required to cover the estimated range of temperature. Each of these problems is considered in detail in the following sections.

2.6.1 Velocity Effects

Just as the measurement of the static pressure of a gas is complicated by pressure disturbances due to the relative motions, temperature measurements are also affected by the motions. The gas in front of the vehicle is accelerated to the vehicle's velocity, and raised in temperature when this increased kinetic energy is converted to thermal energy.

As given by Eckert*, if there is relative motion between the sensor and the gas stream, the total temperature of the gas accelerated to the sensor velocity will be given by

$$\Delta T = T_T - T_S = \frac{V^2}{2g C_p} \quad (1)$$

where T_T = total temperature of the gas - $^{\circ}\text{F}$
 T_S = static temperature of the gas - $^{\circ}\text{F}$
 V = velocity - ft/sec
 g = proportionality constant - ft/sec²
 C_p = specific heat of the gas - ft.-lb./lb. $^{\circ}\text{F}$

For nitrogen at 200 $^{\circ}\text{F}$, Equation (1) reduces to

$$\Delta T = \frac{V^2}{12,550} \quad (2)$$

*Eckert, E. R. G., "Introduction to the Transfer of Heat and Mass," McGraw-Hill, 1950.

In general, any probe or vehicle placed in the gas stream will not recover all of the kinetic energy of the movement as thermal energy. The probe will reach an indicated temperature intermediate between the static and total temperature. A recovery factor for a temperature sensing probe is defined by Equation (3)

$$T - T_S = r \frac{V^2}{2g C_p} \quad (3)$$

or

$$r = \frac{T - T_S}{T_T - T_S} \quad (3a)$$

where

T = temperature reached by probe

r = recovery factor

For flat plates, the recovery factor was shown by Pohlhausen* to be related to the square root of the Prandtl number. For specific types of probes, recovery factors of better than 0.99 have been achieved.

In order to determine the magnitude of the temperature rise due to velocity, the velocity as a function of altitude was determined for the best and extreme I altitudes, and for entry angles of -90° and -15° , with results as shown in Figure 2.6.1. As can be seen, the velocity drops rapidly from about Mach 1 at the upper end of the curves to sub-sonic values. Since the temperature rise depends on the square of the velocity, the temperature rise changes even more rapidly with altitude, as shown in Figure 2.6.2. Soon after the end of telemetry blackout, at sub-sonic velocities, the difference between the static and total temperatures drops below 20°F . In fact, for the major portion of any of the trajectories considered, the temperature rise due to velocity effects is less than 10°F . If the velocity of the vehicle and the recovery factor of the probe are known to any reasonable degree, a correction for velocity can be computed to a good degree of accuracy.

*See Eckert, loc. cit.

2.6.2 Types of Transducers

There are three basic types of temperature sensors used for measurement of temperature in flight vehicles. Sensors may be based on the variation of resistance of a metallic conductor with temperature (resistance thermometer), variation of resistance of a semi-conductor (thermistor), or the generation of a voltage at a junction of two dissimilar metals (thermocouple). It is recommended that sensors for this application be either resistance thermometers or thermistors, and that thermocouples not be used. The principal advantage of the thermocouple is its small size and rapid response. Response time is not a critical parameter for this application. Outweighing this advantage are the thermocouple's disadvantages of low output and the need to provide a reference cold end, since thermocouples can measure only temperature differences and not absolute temperatures.

The choice between a thermistor and a resistance thermometer is dictated by the range of temperatures to be covered and the accuracy required of the measurement. The variation of resistance of a resistance thermometer with temperature is given by an equation of the form of Equation (4):

$$R = R_0 (1 + AT + BT^2) \quad (4)$$

where R = resistance at temperature T

R_0 = resistance at 0°

A, B = coefficients depending on the material used

The coefficient B is usually small, and the linear term coefficient A predominates, so that the resistance varies nearly linearly with temperature over a wide range. The resistance thermometer can thus be used over a wide range of temperatures with nearly constant sensitivity. The resistance-temperature relationship of a thermistor can be approximated by Equation (5).

$$R = R_0 e^{B \left(\frac{1}{T} - \frac{1}{T_0} \right)} \quad (5)$$

where R = resistance at temperature T

R_0 = resistance at temperature T_0

B = constant depending on the thermistor material

Thus, the resistance of the thermistor varies exponentially with temperature, and the range over which it can be used is limited. In practice, the variation in temperature coefficient with temperature, as well as the stability of thermistors, limits their usual range of application to temperatures from around or slightly below 0°C to 200°C maximum. The principal advantage of the thermistor is its increase in sensitivity compared to the resistance thermometer. Most metals used for resistance thermometers have temperature coefficients between 0.4 and $0.5\%/^{\circ}\text{C}$, whereas the coefficient of a thermistor at room temperature is about $4\%/^{\circ}\text{C}$.

There are several excellent sources for resistance thermometers, including RdF Corp., Hudson, N.H., Rosemont Engineering Co., Minneapolis, Minn., and Trans-Sonics, Inc., Lexington, Mass., as well as others. Sources of thermistors are somewhat more limited, but, for temperature measurements, excellent quality units can be obtained from Fenwall, Inc., Ashland, Mass., Gulton Industries, Metuchen, N. J., and Victory Engineering Co., Union, N. J.

If the heat shield is dropped after entry, there are three possible locations for the temperature sensor. The sensor may be located under a thin section of an exposed part of the liner, in a tube leading from the front of the vehicle to the back, with a free flow of gas, or in a boom erected at the side of the vehicle. If the heat shield is not dropped, the sensor must be exposed to the ambient air by either of the latter two methods.

Probes may be evaluated for use in this application on the basis of their recovery factor. Recovery factors can range from zero to one, depending on the basis of design of the probe. The simplest installation would be a sensor located under the surface of the vehicle. Such a probe would have a recovery factor between 0.7 and 0.9. The correct value for the particular configuration could be established by wind tunnel tests. Assuming a 10°F impact temperature rise, an uncertainty in recovery factor of ± 0.1 , and a velocity error of ten per cent, at

a velocity of 400 ft/sec, results in a temperature error of less than 4°F . This would be a maximum and would rapidly drop to less than 1°F at 200 ft/sec.

The most accurate measurement of ambient temperature from aboard a moving vehicle can be made by means of a vortex thermometer. As first described by Vonnegut*, the vortex thermometer has a recovery factor of zero, and measures the ambient temperature directly, with no velocity effect. The operation of the vortex thermometer is based on the Hilsch tube effect except that, instead of separate hot and cold gas streams emerging from the device, the hot and cold gases are mixed in the correct proportions to just cancel the impact heating effects, and the sensing element indicates the ambient air temperature directly. Although no theory of operation of the vortex thermometer has been developed, extensive investigations have been conducted on empirically designed models. Ruskin** reports on careful tests of the NRL axial flow thermometer mounted on a whirling arm. For speeds of up to 500 mph, the speed compensation error did not exceed 0.1°C . Other designs, similar to the tangential model of Vonnegut's, have also been designed and tested. Flight tests on the NRL and Armour Research designs show*** errors from 2 to 5°C for the NRL design, constant to about $M = 0.7$, then increasing, and larger errors, increasing with velocity, for the Armour design. A vortex tube can be designed to read static temperature with a minimum correction for velocity at a given ambient density (altitude). Knowledge of vehicle trajectories thus would permit proper design for the density regime at which the vehicle attains a velocity significantly less than sonic. It appears that a properly designed vortex probe can read static temperatures correct to about 1°C . Independent velocity measurements, combined with calibration of the vortex probe (as installed on the vehicle, would permit determining correction factors, so that temperature could be calculated to about 0.1°C .

*Vonnegut, B., "Vortex Thermometer for Measuring True Air Temperatures and True Air Speeds in Flight," Review of Scientific Instruments, V. 21, No. 1, February, 1950, p. 136.

**Ruskin, Schecter, Dinger, and Merrill, "Development of the NRL Axial-Flow Vortex Thermometer," NRL Report 4008, September 4, 1952.

***Cochran, Roy J., "Flight Tests of Two Experimental Vortex True Free Air Temperature Systems," Technical Note WCF-54-9, WADC, ARDC.

Vortex thermometer probes are made by the Bendix Aviation Corporation, Friez Instrument Division, as part number V-1331245. This instrument is based on the NRL design and is 1 3/8" dia, x 6" long.

The alternative to designing a probe with a zero recovery factor is to design one with a known recovery factor and compensating for velocity effects. Many such probes have been developed for wind tunnel testing and there are many references in the literature to total temperature probes, sonic-flow probes, etc. Most of these were designed for use with thermocouples, however, and would require re-design for use with resistance thermometers or thermistors. The Rosemont Engineering Company, Minneapolis, Minnesota, manufactures a flight test total temperature probe using a resistance thermometer as a sensing element. Their bulletin 7597 describes the characteristics of the probe and indicates a recovery factor of 0.98 for sub-sonic conditions. Among others manufacturing total temperature probes are the Giannini Controls Company whose probe also has a recovery factor of 0.98 and a resistance type sensing element and Aero Research. The data available on the Rosemount probe is more extensive than that on the others, however.

The total temperature probe would have errors due to the uncertainty in recovery factor and velocity. Assuming that its recovery factor is known to within ± 10 per cent, the error would be less than 3°F at 400 ft/sec and less than 1°F at 200 ft/sec. Most of this error is due to uncertainty in velocity.

Since the impact temperature rise is a function of velocity, it is natural to consider using temperature difference to measure velocity. Solving Equation (1) for velocity yields

$$\begin{aligned} V &= 2g C_p \sqrt{T_T - T_S} \\ &= 112 \sqrt{\Delta T} \quad \text{ft/second} \end{aligned}$$

differentiating

$$\frac{dV}{d(\Delta T)} = \frac{112}{2\sqrt{\Delta T}} = \frac{112^2}{2V}$$

The error in velocity for a given temperature error can then be obtained by multiplying the derivative by the temperature error

$$V_E = \frac{dV}{d(\Delta T)} (\Delta T_E) = \frac{112^2}{2V} \Delta T_E$$

when V_E = velocity error

T_E = temperature difference error

Velocity errors for various assumed values of temperature rise errors are plotted in Figure 2.6.3. As shown by this curve, the errors in velocity due to small errors in temperature difference are excessive below 400 ft per second, and it is concluded that this is not a feasible method of measuring velocity for this application.

2.6.3 Ranges

The predicted range of temperatures for altitudes from 0 to 80 KM is from 150 to 750 K. Temperatures at higher altitudes cannot be measured because of dynamic heating effects and telemetry blackout.

Temperatures over this range of values can readily be measured by means of resistance thermometers. An accuracy of ± 1 per cent ($\pm 5^\circ\text{C}$) can be obtained readily. To give some margin on the predicted range, the resistance thermometer should be adjusted to cover from 100 to 800K. For greater accuracy, a more limited range sensor should be included, with its range adjusted for greatest sensitivity at the temperature predicted for about 40KM, where the velocity has become sub-sonic, and telemetry contact has been established. For the best atmospheric model, the temperature at this altitude is about 250K. Thermistors have shown excellent stability and high output at this temperature. Therefore, a second temperature detector should be included, using a thermistor and associated resistors to cover the range from 250K to 350K. Assuming an accuracy of ± 1 per cent, the temperatures can then be measured to $\pm 1^\circ\text{C}$.

2.6.4 Weight, Volume, Power Requirements

The temperature sensors are very simple devices, consisting primarily of the sensing element itself (thermistor resistance wire), a load resistor, and the bias power supply. For the case of the thermistor, a total weight of one ounce, a volume of 1/2 cubic inch, and a power requirement of 1/2 watt seem appropriate. For the case of resistance wires, an amplifier will be required, adding about two ounces and two watts. This amplifier could, of course, be time-shared among several temperature sensors.

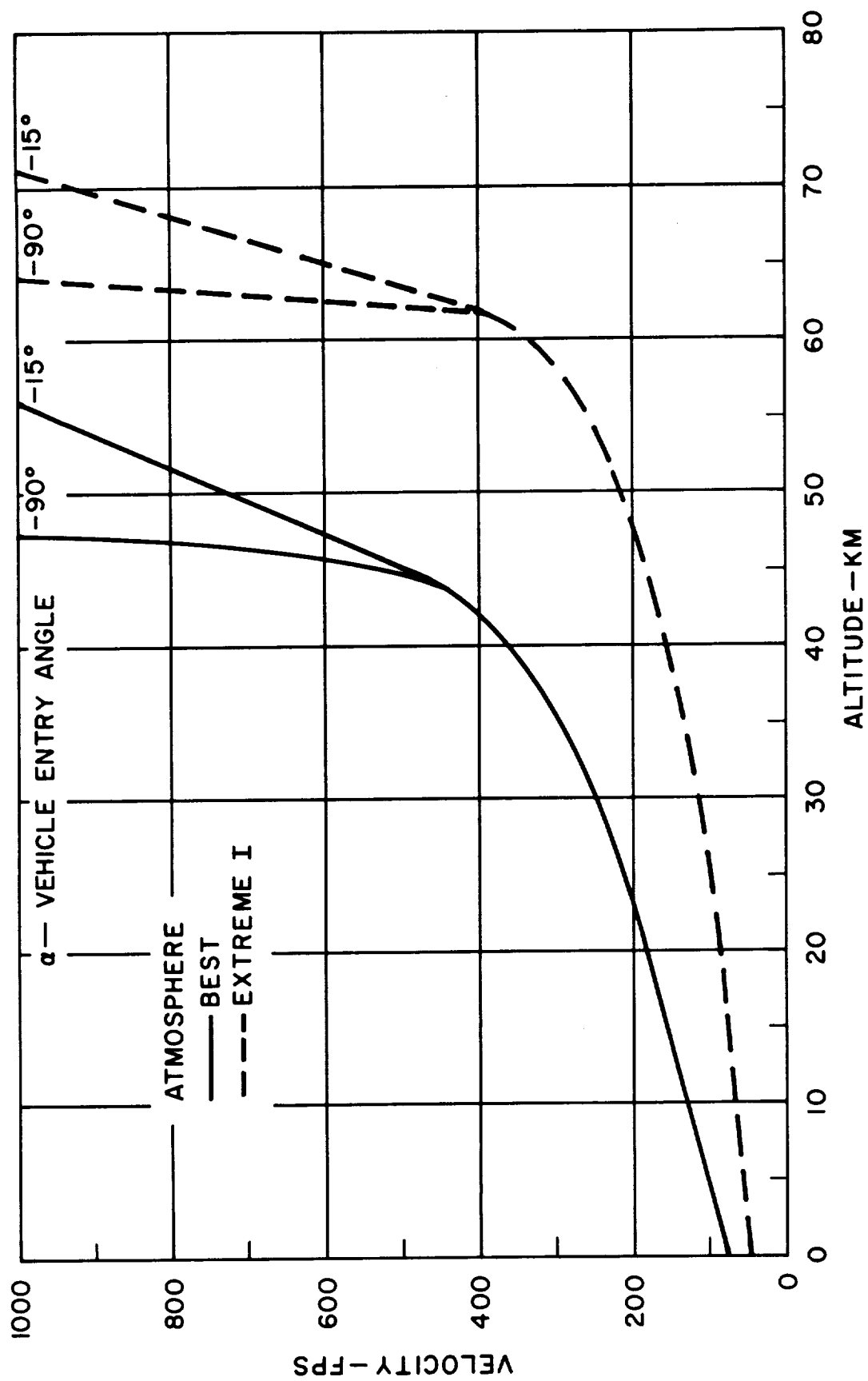


Figure 2.6.1. Capsule Velocity

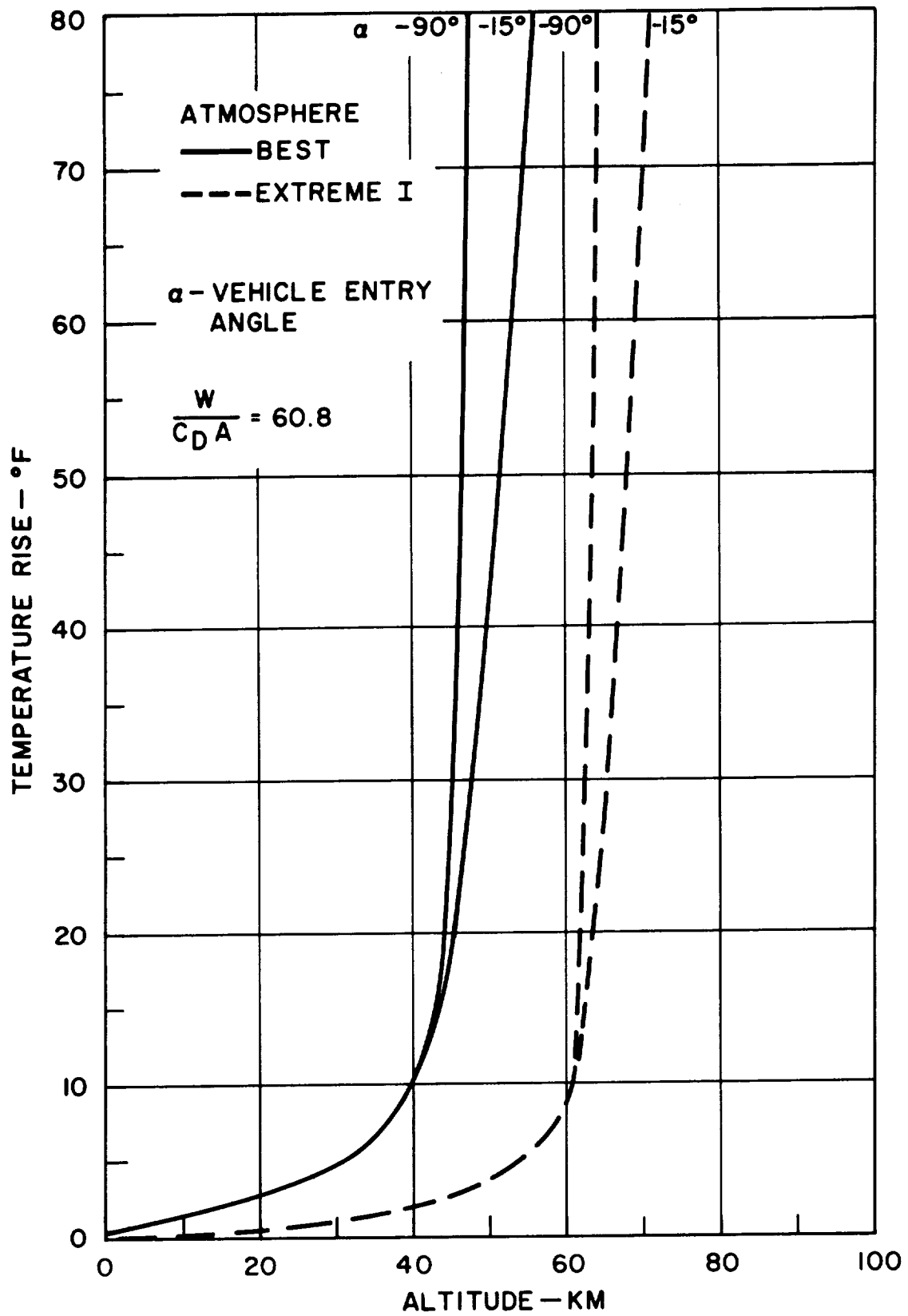


Figure 2.6.2. Subsonic Impact Temperatures

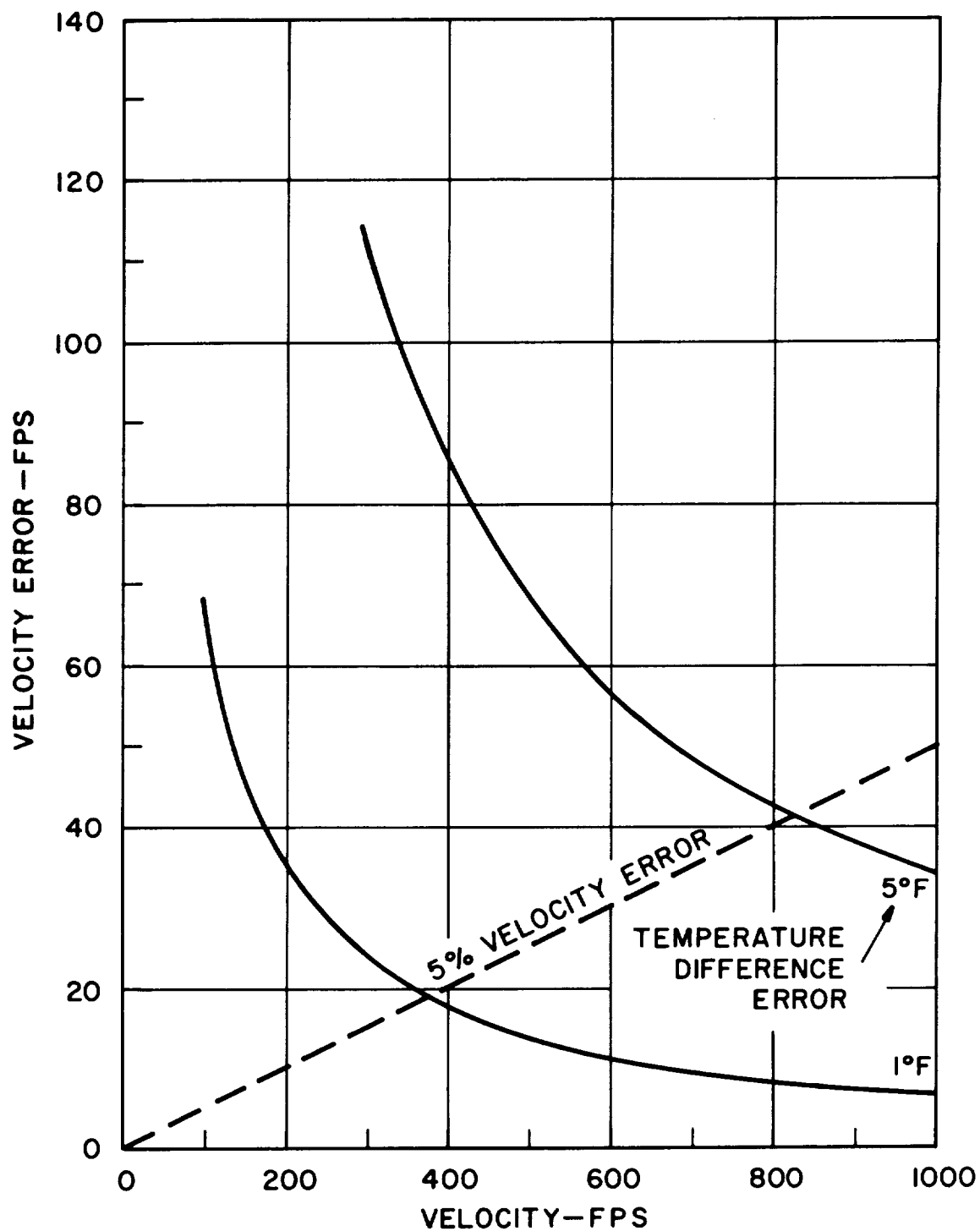


Figure 2.6.3. Effect of Temperature Difference Errors on Velocity Errors

2.7 DENSITY

Conventionally, density is determined by weighing a sample of known volume, and computing the density from the weight and volume information. Such methods cannot be applied in a falling vehicle, and other methods must be employed.

The most promising method of measuring the density of the atmosphere is to employ some form of radio-active gaging. Devices of this type would not be subject to any acceleration, oscillation, or, except for changes in sensitivity of the detector, any temperature effects.

Three types of sources can be used for radio-active gaging: alphas, betas or gammas. The advantages and limitations of each will be compared in the following sections. Each of the three methods can employ either direct absorption techniques, or back-scattering techniques. Comparing the two, the back-scattering methods have the advantage of measuring in the gas stream flowing by the vehicle, with a minimum disturbance to the gas being measured. This assumes that the source and detector can be mounted in the skin of the vehicle, and that the absorption of the skin will not be so high as to mask the measurement. Back-scattering has the additional advantage that the count rate is zero for zero density, and increasing count rate indicates increasing density. Absorption techniques, on the other hand, start with a high count rate at zero density, and decrease with increasing density. This means that the information on density is obtained by subtracting a reading from an originally high count rate.

The absorption technique requires the gas to pass between the source and the detector. The best method of doing this would be to erect the source on a boom outside of the vehicle. This would cause a minimum disturbance to the gas. If this is not feasible, a gas sample would have to be drawn into a chamber within the vehicle. Care would have to be taken to insure that the gas density was not changed by the possible temperature and pressure changes involved in bringing a gas sample within the vehicle.

One advantage of the absorption techniques is that the required source strength would be much less than for the backscattering methods. Calculations have shown, however, that the backscattering required source strength is not prohibitive.

2.7.1 Alpha Particles

2.7.1.1 Alpha Attenuation

Experimental set up: An ionization chamber which has its interior walls coated with an alpha emitter.

Advantages:

1. The value of $\frac{dE}{dx}$ for α - particles in a gas is high.
2. An ionization chamber, whose current is a function of density, can be made quite small.
3. The output signal from the ionization chamber increases with increasing density.
4. Ionization chambers can stand high temperatures quite well. (i.e. temps to 600°K).
5. The output is analog in nature.

Disadvantages:

1. A high voltage supply is needed to collect ions.
2. A stable D.C. current amplifier is needed.

2.7.1.2 Alpha Backscattering

Experimental Set up: Collimated source and detector, both on vehicle surface:

Advantages:

1. The source and detector can be located on skin of vehicle, thus measuring essentially undisturbed conditions.
2. Solid state detectors may be used. (Molechem, Inc., Princeton, N.J.)

Disadvantages:

1. A very good amplification system is needed for solid state detectors.
2. Detector is temperature sensitive, and must be cooled or insulated from the gas stream if the temp is high.
3. Thermal insulation will absorb the α - particles, hence detector must be exposed to ambient temperatures.

2.7.2 Beta Particles

2.7.2.1 Beta Attenuation

Experimental Set up: Beta source and scintillation detector:

Advantages:

1. Source has an energy distribution which is continuous (up to some maximum value).
2. The stopping power in CO_2 - N_2 mixtures does not vary much with composition.
3. β particles will penetrate modest amounts of thermal insulation, if need be.

4. β particles are readily detected in a scintillation crystal.
5. Output signal is in pulse-rate form.

Disadvantages

1. A High Voltage power supply is needed for the photomultiplier
(Note however, that such supplies have been designed so that they are mounted right at the photomultiplier socket, and the entire assembly is potted. In addition, it may be feasible to replace the photomultiplier with a solid state light detector, even though the sensitivity of this is less than that of the photomultiplier tube.)
2. Thermal insulation of detector-scintillator assembly is required to limit the temperature rise to no more than 10°C per hour.
3. NaI (Tl) crystals may not withstand high temperature standard ones will not operate above 71°C (letter from J. G. Bellian). Special crystals will operate to 150°C (Phone conversation with C. A. Ziegler, Parametrics, Inc.)
4. Phototube gain changes with temperature, decreasing about 0.15% per degree rise in temperature. (Letter from J. G. Bellian) between 20°C and 150°C .

2.7.3 Gamma and X-Rays

2.7.3.1 γ Backscattering (using a scintillation crystal detector).

Advantages

1. The source and detector may be mounted on the skin of the vehicle so that the gas is essentially undisturbed while measurements are being taken on it.

Ref: Letter from J. G. Bellian, Technical Sales, Crystal-solid State Division, Harshaw Chemical Co.

2. γ - rays are penetrating, and so the detector may be thermally shielded, if necessary, and yet the γ - rays will easily penetrate the shielding. (e.g., .032" Aluminum will stop only about 5% of incident 70 K ev γ - rays.)
3. Output signal is in pulse-rate form.

Disadvantages

1. A high voltage power supply is needed. (See notes under Beta Attenuation).
2. Thermal insulation of the detector is necessary (see previous section).
3. NaI (Tl) crystals may not withstand high temperatures while working. (See previous section).
4. The phototube changes gain with temperature. (See previous section.)

2.7.3.2 X-Ray Absorption Techniques

One of the X-ray absorption techniques considered in detail used Fe_{55} as the source. The calculations were based on a report by Mullaney* of the use of such a method to determine flame temperatures. Fe_{55} emits radiation with an energy of about 6 KEV. Using the conventional absorption equation given in (1) below:

$$I = I_0 \frac{A}{4 \pi d^2} e^{-\frac{\mu}{\rho} \rho t} \quad (1)$$

*Mullaney, George J. "Temperature Determination in Flames Using a Radio-Active Source of X-Rays," General Electric Report No. 56-RL-1494 February 1956.

where I_o = source intensity

$$\frac{A}{4 \pi d^2} = \text{geometrical factors}$$

l = path length

and assuming a path length of 15 cm, an absorption coefficient $\frac{\mu}{\rho}$ of 18 for nitrogen, a sensitivity relationship with altitude as shown in Figure 2.7.1 was obtained. This figure shows that adequate sensitivity can be obtained by the method, but several problems are anticipated. One is that of obtaining a representative sample and another is to obtain a detector with adequate sensitivity. The radiation proposed is of low energy level, and any detector must have a thin window, with an absorption less than that of the gas. Geiger-Muller tubes with very thin windows might be used, but would have to be specially designed to withstand the entry decelerations.

2.7.4 Summary

Examining the 6 basic schemes of density determination considered, two look significantly more attractive than the others, and these are gamma back-scattering, and beta attenuation.

The gamma backscattering technique has been exhaustively discussed in a report by the Giannini Controls Corp. (GSDP-23a; 16 May 1962). The device, as suggested by them, was designed for Mariner, and would have one serious difficulty if applied to the "Venus Entry Capsule." The problem centers around the thermal requirements of the scintillator-detector combination, as cited in the previous sections. It appears that since gamma radiation in the 70 KEV range is reasonably penetrating (five per cent absorption in 2mm. of plastic or in 1mm. aluminum) it is practical to thermally insulate the detector. Giannini (loc. cit) indicates a weight of 1 1/2 pounds for their entire system, but this might be somewhat larger in the present case, due to the thermal insulation requirements.

Beta attenuation appears quite practical if one considers either a "tube" or open structure for the entry capsule (after the shedding of the heat shield) since in this case one could easily have a 25 cm. or so distance between source and detector. Parametrics has established the feasibility of density measurements using beta attenuation. (C. A. Ziegler, Parametrics, Inc., Waltham, Mass.).

The limit again will be the thermal requirements on the scintillation detector. Thermal insulation is easier in this case than in the previous one from the viewpoint that the detector can be located inside the capsule, rather than near the surface. On the other hand, Beta particles are not very penetrating and one cannot use a window thickness of more than 20 mg/cm.^2 of Aluminum (about 1mm thickness) as thermal insulation between gas and scintillator.

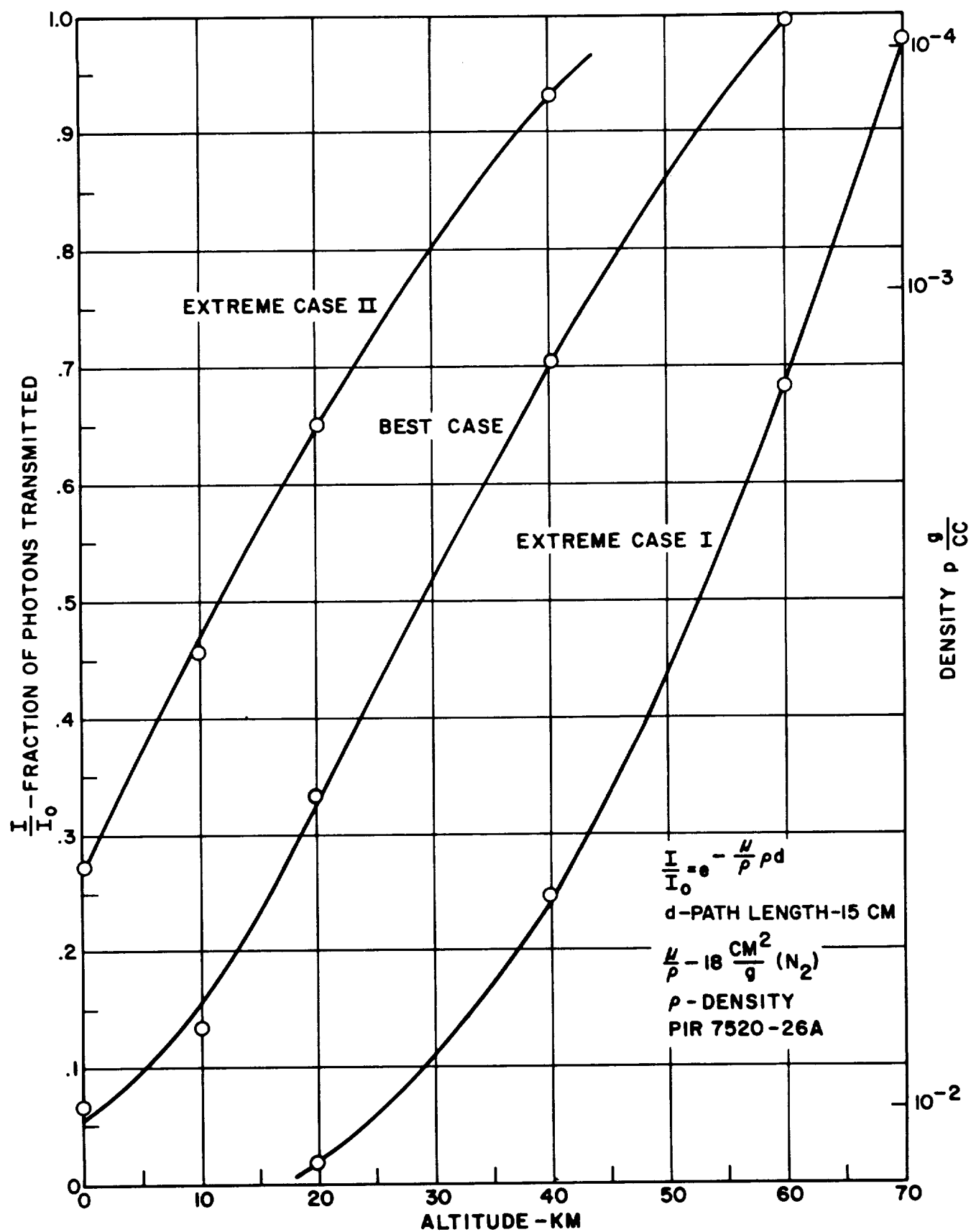


Figure 2.7.1. Density Detector Response

2.8 CARBON DIOXIDE DENSITY MEASUREMENTS

The density of CO₂ in the Venutian atmosphere may be measured in several ways, but only two specific techniques will be considered here: thermal conductivity and infrared optical absorption.

2.8.1 Thermal Conductivity

The principle of the method is that heat is conducted away from a hot body, situated in a gas, at a rate depending upon the nature of the gas; other factors being constant. Sensors based upon this property are known as thermal conductivity cells or katharometers. A katharometer of the usual construction contains either metallic wires (preferably having a high temperature coefficient of resistance) or thermistors mounted in an enclosure containing the gas. Since absolute measurements of thermal conductivity are difficult, a differential procedure is usually employed. Two gas enclosures and detectors (e.g. thermistors) are constructed as nearly identical as possible. One enclosure contains a reference gas, and the other contains the gas whose conductivity is to be compared to that of the sample. The two different conductivities of the gas samples will cause the thermal elements in the enclosures to be at different temperatures and thus at different resistances. The resistances are compared or measured; generally in a bridge circuit.

The katharometer is simple to construct and can be made small, of the order of one cubic inch; light weight, of the order of two ounces; and rugged. In order to obtain useful results, however, certain precautions need be taken to minimize and correct for asymmetry effects, and to obtain calibration curves. Some of the more important asymmetry effects in differential katharometers are:

1. The symmetry of construction of a double enclosure katharometer cannot be relied upon to produce symmetrical output with varying wall temperatures. Typical results* from two precisely-constructed

*A.I. M. Keulemans, "Gas Chromatography," New York, Reinhold Pub. Co., 1959.

double enclosure katharometers containing the same gas showed asymmetrical outputs varying from 0.016 millivolts per degree C to 0.02 millivolts per degree C over a range of $\pm 5^{\circ}\text{C}$ about a balance wall temperature of 25°C . Another pair of cells varied about half this much when balanced at 120°C wall temperature.

2. The output may vary with change in detector operating current. Typical results show a change of 0.013 mv per ma of filament current after the bridge had been balanced at 200 ma. Another double cell varied about half that much.

The output varies with rate of flow of sample gas. This is not an asymmetrical effect. While the thermal conductivity of a gas varies with gas composition, in general, the thermal conductivity of a mixture of gases is not a linear function of composition.

It is customary to calibrate each katharometer rather than to rely upon known construction dimensions and calculated responsivity. Because the environmental conditions are not known in the Venutian atmosphere, the katharometer must be exhaustively calibrated for all expected ranges of parameters before it is sent out. In addition to telemetering katharometer output, the wall temperature and sample gas pressure must be telemetered. Then the CO_2 density is computed assuming that only CO_2 and N_2 make up the Venutian atmosphere.

Since the pressure in the sample chamber will be that of the Venutian atmosphere, there will be only a small portion of the entry time during which the sample chamber and sealed reference chamber will be approximately at the same temperature and pressure. It is during this time that the conductivity measurements will benefit from differential operation. At other times, and therefore pressures, the benefits of differential measurement will be marginal or lost altogether.

2.8.2 Optical Absorption

Many factors place restrictions upon the accuracy of infrared transmission predicted by theoretical or empirical models. Diffraction of light by the experimental apparatus is one of the inherent limitations of usual spectroscopic techniques that present difficulties to the inference of the very fine structure of absorption bands from spectra measured in the laboratory; especially for bands composed of a large number of randomly overlapping spectral lines of randomly sized amplitudes. If the precise position, shape and total intensity of each individual line could be known, and if the exact temperature, pressure, and density of the major absorbing species could be known at all points in an atmosphere, then the optical transmission over a specified path could, in principle, be predicted to any desired degree of accuracy. Such an evaluation represents a formidable task, even for a high speed computer. However, the engineering problem of computing the amount of CO_2 in remote gas sample requires a more practical method.

2.8.2.1 Line-Of-Sight Transmission

In the present case the remote gas sample is the Venutian atmosphere. While the amount of CO_2 is to be found accurately, the instrument to do this need not necessarily measure spectra with a high degree of resolution. In this case, simplifying assumptions are made so that a general expression for the concentration may be formulated as a function of frequency, pressure, temperature and transmission. The formula must be a simple form or else vast computational labor is needed. The greatest drawback is that even if an empirical formula fits laboratory data accurately, there is no assurance that it will apply to long path lengths of varying pressures and temperatures. Lastly, there is no guarantee that the capsule will enter from the sunlit side. For these reasons, the line-of-sight transmission measurements are not as promising as the absorption cell measurements.

2.8.2.2 Absorption Cell Operation

In an optical absorption cell, a light source and a light detector are separated by a volume filled with the gas whose optical transmission is to be measured. The transmission is a function of carbon dioxide content, composition, light wavelength, pressure, and temperature. If all quantities but one are known, the unknown may be determined from the calibration curves.

This instrument is to operate after the entry capsule becomes subsonic, and continue to operate, ideally, to impact. Table 2.8.1 shows the partial pressure of CO₂ for the various per cent compositions and cases.

<u>Case</u>	<u>Altitude (km)</u>	<u>Pressure atm</u>	<u>Tempera- ture - °K</u>	<u>CO₂ Partial Pressure (atm)</u>		
				<u>2.5%</u>	<u>10%</u>	<u>25%</u>
Extreme I	0	56	750	1.4	5.6	14
Extreme I	46	3.7	350	.09	.37	.9
Extreme I	60*	0.4	250	.01	.04	.1
Best	0	16	600	.4	1.6	4
Best	28	2.5	350	.06	.25	.6
Best	45*	0.36	230	.009	.036	.09
Extreme II	0	6	500	.15	.6	1.5
Extreme II	16	2.3	350	.058	.23	.58
Extreme II	30*	.48	250	.012	.048	.12

Table 2.8.1

The partial pressure of CO₂ is shown for the various compositions and cases. The altitudes marked with * are those at which the entry capsule becomes subsonic.

The mixing ratio is assumed to be constant at all altitudes at which measurements will be made. Therefore, one measurement of the transmission will be sufficient to enable the per cent CO₂ to be computed. Several measurements will be redundant, but useful as checks. The capsule may not survive to reach the planet's surface because of the temperature, so it is most important to obtain

measurements in the moderate temperature range 250°K , 350°K soon after the capsule becomes subsonic. Figure 2.8.1 shows the transmission of $\nu = 675\text{ cm}^{-1}$ as a function of path length and pressure. The filter is assumed to be 50 cm^{-1} wide and to have unity response. The data for the solid curves were taken from Stull, Wyatt, and Plass*.

The dashed curves are extrapolations. These data are calculated for 300°K . Thus, the true curves for the temperature range of 250°K to 350°K will be similar. It is seen that if the physical path length of the absorption cell is 10 cm , then the locus of the points representing any given case between the Extreme I & II and any given partial pressure from 2.5 per cent to 25 per cent will lie partially in the transmission region of 0.4 to 0.6. In particular, for the Best Case with ten per cent partial pressure of CO_2 , the transmission varies from 0.8 at 45 km altitude to ~ 0.3 at 28 km altitude. On the basis of this set of curves, then, the absorption cell will be made 10 cm long.

The "Absorption Cell" will be part of the vehicle structure: The interior of the cell wall will be black anodized to prevent reflections. Alternatively, the interior will be coated with a low-reflectance paint as recommended by Hillery & Ramsey**.

The filter will be a reasonably broad one to cover the wave numbers from about 650 cm^{-1} to 700 cm^{-1} . The detector will be either a thermocouple or a thermistor; depending upon other circuiting in the capsule. This cylindrical type of construction is well-suited to withstand high linear accelerations, especially parallel to the axis of symmetry.

The calibration of the completed sensor consists of measuring the transmission of gas samples of known composition of N_2 and CO_2 . In essence, a series

*Stull, V.R., Wyatt, P.J., and Plass, G.N., AFCRL - 62-210 (11) (Dec. 1961)

**D. Hillery and W. Ramsey, Satellite Meteorology Section - U.S. Weather Bureau, Suitland, Md.

of families of curves such as the family shown in Figure 2.8.1 are constructed experimentally for various temperatures. The range of variables should be as follows:

Temperature: 200°K to 400°K .

Total Pressure: 0.1 atm. to 50 atm.

% CO_2 : 1% to 30%

These ranges are adequate to cover the expected variations and to extend somewhat beyond.

In operation, the following data are needed: 1) optical transmission, 2) gas temperature, 3) gas total pressure. During or after entry, by referring to the family of calibration curves for the appropriate temperature, the path length, in atm-cm, may be found corresponding to the measured total pressure and transmission. Division by the length of the absorption cell yields the desired partial pressure of CO_2 .

2.8.2.3 Weight & Power

A typical unit would consist of a source of infrared - typically a 1 mm. diameter wire heated to about 800°K - and two detectors at different distances from the source. In addition four lenses (or mirrors) and two filters would be needed. Total weight would be about 1/2 pound, and power requirements would be about 2w.

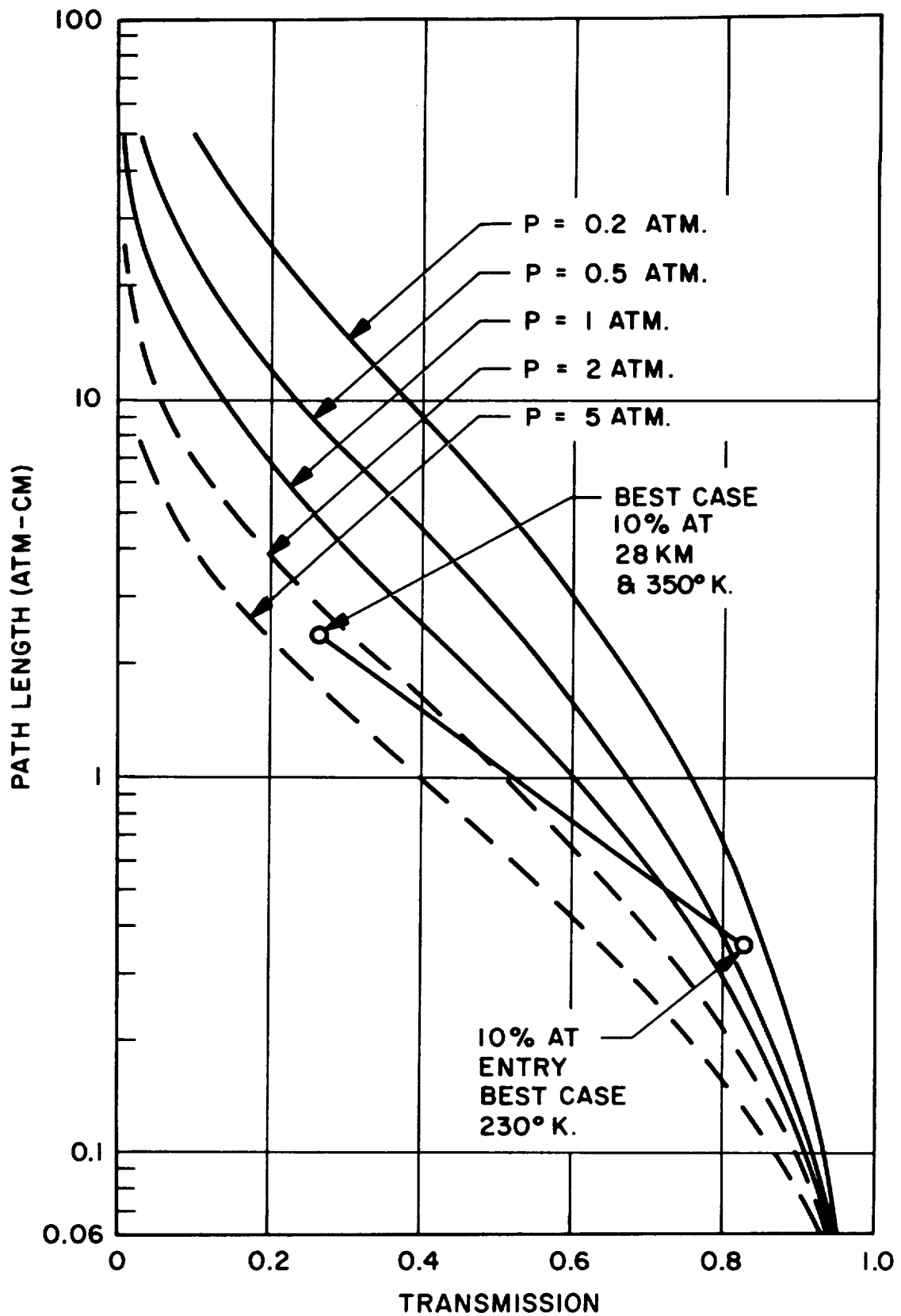


Figure 2.8.1. The Optical Transmission of CO₂ in the Region of 675 cm⁻¹ is Shown as a Function of Path Length for Various Pressures

2.9 MOLECULAR SCATTERING

One technique considered early in the study to determine density as a function of altitude was the attenuation of solar radiation due to molecular scattering. The application of this technique to the Venus entry capsule seems to be brought with serious obstacles, particularly the low probability of seeing the sun during the entry time, the difficulty of determining the solar elevation angle as a function of capsule location, and the possibility of cloud obscuration of the sun, and hence, it is not recommended for the present capsule.

The results of the study of molecular scattering as applied to the atmospheres of Mars and Venus are presented here both for possible utilization on the former planet, and also to indicate the overall possibilities of this technique.

It should be noted this research was primarily supported by funds supplied under the Independent Research and Development Program.

2.9.1 Introduction

With the prospects of probing the atmospheres of Mars and Venus it becomes desirable to determine the optical thickness of those atmospheres, and its dependence on wavelength of incident solar radiation, altitude above the surface of the planet, and composition of the atmosphere itself. Once the optical thickness is determined, a first approximation to the absolute intensity of both the direct and scattered solar radiation as a function of altitude above the planetary surface, as well as distribution of the scattered radiation in the atmosphere, can be obtained from available tables (2)*. These tables are based on the exact theory of scattering in a molecular atmosphere, as developed by Chandrasekhar (1). Refinement of the approximation can be made by taking atmospheric aerosol scattering into account by a method similar to that suggested by Sekera (13), in which the molecular optical thickness is increased appropriately to account in some measure for the aerosol effects.

*Numbers in parentheses denote references listed at the end of this report.

The following discussion deals with the optical thickness for Rayleigh (molecular) scattering only. Molecular scattering must be a major part of the radiative transfer problem in any real planetary atmosphere.

Because of the still largely unknown character of the atmospheres of Mars and Venus a number of atmospheric models have been used for the determinations of optical thickness. The variations of the parameters have been chosen sufficiently large to show the ranges likely to exist.

2.9.2 Method

The equation of radiative transfer in an attenuating medium takes the form

$$dE_{\lambda} = E_{o\lambda} K_{\lambda} dS \quad (1)$$

where $E_{o\lambda}$ is the energy of monochromatic radiation of wavelength λ incident on, and E_{λ} that emerging from, an elemental cylindrical volume of unit cross sectional area normal to the direction of propagation and of length dS taken along the direction of propagation. K_{λ} is the volume attenuation coefficient applicable to the material in the volume. In general, attenuation may be due to both true absorption and scattering of the radiation. Fortunately, for certain spectral regions and certain gases the absorption is negligible compared to scattering, so that the problem can be simplified. For atmospheres composed of nitrogen, oxygen, carbon dioxide, and argon the region of negligible absorption extends from the near ultraviolet through the visible to the near infrared. Within that region, K_{λ} can be replaced by the volume scattering coefficient, β_{λ} , in Equation (1), giving

$$dE_{\lambda} = E_{o\lambda} \beta_{\lambda} dS . \quad (2)$$

Lord Rayleigh (15) showed that for a gas of refractive index n the coefficient β_{λ} is

$$\beta_{\lambda} = \frac{32}{3} \frac{\pi}{\lambda^4} \frac{(n-1)^2}{N} , \quad (3)$$

N being the total number of scattering particles per unit volume of the medium.*
For a given mass density ρ of gas

$$N = \frac{\rho N_A}{M}, \quad (4)$$

where N_A is Avagadro's number and M is molecular weight of the gas. For a mixture consisting of k different gases Equation (4) applies to the i th component of the mixture, and the total number density is obtained by summing over the k component gases. Then the volume scattering coefficient for the mixture takes the final form

$$\beta_\lambda = \frac{32}{3} \frac{\pi^3}{\lambda^4} \sum_{i=1}^k \frac{(n_i - 1)^2}{N_i}, \quad (5)$$

where n_i and N_i are the i th gas. This procedure is valid under the assumption that the molecules are widely spaced in comparison to their size, a condition which is well realized in the planetary atmospheres under consideration. The depolarization factor, arising because of the nonisotropic character of molecules, has been neglected in the foregoing discussion and in the computations. The error introduced thereby, being of the order of a few per cent, is probably of negligible significance in comparison to other uncertainties in planetary atmospheres. A complete discussion of the depolarization effect is given by Partington (10).

Data on refractivity of the various gases were taken from International Critical Tables (9). The wavelength dependence was determined by the relation

$$(n - 1) 10^6 = \frac{\beta'}{(\mu' - \lambda^{-2})}$$

*This form is chosen in place of the more commonly used expression

$$\beta_\lambda = \frac{8}{3} \frac{\pi^3}{\lambda^4} \frac{(n^2 - 1)^2}{N}$$

in order that these computations will be comparable with those of Deirmendjian (3) for the Earth's atmosphere. The two forms are of equivalent accuracy.

for nitrogen and carbon dioxide, and by $(n-1) 10^6 = A + B_{\lambda}^{-2} + C_{\lambda}^{-4}$ for argon and oxygen. Values of the constants, for the gas at STP and wavelength in microns, are given in Table 2.9.1.

Table 2.9.1. Values of Constants Used for Determining Dispersion for Atmospheric Gases at STP and Wavelength in Microns

Constant	A	B	C	β'	μ'
Gas					
Nitrogen	—	—	—	55939	189.94
Carbon Dioxide	—	—	—	69049	156.63
Argon	277.826	1.558	0	—	—
Oxygen	269.74	0.372	0.126	—	—

There is no agreement among various experimenters as to the effects of pressure and temperature on refractivity, except, of course, through their influence on gas density. The experimental results, well summarized by Partington (10), indicate that over the range of pressures and temperatures likely to be encountered in planetary atmospheres the refractivity is, within experimental error, directly proportional to the density. Consequently no other corrections are applied here for atmospheric pressure or temperature effects.

Because of density variations, β_{λ} is dependent on time and position in a planetary atmosphere, as well as on atmospheric composition. However, the time variations of density at a given altitude are relatively small, at least in the Earth's atmosphere, compared to spatial variations existing at any one time. Deirmendjian (3) studied the seasonal changes of optical thickness for a wavelength of 5200 Å at two locations in the United States and found that the seasonal effect varies from only about one per cent at the ground to a maximum of four per cent to six per cent at eight kilometers. From meteorological considerations, the shorter period variations should be of comparable magnitude, as should also the variations in the horizontal direction. Contrasted to these relatively minor variations is the approximately exponential variation of density in the vertical direction. Typically, a six per cent change of density occurs in only 600 meters change of altitude in the Earth's atmosphere. In view of these facts, it is

sufficient for present purposes to consider density being a function of altitude only, the vertical density profile being determined for a number of different atmospheric models.

The flexibility inherent in Equation (5) for taking into account changes of composition is utilized in the present case for studying the scattering by different atmospheric models, a procedure necessitated by the still largely unknown atmospheric compositions existing on Mars and Venus. Hopefully vertical variations of the relative abundances of the constituents will be small so that the computed variations of optical thickness for the appropriate model will approximate reality.

Once the volume scattering coefficient is determined, as a function of wavelength and altitude, determination of the optical thickness is a simple matter. The normal optical thickness of the atmosphere between a point at height z and the effective top of the atmosphere is defined by the relation

$$\tau(\lambda, z) = \int_z^{\infty} \beta(\lambda, z) dz. \quad (6)$$

Qualitatively, τ is strongly dependent on altitude, because of the exponential change of density with altitude, and is strongly dependent on wavelength, because of the well-known negative-fourth-power wavelength dependence of Rayleigh scattering. Numerical values of τ , given in some detail in the following section, typically range between 1.0 and 0.01 for wavelengths between 0.30μ and 1.0μ at sea level in the Earth's atmosphere. As will be seen below, values of τ at the Martian surface will be considerably smaller, and at the surface of Venus considerably larger, than they are at the Earth's surface for equivalent wavelengths.

In order to carry out the integration for the different models, the volume scattering coefficient was put into the form

$$\begin{aligned} \beta(\lambda, z) = \frac{32}{3} \frac{\pi^3}{\lambda^4} m^2 M^2 \left[(C^2N)_{CO_2} + (C^2N)_{N_2} + (C^2N)_A \right. \\ \left. + (C^2N)_{O_2} \right] \frac{P_z}{P_s} \frac{T_s}{T_z} \end{aligned} \quad (7)$$

where m is the unit of molecular weight (reciprocal of Avagadro's number), P is pressure, T is temperature, and the subscripts x and z refer respectively, to standard conditions and conditions at height z in the atmosphere. The following relations are easily shown (see Appendix A) to hold for the cases indicated:

$$P_z = P_o \exp \left[\left(-\frac{gM}{R^* T_o} \right) (z - z_o) \right] \quad (\text{isothermal case}) \quad (8)$$

$$P_z = P_o \left(\frac{T_o + \gamma z}{T_o} \right)^{-\frac{gM}{R^* \gamma}} \quad (\text{non-isothermal case}) \quad (9)$$

Here P_o , T_o , and z_o all refer to conditions at an arbitrary reference level, usually chosen as either the planetary surface or a level at which there is a change of lapse rate, γ . The height z is, of course, taken with respect to that reference level. M is the effective molecular weight of the gaseous mixture, R^* is the universal gas constant, and g is the acceleration of gravity. On substituting Equation (9) into Equation (6) and integrating for the layer between z_o and z_1 over which the lapse rate is considered constant, one obtains the increment of optical thickness

$$\Delta \tau_{z_o, z_1} (\gamma \neq 0) = K_1 \frac{P_o}{T_o} \left[\frac{\left(1 + \frac{\gamma}{T_o} z \right)^{-\frac{gM}{R^* \gamma}}}{-\frac{gM}{R^* T_o}} \right]_{z_o}^{z_1} \quad (10)$$

$$K_1 = \frac{32}{3} \frac{\pi^3}{\lambda^4} m^2 \frac{T_s}{P_s} \sum_{i=1}^4 (C^2 M^2 N)_i, \quad (11)$$

where the summation is taken over the four gases considered. Obviously Equation (10) can be applied to as many layers as necessary to approximate any desired temperature structure.

For present purposes the atmospheric composition is considered to be independent of altitude, for which case one obtains the normal optical thickness in the final form

$$\tau(\lambda, z) = \frac{32}{3} \frac{\pi^3}{\lambda^4} \frac{N_o}{\rho_o} m^2 M^2 C^2 \int_z^{\infty} \rho \, dz. \quad (12)$$

Here M and C are the effective molecular weight and refractivity, respectively, for the mixture.

2.9.3 Atmospheric Models

The atmospheric models selected for Mars and Venus are summarized in Table 2.9.2. They are based on the latest information available, but the observational data from which they are derived are still very sparse, and opinions vary widely among different authors. They should be taken as only tentative estimates of actual conditions.

The models consist of the gaseous composition and the vertical structure of the atmosphere, both of which are included in Table 2.9.2. The arbitrary model numbers listed in the second column are used only for convenience. The composition for Models M1 and M2 corresponds to that suggested by deVaucouleurs (17). The total mass per unit area was estimated from the light-scattering

properties under the assumption that a given mass of the Martian atmosphere scatters light just as does the same mass of the cloudless Earth's atmosphere. The validity of this assumption is unknown but the wavelengths used in the determination were confined to $\lambda > 5000 \text{ \AA}$, in which case multiple scattering effects are minimized. The relative concentrations of large particles are perhaps not too different in general, but the data are still sparse for Mars. By this method deVaucouleurs obtained a surface pressure value of 85 mb, with a probable error of four mb. He considers it unlikely that the actual pressure is different from this by more than ± 40 per cent.

The composition of the Martian atmosphere is still uncertain and estimates are based mostly on indirect evidence. A full discussion of the problem can be found in deVaucouleurs (16). The vertical temperature profiles used are mainly based on conjecture, tempered by comparisons with the Earth's atmosphere. The existence of a stratosphere is by no means certain, being predicated on the assumption that the radiative role of water vapor in the Earth's atmosphere is played by carbon dioxide in the Martian atmosphere. If a stratosphere exists then a tropopause must exist. Estimates of the height of the tropopause range from three km to 45 km, depending on the atmospheric composition and governing processes assumed.

As a first approximation to the vertical structure, an isothermal atmosphere was assumed, the temperature being 223°K (Model M1). This would tend to overestimate surface density and underestimate density at high levels, thereby producing somewhat distorted profiles of volume scattering coefficient and optical thickness. The temperature profile of Model M2 is probably a more realistic one. It is the result of assuming convective equilibrium up to a tropopause height of 24 km, and isothermal conditions above that level. For a surface temperature of 273°K this makes the stratospheric temperature 183°K , in rough agreement with 173°K obtained by Hess (4) for radiative equilibrium. Obviously the possibility of large influences by trace gases in the upper atmosphere, such as the effects of ozone in the Earth's atmosphere, have been neglected.

Table 2.9.2. Composition and Vertical Structure of Planetary Atmospheric Models used in the Present Study

Planet	Model Number	Composition (% by Volume)				Vertical Structure			
		N ₂	O ₂	CO ₂	A	Altitude km	Temp. °K	Pressure ATM.	Lapse Rate between Indicated Levels (°K/km)
Mars	M1	93.8		2.2	4	0	223	8.39×10^{-2}	0-100 km: 0
Mars	M2	93.8		2.2	4	0	273	8.39×10^{-2}	0- 24 km: -3.75
						24	183	2.11×10^{-2}	24-100 km: 0
Venus	V1	80.0	0	20.0	0	0	600	2	0- 48: -7.5
						48	240	4.03×10^{-2}	48-200: 0
	V2	90.0	0	9.0	1.0	0	600	16.6	0-18.8: -8.5
						18.8	440	5.5	18.8-42.9: -8.5
						42.9	235	0.59	42.9-113: -0.4
						113.0	207	3.91×10^{-5}	113- - : +3.0
	V3	90.0	0	9.0	1.0	0	750	54.0	0-36.5: -8.49
						36.5	440	8.07	36.5-60.5: -8.54
						60.5	235	.873	60.5-110: +0.505
						110.0	260	2.037×10^{-3}	110-122: +4.17
						122	310	5.673×10^{-4}	122-133: +5.45
						133	370	2.125×10^{-4}	133-144: +7.27
						144	450	9.405×10^{-5}	144-178: +8.82
						178	750	1.629×10^{-5}	178-200: +8.77
						200	943	7.393×10^{-6}	
	V4	90.0	0	9.0	1.0	0	500	6.3	0-7.1: -8.45
						7.1	440	3.97	7.1-31.2: -8.51
						31.2	235	.426	31.2-41.2: -8.50
						41.2	150	8.63×10^{-2}	41.2- - : 0

The models for Venus are composites derived by various lines of reasoning. Because of the extremely meager available data, they are biased by conditions in the Earth's atmosphere. For instance, the existence of a troposphere-stratosphere structure is mainly conjectural, but it is at least a possible configuration for a planetary atmosphere.

Estimates of atmospheric composition of Venus vary widely. The presence of carbon dioxide was established by spectroscopic methods and there is no doubt that it does indeed exist, but the abundance is still controversial. Estimates of the amount of CO_2 above the effective reflecting level for 8000\AA radiation vary between 100 and 1000 meter-atmospheres (8). Kaplan (7) has reinterpreted some of the earlier data and derived a revised estimate of 15 per cent by volume for CO_2 content. Later estimates (Kaplan - private communication) have given even lower values, perhaps as low as ten per cent or less. It is presumed that the CO_2 mixing ratio is essentially constant throughout the major portion of the Venus atmosphere, as it is in the Earth's atmosphere. There is evidence of a small amount of water vapor above the visible cloud deck. The upper limit of oxygen above the cloud deck is 100 cm-atm (11). There may be trace gases, such as N_2O , CH_4 , C_2H_4 , and others, but they have not been detected so far.

Although there is no direct evidence, it is assumed that the bulk of the Venus atmosphere is N_2 . There is probably about one per cent by volume of argon.

The total mass of the Venus atmosphere and the vertical temperature structure are likewise open to much discussion. For present purposes various models have been assumed without much evidence on which to substantiate them. The troposphere-stratosphere configuration assumed is probably an oversimplification but it serves as a good first approximation. The evidence of a high surface temperature, around 600°K , seems well founded on microwave emission measurements, although the suggestion has been made (8) that the energy in the microwave region is emitted by a Venus ionosphere and does not represent a surface temperature effect. A somewhat sub-adiabatic lapse rate (-7.5°K/km) has been assumed for Model V1. This is still much nearer adiabatic than is the mean

lapse rate of the Earth's atmosphere, but it is justified by the high surface temperature of Venus. This lapse rate is assumed to prevail up to a level at which the temperature is about the thermocouple temperature measured in the 8-13 micron region. This puts the tropopause at 48 kilometers, in rough agreement with the "greenhouse" model depicted by Kellogg and Sagan (8). The surface pressure of two atmospheres for Model V1 is taken as representative of a probable minimum value.

The other models considered, V2, V3, and V4, are those suggested by the Jet Propulsion Laboratory (March 1962, unpublished) for the design of probes. It is pointed out by JPL that they are intended only to establish broad outlines of conditions which might exist. They consider Model V2 to be more realistic than Model V3 or V4. The evidence on which the models are based is a reinterpretation of the early work of Chamberlain and Kuiper on the CO_2 molecular band structure. Details of the reinterpretation are not yet available, but a spectrogram in the 7820\AA CO_2 band was interpreted to give a "mean" pressure of five atmospheres, the pressure at the base of the contributing CO_2 layer being about ten atmospheres. These data may apply to some level above the surface, so the surface pressure may be higher.

Since so little information is available, we have, for present purposes, used Venus models V2, V3, and V4 as they are given by the Jet Propulsion Laboratory.

2.9.4 Computations and Results

2.9.4.1 Mars

Curves of the volume scattering coefficient as a function of altitude for the Martian atmosphere from the surface to 60 kilometers for various wavelengths are given in Figure 2.9.1. Similar curves for three different wavelengths in the Earth's atmosphere, as computed by Deirmendjian (3), are given for comparison. The strong wavelength dependence can be seen in the greater than two orders of magnitude variation of β between $\lambda = 2500\text{\AA}$ and $\lambda = 10,000\text{\AA}$ at any given altitude. The scattering coefficient for the Martian atmosphere is

about an order of magnitude lower than that of the Earth for comparable wavelengths at the surface, but it decreases much less rapidly with altitude than does that of the earth, mainly because of the lower value of Martian gravity. The two are equivalent at about 26 kilometers as shown by the intersection of the curve segments graphically interpolated for $\lambda = 3750\text{\AA}$, 5200\AA , and 8350\AA , with those for the Earth for the same wavelengths. Above 26 kilometers the values of β are greater for Mars than for the Earth, a fact which may be of importance in planetary probes.

Table 2.9.3 gives values of β for several additional altitudes up to 100 kilometers. Deirmendjian's (3) data are included where they are available. By comparing entries in Table 2.9.3 with Figure 2.9.3, it is seen that at 100 kilometers β is about three orders of magnitude lower than at the surface for Mars, while for the Earth β decreases more than six orders in the first 100 kilometers.

Curves of the normal optical thickness as a function of altitude for the eight selected wavelengths are reproduced as Figure 2.9.2. These data are obtained by integration of $\beta(\lambda, z)$ with respect to altitude. Deirmendjian's results for the Earth's atmosphere for the wavelengths available are included. Surface values of optical thickness for Mars are smaller by a factor of four or five than for the Earth, but, as shown in the discussion (Section V), they still fall within a very advantageous range for light-scattering techniques. For instance, the extensive tables of Coulson, Dave, and Sekera (2), specifically for Rayleigh scattering, cover the range of optical thickness $0.02 \leq \tau \leq 1.0$, and the scattering functions computed by Sekera and Ashburn (14) show useful magnitudes down to $\tau = 0.001$. This corresponds to the wavelength range at the surface of Mars of about $2000\text{\AA} \leq \lambda \leq 10,000\text{\AA}$, which is an ideal range from the standpoints of available energy and present techniques of measurement. Furthermore, the relatively slow decrease of τ with altitude on Mars makes light scattering techniques applicable to higher altitudes than in the Earth's atmosphere. For instance, for $\lambda = 2500\text{\AA}$, τ is still greater than 0.01 at 60 kilometers. In comparison, τ for the Earth is the same as for Mars at about 16.5 kilometers. Its rapid-decay with altitude above that level causes light scattering measurements to become inapplicable at much lower levels in the Earth's atmosphere.

Table 2.9.3. Volume Scattering Coefficient at High Altitudes for the Atmospheres of Mars (Model M2) and the Earth. Data for the Earth are Those of Diermndjian (Reference 3).

z (Km)	λ (\AA)	MARS										EARTH		
		2500	3000	3500	4000	5000	6000	8000	10000	3750	5200	8350		
60		8.33×10^{-9}	3.80×10^{-9}	1.99×10^{-9}	1.14×10^{-9}	4.55×10^{-10}	2.17×10^{-10}	6.77×10^{-11}	2.76×10^{-11}	1.77×10^{-10}	4.61×10^{-11}	6.75×10^{-12}		
64		6.28	2.87	1.50	8.59×10^{-10}	3.43	1.64	5.10	2.08					
68		4.73	2.16	1.13×10^{-9}	6.48	2.59	1.23×10^{-10}	3.85	1.57					
72		3.57	1.63	8.50×10^{-10}	4.88	1.95	9.28×10^{-11}	2.90	1.18×10^{-11}					
76		2.69	1.22×10^{-9}	6.41	3.68	1.47	7.00	2.19	8.90×10^{-12}					
80		2.03	9.24×10^{-10}	4.83	2.77	1.11×10^{-10}	5.27	1.64	6.71	1.20×10^{-11}	3.11×10^{-12}	4.56×10^{-13}		
84		1.53	6.97	3.64	2.09	8.35×10^{-11}	3.98	1.24×10^{-11}	5.06					
88		1.15×10^{-9}	5.25	2.74	1.58	6.30	3.00	9.36×10^{-12}	3.81					
92		8.68×10^{-10}	3.96	2.07	1.19×10^{-10}	4.75	2.26	7.05	2.87					
96		6.54	2.98	1.56	8.95×10^{-11}	3.58	1.70	5.32	2.16					
100		4.93×10^{-10}	2.25×10^{-10}	1.17×10^{-10}	6.74×10^{-11}	2.70×10^{-11}	1.28×10^{-11}	4.01×10^{-12}	1.63×10^{-12}	3.76×10^{-13}	9.78×10^{-14}	1.43×10^{-14}		

In addition, ozone absorption below roughly 60 kilometers in the Earth's atmosphere limits the useful wavelength range to $\lambda > 3000\text{\AA}$. Presumably the small oxygen content of the Martian atmosphere would not be conducive to much ozone formation there.

Computed values of the optical thickness at the higher altitudes for the Martian atmosphere Model M2 are listed in Table 2.9.4.

Results for the isothermal model for Mars (Model M1) are not significantly different from those for Model M2. The density, and, hence, the volume scattering coefficient, is higher by a factor of about two at 100 kilometers for the isothermal case, as is shown by the curves of Figure 2.9.3. However, the density difference is less at lower altitudes, so that the optical thickness is essentially the same for the two models throughout most of their vertical extent. The density profile for the 1959 ARDC model of the Earth's atmosphere is included in Figure 2.9.3 for comparison.

2.9.4.2 Venus

Computations have been made for three models of the Venus atmosphere, Models V1, V2, and V3. The large differences in the computed values of β and τ point up the uncertainties with which the atmospheric properties of Venus are presently known.

As discussed previously, Model V1 is a relatively conservative model consisting of a troposphere, in which temperature decreases with increasing altitude, and an isothermal stratosphere which extends to the top of the atmosphere. The volume scattering coefficient for Model V1 is plotted as a function of height for several wavelengths in Figure 2.9.4. The high surface temperature assumed (600°K) keeps β at the surface at about the same value as for the Earth's atmosphere, in spite of the higher surface pressure for Venus (six atmospheres). However, the smaller rate of decrease of β with height for Venus results in an order of magnitude greater values of β for Venus than for the Earth at about 25 kilometers. Two orders of magnitude difference between the two occurs at

Table 2.9.4. Normal Optical Thickness at High Altitudes for the Atmospheres of Mars (Model M2) and the Earth. Data for the Earth are Those of Deirmendjian (Reference 3).

$\frac{\lambda}{z}$ ($\frac{\text{\AA}}{\text{Km}}$)	Mars										Earth		
	2500	3000	3500	4000	5000	6000	8000	10000	3750	5200	8350		
60	1.179×10^{-2}	5.378×10^{-3}	2.089×10^{-3}	1.612×10^{-3}	6.445×10^{-4}	2.008×10^{-4}	9.581×10^{-5}	3.901×10^{-5}					
64	8.887×10^{-3}	4.054×10^{-3}	2.113×10^{-3}	1.215×10^{-3}	4.858×10^{-4}	2.312×10^{-4}	7.221×10^{-5}	2.940×10^{-5}					
68	6.698×10^{-3}	3.055×10^{-3}	1.596×10^{-3}	9.161×10^{-4}	3.662×10^{-4}	1.743×10^{-4}	5.443×10^{-5}	2.216×10^{-5}					
72	5.049×10^{-3}	2.303×10^{-3}	1.203×10^{-3}	6.905×10^{-4}	2.760×10^{-4}	1.313×10^{-4}	4.102×10^{-5}	1.670×10^{-5}	3.7×10^{-5} (70 Km)	9.5×10^{-6} (70 Km)	1.4×10^{-6} (70 Km)		
76	3.805×10^{-3}	1.736×10^{-3}	9.067×10^{-4}	5.204×10^{-4}	2.080×10^{-4}	9.900×10^{-5}	3.092×10^{-5}	1.259×10^{-5}					
80	2.868×10^{-3}	1.308×10^{-3}	6.834×10^{-4}	3.922×10^{-4}	1.568×10^{-4}	7.462×10^{-5}	2.330×10^{-5}	9.488×10^{-6}					
84	2.162×10^{-3}	9.861×10^{-4}	5.151×10^{-4}	2.956×10^{-4}	1.182×10^{-4}	5.624×10^{-5}	1.756×10^{-5}	7.152×10^{-6}					
88	1.629×10^{-3}	7.432×10^{-4}	3.882×10^{-4}	2.228×10^{-4}	8.906×10^{-5}	4.239×10^{-5}	1.324×10^{-5}	5.390×10^{-6}					
92	1.228×10^{-3}	5.602×10^{-4}	2.926×10^{-4}	1.679×10^{-4}	6.713×10^{-5}	3.195×10^{-5}	9.978×10^{-6}	4.063×10^{-6}					
96	9.260×10^{-4}	4.222×10^{-4}	2.205×10^{-4}	1.266×10^{-4}	5.060×10^{-5}	2.408×10^{-5}	7.521×10^{-6}	3.062×10^{-6}					
100	6.976×10^{-4}	3.182×10^{-4}	1.662×10^{-4}	9.541×10^{-5}	3.814×10^{-5}	1.815×10^{-5}	5.669×10^{-6}	2.308×10^{-6}	2.2×10^{-7}	5.8×10^{-8}	8.5×10^{-9}		

Table 2.9.5. Volume Scattering Coefficient β at High Altitudes for the Atmosphere of Venus Model VI

$\frac{\lambda \text{ (Å)}}{z \text{ (km)}}$	2500	3000	3500	4000	5000	6000	8000	10000
60	3.70×10^{-8}	1.68×10^{-8}	8.79×10^{-9}	5.04×10^{-9}	2.01×10^{-9}	9.57×10^{-10}	2.99×10^{-10}	1.22×10^{-10}
80	2.58×10^{-9}	1.17×10^{-9}	6.12×10^{-10}	3.51×10^{-10}	1.40×10^{-10}	6.67×10^{-11}	2.08×10^{-11}	8.48×10^{-12}
100	1.80×10^{-10}	8.18×10^{-11}	4.27×10^{-11}	2.45×10^{-11}	9.77×10^{-12}	4.65×10^{-12}	1.45×10^{-12}	5.91×10^{-13}
120	1.25×10^{-11}	5.70×10^{-12}	2.97×10^{-12}	1.70×10^{-12}	6.81×10^{-13}	3.24×10^{-13}	1.01×10^{-13}	4.12×10^{-14}
140	8.72×10^{-13}	3.97×10^{-13}	2.07×10^{-13}	1.19×10^{-13}	4.74×10^{-14}	2.26×10^{-14}	7.05×10^{-15}	2.87×10^{-15}
160	6.08×10^{-14}	2.77×10^{-14}	1.44×10^{-14}	8.28×10^{-15}	3.31×10^{-15}	1.57×10^{-15}	4.91×10^{-16}	2.00×10^{-16}
180	4.24×10^{-15}	1.93×10^{-15}	1.01×10^{-15}	5.77×10^{-16}	2.30×10^{-16}	1.10×10^{-16}	3.42×10^{-17}	1.39×10^{-17}
200	2.95×10^{-16}	1.34×10^{-16}	7.01×10^{-17}	4.02×10^{-17}	1.61×10^{-17}	7.64×10^{-18}	2.38×10^{-18}	9.70×10^{-19}

between 50 and 55 kilometers, the difference continuing to increase at higher altitudes. Comparisons can be made at altitudes of 60 km, 80 km, and 100 km with Deirmendjian's (3) values for the Earth, which are included as part of Table 2.9.3.

Curves of normal optical thickness from the surface to 60 kilometers for the Venus atmospheric model V1 are reproduced as Figure 2.9.5. Curves as available for the Earth's atmosphere are included in the diagram. Everywhere the optical thickness is greater in the Venus model V1 than for the Earth. The relative difference increases considerably with altitude, due, at least in part, to the lower value of gravity for Venus. If one again uses the criterion of $\tau = 10^{-3}$ as the lower limit for useful light-scattering techniques, such techniques are good in Model V1 up to about 85 kilometers for a wavelength of 2500Å, as can be seen from the tabulated values of normal optical thickness at high levels in Table 2.9.6.

Results of computing the volume scattering coefficient for the more dense atmosphere of Venus Model V2 are given by the curves of Figure 2.9.6. Surface values are roughly an order of magnitude greater than those for Model V1 or for the Earth's atmosphere. The change with altitude is less for Venus than for the Earth, making β at 60 km more than 200 times as great for the Venus V2 model as for the Earth's atmosphere. Selected data for Model V2 at higher altitudes are included as Table 2.9.7.

The vertical profile of normal optical thickness for Model V2 is shown by Figure 2.9.7. The surface values are so great that the shorter wavelengths of direct solar radiation would be essentially all depleted by scattering before reaching the surface. For instance, for normally incident sunlight the fraction which is transmitted directly through the atmosphere is less than 10^{-21} for $\lambda = 2500\text{\AA}$, 10^{-11} for $\lambda = 3000\text{\AA}$, and 6×10^{-4} for $\lambda = 4000\text{\AA}$. About ten per cent of the direct solar radiation at $\lambda = 2500\text{\AA}$ could penetrate down to 40 km altitude in this model. Data for $60 \text{ Km} \leq z \leq 200 \text{ Km}$ are tabulated as Table 2.9.8.

Table 2.9.6. Normal Optical Thickness τ at High Altitudes for the Atmosphere of Venus Model VI

λ (Å) z(Km)	2500	3000	3500	4000	5000	6000	8000	10000
60	2.778×10^{-2}	1.264×10^{-2}	6.59×10^{-3}	3.783×10^{-3}	1.511×10^{-3}	7.187×10^{-4}	2.242×10^{-4}	9.134×10^{-5}
80	1.936×10^{-3}	8.811×10^{-4}	4.596×10^{-4}	2.636×10^{-4}	1.053×10^{-4}	5.008×10^{-5}	1.563×10^{-5}	6.364×10^{-6}
100	1.349×10^{-4}	6.139×10^{-5}	3.203×10^{-5}	1.837×10^{-5}	7.336×10^{-6}	3.490×10^{-6}	1.089×10^{-6}	4.435×10^{-7}
120	9.399×10^{-6}	4.278×10^{-6}	2.232×10^{-6}	1.280×10^{-6}	5.112×10^{-7}	2.432×10^{-7}	7.592×10^{-8}	3.090×10^{-8}
140	6.550×10^{-7}	2.981×10^{-7}	1.555×10^{-7}	8.919×10^{-8}	3.562×10^{-8}	1.694×10^{-8}	5.290×10^{-9}	2.153×10^{-9}
160	4.554×10^{-8}	2.077×10^{-8}	1.084×10^{-8}	6.215×10^{-9}	2.482×10^{-9}	1.181×10^{-9}	3.686×10^{-10}	1.500×10^{-10}
180	3.180×10^{-9}	1.447×10^{-9}	7.551×10^{-10}	4.331×10^{-10}	1.729×10^{-10}	8.228×10^{-11}	2.568×10^{-11}	1.045×10^{-11}
200	2.216×10^{-10}	1.009×10^{-10}	5.262×10^{-11}	3.018×10^{-11}	1.205×10^{-11}	5.733×10^{-11}	1.780×10^{-12}	7.286×10^{-13}

Table 2.9.7. Volume Scattering Coefficient β at High Altitudes for the Atmosphere of Venus Model V2

λ (Å) z(Km)	2500	3000	3500	4000	5000	6000	8000	10000
60	2.710×10^{-7}	1.235×10^{-7}	6.448×10^{-8}	3.700×10^{-8}	1.478×10^{-8}	7.035×10^{-9}	2.197×10^{-9}	8.944×10^{-10}
80	1.882×10^{-8}	8.580×10^{-9}	4.479×10^{-9}	2.570×10^{-9}	1.027×10^{-9}	4.887×10^{-10}	1.526×10^{-10}	6.213×10^{-11}
100	1.185×10^{-9}	5.400×10^{-10}	2.819×10^{-10}	1.618×10^{-10}	6.464×10^{-11}	3.076×10^{-11}	9.606×10^{-12}	3.911×10^{-12}
120	6.348×10^{-11}	2.893×10^{-11}	1.510×10^{-11}	8.667×10^{-12}	3.463×10^{-12}	1.648×10^{-12}	5.146×10^{-13}	2.095×10^{-13}
140	4.751×10^{-12}	2.165×10^{-12}	1.130×10^{-12}	6.487×10^{-13}	2.592×10^{-13}	1.233×10^{-13}	3.852×10^{-14}	1.568×10^{-14}
160	5.820×10^{-13}	2.652×10^{-13}	1.385×10^{-13}	7.946×10^{-14}	3.175×10^{-14}	1.511×10^{-14}	4.718×10^{-15}	1.921×10^{-15}
180	9.964×10^{-14}	4.541×10^{-14}	2.371×10^{-14}	1.360×10^{-14}	5.436×10^{-15}	2.587×10^{-15}	8.077×10^{-16}	3.288×10^{-16}
200	2.174×10^{-14}	9.909×10^{-15}	5.174×10^{-15}	2.969×10^{-15}	1.186×10^{-15}	5.645×10^{-16}	1.763×10^{-16}	7.176×10^{-17}

Table 2.9.8. Normal Optical Thickness τ at High Altitudes for the Atmosphere of Venus Model V2

$\frac{\lambda (\text{\AA})}{z(\text{Km})}$	2500	3000	3500	4000	5000	6000	8000	10000
60	2.041×10^{-1}	9.304×10^{-2}	4.858×10^{-2}	2.78×10^{-2}	1.114×10^{-2}	5.300×10^{-3}	1.655×10^{-3}	6.738×10^{-4}
80	1.368×10^{-2}	6.237×10^{-3}	3.256×10^{-3}	1.868×10^{-3}	7.466×10^{-4}	3.553×10^{-4}	1.109×10^{-4}	4.516×10^{-5}
100	8.30×10^{-4}	3.783×10^{-4}	1.975×10^{-4}	1.133×10^{-4}	4.528×10^{-5}	2.155×10^{-5}	6.729×10^{-6}	2.740×10^{-6}
120	4.778×10^{-5}	2.178×10^{-5}	1.137×10^{-5}	6.524×10^{-6}	2.607×10^{-6}	1.240×10^{-6}	3.874×10^{-7}	1.577×10^{-7}
140	4.518×10^{-6}	2.059×10^{-6}	1.075×10^{-6}	6.169×10^{-7}	2.465×10^{-7}	1.173×10^{-7}	3.663×10^{-8}	1.491×10^{-8}
160	6.687×10^{-7}	3.048×10^{-7}	1.591×10^{-7}	9.130×10^{-8}	3.648×10^{-8}	1.736×10^{-8}	5.421×10^{-9}	2.207×10^{-9}
180	1.342×10^{-7}	6.118×10^{-8}	3.194×10^{-8}	1.833×10^{-8}	7.323×10^{-9}	3.485×10^{-9}	1.088×10^{-9}	4.430×10^{-10}
200	3.360×10^{-8}	1.531×10^{-8}	7.995×10^{-9}	4.588×10^{-9}	1.833×10^{-9}	8.723×10^{-10}	2.724×10^{-10}	1.109×10^{-10}

The very dense atmosphere represented by Model V3 produces correspondingly large values of β and τ . These data are plotted for $0 \leq z \leq 60$ km in Figure 2.9.8 for β and Figure 2.9.9 for τ . Table 2.9.9 and Table 2.9.10 list selected values of β and τ , respectively, for the altitude range 60 Km to 200 Km.

This is indeed an extreme case, as indicated by the label "Extreme Model" applied by JPL when they proposed it. More than 99 per cent of the radiation at all wavelengths less than 6000Å would be scattered out of the direct solar beam in a vertical traverse of the atmosphere. One might remark that to an asbestos-suited surface dweller in such an atmosphere, if his eyes were to have the same spectral sensitivity as ours, the sun would appear only as a dim and dark red disc when directly overhead. It would probably disappear completely by mid-afternoon as the directly transmitted light became less and scattered skylight relatively greater.

If one were to monitor the intensity of the direct solar beam as a capsule enters this atmosphere, as a measure of the atmospheric density profile or as a method of orientation, it would be very advantageous to use different wavelength ranges for different altitude regimes. For instance, 2500Å would be applicable from the highest levels down to perhaps 60-70 km, at which altitude Rayleigh scattering would have depleted more than 90 per cent of the direct beam for vertical incidence, and the scattered skylight would be relatively intense. At that altitude a shift to longer wavelengths would be in order. For instance, 8000Å radiation would have been depleted by only about two per cent at 60 km and 25 per cent would be transmitted entirely through the atmosphere. Thus, the entire altitude range could be covered by using the two wavelengths.

Atmospheric Model V4 was considered by its advocates, namely, the Jet Propulsion Laboratory, to be the second "extreme model." The volume scattering coefficient and normal optical thickness for this model are shown for altitudes up to 60 km by Figure 2.9.11 and Figure 2.9.12, respectively. Selected data for $60 \text{ km} \leq z \leq 200 \text{ km}$ are listed in Table 2.9.11 and Table 2.9.12. The rapid decrease of β and τ with altitude are brought about by the much lower temperatures

Table 2.9.9. Volume Scattering Coefficient at High Altitudes in the Atmosphere of Venus Model V3

λ (Å) z (Km)	2500	3000	3500	4000	5000	6000	8000	10000
60	3.813×10^{-6}	1.738×10^{-6}	9.072×10^{-7}	5.206×10^{-7}	2.080×10^{-7}	9.898×10^{-8}	3.091×10^{-8}	1.258×10^{-8}
80	2.982×10^{-7}	1.359×10^{-7}	7.097×10^{-8}	4.072×10^{-8}	1.267×10^{-8}	7.113×10^{-9}	2.418×10^{-9}	9.843×10^{-10}
100	2.538×10^{-8}	1.157×10^{-8}	6.039×10^{-9}	3.465×10^{-9}	1.384×10^{-9}	6.588×10^{-10}	2.057×10^{-10}	8.276×10^{-11}
120	2.247×10^{-9}	1.024×10^{-9}	5.346×10^{-10}	3.068×10^{-10}	1.226×10^{-10}	5.833×10^{-11}	1.821×10^{-11}	7.415×10^{-12}
140	2.892×10^{-10}	1.318×10^{-10}	6.882×10^{-11}	3.949×10^{-11}	1.578×10^{-11}	7.509×10^{-12}	2.345×10^{-12}	9.546×10^{-13}
160	6.113×10^{-11}	2.786×10^{-11}	1.454×10^{-11}	8.346×10^{-12}	3.335×10^{-12}	1.587×10^{-12}	4.955×10^{-13}	2.017×10^{-13}
180	1.921×10^{-11}	8.756×10^{-12}	4.571×10^{-12}	2.623×10^{-12}	1.048×10^{-12}	4.987×10^{-13}	1.557×10^{-13}	6.340×10^{-14}
200	7.684×10^{-12}	3.502×10^{-12}	1.828×10^{-12}	1.049×10^{-12}	4.192×10^{-13}	1.995×10^{-13}	6.229×10^{-14}	2.536×10^{-14}

Table 2.9.10. Normal Optical Thickness at High Altitudes for the Atmosphere of Venus Model V3

$\lambda(A)$ $z(Km)$	2500	3000	3500	4000	5000	6000	8000	10000
60	3.013×10^0	1.373×10^0	7.169×10^{-1}	4.114×10^{-1}	1.644×10^{-1}	7.822×10^{-2}	2.442×10^{-2}	9.944×10^{-3}
80	2.412×10^{-1}	1.099×10^{-1}	5.739×10^{-2}	3.293×10^{-2}	1.316×10^{-2}	6.261×10^{-3}	1.955×10^{-3}	7.960×10^{-4}
100	2.137×10^{-2}	9.739×10^{-3}	5.085×10^{-3}	2.918×10^{-3}	1.166×10^{-3}	5.547×10^{-4}	1.732×10^{-4}	7.052×10^{-5}
120	2.238×10^{-3}	1.020×10^{-3}	5.326×10^{-4}	3.056×10^{-4}	1.221×10^{-4}	5.811×10^{-5}	1.815×10^{-5}	7.388×10^{-6}
140	4.021×10^{-4}	1.832×10^{-4}	9.567×10^{-5}	5.490×10^{-5}	2.194×10^{-5}	1.044×10^{-5}	3.259×10^{-6}	1.327×10^{-6}
160	1.193×10^{-4}	5.439×10^{-5}	2.840×10^{-5}	1.629×10^{-5}	6.511×10^{-6}	3.098×10^{-6}	9.675×10^{-7}	3.939×10^{-7}
180	4.870×10^{-5}	2.219×10^{-5}	1.159×10^{-5}	6.649×10^{-6}	2.657×10^{-6}	1.264×10^{-6}	3.948×10^{-7}	1.607×10^{-7}
200	2.393×10^{-5}	1.091×10^{-6}	5.694×10^{-6}	3.267×10^{-6}	1.305×10^{-6}	6.212×10^{-7}	1.940×10^{-7}	7.898×10^{-8}

Table 2.9.11 Volume Scattering Coefficient at High Altitudes in the Atmosphere of Venus Model V4

$\frac{\lambda}{z}$ (Å/Km)	2500	3000	3500	4000	5000	6000	8000	10000
60	1.267×10^{-8}	5.782×10^{-9}	3.019×10^{-9}	1.732×10^{-9}	6.921×10^{-10}	3.293×10^{-10}	1.028×10^{-10}	4.187×10^{-11}
80	2.239×10^{-10}	1.020×10^{-10}	5.327×10^{-11}	3.057×10^{-11}	1.221×10^{-11}	5.812×10^{-12}	1.815×10^{-12}	7.389×10^{-13}
100	3.951×10^{-12}	1.801×10^{-12}	9.401×10^{-13}	5.394×10^{-13}	2.155×10^{-13}	1.0264×10^{-13}	3.203×10^{-14}	1.304×10^{-14}
120	6.972×10^{-14}	3.178×10^{-14}	1.659×10^{-14}	9.520×10^{-15}	3.804×10^{-15}	1.810×10^{-15}	5.652×10^{-16}	2.301×10^{-16}
140	1.230×10^{-15}	5.608×10^{-16}	2.928×10^{-16}	1.680×10^{-16}	6.713×10^{-17}	3.194×10^{-17}	9.975×10^{-18}	4.061×10^{-18}
160	2.171×10^{-17}	9.896×10^{-18}	5.167×10^{-18}	2.965×10^{-18}	1.185×10^{-18}	5.637×10^{-19}	1.760×10^{-19}	7.166×10^{-20}
180	3.832×10^{-19}	1.746×10^{-19}	9.118×10^{-20}	5.232×10^{-20}	2.090×10^{-20}	9.948×10^{-21}	3.106×10^{-21}	1.265×10^{-21}
200	6.762×10^{-21}	3.082×10^{-21}	1.609×10^{-21}	9.233×10^{-22}	3.689×10^{-22}	1.755×10^{-22}	5.482×10^{-22}	2.232×10^{-23}

Table 2.9.12. Normal Optical Thickness at High Altitudes for the Atmosphere of Venus Model V4

λ (Å) z (Km)	2500	3000	3500	4000	5000	6000	8000	10000
60	6.285×10^{-3}	2.864×10^{-3}	1.495×10^{-3}	8.581×10^{-4}	3.429×10^{-4}	1.632×10^{-4}	5.095×10^{-5}	2.074×10^{-5}
80	1.109×10^{-4}	5.055×10^{-5}	2.639×10^{-5}	1.514×10^{-5}	6.051×10^{-6}	2.879×10^{-6}	8.991×10^{-7}	3.660×10^{-7}
100	1.957×10^{-6}	8.920×10^{-7}	4.657×10^{-7}	2.672×10^{-7}	1.068×10^{-7}	5.081×10^{-8}	1.587×10^{-8}	6.460×10^{-9}
120	3.454×10^{-8}	1.574×10^{-8}	8.219×10^{-9}	4.716×10^{-9}	1.884×10^{-9}	8.967×10^{-10}	2.800×10^{-10}	1.140×10^{-10}
140	6.095×10^{-10}	2.778×10^{-10}	1.450×10^{-10}	8.323×10^{-11}	3.325×10^{-11}	1.582×10^{-11}	4.941×10^{-12}	2.012×10^{-12}
160	1.076×10^{-11}	4.903×10^{-12}	2.560×10^{-12}	1.469×10^{-12}	5.869×10^{-13}	2.793×10^{-13}	8.720×10^{-14}	3.550×10^{-14}
180	1.898×10^{-13}	8.652×10^{-14}	4.517×10^{-14}	2.592×10^{-14}	1.036×10^{-14}	4.928×10^{-15}	1.539×10^{-15}	6.265×10^{-16}
200	3.350×10^{-15}	1.527×10^{-15}	7.971×10^{-16}	4.574×10^{-16}	1.828×10^{-16}	8.697×10^{-17}	2.716×10^{-17}	1.106×10^{-17}

assumed in the troposphere for this model. This temperature profile results in the optical thickness decreasing by about an order of magnitude more in the first 60 km here than it does in the other Venus models.

2.9.5 Discussion

In evaluating the applicability of these results, one is faced with the problem of establishing the range of values over which optical thickness is a useful parameter for determinations of radiative distribution in an atmosphere. The lower limit for τ is well indicated by the computations of Sekera and Ashburn (14) in which the intensity of scattered sunlight is given for different values of τ . Those tables show useful magnitudes of the intensity of scattered sunlight down to $\tau = 0.0001$. Furthermore, the flux F of the vertical direct solar beam, given by the expression

$$F = F_o e^{-\tau},$$

F_o being the extra-atmosphere solar flux, is attenuated by 0.1 per cent for $\tau = 0.001$. This amount of attenuation is probably sufficient for detection by realistic instrumentation.

For establishing a useful upper limit for τ , one should consider the fact that the extensive tables of Coulson, Dave, and Sekera (2) give values of the intensity of scattered light for $\tau \leq 1.0$. There is not a fundamental reason why this must be the limit for computations, but, as far as is known, the extension beyond $\tau = 1.0$ has not been accomplished. Thus, for present practical purposes $\tau = 1.0$ seems a useful upper limit for considerations of scattered light.

The situation is quite different, however, for the direct solar beam. A value of $\tau = 2.3$ gives ten per cent direct vertical transmission and one per cent transmission occurs for $\tau = 4.3$. Although one per cent of the direct solar beam represents plenty of energy for even narrow-band measurements, one must consider the relative amount of energy which would be contributed by light scattered into the particular instrument by the atmosphere of large optical thickness.

This will be dependent on the field of view of the instrument, so it would have to be evaluated for each case individually. It is likely, however, that measurements of the direct solar beam would be impractical for $\tau > 4.3$.

With these criteria one can evaluate the altitudes and wavelengths at which light-scattering techniques would be most useful for the various atmospheric models. The results of this evaluation are shown in Table 2.9.13 for five different wavelengths. The altitudes are approximate only, having been obtained by graphical interpolation. Entries for the Earth's atmosphere were obtained from a plot of Deirmendjian's (3) data. An extrapolation was required for 3000\AA and $10,000\text{\AA}$, but the values are probably accurate to ± 1 km.

The data of Table 2.9.13 show the significant result that light scattering measurements are applicable at higher altitudes in both the Mars and Venus atmospheres than in the atmosphere of the Earth. The single exception to this indicated in the table is for $\lambda = 10,000\text{\AA}$, for which $\tau = 0.001$ occurs at the lower altitude for Mars. For the very dense atmospheric models V2 and V3, it appears that light-scattering techniques could be used well above 100 km, and for the least dense Venus model V1 measurements to 70 or 80 km seem feasible from these computations. It is unlikely that erroneous assumptions as to atmospheric gaseous composition, including possible diffusive separation at high levels, would change these main conclusions significantly, although, of course, gross changes of temperature structure or total atmospheric mass might do so.

From a practical standpoint it is of interest to know the amount of energy in the direct solar beam as a function of altitude. The fractional transmission T for the direct solar radiation, defined by the expression

$$T = e^{-\tau \sec \theta_0},$$

θ_0 being solar zenith angle, is plotted as a function of altitude for atmospheric models M2, V1, V2, and V3 in Figures 12a, 13a, 14a, and 15a, respectively. The diagrams apply for radiation at four selected wavelengths, and curves are given for two different solar zenith angles, $\theta_0 = 0^\circ$ and 60° . It is seen that there

Table 2.9.13. Altitude Limits for Which Light-Scattering Techniques Would be Most Useful in the Various Atmospheric Models. The Altitude at Which $\tau = 0.001$ (First Column for Each Wavelength) is Considered to be the Upper Limit, That at Which $\tau = 1.0$ the Lower Limit for Scattered Light, and That at Which $\tau = 4.3$ the Lower Limit for the Directly Transmitted Solar Beam.

Wavelength τ Atm. Model	2500 A			3000 A			4000 A			6000 A			10,000 A		
	0.001	1.0	4.3	0.001	1.0	4.3	0.001	1.0	4.3	0.001	1.0	4.3	0.001	1.0	4.3
Mars M1	93	0	0	86	0	0	72	0	0	46	0	0	11	0	0
Mars M2	95	0	0	84	0	0	67	0	0	43	0	0	13	0	0
Venus V1	85	29	8	79	18	0	70	0	0	58	0	0	41	0	0
Venus V2	99	48	36	93	42	27	84	30	0	72	6	0	57	0	0
Venus V3	129	69	57	120	62	49	109	52	34	95	31	1	78	0	0
Venus V4	68	34	21	64	27	6	58	15	0	50	0	0	41	0	0
Earth*	-	-	-	52	1	0	41	0	0	28	0	0	15	0	0

*After Deirmendjian (Reference 3)

is a phenomenal change of transmission with wavelength at the shorter wavelengths. This, of course, arises because of the fourth power wavelength-dependence in Equation (5), and has considerable practical importance in the design of measuring systems.

The flux F_{λ} of solar energy (watts/cm²-μ) in the direct solar beam which would be transmitted down to level z is shown as a function of z in the b-parts of Figures 2.9.12 to 2.9.15, inclusive. These data are computed from the expression,

$$F_{\lambda}(z) = F_o e^{-\tau} \quad (13)$$

where F_o is the extra-atmosphere flux, and the solar zenith angle $\theta_o = 0$ for this case. Data on F_o are obtained by multiplying the solar energy flux for the Earth, as given by Johnson (6), by the appropriate factor

$$\left(\frac{R_e}{R_m} \right)^2 \quad \text{or} \quad \left(\frac{R_e}{R_v} \right)^2 ,$$

R_e , R_m , and R_v being the distances from the sun to the Earth, Mars, and Venus, respectively. The curves show that, except for the lowest layers of the Venus atmospheric models, there is sufficient energy for the use of present instrumentation in making narrow band-pass measurements of the direct solar radiation.

It is instructive to compare conditions in the Mars and Venus model atmospheres with those in the more familiar Earth's atmosphere. Such a comparison can be made from Table 2.9.14, in which the normal optical thickness at one wavelength (4000 Å) for the various models is listed for four altitudes above the planetary surfaces in the first columns under the altitude headings.

In the other columns is a tabulation of the ratio τ_i/τ_e , where subscript e refers to the Earth and i refers to the designated planetary model. Only for the lower levels of Mars is the ratio less than unity. At the higher altitudes the ratio

Table 2.9.14 . Comparison of Optical Thickness of Various Atmospheric Models with that of the Earth's Atmosphere for Wavelength $\lambda = 4000 \text{ \AA}$ at Four Different Altitudes Above the Planetary Surface. The Data for the Earth's Atmosphere Were Obtained by Graphical Interpolation Between Deirmendjian's (Reference 3) Computed Values.

Atmospheric Model	z = 0 km		z = 8 km		z = 20 km		z = 50 km	
	τ	τ/τ_e	τ	τ/τ_e	τ	τ/τ_e	τ	τ/τ_e
Mars M1	8.138×10^{-2}	0.235	5.107×10^{-2}	0.419	2.534×10^{-2}	1.30	2.267×10^{-3}	23.9
Mars M2	8.162×10^{-2}	0.235	5.463×10^{-2}	0.448	2.696×10^{-2}	1.38	3.14×10^{-3}	33.1
Venus V1	9.291×10^{-1}	2.68	5.930×10^{-1}	4.86	2.726×10^{-1}	14.0	1.43×10^{-2}	150
Venus V2	7.337	21.1	4.780	39.1	2.239	115.	2.787×10^{-2}	290
Venus V3	23.87	68.8	17.01	139.	9.553	490.	1.214	13,000
Venus V4	2.784	8.02	1.654	13.6	6.343×10^{-1}	32.5	6.460×10^{-3}	68.0
Earth	3.47×10^{-1}	1.00	1.22×10^{-1}	1.00	1.95×10^{-2}	1.00	9.5×10^{-5}	1.00

REFERENCES

1. Chandrasekhar, S. (1950), Radiative Transfer, Oxford Clarendon Press.
2. Coulson, K. L., Dave, J. V. and Sekera, Z. (1960), Tables Related to Radiation Emerging from a Planetary Atmosphere with Rayleigh Scattering, University of California Press.
3. Deirmendjian, D. A. (1955), "The Optical Thickness of the Molecular Atmosphere," Archiv fur Met., Geoph. und Biokl., Ser. B., 6/4.
4. Hess, S. L. (1950), "Some Aspects of the Meteorology of Mars," Journ. of Meteorology, 7, pp. 1/13.
5. Jet Propulsion Laboratory (March 1962), Requirements for a Venus-Mars Capsule Study, Engineering Planning Document No. 33 (Unpublished).
6. Johnson, F. S. (1954), "The Solar Constant," Journ. of Meteorology, 11:6, pp. 431-439.
7. Kaplan, L. D. (1961), "A New Interpretation of the Structure and CO₂ Content of the Venus Atmosphere," Planet, Space Sci., 8: 1, 23-29.
8. Kellogg, W. W., and Sagan, C. (1961), The Atmospheres of Mars and Venus, Report of the Space Science Board, Nat. Acad. Sci - Nat. Res. Council Pub. 944.
9. National Research Council (1931), International Critical Tables, Vol. 7, New York.
10. Partington, J. R. (1953), An Advanced Treatise on Physical Chemistry, Vol. 4: Physico-Chemical Optics; Longmans, Green & Co.
11. Sagan, C. (1961), "The Planet Venus," Science, 133: 849.
12. Salisbury, F. B. (1962), "Martian Biology," Science, 136, 17-26.
13. Sekera, Z. (1956), "Recent Developments in the Study of the Polarization of Skylight," Advances in Geophysics, III, pp. 43-104.

14. Sekera, Z. and E. V. Ashburn (1953), Tables Relating to Rayleigh Scattering of Light in the Atmosphere, NAVORD Rept. 2061, U. S. Naval Ordnance Test Station, China Lake, Calif. 133 pp.
15. Strutt, J. W. (Lord Rayleigh), (1871), Phil. Mag. 41, 107, 274.
_____ (1881), Phil. Mag., 12, 81
_____ (1899), Phil. Mag., 47, 375
16. deVaucouleurs, G. (1954) - Physics of the Planet Mars, Faber & Faber, London.
17. deVaucouleurs, G. (1960) - "The Physical Environment of Mars," Chap. 13 in Physics and Medicine of the Atmosphere and Space, Ed. O. O. Benson and H. Strughold, John Wiley and Sons, New York.

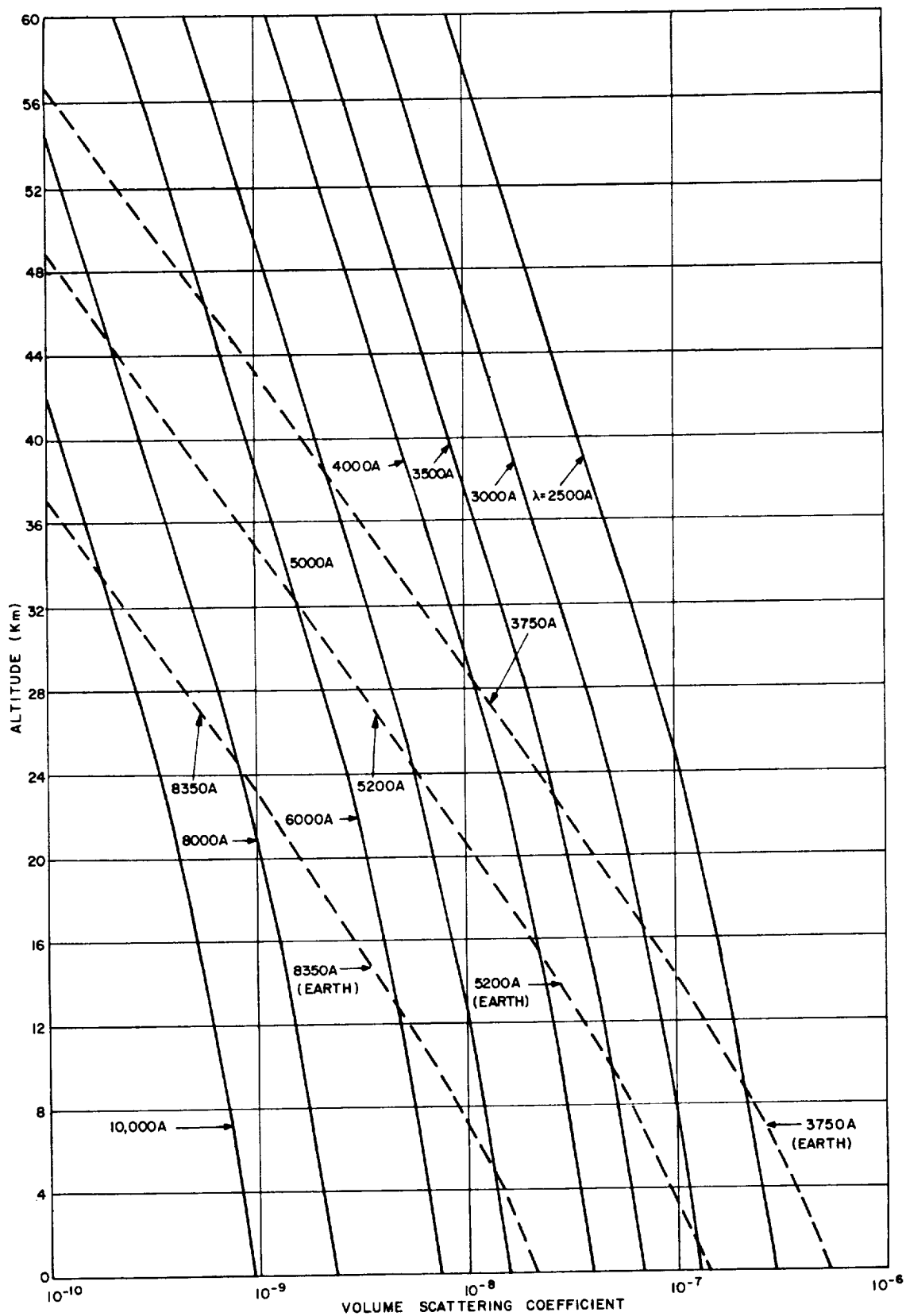


Figure 2.9.1. Volume Scattering Coefficient as a Function of Altitude for the Mars Atmospheric Model M2

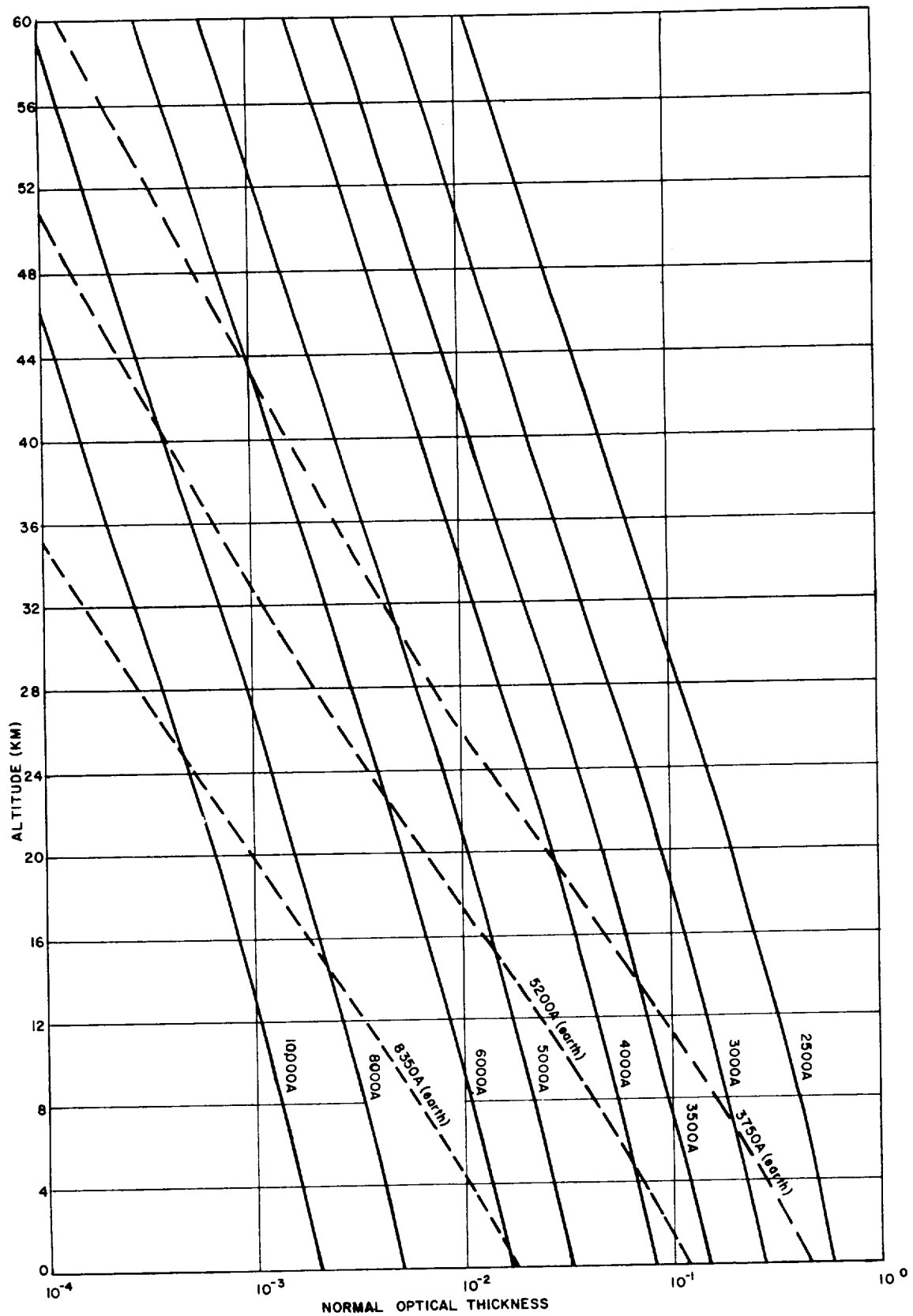


Figure 2.9.2. Normal Optical Thickness as a Function of Altitude for the Mars Atmospheric Model M2

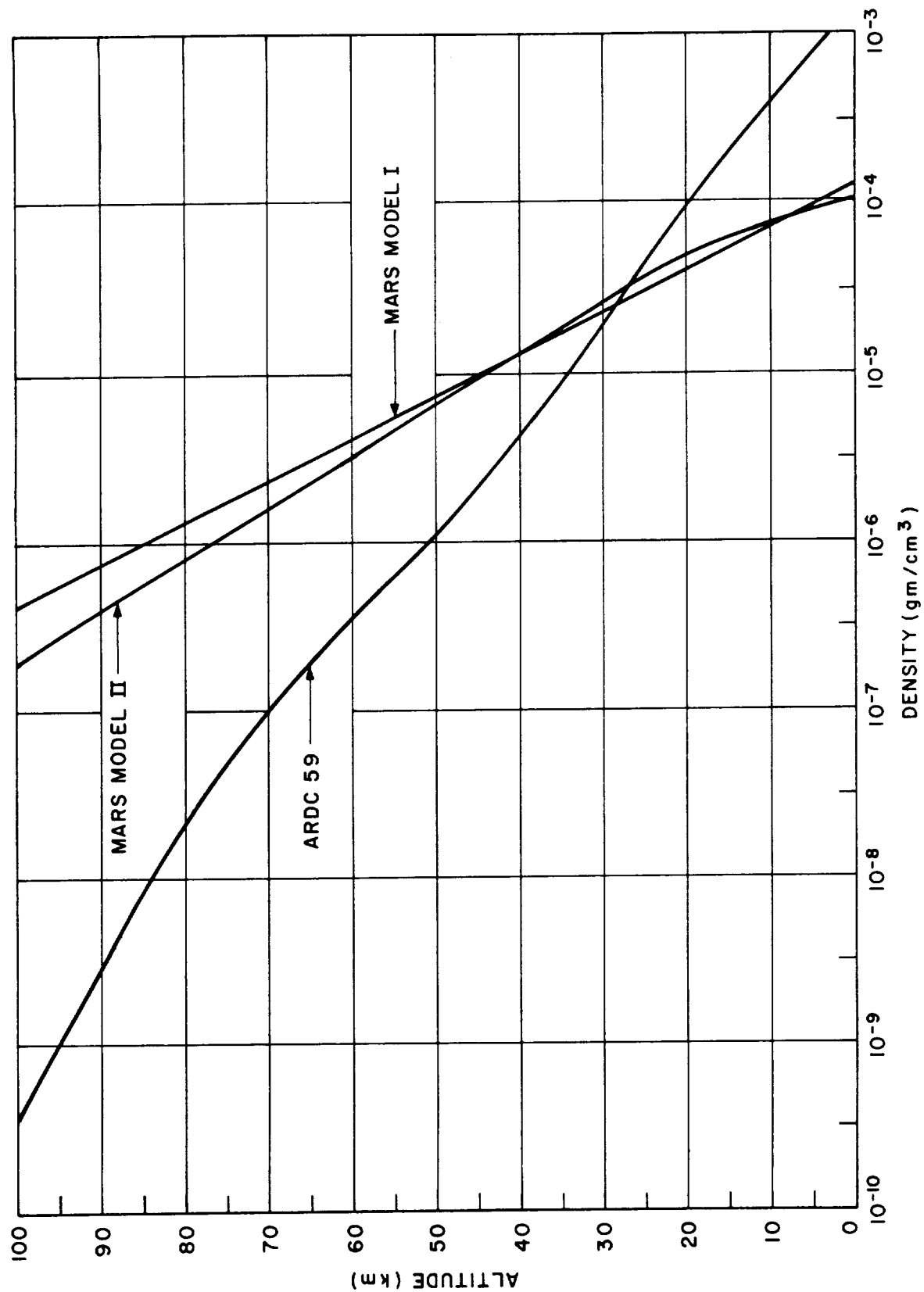


Figure 2.9.3. Vertical Density Profiles for Two Models (M1 and M2) of the Martian Atmosphere and for the 1959 APDC Model of the Earth's Atmosphere

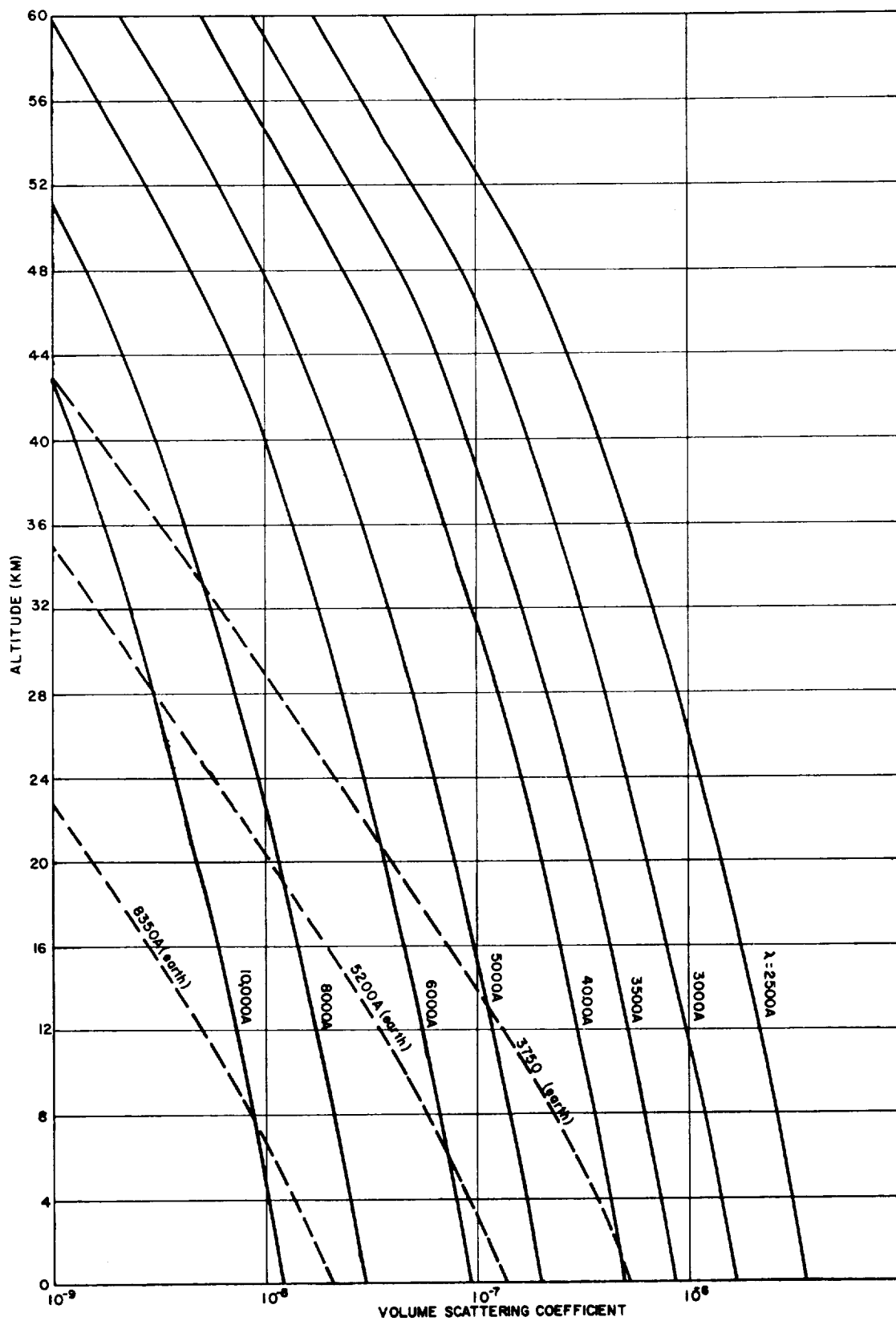


Figure 2.9.4. Volume Scattering Coefficient as a Function of Altitude for Venus Atmospheric Model V1

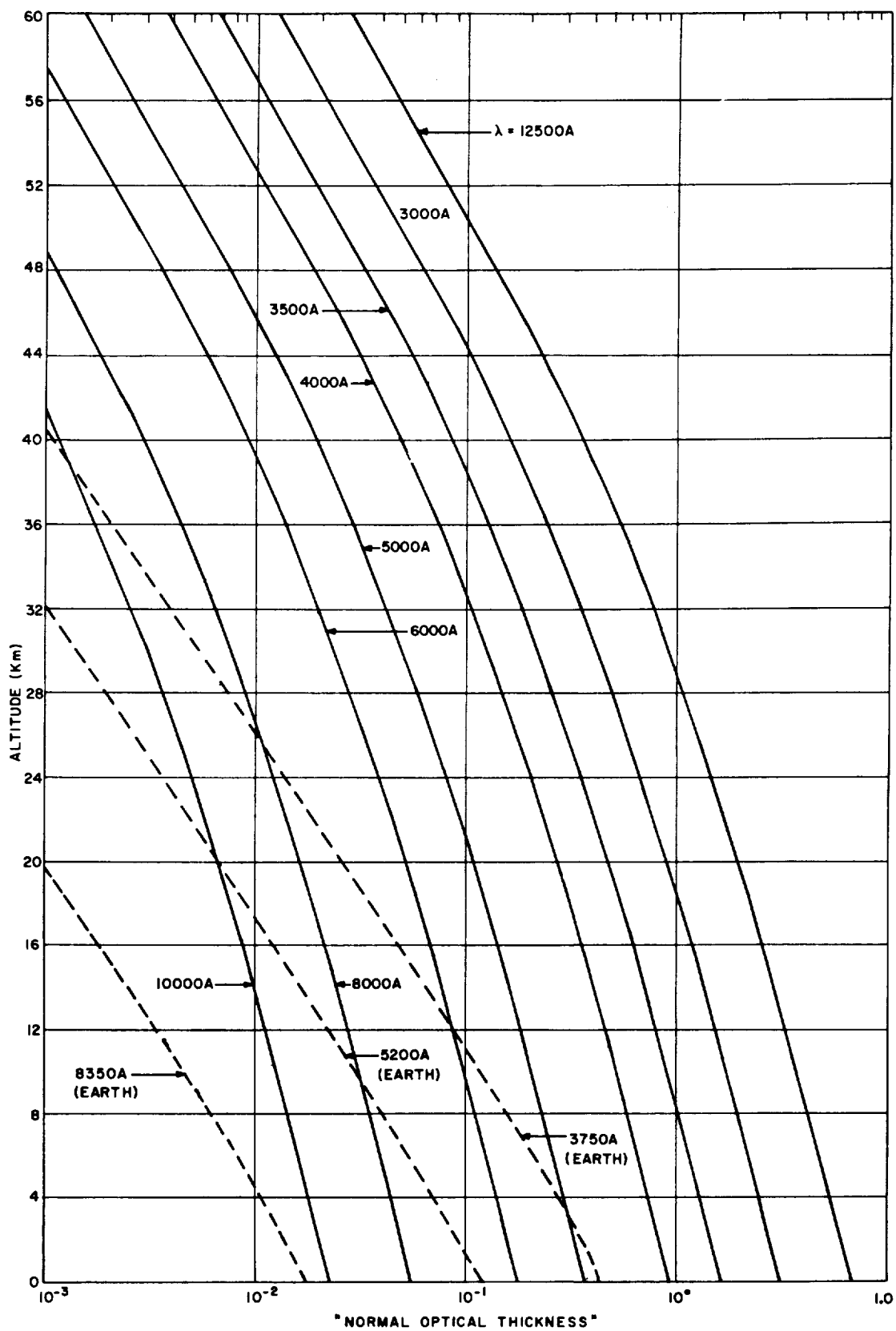


Figure 2.9.5. Normal Optical Thickness as a Function of Altitude for Venus Atmospheric Model V1

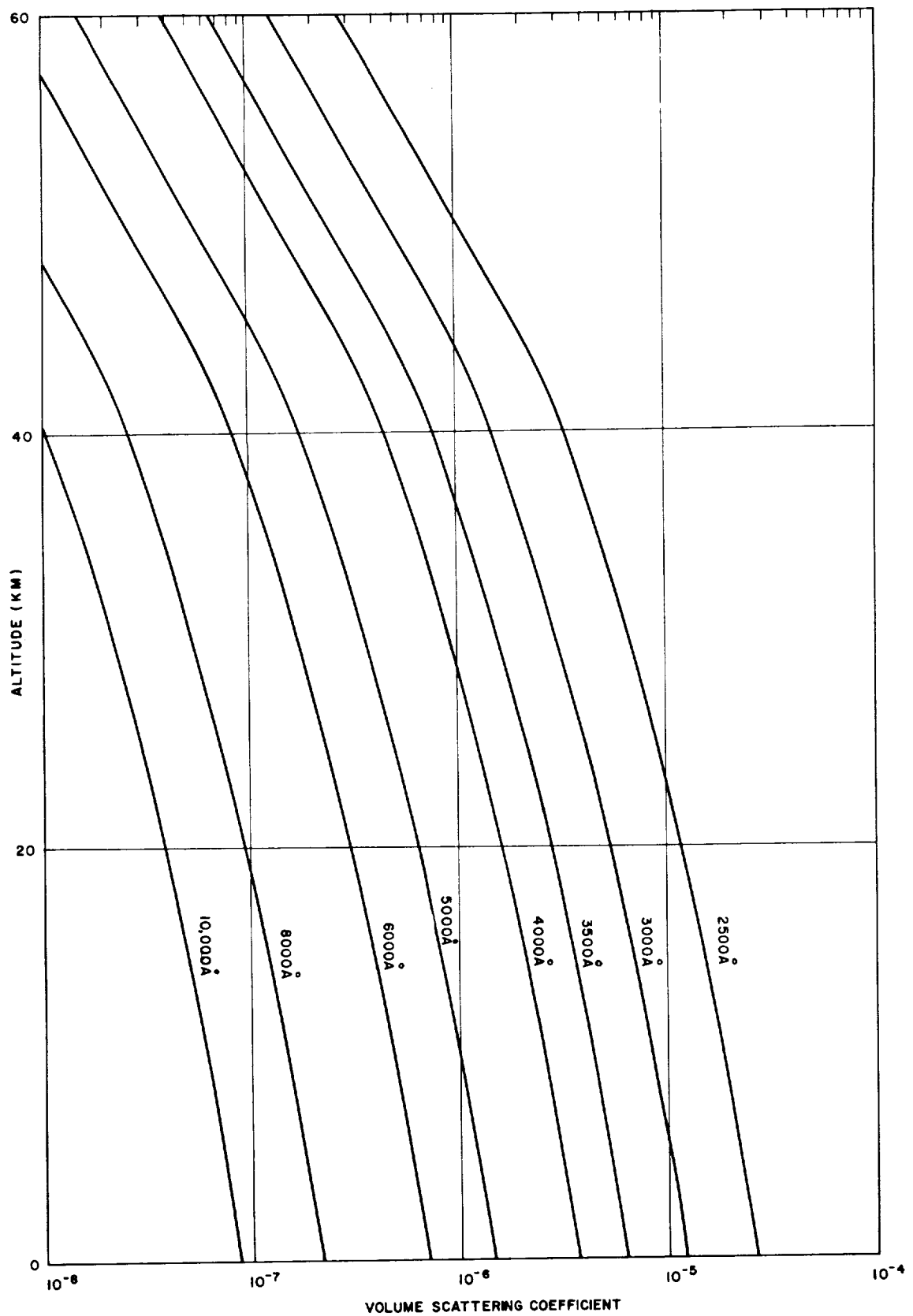


Figure 2.9.6. Volume Scattering Coefficient as a Function of Altitude for the Venus Atmospheric Model V2

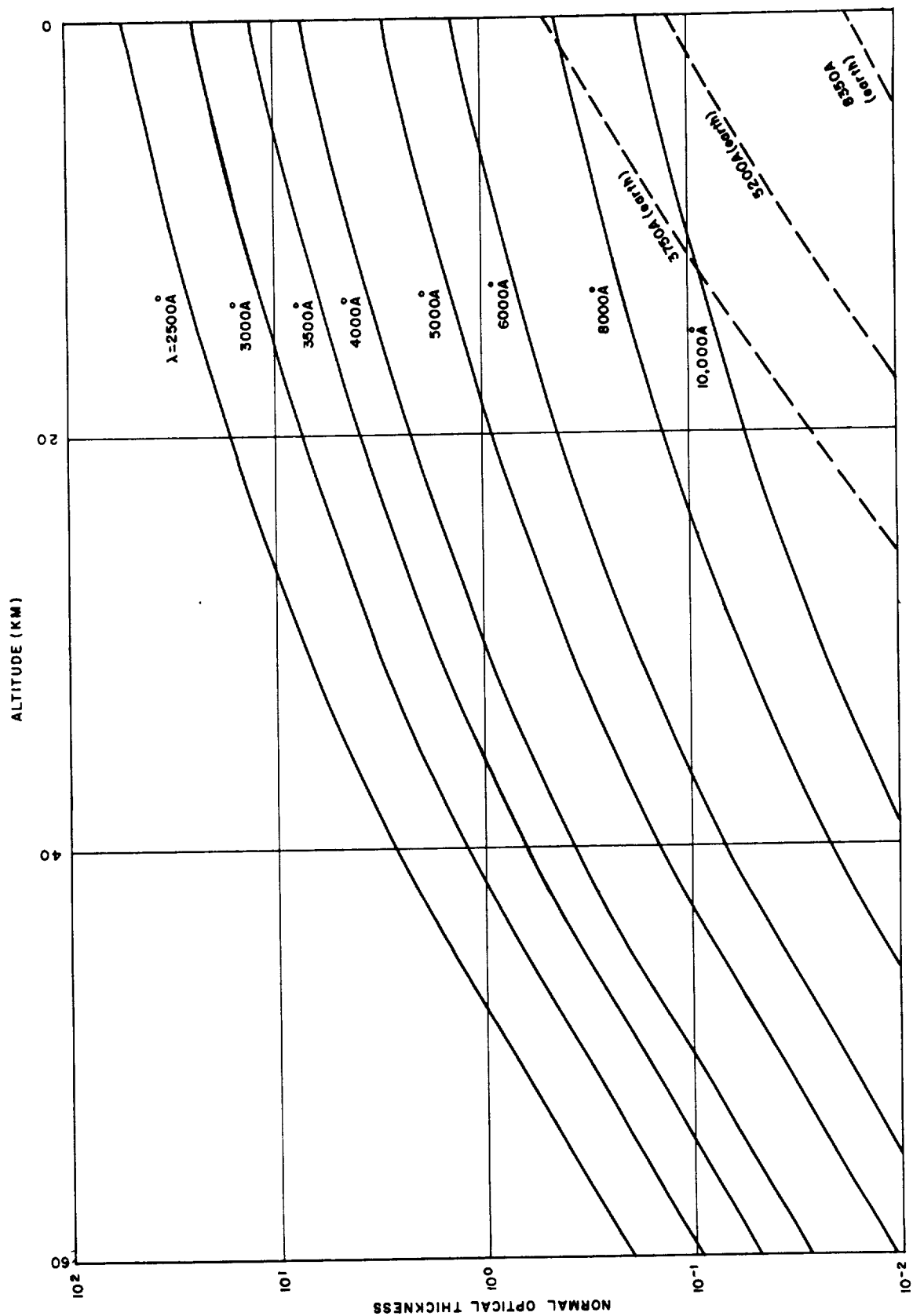


Figure 2.9.7. Normal Optical Thickness as a Function of Altitude for the Venus Atmospheric Model V2

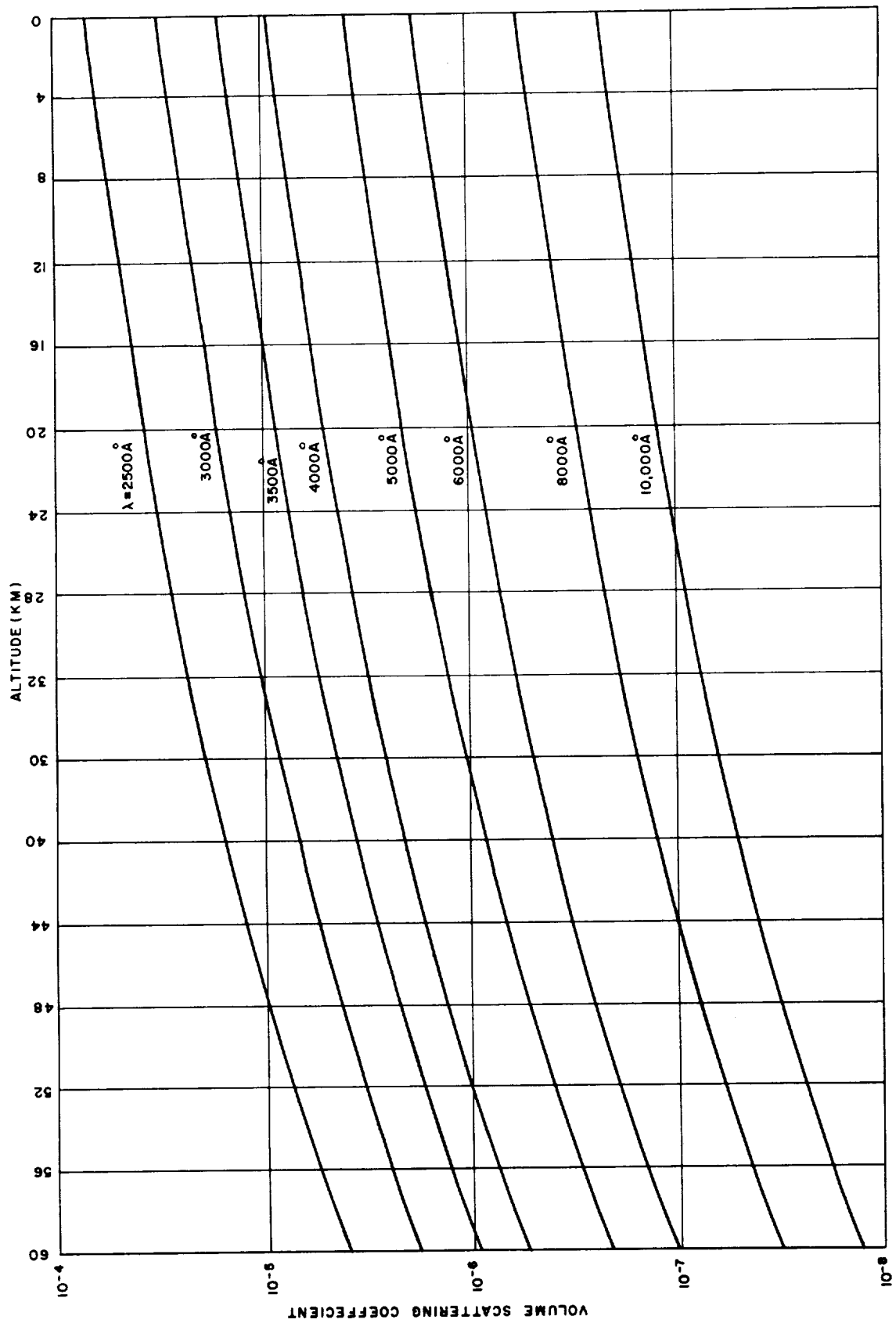


Figure 2.9.8. Volume Scattering Coefficient as a Function of Altitude for Venus Atmospheric Model V3

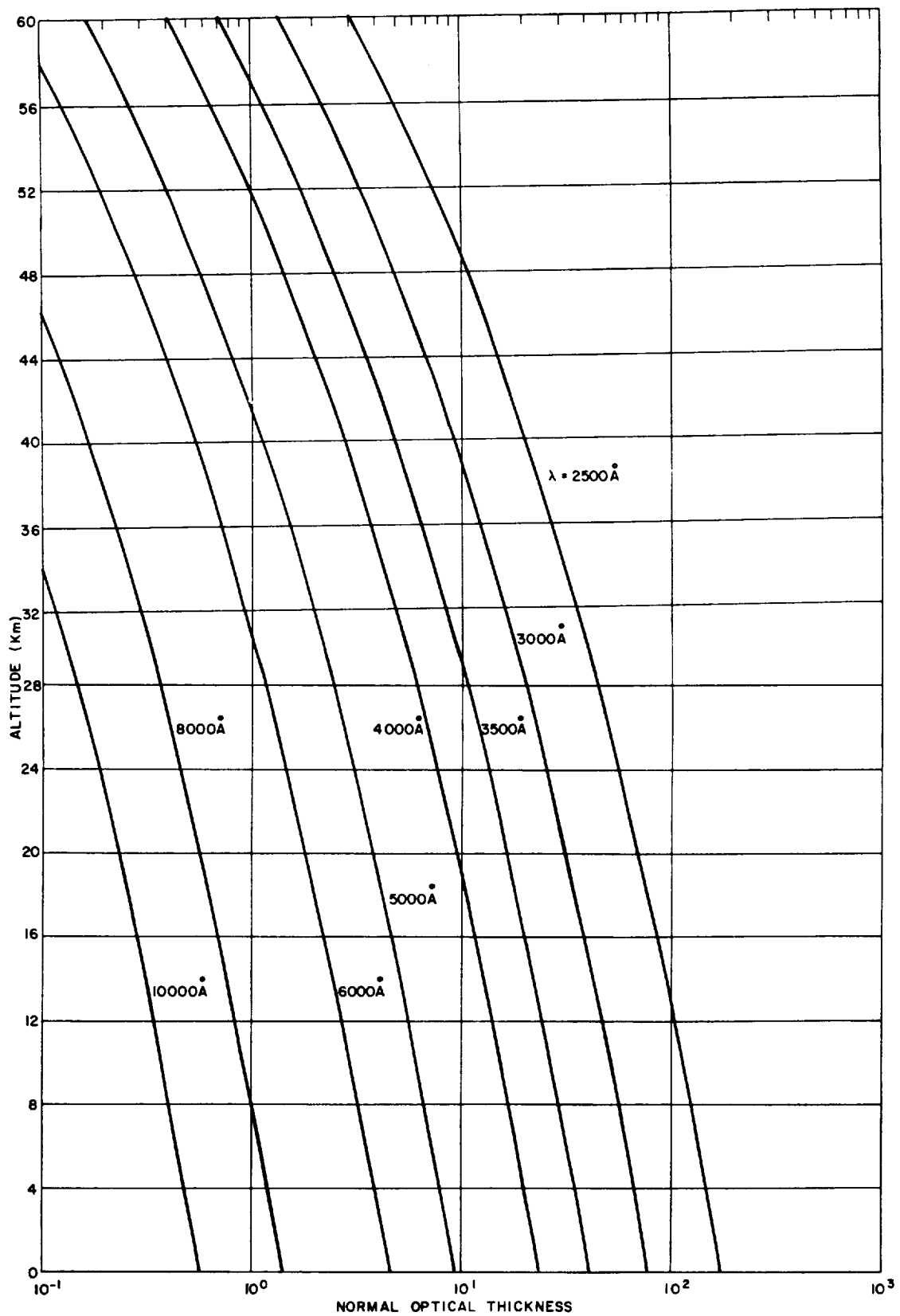


Figure 2.9.9. Normal Optical Thickness as a Function of Altitude for the Venus Atmospheric Model V3

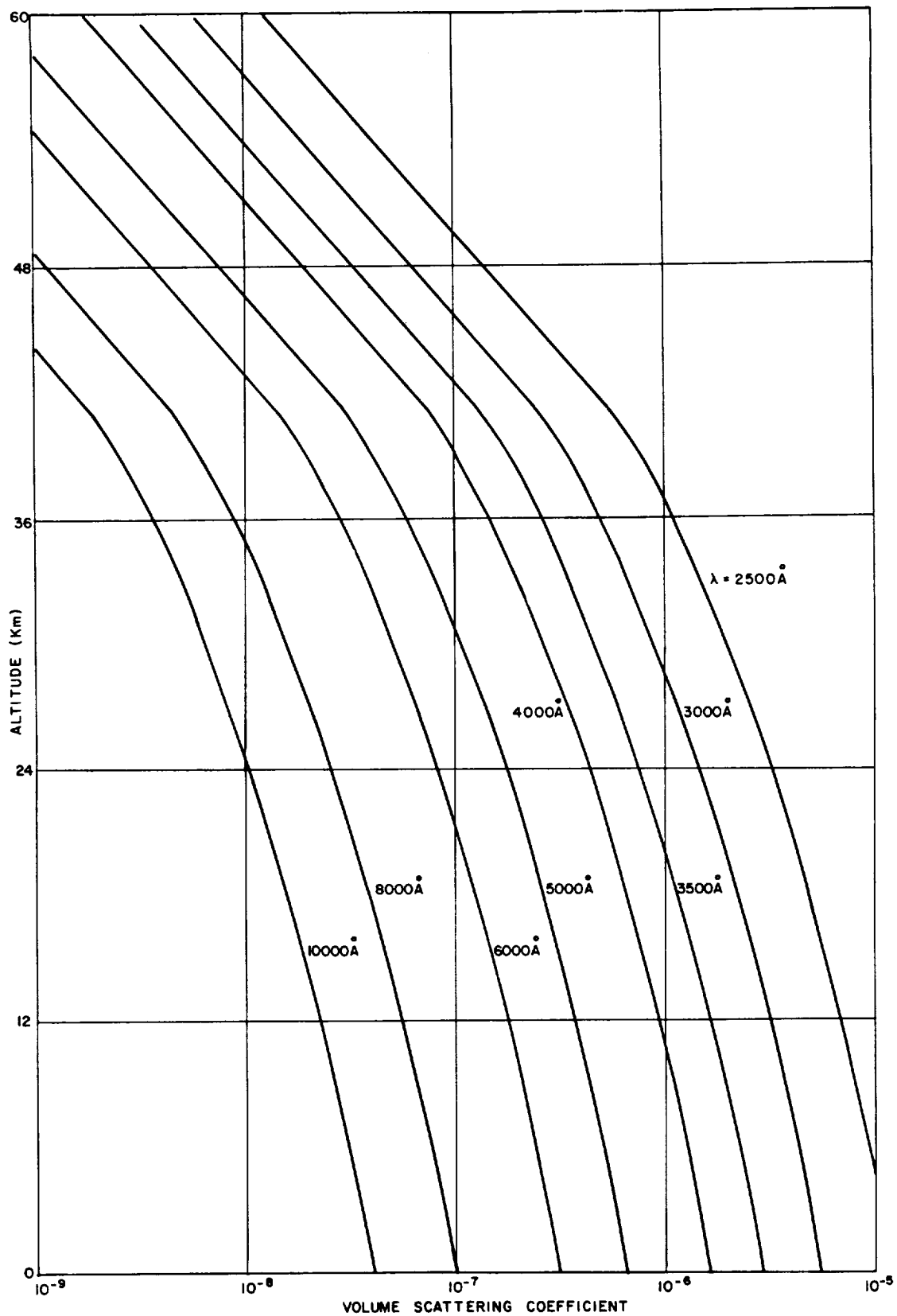


Figure 2.9.10. Volume Scattering Coefficient as a Function of Altitude for Venus Atmospheric Model V4

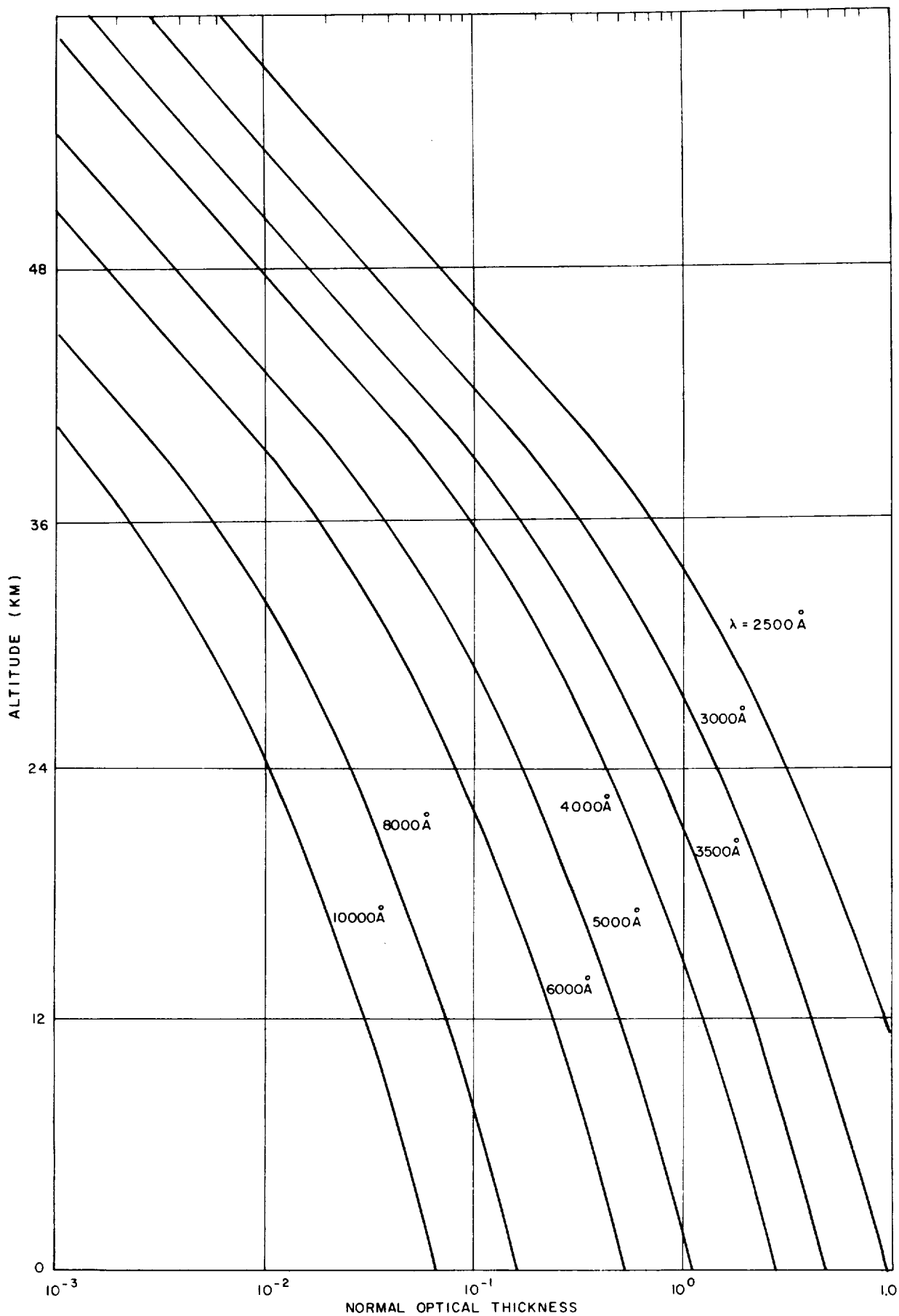


Figure 2.9.11. Normal Optical Thickness as a Function of Altitude
for Venus Atmospheric Model V4
III-2-111

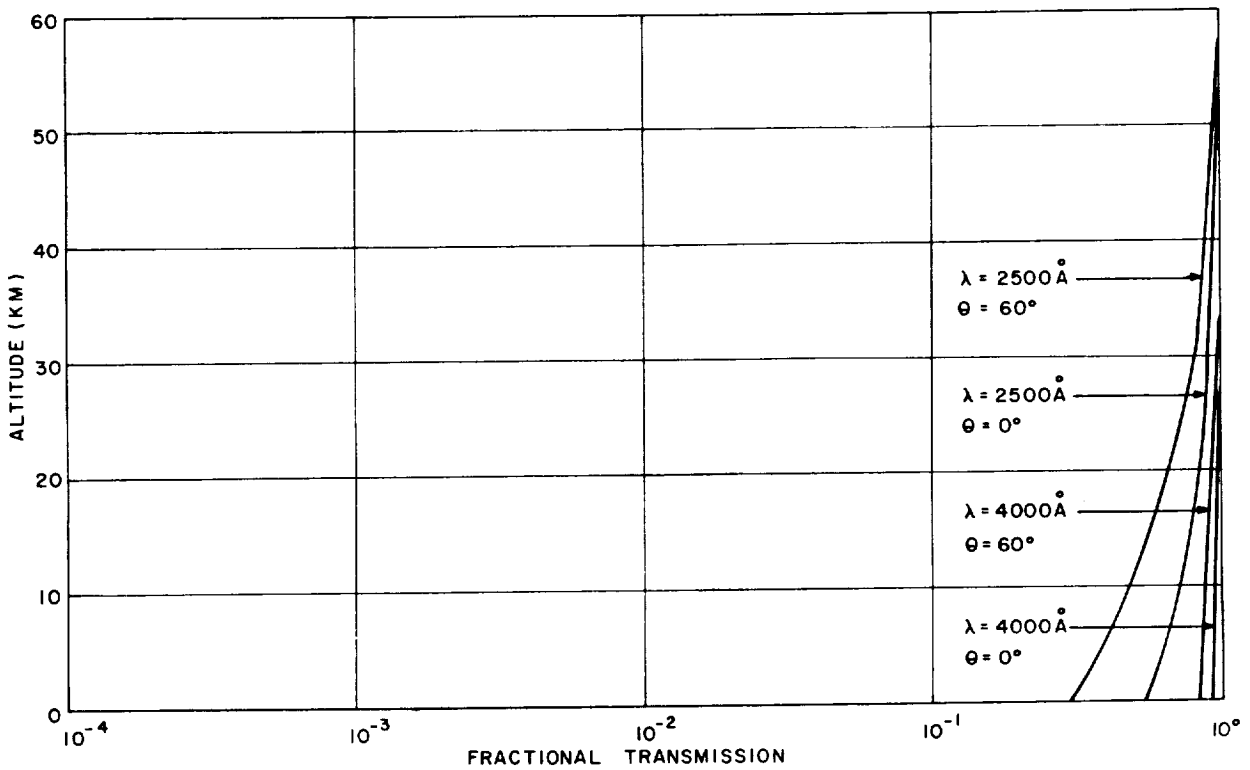
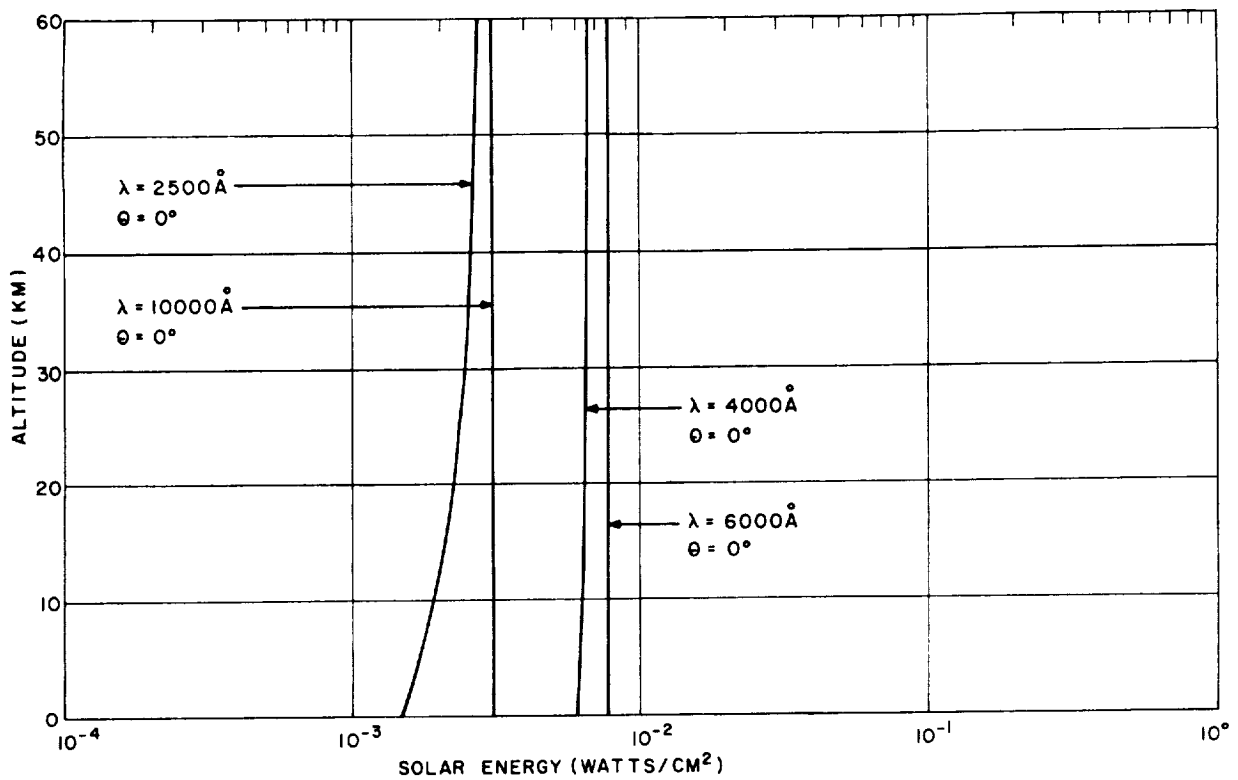


Figure 2.9.12. Energy (Watts/cm² - μ) in the Direct Solar Beams, as a Function of Altitude in Mars model M2 for Four Different Wavelengths. Solar Zenith Angle $\theta_0 = 0^\circ$.

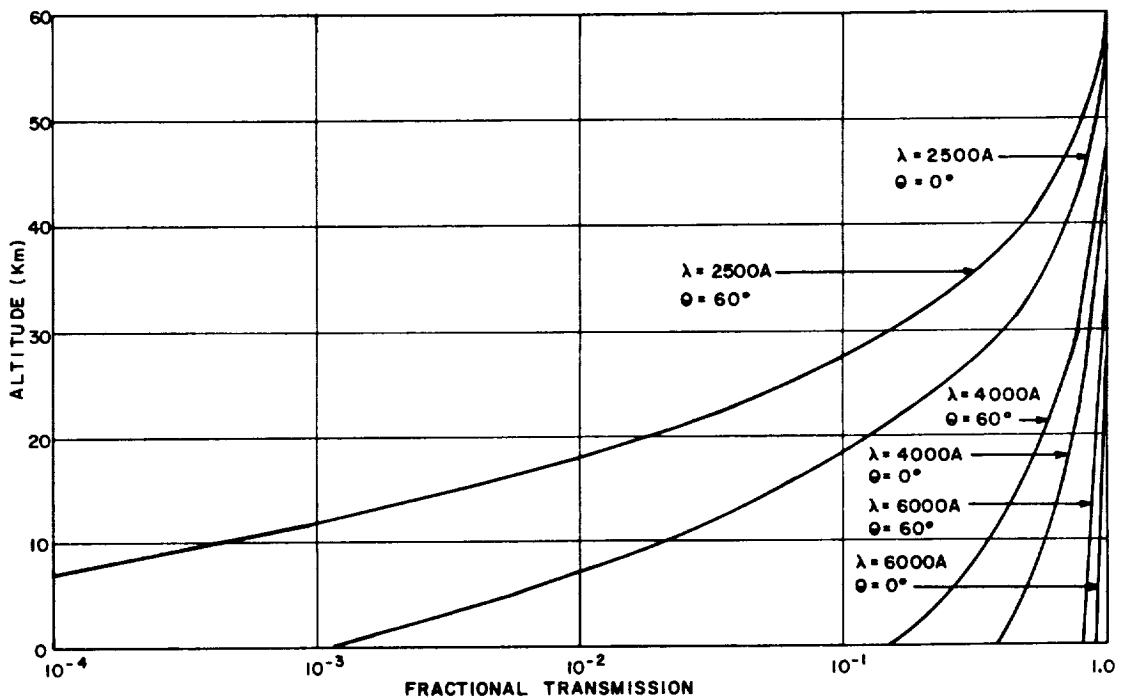
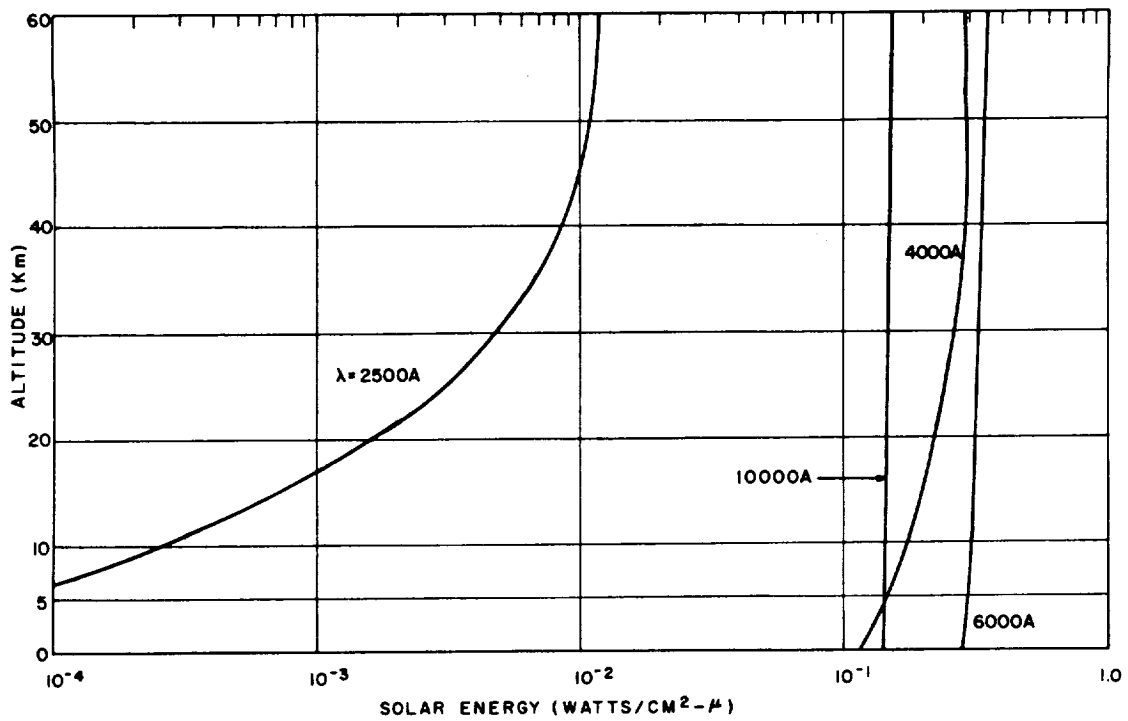


Figure 2.9.13. Energy (Watts/cm² - μ) Direct Solar Beam as a Function of Altitude in Venus Model V1 for Four Different Wavelengths. Solar Zenith Angle $\theta_0 = 0^\circ$.

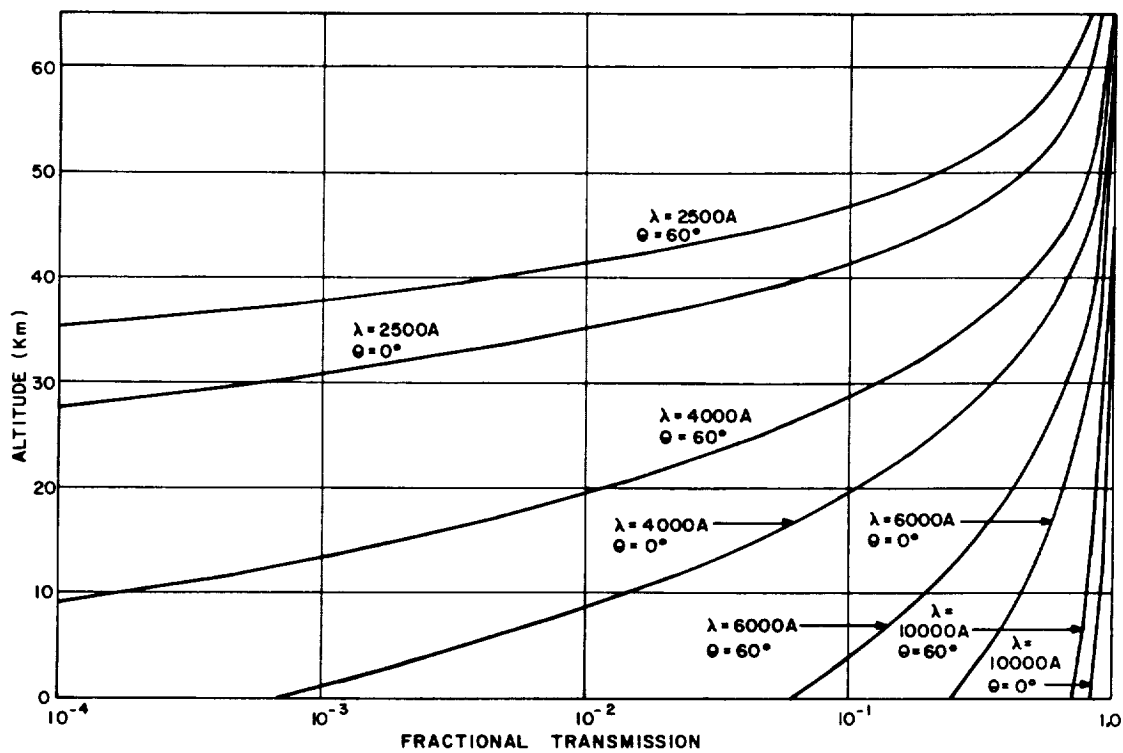
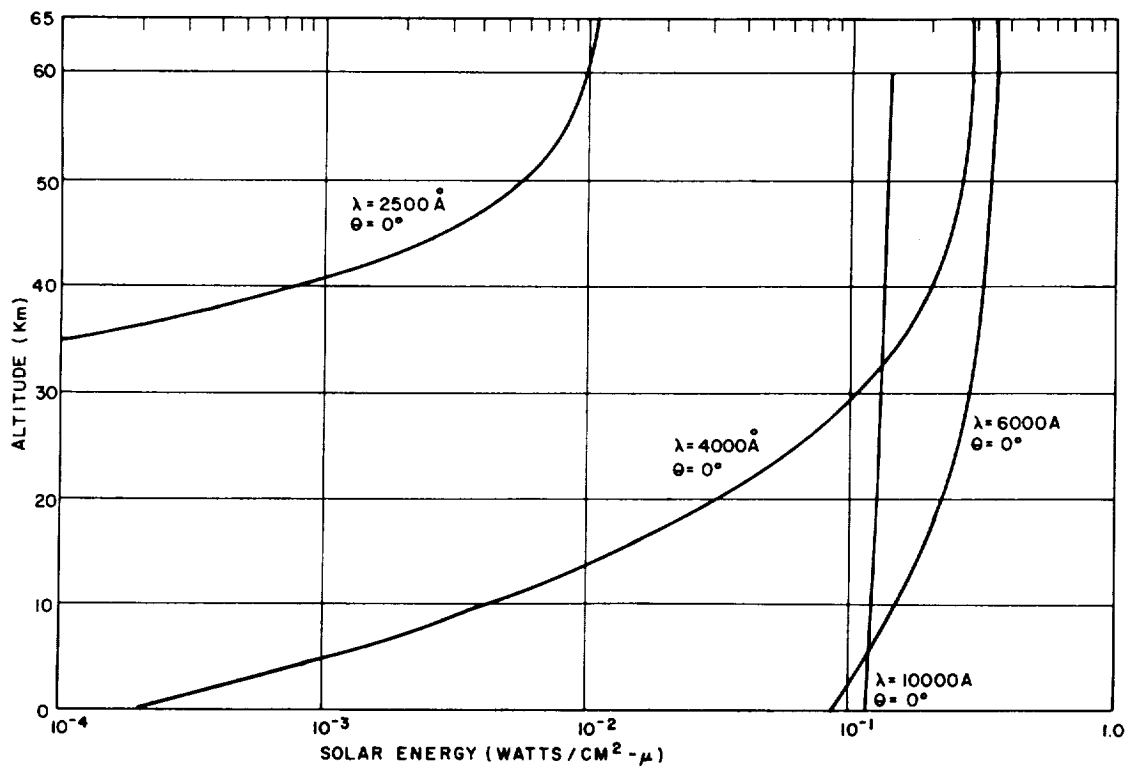


Figure 2.9.14. Energy (Watts/cm² - μ) in the Direct Solar Beams, as a Function of Altitude in Venus model V2 for Four Different Wavelengths. Solar Zenith Angle $\theta_0 = 0^\circ$.

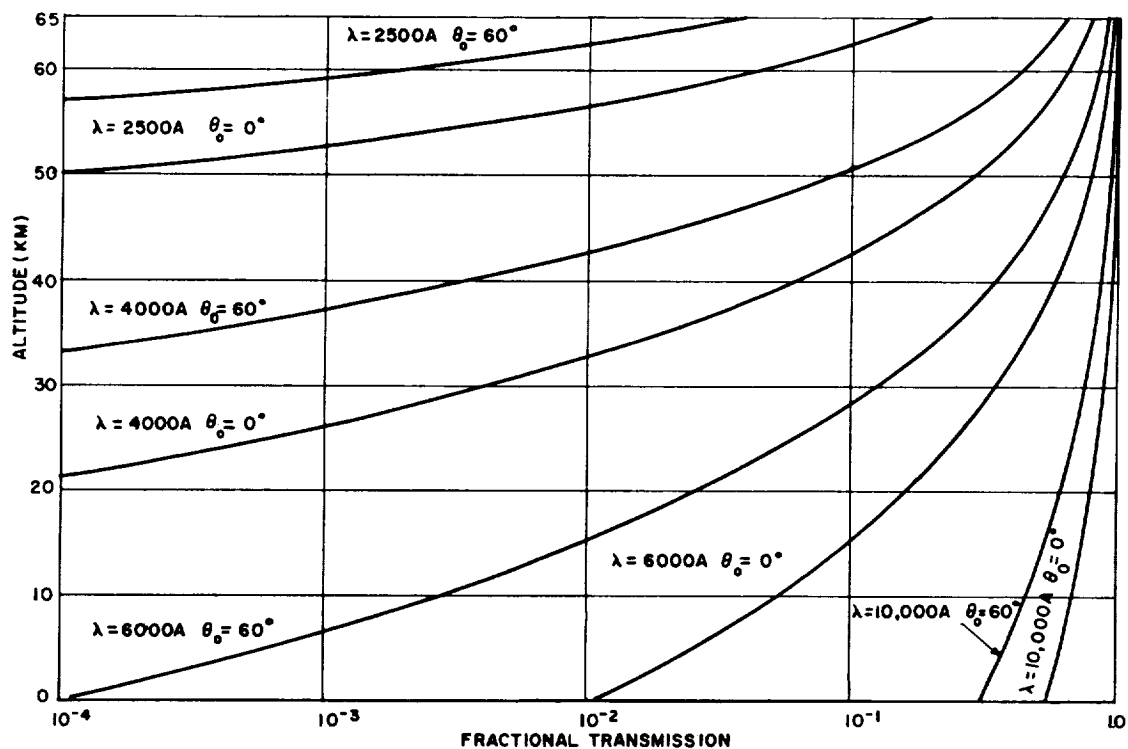
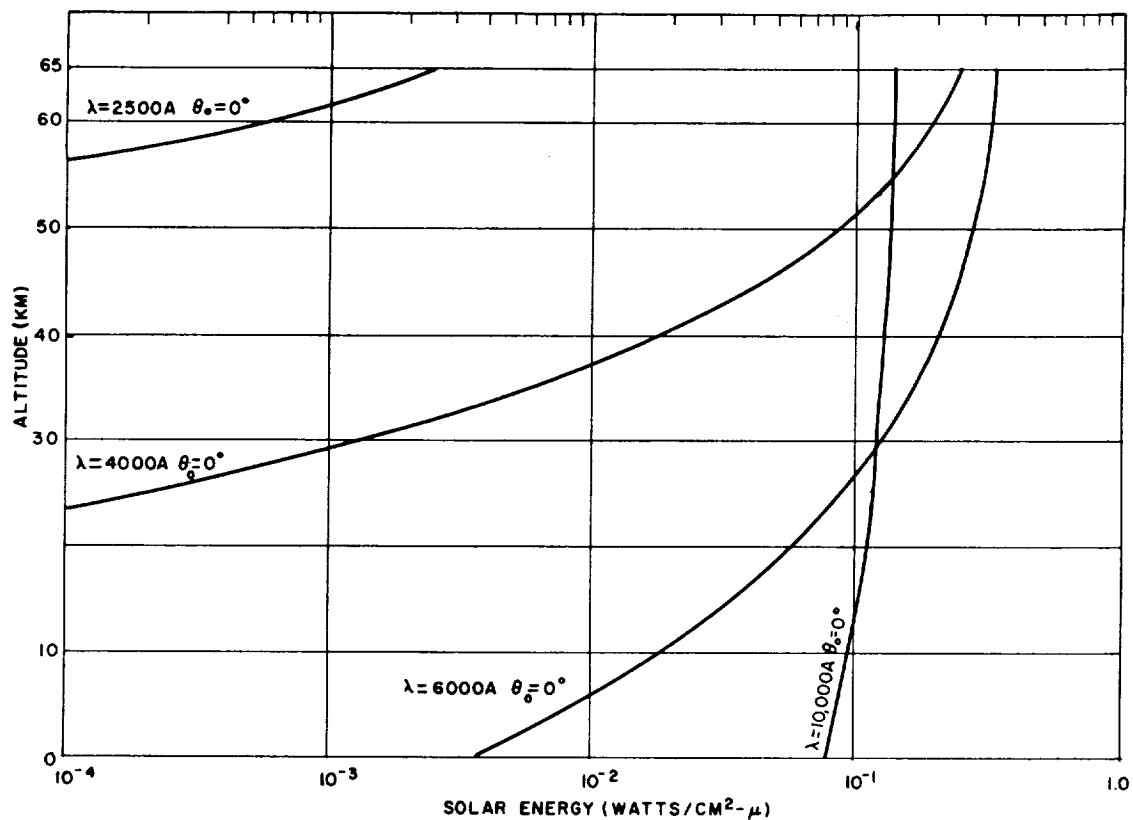


Figure 2.9.15. Energy (Watts/cm² - μ) in the Direct Solar Beam, as a Function of Altitude in Venus Model V3 for Four Different Wavelengths

APPENDIX A

Derivation of Altitude Dependence of Pressure, Density, Scattering Coefficient and Normal Optical Thickness.

The basic relations determining the altitude dependence of the various quantities are the following

$$dP = -g \rho dz: \text{hydrostatic equation} \quad (1)$$

$$P = \rho \frac{R^* T}{M}: \text{equation of state} \quad (2)$$

$$T = T_0 + \gamma z \quad (3)$$

$$\beta = \frac{32}{3} \frac{\pi^3}{\lambda^4} \frac{(n-1)^2}{N} \quad (4)$$

$$\tau = \int_z^{\infty} \beta dz \quad (5)$$

The symbols denote the following quantities:

z = altitude

P = pressure

ρ = density

T = temperature

g = acceleration of gravity

R^* = universal gas constant

M = molecular weight

γ = lapse rate (dT/dz)

β = volume scattering coefficient

λ = wavelength

n = refractive index of gas

m = reciprocal of Avagadro's number

i = index denoting i th gas of mixture of k gases

C = refractivity of gas

N = number density of molecules

τ = normal optical thickness

Subscript 0 denotes conditions at a reference level where $z = z_0$

Subscript s denotes standard conditions (273° K, 760 mm of Hg).

On substitution of Equation (2) into Equation (1), one obtains

$$\frac{dP}{P} = d(\ln P) = \frac{-gM}{R^*T} dz \quad (6)$$

and

$$d(\ln P) = \frac{-gM}{R^*} \frac{dz}{(T_0 + \gamma z)} \quad (7)$$

on substitution of Equation (3) into Equation (6). We now distinguish between two cases of vertical temperature distribution, namely, an isothermal atmosphere or atmospheric layer (Case 1) and a nonisothermal atmosphere or atmospheric layer (Case 2) in which $\gamma = \text{constant} \neq 0$.

Case 1: $\gamma = 0$

For this case Equation (7) reduces to

$$d(\ln P) = \frac{-gM}{R^*T_0} dz \quad (8)$$

and on integration between z_0 and z ,

$$\frac{P}{P_0} = e^{-\frac{gM}{R^*T_0}(z - z_0)} \quad (9)$$

Any change of gravity or composition with altitude is neglected here. This is also the expression for the ratio of densities, as could be anticipated by the constant temperature. Explicitly,

$$\frac{\rho}{\rho_0} = e^{-\frac{gM}{R^*T_0}(z - z_0)} \quad (10)$$

Case 2: $\gamma \neq 0$

For this nonisothermal case, integration of Equation (7) with the assumption of $\gamma = \text{constant}$ gives

$$\frac{P}{P_o} = \left(\frac{T_o + \gamma z}{T_o + \gamma z_o} \right)^{-\frac{gM}{R^*\gamma}} \quad (11)$$

If $z_o = 0$, then

$$\frac{P}{P_o} = \left(\frac{T}{T_o} \right)^{-\frac{gM}{R^*\gamma}} \quad (12)$$

The equivalent expression for density, obtained by substitution of Equation (2) into Equation (12), is

$$\frac{\rho}{\rho_o} = \frac{P}{P_o} \frac{T_o}{T} = \left[\frac{T}{T_o} \right]^{-\left(\frac{gM}{R^*\gamma} + 1 \right)} \quad (13)$$

The number density of molecules is defined

$$N = \frac{\rho}{m M} \quad (14)$$

Since the molecular weight M is assumed constant, it follows that

$$\frac{N}{N_o} = \frac{\rho}{\rho_o} \quad (15)$$

It is convenient to express the index of refraction of a gas in terms of the refractivity C, as

$$C = \frac{n-1}{\rho} . \quad (16)$$

Equation (16) is verified closely by experiment and values of C for the main atmospheric gases are available in tabular form. For an atmosphere consisting of a mixture of k gases the volume scattering coefficient must be appropriately modified to the form

$$\beta = \frac{32}{3} \frac{\pi^3}{\lambda^4} \sum_{i=1}^K \frac{(n_i - 1)^2}{N_i} . \quad (17)$$

On substitution of Equation (16) into Equation (17), we obtain β as

$$\beta = \frac{32}{3} \frac{\pi^3}{\lambda^4} m^2 \sum_{i=1}^K M_i^2 C_i^2 N_i . \quad (18)$$

For purposes of computation it is convenient to express the number density in terms of the mass density as

$$N_i = \left(N_o \frac{\rho}{\rho_o} \right)_i . \quad (19)$$

On introducing β into Equation (5), we obtain the normal optical thickness for wavelength λ for all the atmosphere above altitude z. The integration is facilitated by defining an effective molecular weight for the mixture of gases by the relation

$$M = M_1 \frac{\rho_1}{\rho} + M_2 \frac{\rho_2}{\rho} + . . . , \quad (20)$$

and an effective refractivity by

$$C = C_1 \frac{\rho_1}{\rho} + C_2 \frac{\rho_2}{\rho} + \dots \quad (21)$$

Then

$$\sum M_i^2 C_i^2 N_i = M^2 C^2 N, \quad (22)$$

and the normal optical thickness at altitude z and wavelength λ is

$$\tau(\lambda, z) = \frac{32}{3} \frac{\pi^3}{\lambda^4} \frac{N_o}{\rho_o} m^2 \int_z^{\infty} M^2 C^2 \rho \, dz. \quad (23)$$

Equation (23) is particularly simple for the case in which relative proportions of the components are independent of z . For those conditions

$$\tau(\lambda, z) = \frac{32}{3} \frac{\pi^3}{\lambda^4} \frac{N_o}{\rho_o} m^2 M^2 C^2 \int_z^{\infty} \rho \, dz. \quad (24)$$

For a vertical profile in which the lapse rate or relative composition changes it is necessary to integrate Equation (23) over two or more atmospheric layers. For one such layer

$$\tau(z) = \sum_{j=1}^1 (\Delta \tau)_j \quad (25)$$

the increments of τ being directly additive.

2.10 VELOCITY

Although velocity is not one of the prime measurement parameters, pressure and temperature measurements are velocity sensitive and naturally suggest that they either be used to measure velocity or that velocity measurements be used to correct the temperature and pressure information. Further, if altimeter data were not available, velocity information could be integrated to obtain height data.

The limitations of the use of pressure and temperature for velocity measurements have been discussed previously. Two additional methods, a turbine-type velocity meter and the use of density information, are discussed in the next section.

2.10.1 Turbine Velocity Meter

The basic idea is to use a freely-turning propellor or turbine blade, rotating at a speed proportional to velocity, and count the rate of spin as a measure of velocity. This would be similar in principal to turbine-type flowmeters manufactured, for example, by the Potter Aeronautical Co., N. J.

A number of possible troubles are anticipated. The bearing supporting the turbine blade will be exposed to vacuum for an extended period, and any lubricant may evaporate. This may cause either large errors or failure of the sensing element. Secondly, the gage will have to operate over wide ranges of density. Density information will be available, however, and it should be possible to correct for this effect.

2.10.2 Drag-Velocity Calculations

Soon after entry into the atmosphere, the vehicle velocity drops to subsonic, and then reaches terminal velocity. At terminal velocity, the velocity can be calculated if the force of gravity, atmospheric density, and coefficient of drag are known. The force of gravity is known for Venus, and the atmospheric density is being measured. The drag coefficient can be determined by wind tunnel tests. Hence, sufficient information is available to determine the vehicle velocity.

2.11 RADAR ALTIMETER

2.11.1 Summary and Conclusions

A conventional pulsed radar altimeter system is outlined to obtain altitude data within the Venusian atmosphere subsequent to hard entry conditions and achievement of a capsule speed of Mach 1.

Included are a block diagram of the proposed system, power and weight estimates, radar range equation calculations, receiver noise power calculations, range tracking loop requirements, detection probability calculations and various ancilliary calculations.

It cannot be stated that data can be obtained from a specified altitude above the Venus surface for specific size, weight and power requirements unless prior assumptions are presumed valid.

Additional complications are introduced by the predicted severe environmental conditions to be encountered. High "g" forces at entry and high temperature conditions within the Venusian atmosphere impose restraints upon antenna design and packaging requirements.

Altitude data can be obtained within the Venusian atmosphere by the use of radar altimeter techniques with a high degree of confidence. Prior to the design of a specific instrument however, the design or model conditions must be specified. So long as the actual conditions encountered can be predicted with a reasonable degree of accuracy, an instrument can be constructed which will surely obtain the desired data.

2.11.2 Introduction

Initial penetration of the Venusian atmosphere by a capsule has the primary purpose of gathering data about the properties of that atmosphere. Measurements are intended to be made of pressure, density and temperature as functions of the absolute altitude above the surface of Venus.

Since the data are related to altitude in order to be meaningful, it follows that the altimeter should be a simple, reliable device to ensure the return of information which is definitive.

The studies of atmospheric entry have shown the reduction of capsule speed to approximately Mach 1 at an altitude of approximately 200,000 ft. This range is assumed as the required initial acquisition range of the radar altimeter.

The role of the altimeter as stated above is to measure the range to the planetary surface from the capsule by the use of microwave radar range measuring techniques.

Many system configurations are possible which will solve the altitude measuring problem. Trade-offs can be made utilizing short pulses and higher peak powers that the system outlined herein. Some of the inherent unknowns of the properties of the Venusian atmosphere however have influenced the design choices which were made. One of these is the possibility of high peak powers causing breakdown at the altimeter antenna terminals. Also above a given level an increase in transmitter power causes an inordinate increase in size and weight.

A desire to obtain data prior to hard entry into the atmosphere of a planet can impose serious doubts as to the validity of the system specified. The problems associated with gathering altitude data subsequent and prior to entry are mutually exclusive however in that the types of altimeter system required are completely different due to the order of magnitude differences in range and capsule orientation.

A long range, and a lack of knowledge of capsule orientation suggests the use of an omnidirectional antenna system which for a pulse radar, employed on extended targets, a range attenuation factor of 30 db per octave rather than 20 db per octave as with the directional antenna system. This is identified in radar systems as pulse limiting versus beam limiting conditions.

Simple calculations will show that a radar system required to operate omnidirectionally at approximately four (4) times the range of the present system would require 2×10^5 or 53 db due to pulse limiting at equivalent range plus 120 db

due to a four times increase in range plus 28 db due to lack of the antenna gain factor. This total requirement of approximately 200 db in gain above the present system could be partially offset by the use of a lower frequency (i.e., longer wavelength) of transmission. This inherently only releases 80 db even down to frequency of 1 mc.

It follows, therefore, that some form of pulse compression technique at a relatively low transmission frequency is required for a high altitude omnidirectional system to operate prior to entry into the Venusian atmosphere (i.e., in the free molecular region).

An additional gain can be achieved by an increase of peak power in the order of magnitude of 30 db which would be a maximum. A pulse width change would be offset by a corresponding increase in the noise power of the receiver except the changes in the direction of pulse compression.

Another source of doubt can be generated by an analysis of the initial acquisition range to be preset into the radar altimeter circuitry. Reduction of capsule speed to approximately Mach 1 will occur almost immediately after hard entry. However, the various models of the Venusian atmosphere and various capsule shapes coupled with a variety of entry angles and conditions result in a wide range of expected altitudes for reaching the Mach 1 speed. Present indications are that this range will extend from below 100,000 feet to above 250,000 feet.

Since it is virtually axiomatic that some form of fuzing or preset delay time is required by the radar altimeter in order to achieve automatic tracking of capsule altitude, the lack of a definitive initial acquisition range can create a substantial problem area.

A possible solution would be to preset the initial acquisition range at a value low enough to be assured of the capsule having reached the Mach 1 condition prior to that altitude. This would then impose a requirement of extrapolating the altitude data back to hard entry altitude. Since the temperature conditions are predicted to be extreme in the Venusian atmosphere, it follows that data acquisition at low altitudes may be precluded by component failures induced by the high heat loads imposed.

Note that the use of a swept gate would solve the problem but would also result in a substantial increase in the noise power "on" time or receiver duty ratio which would in turn require a substantial increase in transmitter power. This might be a last resort and could evolve into a trade off of altitude achievable versus power at a maximum allowable weight.

2.11.3 Equipment Characteristics

Functional Characteristics

The role of the altitude sensor in the overall scientific mission of the Venus capsule is to provide altitude data subsequent to entry into the Venusian atmosphere.

Continuous output of range is provided from 200,000 feet to a few thousand feet.

At the time of entry of the capsule into the Venusian atmosphere the radar altimeter should be turned on. At 200,000 feet the radar will lock on and provide a continuous output of altitude in digital form.

Electrical Characteristics

Operating Frequency	10 kmc/sec
Antenna gain	28 db
Pulse Peak Power	50 watts
Pulse Length	5 μ sec
Pulse repetition frequency	500 pps
Duty Ratio	0.25 per cent
Average Power	125 mw
S/N Ratio	20 db
Receiver	
Type	Superheterodyne
Noise Figure	10
Intermediate Frequency	30 mc/sec
I. F. Bandwidth	315 kc/sec
Video Bandwidth	117 kc/sec

Output	Digital
Accuracy	± 5 per cent
Input Power	25 watts @ 28 VDC

Physical Characteristics

Weight	15 lbs including antenna
Volume	500 in ³ plus antenna

2.11.4 System Performance

Signal to Noise

The initial consideration in determining the performance to be expected from a radar altimeter system is the development of the radar equation. Of special interest to a capsule entering the Venusian atmosphere are the back scattering characteristics of the surface of Venus. No specific model is known to be available so that a general discussion on the microwave backscattering characteristics of extended targets is appropos for an engineering estimate of the expected losses which will occur at the surface.*

The return signal power P_r from a single scatterer of backscattering cross section σ (defined as the area intercepting that amount of power which, when scattered isotropically, would produce an echo equal in power to that produced by the actual scatterer) is given by the well-known relation:

$$P_r = \frac{P_t \lambda^2 G^2 \sigma}{(4\pi)^3 R^4}$$

where P_t is the transmitted power, λ is the wavelength of the transmitted radiation, G is the antenna gain, and R is the distance between transmitter-receiver and scatterer.

*Backscattering Characteristics of Land and Sea at X-Band by J. P. Campbell, Proceedings of the National Conference on Aeronautical Electronics, 1958.

When the radar illuminates an extended target which is assumed to be a large collection of independent scatterers, the return signal power is the summation of the powers returned by the individual scatterers:

$$P_r = \frac{P_t \lambda^2}{(4\pi)^3} \sum_K^K \left(\frac{G^2 \sigma}{R^4} \right) \text{ extended target}$$

Where each scatterer has associated with it particular values of G , σ , and R . Since a large number of scatterers are illuminated, the summation can be replaced by an integral. Also since a narrow beam antenna is utilized, R and σ will not vary appreciably over the integral. The equation can now be rewritten as:

$$P_r = \frac{P_t \lambda^2 \sigma_o}{(4\pi)^3 R^2 \cos \psi} \int G^2(q) d\omega$$

Where σ_o is the average backscattering cross section per unit area, defined, for a homogeneous target in which the individual scatterers are distributed in a statistical uniform manner, as σ times the number of scatterers per unit area. ψ is the angle between the direction of incident radiation and the normal to the illuminated area; q is a generalized direction coordinate; $d\omega$ is an element of solid angle. The integral in the above equation is taken over the entire solid angle surrounding the antenna.

The antenna radiation pattern can be defined as:

$$F(q) \equiv \frac{G(q)}{G_o}$$

where G_o is the maximum value of $G(q)$

From the definition of antenna gain

$$G_o \int F(q) d\omega = 4\pi$$

Therefore, the integral of the above equation can be written as:

$$\int G^2(q) d\omega = 4\pi G_o \frac{\int F^2(q) d\omega}{\int F(q) d\omega} = 4\pi G_o [W]$$

where W is defined as the integral quotient shown above.

The quantity W is fixed for a given antenna radiation pattern shape, i.e., it depends only upon the form of F(q) and not upon particular values of antenna radiation pattern parameters such as beamwidth. This is true however only when the preceding assumptions previously made are valid for the extended target.

∴ From the above

$$P_r = \frac{P_t \lambda^2 \sigma_o G_o \omega}{16 \pi^2 R^2 \cos \psi}$$

Since

$$\frac{S}{N} = \frac{P_r}{P_n}$$

where

$$P_n = k T B N.F.$$

and gating is required of the receiver to prevent integration of the noise power after rectification so that $dr \equiv$ duty ratio of the transmitter and $dr' \equiv$ duty ratio of the receiver.

Also: L = plumbing losses

$$\frac{S}{N} = \frac{dr P_t \lambda^2 \sigma_o G_o W L}{16 \pi^2 R^2 \cos \psi KTB N.F. dr'}$$

Detection Probability for a Pulsed Radar Altimeter*

The received signal is assumed to be a pulsed sinusoid. The signal power during a pulse is denoted by S , and the internal noise power referred to the same point in the system is denoted by N .

For this analysis, the essential parts of the receiver consist of a detection amplifier, a square law detector, a pulse integrator, and a decision threshold.

The purpose of this analysis is to predict the probability of detection and lock-on at 200,000 feet, when the capsule flies through the range gate. The analysis will also indicate the probability of a noise pulse unlocking the system by exceeding the threshold of the decision element. This is accomplished by determining when the integrator output is equal to or greater than the threshold voltage. The probability density function for the total voltage at the output of the integrator at the time the desired altitude is reached is $P_n(Z)$ which is a variable of voltage. By definition the probability that a random variable Z will lie between two values such as Z_1 and Z_2 is

$$P = \int_{Z_1}^{Z_2} P_n(Z) dZ$$

The number of independent samples of signal plus noise in the false alarm time is called the false alarm number and is denoted by n . The probability of having a false alarm on a single trial is the reciprocal of the false alarm number.

The probability of a false alarm is defined as the probability that noise alone causes the threshold voltage (b) to be reached or exceeded. Thus,

$$P_F = \frac{1}{n} = \int_b^{\infty} P_n(Z) dZ$$

*A Statistical Theory of Target Detection by Pulsed Radar, J. E. Marcum
Rand Memo, Room 754 and Appendix Room 753.

The probability of detection is defined as the probability that signal plus noise will cause the threshold voltage to be reached or exceeded. Thus, if we call the probability density function at the output of the integrator, when the desired altitude is reached, $P_{(S+N)}(\mu)$ where μ is a variable of voltage, the probability of detection will be

$$P_D = \int_b^{\infty} P_{(S+N)}(\mu) d\mu$$

This technique then consists of selecting a desired false alarm probability, b is determined from the expression for $P_n(Z)$ and used in the expression for $P_{(S+N)}(\mu)$ to determine the probability of detection.

$P_n(Z)$ and $P_{(S+N)}(\mu)$ can be determined by computation utilizing the methods discussed in the referenced report. An analog to our system exists in that the scanning function is essentially the time that the capsule is in the range gate during acquisition.

2.11.5 Functional Description

The basic functional diagram of the pulsed radar altimeter is shown in Figure 2.11.1. The system is composed of an antenna, a pulsed magnetron, a solid state modulator, solid state dc to dc converters, a superheterodyne receiver including an AFC loop and AGC, range tracking circuits, a range computer and suitable digital conversion circuits to provide compatible outputs to the communications system.

The radar makes a simple time echo measurement to determine range along the boresight axis of the antenna. This range determination is made by measuring the time from the leading edge of the transmitter pulse to the centroid of the received pulse energy.

The centroid technique is preferred due to a variety of possible differences from the expected design conditions. The range error will be less than a leading edge determination whenever the extended target is not normal to the antenna

boresight and the angle between the target normal and boresight is continuously changing. Also the narrow receiver passband employed will not maintain a sharp rise on the leading edge of the received pulse.

Altitude or range output is provided by tracking the round trip time of the signal with a split gate time discriminator. As the capsule approaches the planetary surface, the round trip echo time continuously decreases. The tracking loop servoes the range gate to track the delay time of the echo pulse. An error signal is obtained from the range gate when the echo pulse is not equally divided in the early and late halves of the range gate. The time delay measurement, represented by the time between the transmitter and gate signals is provided to the range computer and then converted to a digital output and processed to the communications system.

Upon approach to the planet in question, the capsule will enter the atmosphere and decelerate very rapidly to a velocity of approximately Mach 1. Some means should be provided to turn on the radar altimeter at this time. A simple method could be instrumented to depend upon the large "g" forces which will be encountered at entry.

System

The altitude range measurement is determined by a simple time echo measurement. This function is performed by the pulsed radar altimeter with a superheterodyne receiver and a split range gate tracking loop providing continuous range outputs from 200,000 feet down to a few thousand feet where receiver recovery time prevents further operation.

Transmitter

The magnetron oscillator feeds through the duplexer to the antenna, and the return signal from the target passes from the duplexer to the receiver. An AFC circuit maintains the receiver tuned to the frequency of the magnetron oscillator.

Receiver

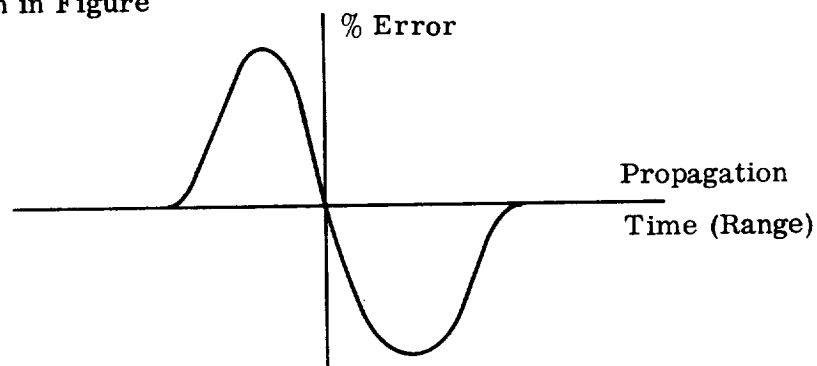
A superheterodyne receiver is apropos beginning with an orthomode balanced mixer which receives the echo signal and the L0 generated signal to be heterodyned. The 30 mc intermediate frequency is then amplified and processed to the second detector.

Range Tracking Loop*

The tracking loop is essentially a servo system which derives an error signal from a time discriminator and compares the signal output from the two range gates. The error signal is used to position the two range gates so that the returned signal is divided equally between each gate which causes the output of the discriminator to be nulled.

The basic physical principle of range tracking technique is one wherein the video signal to be tracked is divided into an early part and late part. The energies in these parts are compared in a differential circuit to develop a voltage proportional to range position error. The dividing line of the video signal is the center of a locally generated reference signal or gate.

Two basic variations of this method are in use. Since the theoretical difference between the methods can be shown to be zero, the "split gate" type will be utilized herein. The pulse energy falling in one gate is subtracted from that in the other to form an error signal. The time discriminator characteristic produced is as shown in Figure



Time Discriminator Curve

*Principles of Guided Missile Design Guidance by Locke, Sect. 10-31.

The split range gate is, therefore, positioned by supplying the output of the time discriminator to the range gate generator to alter the time delay after the transmitter pulse, and therefore the echo time position of the gate. Since the tracking loop is a servo, the stability of the tracking loop is accomplished through normal feedback criteria, the characteristic of the time discriminator curve at the axis crossing and the deceleration of the capsule.

Signal Acquisition

Detection and lock-on of the signal by the tracking loop will be accomplished when the capsule passes through a fixed range gate at approximately 200,000 feet. A fixed time delay circuit positions the split gate at 200,000 feet delay time. When the capsule passes through 200,000 feet, the signal will appear in the early gate first and an error signal will appear at the discriminator. Upon a predetermined threshold being reached, the fixed time delay circuit unlocks and tracking of the signal begins.

Range Computer

The range computer inputs are the two range spikes (transmitted and echo). The computer converts the time delay between them to an analog voltage with a suitable scale factor.

2.11.6 Detailed System Instrumentation

A functional diagram and description of the pulsed radar altimeter has been given in a preceding section.

Antenna

Under normal conditions, the antenna utilized would be a 12-inch paraboloid with feed at the focal point supported by three wires from the circumference of the dish. With the extreme environment conditions anticipated for entry into the Venusian atmosphere, it may be necessary to utilize a linear planar array of equivalent gain mounted to a supporting honeycomb platform for extreme rigidity and strength.

Some advantages would accrue from this configuration by allowing a shallower construction (more useable volume within the capsule), plus a single package altimeter. The transmitter and receiver portion could be mounted directly to the back of the platform minimizing waveguide runs (lower losses) and higher packaging efficiency.

Transmitter

The transmitter will emit X-Band Microwave power. The power will be transmitted in 5 μ seconds 50-watt peak power pulses. The pulse-repetition frequency will be 500 pps.

The main power tube will be a magnetron. A relatively short warmup time can be anticipated so long as the tube chosen is used at a low average power dissipation and the total "on" time is kept short.

Receiver

The received signals will be fed to the orthomode balanced mixer through the duplexer. Local oscillator power is obtained from the reflex klystron via a directional coupler. An AFC control loop is utilized as otherwise explained to maintain the receiver pass band 30 mc displaced from the magnetron frequency.

TR tube protection may be required if the ejection of the heat shield after entry into the Venusian atmosphere could cause strong signal return from the heat shield or in the event of premature turn on of the altimeter prior to the ejection of the heat shield.

An X-band orthomode mixer can be used which has an advantageous form factor and is light-weight. Silicon mixer crystals such as IN23 are available to achieve a low noise figure.

The signal from the mixer is fed directly to the 30 mc amplifier for amplification and gating. The bandpass is 315 kc.

An AGC will probably be required and will need approximately 30 db of dynamic range over the range increment of 200,000 feet down to a few thousand feet.

The range gating will be controlled by the range tracking circuits.

Range Tracking Loop

The split gate tracking technique utilizes time delay circuits, integrators and a differencing amplifier. The outputs of the tracking loop are two voltage spikes, the time displacement of which is proportional to range. These spikes are processed to the range computer. The time delay between the spikes varies from 406 microseconds at 200,000 feet to 6 microseconds at 3,000 feet where the signal will be lost due to receiver recovery time.

A velocity memory feedback circuit can be used to aid in altitude data smoothing. This technique will aid the tracking process during periods of signal fading. Appropriate forward damping can be added to the double integrators as instrumentation for this technique.

Range Computer

The range computer accepts the two range spikes and converts the time delay between them to an analog voltage with a suitable scale factor for later conversion to digital output.

Each of the spikes is fed to a separate bistable multivibrator and the outputs appear as two square waves. A cross coupling network can adjust the phase so that they both start in the same condition.

The two square wave trains are then phase detected in a doubly balanced phase detector. The high frequencies are filtered out, and the resulting DC voltage is fed to an inverting amplifier. When the waves are in phase (echo time equal to zero) the output is maximum, and for the waves 180° out of phase (echo time maximum) the output of the detector is zero. The inverting amplifier with suitable scale factor circuits will provide the requisite output.

2.11.7 Calculations

1-Wavelength

$$\lambda = c/f \text{ where } c = 984 \times 10^6 \text{ ft/sec}$$
$$f = 10 \text{ kmc/sec}$$

$$= \frac{984 \times 10^6}{10^{10}}$$

$$\lambda = 0.0984 \text{ ft}$$

2-Antenna Area

$$A = \frac{\pi D^2}{4} \text{ where } D = \text{antenna diameter in feet}$$

$$= \frac{\pi \times (1)^2}{4}$$

$$A = 0.785 \text{ ft}^2$$

3-Antenna Aperture

$$A_r = A \times b \text{ where } b = \text{illumination efficiency} = 0.6$$

$$= 0.785 \times 0.6$$

$$A_r = 0.471 \text{ ft}^2$$

4-Antenna Gain

$$G_o = \frac{4 \pi A_r}{\lambda^2}$$

$$= \frac{4 \pi \times 0.471}{(0.0984)^2}$$

$$G_o = 611$$

5-Beamwidth

$$\theta = \frac{7 \times 10^4}{f \times D} \quad \text{where } f = \text{frequency in mc} \\ D = \text{diameter in ft}$$

$$= \frac{7 \times 10^4}{10^4 \times 1}$$

$$\theta = 7^\circ$$

6-Doppler Shift

$$f_d = \frac{2V}{c} \times f_t \quad \text{where } f_t = \text{transmitted frequency} \\ v = \text{vehicle velocity}$$

$$= \frac{2 \times 720}{984 \times 10^6} \times 10^{10} = 720 \text{ ft/sec @ } 200,000 \text{ ft}$$

$$f_d = 14.6 \text{ KC/sec}$$

7-Pulse Repetition Frequency

for a $t_g = 200,000 \text{ ft}$. let $T = 220,000 \text{ ft}$

$$T = \frac{220,000 \text{ ft}}{492 \text{ ft}/\mu\text{sec}}$$

$$T = 447 \mu\text{sec}$$

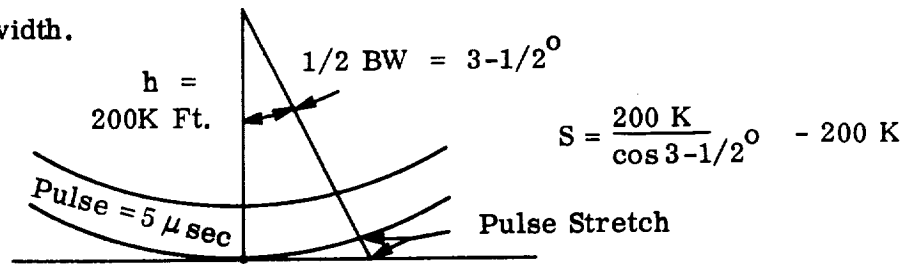
$$\text{PRF} = \frac{1}{T} = \frac{1}{447 \times 10^{-6}} = 2240 \text{ pps Maximum allowable}$$

To reduce the average power requirements but allow a reasonable integration of pulses for signal detection use

$$\text{PRF} = 500 \text{ pps}$$

8-Range Gate Width

The gate width is dependent upon the width of the returned pulse. It is necessary therefore, to calculate the pulse stretching considering pulse length, range and beamwidth.



$$\therefore \text{Stretch} = \frac{381}{492} = 0.775 \mu \text{sec}$$

\therefore the gate width of $6 \mu \text{sec}$ is regarded as a reasonable value for the total gate.

Therefore, $\Delta t_g = 6.0 \mu \text{sec}$ total gate

$$\frac{\Delta t_g}{2} = 3.0 \mu \text{sec} \text{ for each gate}$$

The integrators will be gated each with a $3.0 \mu \text{sec}$ pulse. The time constant of the integrators for build up from 10 to 90 per cent of the value of the voltage pulse is

$$\tau_r = 3.0 \mu \text{sec}$$

Once the input signal is stored in the integrators the time constant changes.

$$\tau_s \gg \tau_r$$

9-Bandwidth of the overall split gate combination for less than five per cent overshoot.

$$\text{BW} = \frac{0.35}{3.0 \times 10^{-6}} = 1.17 \times 10^5 \text{ cps}$$

10- 1-f Bandwidth

$$BW_{IF} = \frac{a}{\tau} \quad \text{where } a = 1.5$$

$\tau = \text{pulse width in sec} = 5 \times 10^{-6}$

$$= \frac{1.5}{5 \times 10^{-6}}$$

$$BW_{IF} = 300 \text{ kc/sec}$$

After allowing for doppler shift

$$BW_{IF} = 300 + 15 = 315 \text{ kc/sec}$$

11-Equivalent Noise Temperature

$$T_{EQ} = \frac{(NF-1) T_r + T_a}{NF} \quad \text{where } NF = \text{receiver noise figure} = 10$$

$$T_r = \text{receive temp} = 290^\circ \text{K}$$

$$T_a = \text{temp antenna secs} = 650^\circ \text{K}$$

$$T_{EQ} = 326^\circ \text{K}$$

12-Noise Power in the Receiver

$$P_n = K \alpha T_{EQ} \times BW_{IF} \times NF \quad \text{where } K = 1.38 \times 10^{-23} \text{ Joules/degree Kelvin}$$

$$= 1.38 \times 10^{-23} \alpha 326 \times 3/5 \times 10^3 \times 10$$

$$P_n = 1.42 \times 10^{-14} \text{ watts}$$

13-Transmitter Power

$$P_T = \frac{S/N \times 16 \times \pi^2 \times r^2 \times P_n \times L}{\lambda^2 \times \sigma_o \times G_o \times W} \times \frac{dr'}{dr} \quad \text{(see section on System Performance)}$$

Assume S/N of 100 \approx 20 db

$$r = 200,000 \text{ ft}$$

$$P_n = 1.42 \times 10^{-14} \text{ watts}$$

$$\lambda = 0.0984 \text{ ft}$$

$$\sigma_o = 0.1$$

$$G_o = 611$$

$$W = 0.6$$

$$L = 2$$

$$\frac{dr'}{dr} = 1$$

$$P_T = \frac{100 \times 16 \times \pi^2 \times (2)^2 \times 10^{10} \times 1.42 \times 10^{-14} \times 2}{(0.0984)^2 \times 0.1 \times 611 \times 0.6} \times \frac{1}{1}$$

$$P_T = 50.6 \text{ watts}$$

14-Average Power

$$\begin{aligned} P_{AVG} &= P_T \times dr \\ &= 50.6 \times \frac{5}{2000} \end{aligned}$$

$$P_{AVG} = 0.126 \text{ watts}$$

15-Video S/N

The video signal to noise is enhanced by an effective narrowing of the receiver bandwidth by the bandwidth of the receiver after the second detector. The overall bandwidth of the receiver is not the video or integrator bandwidth, but an effective bandwidth that takes into consideration the i-f bandwidth, video bandwidth, the effects of video compression and cross beats between receiver and video noise. It is expressed as the bandwidth that would pass an equivalent noise power in the integrator.

$$B_{eff} = \sqrt{2B_{i-f} B_V - B_V^2}$$

where B_{i-f} = i-f bandwidth = 315 kc/sec
 B_V = video bandwidth or integrator bandwidth = 117 kc/sec

$$B_{eff} = \sqrt{2 \times 315 \text{ kc} \times 117 \text{ kc} - (117 \text{ kc})^2}$$

$$= \sqrt{737 \times 10^{10} - 1.37 \times 10^{10}}$$

$$= \sqrt{6 \times 10^5}$$

$$B_{eff} = 2.45 \times 10^5 \text{ cps}$$

$$S/N \text{ Video} = i-f \text{ S/N} \times \frac{BW_{i-f}}{BW_V}$$

$$= 100 \times \frac{315}{245}$$

$$S/N_{(video)} = 128 = 21.1 \text{ db}$$

16-Lock-on S/N

It is desired to have the system unlock as soon as the first half of the split gate is filled with signal, therefore, 3 db loss can be expected. This results in $S/N = 18.1 \text{ db}$.

This figure can be used to predict signal detection probability.

17-Pulses in the Gate

The number of pulses N that the system will see as the capsule flies through the range gate is equivalent to the time for the pulse to go through the early range gate.

The range gate is $3.0 \mu \text{ sec}$ long or 1476 feet long.

The time for the capsule to fly through this gate at 720 fps is:

$$t = \frac{1476 \text{ ft}}{720 \text{ ft/sec}} = 2.05 \text{ seconds}$$

Since the gate is essentially stretched because of the time duration of the video pulse:

$$T = 2t = 4.10 \text{ seconds}$$

The number of pulses (N) seen is then:

$$N = T \times \text{prf}$$

$$= 4.10 \times 500$$

$$N = 2040 \text{ pulses}$$

18-Noise Samples

The number of noise samples seen is based on the number of times the receiver is turned on from hard entry into the Venusian atmosphere, i.e., g switch turn-on of the altimeter prior to 200,000 feet and is equal to the number of times the receiver is gated on with no signals present.

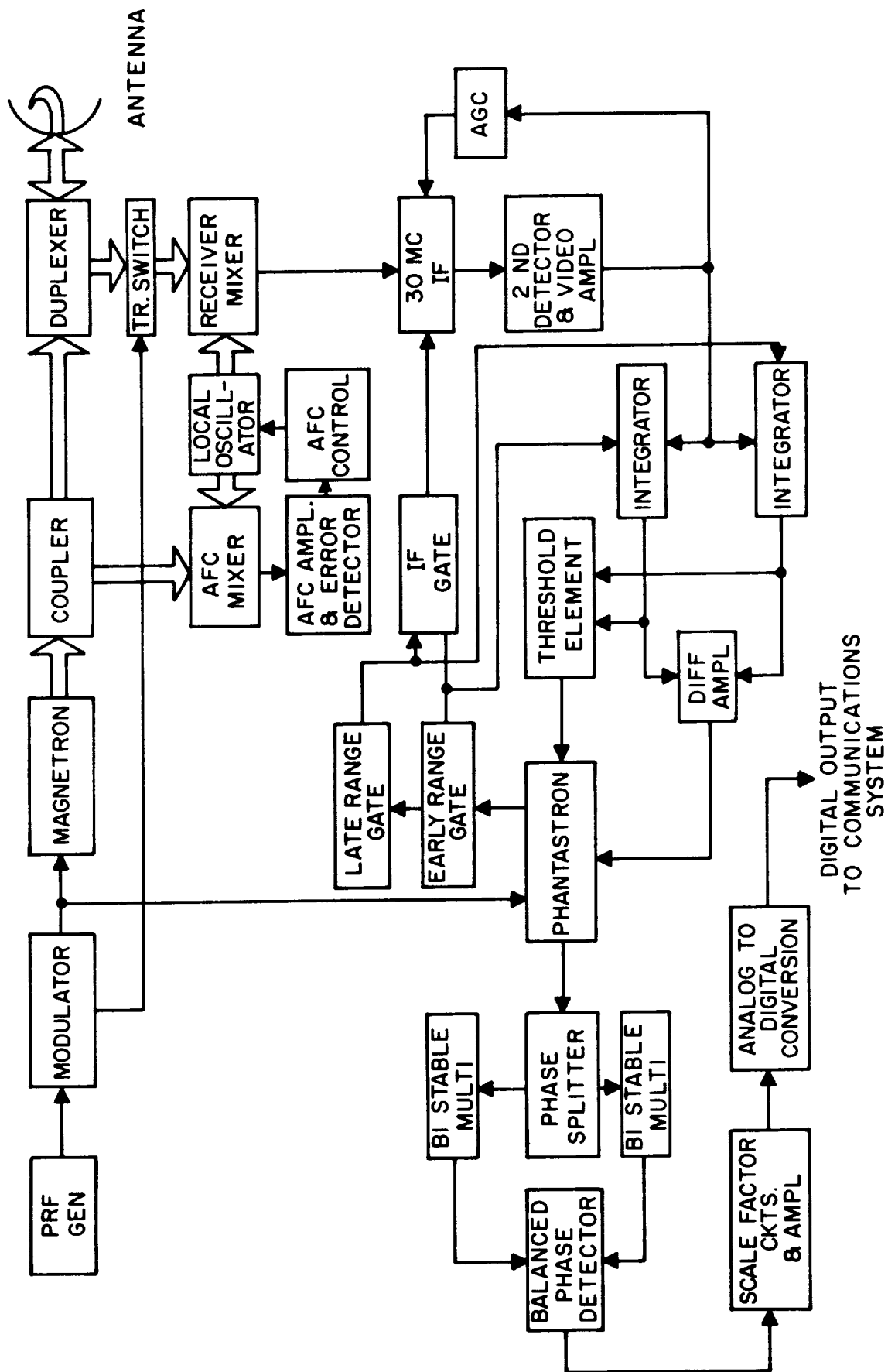


Figure 2.11.1. Radar Altimeter Functional Diagram

2.12 CLOUD DETECTION

One of the phenomena frequently noted in the atmosphere of Venus is the presence of clouds which obscure observation of the planet's surface. The altitude (or altitudes, since it is not known whether they remain at a constant height) of the cloud level is unknown and many phenomena which have been determined at heights above the clouds are hence not fixed in terms of absolute altitude. For this reason, it is of utmost interest to determine the time (that is, altitude) at which the capsule may enter and leave clouds.

In addition, if for power or weight reasons, it does not become practical to have a radar altimeter aboard the capsule, the time at which clouds occur as related to the time of impact, when coupled with velocity measurements would serve to determine the approximate height of the cloud layer.

For these reasons, it is of interest to determine the time at which the capsule enters and/or leaves clouds. The easiest way to accomplish this is to utilize a light source coupled with a simple detector, so arranged that clouds would tend to block the light. The wavelength region that would be selected would be at the red end of the visible spectrum, a region where molecular scattering is at a minimum and where no molecular band absorption is expected.

Two ultimate geometric arrangements could be considered: one would utilize a light source extending out from the vehicle on a boom with the detector looking through a window in the capsule skin. The second arrangement would locate both light source and detector within the capsule and permit the clouds to pass by.

No definite information as to the nature of the clouds on Venus is available. There is a strong suspicion that they may be water vapor clouds, even though there is no evidence of water in the atmosphere of Venus. A second possibility is that one is dealing with dust clouds. A third possibility which attributes the clouds to solid carbon dioxide particles appears inconsistent with the temperatures expected in this altitude regime. (It should be noted that the pressure altitude at which clouds are observed lies somewhere between 20mB and 100mB, the

absolute altitude to which this corresponds is a function of the atmosphere assumed). It would be possible to recognize water vapor clouds by passing them over a screen covered with a material which becomes conducting in the presence of moisture.

It should, of course, be emphasized that there is no assurance that the capsule will at any time pass through a cloud layer.

2.13 HYPersonic REGIME MEASUREMENTS

Measurements during the hypersonic portion of the flight have been considered for two specific objectives. First of all, there is always the possibility of failure prior to attaining subsonic velocities and hence, information obtained during the hypersonic regime would be the only type that was available and might serve to give some indication of the cause of mission failure. Secondly, actual measurements during the hypersonic portion of re-entry will serve to obtain more accurate value for critical capsule design parameters. This, in turn, will permit optimizing the design of subsequent capsules and utilize the weight savings for increased instrumentation or other useful purposes.

In the design of the entry capsule the critical parameters are the heating rates and deceleration as a function of time. This, in turn, results in a given amount and rate of ablation as well as structural loading and stresses of capsule components. In considering possible capsule failure, one finds that it is most likely to occur at times close to those of peak deceleration and/or peak heating rates. Unfortunately, when you examine the problem of transmitting any measurements of these two parameters, one finds that the communication system is blacked out from early entry (above 150 km) down to shortly after deceleration when heating rates have become significant. (Blackout is expected to end at about 70 Km for a vehicle with ballistic coefficient of 60, on a $\gamma = -30^\circ$ trajectory, for an extreme I atmosphere). For this reason, thought was given to significant measurements that could be obtained prior to blackout but unfortunately, it appears that such parameters as deceleration and heat rates have not yet attained significant values at that time. The only possible experiment that might aid in capsule failure analysis would be a check on transmitter failure accomplished by monitoring the time difference between blackout at two different frequencies. (For details see section on Communications).

Since it did not appear practical to make measurements prior to blackout, emphasis was shifted to making measurements during blackout, storing the data and retransmitting the information after blackout has ceased. One strong

implication from this is that it is imperative that the capsule and communication system survive through the peak heating and peak g periods and this implies a conservative design for the first capsule.

The most important information that can be obtained during the hypersonic entry is the determination of the g loading encountered and of the amount of material ablated. A slightly more sophisticated instrumentation system could be used to indicate time of occurrence of specific deceleration forces and specific amounts of heat shield ablated. The minimum hypersonic instrumentation system would consist of an accelerometer along the velocity vector axis of the vehicle. A preferable arrangement would include two more accelerometers on two axes perpendicular to the previously indicated one. These accelerometers would be set to indicate if certain values of g had been exceeded. As an example, the accelerometer along the velocity axes could be set to indicate the maximum g on a scale of 50, 100, 200, 300, 400, 500, 600, 700, 800, 900, 1000 g with the ultimate voltage output serving to indicate which of these steps had been exceeded. Similar devices extending to lower maximum deceleration would be utilized on the other two axes. In the more sophisticated instrumentation system the time at which each of these g values had been exceeded would be recorded.

Similarly, a series of make/break ablation sensors would indicate the depth of material ablated and this could be carried out for about five depths at one point some distance removed from this location. Again, if desired, the time of these events could also be recorded.

The recording device could be exceedingly simple, the signal simply being stored in a series of gates or capacitors. This information would be transmitted at a suitable time after end of blackout as determined by a delayed circuit in conjunction with the g switch.

The accelerometer required for these measurements is well known and have been tested on ballistic missile re-entry. The ablation sensors were developed during the course of nose cone design, and are explained at the end of this section.

Other possible measurements such as heat transfer, shield temperature flight dynamics were considered but the only one that appears to be pertinent for the purposes of interest here might be the measurement of peak temperature reached at the location of a particularly sensitive device.

Ablation Sensors

The use of ablation heat shields brought about the need to measure the loss of material from the re-entry vehicle's heat shield. A number of approaches to the problem were considered, including radio-active and ultra-sonic systems, capacitive and inductive sensors, pneumatic and mechanical, as well as resistive "break-wire" techniques. The resistive or "break-wire" approach was chosen for development as being the simplest and most straightforward approach. The large number of measurements required to define the surface as a function of time made it necessary to develop small sensors that could be located close together. The radio-active sensor would have required a means of installation just prior to flight. Each of the other techniques had similar short-comings, and the major design effort was applied to the "break-wire" approach.

In theory, such an ablation sensor is an extremely simple device, consisting of fine wires embedded in the plastic shield. Loss of the shield material exposes the wires to the hot gases. The resultant melting or breaking causes a step change in resistance in the associated network.

The major problems encountered in reducing this "simple" device to a practical sensor included:

- a. Development of manufacturing methods
- b. Development of installation techniques
- c. Development of suitable circuitry

Since approximately twenty sensors are required for each re-entry vehicle, it was necessary to develop a method of manufacture that would permit the sensors to be produced in quantity and with repeatable accuracy of the location of the breaks. With this in mind, effort was concentrated on the development of a

sensor using printed circuits to locate the break wires. The sensor consists of two cylindrical sections (Figure 2.13.1). The forward section, which contains the break portions of the circuit, is made of blocks of material as similar as possible to the heat shield. These blocks are glued together, turned, and glued into the heat shield. The ablation rate at the detector's surface is then identical to that of the shield. The rear section projects into the missile inner compartment when installed, and contains the resistor network to which the break points are connected. Each sensor is therefore a complete unit, and requires only power to be applied.

The development of suitable installation techniques was a problem with serious ramifications. If the presence of an ablation detector caused a part of the heat shield to be less resistant than the main body, the hot gases could erode more deeply at these points, either giving inaccurate data or possibly destroying the entire re-entry vehicle. Models tested in rocket exhaust actually were destroyed in such a manner. Conversely, if the presence of the detector caused a part of the shield to be extra resistant, the data would again be inaccurate and the aerodynamic characteristics of the vehicle might be affected.

Matching the characteristics of the shield and sensor require that the material used in the body of the sensor match that of the shield and that the glue joints were not a point of weakness. The first requirement was met by very close control of the materials used, requiring that they be obtained from the same source and to the same specifications and heat treatment as the shield. Various techniques were tested to determine that the glue joint strength was adequate. Plugs of various diameters and with varying clearances were glued into test models and burned in a rocket exhaust. It was generally found that the plug diameter was not critical, and that clearances of up to 0.010 inch were acceptable. However, the type of glue and cure used varied with the shield material. A wide variety of combinations were tried as the program progressed, and various materials were considered for use as a shield.

On the surface, the problem of designing the detector is a simple one. There is a serious complication, however, in that the ablative type materials employed to date char in advance of the ablating surface, and this char is electrically conductive. Thus, after a wire loop is broken open, it may again be "closed" by this char, thereby affecting the indicated depth. The obvious solutions are to make the impedance loads within the sensor low in comparison to the char resistance, and to increase the char resistance by adding insulation on either side of the printed circuit. Due to battery power limitations, there is a minimum resistance which can be employed and extreme care must be used in the selection of the insulating board material to prevent preferential ablation. In one case, quartz was selected for its good high-temperature insulation. In a rocket test of this combination, the ablation at the sensor location was greater than the main body by a factor of three. It is thought that heat radiated down the quartz insert weakened the glue bond and led to the undesirable results obtained.

It has also been proposed that the char be used to complete the circuit. For some materials, this method works well, but for most of the ablating materials, the char is very weak, and is sheared off by the gas flow resulting in inconsistent or varying resistance levels and an indeterminant output. Although, as shown in Figure 2.13.2, satisfactory results have been obtained in comparing flight data with measurement of material erosion made on shields of recovered vehicles, attempts to develop better sensors were continued.

Several alternate types of circuits other than the all resistor circuit have been considered. In one circuit, diodes are used instead of resistors, so that the effect of the char leakage resistance in altering the voltage output is reduced by the diode Zener action. A second variation consists of using transistor switching circuits which function as soon as the resistance across the break point increases to a predetermined level. Some other circuits were also tested, with varying degrees of success.

The best results were obtained with the circuit shown in Figure 2.13.3. In this circuit, the approach of the char layer forms a conductive path across the printed circuit from A to B. This current flow changes the bias on the

transistor and permits a current flow which is limited by the resistor R_3 , thus developing a known voltage across R_4 . As the surface recedes, the point B will be broken. Breakage of point B will attempt to further change the transistor bias in the same way that leakage from B to A did, and the transistor will continue to conduct at a current limited by R_3 . If the surface char flakes off or is otherwise removed, the resistance across the open points of B will maintain the transistor bias such that it will conduct at the current limit set by R_3 .

In the event that the surface recedes without forming a layer of char, the breakage of B as the surface reaches the level of the break will cause the necessary transistor switching action and the step change in output. Further recession of the surface is noted by the breaking of B or the charring from A to B of succeeding circuits.

Two phenomena overlap in their action. Initially, the voltage output is zero since the resistance across B is zero, giving zero output, and the resistance from A to B decreases or B breaks with an increase in resistance, the output will increase to a value limited by the current through R_3 . Since A and B are physically located very closely together, the char resistance across B or from A to B will be nearly equal. In this event, no matter what the resistance is, the output will depend only on the current flow through R_3 which is unaffected by such a change of resistance.

An ablation damage detector containing a circuit such as that shown in Figure 2.13.3 was subjected to a rocket exhaust to simulate re-entry conditions and the test results indicated that the voltage predicted by pre-test calibration was realized for each voltage step and that the breaks were clearly defined. Similar good results were obtained from sensors installed and flown in the RVX-2 series of re-entry vehicles.

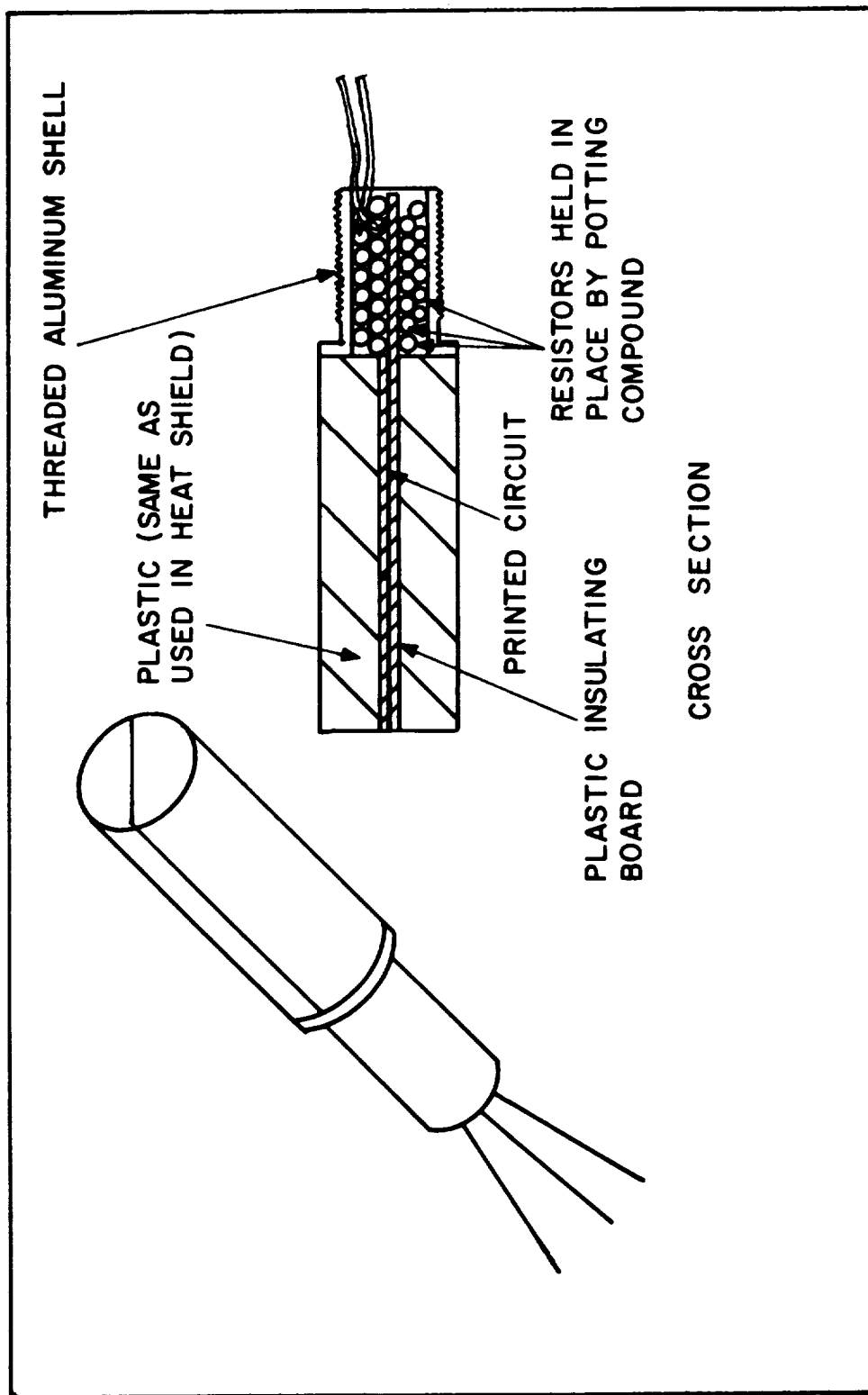


Figure 2.13.1. Ablation Sensor

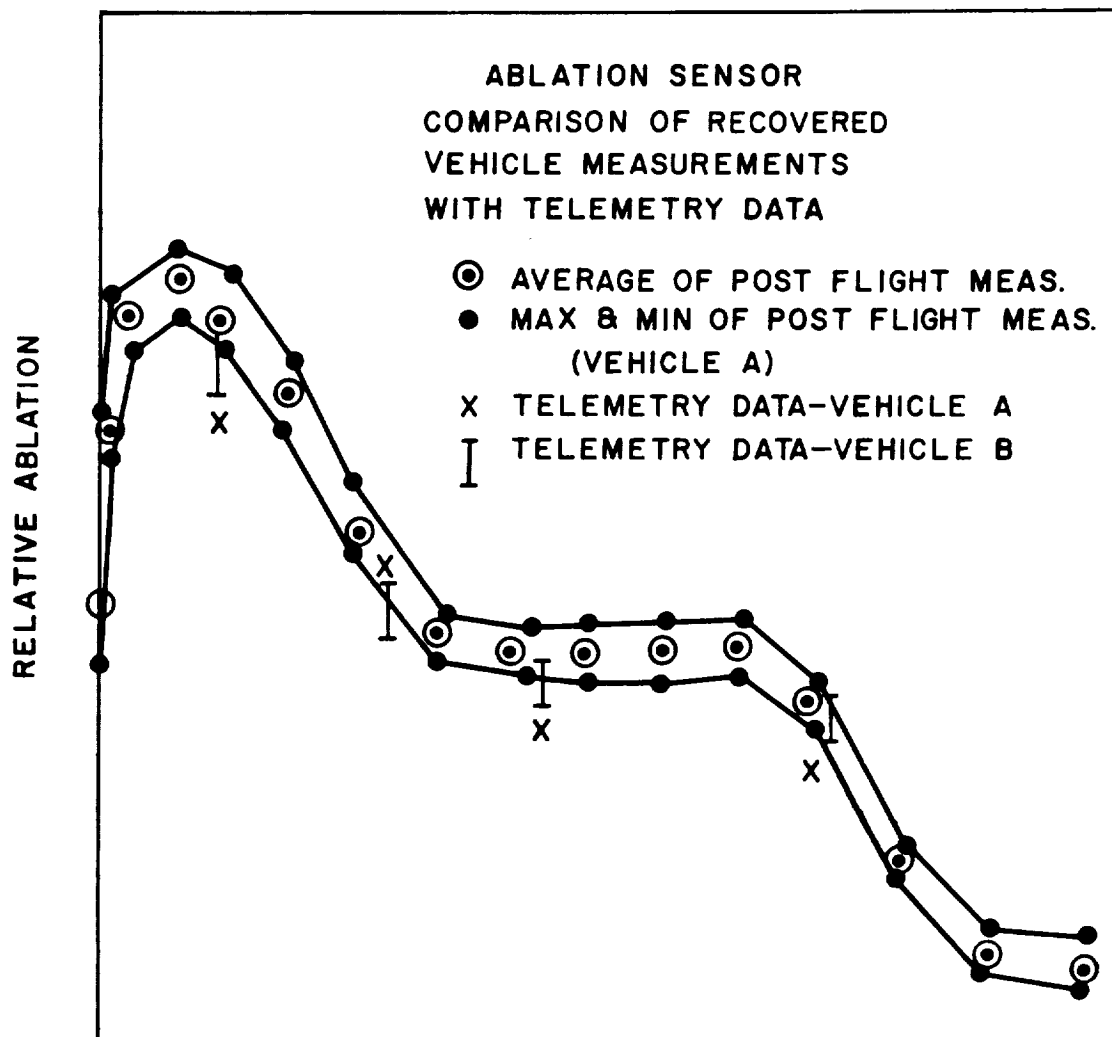


Figure 2.13.2. Axial Distance

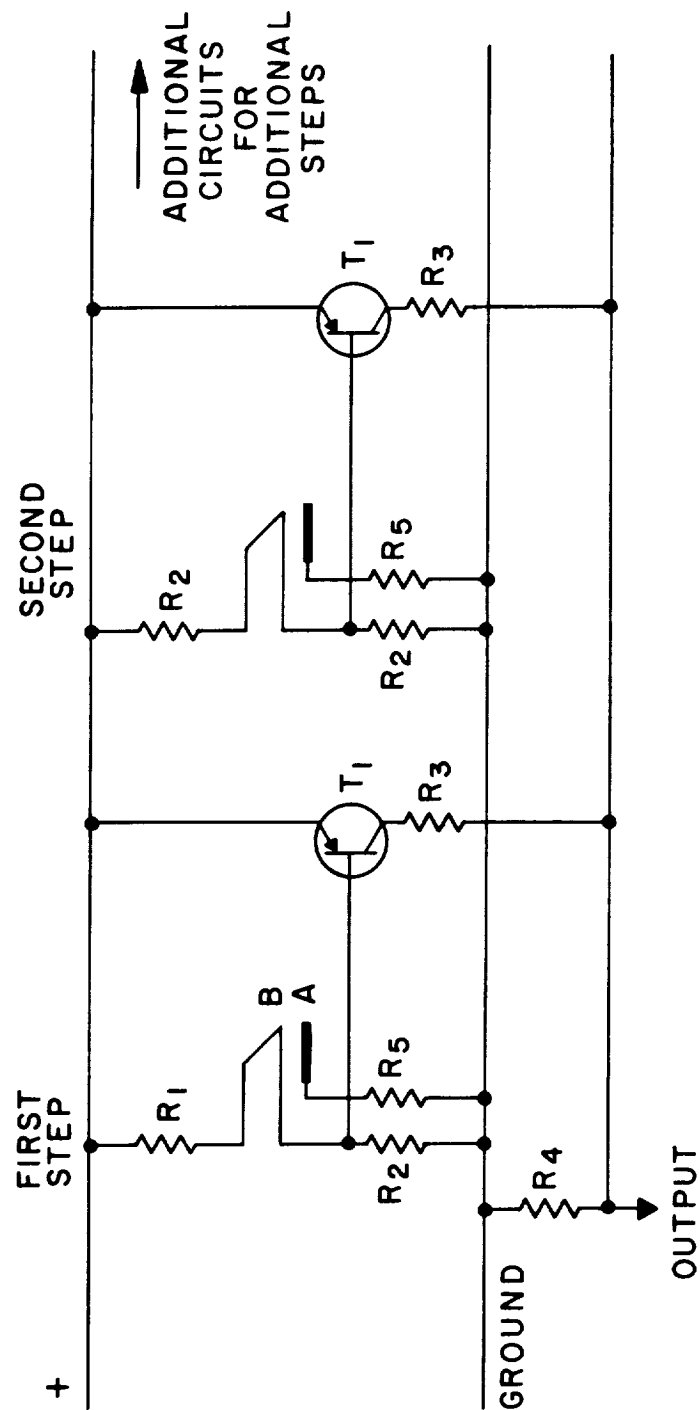


Figure 2.13.3. Ablation Detector Circuit

3.0 COMMUNICATIONS

3.1 SUMMARY OF RESULTS

3.1.1 Introduction

This section contains analyses and discussions of the problem areas and trade-offs occurring in the capsule telemetry system. Both a relay link to the Mariner spacecraft and a direct link to a DSIF ground station have been considered.

3.1.2 Comparison of System Capabilities

The communication system calculations have been based on the nominal parameters tabulated in Sections 3.1.3 and 3.1.4. Although these particular values are not unreasonable, they should not be taken as a precise definition of the communication problem, but merely as a point to permit a comparative analysis between systems. If a certain amount of caution is exercised, excursions can be made from these nominal parameters by using the conversion factors of Section 3.2.

The data rate has been taken as a variable in the analyses. The typical instrumentation system presented in Section 2 of this report requires a rate of eight bits/sec.

Data rates in the vicinity of 25 bits/sec or more appear feasible on the relay link with a 25-watt transmitter, using any one of several modulation techniques, as shown in Figure 3.1-1.

For the direct link, the carrier-tracking power alone (with an 85-foot paraboloid) requires about 33 watts of transmitter output power. Using a 50-watt transmitter, a PCM/PS system offers a communication capacity of about six bits/sec, while a PCM/PS/PM system offers about two bits/sec, as shown in Figure 3.1-2.

In a broad analysis of this type, numerical results such as the above are more valid on a comparative basis than on a definite basis. Time did not permit the optimization of all parameters nor the precise evaluation of gain and

attenuation estimates. Before starting the system design, a rigorous analysis of the selected system must be made. By that time the mission parameters should also be better defined.

The broad analyses showed further that a non-coherent relay link, using PPM/AM or PCM/FM, does not appear feasible unless the frequency uncertainty region (due primarily to doppler effect and long-term oscillator instability) can be made very small.

Periodic checkouts of the transmission equipment during the transit time between capsule separation and entry appear possible by using a small solar cell-battery power supply system. If adequate power is available in the spacecraft, it would be better to operate the spacecraft receiver continuously and to program only the capsule transmitter on for a period of perhaps 1-2 minutes every other day. This would avoid the long power-consuming transmitting periods which timing inaccuracies would require if the receiver were also programmed.

The requirement for isotropic antenna pattern coverage for this checkout function will be determined by the maximum rate of capsule tumble and the acquisition time of the receiver. Tumbling rates as high as six rpm might be permissible without losing lock.

It might also be desirable to check out the capsule transmitter prior to separation from the spacecraft. It does not seem necessary nor desirable to do this more than once. Such a check might range from a simple monitoring of the DC voltage test points (requiring an umbilical connection) to actually taking a calibrated RF wattmeter reading near the capsule antenna. If the latter is done, extreme care must be taken in the design to prevent damaging the transmitter through impedance mismatch due to the proximity of the spacecraft to the capsule antenna.

3.1.3 Nominal Relay Link Parameters

The nominal parameters used to permit comparative analyses of the modulation techniques for the relay link are listed in Table 3.1.1.

TABLE 3.1.1

Nominal Parameters for Relay Link

- (1) Maximum transmission distance: 50,000 km
- (2) Data rate: variable. Presently estimated requirements are in the vicinity of 8-25 bits/sec.
- (3) Frequency: 100 mc
- (4) Maximum range rate: 8 km/sec
- (5) All sources of frequency uncertainty except doppler effect are assumed negligible.
- (6) Allowable acquisition time: one per cent of total communication time
- (7) Capsule antenna gain: 0 db
- (8) Spacecraft receiving antenna gain: 0 db
- (9) Receiving system noise figure: 10 db (This noise figure includes estimated galactic noise and noise contributed by Venus itself, as well as receiver noise. It should be refined before starting a specific system design.)
- (10) Margin: 8 db
- (11) Misc. RF losses: 3 db
- (12) Maximum phase-modulation index: 1.4 radians

3.1.4 Nominal Direct Link Parameters

The nominal parameters used to permit comparative analyses of the modulation techniques for the direct link are listed in Table 3.1.2.

TABLE 3.1.2

Nominal Parameters for Direct Link

- (1) Maximum transmission distance: 60×10^6 km
- (2) Data rate: variable. Presently estimated requirements are in the vicinity of 8-25 bits/sec.
- (3) Frequency: 2295 mc
- (4) DSIF ground receiving station, having 85-ft (51.8 db) and 210-ft (61 db) paraboloids and a 50° noise temperature.
- (5) Capsule oscillator stability is adequate to permit operation in a 3-cps receiver loop bandwidth.
- (6) Capsule antenna gain: 0 db
- (7) Margin: 8 db
- (8) Misc. RF losses: 3 db
- (9) Maximum phase-modulation index: 1.4 radians

3.1.5 Factors Affecting Venus Capsule Telemetry Power Requirements

The factors listed in Table 3.1.3 significantly affect the prime power requirements of the capsule telemetry transmitter.

TABLE 3.1.3

Factors Affecting Telemetry Prime Power Requirement

FACTOR		RELAY LINK	DIRECT LINK
1.	Venus miss distance (affects doppler rate and transmission distance)	X	
2.	Transmitter efficiency (depends in turn on transmission frequency and power level)	X	X
3.	Communication time (T)	X	X
4.	Data rate (includes sampling rate and encoding accuracy)	X	X
5.	Modulation technique (reliability vs. efficiency)	X	X
6.	Allowable acquisition time (T_L)	X	X
7.	Transmission frequency	X	X
8.	Antenna pattern, as dictated by encounter geometry	X	X
9.	Range to Venus at encounter		X
10.	Range rate to capsule		X
11.	Output S/N ratio or error rate required	X	X
12.	Error correction coding	X	X
13.	Capsule stabilization prior to entry.	X	X

3.1.6 Communication System Weight Considerations3.1.6.1 Method of Approach

In such a small vehicle as this capsule, the weight of the payload is of prime importance. Thus, it is mandatory to compare the systems from the point of view of available communication capacity versus the weight of the communication

equipment and its batteries. This can be determined by combining the transmitter equipment data for the relay link in Section 3.10 with the power supply weights of Section 4, producing Figure 3.1.5 from Figures 3.1.3 and 3.1.4. Then from the frequency considerations of Section 3.3 and the modulation system analyses of Section 3.5, a curve of communication capacity versus frequency can be plotted for each modulation system. This has been done for three typical systems in Figures 3.1.6, 3.1.8 and 3.1.10 (PCM/FM/PM, PCM/PS/PM, and PCM/PS, respectively). Each of these can then be combined with Figure 3.1.5 to yield the desired plot of communication capacity vs. weight. This has been done for the three systems in Figures 3.1.7, 3.1.9 and 3.1.11.

3.1.6.2 Discussion of Results

Figures 3.1.6, 3.1.8 and 3.1.10 indicate the additional transmitter power that is required to provide a given communication capacity at higher carrier frequencies. This is due to the considerations presented in Section 3.2. However, the antenna weight decreases considerably at higher frequencies, and the required increase in battery weight is rather small. Therefore, the entire variation in weight with a change in carrier frequency is only a few pounds.

If weight alone were the sole criterion, these results would indicate that 500 mc is the optimum carrier frequency for low data rate systems. However, weight alone is not an adequate criterion. Other factors which must be considered are thermal dissipation, reliability, design simplicity, availability of qualified components, past experience, etc. These considerations generally point toward the 100-mc equipment. This is particularly attractive because of the possibility of a completely solid-state transmitter. Since such a transmitter would not require any warm-up time, it could be activated by a "g" switch upon entry and perhaps eliminate the need for an accurate timer.

Therefore, on the basis of these considerations, a 100-mc solid-state transmitter appears the most attractive.

3.1.7 Signal Acquisition and Tracking

The results of the tracking and acquisition analysis indicated that for the relay link a few watts of carrier power will give quite good performance for ranges in the order of 20,000 to 30,000 km., if the carrier frequency is in the lower portion of the 100-500 mc band. This lower frequency will also place less stringent requirements on the stability of the oscillators.

The results of the direct link analysis are more difficult to evaluate, since two major problem areas require further resolution: oscillator stability and pre-detection recording. There appears to be no oscillator presently available which has been qualified to survive such an entry and still maintain adequate stability to operate in a 3-cps receiver loop bandwidth. If such an oscillator is developed, there still remains the problem of real-time acquisition by the DSIF. This might be obviated by the use of pre-detection recording, allowing the use of optimum filtering techniques for post-flight signal processing. The problems involved here require further, more specific investigation.

3.1.8 Propagation Effects

The propagation effects investigated in this study include Venus ionospheric attenuation, multipath effect, and communication during entry.

Calculations using the JPL model atmospheres showed the maximum ionospheric attenuation to be 1.35 db in the Extreme II atmosphere. The attenuation was found to be less than one db with the other atmospheric models as well as at higher frequencies. Calculations showed that the multipath problem (from the surface of Venus) for the relay link could be obviated by adequate suppression of forward gain of the capsule antenna radiation pattern.

Calculation of the entry plasma characteristics showed that radio frequency blackout will occur upon entry for the blunt capsule both at Venus and at Mars. The only possibility found for entry communication is to use a flared-cone configuration, and even then, an unseparated flow field condition would have to exist at least in the neighborhood of the antenna.

3.1.9 Frequency Considerations for Post-Entry Communication

The transmission frequency of the direct link was constrained for the purposes of the study to 2295 mc, and that of the relay link to the 100-500 mc range. Taking account of transmitting equipment capabilities, antenna size, weight and losses, noise, doppler, and free-space attenuation, it appears that for the relay link a 100-mc carrier (permitting the use of a solid-state transmitter which at present can be obtained with up to 25 watts of RF output power) would be most desirable, provided that the aft bulkhead or cover of the vehicle is large enough to contain the rather large crossed-slot antenna which is required at that frequency.

3.1.10 Error-Correction Coding

A brief study was made regarding the weight and effectiveness of a single-bit parity encoder and its corresponding decoder. It was found that for a seven-bit word, the use of such a Wagner code would reduce the required transmitter power by about 2.5 db for 10^{-3} and 10^{-4} bit-error rates.

The encoding equipment in the capsule would weigh about five pounds and draw about five watts of power. The corresponding decoding equipment on the spacecraft (for a relay link) would weigh about ten pounds and draw about ten watts of power. (Of course, these decoder requirements would not be a significant factor in the direct link.)

Since the capsule's transmitting equipment and battery power supply are quite lightweight, it appears that, for the low data rates presently anticipated, the reduction offered in transmitter power does not justify the additional weight and complexity of the error-correction equipment. However, for higher data rates requiring higher transmitter powers, the reduction in transmitter complexity (through lowering the required power output) might make error-correction coding appear attractive, even though it would not reduce the payload weight significantly.

3.1.11 Relay Equipment for the Spacecraft

In comparing the relay link to the direct link, due account must be taken of the receiving equipment required in the Mariner spacecraft. In this study this has been considered as only a secondary factor and in the binary form, "too heavy" or "not too heavy."

It was readily found that the receiving equipment did not appear to be too heavy. A typical receiver (to produce a demodulated digital output) would weigh about five pounds, require about 15 watts, and be about 4 X 4 X 7 inches in size. It could be completely solid-state with a low-noise Germanium transistor front end, and would thus have a very high reliability.

A crossed-dipole receiving antenna mounted either on the planet horizontal platform (PHP) or on the favored side of the vehicle (i.e., the side predicted to be toward Venus, based on ephemeris data of the Sun and Canopus), and having about a hemisphere of coverage appears to be satisfactory. This would weigh only about one to two pounds, including its matcher and cabling.

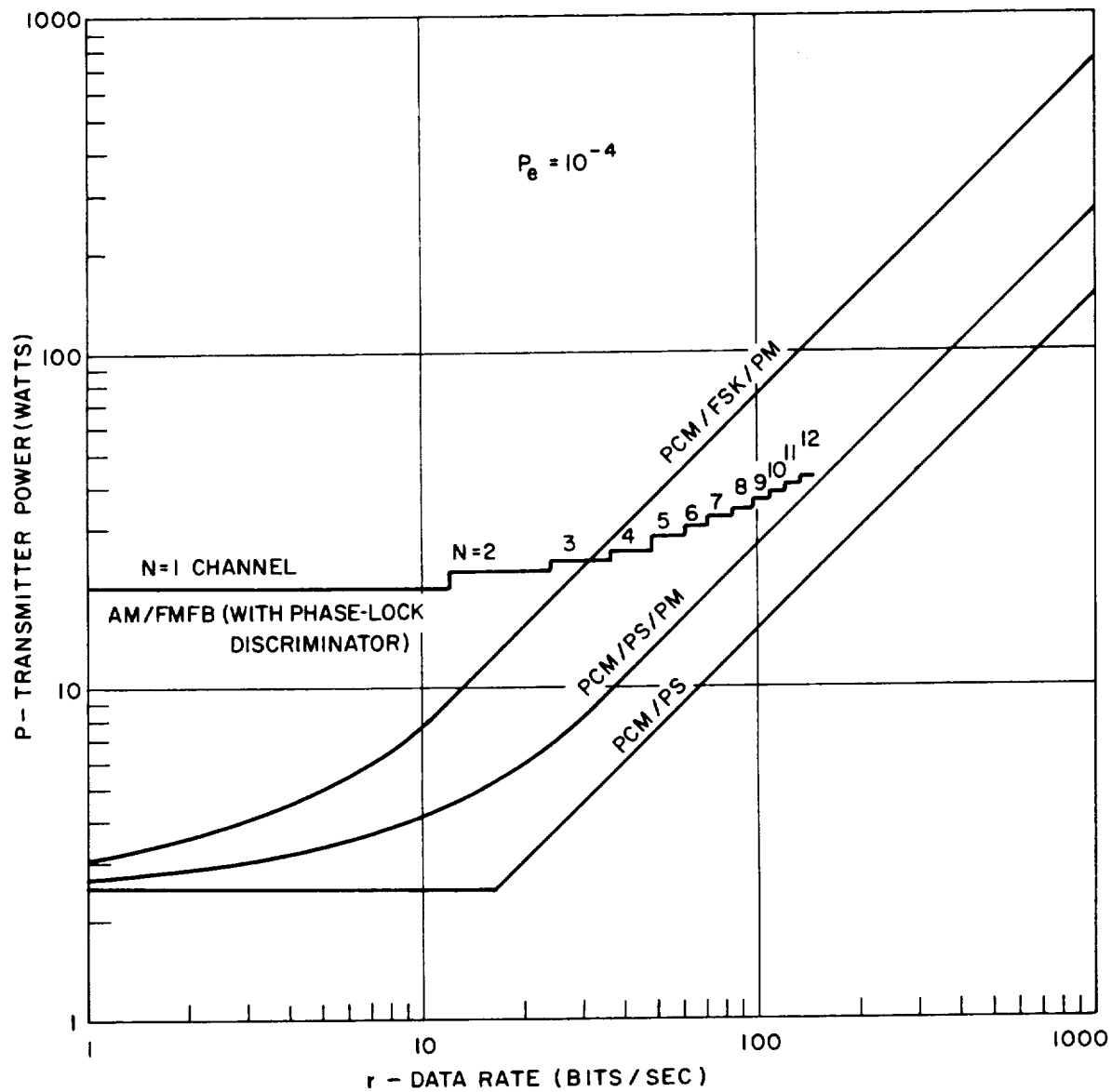


Figure 3.1.1. Transmitter Power Required for Relay Link
(For System Parameters, See Table 3.1.1)

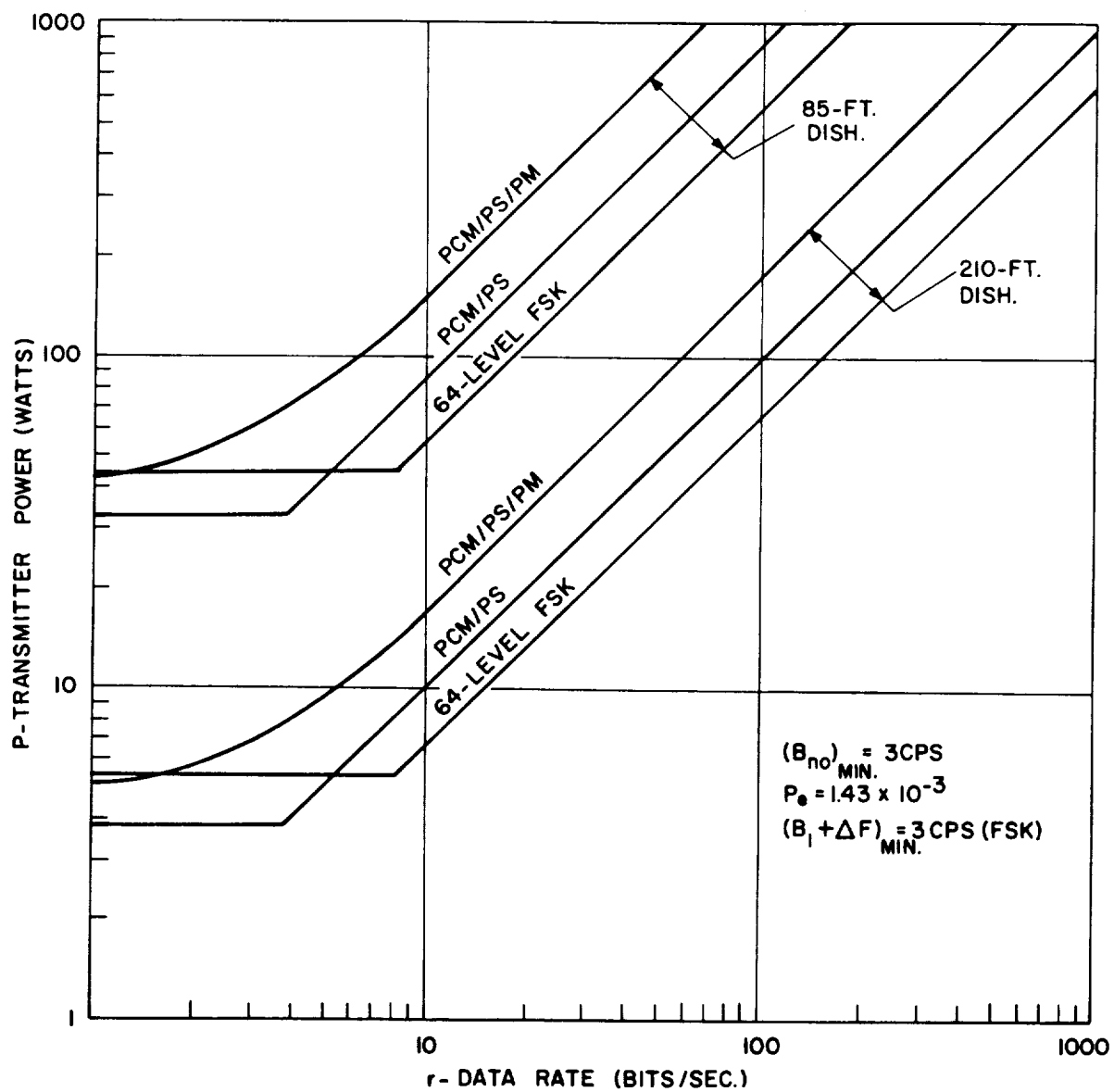


Figure 3.1.2. Transmitter Power Required for Direct Link
(For System Parameters, See Table 3.1.2)

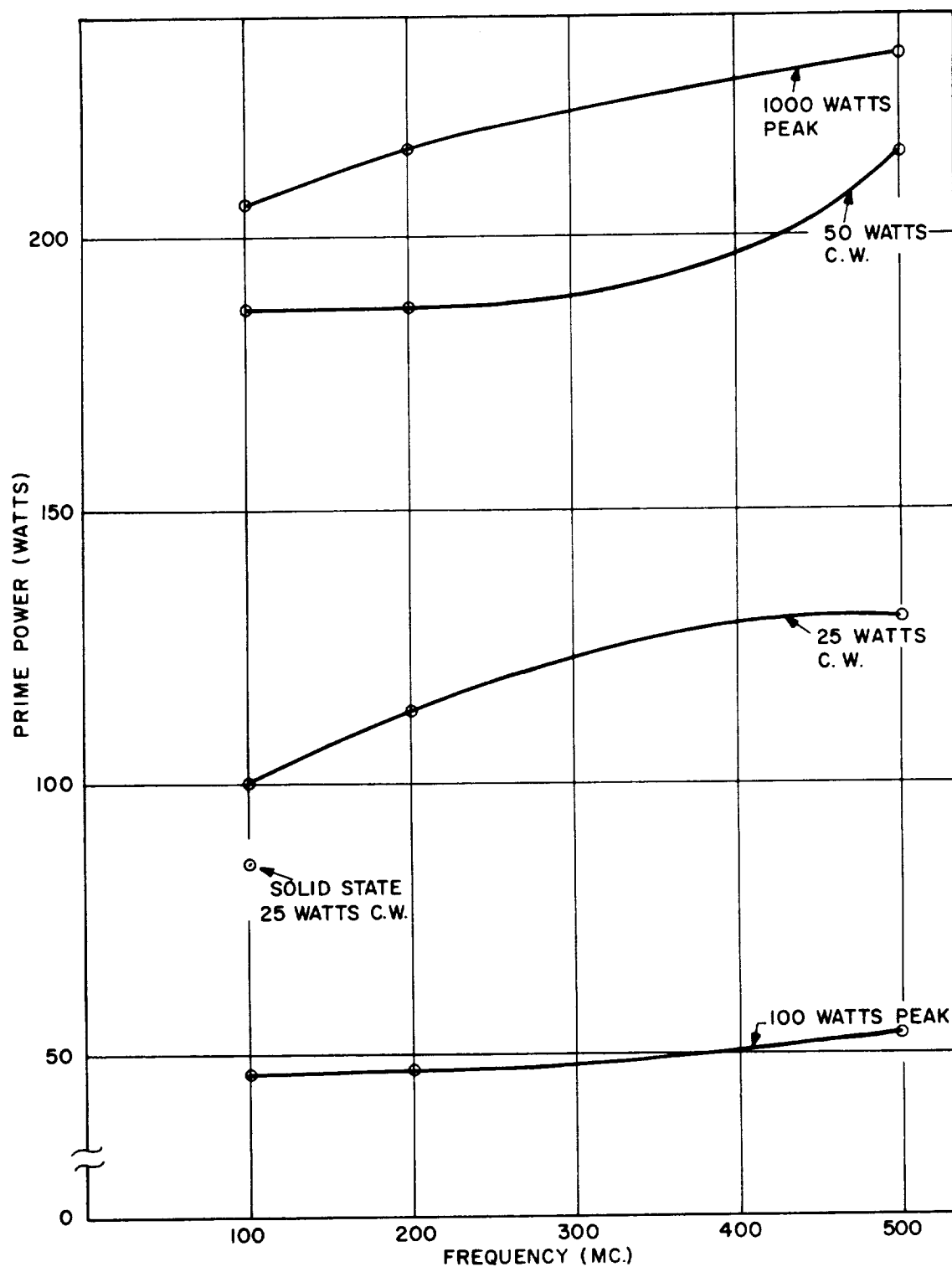


Figure 3.1.3. Prime Power (28V DC \pm 10%) Required by Communication System for Several RF Output Powers

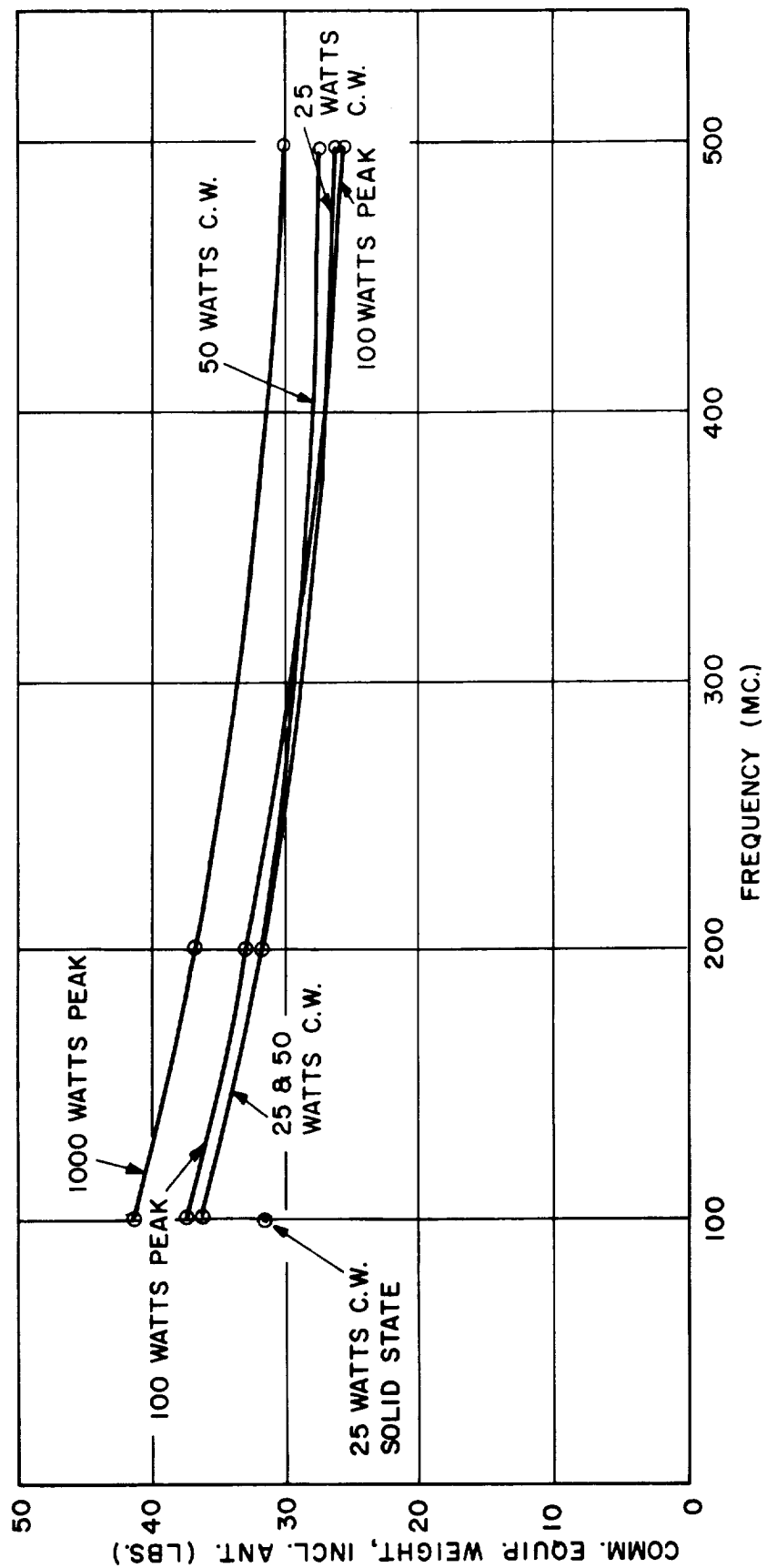


Figure 3.1.4. Weight of Communication Equipment vs. Frequency

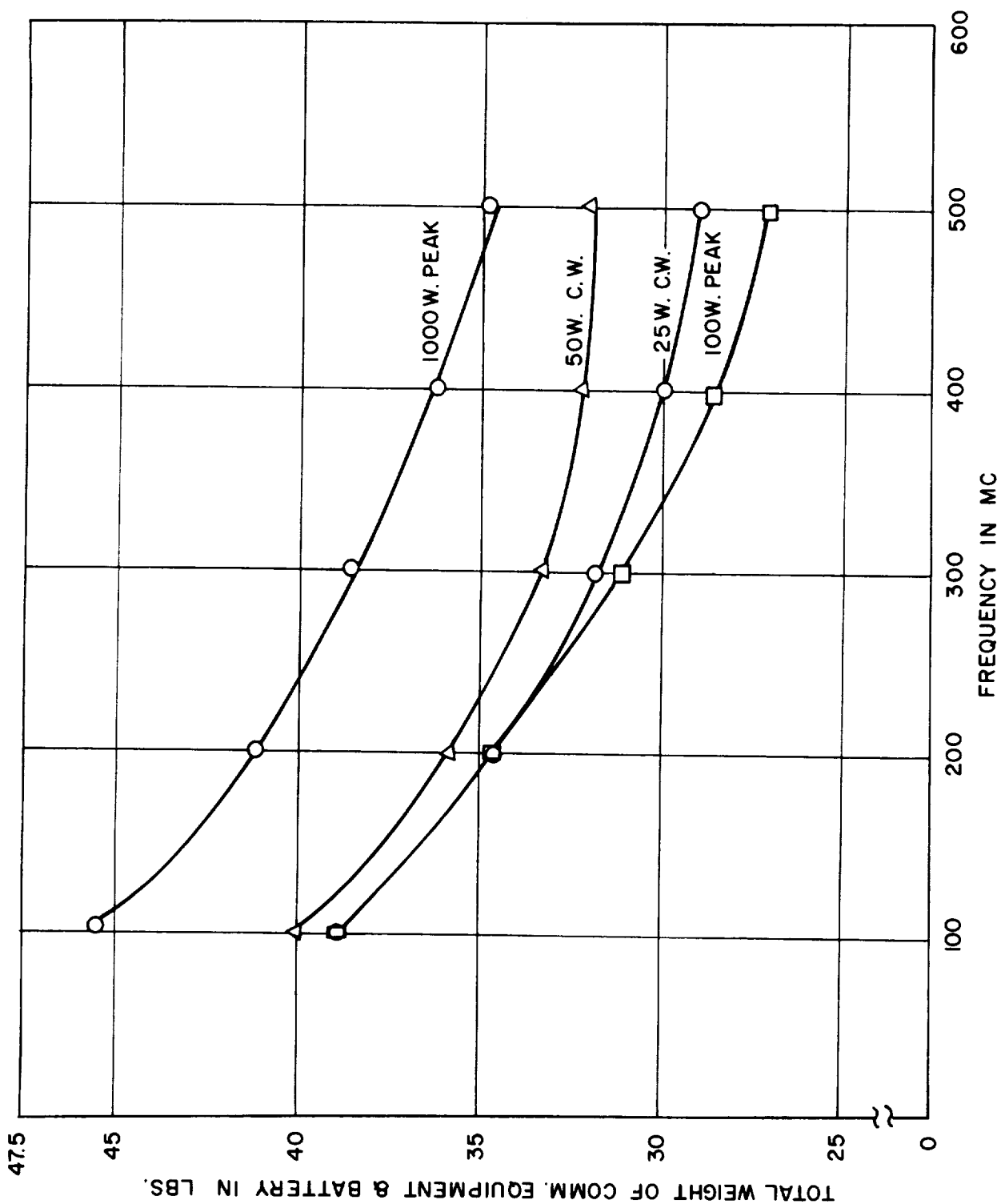


Figure 3.1.5. Weight of Communication Equipment and Battery vs. Frequency

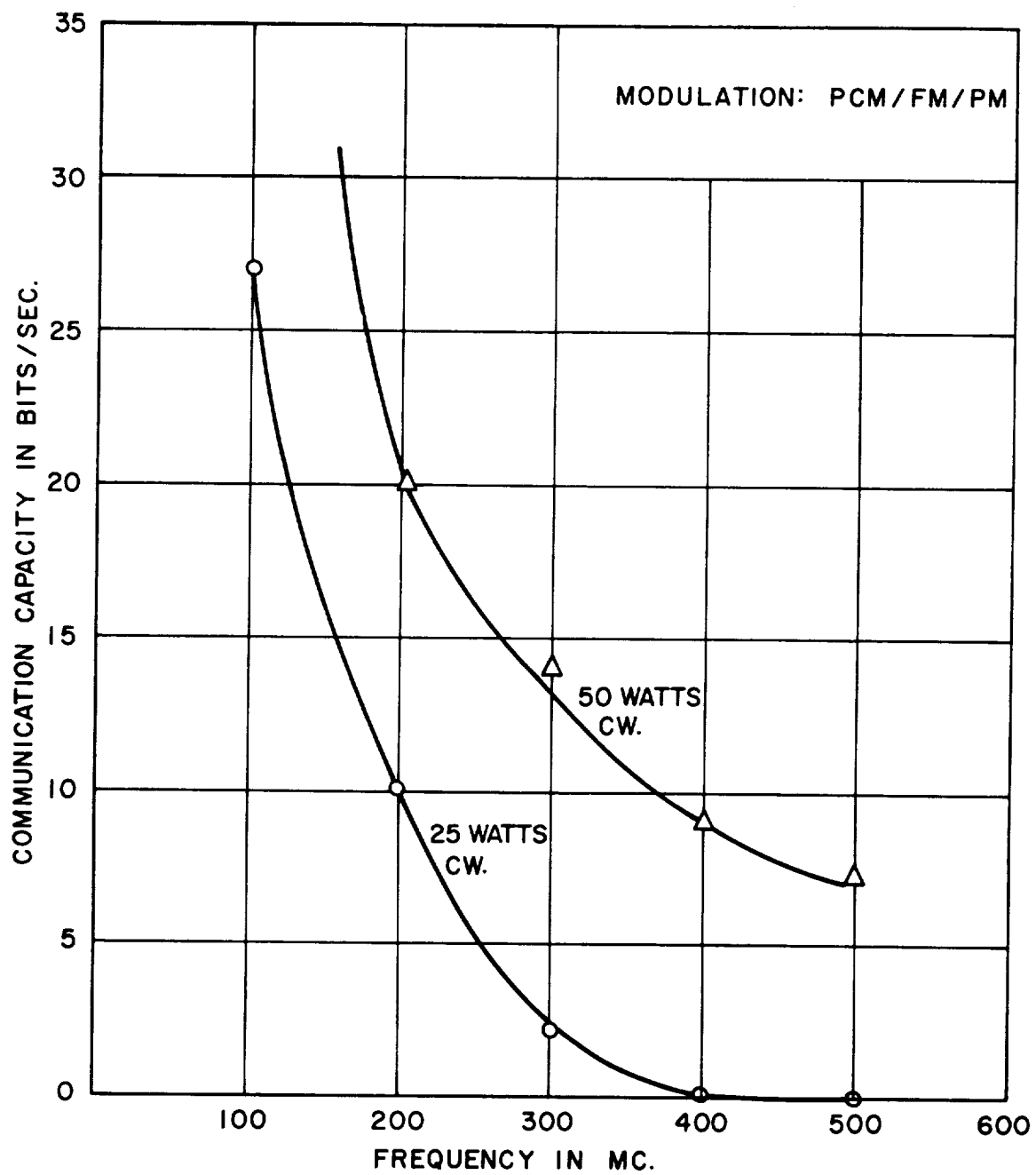


Figure 3.1.6. Relay Link Communication Capacity vs. Carrier Frequency

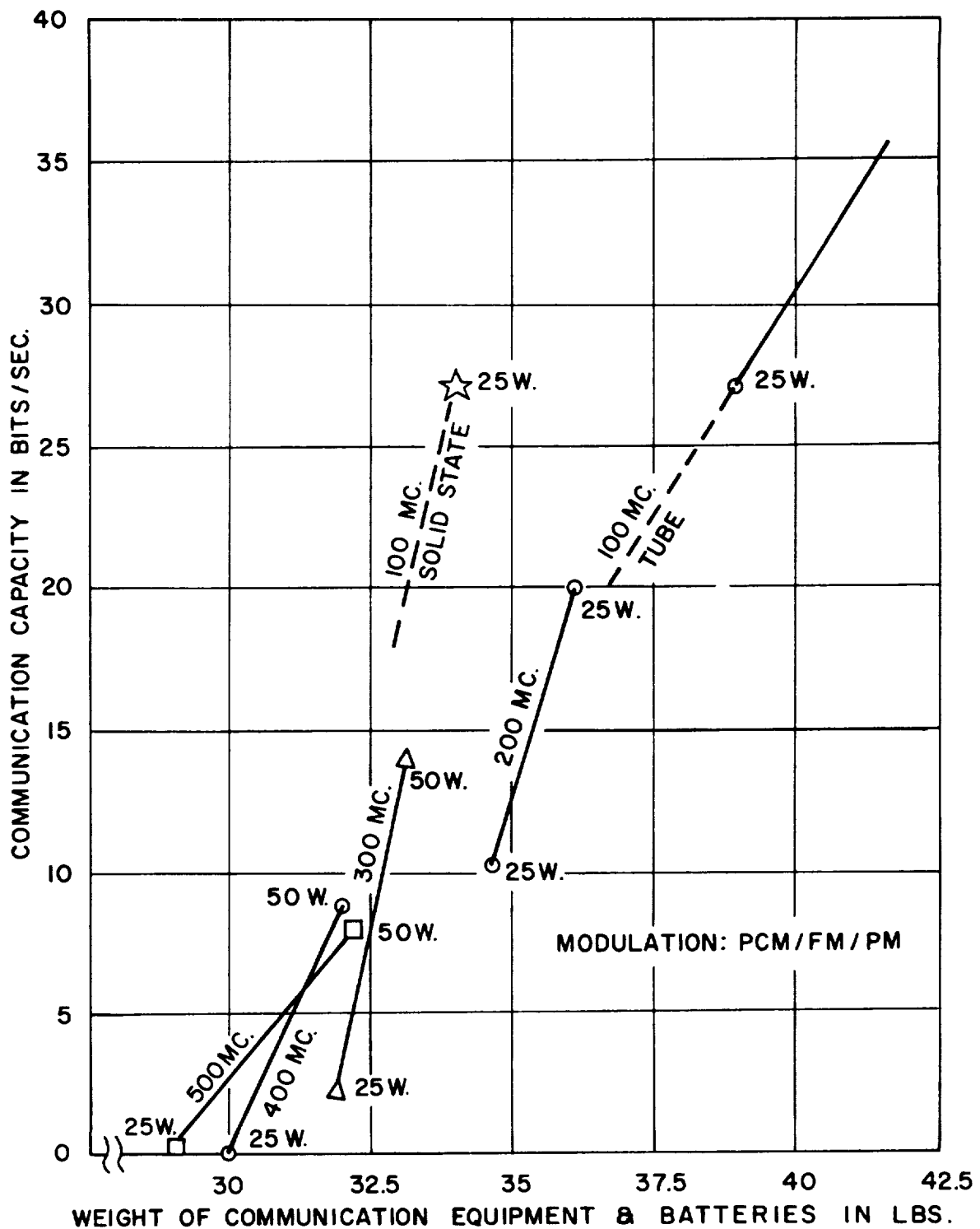


Figure 3.1.7. Communication Capacity vs. Weight

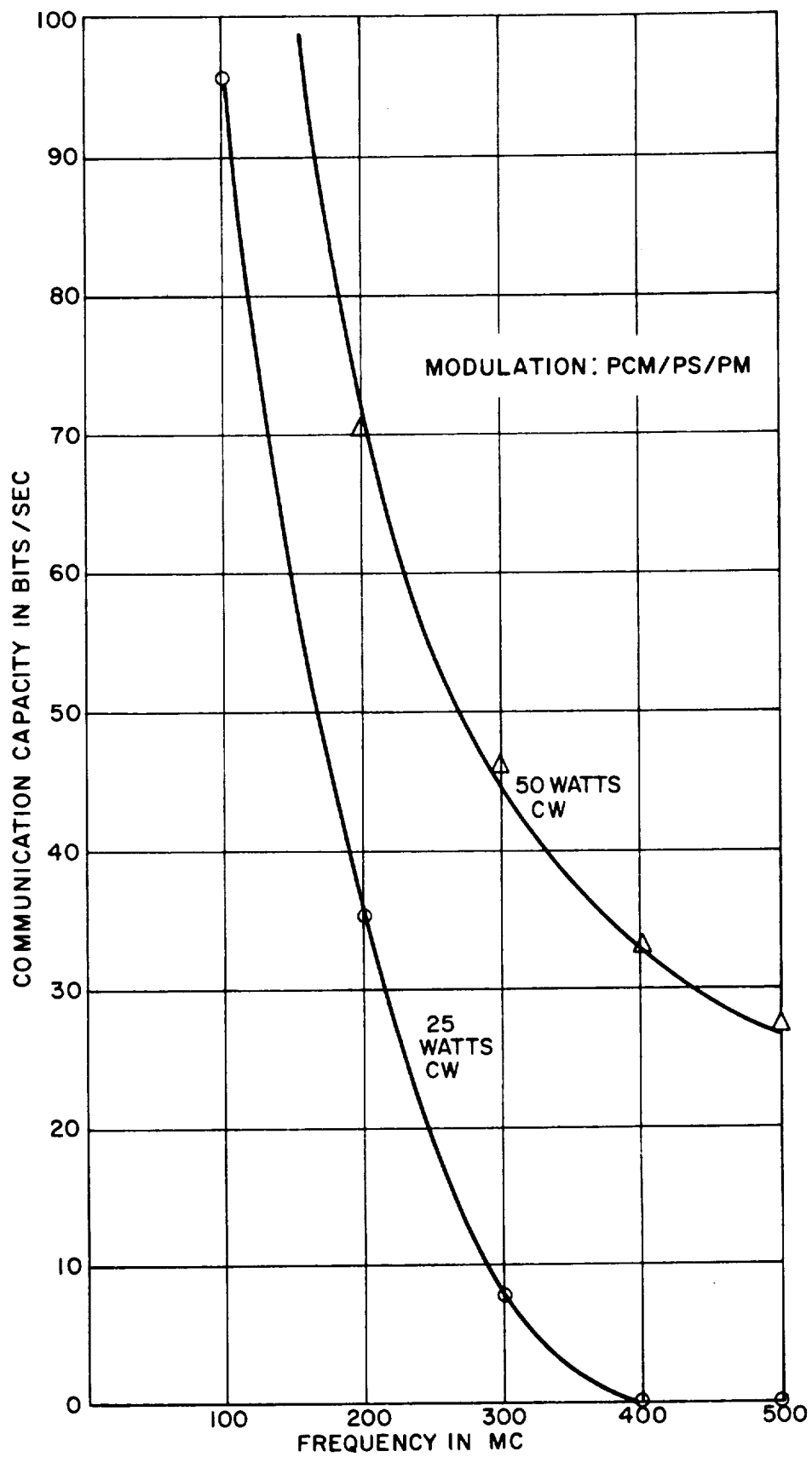


Figure 3.1.8. Relay Link Communication Capacity
vs. Carrier Frequency

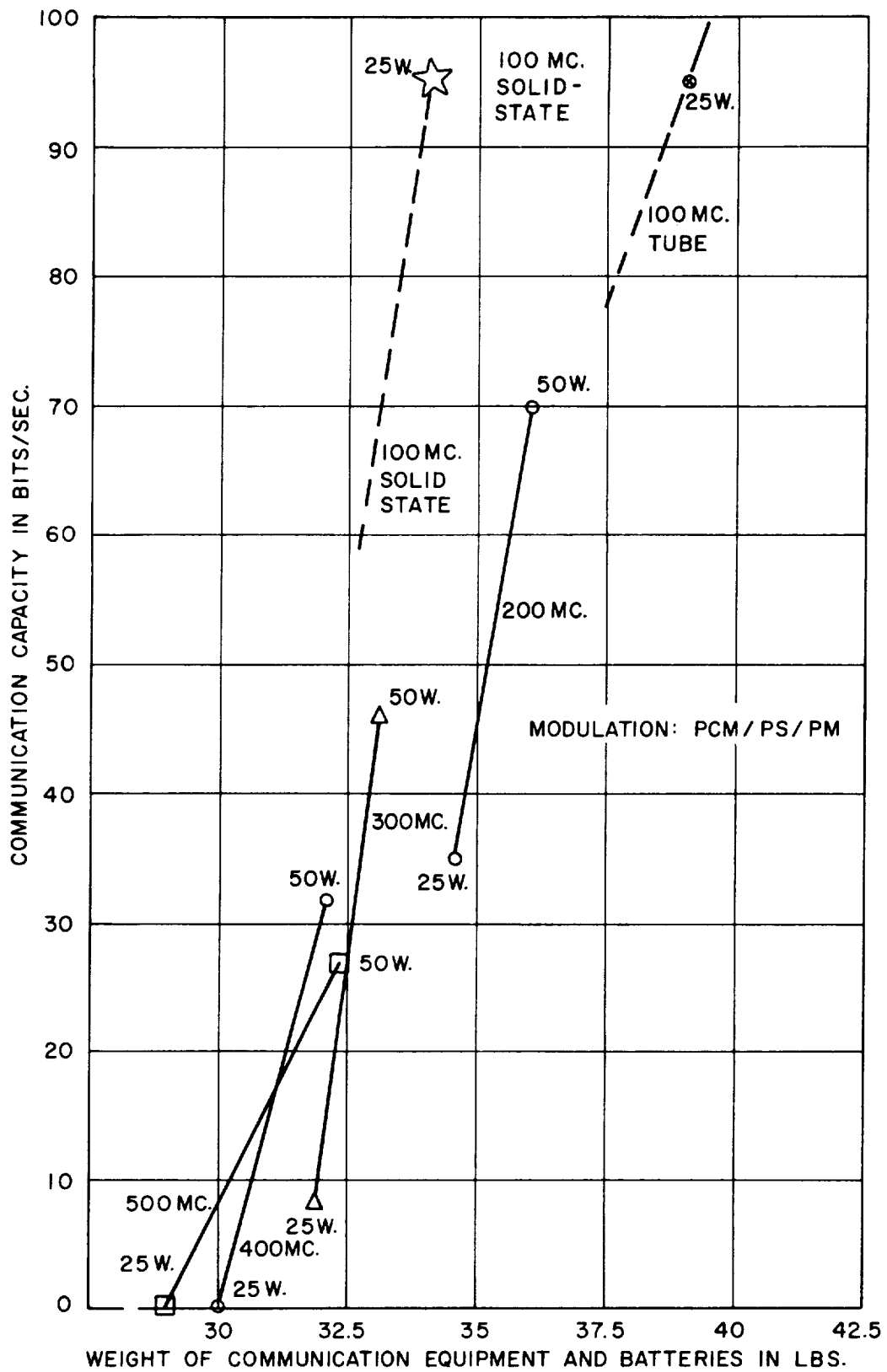


Figure 3.1.9. Communication Capacity vs. Weight

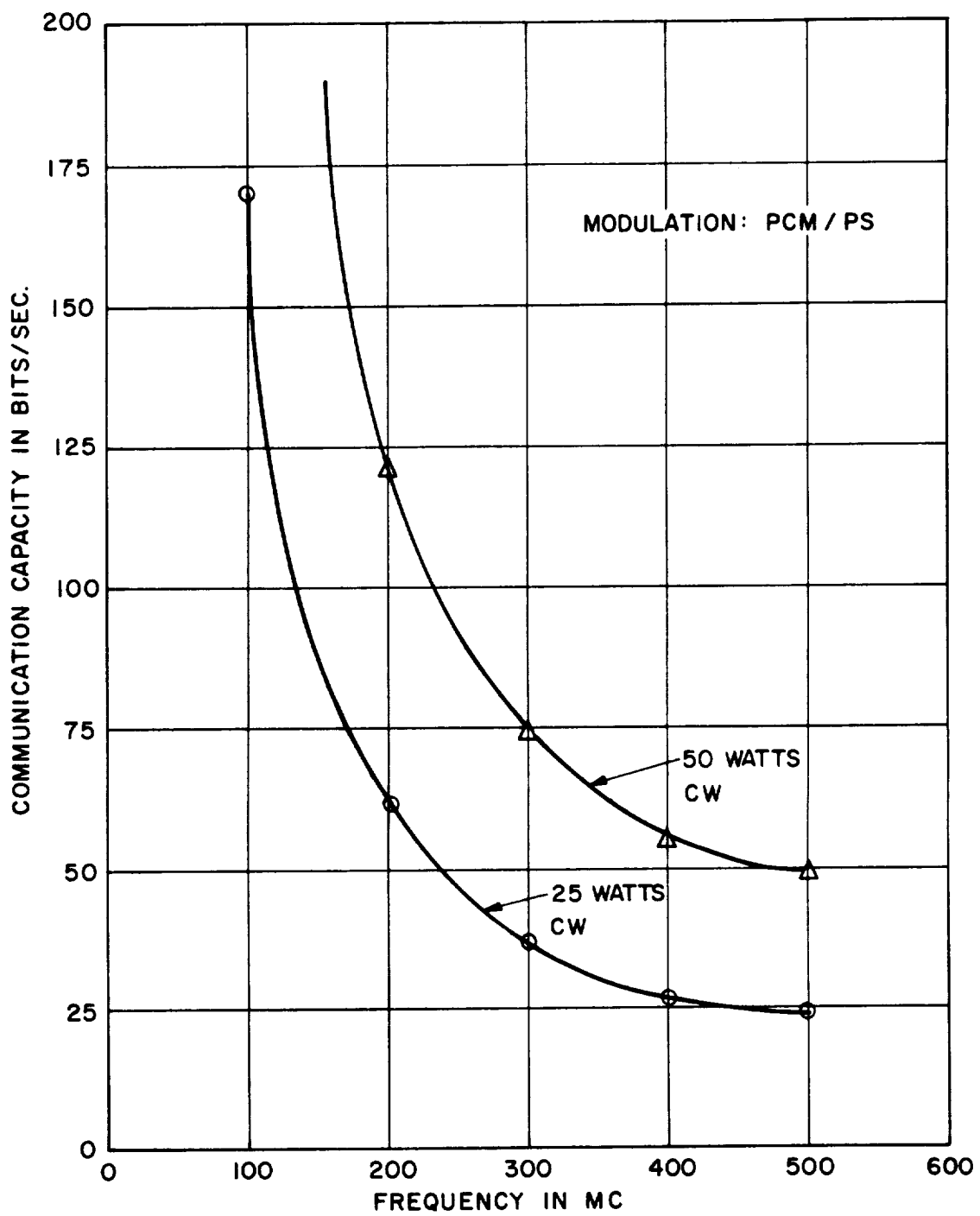


Figure 3.1.10. Relay Link Communication Capacity vs. Carrier Frequency

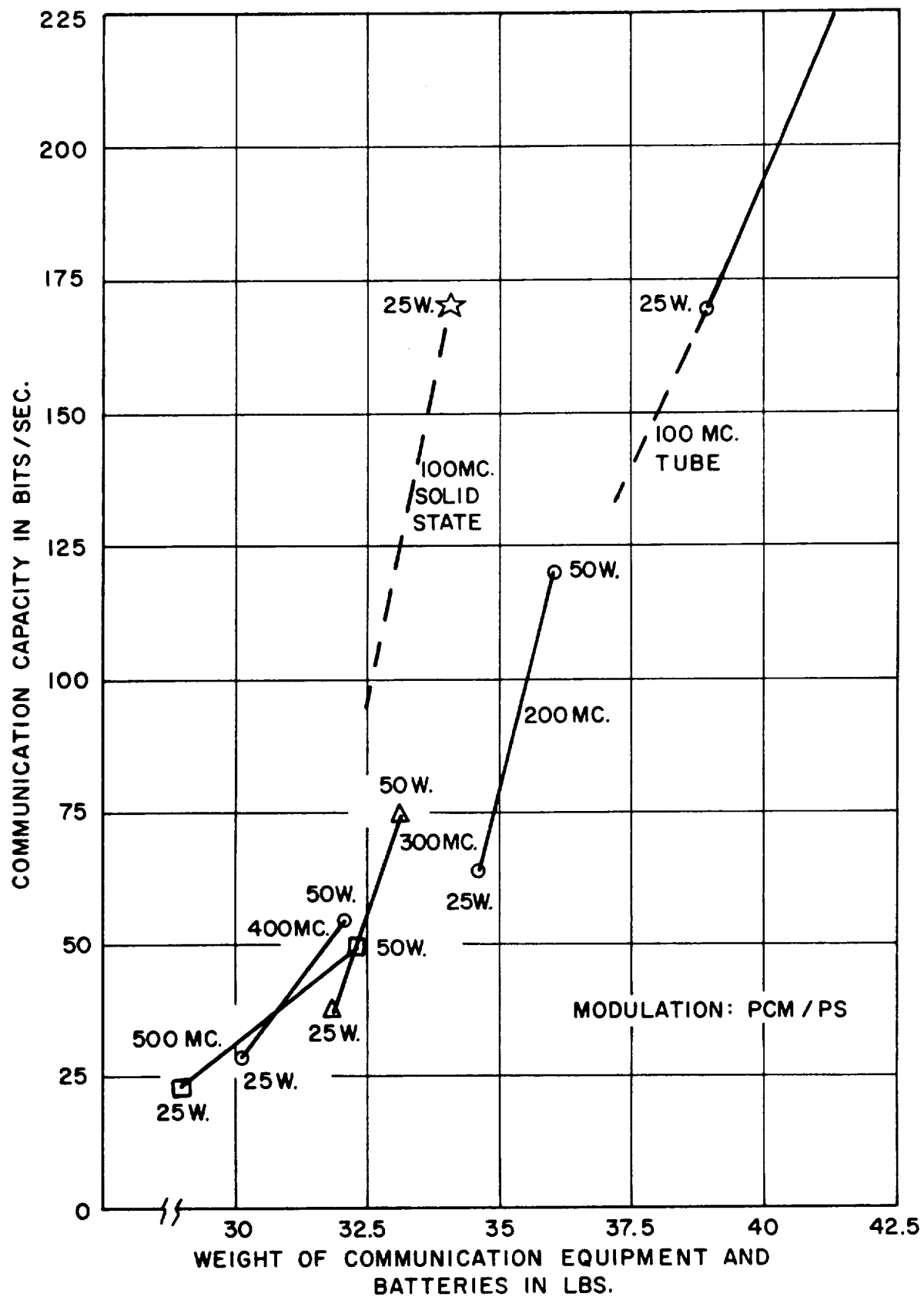


Figure 3.1.11. Communication Capacity vs. Weight

3.2 CONVERSION FACTORS

In this section will be pointed out some of the more obvious conversion factors which can be used when deviating from the nominal parameters of Tables 3.1.1 and 3.1.2, on which the analyses have been based.

- (1) Transmission Distance - The required transmitter power will vary with the square of the transmission distance. It should be noted here that this refers to the maximum transmission distance, not to the miss distance. If the miss distance is changed significantly, this will affect the acquisition time, and reference must be made to Section 3.4.
- (2) Carrier Frequency - Section 3.3 contains a discussion of the frequency-dependent variables in this analysis. In particular, a change in carrier frequency will significantly affect the following quantities:
 - (a) Free-space attenuation
 - (b) Noise level
 - (c) Antenna losses
 - (d) Threshold carrier power requirement
 - (e) Pre-detection bandwidth

Quantities (a), (b), and (c) have been lumped together and plotted in Figure 3.2.1. This can be used over the linear region of the power versus data rate curves for the coherent systems. Multiplication of $K(f)$ times the 100-mc power yields an equivalent 100-mc power for systems operating above 100 mc.

In the region below threshold it should be noted that the frequency uncertainty is directly proportional to the carrier frequency (due to doppler effect). Therefore, the loop bandwidth - hence, the minimum carrier power requirement - must be increased as the square root of the carrier frequency, in order to hold the acquisition time constant. When operating in the threshold region, this correction must be applied over and above that shown in Figure 3.2.1.

The pre-detection bandwidth is directly proportional to the carrier frequency, due to doppler effect. This correction applies to the noncoherent systems (such as PPM/AM) with their RF thresholding problems.

- (3) Acquisition Time - The allowable acquisition time has been chosen to be one per cent of the total communication time, i.e., a nominal 18 seconds for a 30-minute descent. Conversion to other acquisition times is covered in Section 3.4.
- (4) Other Variables - Values other than the nominal values used for such quantities as antenna gains, noise figure, miscellaneous RF losses, and margin may be directly substituted into the transmitter power requirements.

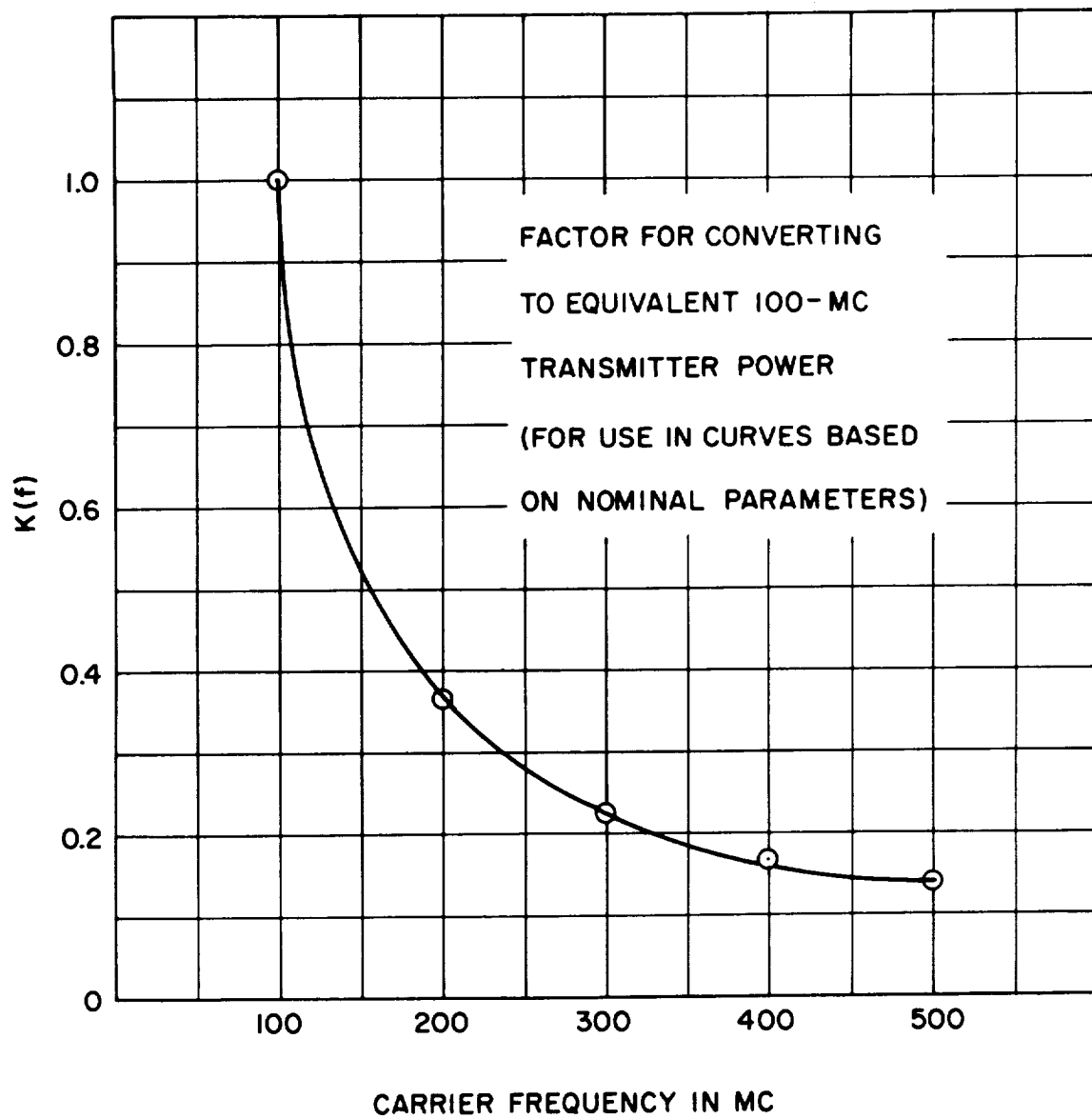


Figure 3.2.1
III-3-23

3.3 FREQUENCY CONSIDERATIONS FOR RELAY LINK

The transmission frequency of the relay link is constrained in the study to the band from 100 mc to 500 mc. The results of the study indicate that the optimum frequency does indeed lie within this band. The primary factors which prescribe these limits are the antenna size, antenna losses and galactic noise which increase with decreasing frequency and free-space attenuation which increases with increasing frequency. These and other factors are considered in this section. Those factors which are described in more detail in other sections are discussed only briefly here. The overall relationships among data rate, communication system weight, and frequency are illustrated in the summary (Section 3.1).

3.3.1 Transmitter Size, Weight and Efficiency

The size, weight and prime power requirements of the transmitters utilizing a tube in the power amplifier stage and having equal RF power output tend to increase with increasing frequency (see Section 3.10); however, the variation is not significant. If no more than 25 watts of transmitter power are required, a solid-state transmitter can be utilized at the low end of the band (≈ 100 mc). This not only results in a reduction of size, weight, and prime power over tube transmitters, but also eliminates warm-up requirements and offers greater reliability.

3.3.2 Transmitter Antenna Weight, Efficiency and Breakdown

Transmitter antenna weight and loss increase as frequency decreases under the constraints placed on the system as described in Section 3.11. The variations with frequency are shown in Figure 3.3.1.

The power level at which the antenna breaks down is expected to be slightly higher at the upper end of the frequency band. The actual magnitude is unknown but is expected to be higher than that in the earth's atmosphere (see Section 3.11).

3.3.3 Transmitter Frequency Stability

Both frequency drift and oscillator phase jitter in the transmitter and receiver oscillators increase with increasing frequency. Frequency drift is objectionable since the band which the acquisition circuit sweeps must be increased by the value of the possible drift between the two oscillators. This, of course, increases the acquisition time. Oscillator phase jitter can cause degradation of the signal and loss of phase lock. As phase jitter increases, the loop bandwidth and, therefore, RF signal power must increase if performance is to remain constant.

Ordinarily, neither drift nor jitter would pose a significant problem in the system at the frequencies being considered using available crystals. The slow drift during the mission could be corrected periodically prior to entry. Phase jitter would be relatively small compared to that allowable with the broad phase lock loop bandwidth required for fast acquisition. However, contacts with vendors and the U.S. Army Signal Corps at Fort Monmouth, N.J., indicate that no oscillators have previously been subjected to the environment expected in the capsule at entry. Therefore, further development may be required to obtain a suitable oscillator for the transmitter. In this case, the desirability of using a low frequency to reduce the stability requirements will depend on the relative ease or difficulty with which the stability requirements can be met at the higher frequencies under the capsule environmental specifications.

3.3.4 Free-Space Attenuation

Free-space attenuation $(4\pi R/\lambda)^2$ is the dominant factor which degrades the communication capability with increasing frequency. Free-space attenuation, of course, is a factor used in the range equation for mathematical convenience. The physical cause of the degradation is the reduction of the effective area of the receiving antenna with increasing frequency in order to hold the antenna beamwidth relatively constant.

As may be noted from the above expression, free-space attenuation reduces the communication capability by a factor of 25 (14 db) as frequency is increased from 100 to 500 mc; however, since this is accompanied by a reduction of antenna size and weights, the overall effect on the capsule is not as significant.

3.3.5 Receiver System Noise Temperature

The noise temperature of the receiving system is derived from receiver noise and RF losses inside the spacecraft and the effective noise temperature which the antenna "sees" external to the spacecraft.

Inside the spacecraft the noise will be due primarily to the receiver itself. The noise figures given in Section 3.12 for receivers in the frequency range of interest has been converted to noise temperature and plotted in Figure 3.3.2. The relation utilized for the conversion was

$$T = 290^{\circ} (F-1)$$

where F is the receiver noise factor.

The external noise temperature is plotted in Figure 3.3.2. The assumption has been made that the galactic plane is included in only a small portion of the hemispherical antenna pattern and that the major portion of the noise is derived from galactic noise in the direction normal to the galactic plane. The noise from the Sun and Venus has also been neglected. These assumptions result in optimistic values, especially at the higher frequencies where Venus, if closely approached, might contribute significantly compared to the value given for galactic noise.

The sum of the internal and external noise is shown in the same Figure.

3.3.6 Plasma Attenuation

Transmission through the plasma during entry appears feasible only for a sharp-nosed body, and then only for "no separation" flow. In general, attenuation decreases with increased frequency. The variations are shown in Section 3.8.

Losses due to plasma attenuation are not included in the calculations of RF power requirements for the various communication systems in this report.

3.3.7 Ionosphere Attenuation

Ionospheric attenuation increases with decreasing frequency; however, calculations in Section 3.6 indicate that it is negligible in the frequency band of interest. The highest value to be expected occurs in the Extreme I atmosphere at 100 mc and is less than 2 db. As with plasma losses, no values of ionospheric attenuation have been inserted in the RF power requirements calculations.

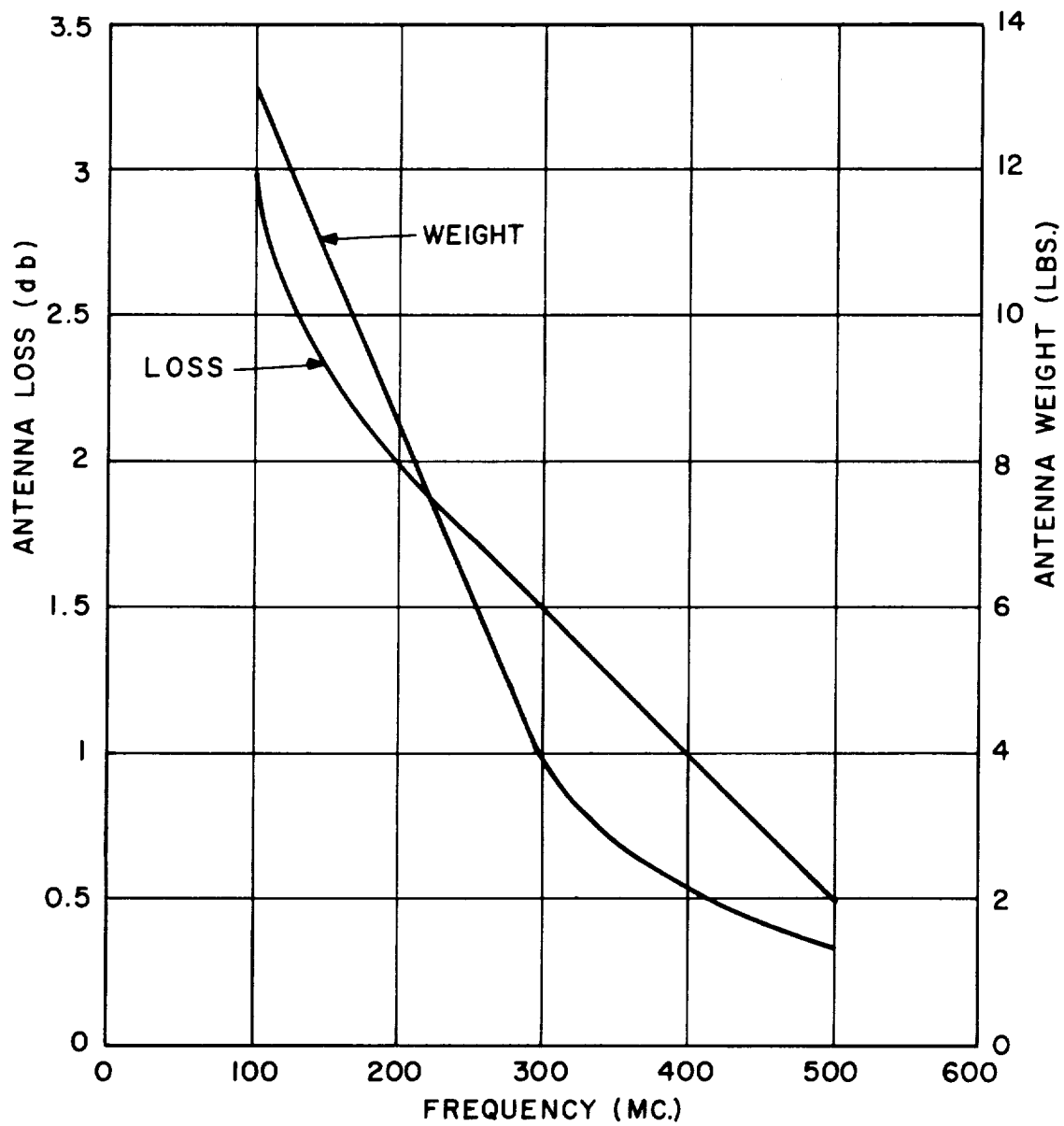


Figure 3.3.1. Capsule Antenna Loss and Weight vs. Frequency
III-3-28

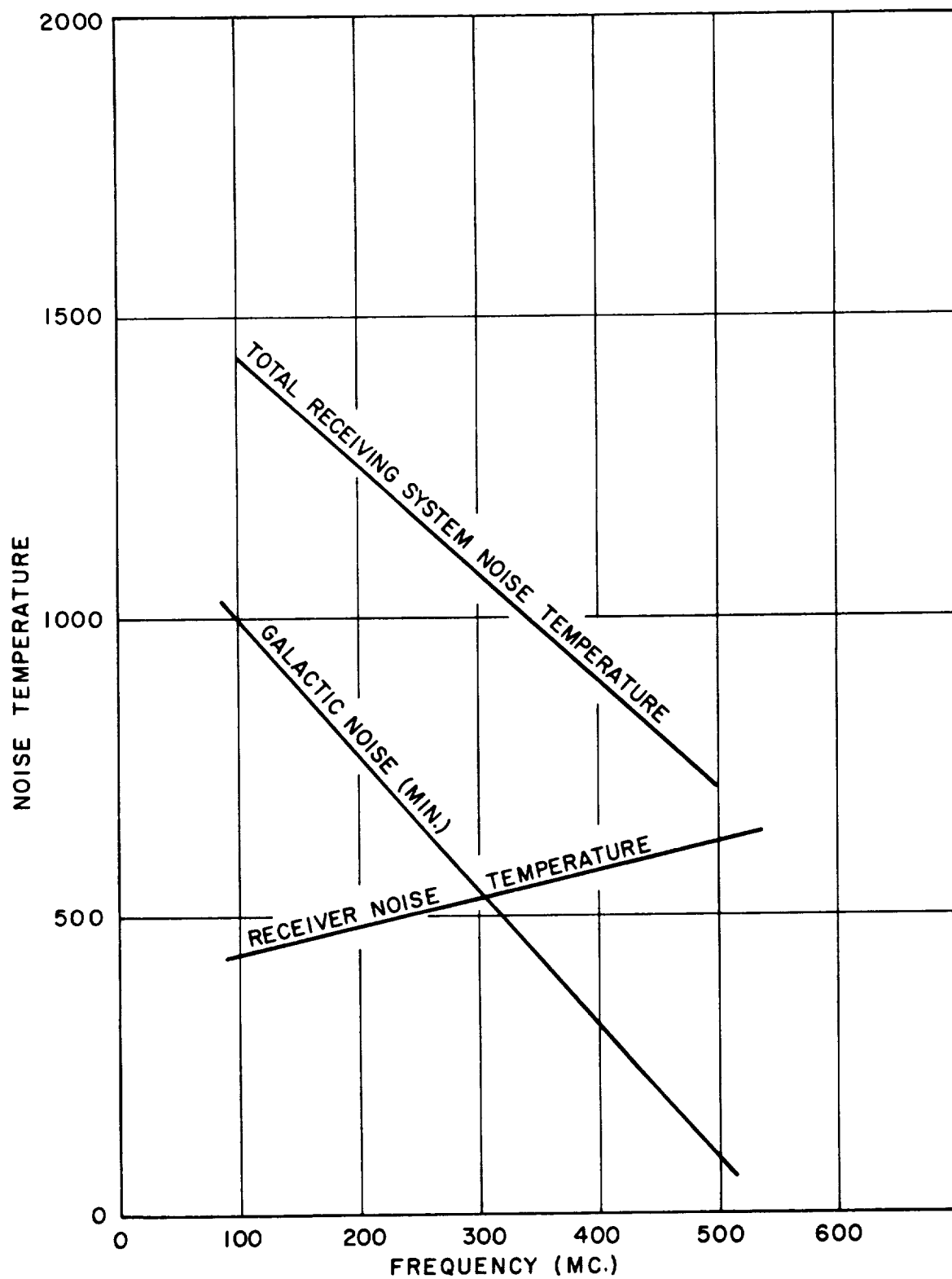


Figure 3.3.2. Noise Temperature vs. Frequency

3.4 SIGNAL ACQUISITION AND TRACKING

3.4.1 Introduction

Several of the detection processes investigated in this report require coherent tracking of a carrier signal received from the capsule. The frequency of the received signal must first be located; then, an internally generated signal at the receiver must be locked in phase with the received carrier and must be capable of following all further phase variations of the carrier.

The capability of a phase-lock loop which will acquire and track the signal is determined in this section. Its parameters are then related to those of the relay and direct communication links.

In the analysis it will be assumed that a carrier signal is present without regard to how it is derived from the power transmitted from the capsule; i.e., it is of little importance here whether the carrier is transmitted as a carrier (such as in PCM/PS/PM) or is derived from the spectrum containing the information (as in PCM/PS). This will affect the efficiency of the communication system, but will be taken into account in the evaluation of the modulation techniques.

3.4.2 Factors Affecting System Capability

A phase-lock loop will be considered for the purpose of tracking the frequency and phase of the received signal. The parameters of interest in the loop are the effective noise bandwidth and the signal-to-noise ratio required in that bandwidth, since they determine the amount of transmitter power required in the carrier. Several factors must be taken into account in determining the noise bandwidth. These include:

1. thermal noise
2. phase jitter due to instability of the transmitter and receiver oscillators
3. sweep rate for signal acquisition
4. doppler rate

Although it is desirable to reduce the bandwidth toward zero in order to minimize thermal noise, the latter three factors tend to restrict the reduction.

The phase variations due to oscillator instability should be followed as closely as possible not only to reduce degradation of the information accompanying the transmitted carrier, but also to reduce the probability of losing lock and thereby losing all information. As oscillator instability increases, the noise bandwidth of the loop must also be increased in order to hold information degradation and probability of losing lock constant.

Acquisition of the incoming signal is accomplished by sweeping the internally generated signal through the frequency band in which the former is known to exist. A low probability of phase lock will exist unless the loop can respond adequately to the transient resulting from the coincidence of the two signals. The signal acquisition capability of a loop can be increased by broadening the loop bandwidth and/or decreasing the frequency uncertainty. Frequency uncertainty can result from:

1. long-term oscillator drift during the journey of greater than 100 days.
2. abrupt oscillator frequency change due to high g-loading during capsule entry.
3. oscillator frequency change due to temperature variation if adequate temperature control cannot be maintained during entry and the subsonic descent of the capsule into the relatively hot Venusian atmosphere.
4. doppler shift.

In addition to oscillator phase jitter and the sweeping action for acquisition, doppler rate also precludes the possibility of reducing the loop noise bandwidth to zero. In effect doppler rate places approximately the same requirement on the loop bandwidth as an equal sweep rate for acquisition.

The applicability of the above mentioned factors to each of the types of links and methods of reducing their effects are discussed below.

In the analysis to be presented for the relay link, it will be assumed that all factors causing frequency uncertainty are negligible or can be made negligible except the doppler shift. Long term drift can be eliminated by comparing and correcting the frequency of the receiver both prior to capsule separation from the spacecraft and periodically after separation until entry occurs. If capsule propulsion is utilized so that separation can occur a relatively short time prior to entry, no post-separation corrections appear to be necessary. Temperature change and g-loading should not result in significant frequencies if proper design techniques are utilized.

The doppler shift has been determined in Appendix A under the assumption that the trajectories of the capsule and spacecraft with respect to Venus and each other can be predicted to a relatively high degree. This allows optimization of the system; any uncertainty in parameters such as range, communication time, and spacecraft velocity will result in more stringent requirements on the tracking system than those determined in the analysis. Adequate information is contained in the analysis, however, to allow corrections to be made where conditions are other than those assumed.

3.4.2.1 Relay Link

The results of the following sections indicate that the dominant factor that limits the minimum loop bandwidth in the relay link is the sweep rate required for signal acquisition. Since only a few minutes of communication will be available, fast acquisition time is mandatory. As noted later the sweep rate required for acquisition should be much greater than the doppler rate and, therefore, the effects of the latter will be negligible. This suggests the possibility of an adaptive system which will switch to a narrow bandwidth after the signal has been acquired. This would yield good loop dynamic characteristics during acquisition and reduce phase jitter due to thermal noise during the tracking phase, thereby reducing the probability of loss of lock. Although this procedure is described in the literature, no reference to a working model has been found.

Considering the bandwidth which will be shown to be available on the basis of transmitted power, range, etc., and considering the low transmission frequency, the oscillator stability requirements will not be difficult to meet. However, if an adaptive loop is implemented as mentioned above, the stability must be consistent with the minimum bandwidth utilized.

3.4.2.2 Direct Link

The factor in the direct link which places a lower limit on loop bandwidth appears to be oscillator instability. This is a critical problem, since the minimum loop bandwidth predicted for the DSIF with crystal oscillators is 3 cps, while it will be shown that less bandwidth is desirable if an 85-ft. dish is utilized. The problem becomes even more severe since there does not appear to be an oscillator at the present time with adequate stability to satisfy this requirement in the high-g environment expected in the capsule. This problem is not as critical in the relay link, since the signal frequency is expected to be an order of magnitude lower, and power is available to allow a much larger loop bandwidth.

Allowable loop acquisition time for the direct link is a more nebulous quantity than that for the relay link. In the latter, real-time acquisition was mandatory; however, for the direct link it appears that the probability of rapid acquisition in real time is very low. This is due to both the narrow loop bandwidth required and the relatively large region of frequency uncertainty which may exist. The latter may result from the inability to acquire the signal for a long period prior to entry due to vehicle tumbling combined with the limited periods of transmitter "on-time"; or, even if the signal is acquired just prior to entry but lost during entry, the transmitter frequency may change considerably during entry (in comparison to the loop bandwidth) due to the severe environment and result in a prolonged search for re-acquisition. Because of these possibilities, predetection recording in the uncertainty bandwidth appears desirable as a back-up; however, it is recognized that there may be many problems inherent in this technique, such as limited dynamic range and time-base stability of the record/reproduce operation, which require further investigation. If, however, predetection recording proves

feasible, acquisition time is of no consequence since the data can be played back continually until phase-lock is achieved.

The remaining factor, doppler rate due to the relative motion between the Earth and Venus, which would ordinarily place a requirement on the loop bandwidth should be no problem. It can be removed by means of an ephemeris-controlled oscillator as was used in the DSIF for the radar exploration of Venus.

3.4.3 Description of Phase-Lock Loop

The phase-lock loop considered in this report is a basic type II loop with the addition of a limiter at the output of the IF section. The limiter provides a gain control function since the gain of the loop depends upon the amplitude of the incoming signal. The advantages of limiting were set forth in Reference 3 and the acquisition characteristics of a type II loop with limiting in the presence of noise were recently determined by the Defense Systems Department of General Electric (Reference 1) utilizing a GEESE* model of the system. The results of the latter will be used in the following analysis. Since the type II loop has been discussed extensively in the literature, the theory of operation will not be re-derived here and only the resulting equations and a brief discussion will be given.

The block diagram of the particular phase-lock loop considered in the computer simulation described in Reference 1 is shown in Figure 3.4.1. The incoming signal is mixed with the local oscillator signal and filtered in the IF amplifier. It is then fed into a band-pass limiter. In the locked condition, the IF signal is of exactly the same frequency as the reference oscillator, and only a phase difference exists between them. The phase detector senses any phase error, and its output is a voltage proportional to the sine of the phase difference. This error voltage is filtered and applied to the VCO (Voltage-Controlled Oscillator) to control the VCO frequency. The dynamic characteristics of the loop are

*General Electric Electronic System Evaluator

determined primarily by the characteristics of the control filter, $H(s)$, which is a proportional plus integral filter.

The loop transfer function is (for $\omega_n \gg \omega_1$).

$$\frac{\phi_{VCO}(S)}{\phi_{SIG}(S)} = \frac{K (\omega_2/\omega_1) (S + \omega_1)}{S^2 + [\omega_2 + K (\omega_2/\omega_1)] S + \omega_n^2} \quad (3.4-1)$$

or

$$\frac{\phi_{VCO}(S)}{\phi_{SIG}} = \frac{K (\omega_2/\omega_1) (S + \omega_1)}{S^2 + 2 \zeta \omega_n S + \omega_n^2} \quad (3.4-2)$$

where,

ω_2 and ω_1 are the critical frequencies of the loop filter

$$H(s) = (S + \omega_1)/(S + \omega_2)$$

K is the loop velocity constant

ω_n is the loop undamped natural frequency ($\sqrt{K \omega_2}$)

ζ is the loop damping factor ($\approx 1/2 \sqrt{K \omega_2/\omega_1^2}$)

The phase error response is

$$\frac{\phi_{ERROR}(S)}{\phi_{SIG}(S)} = \frac{S (S + \omega_2)}{S^2 + 2 \zeta \omega_n S + \omega_n^2} \quad (3.4-3)$$

3.4.4 Acquisition Capability of Phase-Lock Loop in the Presence of Noise

In the particular loop utilized in the computer simulation, for a given equivalent noise bandwidth, B_n , the natural frequency, ω_n , is a maximum for a loop damping factor of $\zeta = 1/2$. Conversely for a given natural frequency, the noise bandwidth is minimum when $\zeta = 1/2$. The comparative data on systems with damping factors indicate that for $\zeta > 1/2$ there is no marked change in acquisition characteristics; but for $\zeta = 1/3$, the acquisition performance is significantly poorer than for $\zeta \geq 1/2$. When the IF signal is limited, the loop can be designed so that at some S/N ratio, a high probability of acquisition is obtainable for a given sweep rate. The limiter performs a gain control function which provides good dynamic performance. In addition, when using the limiter and "matching" the gain at some minimum expected S/N ratio, the loop operates as well at the match point as would a linear loop. (Any increase in S/N ratio will improve acquisition performance over that obtainable with a linear loop.) The overall system performance is generally better for $\zeta = 1/2$, inasmuch as the decrease in probability of acquisition is not as rapid with increasing sweep rate and noise does not degrade the performance as much. The apparent improvement in maximum sweep rate for higher damping factors, and the decrease for lower damping factors, are due to the relative stability of the loops.

From the results an empirical formula was developed in Reference 1 to predict the sweep rate for a 90 per cent probability of acquisition. The accuracy of the formula in predicting the 90 per cent point is within 10 per cent of the measured values, and holds for damping factors equal to, or greater than, 0.5 ($\zeta \geq 1/2$).

$$R_{90} \text{ (cps/sec)} = \frac{(\pi/2 - 2.2 \sigma_o) (0.9 \frac{\alpha}{\alpha_o} \omega_{no}^2)}{2 \pi (1 + \delta)} \quad (3.4-4)$$

*"Matching" is the procedure whereby the loop gain is set to give a minimum noise bandwidth ($\zeta = 1/2$) at one S/N ratio in the IF, $(S/N)_{IF}$. Figure 3.4.4 shows the factor, α , by which the signal voltage out of a limiter varies as a function of S/N ratio into the limiter, $(S/N)_{IF}$. The point at which $\zeta = 1/2$ is set is designated α_o .

where

- σ_o = calculated rms output phase jitter
- δ = overshoot
- α = signal suppression factor in limiter
- α_o = suppression factor for the $(S/N)_{IF}$ for which loop is "matched"
- ω_{no} = natural frequency of loop at matched point

The calculated rms output phase jitter, σ_o , is given by

$$\sigma_o = \left[\frac{1}{2} (N/S)_{IF} (B_n/B_{IF}) \right]^{1/2} = \left[\frac{1}{2} (N/S)_{out} \right]^{1/2} \quad (3.4-5)$$

where,

- $(S/N)_{IF}$ is the signal-to-noise ratio in the IF section
- B_{IF} is the IF bandwidth
- B_n is the loop bandwidth
- $(S/N)_{out}$ is the signal-to-noise ratio in the loop noise bandwidth

This equation is plotted in Figure 3.4.2 along with a curve showing the average experimental values obtained. The calculated value given above is to be used with Equation (3.4-4); however, the predicted value of phase jitter for a given $(S/N)_{out}$ is to be taken from the experimental curve.

The overshoot, δ , is obtained by considering the phase response of the loop to an input ramp of frequency and is given by

$$\delta = \exp \left[- \frac{\zeta \pi}{1 - \zeta^2} \right] \quad (3.4-6)$$

This function is plotted in Figure 3.4.3.

The signal suppression factor, α , results from the characteristics of an ideal limiter in the presence of noise. The variation of α with S/N at the input to the limiter is shown in Figure 3.4.4.

The noise bandwidth of the loop, B_n (cps), is related to the natural frequency of the loop, ω_n (rad/sec), by

$$B_n \approx \frac{\omega_n}{4 \zeta} (1 + 4 \zeta^2) \quad (3.4-7)$$

B_n is minimum when $\zeta = 1/2$. Its value at that point is $B_n = \omega_n$.

3.4.5 Analysis

3.4.5.1 Relay Link

In the following analysis the relationships among transmission range, frequency, loop noise bandwidth and the transmitter power required are first determined; then the required loop noise bandwidth will be determined in terms of the closest approach of the spacecraft to the capsule and the acquisition capability of loop.

The system described in Section 3.1 will be utilized for the calculations. An allowable rms phase jitter of 20^0 will be assumed which results in a required signal-to-noise ratio of 7.5db in the loop noise bandwidth, B_{no} (Appendix B). The relationship between transmitted power and bandwidth for a transmission range of 10,000 km and a transmission frequency of 100 mc is determined in Table 3.4.1.

Table 3.4.1

Carrier Power Transmitted	$10 \log P_c$ dbw
Transmitter Antenna Gain	0.0 db
Propagation Loss (100 mc; 10000 km)	- 152.5 db
Receiver Antenna Gain	0.0 db
Miscellaneous Losses	<u>- 3.0 db</u>
Carrier Power Available at Receiver:	$10 \log P_c - 155.5$ dbw
Receiver Noise per cps	- 204.0 dbw
Bandwidth	$10 \log B_{no}$ db
Noise Figure	10.0 db
S/N Required	7.5 db
Margin	<u>8.0 db</u>
Power Required at Receiver:	$10 \log B_{no} - 178.5$ dbw

Then,

$$10 \log P_c - 155.5 = 10 \log B_{no} - 178.5$$

or,

$$10 \log P_c = 10 \log B_{no} - 23 \text{ dbw} \quad (3.4-8)$$

This function is utilized to plot figures 3.4.5, 3.4.6 and 3.4.7 for 4 values of range and 3 values of frequency. This then gives the available loop noise bandwidth in terms of the system parameters.

The results of Appendices A and B can now be used to determine the required loop noise bandwidth. In Appendix A the total doppler shift observed by the receiver was found to be described by (Equation A-8).

$$B_S = \dot{f}_{d \max} T \quad (3.4-9)$$

where,

$\dot{f}_{d \max}$ is the maximum doppler rate

T is the communication time (time from capsule entry to impact)

Appendix B gives the loop noise bandwidth at the "match" point as a function of sweep rate for 90 per cent probability of acquisition in a single sweep (Equation B-7):

$$B_{no} = \sqrt{9 R_{90}} \quad (3.4-10)$$

Neglecting frequency uncertainties in the capsule-to-spacecraft link other than the doppler shift given by Equation (3.4-9), the sweep rate can be written as

$$R_{90} = \frac{B_S}{T_L} = \frac{\dot{f}_{d \max} T}{T_L} \quad (3.4-11)$$

where T_L is the time required for one complete sweep of the defined frequency band, B_S , and is interpreted as the maximum time "lost" in acquiring the signal after loss of phase lock (neglecting the 10 per cent probability that more than one sweep is required).

Utilizing Equations 3.4-10 and 3.4-11, the required loop noise bandwidth can be expressed as

$$B_{no} = \sqrt{9 \dot{f}_{d \max} \frac{T}{T_L}} \quad (3.4-12)$$

Defining $\epsilon = \frac{T_L}{T}$, the maximum percentage of communication time or data that is lost during a single acquisition, Equation 3.4-12 becomes

$$B_{no} = \sqrt{9 \frac{\dot{f}_{d \max}}{\epsilon}} \quad (3.4-13)$$

The required bandwidth is shown in Figures 3.4.5, 3.4.6 and 3.4.7 for different values of ϵ and assuming $V_S = 8$ km/sec. The intersections of the curves (dashed lines) for available and required bandwidth therefore indicate the minimum signal power required as a function of range, frequency, and per cent of lost communication time per acquisition.

It may be noted that the form of the above equation is identical to that commonly used for determining the bandwidth required for loop hold-in in the presence of doppler where $\epsilon \approx 1$. Since, for essentially continuous communication, ϵ must be much less than unity, the requirements for doppler hold-in will be

negligible compared to those for acquisition. In fact, the doppler rate can be utilized to advantage if the frequency sweeping for acquisition is always in the direction of the doppler change (continuously decreasing frequency). The fact that the function is monotonic also leads to the possibility of continually reducing the highest frequency of the sweep band to the frequency being observed.

The preceding analysis and the above comments apply only if no communication is attempted during capsule entry. During capsule entry both the entry plasma attenuation and an increased doppler rate will complicate the situation. The behavior of the doppler frequency may be described qualitatively as follows: There is negligible doppler prior to entry, and the receiver observes the transmitter frequency, f_0 ; during the relatively few seconds of entry, the frequency observed will increase to the value corresponding to that for the particular trajectory geometry at that time and for a stationary capsule (Figure A-1, Appendix A). The doppler rate during entry is therefore dependent upon the deceleration of the capsule and the value of θ (Figure A-1) during entry. For $\theta \approx 0$ during entry the doppler rate can be very low; however, significant values of θ are expected.

The dashed lines on the graphs through the intersections of the curves for available and required bandwidth were drawn for convenience. It should be noted, however, that in drawing these lines, the approximation $R = R_0$ (where R is the communication range used to determine available bandwidth and R_0 is the distance from capsule to spacecraft at closest approach used to determine required bandwidth) was made. The effect of this approximation depends on the maximum value of θ during the communication period; for instance, if $\theta_{\max} = 30^\circ$, the actual value of available bandwidth will be three-fourths $\left[\left(\frac{R_{\max}}{R_0} \right)^2 = \cos^2 \theta \right]$ that shown on the graphs. For a more precise determination of system capability than indicated by the dashed lines, the predicted maximum value of R and minimum value of R_0 should be used.

3.4.5.2 Direct Link

The parameters of the reference system described in Section 3.1 will be utilized to determine the relationship between loop noise bandwidth and the

transmitted carrier power required in the direct link. As in the relay link, the rms phase jitter will be taken as 20° , which results in a required signal-to-noise ratio of 7.5 db in the loop bandwidth. The calculations are shown in Table 3.4.2.

Table 3.4.2

Transmitter Carrier Power	$10 \log P_c$ dbw
Transmitter Antenna Gain	0.0 db
Propagation Loss	- 255.3 db
Receiver Antenna Gain (85 ft-dish)	51.8 db
Miscellaneous Losses	- 3.0 db
<hr/>	
Carrier Power Available at Receiver:	$10 \log P_c - 206.5$ dbw
Receiver Noise per cps	- 211.6 dbw
Bandwidth	$10 \log B_{no}$ db
S/N Required	7.5 db
Margin	8.0 db
<hr/>	
Carrier Power Required at Receiver:	$10 \log B_{no} - 196.1$ dbw

Then,

$$10 \log P_c - 206.5 = 10 \log B_{no} - 196.1$$

or,

$$10 \log P_c = 10 \log B_{no} + 10.4 \quad (3.4-14)$$

This relationship is plotted in Figure 3.4.8.

Also, the function is plotted for the same system with a 210-foot dish (61 db gain) instead of the 85-foot dish. Note that 33 watts of carrier power are required if an 85-foot dish is used, even if the noise bandwidth can be held to 3 cps, the present minimum for DSIF. Only 4 watts are required with the 210-foot dish.

The frequency search capability of the system can be determined by comparing the available bandwidth plotted in Figure 3.4.8 with the loop noise bandwidth of Figure B-1. For a loop bandwidth of 3 cps, the sweep rate is found to be 1 cps/sec.

3.4.6 Results

3.4.6.1 Relay Link

The results of the analysis are illustrated in Figures 3.4.5, 3.4.6 and 3.4.7. The curves may be summarized as follows: The solid slanted lines indicate the available bandwidth as a function of carrier power transmitted (P_c) signal frequency (f_o), and path length (R); the solid vertical lines indicate the bandwidth required as a function of signal frequency, path length at closest approach (R_o), and the maximum percentage of total communication time lost for each acquisition of the signal when phase lock is lost (ϵ); the slanted dashed lines drawn through the intersections of the preceding curves for $R = R_o$ (the effect of this approximation is discussed in Section 3.4.5.1), therefore, define the minimum carrier power required for particular values of the parameters f_o , R and ϵ .

These results indicate that a few watts of carrier power will give good tracking and acquisition performance for ranges in the order of 20,000 to 30,000 km if the carrier frequency is in the lower portion ($f_o \sim 100$ mc) of the frequency band considered. A low frequency is not only desirable because of the lower power required, but also because it will place less stringent requirements on the stability of the oscillators. Although it appears from the analysis that a frequency less than 100 mc might be advantageous, ionospheric reflection and antenna size and efficiency will probably not allow the use of a lower frequency.

3.4.6.2 Direct Link

The results of the direct link analysis are more difficult to evaluate, since two problems which appear to be major must yet be resolved: oscillator stability and predetection recording. If the 85-foot dish is utilized, a narrow loop

bandwidth is mandatory. With the present minimum bandwidth allowed for the DSIF (3 cps), 33 watts of carrier power are required. The magnitude of the problem of obtaining an oscillator which will survive entry and maintain adequate stability to operate in this bandwidth is not presently known. None have been found to be available at present; however, there are indications that one could be developed (see Section 3.10). If such an oscillator is made available, there yet remains the problem of real-time acquisition. A 3-cps loop bandwidth allows a sweep rate of 1 cps/sec. This may be adequate if the signal can be acquired prior to entry and if the oscillator frequency changes no more than a few cps due to the entry environment. Tests will be required to determine these characteristics. If real-time acquisition is unlikely, predetection recording will be necessary. As mentioned previously there appear to be several problems to be resolved, such as dynamic range and time base stability of the record/reproduce operation, before this technique can be utilized effectively.

If the 210-foot dish is available, 25 watts of transmitted carrier power will result in an allowable loop bandwidth of approximately 20 cps. This not only relieves to a certain extent the oscillator stability requirement, but also allows a sweep rate of 40 cps/sec for real-time acquisition purposes.

Another possibility for reducing the oscillator stability problem is the utilization of a transmission frequency lower than 2295-mc. Since the capsule antenna is gain limited and the ground antenna is area limited there is no theoretical loss associated with a reduction of frequency ($G_t G_r \alpha = \text{constant}$, where α is free-space attenuation). The factor which will probably place the lower bound on frequency is sky noise; however, spectrum allocation and ground equipment availability are other factors which must be considered. The present 960 mc DSIF frequency appears to satisfy these constraints. Although the frequency advantage is relatively small (frequency reduction of 2.4:1), this possibility should be considered along with the possibility of utilizing a lower frequency.

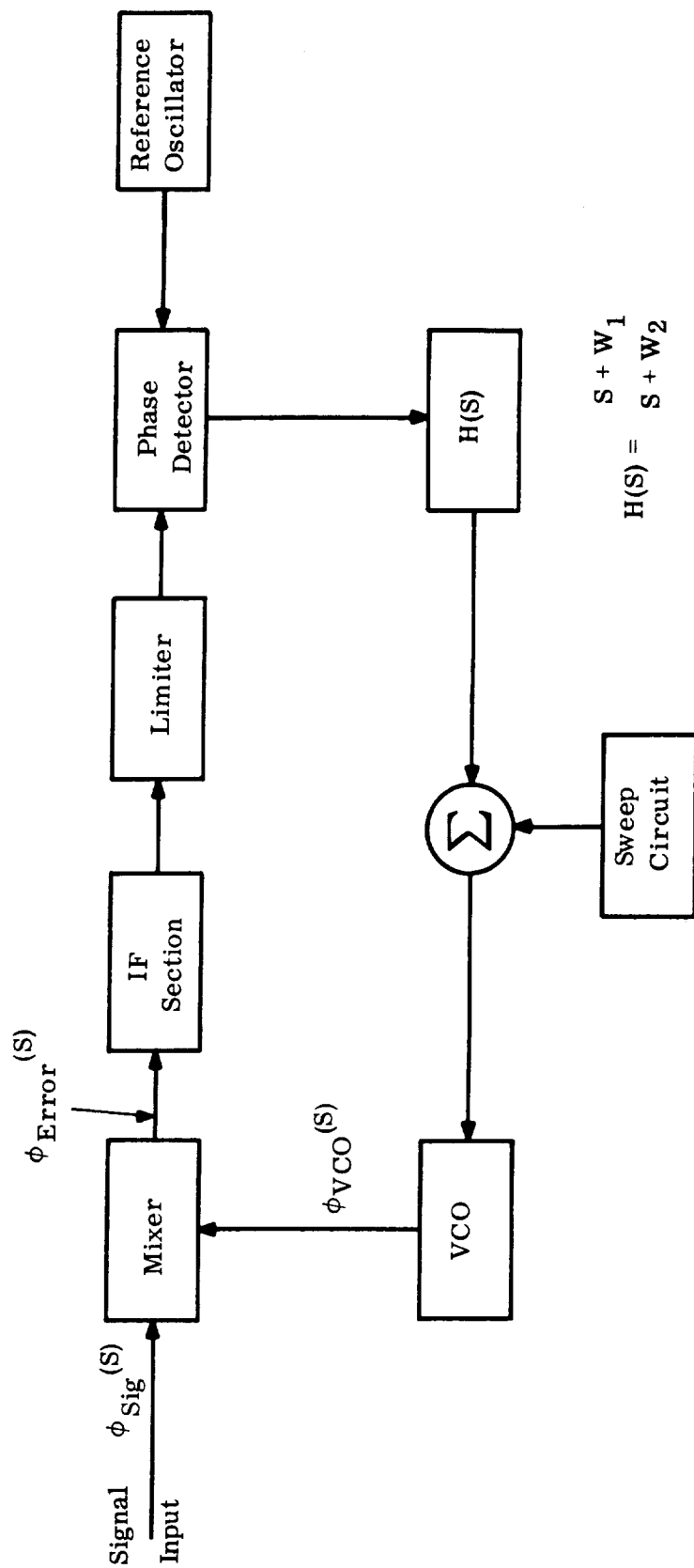


Figure 3.4.1. Phase-Lock Loop Block Diagram

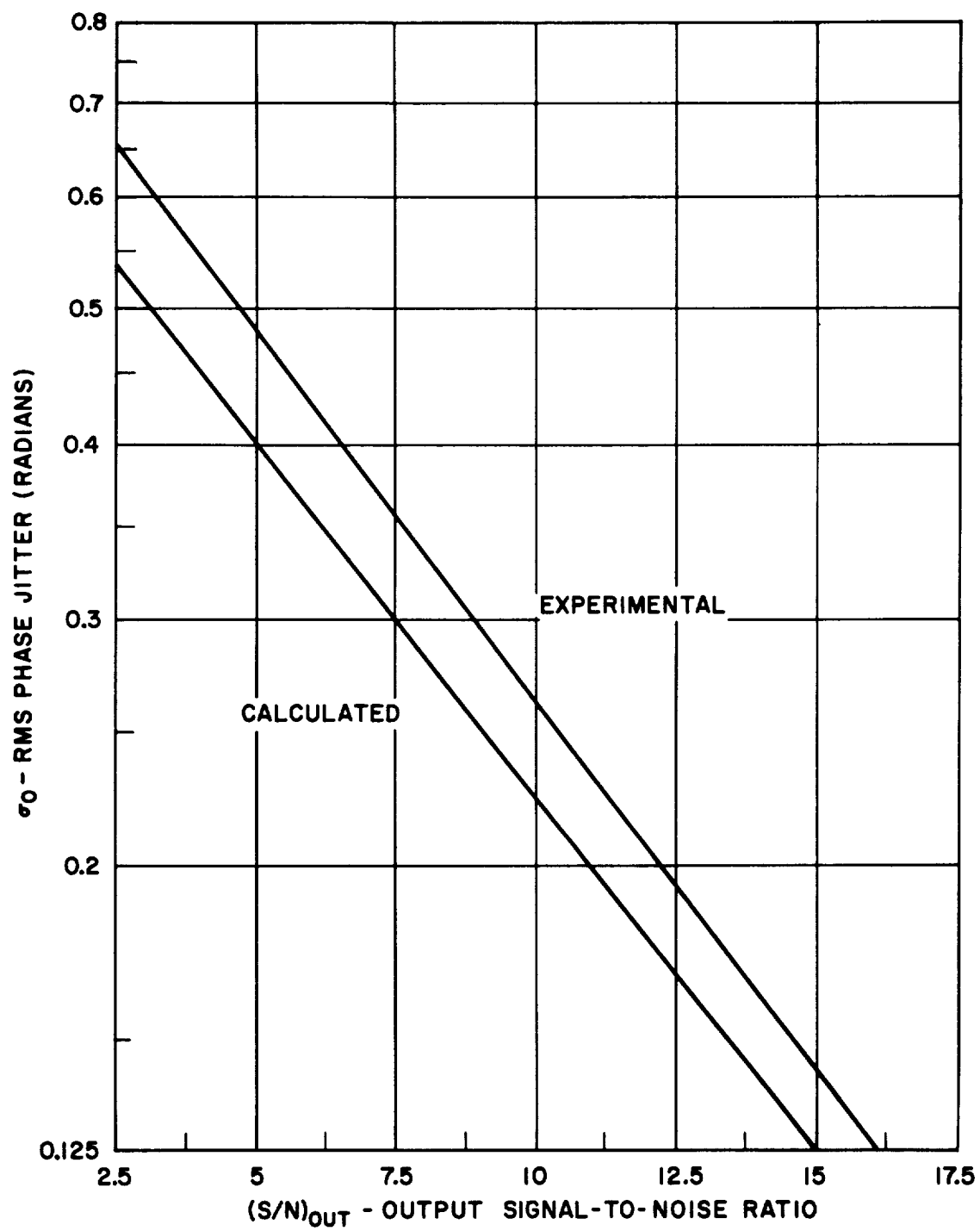


Figure 3.4.2. RMS Phase Jitter vs. Output Signal-to-noise Ratio

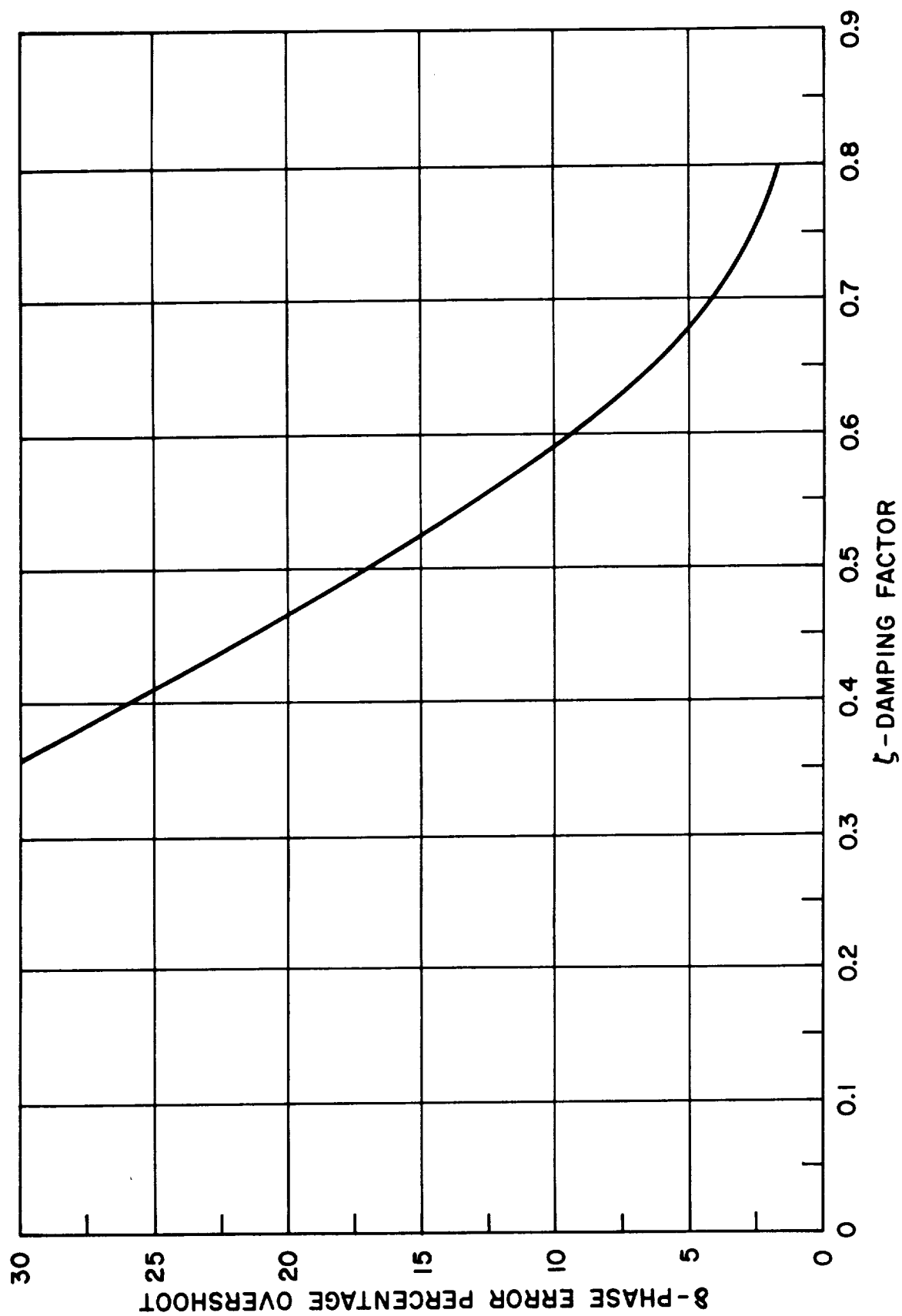


Figure 3.4.3. Phase Error Percentage Overshoot as a Function of Damping Factor for a Linearly Changing Input Frequency

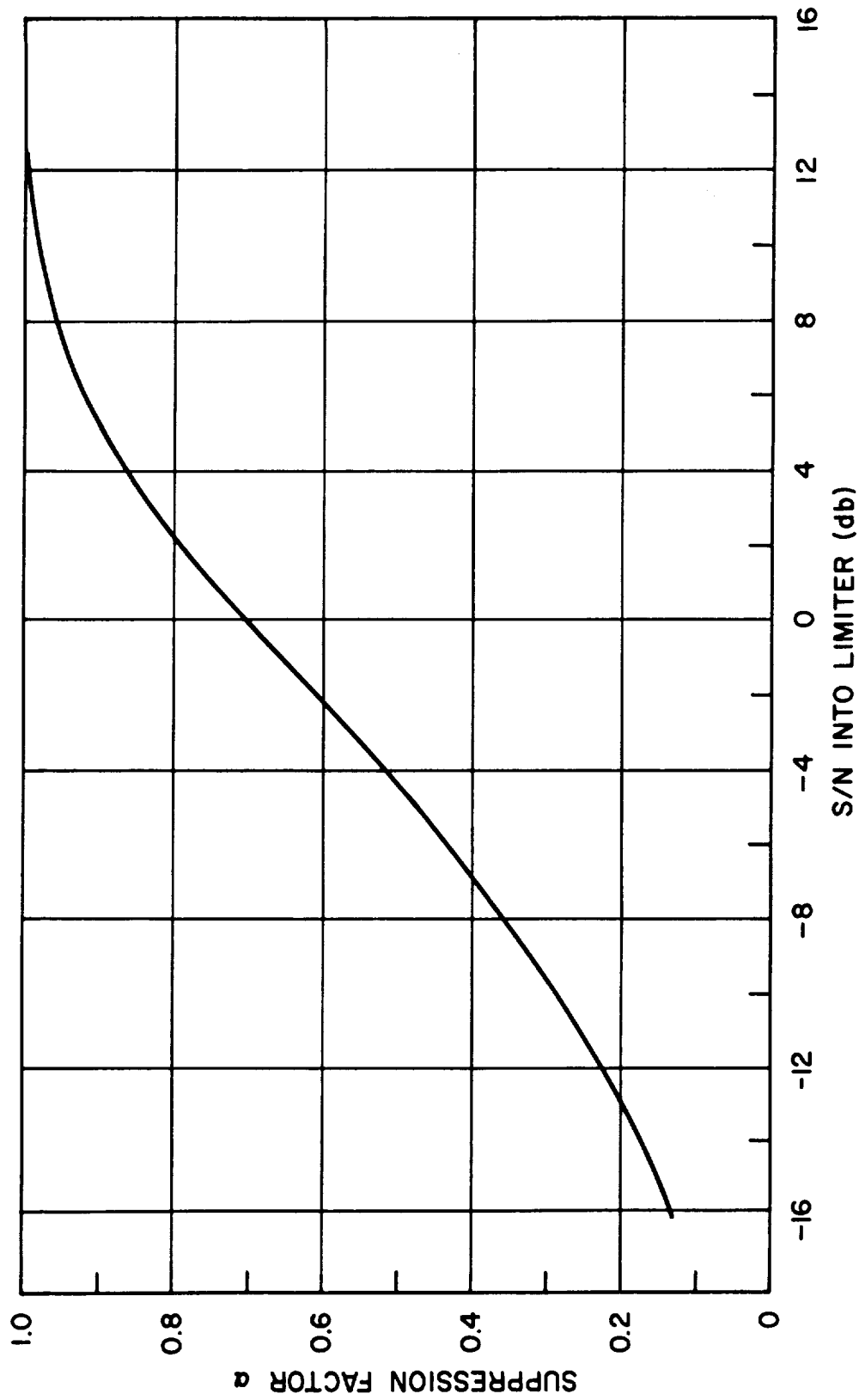


Figure 3.4.4. Output Signal Voltage Suppression Factor in an Ideal Bandpass Limiter as a Function of Input Signal-to-Noise Ratio

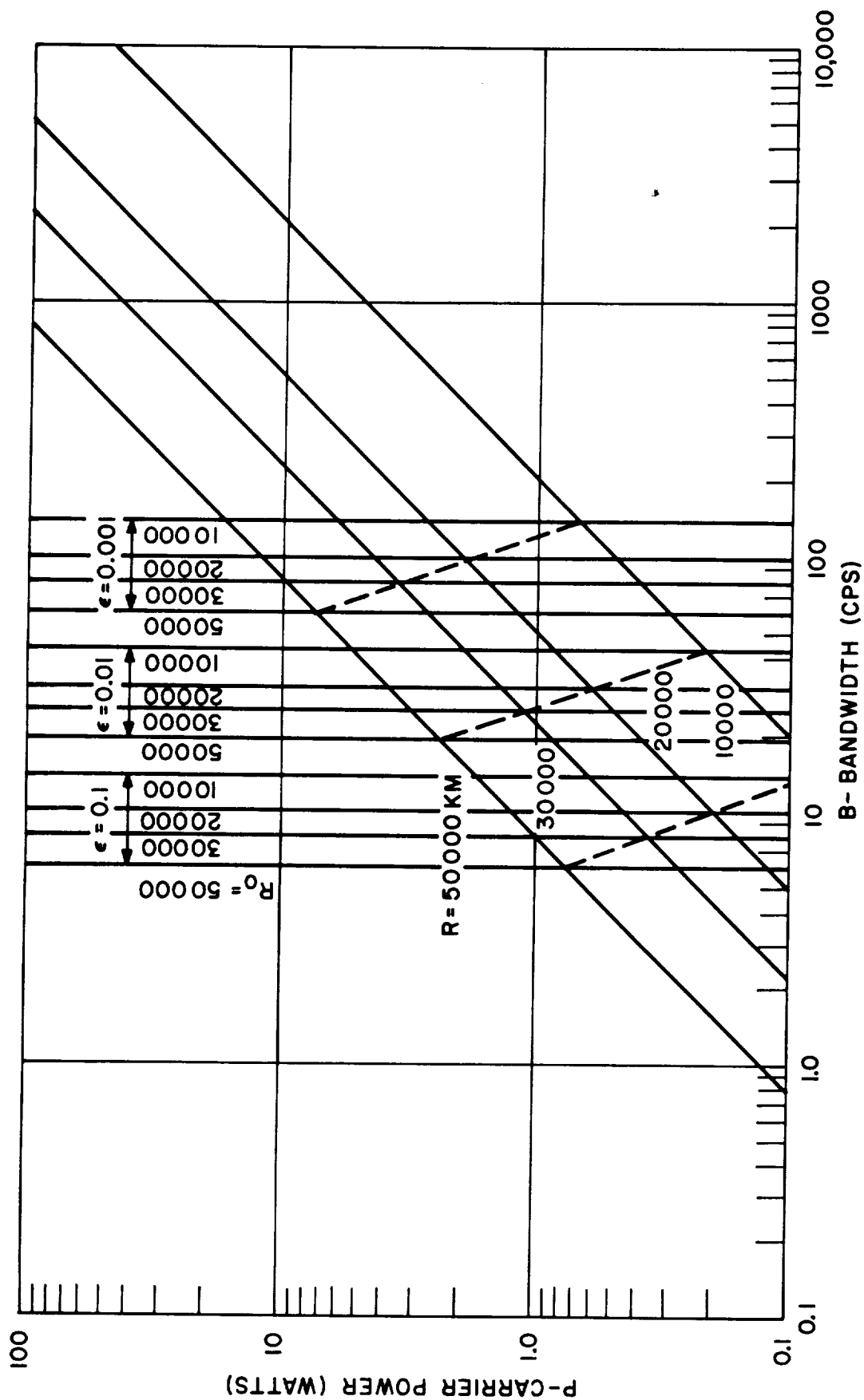


Figure 3.4.5. Power Requirements for Acquisition (100 megacycles)

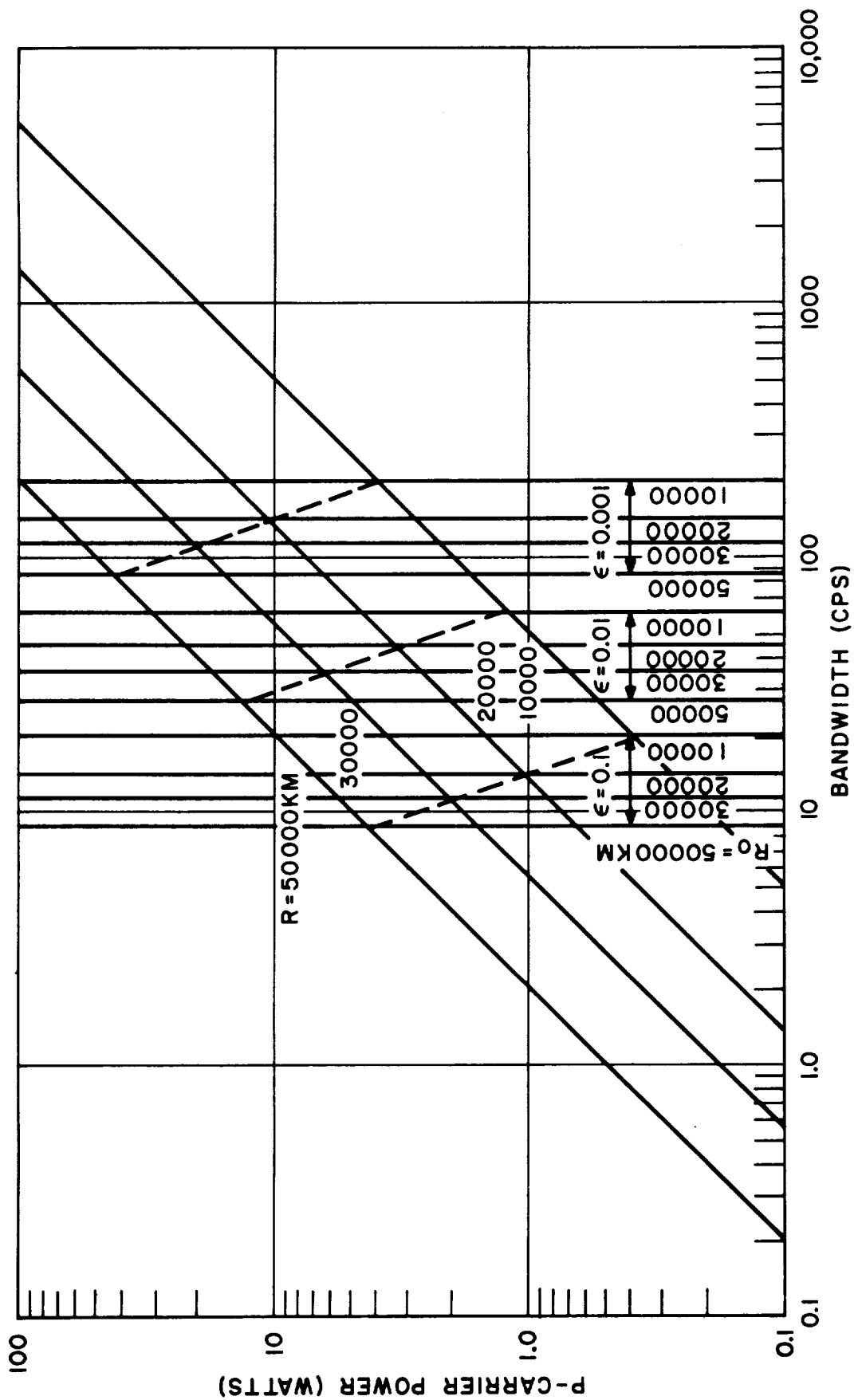


Figure 3.4.6. Power Requirements for Acquisition (200 megacycles)

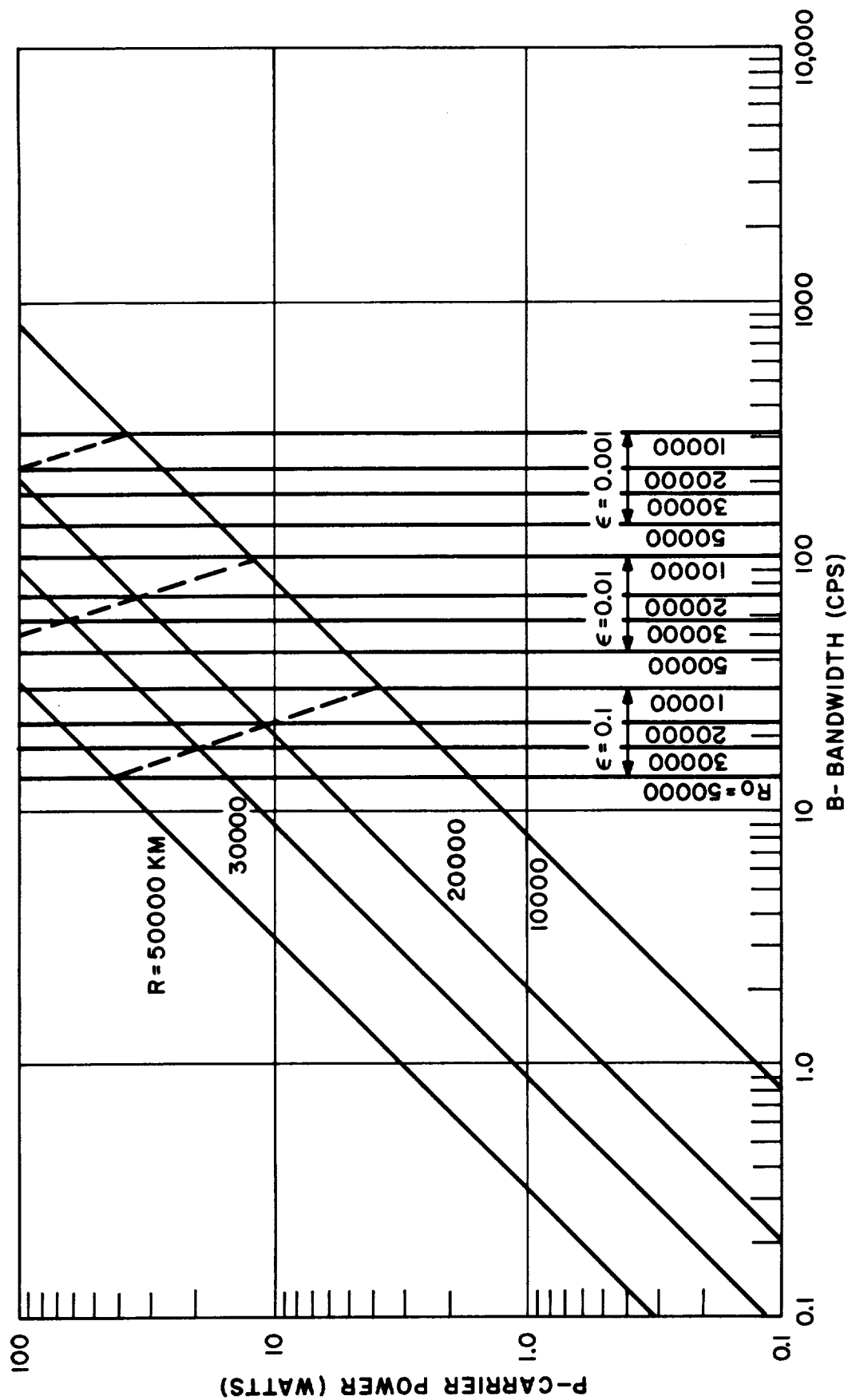


Figure 3.4.7. Power Requirements for Acquisition (500 megacycles)

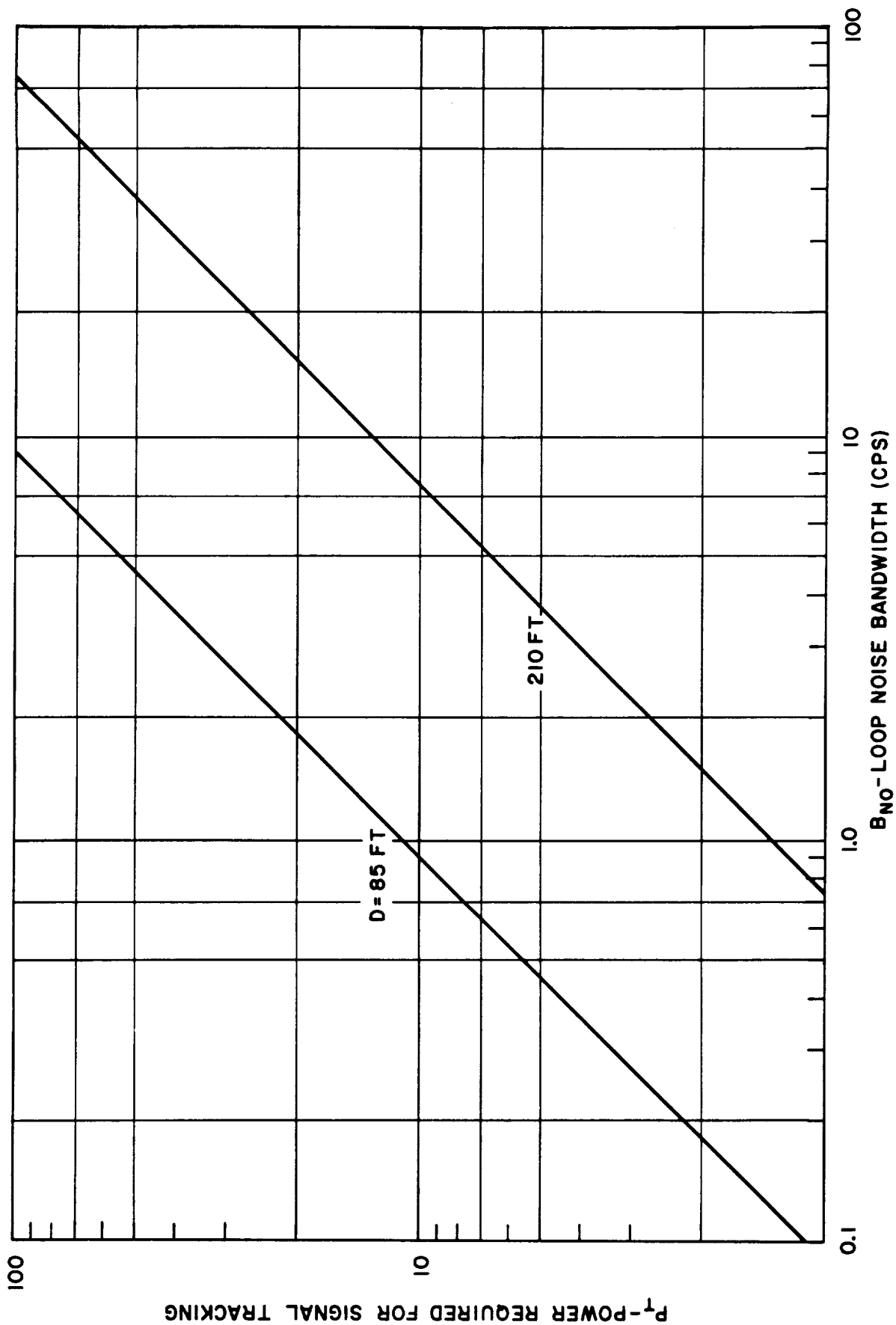


Figure 3.4.8. Power Required for Signal Tracking vs. Loop Noise Bandwidth

APPENDIX A

DETERMINATION OF DOPPLER VARIATIONS

For the purpose of determining the doppler shift observed at the spacecraft receiver we shall utilize the trajectory geometry indicated in Figure A-1a. A straight-line, constant velocity (V_S) spacecraft trajectory is assumed. The doppler frequency is then given by

$$f_d = \frac{V_r}{C} f_o \quad (A-1)$$

where

V_r is the relative velocity between the spacecraft and capsule (km/sec)

C is the velocity of light (3×10^5 km/sec)

f_o is the transmitter frequency (cps)

The relative velocity may be determined from the geometry and is

$$\begin{aligned} V_r &= \frac{dR}{dt} = \frac{d}{dt} \left[(R_o^2 + X_S^2)^{1/2} \right] \\ &= \frac{d}{dt} \left[R_o^2 + (V_S t)^2 \right]^{1/2} \\ &= \frac{V_S^2 t}{\left[R_o^2 + (V_S t)^2 \right]^{1/2}} \end{aligned} \quad (A-2)$$

where

R is the range from spacecraft to vehicle (km)

R_o is the range from closest approach (km)

X_S is the distance from spacecraft to the point of closest approach (km)

V_S is the spacecraft velocity with respect to Venus (km/sec)

t is time (sec)

From (A-1) and (A-2) the doppler frequency is

$$f_d = \frac{V_S f_o}{C} \frac{V_S t}{\left[R_o^2 + (V_S t)^2 \right]^{1/2}} = \frac{V_S f_o}{C} \frac{X_S}{\left[R_o^2 + X_S^2 \right]^{1/2}} \quad (\text{A-3})$$

This function is sketched in Figure (A-1b)

The maximum total doppler shift which can occur is then

$$B_{s \max} = f_d(t = \infty) - f_d(t = -\infty) = 2 \frac{V_S f_o}{C} = 2f_{d \max} \quad (\text{A-4})$$

If, then, transmission is to start when the spacecraft is a large distance from the point of closest approach ($X_S \gg R_o$) and end when it is a large distance past the point of closest approach, (A-4) gives the minimum bandwidth which must be swept by the receiver in order to be assured that the received signal is within the sweep band. This case, however, is pessimistic since the receiver will never observe the signal when it is at $f_o \pm f_{d \max}$. The actual doppler shift is given by

$$B_S = \frac{V_S f_o}{C} \left[\frac{V_S t_2}{\left[R_o^2 + (V_S t_2)^2 \right]^{1/2}} - \frac{V_S t_1}{\left[R_o^2 + (V_S t_1)^2 \right]^{1/2}} \right] \quad (\text{A-5})$$

where

t_1 is the time at which communication begins referred to $t = 0$ at $x = 0$
(assumed here to be immediately after capsule entry)

t_2 is the time at which communication ceases (assumed to be at capsule impact)

In order to simplify further analysis the assumptions will be made that the communication period, T , is centered about $t = 0$; i.e., $t_1 = t_2 = \frac{T}{2}$ and that

$R_o > \frac{V_s T}{2}$. The resulting value of B_s will be slightly pessimistic but will be reasonably close to the actual value for the trajectories which are expected (spacecraft is several thousand kilometers from capsule impact area and lags capsule by a few minutes). With this assumption Equation A-5 may be rewritten as

$$B_s = \frac{V_s f_o}{C} \frac{V_s T}{R_o} \quad (A-6)$$

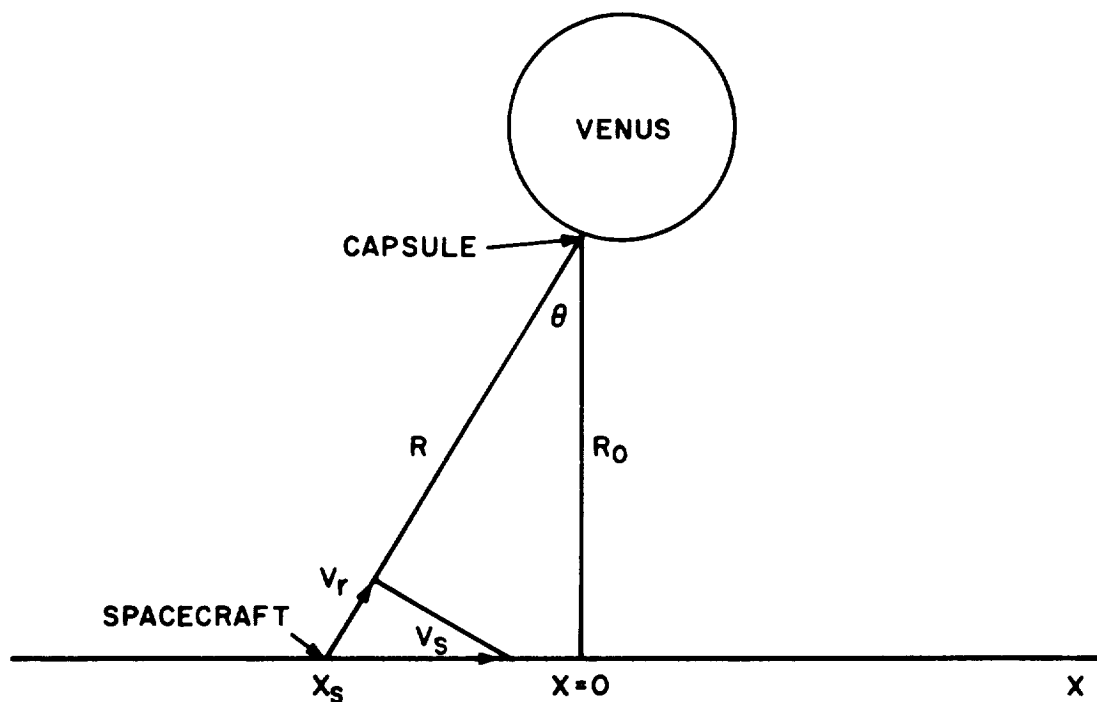
Since the maximum doppler rate, $\dot{f}_{d \max}$, can be shown to be

$$\dot{f}_{d \max} = \frac{V_s^2 f_o}{C R_o} \quad (A-7)$$

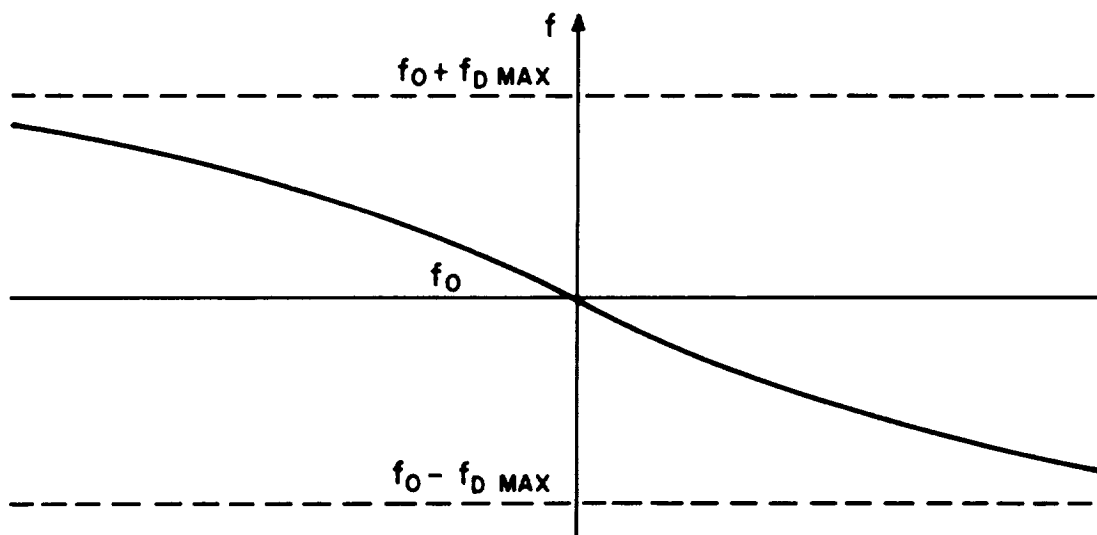
then equation A-6 may be rewritten as

$$B_s = \dot{f}_{d \max} T \quad (A-8)$$

The above assumptions have therefore led to the case where the doppler shift is approximated by the product of the maximum doppler rate and communication time.



A. TRAJECTORY GEOMETRY FOR DOPPLER CALCULATIONS



B. CORRESPONDING DOPPLER VARIATION (FOR STATIONARY CAPSULE)

Figure A-1. Trajectory Geometry and Resulting Doppler

APPENDIX B

BANDWIDTH REQUIREMENTS FOR ACQUISITION

From Section 5.4 the sweep rate for a 90-per cent probability of acquisition is given by

$$R_{90} \text{ (cps/sec)} = \frac{\left(\frac{\pi}{2} - 2.2 \sigma_o \right) \left(0.9 \frac{\alpha}{\alpha_o} \right) \omega_{no}^2}{2 (1 + \delta)} \quad (\text{B-1})$$

Since a damping factor of $\frac{1}{2}$ was determined to be optimum, this value will be used. Then, from Figure 3.4.3

$$\delta = 0.17 \quad (\text{B-2})$$

and from Equation 4-4 the noise bandwidth equals the natural angular frequency of the loop

$$B_n = \omega_n \quad (\text{B-3})$$

or, at the "match" point

$$B_{no} = \omega_{no} \quad (\text{B-4})$$

The allowable rms phase jitter at the match point will be designated to be 20° or 0.35 radians. Figure 3.4.2 then indicates that a $(S/N)_{out}$ of 7.5 db is required. The calculated phase jitter, σ_o , is found from the same figure to be 0.3 radians.

At the "match" point $\alpha = \alpha_o$; therefore,

$$\frac{\alpha}{\alpha_o} = 1 \quad (\text{B-5})$$

Utilizing the values determined here, Equation B-1 may be reduced to

$$R_{90} = \frac{\left[\frac{\pi}{2} - (2.2) (0.3) \right] \left[0.9 B_{no}^2 \right]}{2 \pi (1 + 0.17)} \quad (B-6)$$

$$= 0.111 B_{no}^2$$

or

$$B_{no} = \sqrt{9 R_{90}} \quad (B-7)$$

In terms of sweep bandwidth B_S and duration of a single sweep T_L this becomes

$$B_{no} = \sqrt{9 \frac{B_S}{T_L}} \quad (B-8)$$

This function is plotted in Figure B-1.

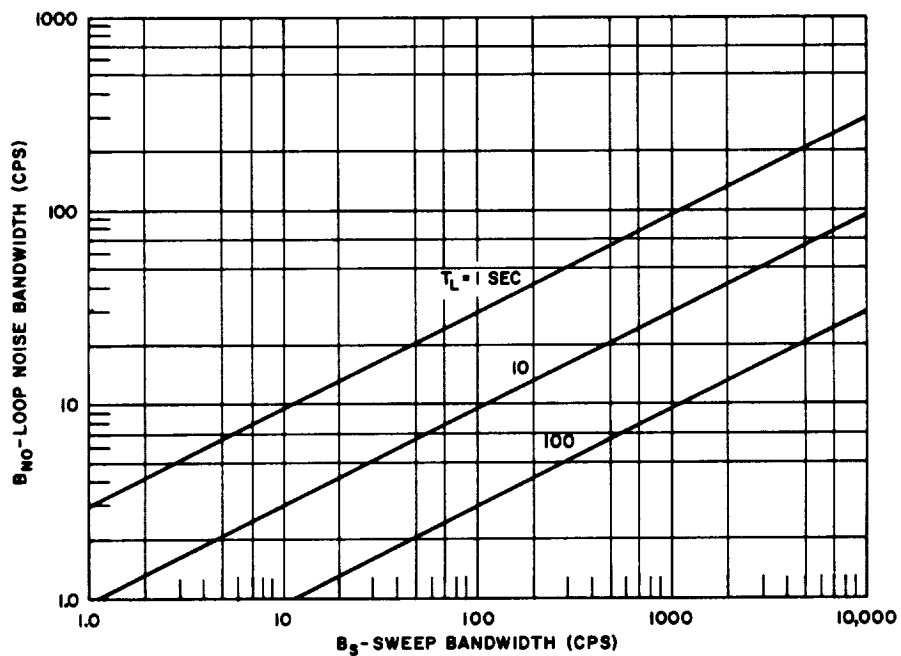


Figure B-1. Noise Bandwidth vs. Sweep Bandwidth

APPENDIX C

NOMENCLATURE

$H(S)$	Loop filter transfer function
K	Velocity gain constant
ω_1	Upper critical frequency of loop filter
ω_2	Lower critical frequency of loop filter
ζ	Loop damping factor
ω_n	Loop undamped natural frequency
ω_{no}	Loop undamped natural frequency at "match" point
B_n	Loop noise bandwidth
B_{no}	Loop noise bandwidth at match point
B_{IF}	Bandwidth of intermediate frequency section
B_S	Bandwidth to be swept by frequency sweep circuit
P_c	Carrier power for tracking
$(S/N)_{IF}$	Signal-to-noise ratio at the output of the IF section
$(S/N)_{out}$	Signal-to-noise ratio in the loop noise bandwidth
R_{90}	Sweep rate for 90 per cent probability of acquisition
σ_o	RMS phase jitter in the output signal
α	Signal suppression factor in limiter
α_o	Signal suppression factor for a damping factor of $\frac{1}{2}$
δ	Per cent overshoot in phase error for a VCO frequency ramp
f_d	Doppler frequency
$f_{d \max}$	Maximum doppler frequency
$\dot{f}_{d \max}$	Maximum doppler rate of change with time
T	Communication period (duration of subsonic capsule)
T_L	Time required for one complete sweep by sweep circuit
ϵ	Ratio of T_L to T
V_r	Relative spacecraft velocity in direction of capsule
V_S	Velocity of spacecraft
f_o	Carrier frequency
C	Speed of light

R	Range from capsule to spacecraft
R_o	Closest distance of approach of spacecraft to capsule
X_S	Position of spacecraft along trajectory
θ	Angle between the vectors R and R_o

REFERENCES

1. Frazier, J. P. and Page, J. ; "Phase-Lock Loop Frequency Acquisition Study," General Electric Company, TIS No. R61DSD25, 1 September, 1961.
2. Gruen, W. J. ; "Theory of AFC Synchronization," Proceedings of the IRE, August, 1953.
3. Jaffe, R. and Rectin, E. ; "Design and Performance of Phase-Lock Circuits Capable of Near-Optimum Performance Over a Wide Range of Input Signal and Noise Levels," IRE Transactions on Information Theory, Volume IT-1, pp. 66-67; March, 1955.
4. Woods, C. R. ; "A Mathematical Model Representing Oscillator Short-Term Stability," General Electric Company, TIS No. R61DSD35, 20 September, 1961.
5. "Stable Oscillator Investigation," Jet Propulsion Laboratory Research Summary 36-3.
6. Eveleigh, V. W. ; "Adaptive Phase Locked Loop Study," General Electric Company, TIS No. R62ELS-3, 2 January, 1962.

3.5 MODULATION SYSTEM ANALYSES

3.5.1 Introduction

Many possibilities exist for an appropriate modulation system for the capsule telemetry link, since most of the constraints usually imposed by existing ground receiving installations or local frequency and bandwidth allocations are not present. This has allowed the approaches to be based primarily on theoretical and technological considerations.

Although it was neither possible nor practical to analyze all the possible modulation techniques, several of the more promising approaches were analyzed and are presented in this section. These systems include those suggested early in the program by JPL, when it was indicated that a broad look at suitable systems was desired, including such well-known and readily implemented techniques as FM/FM, as well as the less-common systems showing high theoretical efficiencies.

As noted in Section 3.4, "Signal Tracking and Acquisition," due to the nature of the capsule's mission, frequency uncertainties will exist between the signal arriving at the spacecraft or Earth receiver and that predicted at the receiver. The modulation techniques analyzed in this section involve two general approaches to this frequency uncertainty problem - noncoherent receiving systems and coherent receiving systems.

In the noncoherent receiving systems, the receiver bandwidth is made wide enough to include any predicted incoming signal. This, of course, can lead to excessive noise bandwidths and, therefore, excessive transmitter power requirements to overcome thresholding. The noncoherent techniques included in this report are PPM/AM, FM, FM/FM, and FSK.

In the coherent receiving systems, the frequency of the incoming signal is tracked, so that the receiver bandwidth can be made as narrow as desired. The major problem in a coherent system then becomes that of signal acquisition instead of the thresholding problem of a noncoherent system. A coherent receiving system usually requires more complex equipment, but may be required if other simpler methods prove unsatisfactory. Coherent systems included in this report are phase modulation and frequency modulation with feedback.

Analyses of both the direct and relay links have been included, using the nominal parameters listed in Section 3.1. The results are presented as required transmitter output power versus data rate, a form useful to the vehicle system engineers. To allow for changes from the typical values which have been chosen for the comparison of the various systems, a table of conversion factors appears in Section 3.2.

Estimates of suitable capsule transmitter equipment are included in Section 3.10, and spacecraft receiving equipment suitable for the relay function is described in Section 3.12.

The modulation techniques analyzed for this application are defined as follows:

PPM/AM Technique

PPM/AM is a form of pulse modulation in which the time of occurrence of an RF pulse is varied in proportion to the magnitude of the sampled modulating signal.

Pulse-Code Modulation Techniques

PCM/PS: A PCM/PS system is based on the use of pulse-code modulation (PCM) with phase-shift (PS) keying of the transmitted radio-frequency carrier signal. Each sample of the information to be transmitted is encoded into a series of positive or negative pulses. Each change between positive and negative values causes a 180° phase shift in the carrier, which results in a double-sideband suppressed-carrier (DSSC) transmission.

PCM/PS/PM: A PCM/PS/PM system involves a PCM/PS signal on a sub-carrier, which in turn phase-modulates the main carrier.

PCM/FM: A PCM/FM system is based on the use of pulse-code modulation (PCM) which is low-pass filtered prior to frequency-modulating the carrier.

PCM/FM/PM: A PCM/FM/PM system involves a PCM/FM signal on a subcarrier, which in turn phase-modulates the main carrier.

PCM/FSK: A PCM/FSK system employs a PCM signal which frequency-modulates the carrier without being previously low-pass filtered (i.e., each binary digit frequency-shift keys the transmitter). Only two frequencies are required, since this is a binary system.

Frequency Modulation Techniques

FM: Frequency modulation (FM) is angle modulation in which the instantaneous frequency of a sinusoidal carrier is caused to depart from the carrier frequency by an amount proportional to the instantaneous value of the modulating wave. For this application it will be assumed that the individual channels are frequency-division multiplexed (FDM) before modulating the carrier. In this case they will amplitude-modulate the subcarriers. This will yield a resultant modulation of AM/FM.

FM/FM: In an FM/FM system, the transmitter is frequency-modulated simultaneously with the output of one or more subcarrier oscillators (SCO) which in turn have been frequency-modulated by data signals.

Frequency-Shift Keying Techniques

FSK: Multi-level FSK or quantized FSK (noncoherent) is used with a sampled-data system (time-division multiplex) in which the transmitted frequency is shifted in accordance with the quantized amplitude of each sample in turn. Note that binary (i.e., two-level) FSK is essentially PCM/FSK.

Phase-Shift Keying Techniques

PSK: Multi-level PSK or quantized PSK is a coherent sampled-data system in which the carrier phase is shifted in accordance with the quantized amplitude of each sample in turn.

3.5.2 PPM/AM Telemetry System Analysis

3.5.2.1 Introduction

Pulse position modulation - amplitude modulation (PPM/AM) is a particular form of pulse modulation in which the time of occurrence of an RF pulse is varied in proportion to the amplitude of the sampled modulating signal. It can achieve very high output S/N ratios and has the property of being able to work through channels where multipath or common RF channel interference is a problem.

It has been shown* that for a given required output S/N ratio, a PPM/AM telemetry system requires the lowest average power of all the various telemetry systems. This is due largely to the fact that the transmitter duty cycle for PPM/AM is quite low.

One of the main reasons that PPM/AM is not more widely used in terrestrial applications is because it does not trade bandwidth for power so efficiently as the PCM techniques do. However, this is not a constraint on the Venus relay link, since there are no known legislative limits on RF bandwidth occupancy at Venus. Therefore, PPM/AM should be considered a contender for this application.

3.5.2.2 Calculation of Output S/N Ratio

A convenient and realizable type of pulse to use as a basis of this analysis is the "raised cosine" pulse, shown in Figure 3.5.1. The mathematical expression for such an envelope is:

$$g(t) = \frac{A}{2} (1 + \cos 2\pi f_o t) \quad (3.5-1)$$

where,

$$f_o = 1/2T \quad (3.5-2)$$

*See, for example, Nichols and Rauch (Reference 6).

is the fundamental frequency of the cosine pulse. The corresponding Fourier transform is:

$$G(f) = \int_{-T}^T \frac{A}{2} (1 + \cos 2\pi f_0 t) \exp(-j 2\pi f t) dt \quad (3.5-3)$$

$$= \frac{A \sin(\pi f/f_0)}{2\pi f (1 - f^2/f_0^2)} \quad (3.5-4)$$

The power density spectrum for this is shown in Figure 3.5.2. It has its first nulls at $\pm f_0$ and is small outside this range. For practical purposes, the bandwidth required for transmission of the pulse may be taken as the range between the first nulls.

Pulses in channels adjacent in time can just touch when full-load signals are impressed on each. The "slicer" operates at half the pulse height, which, for the assumed pulse shape, is also the point of maximum slope. The time available for modulating the pulse position is equal to the channel time minus the pulse duration ($2T$). The appropriate combination of these factors leads to the PPM "slicer advantage" which, when applied to the RF pulse-to-noise ratio, gives the output S/N ratio in each channel.

As shown in Figure 3.5.3 a small noise voltage V_n displaces the time of observation by an increment τ , where

$$\frac{V_n}{\tau} \approx g'(-T/2) = \pi f_0 A \quad (3.5-5)$$

in which $g'(t)$ is the time derivative of $g(t)$. The mean-square position error produced by noise may be obtained from Equation (3.5-5) as:

$$\overline{\tau^2} = \frac{\overline{V_n^2}}{(\pi f_0 A)^2} \quad (3.5-6)$$

Now consider the detection technique illustrated (for a single channel) in Figure 3.5.4. Assuming a white noise spectral density N_o , with a predetection bandwidth B and a receiver input resistance R , the mean-square noise voltage at the slicer is:

$$\overline{V_n^2} = N_o B R \frac{f_o}{B} = N_o f_o R \quad (3.5-7)$$

Substitution of this into Equation (3.5-6) yields the mean-square pulse-position error due to this noise:

$$\overline{\tau^2} = \frac{N_o f_o R}{(\pi f_o A)^2} = \frac{N_o R}{\pi^2 f_o A^2} \quad (3.5-8)$$

For a modulating signal causing a peak pulse-position displacement of $\pm t_m$, with all signal levels assumed equally likely, the mean-square signal output voltage (power across a unit resistance) is:

$$\overline{S^2} = \frac{1}{2t_m} \int_{-t_m}^{t_m} S^2 dS = t_m^2/3 \quad (3.5-9)$$

The output S/N ratio $(S/N)_o$ may now be calculated from Equations (3.5-8) and (3.5-9):

$$(S/N)_o = \frac{\overline{S^2}}{\overline{\tau^2}} = \frac{t_m^2 \pi^2 f_o A^2}{3 N_o R} \quad (3.5-10)$$

Since the peak signal envelope power received is A^2/R , and the predetection noise power is $N_o B$, Equation (3.5-10) may be written:

$$(S/N)_o = \frac{t_m^2 \pi^2 f_o B A^2/R}{3 N_o B} = (S/N)_i \pi^2 t_m^2 f_o B/3 \quad (3.5-11)$$

where $(S/N)_i$ is the peak signal to rms noise ratio in the receiver IF section. This demonstrates the S/N improvement factor of PPM. In decibel form, Equation (3.5-11) may be written:

$$(S/N)_o = (S/N)_i + 20 \log t_m + 10 \log f_o + 10 \log B + 5.1 \text{ (db)} \quad (3.5-12)$$

It should be noted here that, when operating with large doppler shifts and narrow information bandwidths, the IF bandwidth will be determined by the doppler, rather than by the pulse width. In the absence of doppler, the IF bandwidth could be made approximately $2f_o$.

This analysis has, of course, assumed a peak pulse to noise ratio sufficiently high so that noise by itself rarely rises to the slicing level; nor is it large enough in the negative direction to suppress a pulse completely. When the pre-detection bandwidth becomes large, a substantial number of false pulses caused by noise begins to occur. This is the threshold point, at which the signal will tend to lose its information-bearing properties completely. This important problem is considered in the next section.

3.5.2.3 Thresholding

As with all systems that exchange bandwidth for noise improvement, PPM experiences a marked improvement threshold. In the PPM/AM detection technique of Figure 3.5.4, two thresholds must be considered, viz, the RF threshold of the linear detector and the PPM threshold at the slicer. In conventional PPM/AM systems, the IF bandwidth is $2f_o$, so these two thresholds are related and need not be considered separately. However, when the required IF bandwidth is determined by the doppler shift, then both thresholds must be calculated.

The RF detection threshold is based on the point where the peak noise amplitude equals the peak signal amplitude. A "crest factor" of four is usually assumed for random noise, meaning that the peak-to-rms noise voltage ratio is 4(12db). Assuming the random noise has a normal probability distribution, the probability of the noise voltage exceeding a crest factor of 4 is about 6.3×10^{-5} ,

which is indeed quite small. Since the peak-to-rms voltage ratio of the sinusoidal RF signal is 3db, and the peak-to-rms voltage ratio of the noise is 12db, when these peaks are equal the ratio of rms signal voltage to rms noise voltage is 9db. AM thresholding is a rather gradual process (unlike FM or PM), so just how far above this point one should call "threshold" is somewhat arbitrary, depending upon how much signal degradation can be tolerated. Since the system of Figure 3.5.4 includes post-detection filtering, much of the random noise which arrives in the absence of signal will not be passed by the low-pass filter anyway. Because of this and the fact that AM thresholding is so gradual, an RF threshold of 9db (PEP/rms noise) appears adequate here.

The PPM threshold (at the slicer) is dictated by the general requirement that the noise voltage alone cannot have a significant probability of rising above the slicing level. Therefore, the PPM threshold will be taken to occur when the peak noise (crest factor of 4) equals half the demodulated pulse amplitude. The probability of noise exceeding this level will then be 3.4×10^{-4} *. As a rough approximation of the error rate in the slicer, we may consider each cps of low-pass filter bandwidth to be represented by two degrees of freedom, that is, there are two samples/sec of noise per unit bandwidth, or a total of $2f_o$ samples/sec of noise. The rate of occurrence of samples above the slicing level is then $2f_o \times 3.4 \times 10^{-4} = 6.8 \times 10^{-4} f_o$. For f_o on the order of 50 cps, this would yield an error rate of about 0.034 pps, or about one error every 30 seconds, which appears to be a reasonable threshold in this application. Therefore, the PPM threshold will be set at a peak signal/rms noise ratio of 18db (for a peak signal amplitude of twice the peak noise amplitude).

A comparison of the IF bandwidth (of perhaps 10 kc) with the post-detection bandwidth (of perhaps 50 cps) shows that, unless the IF bandwidth is considerably narrower than this, the RF detection threshold (9db in the IF bandwidth) will be the limiting factor.

*Based on a Rayleigh distribution, which is the distribution of the noise envelope.

3.5.2.4 Transmitter Power Calculations

The required S/N ratio at the receiver will be determined by the two threshold requirements determined in the preceding section. The pertinent bandwidths are shown in Figure 3.5.5.

Due to doppler effect, the signal spectrum may be received anywhere within the IF bandwidth B. For a wide IF bandwidth, the RF threshold will determine the required S/N ratio; while, for a relatively narrow IF bandwidth, the PPM threshold will determine the required S/N ratio. Since there is a 9db difference between the RF threshold and the PPM threshold, the PPM threshold will become dominant for systems where

$$10 \log \frac{B}{f_o} < 9\text{db} \quad (3.5-13)$$

The nominal parameters for the capsule-to-spacecraft communication link which have been assumed for this calculation are given in Section 3.1.

From those parameters the following transmitter power requirement can be calculated as in Table 3.5.1.

Table 3.5.1

Transmitter peak envelope power (PEP)	10 log P	dbw
Capsule Antenna Gain	0 db	
Path Attenuation	-152.5 db	
Receiving Antenna Gain	0 db	
Misc. RF Losses	-3 db	
Peak Signal Power Available at Receiver:	<hr/> 10 log P-155.5 dbw	

Receiver noise density per cps (KTF)	-194 dbw
Bandwidth	10 log B
S/N required (in B)	+9 db
Margin	+8 db
Peak signal power required at receiver:	<hr/> 10 log B - 177 dbw

Therefore,

$$10 \log P - 155.5 = 10 \log B - 177 \quad (3.5-14)$$

which yields:

$$10 \log P = 10 \log B - 21.5 \text{ dbw} \quad (3.5-15)$$

Equation (3.5-15) has been plotted in Figure 3.5.6.

3.5.2.5 Typical System Block Diagrams

Figure 3.5.7 shows one possible block diagram of a typical n-channel PPM/AM transmitting system*. The frame sampling rate is established by a ring counter chain which is triggered by a master pulse generator. The pulses from the generator cause successive stages to conduct in sequence and to generate pulses distributed uniformly in time. The pulse from one of the counter chain stages is coded and is used as a frame synchronizing signal. Each channel pulse produced in the counter chain passes to a corresponding pulse position modulator which generates a pulse delayed with respect to the pulse from the counter chain, the delay being proportional to the modulating signal from the corresponding sensor. The n pulses from the pulse position modulators, together with the coded frame synchronizing signal, pass to a mixer and then to the amplitude modulator of the transmitter, as shown in Figure 3.5.7.

Figure 3.5.8 shows a block diagram for a typical n-channel PPM/AM receiving system. The multi-channel sequence of pulses from the radio receiver passes to a channel synchronizing pulse generator which electronically separates

*Reference 7, pp. 307-308.

the coded frame synchronizing pulse from the incoming pulse train and develops a sequence of channel synchronizing pulses which mark the reference time for the separate channels. Each of these channel synchronizing pulses triggers a variable pulse-width generator in which the pulse width is initiated by the channel synchronizing pulse and terminated by the corresponding channel signal pulse which is also fed into the pulse-width generator. Thus, for each channel, a pulse is generated having a width which varies in accordance with the modulation produced by the corresponding instrumentation sensor. These variable-width channel pulses, recurring at the sampling rate generated at the transmitter, pass to suitable metering circuits, where they are then converted to analog signals.

3.5.1.6 Bibliography

1. Black, H. S. Modulation Theory, D Van Nostrand Co., Inc., New York, N. Y., 1953.
2. Bennett, W. R. "Effect of Random Noise on Sinusoidal and Pulse Systems," Lecture given at MIT Special Summer Program 6.57s, Aug., 1960.
3. Golay, M. "Note on the Theoretical Efficiency of Information Reception with PPM," Proc. IRE, Sept., 1949.
4. Jacobs, I. "Theoretical and Practical Limitations of Weak-Signal Processing Techniques," COSPAR Symposium, April 10, 1961.
5. Kotelnikov, V.A. The Theory of Optimum Noise Immunity, McGraw-Hill Book Co., New York, N. Y., 1959.
6. Nichols, M. H. and Rauch, L. L. Radio Telemetry, John Wiley and Sons, Inc., New York, N. Y., 1956.
7. Pawley, M. G. and Triest, W. E. "Multichannel Radio Telemetering," Chapter in Advances in Electronics, Vol. IV, Edited by L. Marton, Academic Press, Inc., New York, N. Y., 1952.
8. Putschi, H. N. "Evaluation and Development of a PCM-PS Radio Telemetry System," GE TIS No. R59ELS-34, May 7, 1959.
9. Schwartz, M. Information Transmission, Modulation, and Noise, McGraw-Hill Book Co., New York, N. Y., 1959.
10. Uglow, K. M. "Transmission Systems for Re-entry Telemetry," Report 1201-3, July 30, 1958 (under a consulting contract with G.E.).

3.5.3 PCM Telemetry System Analyses

3.5.3.1 General PCM Considerations

Some general considerations of PCM systems are presented in the opening sections.

3.5.3.1.1 Data Handling in Spacecraft for Relay Link

There are basically two methods by which the relay function can be performed in the spacecraft. These are the "repeater" method and the "demodulator" method. A functional block diagram of each is shown in Figure 3.5.9. In the former the signal is received, amplified and retransmitted. In the latter the signal is received, amplified, demodulated, and then retransmitted utilizing either the original or a new modulation technique. There are several ways to perform the latter. These include (assuming PCM/PS/PM is used on the spacecraft-to-Earth link):

1. Time multiplexing the capsule information onto the same carrier used for the spacecraft information [either directly or via an A/D encoder depending on whether bit or word (such as PPM/AM) demodulation is used).]
2. Frequency multiplexing the signal outside the spacecraft data spectrum on a separate subcarrier.
3. Transmitting the capsule data back by itself (either immediately or after recording).

Since two receivers (spacecraft and ground) are required in both the repeater and demodulator systems, noise will be added to the signal twice prior to bit detection on the ground. In the case of the repeater, the noise is considered to be thermal in both receivers; however, for the demodulator system the "noise" contributed at the spacecraft will be in terms of the bit error rate at that point in the system and is additive to the bit error rate caused by noise at the ground receiver. Therefore, it is apparent that the signal-to-noise ratio in each separate link must be greater than the final over-all signal-to-noise ratio required.

In order to indicate the increased performance required for the repeater and demodulator techniques, both cases will be evaluated and compared.

1. Repeater Techniques

A signal flow diagram for the linear repeater system is shown in Figure 3.5.10. $(S/N)_0$ is the minimum allowable signal-to-noise ratio for a particular probability of error (P_{eo}). $(S/N)_1$ and $(S/N)_2$ are the signal-to-noise ratios at the repeater and ground receiver, respectively, based on power transmitted and noise from natural sources.

The noise N_1 transmitted from the spacecraft is therefore included in the signal power received at the ground station S_2 and not in the value of the noise N_2 when calculating $(S/N)_2$.

Then,

$$(S/N)_2 = \frac{K (S_1 + N_1)}{N_2} \quad (3.5-16)$$

The overall signal-to-noise ratio, i.e., that which will actually determine the ultimate probability of error, includes the noise from both sources (N_1 and N_2).

This is given by

$$\begin{aligned} (S/N)_0 &= \frac{S_{\text{total}}}{N_{\text{total}}} = \frac{KS_1}{KN_1 + N_2} \\ &= \frac{1}{\frac{KN_1}{KS_1} + \frac{N_2}{KS_1}} \end{aligned} \quad (3.5-17)$$

Assuming

$$S_1 \gg N_1$$

then from Equation 3.5-16

$$S_2 \approx KS_1 \quad (3.5-18)$$

and Equation (3.5-17) may be rewritten as

$$(S/N)_o = \frac{1}{(N/S)_1 + (N/S)_2}$$

or

$$\frac{(S/N)_1}{(S/N)_o} = \frac{1}{1 - \frac{(S/N)_o}{(S/N)_2}} \quad (3.5-19)$$

This function is plotted in Figure 3.5.12. It describes the possible relationship between the S/N ratios at the spacecraft and the ground station.

The significance of the assumption that $S_1 \gg N_1$ should be noted. The assumption is that the total power transmitted from the spacecraft $P_t = K_1(S_1 + N_1)$ consists mainly of signal and that the fraction of power in the noise transmitted is negligible. This is a reasonably good assumption if the bandwidth of the spectrum is limited to approximately the bit rate at IF. In this case the signal-to-noise ratio in the IF should be at least 9 or 10 db for a practical error rate. The error resulting from the approximation is then about 0.5 db. However, the $(\sin x/x)^2$ spectrum of keyed pulses should have at least two or three times the IF bandwidth indicated above, so that an integrate-and-dump circuit is reasonably matched to the signal. This would indicate that other shaped pulses which have relatively narrow spectra and detection methods reasonably matched to these pulses might give equal or better performance if a repeater technique is used.

2. Demodulator Technique

The signal flow diagram for the demodulator technique is shown in Figure 3.5.11. The maximum probability of bit error P_{eo} is related to the error probabilities in the individual bit detectors by:

$$P_{eo} = P_{e1} + P_{e2} - P_{e1} P_{e2} \quad (3.5-20)$$

where P_{e1} and P_{e2} are the probabilities of bit error corresponding to $(S/N)_1$ and $(S/N)_2$ in the spacecraft and ground receivers, respectively. Since P_{e1} and P_{e2} will both be less than 10^{-2} for the problem of interest, the above equation may be rewritten as

$$P_{eo} = P_{e1} + P_{e2} \quad (3.5-21)$$

i.e., double errors may be neglected.

In the repeater analysis of the previous section, the final results were independent of the numerical value of P_{eo} and the error probability versus signal-to-noise ratio characteristic of the bit detector. This is not true for the present case; therefore, an overall probability of bit error equal to 1.43×10^{-3} (word error probability equals 10^{-2} for 7-bit word) will be assumed. Also, the P_e versus $(S/N)_o$ characteristic is assumed to be the same as that for a matched filter as shown in Figure A-1, Appendix A, except that it will be displaced to the right in the figure by a factor equal to its efficiency. For instance, if the bit detector is 2 db less efficient than a matched filter, it requires a signal-to-noise ratio of 11.8 db to attain a bit error probability of 10^{-3} as compared to the 9.8 db required with a matched filter. Since a spaceborne demodulator will undoubtedly be less efficient than one on the ground, three cases will be considered: demodulation 0 db, 1.5 db, and 3.0 db less efficient in the spacecraft than on the ground. Letting $(S/N)_o$ be the reference signal-to-noise ratio required in the ground receiver for a 1.43×10^{-3} error rate (including efficiency), and

utilizing the curve of Figure A-1, Figure 3.5.12 has been plotted to show the relationships between $\frac{(S/N)_1}{(S/N)_0}$ and $\frac{(S/N)_2}{(S/N)_0}$ which satisfy Equation (3.5-21).

3.5.3.1.2 Output Signal-to-Noise Ratio in PCM Systems

In pulse-code modulation (PCM) communication systems there are two general types of noise to contend with, viz:

1. Noise due to quantization of the signal
2. Noise due to digit error rate.

Most systems are normally operated such that the former predominates. However, for a deep-space telemetry link, where low received S/N ratios (with accompanying high digit error rates) may be anticipated, it is worthwhile to investigate the resultant noise power caused by the digit error rate. This will give an indication of the number of quantization levels it is practical to use to be consistent with an anticipated error rate.

Calculation of the effective rms output S/N ratio of a PCM system will also serve as a tool in making a quantitative comparison between the performance of a PCM system and that of analog systems. For this purpose it is convenient to relate the digit error probabilities to the rms signal output errors they cause. The result can then be combined with the PCM quantization error to obtain a composite rms output S/N ratio for a PCM system.*

It is, of course, well-known that a PCM system is a sharp threshold system. As long as the signal is strong (thus keeping the digit error rate low), the

*This is not quite a fair comparison, because the noise in digital systems is of a different nature than the fluctuation noise of analog systems. An example of this is the contouring effect noticeable in PCM television pictures. However, for usual telemetry data this effect would not be so objectionable.

output S/N ratio will be determined by the quantization noise. It can get no better than this, no matter how strong the signal becomes. However, as the signal strength is decreased, the point is reached where the noise due to the increased digit error rate becomes excessive, and the output S/N ratio drops off sharply.

Thus, for comparison purposes the system performance may be measured by its margin above the signal strength which would provide the desired digit error rate.

Output Signal Power

In order to encode a continuous signal, its samples must first be quantized into discrete amplitude levels. The power in such a signal depends on the probability distribution of the original signal. In this particular analysis it will be assumed that all signal levels have equal probability of occurrence, i.e., a uniform probability distribution.*

The average value of the signal will be taken to be zero, and the signal will be linearly quantized in the general manner shown in Figure 3.4.13.

For an even number of levels L^{**} , the quantized signal levels as shown in Figure 3.5-13 are given by:

$$\pm q/2, \pm 3q/2, \pm 5q/2, \dots, \pm (L-1) q/2 \quad (3.5-22)$$

and the mean-square signal is thus:

$$\overline{s^2} = \frac{2}{L} \frac{[1^2 + 3^2 + 5^2 + \dots + (L-1)^2]}{L} \left[\frac{q^2}{4} \right] \quad (3.5-23)$$

$$= \frac{2}{L} \left[\frac{L(L^2-1)}{6} \right] \left[\frac{q^2}{4} \right] \quad (3.5-24)$$

$$= (L^2 - 1) q^2 / 12 \quad (3.5-25)$$

*This is a reasonable assumption if nothing more is known regarding the statistics of the signals to be transmitted.

**For the usual binary system, L will always be even. However, even if a different base is used, yielding an odd number of levels, the analysis is similar and the results are identical to Equation (3.5-25).

Quantization Noise

Once quantized, the instantaneous values of the continuous signal can never be restored exactly. This gives rise to random errors which are called quantization noise. Instead of fluctuation noise which an analog system would have, there is now artificially introduced quantization noise. This can be reduced to any desired degree, however, by choosing the quantum steps to be sufficiently fine. The available output S/N ratio will be a function of the quantization noise, i.e., a function of the number of quantum steps used to represent the signal.

Assuming that over a long period of time all amounts of quantization error up to \pm half a quantum step are equally likely, the probability distribution of the quantization error (noise) is uniform, as shown in Figure 3.5.14.

The mean-square quantization noise is given by:

$$N_q = \overline{e^2} = \frac{1}{q} \int_{-q/2}^{+q/2} e^2 de = q^2/12 \quad (3.5-26)$$

where q is the height of a quantum step.

Output Noise Due to Bit Error Rate

To relate bit error rate to equivalent analog S/N ratio, the following assumptions will be made:

1. For each digit, $P(\text{mark}) = P(\text{space}) = 1/2$.
2. All digits in a word have equal probability of being in error.
3. Not more than one bit error occurs in a word (containing n bits).

The weight of the k th digit in a binary word is*:

$$W(k) = 2^{k-1} q \quad (3.5-27)$$

where $k = 1, 2, 3, \dots, n$

*This is valid for a binary system regardless of where the zero level of the scale is located.

Now, given that a particular word contains one bit in error, the mean-square word error (i.e., average over the n bits of the word) is:

$$\overline{e^2} = \frac{1}{n} \left[1^2 + 2^2 + 4^2 + \dots + (2^{n-1})^2 \right] q^2 \quad (3.5-28)$$

If there are W_e words in error out of a total number of W words, then the mean-square total error (i.e., average over the entire message of W words) is:

$$\left\langle \overline{e^2} \right\rangle = \frac{W_e}{W} \overline{e^2} = P_W \overline{e^2} \quad (3.5-29)$$

for large W , where P_W is the probability of word error. But, for reasonably small probabilities of error, the bit error rate is related to the word error by:

$$P_W = n P_e \quad (3.5-30)$$

Therefore, Equation (3.5-29) may be written:

$$N_e = \left\langle \overline{e^2} \right\rangle = n P_e \overline{e^2} \quad (3.5-31)$$

Substitution of Equation (3.5-28) into this yields:

$$N_e = \left[1^2 + 2^2 + 4^2 + \dots + (2^{n-1})^2 \right] q^2 P_e \quad (3.5-32)$$

$$= \left[(2^2)^0 + (2^2)^1 + (2^2)^2 + (2^2)^3 + \dots + (2^2)^{n-1} \right] q^2 P_e \quad (3.5-33)$$

This type of series may be written in closed form as:

$$(1 + r + r^2 + r^3 + \dots + r^{n-1}) = \frac{r^{n-1}}{r-1} \quad (3.5-34)$$

In this case:

$$r = 2^2 \quad (3.5-35)$$

So Equation (3.5-33) becomes:

$$N_e = \frac{2^{2n} - 1}{2^2 - 1} q^2 P_e \quad (3.5-36)$$

$$= \frac{L^2 - 1}{3} q^2 P_e \quad (3.5-37)$$

where L is the number of levels, given by:

$$L = 2^n \quad (3.5-38)$$

Composite Output S/N Ratio

The decoded output (from the D/A converter) contains the signal power given by:

$$S = \frac{(L^2 - 1) q^2}{12} \quad (3.5-25)$$

the quantization noise, given by:

$$N_q = q^2/12 \quad (3.5-26)$$

and the error-rate noise, given by:

$$N_e = \frac{L^2 - 1}{3} q^2 P_e \quad (3.5-37)$$

The total output noise power is given by the sum of (3.5-26) and (3.5-37).

$$N = N_e + N_q = \left[\frac{1}{4} + (L^2 - 1) P_e \right] q^2/3 \quad (3.5-39)$$

Therefore, the composite output S/N ratio is given by:

$$S/N = \frac{S}{N_e + N_q} \quad (3.5-40)$$

$$= \frac{(L^2 - 1) q^2}{12 \left[\frac{1}{4} + (L^2 - 1) P_e \right] q^2 / 3} \quad (3.5-41)$$

$$S/N = \frac{(L^2 - 1)}{1 + 4 (L^2 - 1) P_e} \quad (3.5-42)$$

where $L \equiv 2^n$.

This has been plotted for several values of n in Figure 3.5.15.

For low bit-error probabilities, the quantization noise predominates, and Equation (3.5-42) reduces to:

$$\begin{aligned} S/N_q &= L^2 - 1 \\ &\doteq 2^{2n} \end{aligned} \quad (3.5-43)$$

For high bit-error probabilities, the error-rate noise predominates, and Equation (3.5-42) reduces to:

$$S/N_e = \frac{1}{4 P_e} \quad (3.5-44)$$

This sets the PCM video threshold, as indicated in Figure 3.5.15.

Figure 3.5-15 relates the output S/N ratio to the bit error rate and the number of bits per word. It is applicable to all PCM systems. For a given RF modulation scheme, one must determine the relationship between predetection (IF) S/N ratio and output bit error rate. Then Figure 3.5.15 permits relating this IF S/N ratio directly to the output S/N ratio it will produce.

Accuracy of PCM Data

Assuming that the output of the transducer can be quantized (in the A/D encoder) to \pm one-half a quantum step, the accuracy of the data may be expressed as:

$$\begin{aligned} E &= \pm \frac{1}{2} \cdot 1/L \\ &= \pm \frac{1}{2^{n+1}} \end{aligned} \quad (3.5-45)$$

where $L \equiv 2^n$.

Therefore, the accuracies are as shown below:

Table 3.5.2. Quantization Error

<u>n</u>	<u>E</u>
4	$\pm (1/2)^5 \doteq \pm 3\%$
5	$\pm (1/2)^6 \doteq \pm 1.5\%$
6	$\pm (1/2)^7 \doteq \pm 0.8\%$
7	$\pm (1/2)^8 \doteq \pm 0.4\%$
8	$\pm (1/2)^9 \doteq \pm 0.2\%$

3.5.3.2 Phase-Shift RF Keying

3.5.3.2.1 PCM/PS

This term is used for the modulation with binary signals of an AM channel with carrier suppression. For a binary "1" full amplitude RF carrier signal of reference phase α is transmitted; for a binary "0" the transmitted phase is $180^\circ + \alpha$. If the modulation wave-shape is a square wave, then the changeover is instantaneous and can be considered PM with $\pm \pi/2$ phase deviation.

Detection of PS signals requires the re-insertion of a carrier of equal frequency and phase as the originally suppressed carrier. Since a product detector can be used, threshold-free detection is possible. The basic block diagram

of the phase-lock servo loop of a synchronous detection receiver for PCM/PS is shown in Figure 3.5.16.

PCM/PS is the most efficient of the PCM phase-lock techniques. It is unique in that all the transmitted power can be utilized both for transmission of data and as a tracking signal. When used with a matched filter, the error rate is equal to that shown in Figure A-1, where the noise bandwidth is equal to one-half the bit rate. Also, the carrier power derived from the signal is equal to the power received.

PCM/PS Relay Link

Each of the systems utilizing phase-shift keying requires carrier acquisition. The minimum power which can be transmitted will therefore be determined by the signal tracking and acquisition requirements of the system. The nominal relay link parameters given in Section 3.1 will be used in calculating the required transmitter power.

A bit error probability of 10^{-4} will also be assumed. This error rate will result in a negligible degradation of the signal, since the spacecraft-to-earth link is designed for a bit error probability of 1.43×10^{-3} . From Figure A-1 the required signal-to-noise ratio is found to be 11.4 db. The noise bandwidth of the data system will be taken at its theoretical value, $b = r/2$ where r is the data rate in bits per second.

The transmitter power calculation using the parameters defined in Section 3.1 is given below.

Table 3.5.3

Transmitter Power	10 log P	dbw
Capsule Antenna Gain	0	db
Path Attenuation (50,000 km)	-166.4	db
Receiving Antenna Gain	0	db
Misc. RF Losses	-3	db

Signal Power Available at Receiver: 10 log P - 169.4 dbw

Receiver Noise per cps (KTF)	-194	dbw
Bandwidth (b = r/2)	10 log r/2	db
S/N required (in b)	11.4	db
Margin	8	db

Signal Power Required at Receiver: $10 \log r/2 - 174.6 \text{ dbw}$

then

$$10 \log P - 169.4 = 10 \log r - 3 - 174.6$$

or

$$10 \log P = 10 \log r - 8.2 \quad (3.5-46)$$

As mentioned previously, the lower limit on power transmitted is determined by the acquisition requirement of the system. This is found from the "Signal Tracking Acquisition" Section and is

$$P = 0.75 \text{ watts for } \epsilon = 10\%$$

$$P = 2.4 \text{ watts for } \epsilon = 1\%$$

$$P = 7.5 \text{ watts for } \epsilon = 0.1\%$$

where ϵ is the percentage of the communication time required for acquisition. Equation (3.5-46) is plotted in Figure 3.5.17 with the above power levels determining the lower limits.

PCM/PS Direct Link

As noted in the "Signal Tracking and Acquisition" Section, all modulation techniques requiring coherent detection may be severely limited unless rugged oscillators with adequate stability can be found. However, the minimum phase-lock loop bandwidth given for the DSIF (3 cps) will be used here in order to compare the systems. The transmitter power requirements are determined below:

Table 3.5.4. PCM/PS Direct Link

Transmitter Power	10 log P dbw
Vehicle Antenna Gain	0.0 db
Path Attenuation (60×10^6 KM)	-255.3 db
Receiving Antenna Gain (85-ft dish)	51.8 db
Misc. RF Losses	<u>-3.0 db</u>
Signal Power Available at Receiver: 10 log P - 206.5 dbw	
Receiver Noise per cps ($T_e = 50^\circ\text{K}$)	-211.6 dbw
Bandwidth ($b = r/2$)	10 log r/2 db
S/N Required [for $P_e = 1.43 \times 10^{-3}$, (Figure A-1)]	9.5 db
Margin	<u>8.0 db</u>
Power Required at Receiver: 10 log r/2 - 194.1 dbw	

then,

$$10 \log P = 206.5 = 10 \log r - 3 - 194.1$$

or

$$10 \log P = 10 \log r + 9.4 \text{ dbw} \quad (3.5-47)$$

This relationship is plotted in Figure 3.5.18. The minimum transmitter power shown (33 watts) is that required for signal tracking as determined in Section 3.4 for a 3 cps loop bandwidth. Performance with a 210-ft. dish (61 db gain) is also indicated in the graph.

3.5.3.2.2 PCM/PS/PM

The PCM/PS/PM modulation technique requires that the binary information first be placed on a subcarrier by means of phase-shift modulation. This, in turn, is used to phase-modulate the carrier. This technique derives its advantage from the fact that it provides a clean carrier for signal tracking. Its disadvantage, compared to PCM/PS, is that the power in the carrier cannot be utilized to transmit data. A modulation index of 1.4 will be utilized for the

calculations. The fraction of transmitted power used for the carrier is then

$$J_0^2(1.4) = (0.57)^2 = 0.324 \quad (3.5-48)$$

where J_0 is the Bessel function of zero order. Assuming that the information is recovered only from the first set of sidebands, the fraction of power in the data is

$$2J_1^2(1.4) = 0.583 \quad (3.5-49)$$

where J_1 is the Bessel function of the first order.

PCM/PS/PM Relay Link

The calculations for PCM/PS/PM are the same as those utilized for PCM/PS except that the loss of power due to the carrier and outer sidebands must be accounted for. The fraction of 0.583 determined previously results in an increase of 2.4 dbw of power required for the same data rates available with PCM/PS.

This gives (from Equation (3.5-46)):

$$10 \log P - 2.4 = 10 \log r - 8.2$$

or

$$10 \log P = 10 \log r - 5.8 \text{ dbw} \quad (3.5-50)$$

This function is plotted in Figure 3.5.17. The minimum allowable power is determined in the table below for the three acquisition capabilities used previously.

Table 3.5.5

ϵ	P_c (watts)	Required Power $= P_c / 0.324$ (watts)
10%	0.75	2.3
1%	2.4	7.4
0.1%	7.5	23.2

Note that the values given above were determined under the assumption that the modulation index remains at 1.4 for all bit rates. By reducing the modulation index as the data rate requirement rate is reduced, the ultimate threshold is equal to that for PCM/PS; however, at this limit (modulation index 0), all the power is in the carrier and no data transmission capability exists. The modulation index has been reduced in this manner in Figure 3.5.17.

PCM/PS/PM Direct Link

As in the Relay Link analysis, the only difference as compared to PCM/PS is the separate carrier and sideband power requirement. Utilizing Equation (3.5-47), the power required is given by:

$$10 \log P - 2.4 = 10 \log r + 9.4 \text{ dbw}$$

or

$$10 \log P = \log r + 11.8 \quad (3.5-51)$$

This is plotted in Figure 3.5.18.

The minimum allowable transmitter power for $M = 1.4$ is:

$$P = \frac{P_c}{J_o^2 (1.4)} = \frac{33}{0.324} \approx 100 \text{ watts} \quad (3.5-52)$$

In Figure 3.5.18 the modulation index has been reduced in a manner such that $P_c = 33$ watts for $P < 100$ watts. Performance with a 210-ft. dish (61 db gain) is also indicated.

3.5.3.3 Frequency - Modulation RF Keying

3.5.3.3.1 General Considerations

Figure 3.5.19 is a general block diagram of a PCM/FM system. Ideal bandpass filter characteristics will be assumed for the purpose of this analysis. Synchronizing signals are contained in the code, and a suitable method of extracting them at the receiver is assumed.

Ideally speaking, the bandwidths of the premodulation and post-detection filters should be equal to one-half the bit rate, since this is the highest fundamental frequency which can exist in the code.

McRae* has shown that the optimum value of deviation ratio to use is 0.7, as a compromise between RF thresholding (in the absence of doppler effect) and PCM video thresholding considerations.

McRae also showed that for a 0.7 deviation ratio, the RF bandwidth required to pass the signal** is approximately 1.4 times the bit rate. Since the IRIG standards recommend 1.5 times the bit rate, this latter bandwidth will be used. IRIG standards also recommend the following predetection S/N ratios for the indicated bit error probabilities:

Table 3.5.6. IRIG Predetection S/N Ratios for PCM/FM

13 db for $P_e = 10^{-5}$

15 db for $P_e = 10^{-6}$

17 db for $P_e = 10^{-7}$

(Note that these standards imply a detection system which is about 1.5 db less efficient than a matched filter).

Since the Mariner spacecraft-to-earth link operates at an error rate of 1.43×10^{-3} , it appears that S/N ratios as high as these standards will not be necessary. Therefore, 12 db will be used in these calculations. The digit errors contributed by the capsule-to-spacecraft link will still be insignificant compared to those of the spacecraft-to-earth link, and the FM discriminator will be operating at threshold. The probability of error will be about 10^{-4} .

*McRae, D. D., "Considerations of RF Parameters for PCM Telemetry Systems," IRE PGSET Transactions, June, 1959.

**i.e., to pass 90 per cent of the power in the highest fundamental frequency of the code.

3.5.3.3.2 PCM/FM Relay Link

The first PCM/FM system to be analyzed is that of the relay link, involving transmission from the capsule to the Mariner spacecraft. In this situation, the transmitter power requirement will be determined largely by the signal power required to prevent thresholding in the discriminator.

Conventional Discriminator

In this section an analysis will be made of a PCM/FM link employing a conventional discriminator (e.g., a Foster-Seeley discriminator or a ratio detector) in which the predetection bandwidth is made large enough to include the doppler shift. For purposes of comparing the system, the nominal relay link parameters of Section 3.1 have been assumed.

a. Thresholding

Using the same general line of reasoning as in the PPM/AM analysis, to prevent thresholding in a conventional FM discriminator the predetection C/N ratio requirement is usually taken to be 12 db*.

As shown in a previous section, the PCM video threshold (due to digit error rate) depends on the number of bits per sample (if this threshold is taken to occur at the point where digit error noise equals quantization noise). This yields:

Table 3.5.7

<u>No. Bits/word</u>	<u>P_e at Threshold</u>	<u>S/N Required**</u>
7	1.6×10^{-5}	12.4 db
6	6.0×10^{-5}	11.7 db
5	2.6×10^{-4}	10.8 db

*This will be discussed later in more detail with regard to FM in Section 3.5.4.3.

**From Figure A-1

The S/N out of the discriminator is related to the C/N into the discriminator by the well-known FM relationship:*

$$S/N = C/N + 10 \log 3M^2 + 10 \log B/2b \quad (3.5-53)$$

Since there is a 12 db predetection threshold, and the PCM video thresholds are as indicated in the above table, the PCM threshold will become dominant for:

$$(10 \log \frac{B}{2b} + 10 \log 3M^2) \begin{cases} 0.4 \text{ (for } n = 7) \\ -0.3 \text{ (for } n = 6) \\ -1.2 \text{ (for } n = 5) \end{cases} \text{ db} \quad (3.5-54)$$

For small deviation ratios and wide IF bandwidths, the second term is insignificant compared to the first term. Therefore, the PCM video threshold will become predominant only for IF bandwidths B approximately equal to twice the post-detection bandwidth. For low data rates and high doppler shifts this situation will not occur, so the transmitter power required will be determined by the RF threshold requirement.

b. Transmitter Power Calculations

Using the parameters previously listed, the following transmitter power calculation may be made for the relay link:

Table 3.5.8

Transmitter Power	10 log P dbw
Capsule Antenna Gain	0 db
Path Attenuation (at 50,000 km)	-166.4 db
Receiving Antenna Gain	0 db
Misc. RF Losses	<u>-3 db</u>
Signal Power Available at Rec.: 10 log P - 169.4 dbw	
Receiver Noise Density per cps (KTF)	-194 dbw
Bandwidth	10 log B db
S/N Required (in B)	+ 12 db
Margin	<u>+8 db</u>
<u>Signal Power Required at Rec.: 10 log B-174 dbw</u>	

*cf. Section 3.5.4.2.

Therefore:

$$10 \log P - 169.4 = 10 \log B - 174 \text{ dbw} \quad (3.5-55)$$

which yields:

$$10 \log P = 10 \log B - 4.6 \text{ dbw} \quad (3.5-56)$$

This has been plotted in Figure 3.5.20. (Note that the average power required is twice as great as the peak power required for PPM/AM.)

c. Numerical Example

As a typical example of the use of Figure 3.5.19, consider the maximum range rate to be equal to the spacecraft velocity of 8 km/sec. The maximum doppler shift of a 100 mc carrier frequency then will be:

$$f_d = \pm \frac{8}{3 \times 10^5} \times 100 \times 10^6 = \pm \frac{8000}{3} = \pm 2667 \text{ cps} \quad (3.5-57)$$

It should be possible to predict the trajectory such that the frequency uncertainty will be only half this value. Figure 3.5.20 then shows a typical value of 934 watts would be required from the transmitter under these conditions.*

Phase-Lock Discriminator

The thresholding problem encountered with the conventional discriminator can be reduced by using a phase-lock discriminator, although acquisition time now becomes a problem. However, since the input C/N requirement is not below the threshold of a conventional discriminator, the use of a phase-lock discriminator would not reduce the transmitter power requirement at all. Its use would, however, tend to extend the margin above threshold, i.e., serve as somewhat of a safety factor.

*It has been implicitly assumed here that doppler shift is the only cause of frequency uncertainty. Other effects such as oscillator instability might be significant, too.

a. General Description

Figure 3.5.21 shows a conceptual block diagram of a phase-lock FM discriminator. The conventional FM discriminator is replaced by a phase-lock loop consisting principally of a phase-detector, a voltage-controlled oscillator (VCO), and appropriate filters.

When the loop is locked, the IF input and the VCO input to the phase detector (multiplier) are identical in frequency and only slightly different in phase. Since the process of multiplication of these two inputs produces a voltage at baseband roughly proportional to their phase difference, a voltage is available at the output of the multiplier for phase control. This baseband voltage is filtered and applied to the VCO to complete the feedback loop. Since the frequency of the VCO is proportional to its control voltage, the variations of the control voltage will be proportional to the frequency modulation of the signal, provided, of course, that the loop bandwidth, gain and filter characteristics have been properly selected.

b. Required S/N Ratio at Threshold

In a typical phase-lock FM discriminator, a JPL source has stated that a 5.6 db S/N ratio measured in the loop noise bandwidth (about 6.7 times the bit rate) is required to keep the peak phase error less than 30 degrees.

3.5.3.3.3 PCM/FM/PM Relay Link

General Description

The PCM/FM/PM modulation technique leaves an uncluttered carrier signal available for tracking purposes. This eliminates the doppler shift problem, but causes an acquisition problem. It can be used with either a conventional FM discriminator or a phase-lock FM discriminator. The latter case, of course, involves two acquisitions; but the subcarrier acquisition problem is not so severe as the carrier acquisition problem.

A conceptual block diagram of a typical PCM/FM/PM receiver is shown in Figure 3.5.22. A typical mode of operation would be to frequency-modulate a 400-cps subcarrier with an NRZ(c) PCM signal, using a deviation ratio of 0.7. A maximum carrier modulation index of 1.4 radians appears suitable.

Transmitter Power Calculations

The discriminator shown in Figure 3.5.21 may be either a conventional discriminator or a phase-lock discriminator.

In either case, the sideband power from the output of the phase detector for a modulation index of 1.4 is:

$$P_S = 2 J_1^2(1.4) P_r = 0.583 P_r \quad (3.5-58)$$

where P_r is the total received signal power, and J_1 is the Bessel function of the first kind of order one. In decibels this may be written:

$$P_S = P_r - 2.4 \text{ db} \quad (3.5-59)$$

a. C/N Requirement

The predetection bandwidth will be taken to be 1.5 times the bit rate. Therefore, (as discussed in Section 3.5.3.3.1), the discriminator will require a 12 db S/N ratio in a bandwidth of 1.5 r, and the signal power required at the receiver is now (from Table 3.5.8):

$$P_S = 10 \log 1.5 r - 174 \text{ dbw} \quad (3.5-60)$$

Furthermore, due to putting power into the carrier, the signal power has now been reduced by 2.4 db over the PCM/FM case. Therefore, the power balance equation now becomes:

$$10 \log P - 169.4 - 2.4 = 10 \log 1.5 r - 174 \quad (3.5-61)$$

$$10 \log P = 10 \log 1.5 r - 2.2 \text{ dbw} \quad (3.5-62)$$

This has been plotted in Figure 3.5.23.

b. Carrier Power Requirement

In a phase-lock receiver it is necessary to maintain sufficient carrier power to acquire and track the signal.

Of the total received signal power, the fraction which is carrier power is $J_0^2(m)$, where J_0 is the Bessel function of zero order, and m is the modulation index. For a modulation index of $m = 1.4$, we have:

$$J_0^2(1.4) = (0.57)^2 = 0.324 \quad (3.5-63)$$

Figure 3.4.5 in the "Signal Acquisition and Tracking" Section shows the carrier power (P_c) requirements for a 100-mc link at 50,000 km range. Using these requirements, the following table can be constructed.

Table 3.5.9

ϵ^*	P_c (watts)	$\frac{\text{Req'd } P = P_c / 0.324 \text{ (watts)}}{\text{for } m = 1.4}$
10%	0.75	2.3
1%	2.4	7.4
0.1%	7.5	23.3

When the transmitter power required by the data rate falls below that given by Table 3.5.9, the latter becomes the limiting requirement.

*It may be recalled that ϵ is the fraction of total communication time which is allowed for initial acquisition.

For relatively low data rate requirements, the modulation index can be optimized such that the minimum sideband power requirement and the minimum carrier power requirement both correspond to the same value of total transmitter power; however, due to distortion effects in the phase detector, the modulation index should generally not be more than 1.4 radians. This optimization has been made in Figure 3.5.23.

3.5.3.3.4 PCM/FM/PM Direct Link

In this section the problem of transmitting a PCM/FM signal from the Venus capsule directly back to a DSIF earth station will be analyzed. In order to be compatible with the DSIF, the PCM/FM signal will be placed on a subcarrier which will phase-modulate the main carrier.

Transmitter Power Calculations

Using the nominal direct-link parameters given in Section 3.1, the following calculation can be made:

Table 3.5.10

Transmitter Power	10 log P	dbw
Subcarrier Suppression Factor	-2.4	db
Vehicle Antenna Gain	0	db
Path Attenuation (60×10^6 km)	-255.3	db
Receiving Antenna Gain	51.8	db
Misc. RF Losses	-3	db

Signal Power Available at Receiver: $10 \log P - 208.9$ dbw

a. C/N Requirement

As shown in preceding sections, the discriminator will require a 12 db S/N ratio in a predetection bandwidth of 1.5r. Therefore, the receiver sensitivity calculation may be made as follows:

Table 3.5.11

Receiver Noise Density per cps (KT_e)	-211.6	dbw
Bandwidth	10 log 1.5r	db
S/N ratio Required	+12	db
Margin	+8	db

Signal Power Required at Ground Receiver: 10 log 1.5r - 191.6 dbw

The power balance equation now becomes:

$$10 \log P - 208.9 = 10 \log 1.5r - 191.6 \quad (3.5-64)$$

$$10 \log P = 10 \log 1.5r + 17.3 \text{ dbw} \quad (3.5-65)$$

which has been plotted in Figure 3.5.24.

b. Carrier Power Requirements

As shown in Section 3.4, a carrier power of 33 watts is necessary to provide a 7.5 db S/N ratio in a 3-cps tracking loop bandwidth. Therefore, by the same reasoning as in Section 3.5.3.3.3, the minimum total transmitter power for a modulation index of 1.4 must be

$$P_{\min} = 33/0.324 = 102 \text{ watts for } m = 1.4 \quad (3.5-66)$$

Here again, for relatively low data rate requirements, the modulation index can be optimized such that the minimum sideband power requirement and the minimum carrier power requirement both correspond to the same value of total transmitter power. This has been done in Figure 3.5.24.

3.5.3.3.5 PCM/FSK

General Description

PCM/FSK modulation is implemented by switching the frequency of the transmitted carrier between two possible values to indicate binary "1's" and "0's." Although either coherent or noncoherent detection of the resulting signal is possible, only a noncoherent technique will be considered here. In particular the assumed receiver is a dual-filter linear receiver as shown in Figure 3.5.24. The two frequencies to be used are assumed to be separated adequately to reduce their cross-correlation coefficient to a value near zero. The dual bandpass filters are then centered about the individual frequencies. Each filter must have a bandwidth broad enough to include the signal spectrum and any short-term oscillator instability. Envelope detectors are utilized to detect the signals from the filters. These are followed by low-pass filters having only enough bandwidth to include the signal. The outputs of the low-pass filters are then subtracted, and the resultant signal is amplified. Binary information previously contained in the two frequencies is now contained in the polarity of the output signal. Further processing, such as matched filter detection, can be utilized to enhance the signal-to-noise ratio prior to the determination of the signal polarity.

Analysis of Receiver

In the following analysis the signal will be traced through the receiver illustrated in Figure 3.5.24, as given by Glenn*. The passband of each filter is taken as $B_1 + \Delta F$ where B_1 is the matched filter bandwidth ($B_1/f_m = 2$, f_m being the bandwidth of the output filter) and ΔF is the frequency uncertainty. Therefore, the approximate total noise bandwidth is $B_{IF} \approx 2(B_1 + \Delta F)$. The S/N ratio after either filter, at point b is

$$(S/N)_b = (C/N)_{B_{IF}} \frac{B_{IF}}{B_1 + \Delta F} \quad (3.5-67)$$

For envelope detection the S/N at b must be at least 3 (4.8 db) for negligible degradation of the output S/N. After detection the S/N at point c is then:

$$(S/N)_c \approx (S/N)_b \text{ for } (S/N)_b > 3 \quad (3.5-68)$$

The S/N at point d after the low-pass filter with a bandwidth f_m for optimum S/N is approximately:

$$(S/N)_d \approx (S/N)_b \frac{(B_1 + \Delta F) / 2}{f_m} \quad (3.5-69)$$

where

$$f_m = B_1 / 2$$

Glenn then states that the output S/N at point e is approximately

$$(S/N)_{out} \approx 0.84 (S/N)_d \approx 0.84 (C/N)_{B_{IF}} \frac{B_{IF}}{B_1} \quad (3.5-70)$$

for $(S/N)_b > 3$

*Glenn, A. B., "Comparison of Binary Coded Transmission Systems," IRE Transactions on Communications Systems, June, 1960.

The coefficient is 0.84 instead of 0.5 for large S/N because the noise contributed by the channel which contains the desired signal is greater than the noise contributed by the channel which does not contain the desired signal.

The error probability for noncoherent FSK is given by Lawton and Becker*

$$P_e = \frac{1}{2} e^{-\frac{E}{2 N_o}} \quad (3.5-71)$$

where E/N_o is the normalized S/N. (E is signal energy per bit, N_o is noise power unit bandwidth.) This function is plotted in Figure 3.5.25. The relation between average and normalized S/N for a matched filter is:

$$S/N = E/N_o \quad \text{or} \quad B_1/f_m = 1 \quad (3.5-72)$$

Therefore, for the receiver of interest:

$$\begin{aligned} E/N_o &\approx 0.84 (C/N)_{B_{IF}} \frac{B_{IF}}{B_1} \\ &= 0.84 (C/N)_{B_{IF}} \frac{2(B_1 + \Delta F)}{B_1} \\ &= 0.84 (S/N)_{B_1} \end{aligned} \quad (3.5-73)$$

The threshold condition is

$$(S/N)_{B_1} + \Delta F > 3 \text{ (4.8 db)} \quad (3.5-74)$$

*Lawton, J. G. and Becker, H. D., "Theoretical Comparison of Binary Data Transmission Systems," Cornell Aeronautical Laboratory Report No. (A-1172-5-1), AD148803, May, 1958.

Direct Link

In order to indicate the capability of the direct link, the relationship between the filter bandwidth ($B_1 + \Delta F$) and data rate must be determined. Although the S/N in each bandpass filter can be 9 db, the S/N at the output must be greater in order to attain the required value for probability of error. This can be determined from Figure 3.5.26 and Equation (3.5-73). Figure 3.5.26 indicates that the ratio E/N_o must be equal to 10.4 db (11) in order to attain an error probability of 1.67×10^{-3} (word error probability equals 10^{-2} ; 6 bits per word). Then, from Equation (3.5-73),

$$\begin{aligned} (S/N)_{B_1} &= \frac{1}{0.84} E/N_o \\ &= \frac{11}{0.84} = 13.1 \text{ (11.2 db)} \end{aligned} \quad (3.5-75)$$

The maximum ratio of filter bandwidth ($B_1 + \Delta F$) to matched filter bandwidth (B_1) is then:

$$\frac{B_1 + \Delta F}{B_1} = \frac{(S/N)_{B_1}}{(S/N)_{B_1 + \Delta F}} = \frac{13.1}{8} = 1.64 \quad (3.5-76)$$

The filter bandwidth B_1 is equal to the reciprocal of the bit duration or equal to the bit rate r . Then from Equation (3.5-76),

$$B_1 + \Delta F = 1.64 r \quad (3.5-77)$$

The bandwidth of each filter can, therefore, be increased to 1.64 times the data rate of B_1 in order to allow for frequency instability.

The relationship between transmitted power and the data rate is determined below, utilizing the above equation and the nominal parameters given in Section 3.1.

Table 3.5.13

Signal Power Available at Receiver: (from Table 3.5.4)	10 log P - 206.5 dbw
Receiver Noise per cps ($T_e = 50^\circ \text{K}$)	- 211.6 dbw
Bandwidth ($B_1 + \Delta F$)	10 log 1.64 r db
S/N Required (in $B_1 + \Delta F$)	9.0 db
Margin	<u>8.0 db</u>
Signal Power Required at Receiver:	10 log 1.64 r - 194.6 dbw

Then,

$$10 \log P - 206.5 = 10 \log 1.64 r - 194.6$$

or,

$$10 \log P = 10 \log r + 14 \text{ dbw} \quad (3.5-78)$$

This relationship is shown in Figure 3.5.27.

The power level at which the system thresholds can also be determined from the results of Table 3.5.13 by replacing 1.64 r by ($B_1 + \Delta F$) as given by Equation (3.5-77).

$$10 \log P = 10 \log (B_1 + \Delta F) + 11.9 \text{ dbw} \quad (3.5-78)$$

The thresholds for bandpass filters having bandwidths ($B_1 + \Delta F$) equal to 3, 15, and 50 cps then occur at $P = 47$, 232, and 720 watts, respectively. These values are shown in Figure 3.5.27.

The relationship between transmitter power and data rate is also shown for the system with the 85-ft. dish replaced by a 210-ft. dish (61 db gain).

The maximum allowable data rate is proportional to the energy transmitted while the maximum bandwidth allowable without signal thresholding is proportional to the peak envelope power (PEP). This suggests the desirability of transmitting noncontiguous pulses to alleviate the frequency stability problem. For instance, the analysis shows that with 50 watts of average power transmitted, the data rate is 2 bits/sec. and the maximum allowable width of the bandpass filters is 1.64 r = 3.3 cps, if contiguous pulses are transmitted. If the peak envelope power is

increased to 500 watts and the duty cycle is decreased to ten per cent, so that the average power is still 50 watts, the data rate remains at two bits/sec while the bandwidth can be increased to 33 cps. The increase in bandwidth will also allow an increase in sweep rate for real-time acquisition by a factor of ten over the contiguous pulse case. The bandwidth of a predetection recorder can also be increased by a factor of ten over a CW system since the signal power during a pulse is ten times as great.

Noncoherent PCM/FSK also has an advantage over coherent techniques (as do other noncoherent techniques) if predetection recording is utilized in that the time-base stability of the record/reproduce operation is not critical.

Other factors such as prime power, weight, thermal dissipation, and power level at antenna breakdown must be taken into account before the overall merits of such a technique can be determined.

3.5.3.3.6 PCM/FSK/PM

PCM/FSK/PM is similar to PCM/FSK in that the binary information takes the form of pulses at two different frequencies; however, in PCM/FSK/PM this is carried out at a low frequency, and the resulting signal is used to phase-modulate the carrier. A maximum modulation index of 1.4 will be used as in Section 3.5.3.2.1. This results in the following distribution of power between the carrier and the first set of sidebands:

$$\text{Carrier power} = 0.324 P$$

$$\text{Sideband (data) power} = 0.583 P$$

PCM/FSK/PM Relay Link

The nominal system parameters listed in Section 3.1 will be utilized in the determination of the system capability. For an error probability of 10^{-4} , Figure 3.5.26 indicates that the value of E/N_0 required is 12.1 db (16.2). The signal-to-noise ratio required is then given by Equation (3.5-73).

$$(S/N)_{B_1} = \frac{E/N_0}{0.84} = \frac{16.2}{0.84} = 19.3 \text{ (12.9 db)} \quad (3.5-79)$$

The relationship between transmitter power and data rate is calculated below.

Table 3.5.14

Total Power Available at Receiver: (from Table 3.5.3)	10 log P - 169.4 dbw
Subcarrier Suppression Factor (0.583):	<u>-2.4 db</u>
Signal Power Available at Receiver:	10 log P - 171.8 dbw
Receiver Noise per cps	-194.0 dbw
Bandwidth ($B_1 = r$)	10 log r db
S/N Required	12.9 db
Margin	<u>8.0 db</u>
Signal Power Available at Receiver:	10 log r - 173.1 dbw

Then,

$$10 \log P - 171.8 = 10 \log r - 173.1$$

or,

$$10 \log P = 10 \log r - 1.3 \text{ dbw} \quad (3.5-80)$$

This relationship is plotted in Figure 3.5.28. Table 3.5.5 lists the carrier power required for three values of ϵ , the percentage of communication time taken for acquisition. It also gives the total power required for these values of ϵ and a modulation index of 1.4. In Figure 3.2.28, the modulation index (M) is adjusted such that the carrier power, and therefore, the acquisition time, remains constant below the threshold for $M = 1.4$.

PCM/FSK/PM Direct Link

The theoretical capability of the PCM/FSK/PM system in the direct link differs from that of the PCM/FSK system only in that part of the total power is utilized for the carrier. Since the loss of power in the data spectrum is -2.4 db, for a modulation index of 1.4, the transmitter power versus data rate relationship can be determined directly from Equation (3.5-78) for PCM/FSK

$$10 \log P - 2.4 = 10 \log r + 14$$

or

$$10 \log P = 10 \log r + 16.4 \quad (3.5-81)$$

This relationship is shown in Figure 3.5.29 along with the relationship for a system utilizing a 210-ft. dish (61 db gain). As in the PCM/PS/PM system the modulation index is varied to satisfy the power requirements for tracking in a 3 cps loop bandwidth.

3.5.3.3.6 Summary of Capabilities of PCM Systems

Relay Link

The data transmission capabilities of the PCM systems in the relay link are illustrated in Figure 3.5.30. The nominal parameters defined in Section 3.1 have been assumed for all the systems. A probability of bit error of 10^{-4} has also been assumed, along with a value of one per cent for the maximum communication time lost during acquisition (see Section 3.4).

The threshold effect noted at low data rates is a result of the minimum value of carrier power (2.4 watts) required for acquisition of the signal under the constraint that $\epsilon_{\max} =$ one per cent. The threshold is sudden for PCM/PS, since all the received power is used for both signal acquisition and data. In the other systems the power required for acquisition is in the carrier of the spectrum of the transmitted signal, while the data is contained in the first set of sidebands. The relative amount of power in each is determined by the modulation index. The maximum value which has been used for modulation index is 1.4. The point on each curve at which threshold begins is the point at which the carrier power transmitted is equal to 2.4 watts. Above this point, the modulation index is 1.4 and the carrier power is greater than 2.4 watts; ϵ is therefore one per cent at the threshold point and less above this point. Below the threshold point the carrier power transmitted is held constant at 2.4 watts by decreasing the modulation index. Since this is done at the expense of the power in the sidebands, the data rate decreases more rapidly. The limiting condition is, therefore, reached when the power transmitted is 2.4 watts, and the modulation index is zero; i. e.,

the acquisition constraint is satisfied but no data is transmitted. The regions of the curve can, therefore, be summarized by the following:

Above threshold: $M = 1.4$, $\epsilon < 1$ per cent

At threshold: $M = 1.4$, $\epsilon = 1$ per cent

Below threshold: $M < 1.4$, $\epsilon = 1$ per cent

Direct Link

Figure 3.5.31 shows the data transmission capabilities of the PCM systems for the direct link. The nominal direct link parameters given in Section 3.1 have been assumed. The probability of bit error is taken as 1.43×10^{-3} * (10^{-2} word error probability for a seven-bit word). The minimum bandwidth available at the ground receiver has been assumed to be 3 cps. Note that the 3 cps refers to the bandwidth of the bandpass filters for noncoherent PCM/FSK while it refers to the noise bandwidth of the phase lock loop for the other modulation techniques. Therefore, PCM/FSK should not be compared directly with the other techniques in the threshold region.

The data rates in the threshold region for the systems other than PCM/FSK have been determined in the same manner as that described for the relay link. Here, the condition to be satisfied is that a minimum signal-to-noise ratio of 7.5 db be available in the 3 cps bandwidth. This is the same as for the relay link except that the bandwidth in that case was defined in terms of the acquisition parameter, ϵ . Further discussion of the signal tracking and acquisition problem for the direct link is given in Section 3.4.

The threshold criterion for the noncoherent PCM/FSK system is that the signal-to-noise ratio in the bandwidth of the bandpass filters be at least 9 db. Reducing the signal-to-noise ratio below this value results in rapid degradation of the signal in the envelope detector, thereby increasing the error rate.

*Note that this differs from the bit error probabilities used in the previous individual analyses of some of the systems; therefore, adjustments have been made where necessary to present the systems on an equal basis. A bit error probability of 1.66×10^{-3} was used previously for the PCM/FSK and PCM/FSK/PM analyses and 10^{-4} for the PCM/FM/PM analysis.

APPENDIX A

Bit Error Probability for PCM/PS with Matched Filter Detection

(a) Determination of Peak Signal-to-Mean Square Noise Power Ratio

Since PCM/PS modulation combined with matched filter detection is theoretically the most efficient binary system available, its bit error probability versus signal-to-noise ratio will be used as a standard. Squarewave modulation will be assumed, i. e., the waveform of a single bit after synchronous detection is

$$f(t) = \begin{cases} V & \text{for } -\frac{T}{2} \leq t \leq \frac{T}{2} \\ 0 & \text{elsewhere} \end{cases} \quad (\text{A-1})$$

A matched filter for any signal must have an impulse response equal to the reverse of the time function to be detected. This is given by

$$h(t) = f(T - t) \quad (\text{A-2})$$

Since the squarewave time function to be detected is symmetrical about the time-axis

$$h(t) = f(T - t) = f(t) \quad (\text{A-3})$$

A filter satisfying this requirement is an integrate-and-dump circuit.

The frequency response of the integrate-and-dump circuit is then

$$\begin{aligned} H(w) &= \int_{-\infty}^{\infty} h(t) e^{jwt} dt \\ &= V \int_{-\frac{T}{2}}^{\frac{T}{2}} e^{jwt} dt \end{aligned}$$

$$\begin{aligned}
&= V \frac{e^{j\omega T/2} - e^{-j\omega T/2}}{j\omega} \\
&= VT \frac{\sin \omega T/2}{\omega T/2}
\end{aligned} \tag{A-4}$$

The mean noise power output from the filter is given by

$$\begin{aligned}
N_f &= \frac{N_o}{2\pi} \int_0^\infty |H(\omega)|^2 d\omega \\
&= \frac{N_o}{2\pi} \int_0^\infty \left| VT \frac{\sin \omega T/2}{\omega T/2} \right|^2 d\omega \\
&= \frac{V^2 N_o}{2\pi} 2T \int_0^\infty \left| \frac{\sin \omega T/2}{\omega T/2} \right|^2 d\omega T/2 \\
&= \frac{V^2 N_o T}{\pi} \frac{\pi}{2} = \frac{V^2 N_o T}{2}
\end{aligned} \tag{A-5}$$

where N_o is the noise power per unit bandwidth. The noise is assumed to be white and to have a gaussian distribution.

The peak signal voltage from a matched filter is equal numerically to the energy in the input signal. This is determined as follows

$$V_o = \int_{-\infty}^{\infty} S^2(t) dt$$

$$\begin{aligned}
&= \int_{-\frac{T}{2}}^{\frac{T}{2}} V^2 dt \\
&= V^2 T
\end{aligned} \tag{A-6}$$

The peak signal power is then

$$S_f = V^4 T^2 \tag{A-7}$$

The ratio of peak signal power to mean noise power defined in Equations (A-5) and (A-7) is

$$\begin{aligned}
\frac{S_{fp}}{N_f} &= \frac{V^4 T^2}{V^2 N_o T/2} \\
&= \frac{2 V^2 T}{N_o}
\end{aligned} \tag{A-8}$$

It is now desirable to relate this expression to the signal-to-noise ratio S/N , where S is the average power of the PCM/PS signal received and N is the receiver noise power in the equivalent bandwidth of the matched filter ($N_o B$). To do this we consider the synchronous detection of the signal during a single bit period and use the following representation of the signal and noise at IF.

$$f_{IF}(t) = \sqrt{2S} \cos wt \tag{A-9}$$

$$n_{IF}(t) = \sqrt{N_o B_{IF}}(t) \cos wt + \sqrt{N_o B_{IF}}(t) \sin wt \tag{A-10}$$

$$c(t) = C \cos wt \tag{A-11}$$

where S is the average signal power

$n_{IF}(t)$ is a mathematical representation of narrowband gaussian noise in the IF bandwidth in terms of the in-phase and quadrature components.

$c(t)$ is the in-phase reinserted carrier.

The components of signal and noise at baseband are then

$$\begin{aligned} f_b(t) &= \sqrt{2S} \cos \omega t \quad C \cos \omega t \\ &= \frac{C \sqrt{2S}}{2} \end{aligned} \quad (A-12)$$

and

$$n_b(t) = \sqrt{2 N_o b} \cos \omega t \quad C \cos \omega t + \sqrt{2 N_o b} \sin \omega t \quad C \cos \omega t$$

$$= \frac{C \sqrt{2 N_o b}}{2} (t) \quad (A-13)$$

where b is the width of the baseband and is equal to $B_{IF}/2$.

The signal-to-noise power ratio ahead of the matched filter is therefore (from A-12 and A-13)

$$\left(\frac{S}{N} \right)_b = \frac{S}{N_o b} \quad (A-14)$$

Since the value of the noise in this case is exactly the same as that used in the derivation of signal-to-noise ratio at the matched filter output (noise density = N_o ; total noise = $N_o \times$ bandwidth) then S is the true average power in the assumed signal, i.e., $V^2 = S$. Therefore Equation A-8 may be rewritten as

$$\frac{S_{fp}}{N_f} = \frac{2 ST}{N_o} \quad (A-15)$$

The last step is to determine the equivalent bandwidth of the filter. It may be found from the following definition:

$$B_{eq} = \frac{\frac{1}{2\pi} \int_0^{\infty} |H(w)|^2 dw}{|H(o)|^2} \quad (A-16)$$

Then, from Equation A-4

$$\begin{aligned} B_{eq} &= \frac{\frac{1}{2\pi} \int_0^{\infty} \left| VT \frac{\sin wT/2}{wT/2} \right|^2 dw}{(VT)^2} \\ &= \frac{2}{2\pi T} \int_0^{\infty} \frac{\sin wT/2}{wT/2} d wT/2 \\ &= \frac{1}{2T} \end{aligned} \quad (A-17)$$

Substitution into Equation A-15 yields

$$\frac{S_{fp}}{N_f} = \frac{S}{N_o B_{eq}} = \frac{S}{N} \quad (A-18)$$

Therefore, the ratio of peak signal power to mean noise power at the output of the filter is equal to the ratio of average received signal power to mean noise power in the receiver where the latter noise is calculated in a bandwidth equal to one-half the bit rate.

(b) Bit Error Probability

Assuming errors in the "1's" and "0's" are equally probable and a balanced amplitude sampling system is utilized, the probability of error in a "1" or "0" is given by the normal probability density function

$$P(1/0) = P(0/1) = 1/2 - \frac{1}{\sqrt{2\pi}\sigma} \int_0^x e^{-1/2 \frac{x^2}{\sigma^2}} dx \quad (A-19)$$

where

$P(1/0)$ = probability of receiving 1; 0 transmitted

$P(0/1)$ = probability of receiving 0; 1 transmitted

x = peak signal amplitude at filter output

σ = rms noise amplitude

Therefore, for the system being considered, the above definitions lead to (from Equation A-18)

$$\frac{x^2}{\sigma^2} = \frac{S_{fp}}{N_f} = \frac{S}{N} \quad (A-20)$$

Letting $S/N = t$, Equation A-19 may be rewritten as

$$\begin{aligned} P(1/0) = P(0/1) &= 1/2 - \frac{1}{\sqrt{2\pi}} \int_0^t e^{-\frac{t^2}{2}} dt \\ &= 1/2 - \int_0^t \phi(t) dt \end{aligned} \quad (A-21)$$

The probability of bit error is

$$P_e = P(0) P(1/0) + P(1) P(0/1) \quad (A-22)$$

where $P(0)$ and $P(1)$ are the probabilities of transmitting a "1" and "0" respectively and will be assumed to be equal (0.5). Then from Equations A-21 and A-22

$$\begin{aligned} P_e &= 1/2 \left\{ 2 \left[1/2 - \int_0^t \phi(t) dt \right] \right\} \\ &= 1/2 - \int_0^t \phi(t) dt \end{aligned} \quad (A-23)$$

Using values from tables of the normal probability functions this function is plotted in Figure A-1.

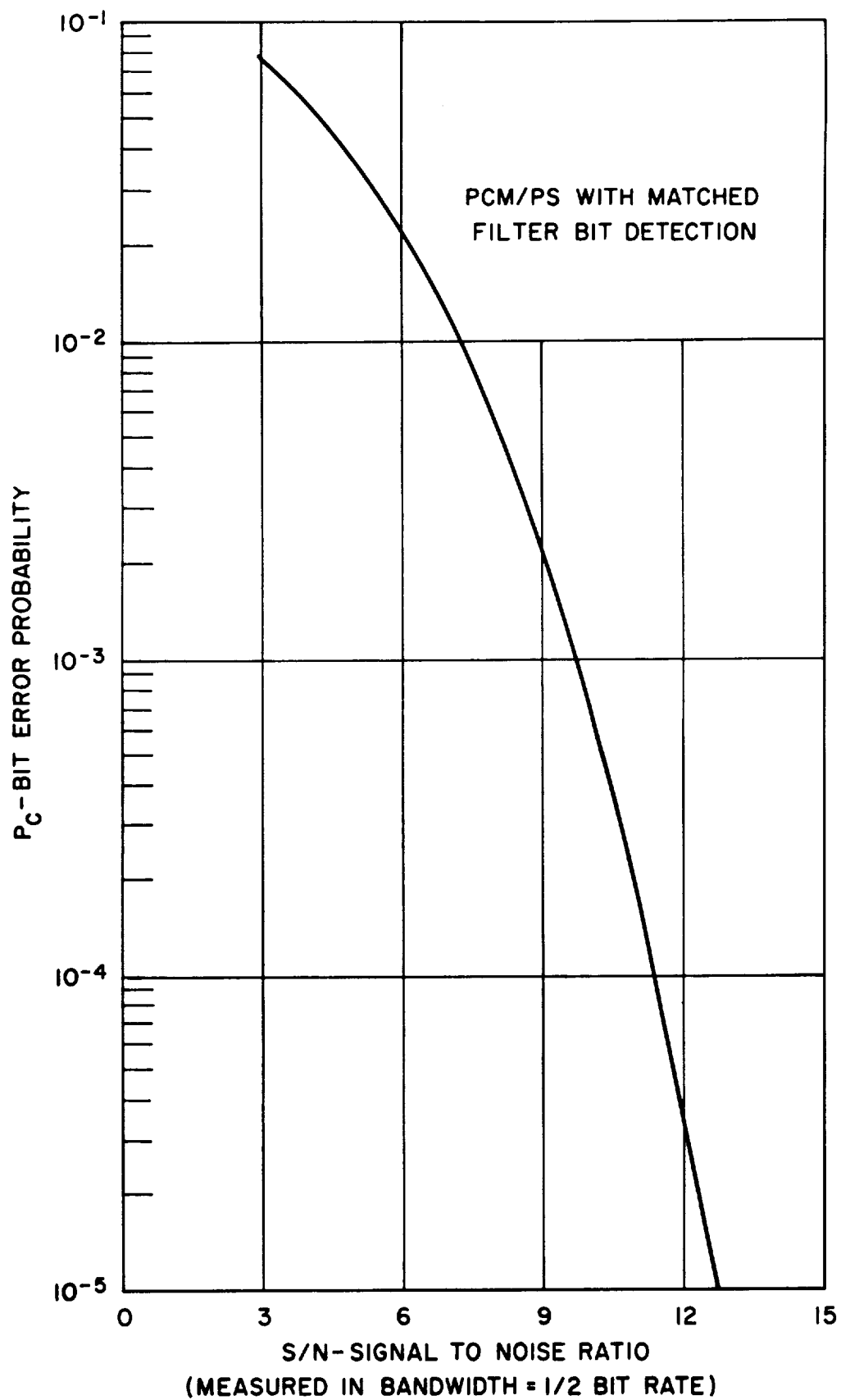


Figure A-1. Probability of Bit Error vs. Signal to Noise Ratio

3.5.4 FM and FM/FM Telemetry System Analyses

3.5.4.1 General Considerations

In this analysis it will be assumed that the individual data channels are frequency-division multiplexed (FDM) before modulating the carrier. In the FM analysis they will amplitude-modulate the subcarriers. This will yield a resultant modulation of AM/FM. In the FM/FM analysis, they will frequency-modulate the subcarriers.

3.5.4.2 Noise Improvement Factor of FM (Single-Channel)

Appendix A of this section shows the derivation (from Black*) that for a sinusoidal modulating signal the S/N ratio at the output of an FM receiver is given by**:

$$S/N = 3 M^2 P_c / 2bn \quad (3.5-82)$$

where:

M = modulation index

P_c = carrier power

b = noise bandwidth of output filter

n = noise power spectral density

The carrier-to-noise (C/N) ratio before detection is given by:

$$C/N = P_c / Bn \quad (3.5-83)$$

where B is the predetection bandwidth.

Therefore, Equation (3.5-82) may be written:

$$S/N = (3M^2) (C/N) (B/2b) \quad (3.5-84)$$

In decibels this becomes:

$$S/N = C/N + 10 \log 3M^2 + 10 \log B/2b \text{ (db)} \quad (3.5-85)$$

*Black, H.S. Modulation Theory, Van Nostrand Co., 1953, page 224.

**Assuming an ideal FM detector, which is insensitive to amplitude modulation, distortionless, and noise-free.

Even with a sinusoidal modulating signal, the spectrum of a frequency-modulated wave extends over an infinite bandwidth. However, in practical applications the significant range of the spectrum is often approximated by:

$$B \approx 2 (M + 1)b = 2 (F + b) \quad (3.5-86)$$

where:

b is the information bandwidth (baseband)

F is the frequency deviation $\equiv Mb$

In a conventional FM receiver (neglecting doppler effect) the predetection bandwidth B is equal to the R.F. bandwidth. Therefore, Equation (3.5-84) may be written:

$$S/N = (3M^2) (C/N) (B/2b) \quad (3.5-87)$$

$$= (C/N) (3M^2) (M + 1) \quad (3.5-88)$$

for conventional FM.

3.5.4.3 The Threshold Effect

The threshold C/N ratio will be defined as that at which the demodulated output S/N ratio begins to decrease more rapidly than the input C/N ratio. At C/N ratios less than this, the full noise improvement capability of FM is not realized. Figure 3.5.32 shows an example of the FM threshold effect. This FM threshold effect is actually a result of the so-called "capture effect" which occurs in the situation where two (or more) FM signals are operating on a common frequency or are separated by a relatively small frequency difference. In the FM demodulation process, the weaker signal then becomes suppressed by the stronger*. When the peak amplitude of the interfering signal is equal to the peak amplitude of the desired signal, the interfering signal then "captures" the receiver, i.e., it suppresses the desired signal. This same effect occurs when noise is the "interfering signal," since noise may be represented by an ensemble of sinusoidal elements, unrelated in phase and frequency**.

*Just how much stronger the desired signal must be to suppress the weaker signal adequately depends on the receiver characteristics. A factor of 3 db is sufficient in all receivers of interest.

**Black, loc. cit., page 222.

To evaluate the threshold level for random noise interference, it is first necessary to establish the peak amplitude of the noise and then equate this to the peak carrier amplitude. A "crest factor" of four is frequently assumed for random noise, meaning that the peak-to-rms noise voltage ratio is 4(12 db)*. With the receiver bandwidths used in practical communication systems, the probability of any noise peak substantially exceeding four times the rms level is very remote.

Since the amplitude of the random noise is often assumed to have a Gaussian probability distribution, as shown in Figure 3.5.33, it is of interest to see what the probability of a noise peak exceeding four times the rms level is in this case.

The rms noise voltage is σ , so the probability of exceeding a crest factor of four in Gaussian noise is the probability that the noise voltage will be greater than $\pm 4\sigma$ at any instant. Statistical tables show this probability to be 6.3×10^{-5} , which is indeed quite small.

The peak-to-rms voltage ratio of the sinusoidal carrier wave is 3 db, and that of the random noise is 12 db (assuming a crest factor of four). Therefore, when the peak noise voltage is equal to the peak carrier voltage, the ratio of rms carrier voltage to rms noise voltage is approximately 9 db. At this point, the performance is about the same as that of AM**. How much higher than this the C/N ratio must be to realize the full noise improvement of FM depends on the receiver characteristics. In general, it should be 3 or 4 db above equality of peak carrier and peak noise (in the predetection bandwidth)**. Thus, as shown in Figure 3.5.32, the FM threshold occurs at a C/N ratio of approximately 12 db.

Since the FM threshold occurs when the peak carrier power is about 3 db greater than the peak noise power (in the predetection bandwidth), it follows that wide-deviation FM will require more carrier power in order to rise above

*Nichols, M. H. and Rauch, L. Radio Telemetry, Second Edition, Wiley, New York, N. Y., 1956.

**Crosby, M. G., "Frequency Modulation Noise Characteristics," Proc., IRE, April, 1937.

threshold than will narrow-deviation FM. Thus, the price paid for the large noise improvement factor of wide-deviation FM employing a conventional FM receiver is that of overcoming a high threshold requirement. (However, with an FMFB receiver, it is possible to employ a wide deviation without encountering the high threshold problem. This is discussed in Section 3.5.6 of this analysis).

3.5.4.4 Pre-Emphasis

The analysis of Section 3.5.3 has considered only one sinusoidal component of the modulating signal. Equation (3.5-88) showed that the noise improvement factor is determined by the modulation index M , defined by:

$$M = F/f \quad (3.5-89)$$

where F is the frequency deviation caused by the modulating sinusoid of frequency f . Clearly, the higher the modulating frequency f , the lower is the noise improvement factor. This is because the modulation index corresponding to a given frequency deviation produced by the signal is less*. As a result, it has been found advantageous to increase the amplitude of the higher frequencies before modulation at the transmitter. This pre-emphasis improves the noise suppression at the receiver by making the modulation index at high frequencies greater than would otherwise be the case, and the receiver output retains this improvement in S/N ratio after performing appropriate de-emphasis.

The amount of pre-emphasis is often specified as the number of decibels of amplification of the highest baseband frequency above that of the lowest baseband frequency (e.g., 10 db of pre-emphasis). Assuming a straight line connecting these two points, the average pre-emphasis in the baseband can be readily calculated. Passive networks at the transmitter and receiver can be used for pre-emphasis and de-emphasis.

*cf. Terman, F. E. Radio Engineering, Third Edition, McGraw-Hill, New York, N. Y., 1947. This can also be explained by the "triangular output noise voltage spectrum" of FM, as explained by Tibbs, C. E. and Johnstone, G. G., in Frequency Modulation Engineering, Wiley, N. Y., 1950.

3.5.4.5 Multi-Channel Baseband FM

Section 3.5.2 has dealt with the case of a single-channel baseband transmitted by frequency modulation. This section will show how the noise improvement factor changes for the case of a multi-channel baseband. Here the baseband will be assumed to be composed of many frequency-division-multiplexed channels, such as shown in Figure 3.5.34.

As shown in Section 3.5.4.4, the noise which falls in the baseband of an FM radio system increases with the baseband frequency. Consequently, the noise is greatest in the highest frequency channel. Thus, the S/N ratio will be evaluated in the highest frequency channel.

Appendix B shows that the output S/N ratio in the highest channel may be written:

$$S/N = (F/f_m)^2 (P_c/2bn) \quad (3.5-90)$$

This corresponds to Equation (3.5-82) in the single-channel case. Using Equation (3.5-83), this may be written:

$$S/N = (F/f_m)^2 (C/N) (B/2b) \quad (3.5-91)$$

In decibels this becomes:

$$S/N = C/N + 20 \log \frac{F}{f_m} + 10 \log \frac{B}{2b} \text{ (db)} \quad (3.5-92)$$

which corresponds to Equation (3.5-85) in the single-channel system.

Using Equation (3.5-92), one may assign values to the desired S/N ratio, bandwidths, and frequency deviation to arrive at the required C/N ratio. The required transmitter power will then be that required to establish the required C/N ratio in the predetection bandwidth B.

3.5.4.6 FM With Feedback

Originally conceived at the Bell Telephone Laboratories in 1939, FM with feedback (FMFB) is presently being used in communication satellite systems. The modulation is actually wide-deviation FM; the feedback is applied only in the receiver to reduce the deviation in the I. F. stages. This is done by using the output of the discriminator to cause a local oscillator to partially track changes in the instantaneous frequency of the received signal. The local oscillator output is then mixed with the received signal to yield a comparatively narrow difference frequency band which becomes the I. F. bandwidth.

The theoretical advantage of FMFB (over conventional FM reception) is that, due to the narrowing of the I. F. bandwidth by the feedback process, the noise admitted to the discriminator in an FMFB receiver will be much less than that in the total R. F. bandwidth. Thus, the carrier power required to maintain the predetection carrier-to-noise ratio above threshold (about 12 db in the predetection bandwidth) is much less with feedback than it would be without feedback. This permits the use of wide deviation FM at the transmitter (with its large inherent noise improvement factor) without experiencing the high threshold requirement of conventional wideband FM reception.

One way of implementing an FMFB receiver is shown in Figure 3.5.35. The discriminator output causes the local oscillator to partially track changes in the instantaneous frequency of the receiver signal such as to reduce the deviation ratio in the I. F. amplifier. Appendix C shows from elementary servo theory that the I. F. modulation index becomes:

$$M_{IF} = \frac{M}{1 + \mu} \quad (3.5-93)$$

where:

- M = the transmitted modulation index
- M_{IF} = the I. F. modulation index
- μ = the feedback factor (loop gain)

Equation (3.5-93) then shows that the I. F. bandwidth is approximately:

$$B' = 2 \left(\frac{M}{1 + \mu} + 1 \right) b \quad (3.5-94)$$

Thus, the minimum theoretical I. F. bandwidth possible is twice the baseband.

$$B' \longrightarrow 2b \quad (3.5-95)$$

This would require an infinite feedback factor. However, a significant bandwidth reduction can be made with values of μ even on the order of 10 or 20.

In FMFB, the ideal predetection bandwidth approaches $2b$, to reduce the threshold requirement. Thus, in FMFB Equation (3.5-84) approaches:

$$\begin{aligned} S/N &= (3M^2) (C/N) (B/2b) \\ &= (3M^2) (C/N) (2b/2b) \\ &= (3M^2) (C/N) \end{aligned} \quad (3.5-96)$$

From a first glance at Equations (3.5-88) and (3.5-96), one might infer that FMFB has lost something through the dropping of the $(M + 1)$ factor. However, this is not the whole story, since it should be recalled that FMFB permits the use of a larger value of M than conventional FM does, without encountering the high threshold requirement of conventional FM.

For example: In conventional FM a modulation index of four might be used. Equation (3.5-88) shows the noise improvement factor would be:

$$3M^2 (M + 1) = 48 \times 5 = 240 = 24 \text{ db} \quad (3.5-97)$$

In FMFB, however, a modulation index of ten (or even higher) might be used. For $M = 10$, Equation (3.5-96) shows the noise improvement factor would be:

$$3M^2 = 300 = 25 \text{ db} \quad (3.5-98)$$

which is slightly better than that of the conventional FM system of Equation (3.5-97). However, the conventional FM system must provide a 12 db C/N ratio in a predetection bandwidth of:

$$B = 2(M + 1)b = 10b \quad (3.5-99)$$

while the ideal (infinite feedback) FMFB system must provide the 12 db C/N ratio in a predetection bandwidth of only 2b. Since the noise power in the 10b bandwidth would be five times that in the 2b bandwidth, the FMFB system would produce the same noise improvement factor as the conventional FM system with only 1/5 the transmitter power. Conversely, for equal transmitter powers, the signal-to-noise ratio of the FMFB system would be 8 db better than the conventional FM system in this simple example.

3.5.4.7 Establishment of Required Analog Output S/N Ratio

In order to make a comparison between analog modulation systems and digital modulation systems, it is necessary to establish the output S/N ratio required as a function of the accuracy requirements of the data. (This is analogous to Table 3.5.2 in the PCM analysis, where the data accuracies were related to the required encoding accuracy, hence, to the quantization noise.)

The accuracy comparison is admittedly somewhat arbitrary, since quantization noise has a uniform (rectangular) distribution while thermal (analog system) noise has a gaussian distribution. Therefore, one can speak of maximum error for a digital system, while it is more common to require a corresponding rms error from an analog system*. Therefore, an analog accuracy requirement of ± 1 per cent is taken to mean a ratio of full-scale signal voltage-to-rms noise voltage of 100, i.e., 40 db. Figure 3.5.36 has been plotted on this basis.

3.5.4.8 Calculation of Required FM Transmitter Power

3.5.4.8.1 Subcarrier Frequencies

Although it would be desirable (from an implementation viewpoint) to use standard IRIG SCO frequencies, these subcarrier frequencies would result in a base bandwidth considerably greater than is necessary for this application. Since the individual channel signal bandwidths are only a few cps, the use of AM subcarrier modulation (instead of SSB) will not result in an excessive multi-channel base bandwidth and will allow a considerably simpler receiver.

*If it is desired to compare this to the performance of the digital system on the basis of rms errors, the rms value of a uniform distribution is 1/3 of the peak value.

If suitable active (feedback) bandpass filters are used in the receiver, then the receiving channel bandwidths can be narrow enough to permit the use of relatively close-spaced subcarrier frequencies. Typical channel allocations might be spaced every 10 cps, as shown in Table 3.5.15.

Table 3.5.15

<u>Channel No.</u>	<u>SCO Frequency</u>	<u>Band</u>
1	100 cps	99 - 101
2	110	109 - 111
3	120	119 - 121
4	130	129 - 131
5	140	139 - 141
6	150	149 - 151
7	160	159 - 161
8	170	169 - 171
9	180	179 - 181
10	190	189 - 191
etc.		

Using these subcarriers, the multi-channel bandwidth of the system may be approximated by:

$$\begin{aligned}
 f_{\text{max SC}} &= 100 + 10 (N-1) & (3.5-100) \\
 &= 10 (N + 9)
 \end{aligned}$$

where N is the number of channels.

3.5.4.8.2 Conventional FM

The nominal parameters given in Section 3.1 will be used for the FM relay link calculations.

The transmitter power required for conventional FM at low data rates will be that required to provide a 12 db C/N ratio in the I. F. bandwidth. Since this

is the same requirement as that of the conventional PCM/FM analysis, Figure 3.5.20 is equally applicable to the conventional FM analysis. This shows it is not a desirable receiving system.

3.5.4.8.3 FM With Feedback

For the analysis of FM with feedback, a receiving system of the nature of that shown in Figure 3.5.37 will be assumed, along with a linear pre-emphasis taper such that the output S/N ratio is the same from each channel. Equation (3.5-92) then yields the channel output S/N ratio:

$$S/N = C/N + 20 \log M + 10 \log \frac{B'}{2b} \quad (3.5-92)$$

where b is the channel base bandwidth

F is the channel peak deviation

f_{SC} is the channel subcarrier frequency

M is the modulation index = F/f_{SC} , a constant due to linear pre-emphasis

$B' \longrightarrow 2 f_{SC}$
max

It is now required to choose the required S/N ratio from Figure 3.5.36 and to calculate the frequency-modulation index required to produce this S/N from the threshold value of C/N, utilizing Equations (3.5-93) and (3.5-94).

For example, for ± 1 per cent accuracy, Figure 3.5.36 shows that S/N = 40 db is required. However, for 100 per cent amplitude-modulation of the sub-carrier, only 1/3 of the total channel power is available in the sidebands, the remaining 2/3 lying in the carrier. Therefore, when considering useful sideband power, an extra 4.8 db must be required in the S/N ratio of Equation (3.5-92). Substitution of Equation (3.5-100) into Equation (3.5-92) then yields:

$$44.8 = 12 + 20 \log M + 10 \log \frac{20 (N + 9)}{4} \quad (3.5-101)$$

(where it has been assumed that a channel having a nominal 3-db base bandwidth of 1 cps would have a noise bandwidth of 2 cps). Solution of Equation (3.5-101) for

M shows that the required channel modulation index varies from 3.5 to 2.9 as the number of channels N varies from 1 to 10. This is a reasonable value of M.

The transmitter power requirement, therefore, is such that at least a 12 db C/N ratio must be established in a bandwidth approximately equal to twice the highest subcarrier frequency.

Using the nominal parameters given in Section 3.1 together with Equation (3.5-100) now, it is possible to calculate the transmitter power required as a function of the number of channels, as shown in Table 3.5.16.

Table 3.5.16

Transmitter Power	10 log P dbw
Capsule Antenna Gain	0.0 db
Path Attenuation (at 50,000 km)	-166.4 db
Receiving Antenna Gain	0.0 db
Miscellaneous RF Losses	<u>-3.0 db</u>
Carrier Power Available at Receiver:	10 log P - 169.4 dbw
Receiver Noise Density per cps (KTF)	-194.0 dbw
Base Bandwidth	10 log 20 (N + 9) db
C/N Required	12.0 db
Margin	<u>8.0 db</u>
Carrier Power Required at Receiver:	10 log 20 (N + 9) - 174 dbw

Therefore, the power balance equation becomes:

$$10 \log P - 169.4 = 10 \log 20 (N + 9) - 174 \text{ dbw} \quad (3.5-102)$$

which yields:

$$10 \log P = 10 \log 20 (N + 9) - 4.6 \text{ dbw} \quad (3.5-103)$$

This has been plotted in Figure 3.5.38.

If the discriminator of Figure 3.5.37 is a phase-lock discriminator* with a threshold of 6.5 db instead of the conventional 12 db, then the required transmitter power would be reduced by a factor of 1/3.5. This has also been plotted in Figure 3.5.38. The modulation index required would then be slightly greater to provide the same output S/N ratio, but it would still not be excessive.

3.5.4.9 Calculation of Required FM/FM Transmitter Power

3.5.4.9.1 Subcarrier Frequencies

In FM/FM telemeters a deviation ratio of five is commonly used. The exact value, of course, should be optimized for this application before starting a system design. A modulation index in the neighborhood of unity will result in a performance comparable to the AM/FM system previously analyzed. Therefore, in order to examine the difference between AM/FM and FM/FM in this application a deviation ratio of five will be used for this analysis.

A suitable selection of subcarrier frequencies must be based on a precise knowledge of individual channel bandwidth requirements, as well as adequate suppression of inter-channel cross-talk. Based on rough estimates of the required bandwidth for 50-db FM sideband suppression, the channel allocations listed in Table 3.5.17 appear as though they might be satisfactory.

*The resulting FMFB-phase-lock receiver would be similar to a tracking beacon presently being developed by GE-MSD on another spacecraft program.

Table 3.5.17

<u>Channel No.</u>	<u>SCO Frequency</u>	<u>Band</u>
1	50 cps	45 - 55 cps
2	80 cps	75 - 85
3	110 cps	105 - 115
4	140 cps	135 - 145
5	170 cps	165 - 175
6	200 cps	195 - 205
7	230 cps	225 - 235
8	260 cps	255 - 265
9	290 cps	285 - 295
10	320 cps	315 - 325
etc.		

Using these subcarriers, the multi-channel base bandwidth of the system may be approximated by:

$$\begin{aligned} f_{\max} &= 50 + 30 (N - 1) \\ &= 20 (1.5N + 1) \end{aligned} \quad (3.5-104)$$

3.5.4.9.2 Conventional FM/FM Receiver

Just as in conventional FM and PCM/FM, the transmitter power required for conventional FM/FM at low data rates will be that required to provide a 12 db C/N ratio in the IF bandwidth, which is a function of the frequency uncertainty. Therefore, Figure 3.5.20 is equally applicable to the FM/FM analysis.

3.5.4.9.3 FM/FM With Feedback

FM/FM with a feedback receiver will be similar to the previously analyzed AM/FM with feedback, although the system base bandwidth will be greater, due to the frequency-modulation of the subcarrier resulting in a wider spectrum than amplitude modulation (Equation 3.5.-100) would. This is given as Equation (3.5.-104).

The FM equation for an individual channel is:

$$S/N = SC/N + 10 \log 3M^2 + 10 \log \frac{B}{2b} \quad (3.5-105)$$

which for ± 1 per cent accuracy becomes:

$$\begin{aligned} 40 &= SC/N + 10 \log 3(25) + 10 \log 10/4 \\ SC/N &= 40 - 18.7 - 4 \\ SC/N &= 17.3 \text{ db} \end{aligned} \quad (3.5-106)$$

This required SC/N ratio of 17.3 db in a 10 cps bandwidth must be obtained from the output of the FMFB receiver. The appropriate FM equation (assuming linear pre-emphasis) is:

$$\begin{aligned} S/N &= C/N + 10 \log M^2 + 10 \log \frac{40 (1.5N + 1)}{20} \\ 17.3 &= 12 + 10 \log M^2 + 10 \log 2(1.5 N + 1) \\ 10 \log M^2 &= 5.3 - 10 \log 2 (1.5 N + 1) \end{aligned} \quad (3.5-107)$$

This shows that a deviation ratio on the order of unity will be quite adequate. (The required FM improvement here has been obtained through the subcarrier discriminators.)

Therefore, the transmitter power requirement is that of producing a 12 db C/N ratio in a bandwidth of approximately $40 (1.5N + 1)$, which corresponds to the $20 (N + 9)$ bandwidth of the AM/FM system. This has been plotted in Figure 3.5.38.

It appears that, by choosing the AM/FM subcarriers at slightly lower frequencies than those of Table 3.5.15, the AM/FMFB performance can be made to exceed the FM/FMFB performance regardless of the number of channels. Since the AM channels are simpler to implement than the FM, the AM/FMFB system is, therefore, recommended over the FM/FMFB system.

3.5.4.10 Determination of Equivalent Digital Data Rate

Although the comparison is actually somewhat artificial without more knowledge of the statistics of the data, for purposes of comparison with the digital

systems analyzed for this application, it is of interest now to convert the independent variable of Figure 3.5.38 from the number of channels N to an equivalent binary data rate. The theoretical maximum number of independent samples per second available from each channel is equal to twice the channel base bandwidth. Therefore, a one-cps channel carries the equivalent of up to two independent samples per second. The number of equivalent bits per sample (i.e., the resolution of each sample) depends on the analog S/N ratio. Comparison of Figure 3.5.36 to Table 3.5.2 (in the PCM analysis) permits the association of S/N ratio and accuracy with an equivalent number of bits per sample. For example, 6-bit PCM offers an accuracy of ± 0.8 per cent, which corresponds to an equivalent analog S/N ratio of 41.7 db in a one-cps data channel. This could be said to convey up to $2 \times 6 = 12$ bits/sec. of data. In general, this line of reasoning leads to an equivalent digital data rate per channel of:

$$0 < r < 2nb \quad (3.5-108)$$

Since the modulation index can be increased to provide a higher output channel S/N ratio with only a slight increase in predetection bandwidth, the equivalent value of n has only a secondary effect in this comparison. Therefore, in order to simplify the comparison, a value of $n = 6$ bits/sample will be used. In this manner, the results presented in Figure 3.5.38 have been translated to those of Figure 3.5.39.

APPENDIX A

Derivation of FM Output S/N Ratio*

Frequency modulation of a sinusoidal carrier by a sinusoidal modulating wave may be represented by:

$$M(t) = A \sin \left(2\pi f_c t + \frac{F}{f} \sin 2\pi ft \right) \quad (\text{A-1})$$

where:

F is the frequency deviation

f is the frequency of the modulating wave

f_c is the carrier frequency

The instantaneous frequency (defined as the time rate of change of the argument, divided by 2π) is given by:

$$f_i = f_c + F \cos 2\pi ft \quad (\text{A-2})$$

The output voltage of an ideal FM detector will be proportional to the amount this instantaneous frequency varies from the carrier frequency. Thus:

$$e_s = m F \cos 2\pi ft \quad (\text{A-3})$$

where m is a factor of proportionality.

The corresponding average output power (in a one-ohm circuit) is:

$$S = \overline{e_s^2} = \frac{1}{2} m^2 F^2 \quad (\text{A-4})$$

where the bar denotes the time average.

The noise output power will now be calculated, assuming that uncorrelated noise is uniformly distributed in frequency over the frequency range accepted at the detector input. The band of noise of power spectral density n will be represented by a large number of sinusoidal elements, separated in frequency by increments Δf . The sinusoidal components will each have a peak amplitude of $\sqrt{2n \Delta f}$,

*From Black, loc. cit., pp. 221-224.

and will be unrelated in phase and frequency. The sum of a particular incremental noise sinusoid and the unmodulated carrier may be written in the form:

$$R = A \sin \omega_c t + \sqrt{2n \Delta f} \sin (\omega_c + \omega) t \quad (A-5)$$

$$= A \left[\sin \omega_c t + X \sin (\omega_c + \omega) t \right] \quad (A-6)$$

where:

$$\omega = 2 \pi f$$

$$\omega_c = 2 \pi f_c$$

$$n = \text{input noise power density}$$

$$\Delta f = \text{input bandwidth increment}$$

$$X = \sqrt{2n \Delta f} / A \ll 1$$

Then, by mathematical identity, Equation (A-6) may be written:

$$R = A (1 + X^2 + 2X \cos \omega t)^{1/2} \sin(\omega_c t + \theta) \quad (A-7)$$

where:

$$\theta = \tan^{-1} \left[\frac{X \sin \omega t}{1 + X \cos \omega t} \right]$$

$$\approx X \sin \omega t \text{ for } X \ll 1$$

Thus, for small values of X, Equation (A-7) may be written:

$$R \approx A (1 + 2 X \cos \omega t)^{1/2} \sin (\omega_c t + X \sin \omega t) \quad (A-8)$$

As in Equation (A-2), the instantaneous frequency is given by:

$$f_i = f_c + X f \cos 2 \pi f t \quad (A-9)$$

So, when the wave described by Equation (A-8) is applied to an ideal FM detector, the output voltage will be given by:

$$e_n = m X f \cos 2 \pi f t$$

$$= \frac{mf \sqrt{2n \Delta f}}{A} \cos 2 \pi f t \quad (A-10)$$

This will yield an incremental noise power (in an assumed one-ohm output circuit) given by:

$$\Delta N = \overline{e_n^2} = \frac{m^2 n f^2}{A^2} \Delta f \quad (A-11)$$

Going to the limit as $\Delta f \rightarrow 0$, yields:

$$dN = \overline{e_n^2} = \frac{m^2 n f^2}{A^2} df \quad (A-12)$$

The average noise power output may be obtained by integrating this over the range of noise frequencies of f in Equation (A-5) which will appear in the output of the low-pass output filter of bandwidth b .

$$N = \int_{-b}^b dN = 2 \int_0^b dN = \frac{2m^2 n}{A^2} \int_0^b f^2 df = 2m^2 n b^3 / 3A^2 \quad (A-13)$$

Since the carrier power is given by:

$$P_c = A^2 / 2 \quad (A-14)$$

Equation (A-13) may be written:

$$N = m^2 n b^3 / 3 P_c \quad (A-15)$$

Division of Equation (A-4) by Equation (A-15) yields the output S/N ratio:

$$S/N = 3 (F/b)^2 (P_c / 2 bn) \quad (A-16)$$

Since an output bandwidth b will accommodate a modulating signal frequency up to b , this may be written:

$$S/N = 3 M^2 P_c / 2 bn \quad (A-17)$$

where M is the modulation index $= F/b$. This is Equation (3.5-82) in the body of this report.

APPENDIX B

Derivation of FM Output S/N Ratio in Highest Channel of Baseband

Appendix A has shown the output S/N ratio derivation for the case of a single channel output of bandwidth 0 to b cps. This appendix will show the derivation of the output S/N ratio in the worst* (i.e., highest frequency) channel, with a bandwidth lying between f_1 and f_2 cps, as shown below in Figure B-1.

All of the reasoning up to Equation (A-12), in Appendix A still applies. However, the integration limits of Equation (A-12) now become f_1 to f_2 instead of 0 to b, yielding:

$$N = 2 \int_{f_1}^{f_2} dN = \frac{2 m^2 n}{A^2} \int_{f_1}^{f_2} f^2 df \quad (B-1)$$

$$= (2m^2 n/3A^2) (f_2^3 - f_1^3) \quad (B-2)$$

$$= (2m^2 n/3A^2) (f_2 - f_1) (f_2^2 + f_1 f_2 + f_1^2) \quad (B-3)$$

Now letting:

$$f_2 - f_1 = b$$

$$(f_2^2 + f_1 f_2 + f_1^2) \approx 3f_m^2 \quad (B-4)$$

$$(\text{for } f_2 \approx f_1 \approx f_m)$$

where f_m is the mean frequency of the channel under consideration, yields:

$$\begin{aligned} N &= (2m^2 n/3A^2) (b) (3f_m^2) \\ &= (2m^2 n/A^2) (b) (f_m^2) \end{aligned} \quad (B-6)$$

*As shown in Section 3.5.4.4, the noise which falls in the baseband of an FM signal increases with the baseband frequency. Thus, the noise is greatest in the top channel, corresponding to the highest frequency in the baseband.

**The fractional error in the approximation in the top channel of a system is as follows: 300 channels -9.3×10^{-7} ; 12 channels -6.3×10^{-4} ; 6 channels -2.7×10^{-3}

Since the carrier power is given by Equation (A-13)

$$P_c = A^2/2 \quad (A-13)$$

Equation (B-6) may be written:

$$N = (m^2 n/P_c) (b f_m^2) \quad (B-7)$$

Division of Equations (A-4) by (B-7) then yields the output S/N ratio:

$$S/N = (F/f_m)^2 (P_c/2 bn) \quad (B-8)$$

This may be written

$$S/N = M^2 P_c/2 bn \quad (B-9)$$

where M is the modulation index of the mean frequency in the channel*. Note that the factor of 3 in Equation (A-16) has disappeared in Equation (B-9).

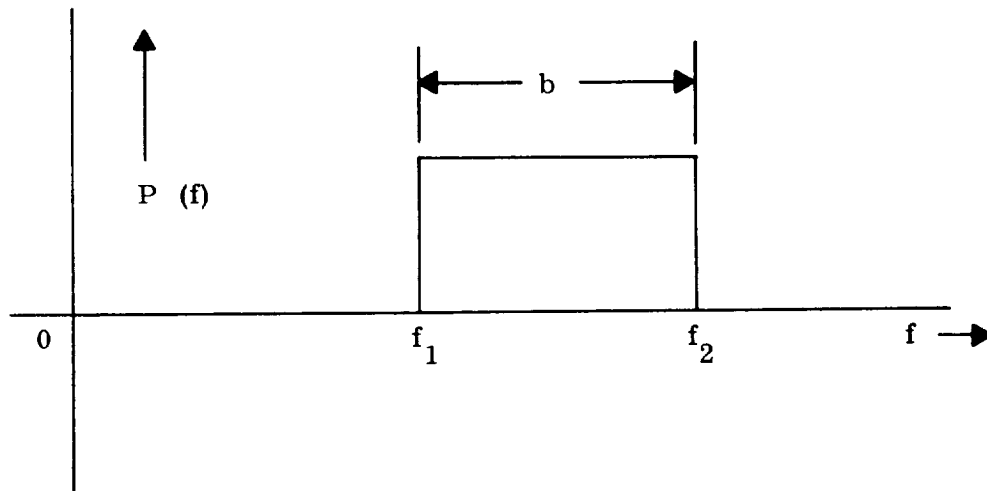


Figure B-1. Spectrum of Highest Channel

*Note that, with a large number of channels in the system, the modulation index does not vary significantly over the channel bandwidth of the high channels.

APPENDIX C

Derivation of I. F. Modulation Index

Equation (3.5-93) may be readily derived from elementary servo theory.

Consider the receiver feedback loop of Figure C-1.

The function of the loop is to drive the frequency deviation F_2 to the value of F_1 . The error in doing this is indicated by ΔF .

Let the loop gain be given by:

$$\mu = K_1 K_2 \quad (C-1)$$

Then:

$$\begin{aligned} \Delta F &= F_1 - F_2 \\ &= F_1 - \Delta F \mu \end{aligned} \quad (C-2)$$

Solution for ΔF yields:

$$\Delta F = \frac{F_1}{1 + \mu} \quad (C-3)$$

Thus, from the definition of modulation index (Equation 3.5-89) the I. F. modulation index is given by:

$$M_{IF} = \frac{M}{1 + \mu} \quad (C-4)$$

where M is the modulation index associated with F_1 .

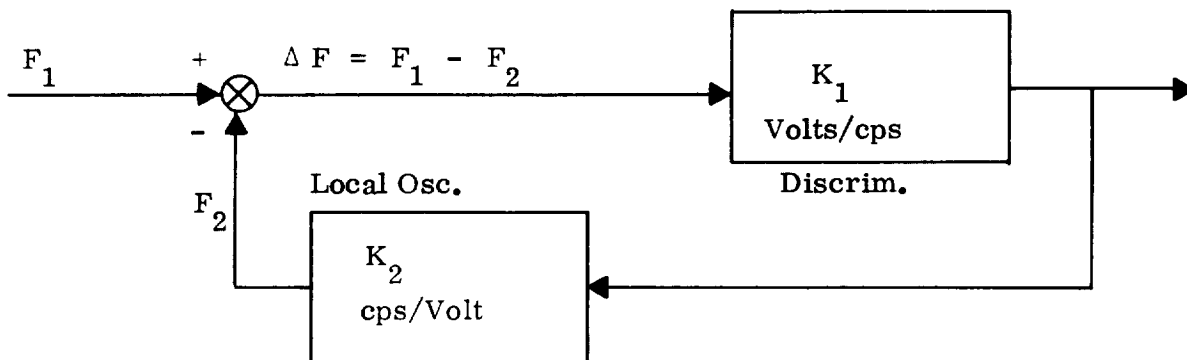


Figure C-1. Receiver Feedback Loop

APPENDIX E

Nomenclature

b	Channel information bandwidth (cps)
B	predetection bandwidth (cps)
B'	loop bandwidth in FMFB receiver (cps)
C/N	predetection carrier-to-noise power ratio
D	deviation ratio, the ratio of the maximum frequency deviation to the maximum modulating frequency
e_n	noise voltage out of FM detector (volts)
e_s	signal voltage out of FM detector (volts)
f	a typical frequency (cps)
f_m	mean frequency of the channel under consideration (cps)
F	frequency deviation, the maximum instantaneous frequency excursion (cps)
FMFB	frequency modulation with feedback
m	factor of proportionality in FM detector
M	modulation index, the deviation ratio when the modulating signal is a single sinusoid
n	noise power spectral density (single-sided spectrum) (watts/cps)
P_c	unmodulated carrier power (watts)
$p(V_n)$	probability density function of predetection noise voltage amplitude (volts) ⁻¹
S/N	detected signal-to-noise ratio
V_n	instantaneous amplitude of the predetection noise voltage (volts)
μ	feedback factor (loop gain) of the feedback receiver

APPENDIX D

Bibliography

1. Chaffee, J. G. "The Application of Negative Feedback to Frequency-Modulation Systems," Bell System Technical Journal, July, 1939.
2. Carson, J. R. "Frequency - Modulation: Theory of the Feedback Receiving Circuit," Bell System Technical Journal, July, 1939.
3. International Telephone and Telegraph Corp., Reference Data for Radio Engineers, Fourth Edition, New York, N. Y., 1956.
4. Tibbs, C. E. and Johnstone, G. G. Frequency Modulation Engineering, Wiley, New York, N. Y., 1950.
5. Black, H. S. Modulation Theory, Van Nostrand, New York, N. Y., 1953.
6. Nichols, M. H. and Rauch, L. L. Radio Telemetry, Second Edition, New York, N. Y., 1956.
7. Crosby, M. G. "Frequency-Modulation Noise Characteristics," Proc. IRE, April, 1937.
8. Pierce, J. R. and Kompfner, R. "Transoceanic Communication by Means of Satellites," Proc. IRE, March, 1959.
9. Terman, F. E. Radio Engineering, Third Edition, McGraw-Hill, New York, N. Y., 1947.
10. Ordway, F. I., Editor. Advances in Space Sciences, Vol. 1, pp. 55-108, "Interplanetary Communications" (by J. R. Pierce and C. C. Cutler), Academic Press, New York, N. Y., 1959.
11. Martin, B. D. "Threshold Improvement in an FM Subcarrier System," IRE PGSET Transactions, March, 1960.
12. Holbrook, B. D. and Dixon, J. T. "Load Rating Theory for Multi-Channel Amplifiers," Bell System Technical Journal, October, 1939.

Noncoherent Multi-level FSK Direct Link

Multi-level FSK or quantized FSK is used with a sample-data system (time-division multiplex) in which the carrier frequency is keyed in accordance with the quantized amplitude of each sample in turn. The number of levels of frequency required is determined by the required resolution of the measurement. If M levels are utilized, the resolution is equivalent to that of an N -bit binary system where $N = \log_2 M$, as given in Table 3.5.2.

Noncoherent detection is assumed. In particular, the receiver consists of a bank of M bandpass filters, each centered about a particular frequency to be transmitted. Each bandpass filter is followed by an envelope detector, which in turn is followed by a matched filter. The decision is based on the relative amplitudes of the waveforms emanating from the matched filters; i.e., the signal is assumed to be at the frequency of the matched filter having the greatest output.

Reiger* gives the probability of error for such a system as

$$P_{eM} = \frac{e}{M} e^{-E/N_o} \sum_{r=2}^M (-1)^r \binom{M}{r} e^{E/rN_o} \quad (3.5-109)$$

Since an evaluation of this expression for $M = 64$ (6-bit accuracy) was not found in the literature, an approximation will be made by considering the probability of error for a 64-level coherent FSK system given by Viterbi** and by a comparison of the relative performance of a noncoherent and coherent binary system. The required probability of error will be assumed to be 0.01. The normalized S/N ratio (E/N_o) required for the coherent FSK system is approximately 11 db according to Viterbi. To this will now be added the difference between the values of (E/N_o), for the noncoherent and coherent binary systems which is approximately 1.5 db. Therefore, the required value of (E/N_o) is assumed to be 12.5 db.

*Reiger, S. "Error Rates in Data Transmission," Proceedings of the IRE, May, 1958.

**Viterbi, A. "Classification & Evaluation of Coherent Synchronous Sample Data Telemetry System," Transactions on Space Electronics & Telemetry, March, 1962.

The difference between this and the value obtained using Equation 3.5-109 is negligible for the purpose of this analysis. Assuming further that the double-ended bandwidth of each matched filter is equal to the reciprocal of the pulse length T, then

$$\left(\frac{E}{N_o} \right) \approx (S/N)_{B_1} = 12.5 \text{ db (17.8)} \quad (3.5-110)$$

Threshold in the bandpass filters will be taken as 9 db (8). The bandwidth of the bandpass filters can, therefore, be greater than that of the matched filter in order to allow for frequency instability. The maximum ratio of the two bandwidths is then,

$$\frac{B_1 + \Delta F}{B_1} = \frac{(S/N)_{B_1}}{(S/N)_{B_1} + \Delta F} = \frac{17.8}{8} = 2.2 \quad (3.5-111)$$

Since the sample rate is equal to B_1 and 6-bit samples have been assumed, the bit rate r is given by

$$r = 6B_1 \quad (3.5-112)$$

In terms of the bandwidth of the bandpass filters,

$$r = 6 \frac{B_1 + \Delta F}{2.2} = 2.72 (B_1 + \Delta F)$$

or

$$B_1 + \Delta F = 0.368 r \quad (3.5-113)$$

This relation is used to determine the system capability in the following table.

Table 3.5.18

Signal Power Available at Receiver	10 log P - 206.5 dbw
Receiver Noise per cps ($T_e = 50^{\circ}\text{K}$)	- 211.6 dbw
Bandwidth ($B_1 + \Delta F$)	10 log 0.368 r db
S/N Required (in $B_1 + \Delta F$)	9.0 db
Margin	<u>8.0 db</u>
Signal Power Required at Receiver: 10 log 0.368 r - 194.6	

Then,

$$10 \log P - 206.5 = 10 \log 0.368 r - 194.6$$

or,

$$10 \log P = 10 \log r + 7.7 \text{ db} \quad (3.5-114)$$

This relationship is plotted in Figure 3.5.40.

The power levels at which the threshold condition is reached for a given bandwidth can be determined from the above calculations letting ($B_1 + \Delta F$) equal 0.368 r.

Then,

$$10 \log P = 10 \log (B_1 + \Delta F) + 11.9 \quad (3.5-115)$$

For ($B_1 + \Delta F$) = 3, 15 and 50 cps the power levels at threshold are then 47, 232, and 720 watts, respectively.

Note that advantage can be taken of the noncoherent nature of multi-level FSK as was discussed with respect to PCM/FSK (Section 3.5.3.3.5). The high theoretical efficiency of this technique combined with the possibility of utilizing the advantages of a noncoherent pulse system make the technique look very attractive for the direct link. Since the bandwidth of the signal is much greater than that of most other systems, application of the technique in an earth link is limited by frequency allocation considerations; however, with the low data rates expected in the direct link, this should present no problems in this application.

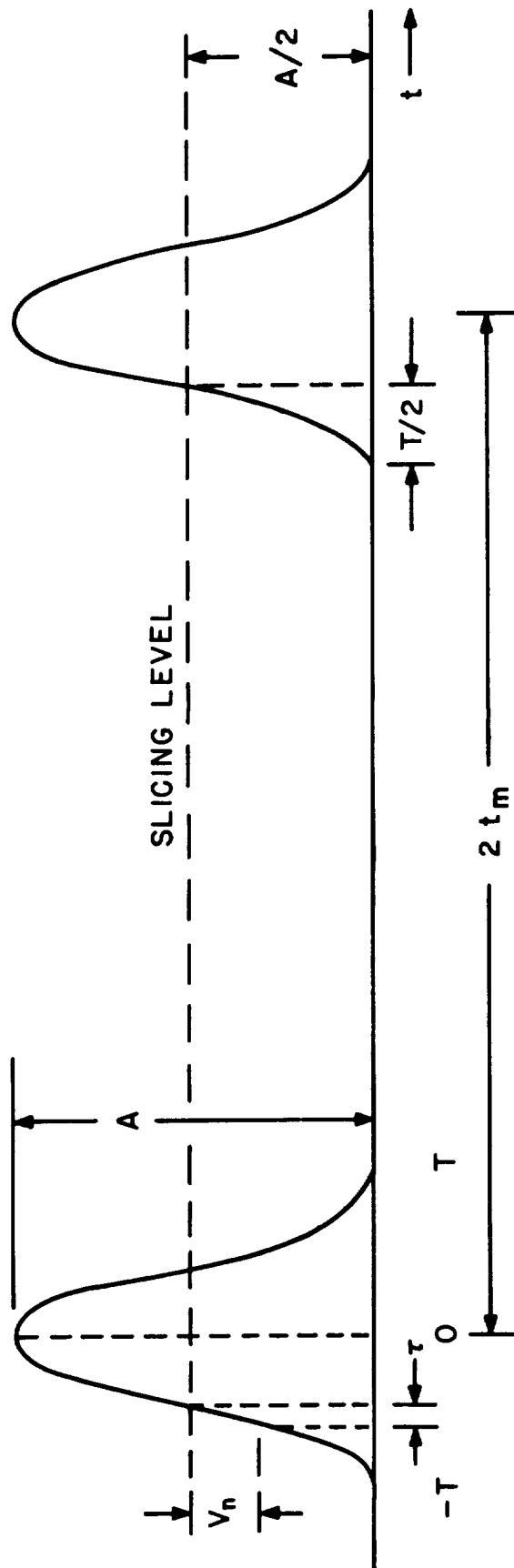


Figure 3.5.1. Raised Cosine Pulse Waveforms

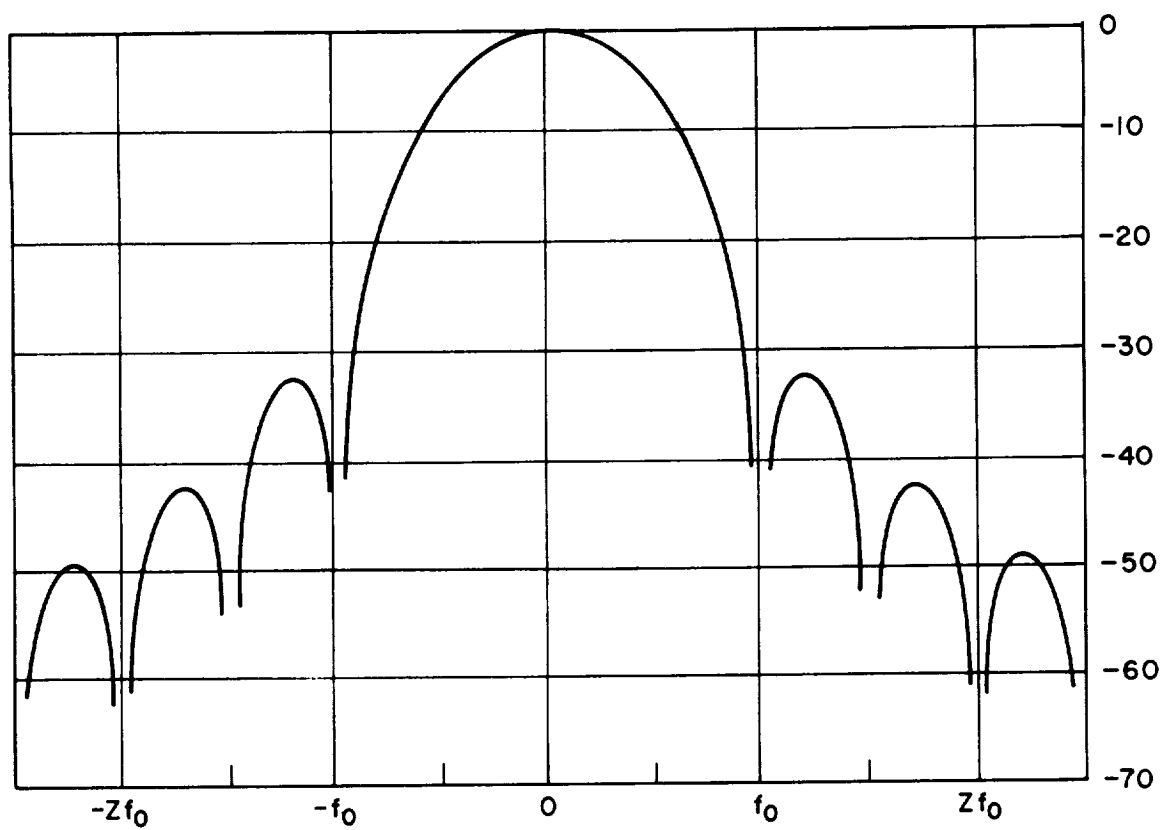


Figure 3.5.2. Power Density Spectrum of Raised Cosine Pulse

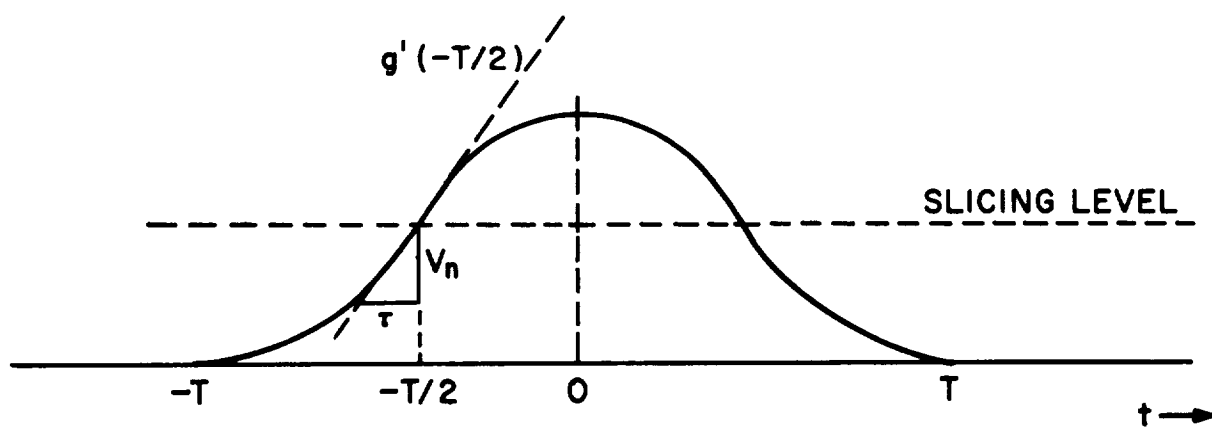


Figure 3.5.3. Effect of Additive Noise

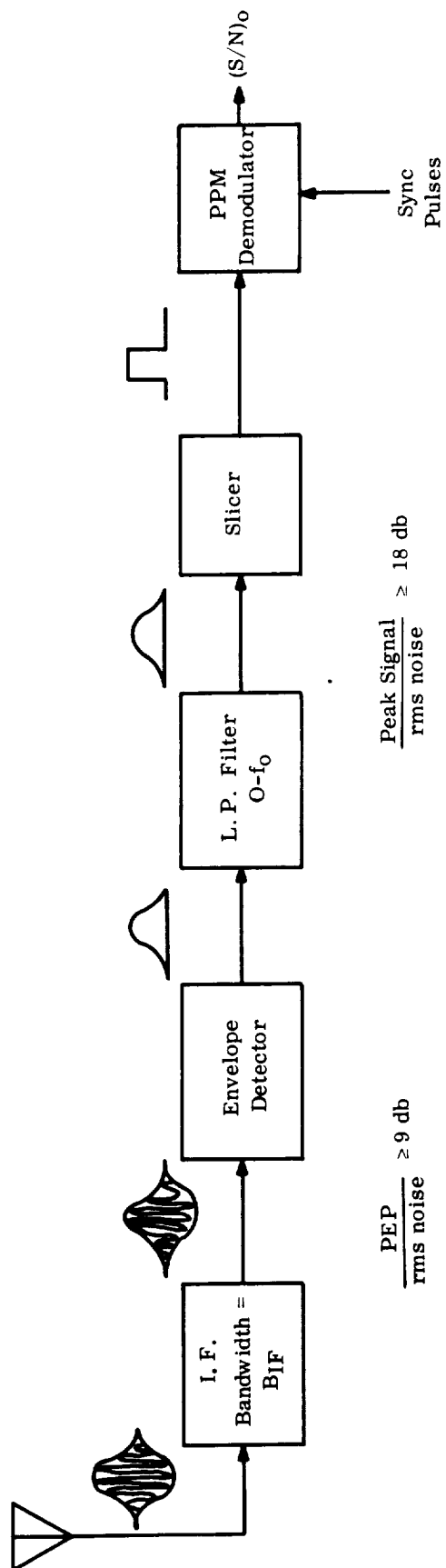


Figure 3.5.4. PPM/AM Detection Technique

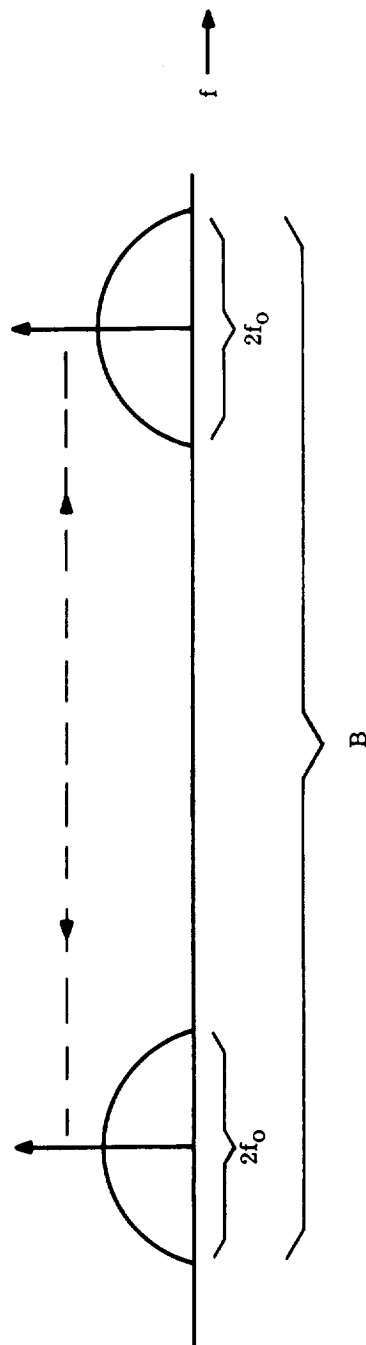


Figure 3.5.5. Spectra of Received Signal

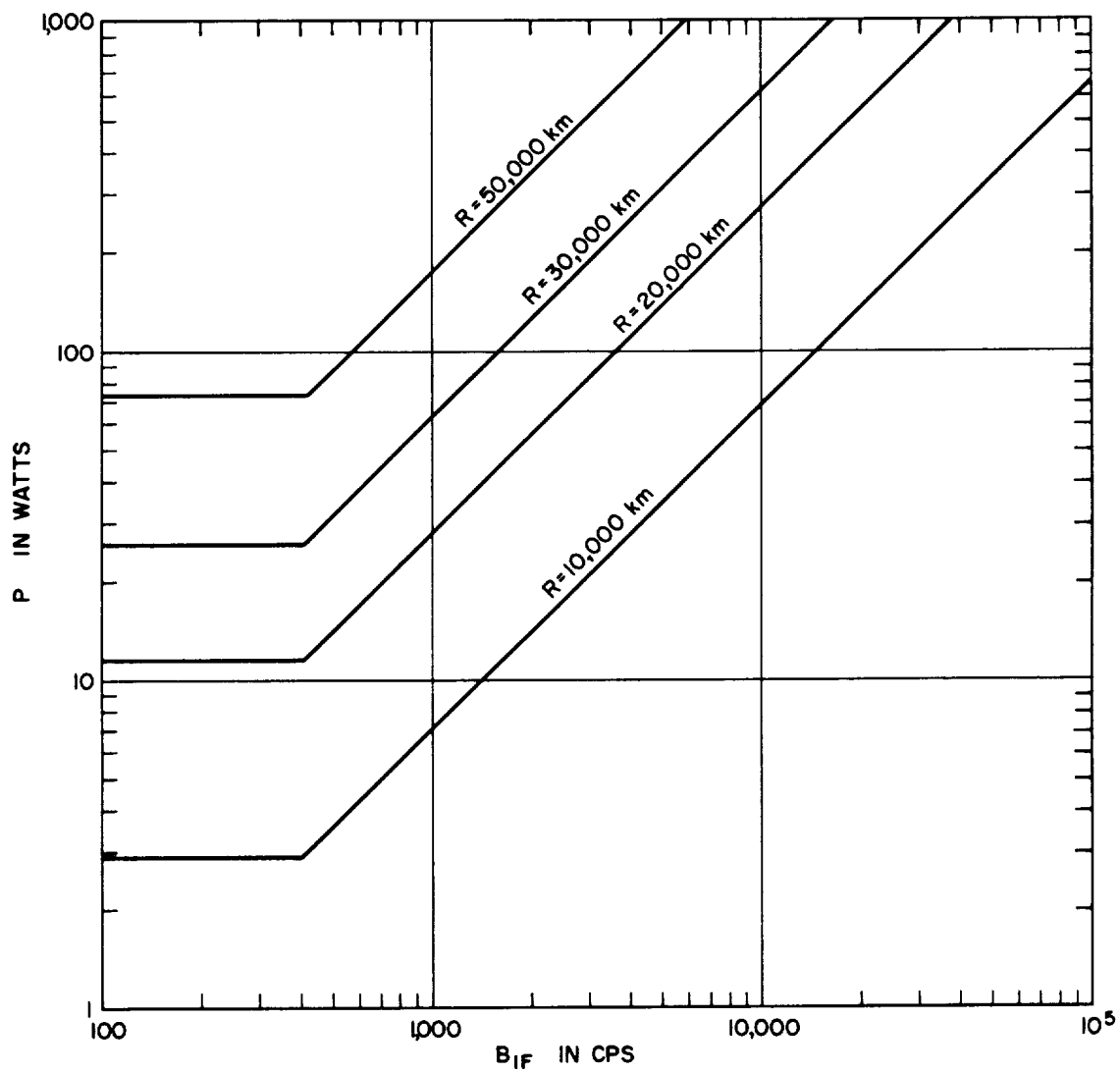


Figure 3.5.6. Transmitter PEP Required for Operation above Thresholds

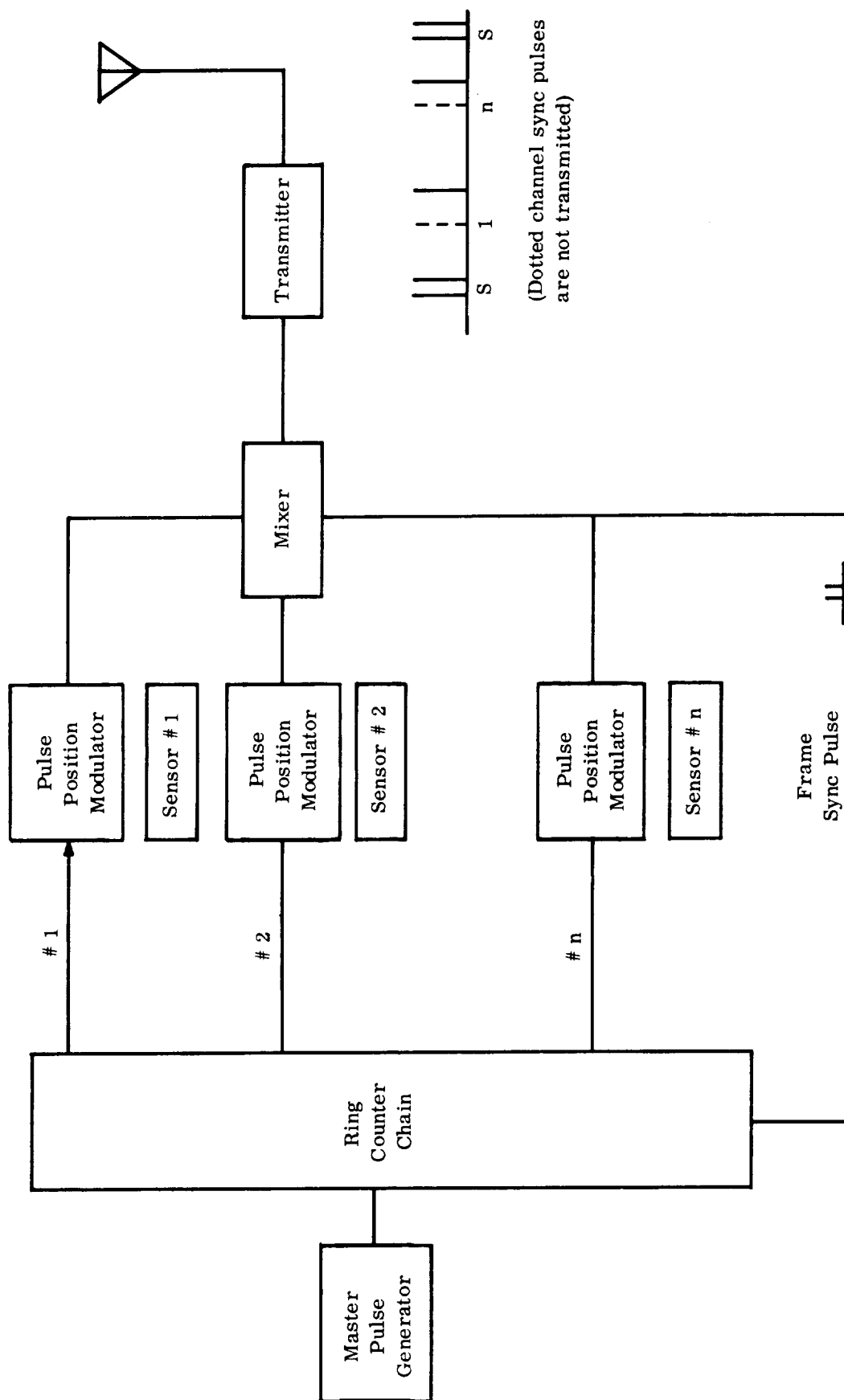


Figure 3.5.7. PPM/AM Transmitting System

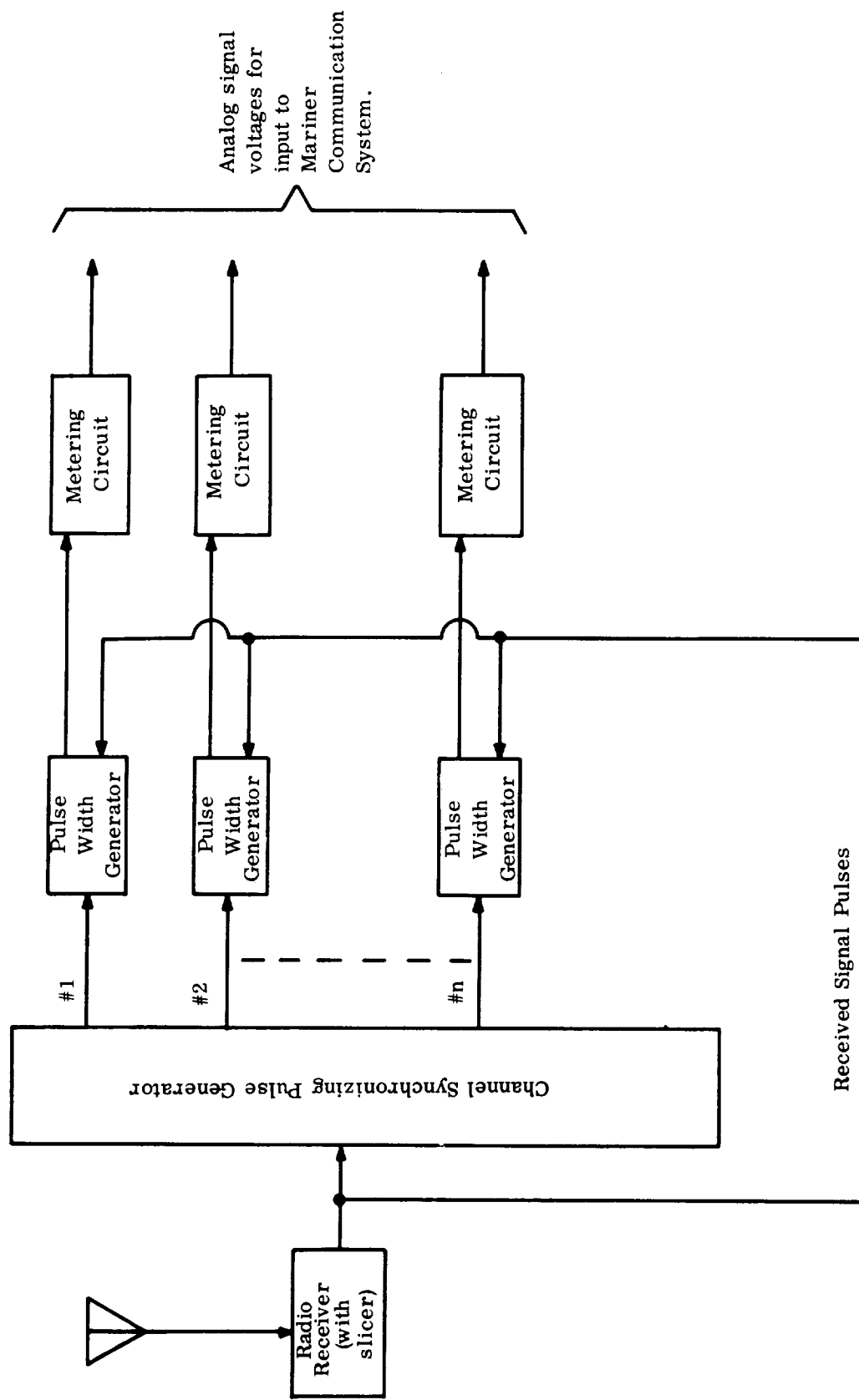


Figure 3.5.8. PPM/AM Receiving System

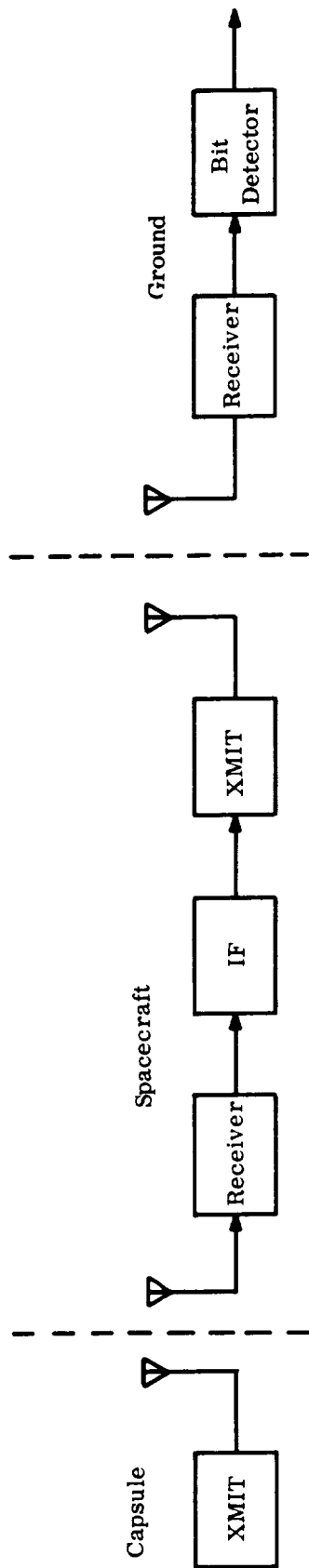


Figure 3.5.9a. Basic Block Diagram of "Repeater" System

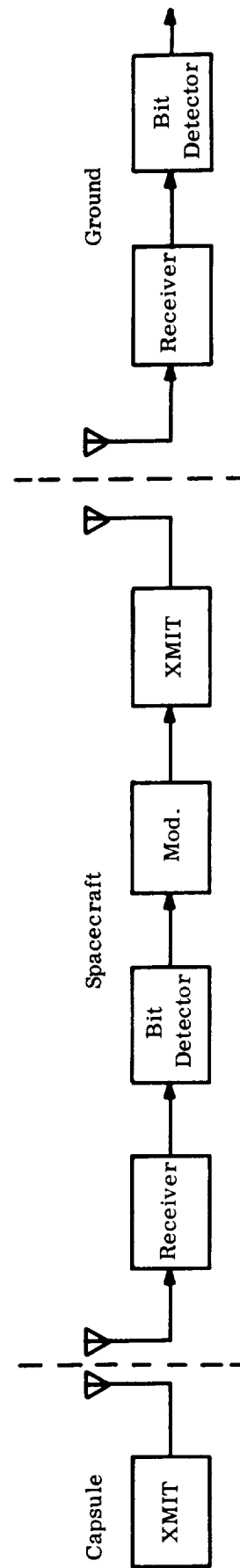


Figure 3.5.9b. Basic Block Diagram of "Demodulator" System

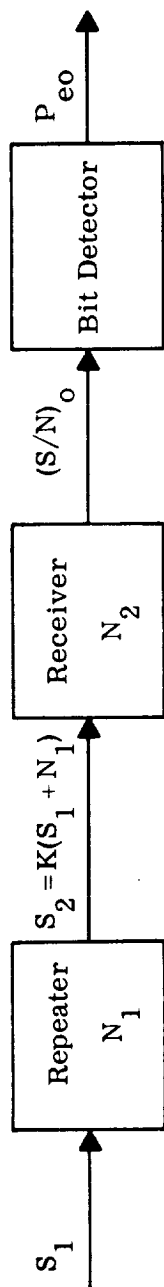


Figure 3.5.10. Signal Flow Diagram for Linear Repeater

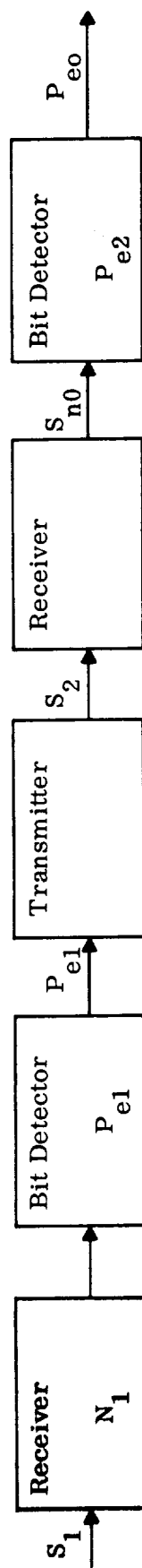


Figure 3.5.11 Signal Flow Diagram for Demodulator Technique

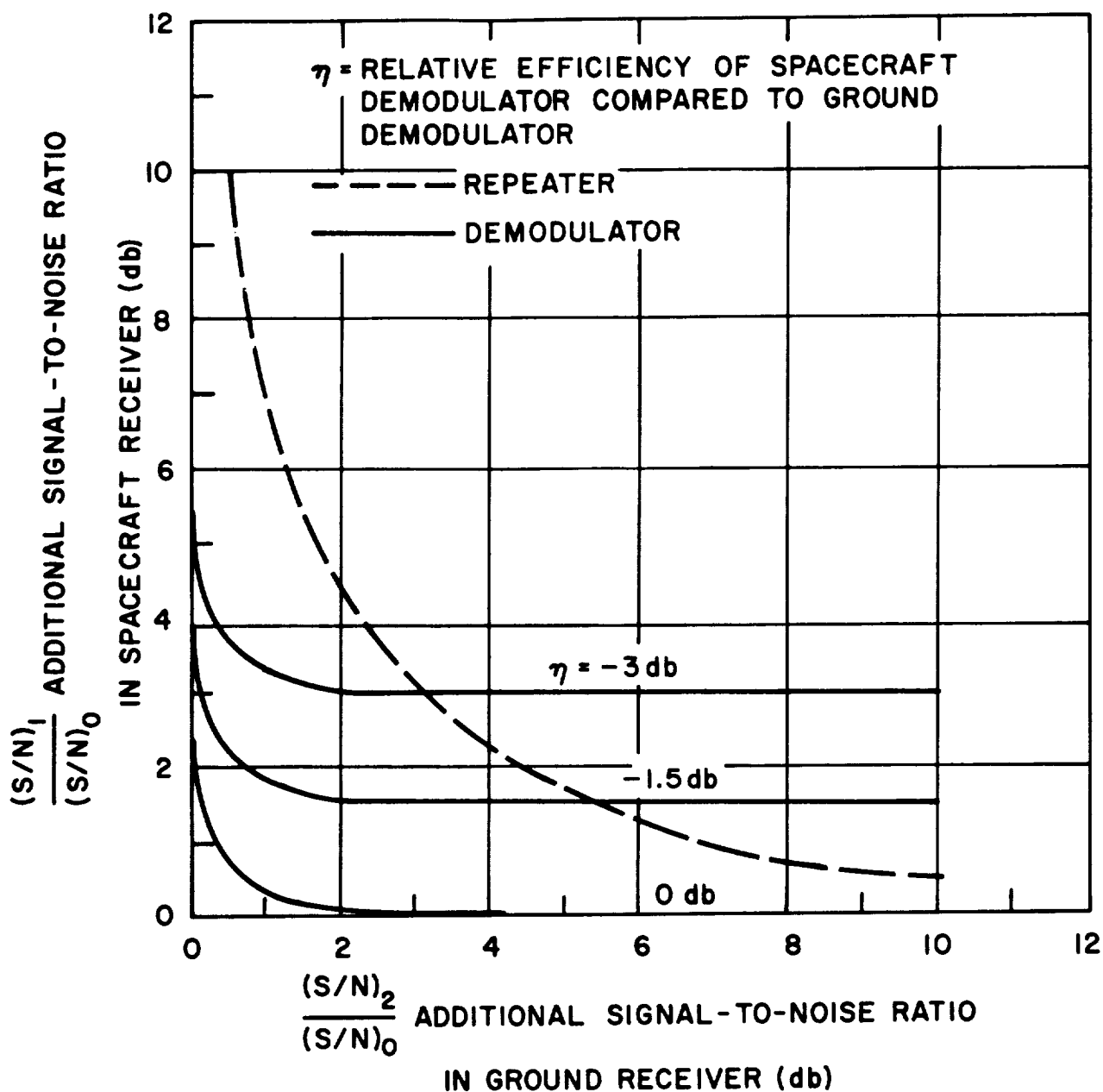


Figure 3.5.12. Relationships Between Signal-to-Noise Ratios in Spacecraft and Ground Receivers to Obtain Required Error Rate

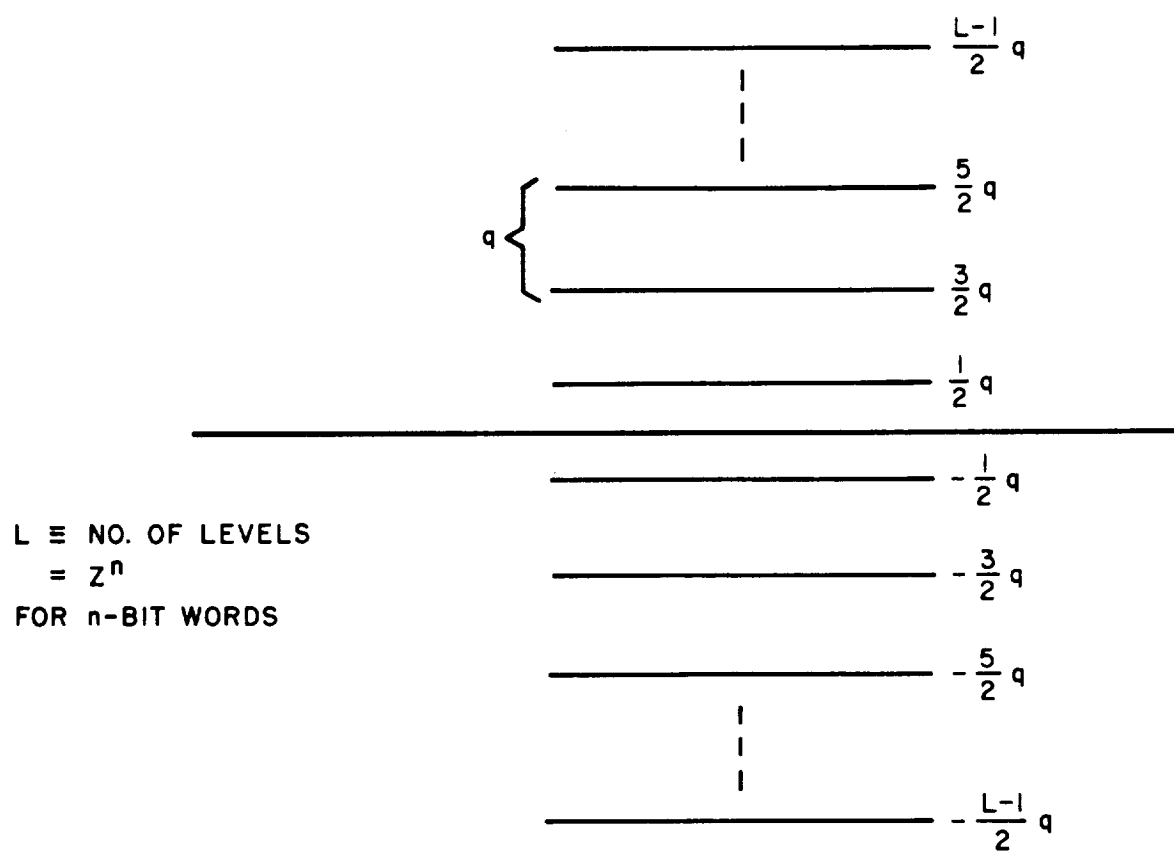


Figure 3.5.13. Linear Quantization Levels

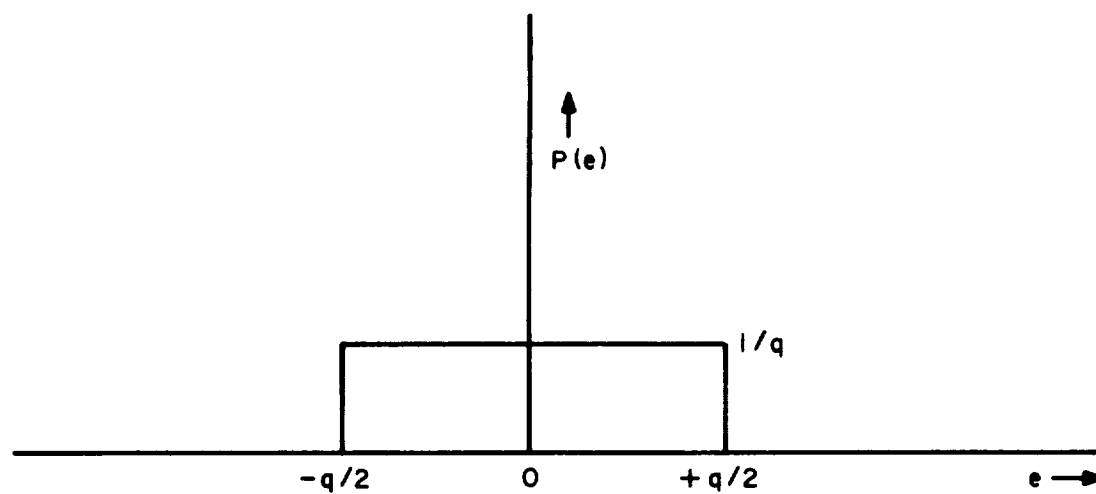


Figure 3.5.14. Probability Distribution of Quantization Error

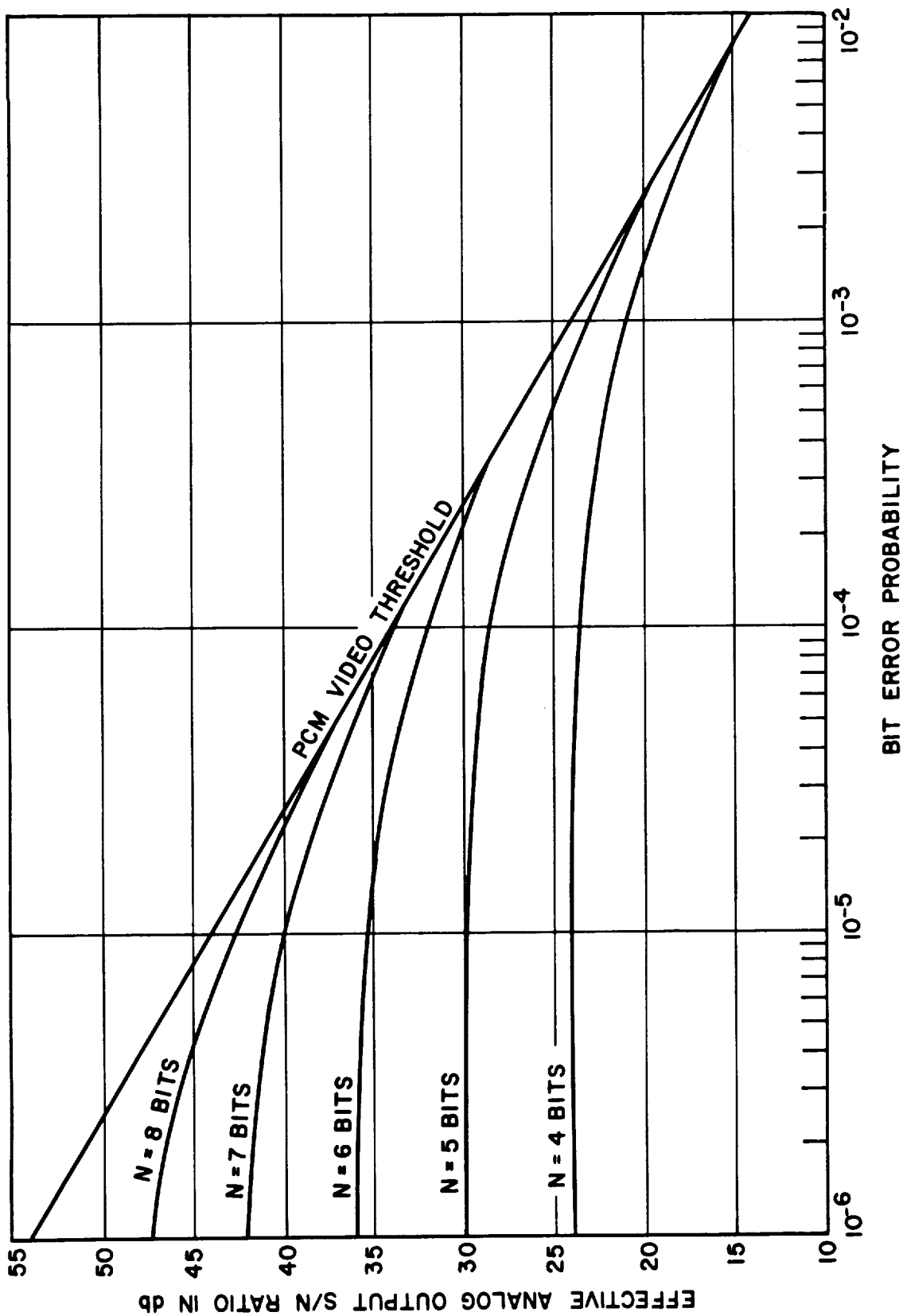


Figure 3.5.15. PCM Output S/N Ratio vs. Bit Error Probability for Various Quantization Accuracies
(Assuming all Signal Levels Equally Likely)

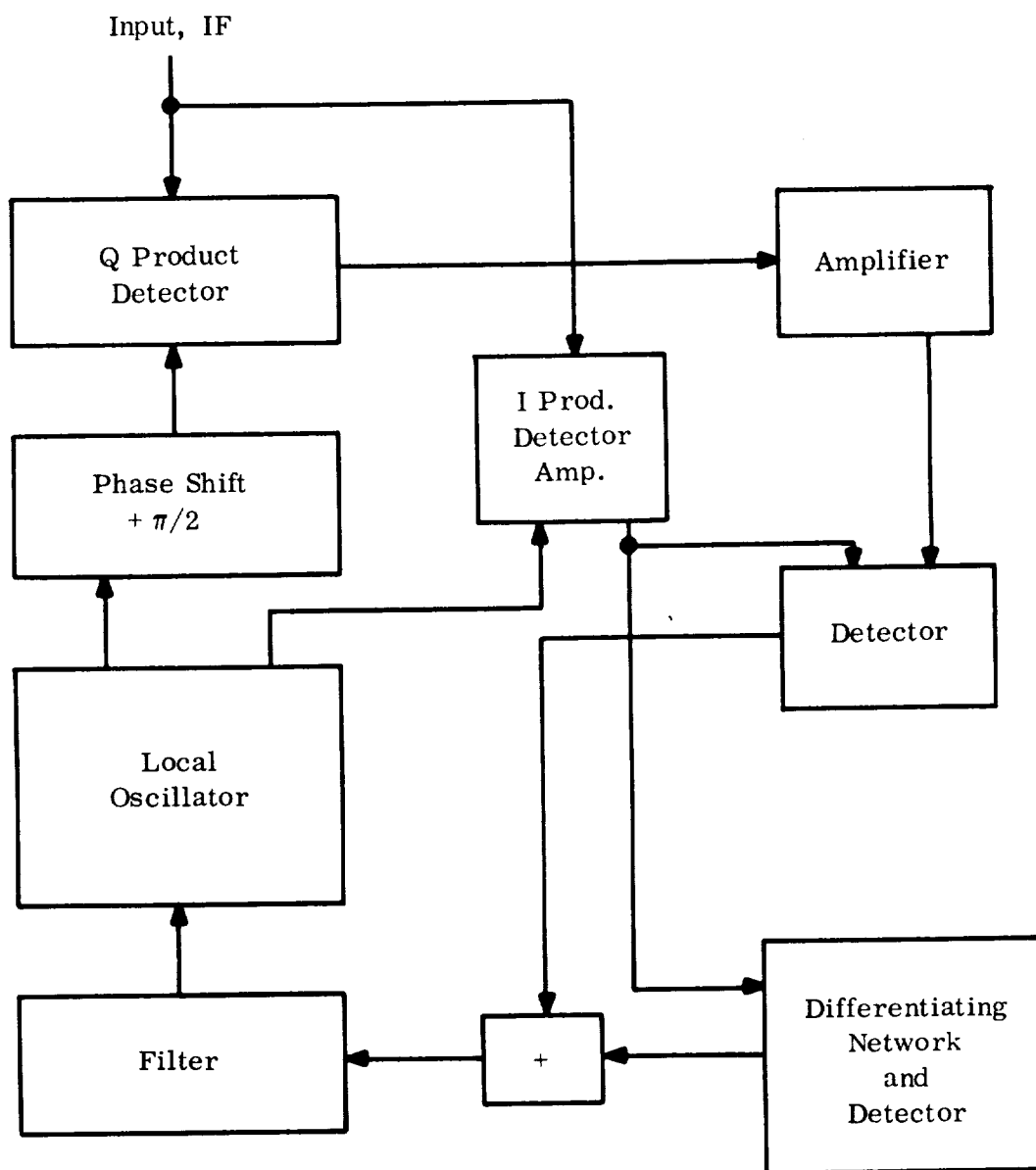


Figure 3.5.16. Synchronous Detection Receiver Phase Lock Servo Loop

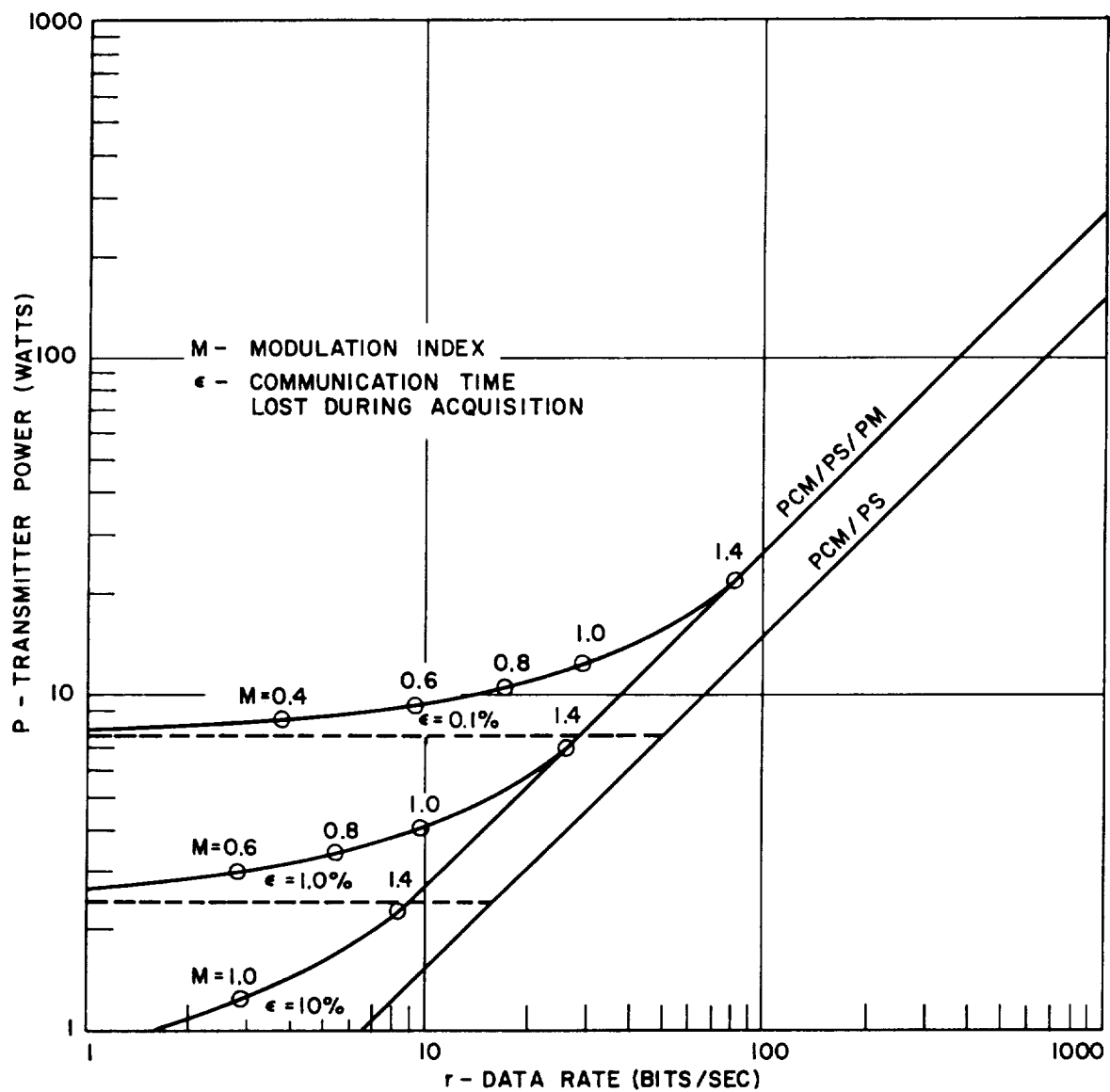


Figure 3.5.17. Transmitter Power Required for PCM/PS and PCM/PS/PM Relay Link

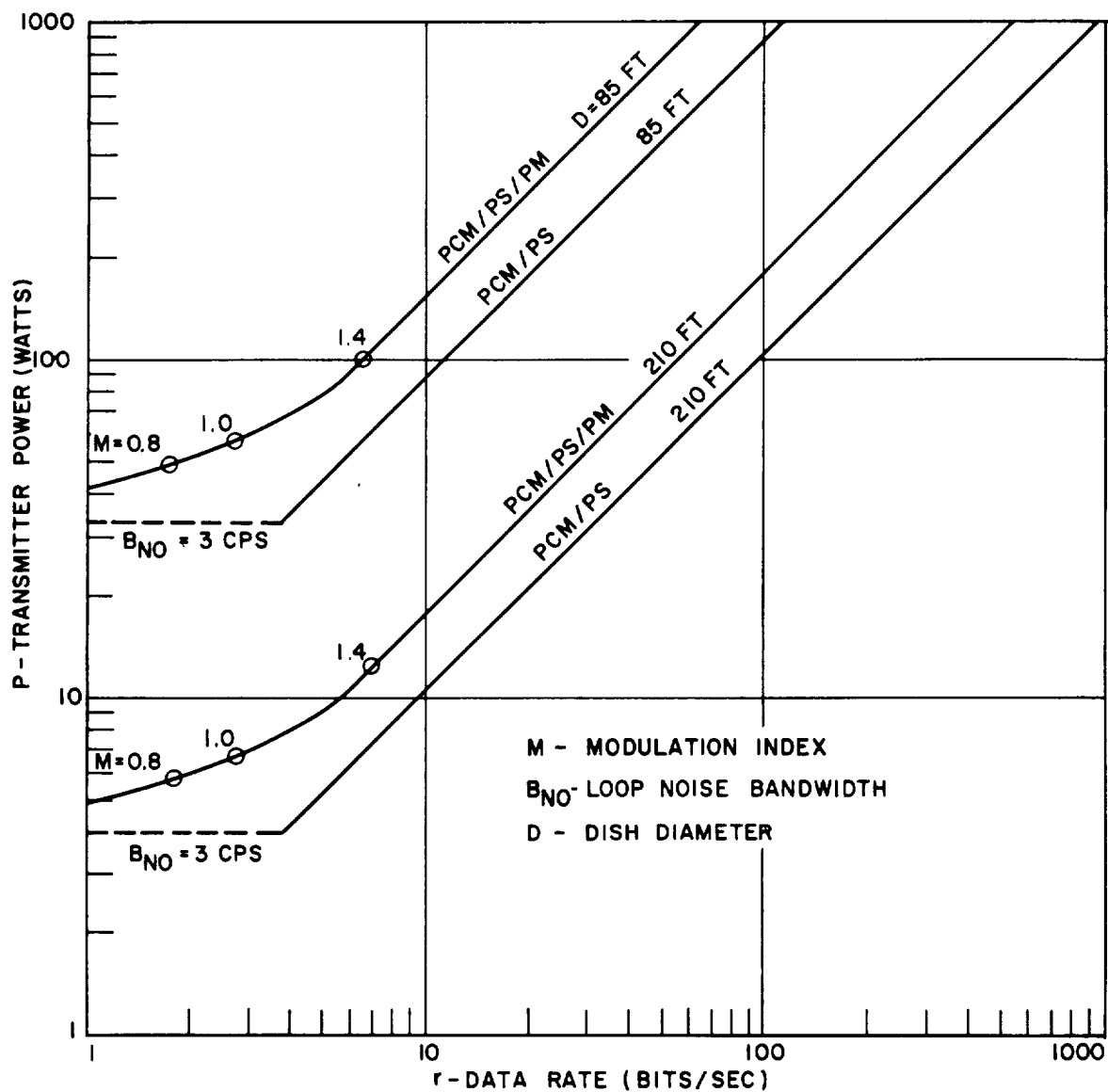


Figure 3.5.18. Transmitter Power Required for PCM/PS and PCM/PS/PM Direct Link

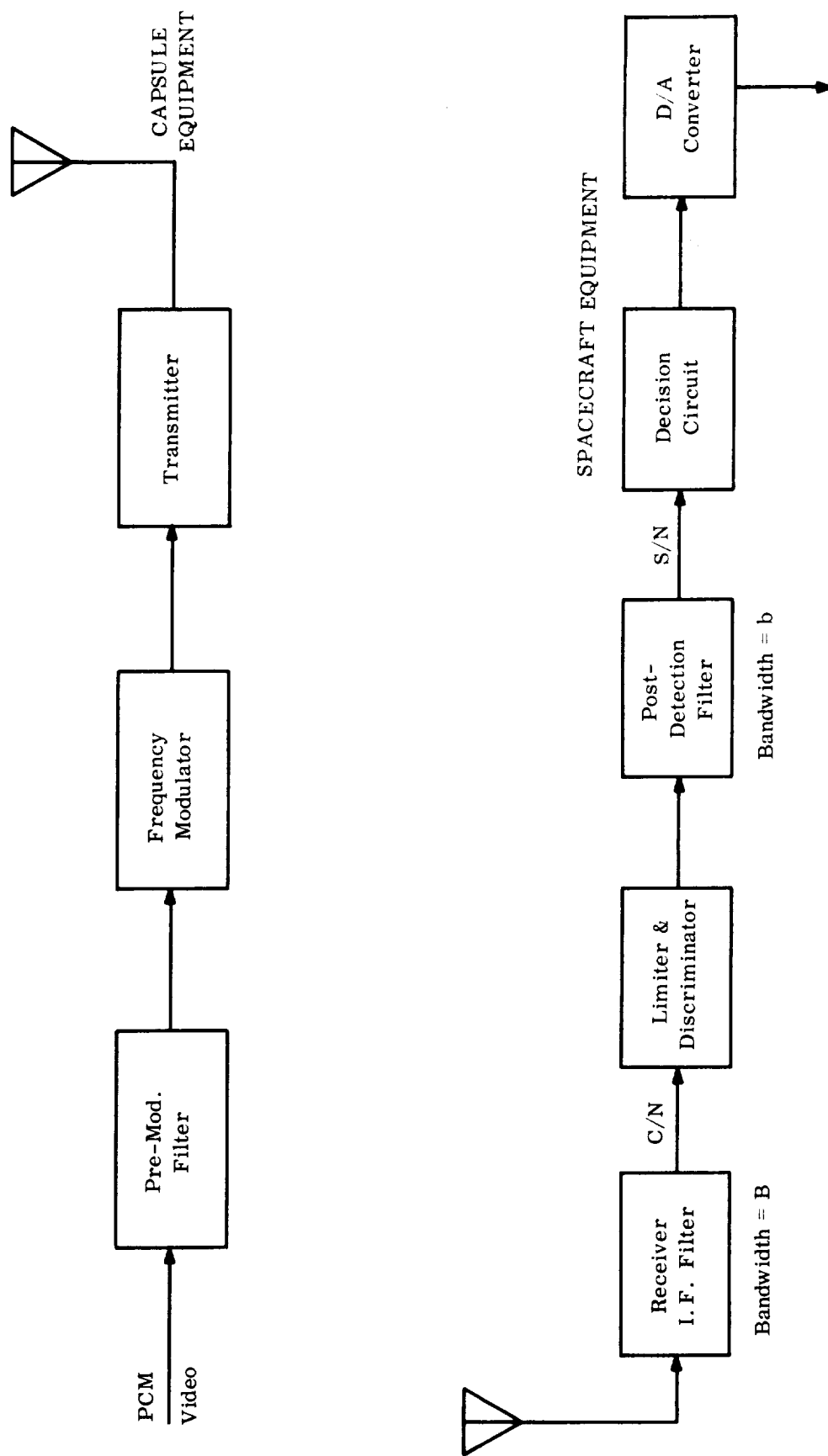


Figure 3.5.19. General PCM/FM System

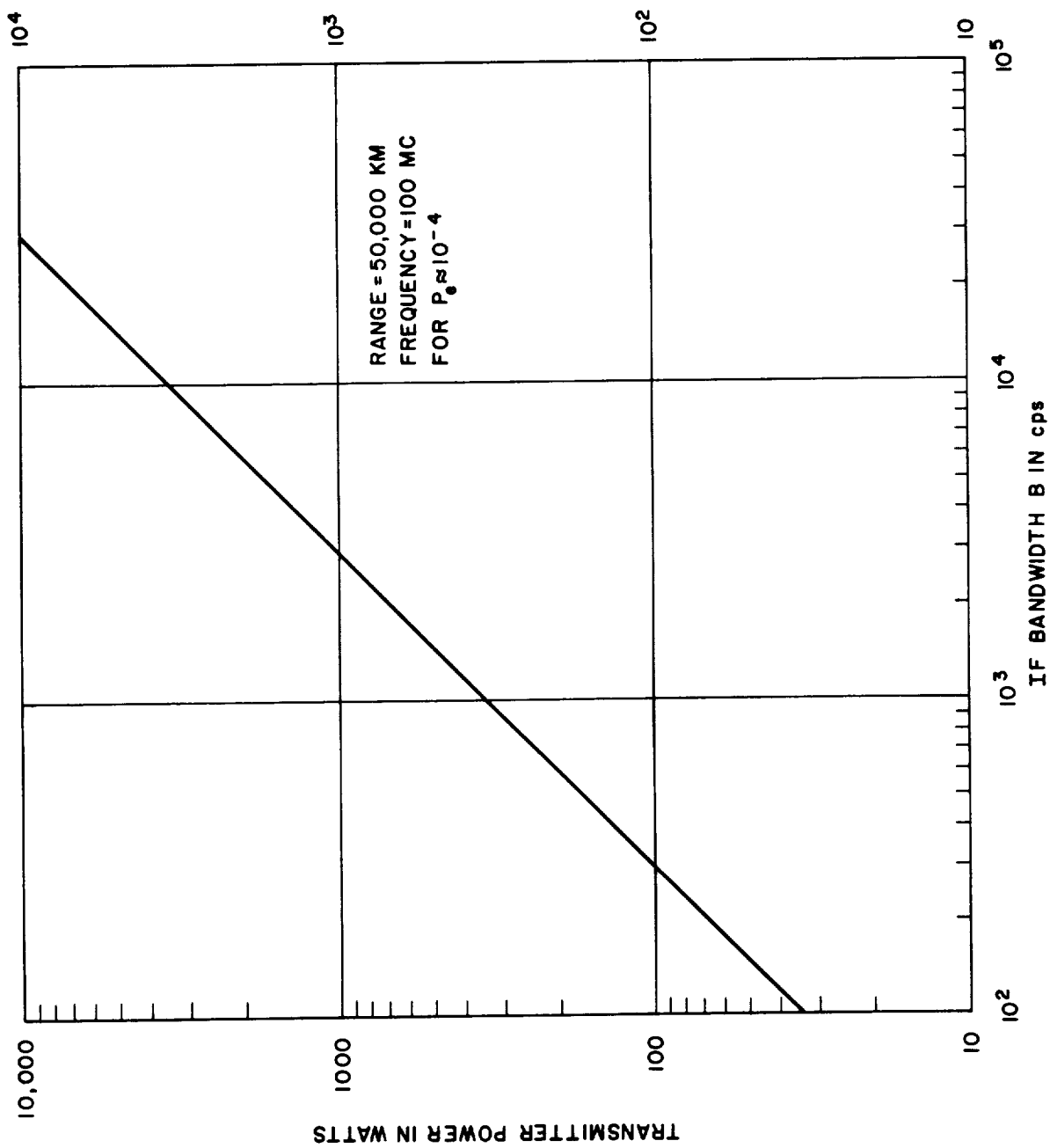


Figure 3.5.20. Transmitter Power Required for PCM/FM Relay Link

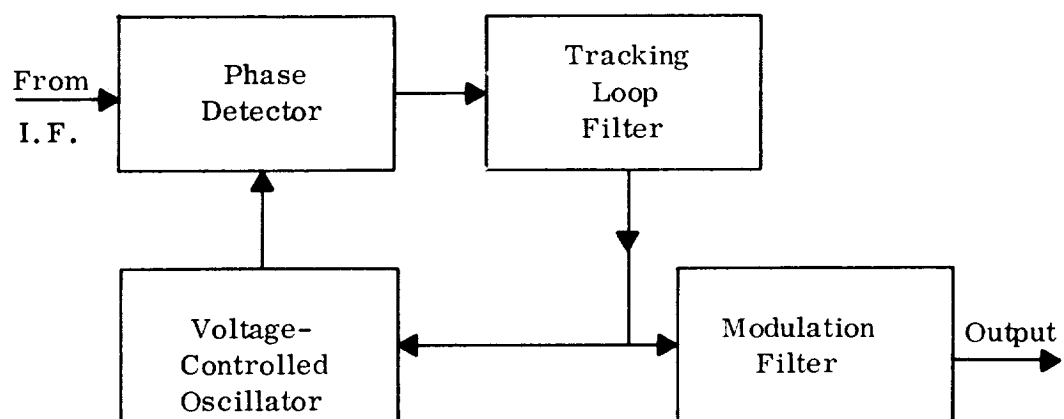


Figure 3. 5. 21. Block Diagram of Phase-Lock FM Discriminator

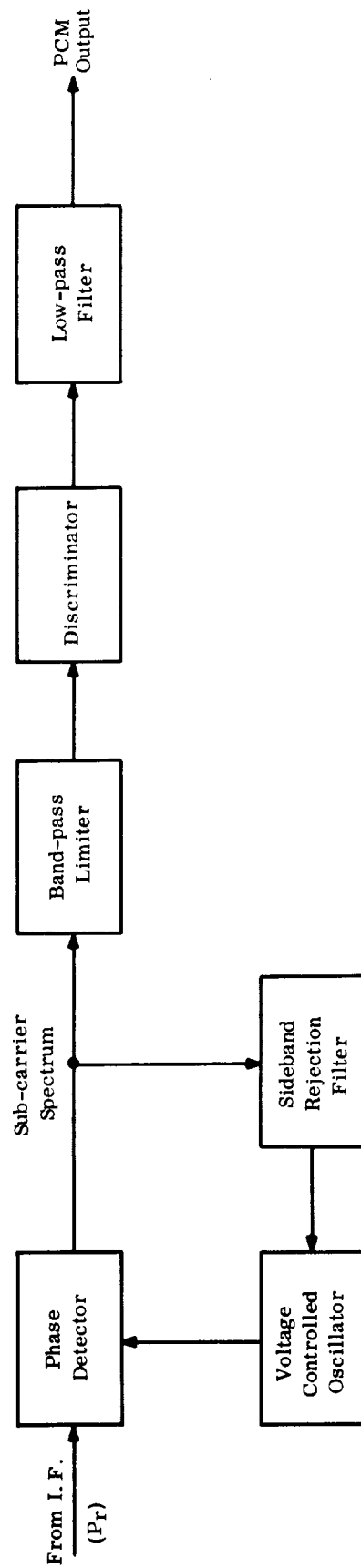


Figure 3.5.22. Block Diagram of PCM/FM/PM Receiver

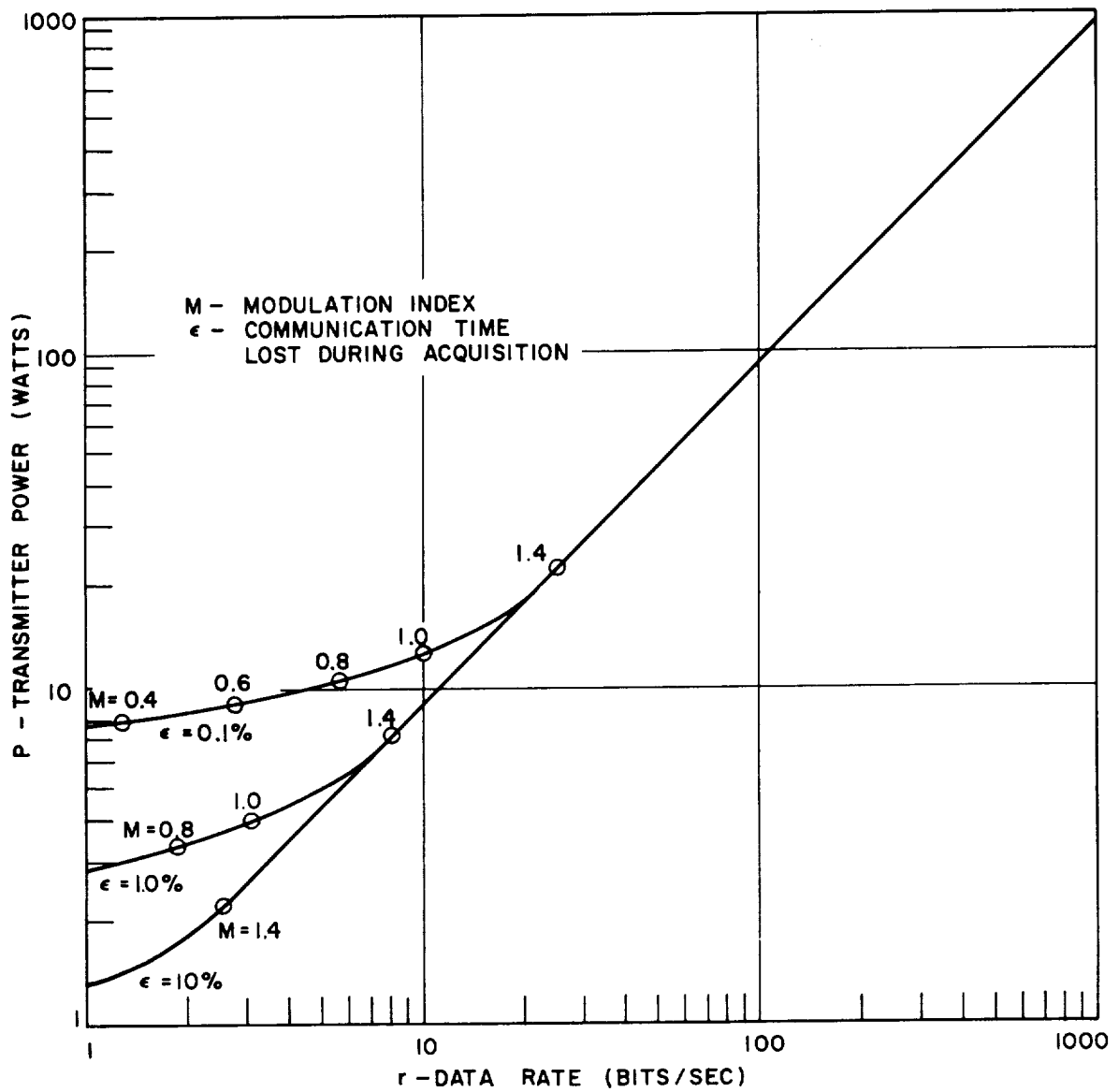


Figure 3.5.23. Transmitter Power Required for PCM/FM/PM Relay Link

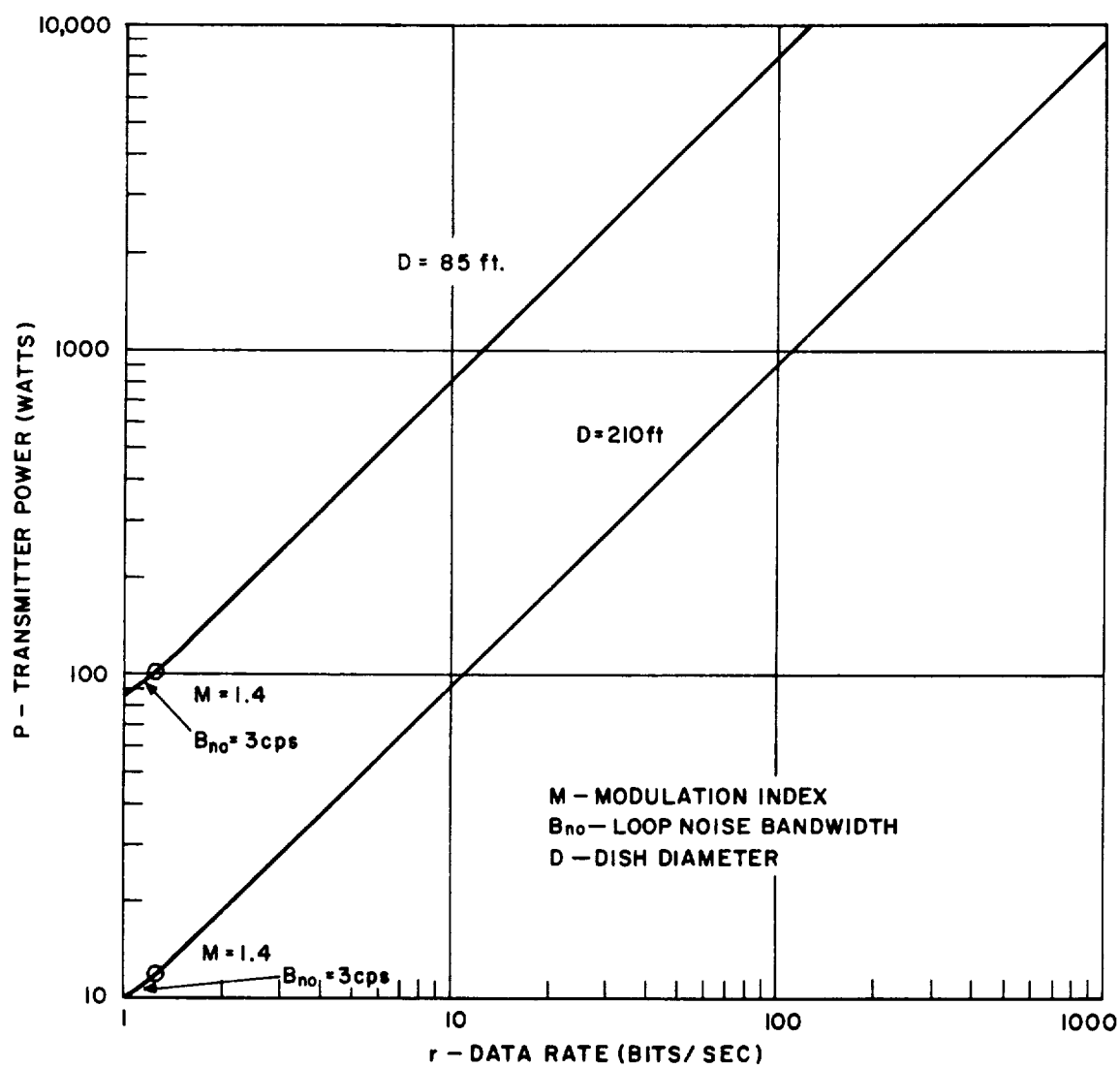


Figure 3.5.24. Transmitter Power Required for PCM/FM/PM Direct Link

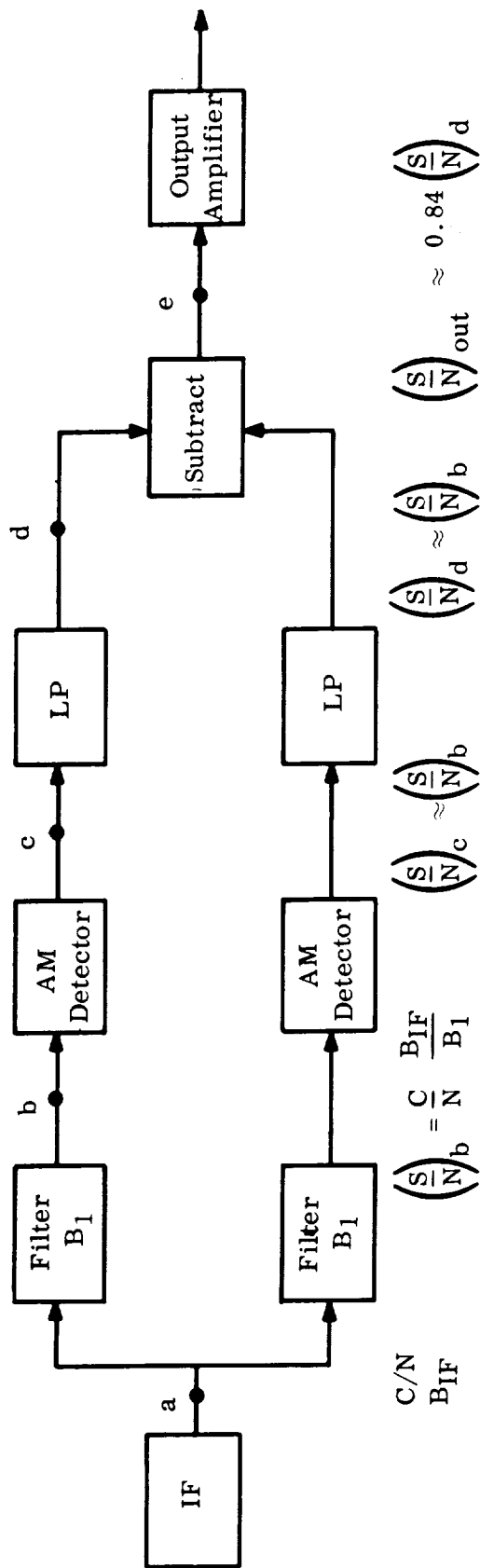


Figure 3.5.25. Block Diagram of Non-Coherent PCM/FSK Receiver

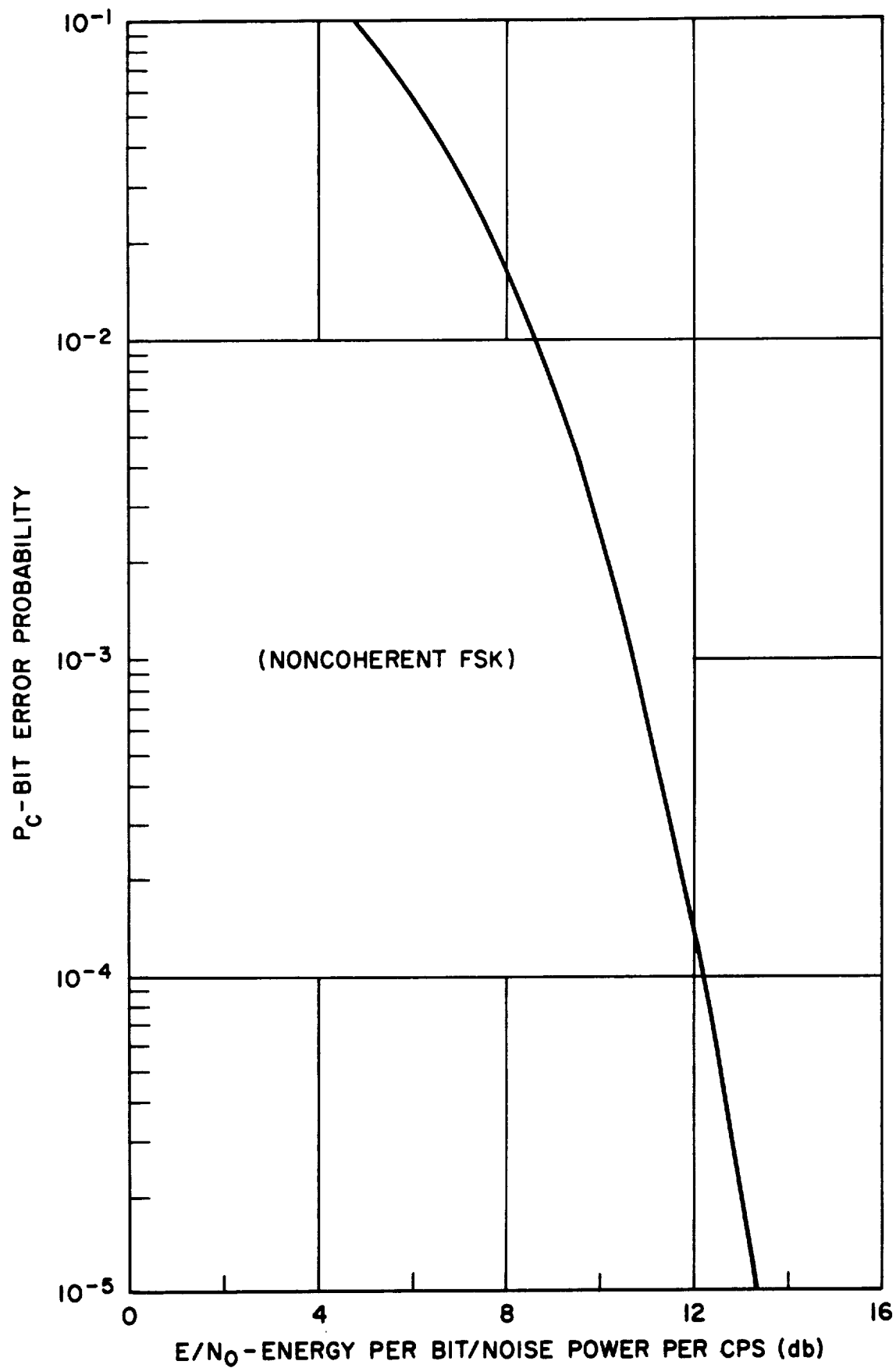


Figure 3.5.26. Bit Error vs. Normalized Signal-to-noise
(Non-Coherent FSK)

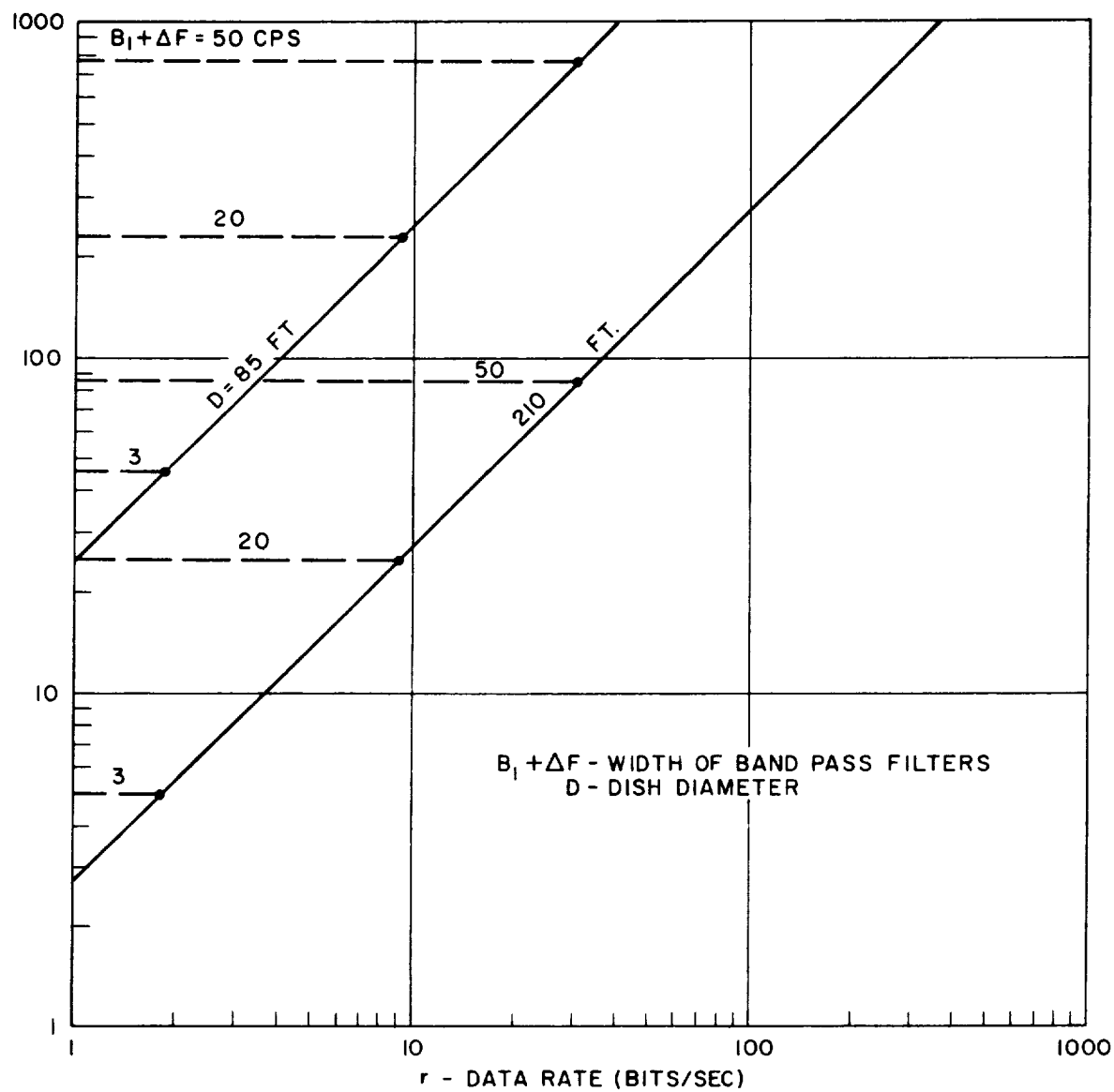


Figure 3.5.27. Transmitter Power Required for PCM/FSK Direct Link

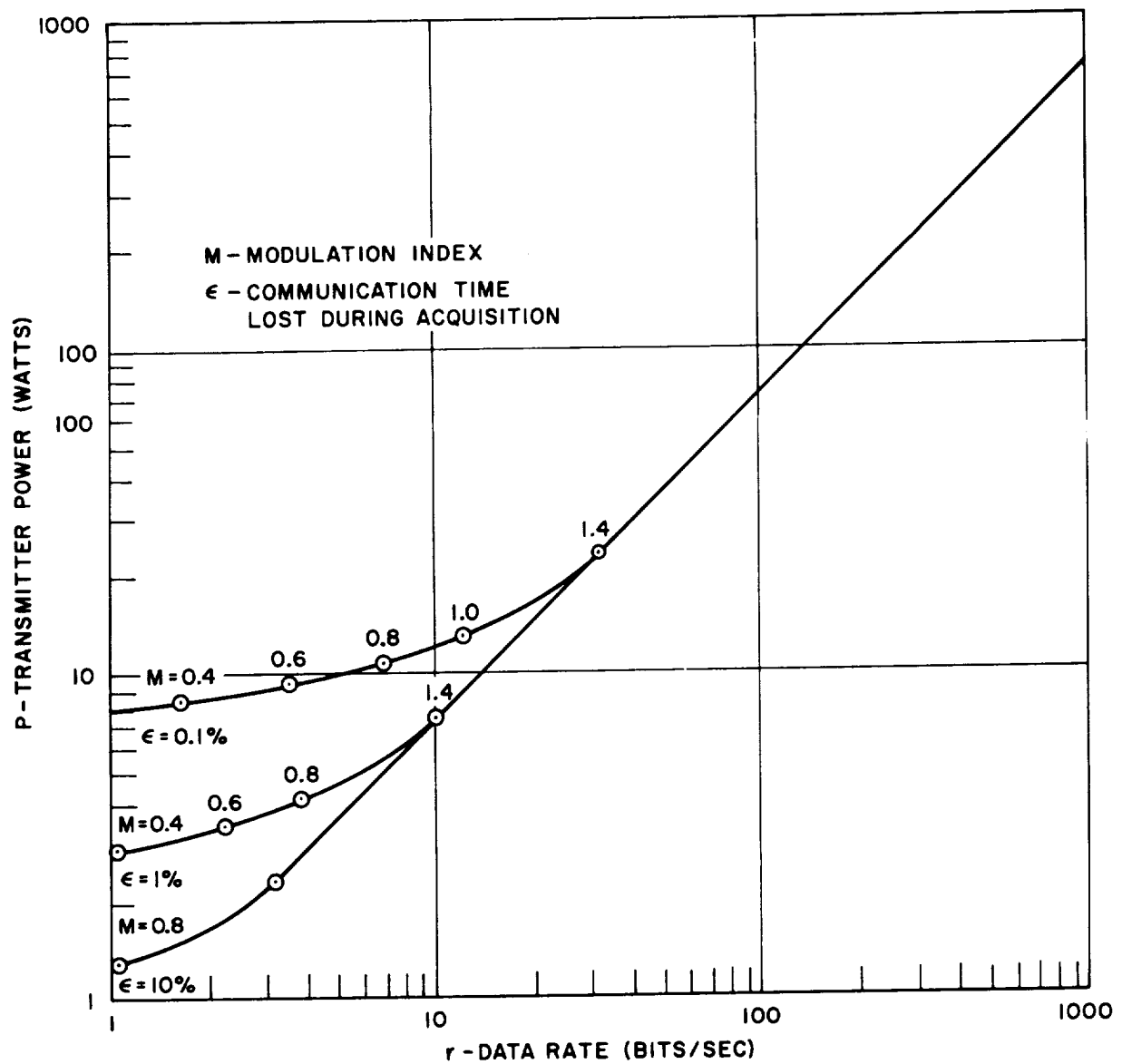


Figure 3.5.28. Transmitter Power Required for PCM/FSK/PM Relay Link

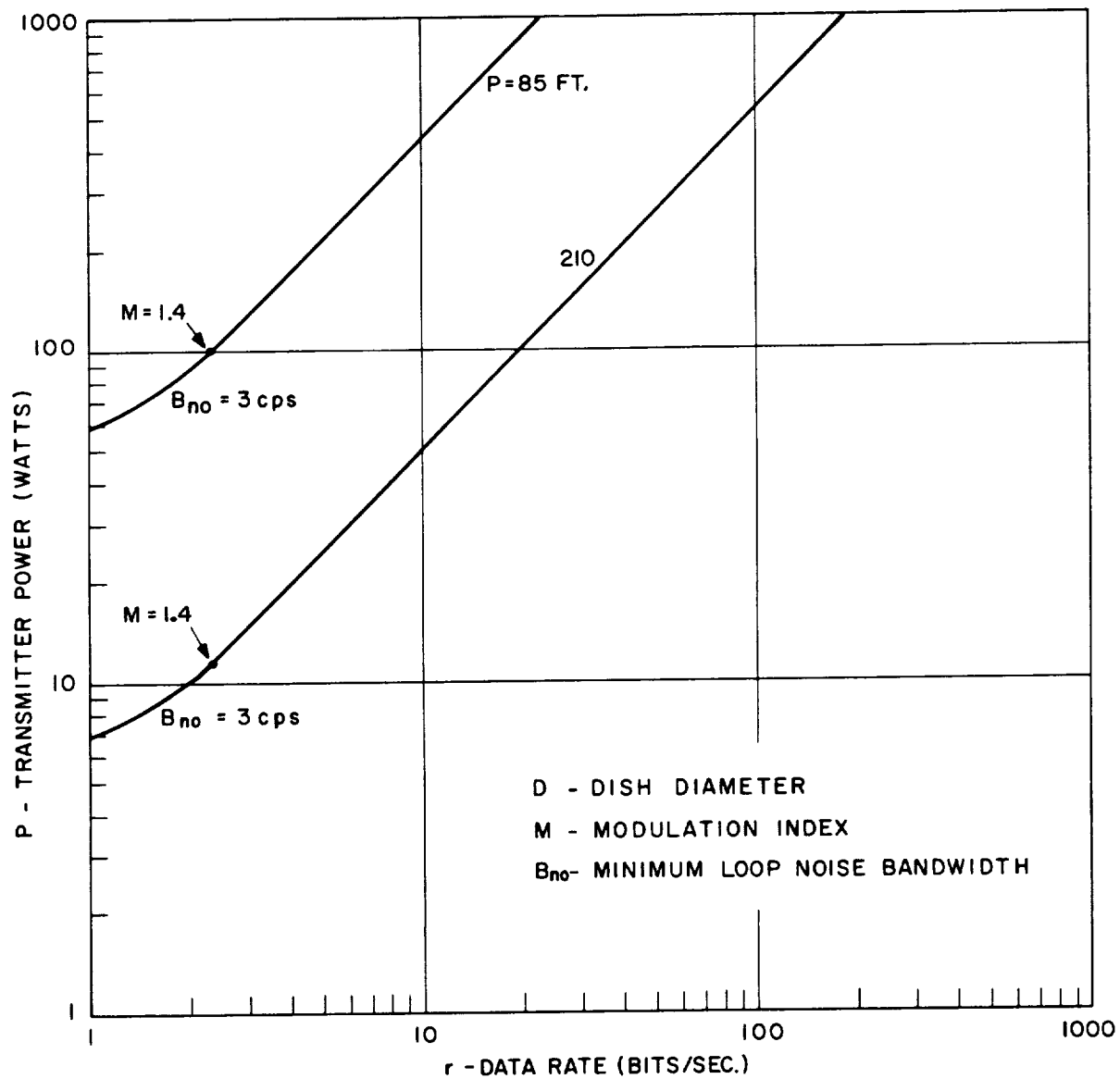


Figure 3.5.29. Transmitter Power Required for PCM/FSK/PM Direct Link

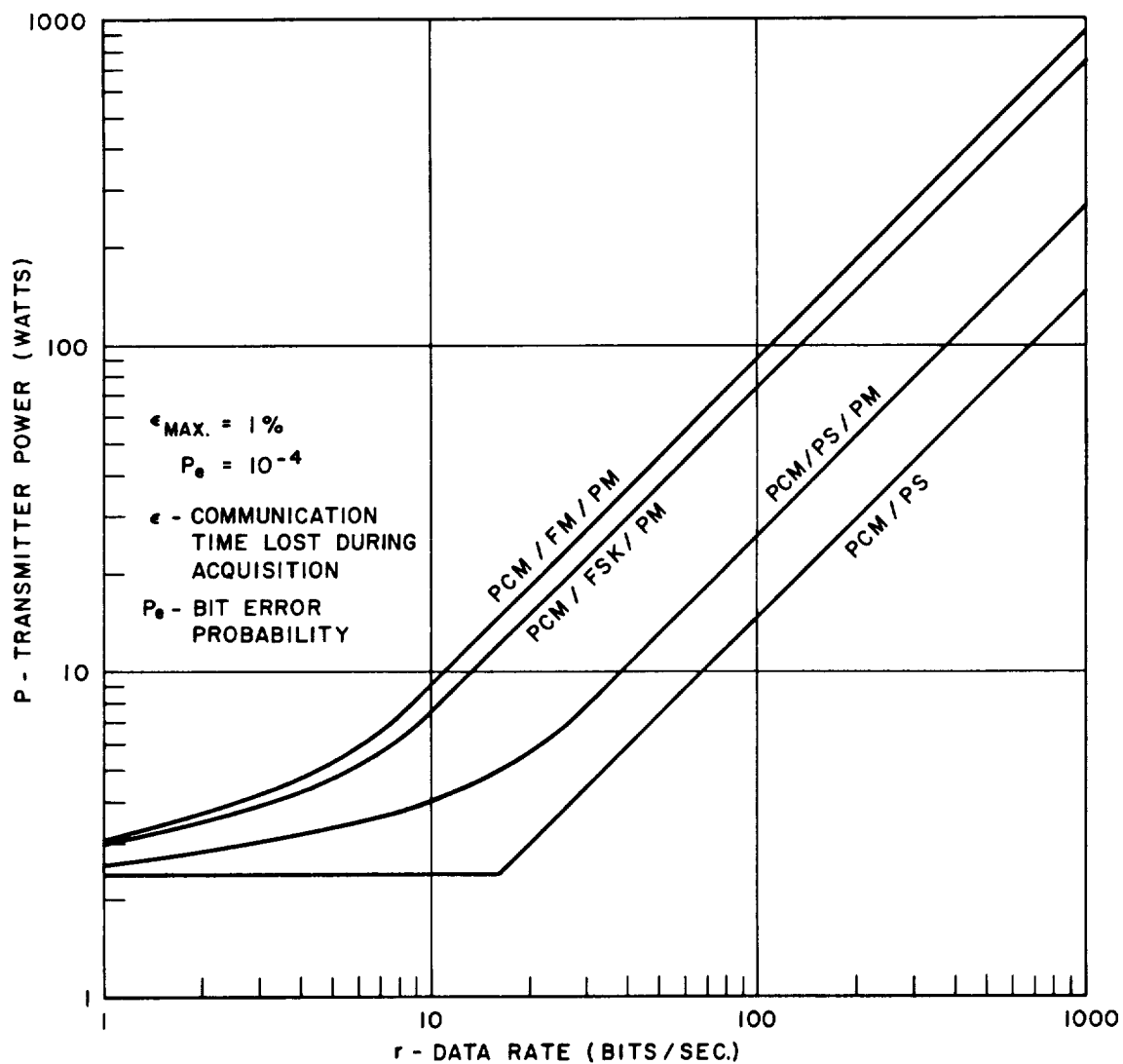


Figure 3.5.30. Transmitter Power Required for Relay Link Utilizing PCM Systems

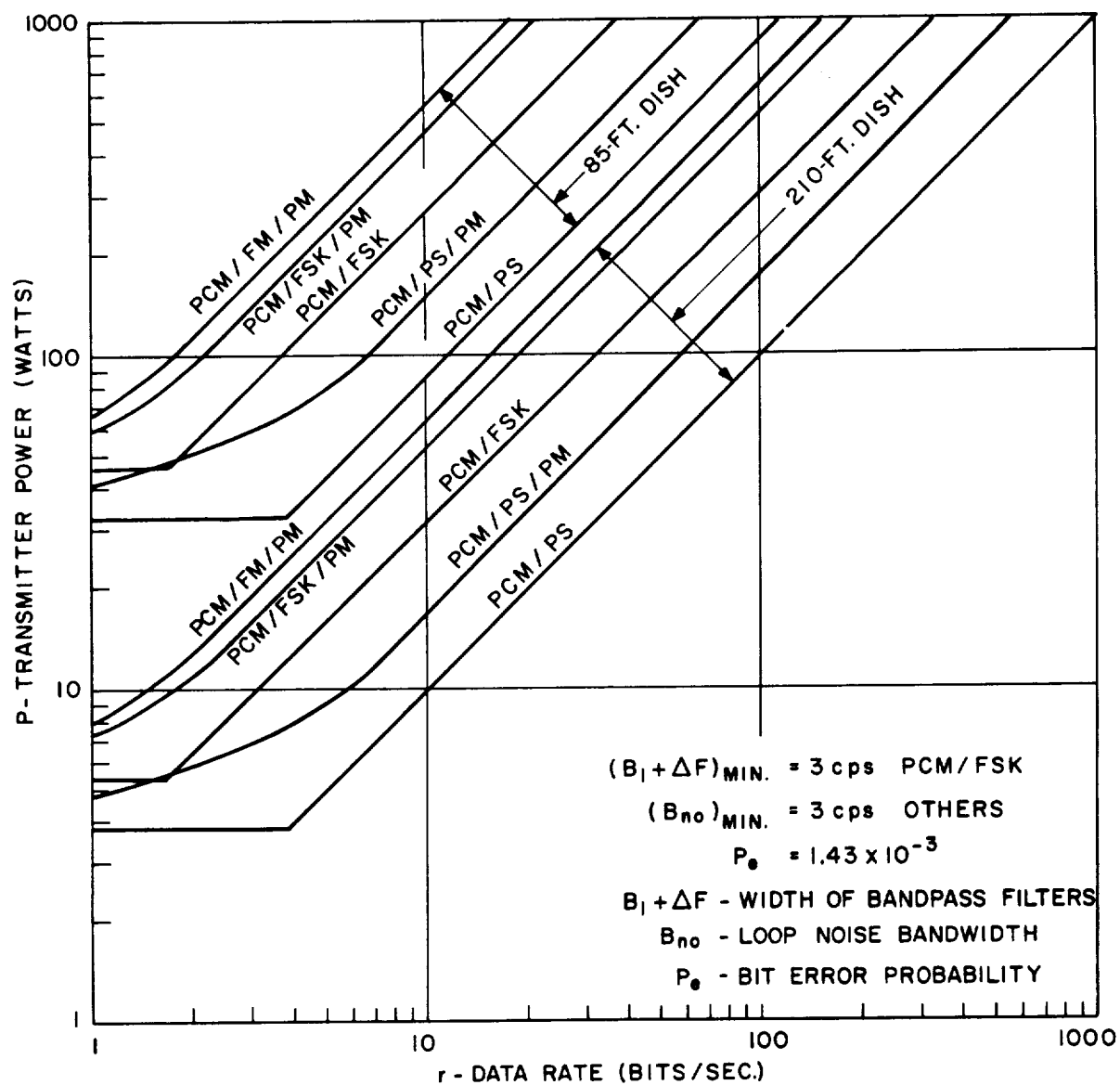


Figure 3.5.31. Transmitter Power Required for Direct Link Utilizing PCM Systems

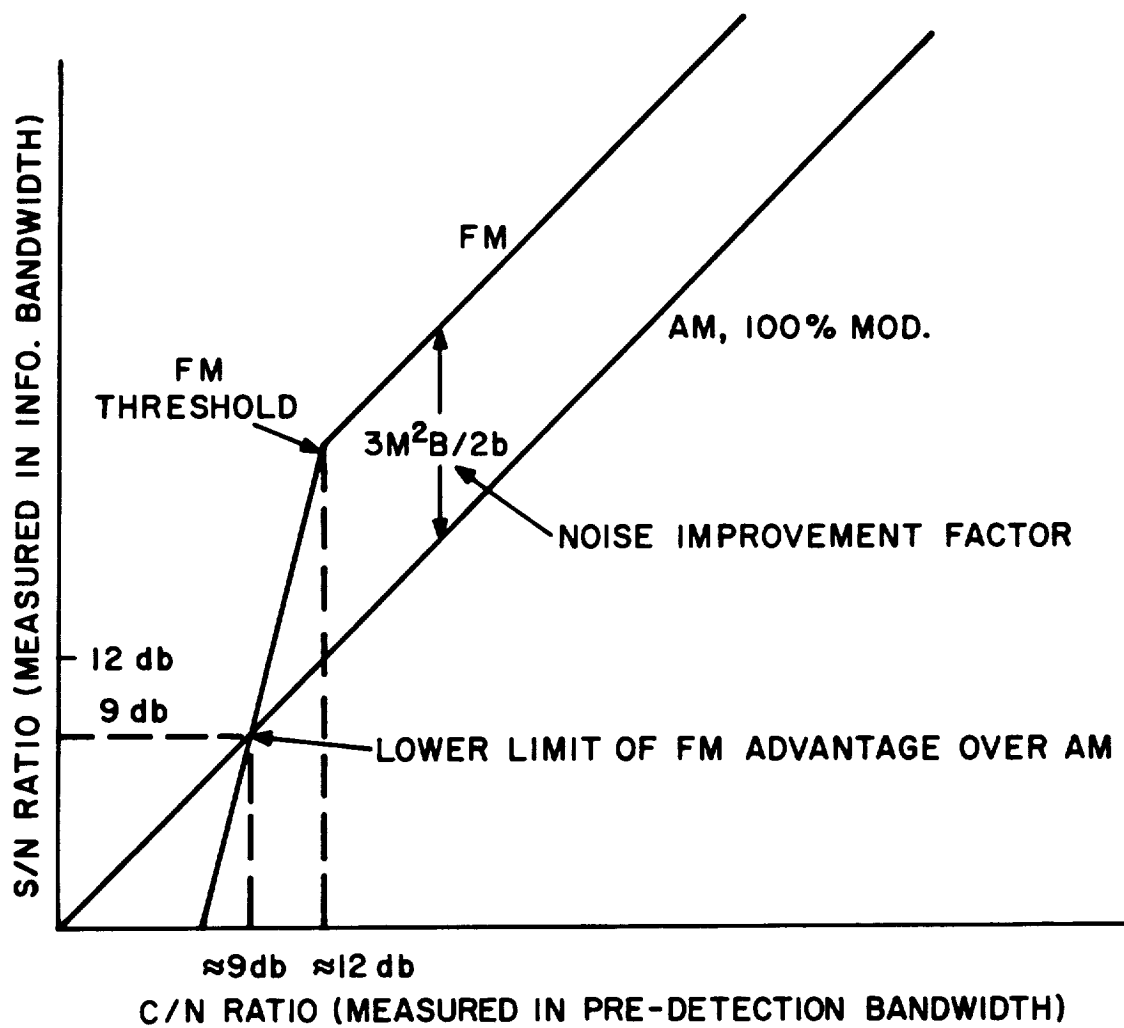


Figure 3.5.32. Example of FM Threshold Effect

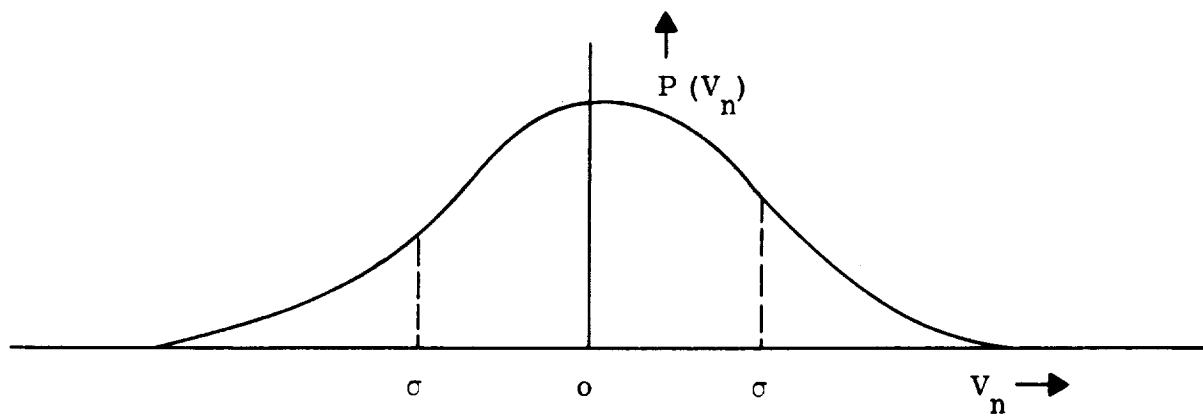


Figure 3.5.33. Gaussian Probability Distribution of Noise Voltage

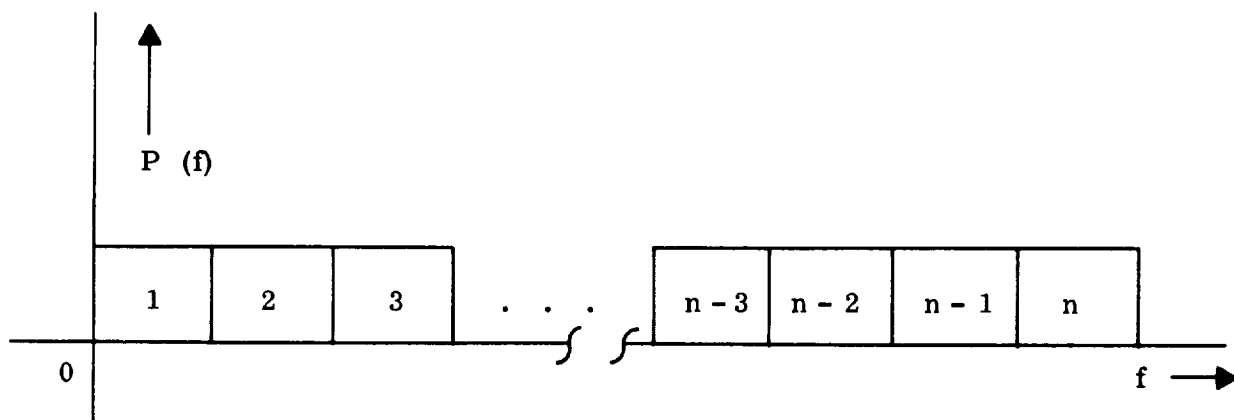


Figure 3.5.34. Channels in the Baseband

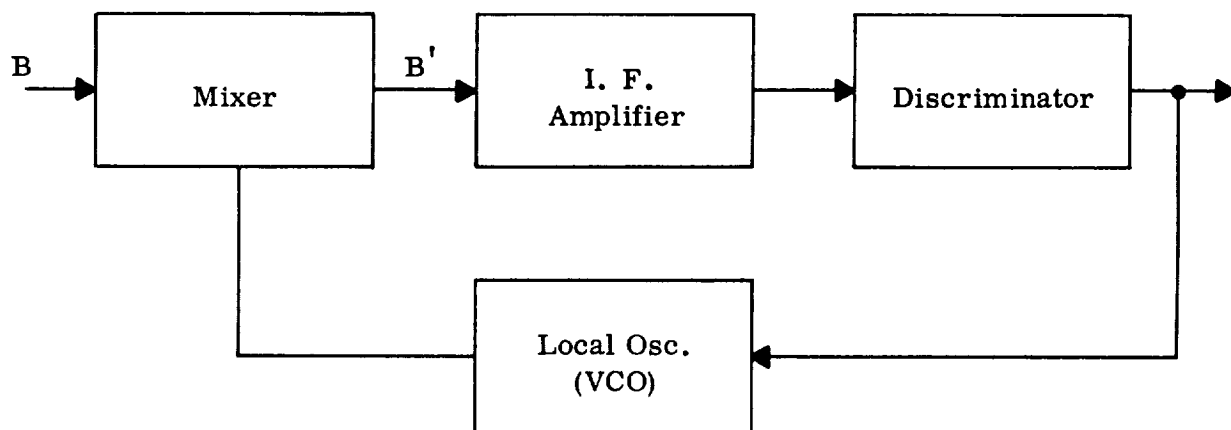


Figure 3.5.35. FMFB Receiver

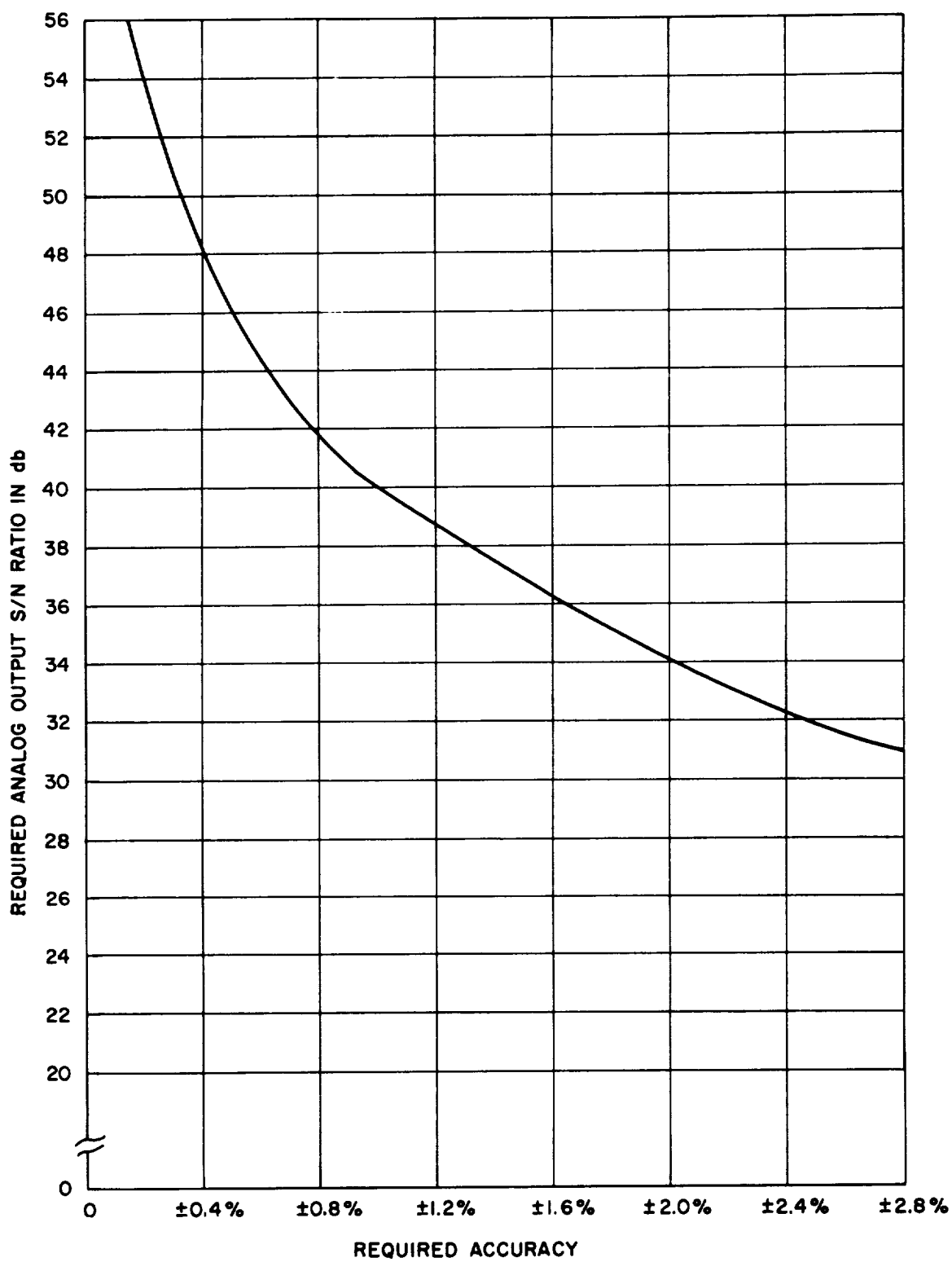


Figure 3.5.36. Analog Output S/N Ratio vs. Channel Accuracy Requirement

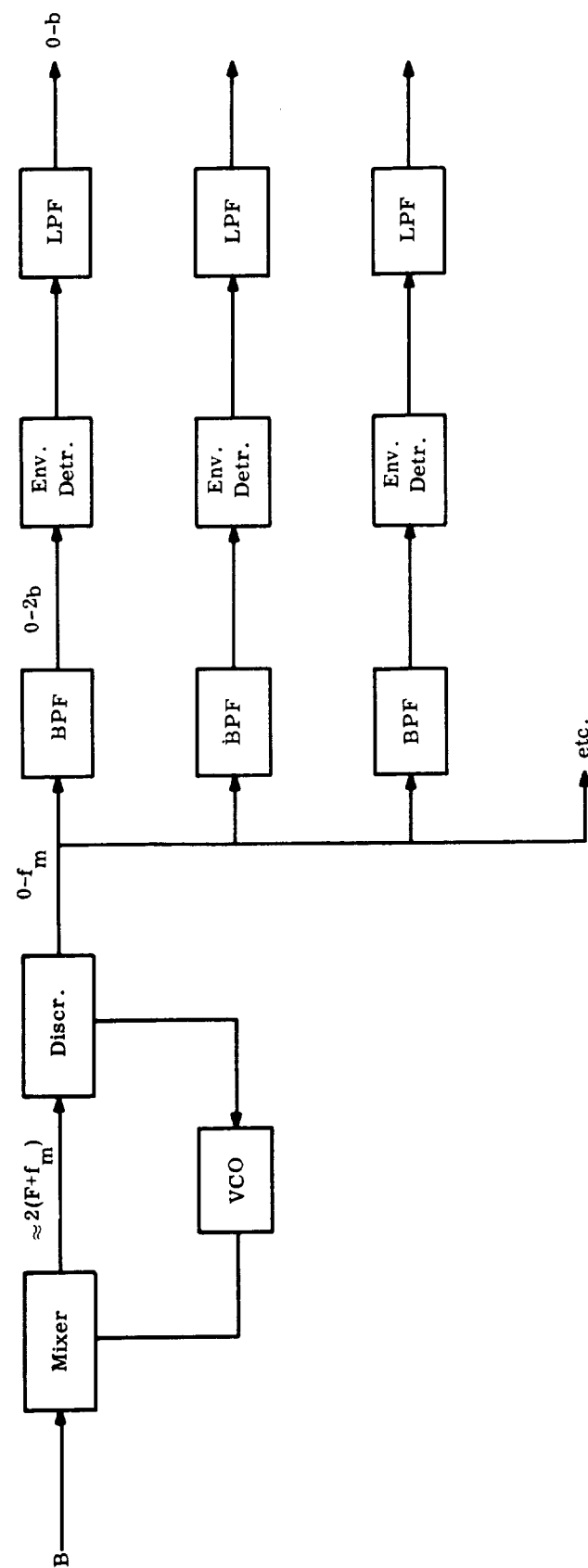


Figure 3.5.37. Conceptual Block Diagram of AM/FMFB Receiver (Showing Significant Bandwidths)

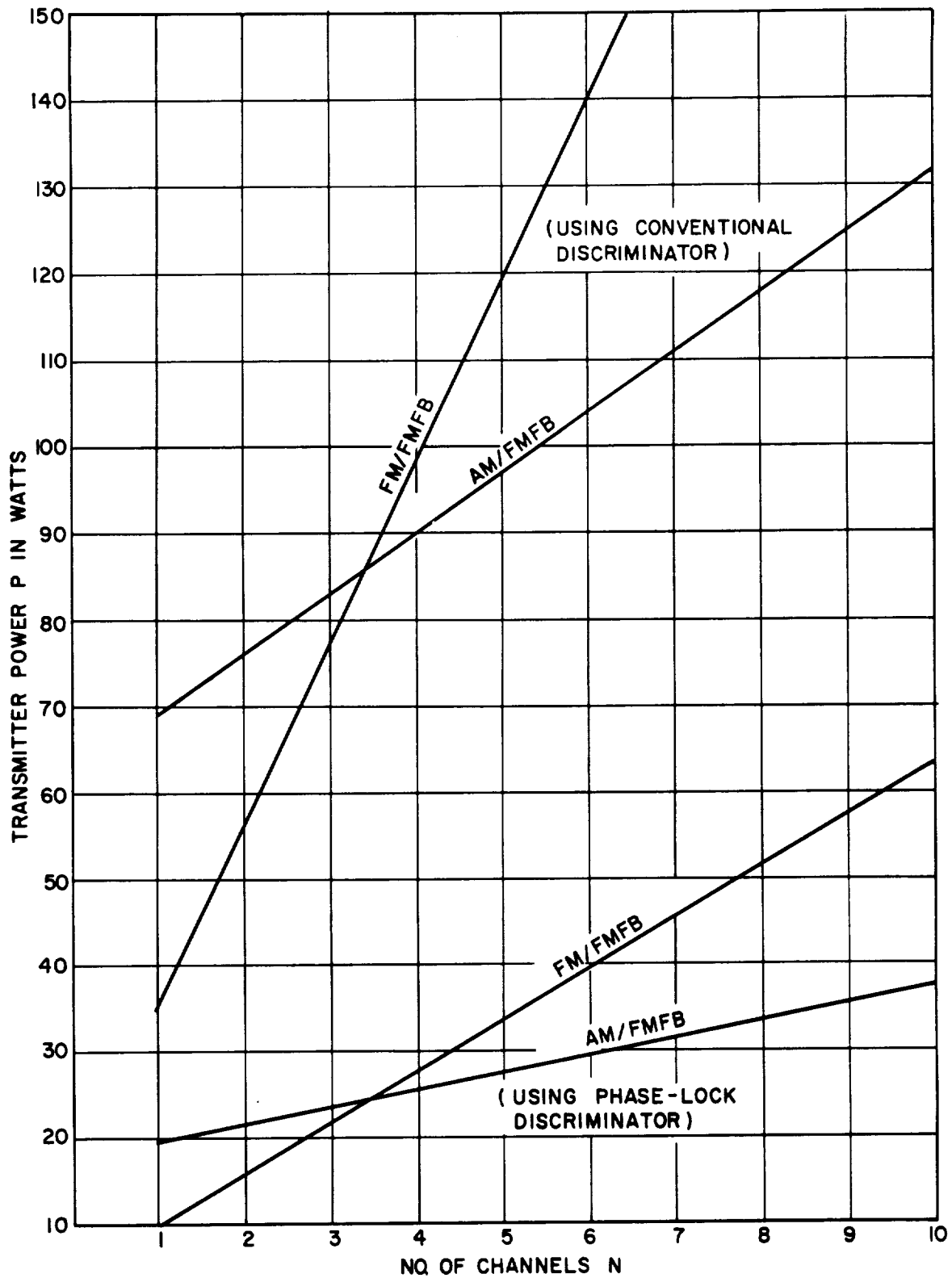


Figure 3.5.38. Transmitter Power vs. No. of Channels for AM/FMFB and FM/FMFB Relay Systems

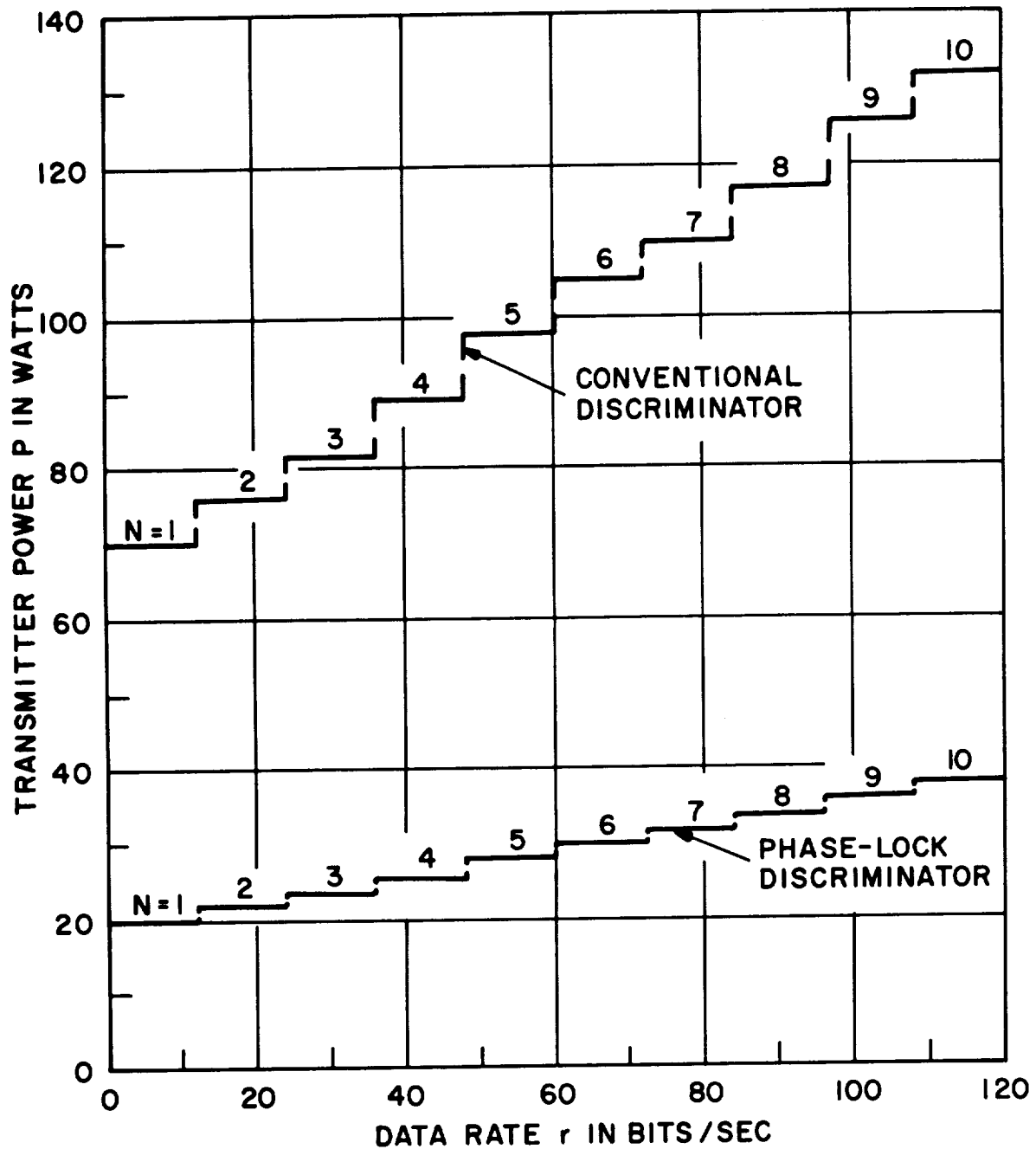


Figure 3.5.39. Transmitter Power vs. Equivalent Binary Data-Rate for an N-Channel AM/FMFB Relay System (Having One-cps Channel Base Bandwidths)

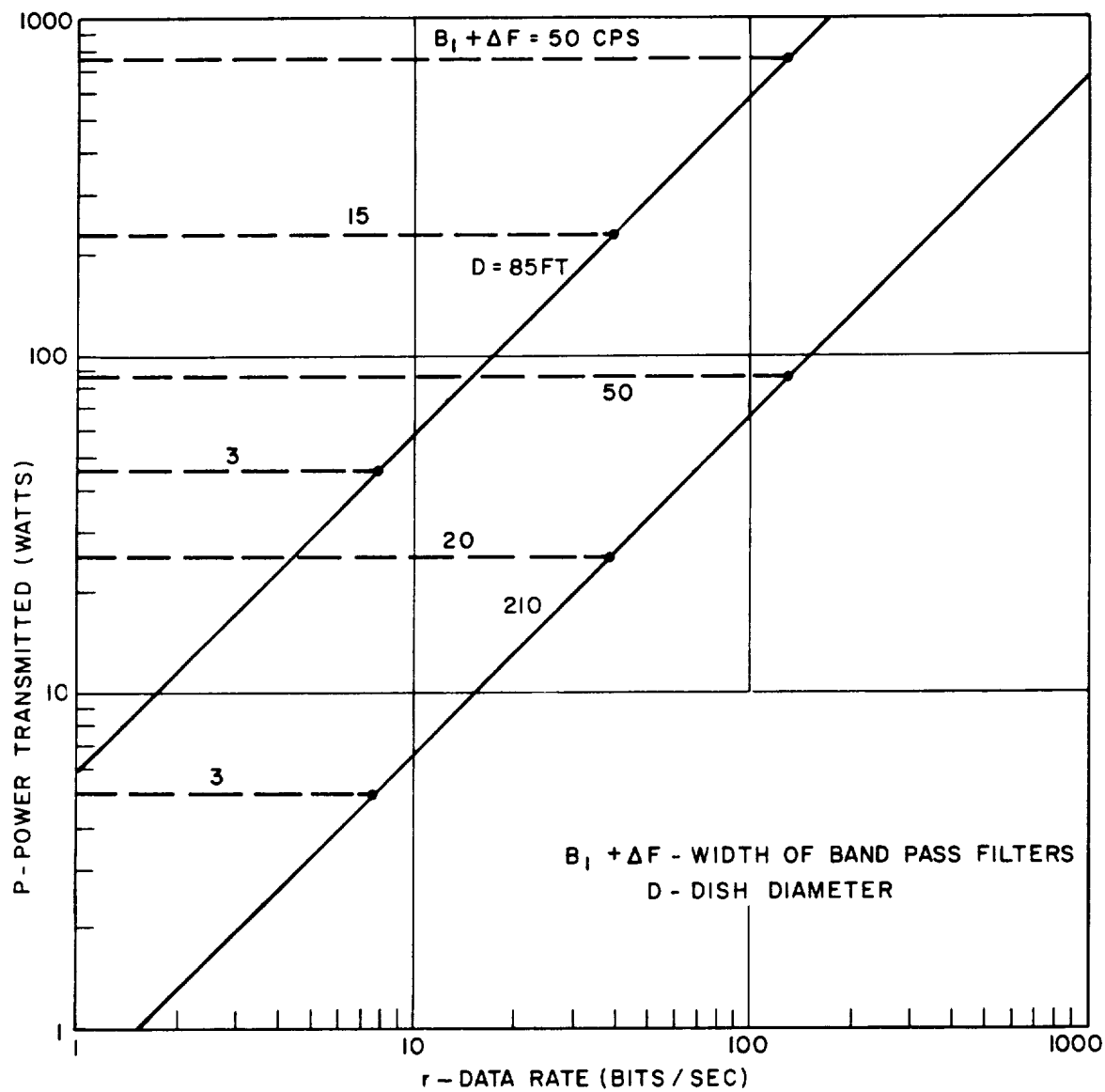


Figure 3.5.40. Transmitter Power Required for 64-Level FSK Direct Link

3.6 VENUS IONOSPHERIC ATTENUATION

3.6.1 Introduction

The object of this part of the study program was to determine the expected amount of attenuation of a radio-frequency signal passing through the ionosphere of Venus. The attenuation of a signal in the ionosphere depends on the electron concentration and the collision frequency, which in turn depend quite critically on the atmospheric composition. The composition data used for the three models are those given in Section I of this report. The attenuation has been calculated for transmission frequencies of 100 mc and 500 mc.

Initial considerations of the atmospheric models provided by JPL indicated that losses in the ionosphere would be sufficiently small that mathematically convenient assumptions might yield results of acceptable accuracy for the present study. The results appear to justify these assumptions. The two basic assumptions are that the propagation can be treated in a piecewise-linear manner and that reflection at the boundaries can be neglected. The resulting expression is:

$$P = P_o e^{-\sum_i \alpha(z_i) (\Delta z)_i} \quad (3.6-1)$$

where P_o is the power incident on the ionosphere and $\alpha(z)$ is the attenuation coefficient, given by:*

$$\alpha(z) = (f_p/f)^2 \nu(z) (1 - f_p^2/f^2)^{-1} c^{-1} \quad (3.6-2)$$

where,

$$f_p = e \sqrt{N_e / \pi m} \quad (3.6-3)$$

is the critical frequency

N_e is the electron concentration, given by JPL as $10^6/\text{cc}$.

f is the signal frequency

c is the velocity of light

$\nu(z)$ is the collision frequency of the electrons

*Drummond, J. E. Plasma Physics, McGraw-Hill Company, 1961

3.6.2 Collision Frequencies for the Three Atmospheric Models

The collision frequency is given by:*

$$\nu(z) = N(z) \sigma_{\text{eff}} V \quad (3.6-4)$$

where,

$N(z)$ is the density of the electrically neutral particles at altitude z

σ_{eff} is the effective cross section of the electrons

T is the temperature of the electrons

V is the mean velocity of the electrons, given by

$$V = \left(\frac{8KT}{\pi M} \right)^{1/2} \quad (3.6-5)$$

The effective collision cross section for the Venus model atmospheres is subject to considerable uncertainties. As observed from experimental work reported in Massey & Burhop,* and also in Brown** experimental data in the energy ranges of interest (considerably less than one electron volt) is sufficiently scarce as to be unreliable. Extrapolation of experimental data permits a reasonable choice within a range of about an order of magnitude.

For the purposes of this study, the effective cross sections for the three model atmospheres are taken as follows:

$$\begin{aligned} \text{Best Model: } \sigma_{\text{eff}} &= 7.64 \times 10^{-16} \text{ cm}^2 \\ \text{Extreme I: } \sigma_{\text{eff}} &= 7.2 \times 10^{-16} \text{ cm}^2 \\ \text{Extreme II: } \sigma_{\text{eff}} &= 8.73 \times 10^{-16} \text{ cm}^2 \end{aligned}$$

The collision frequencies were computed from Equation (3.6-4), using these values of the cross section and the corresponding values for the neutral density N and the thermal velocity. The results of these calculations are given below in Table 3.6.1.

*Massey, H. S. M. and Burhop, E. H. S., Electronic and Ionic Impact Phenomena, Oxford University Press, London, 1952.

**Brown, S. C., Basic Data on Plasma Physics, Wiley, 1959.

Table 3.6.1

Best Atmosphere

<u>Height in km</u>	<u>Collision Frequency no/sec</u>
110	7.52×10^5
122	1.31×10^5
133	3.62×10^4
144	1.19×10^4
178	8.12×10^2
235	8.16×10^1
292	0.11

Extreme I

<u>Height in km</u>	<u>Collision Frequency no/sec</u>
110	9.58×10^5
122	2.94×10^5
133	3.67×10^4
144	6.44×10^3
178	7.70×10^2
235	2.73×10^2

Extreme II

<u>Height in km</u>	<u>Collision Frequency no/sec</u>
100	1.69×10^5
150	0.6
200	2.28×10^{-4}
250	6×10^{-10}
300	3×10^{-14}

3.6.3 Attenuation in the Venusian Ionosphere

The critical frequency for the Venusian ionosphere, taking the electron concentration as 10^6 /cc is

$$f_p = 8.984 \text{ mc} \quad (3.6-6)$$

The attenuation $\alpha(z)$ has been computed for the three models using equation (3.6-2) and the above data. The results are presented in Table 3.6.2 below for the signal frequencies $f = 100 \text{ mc}$ and 500 mc .

Table 3.6.2

Height in km	<u>Best Atmosphere</u>	
	Attenuation in cm^{-1} ($f = 100 \text{ mc}$)	Attenuation in cm^{-1} ($f = 500 \text{ mc}$)
110	1.023×10^{-7}	3.76×10^{-9}
122	1.78×10^{-8}	6.56×10^{-10}
133	4.92×10^{-9}	1.81×10^{-10}
144	1.62×10^{-9}	5.94×10^{-11}
178	1.10×10^{-10}	4.06×10^{-12}
235	1.11×10^{-11}	4.08×10^{-13}
292	1.50×10^{-14}	5.50×10^{-16}

Height in km	<u>Extreme I</u>	
	Attenuation in cm^{-1} ($f = 100 \text{ mc}$)	Attenuation in cm^{-1} ($f = 50 \text{ mc}$)
110	1.30×10^{-7}	4.79×10^{-9}
122	4.00×10^{-8}	1.47×10^{-9}
133	1.40×10^{-8}	5.14×10^{-10}
144	4.50×10^{-9}	1.84×10^{-10}
178	8.76×10^{-10}	3.22×10^{-11}
235	1.05×10^{-10}	3.85×10^{-12}
292	3.71×10^{-11}	1.37×10^{-12}

Extreme II

Height in km	Attenuation in cm^{-1} (f = 100 mc)	Attenuation in cm^{-1} (f = 500 mc)
100	2.30×10^{-8}	8.45×10^{-10}
150	8.16×10^{-14}	3.08×10^{-15}
200	3.82×10^{-17}	1.15×10^{-18}

The total attenuation was obtained by summing the contributions from the altitude-increments:

$$\alpha_{\text{TOTAL}} = \sum_i \alpha(z_i) (\Delta z)_i$$

The calculated attenuations in decibels are given in Table 3.6.3 for the three atmospheric models.

Table 3.6.3

<u>Model</u>	<u>Path Length</u>	Total Attenuation at 100 mc	Total Attenuation at 500 mc
Best	182 km	0.80 db	0.02 db
Extreme I	182 km	0.52 db	0.017 db
Extreme II	100 km	1.35 db	0.05 db

These attenuations, of course, are for a vertical propagation path through the ionosphere. The attenuation vs. path length and altitude is shown in Figures 3.6.1 and 3.6.2.

Table 3.6.3 shows that there is no problem in communicating through the ionosphere of Venus. The Extreme II model yields the pessimistic estimate, and Extreme I yields the optimistic estimate. It should be pointed out, however, that it is not known exactly where the ionosphere of Venus begins; it has been estimated that it starts around 100 km. For a true evaluation of the attenuation, one should know the variation of the electron concentration with altitude, particularly around

100 km where the collision frequency gets higher, and this aspect needs to be investigated more carefully when better knowledge of the composition of the Venusian atmosphere becomes available.

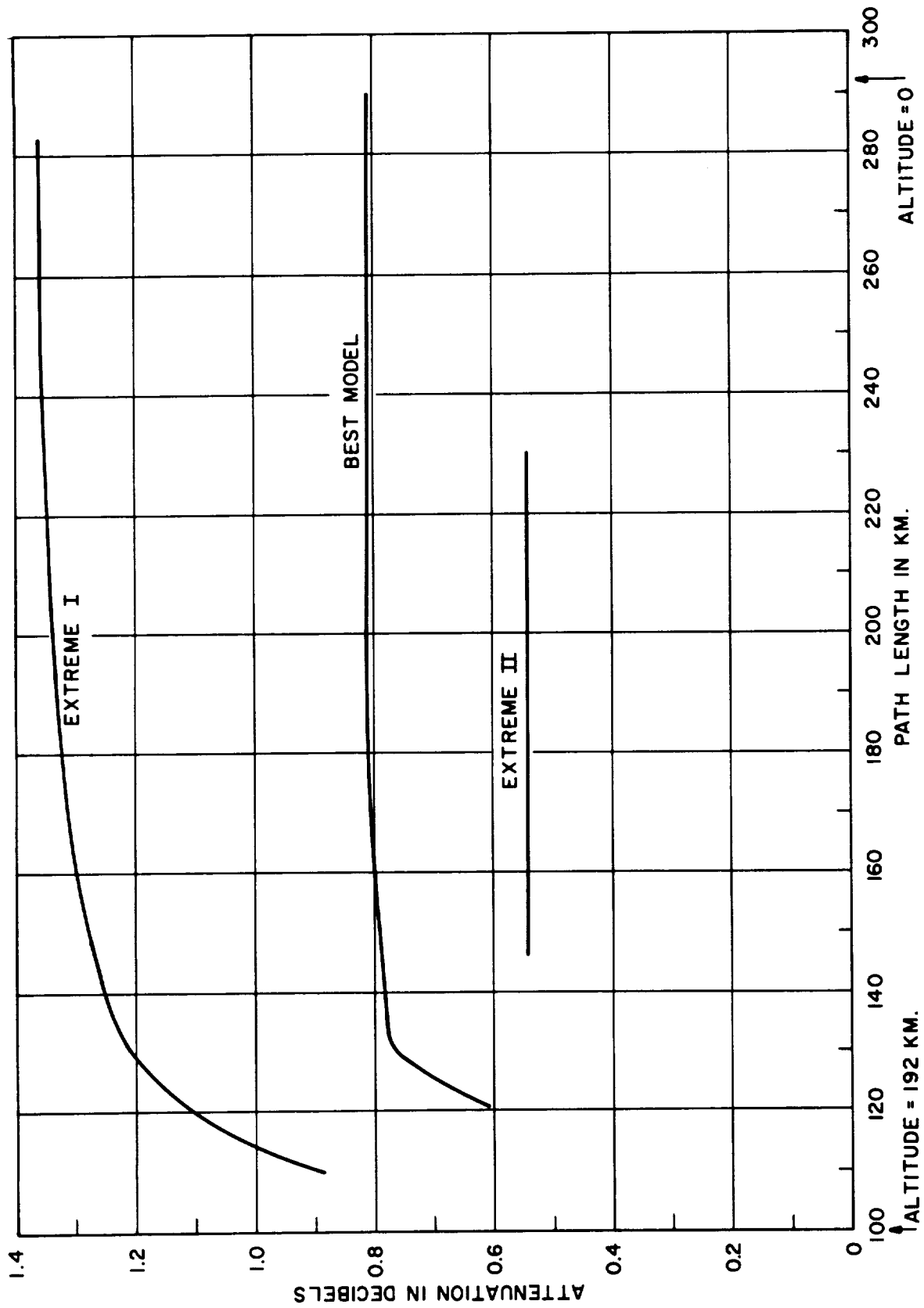


Figure 3.6.1. Venus Ionospheric Attenuation vs. Path Length at $f = 100$ mc.

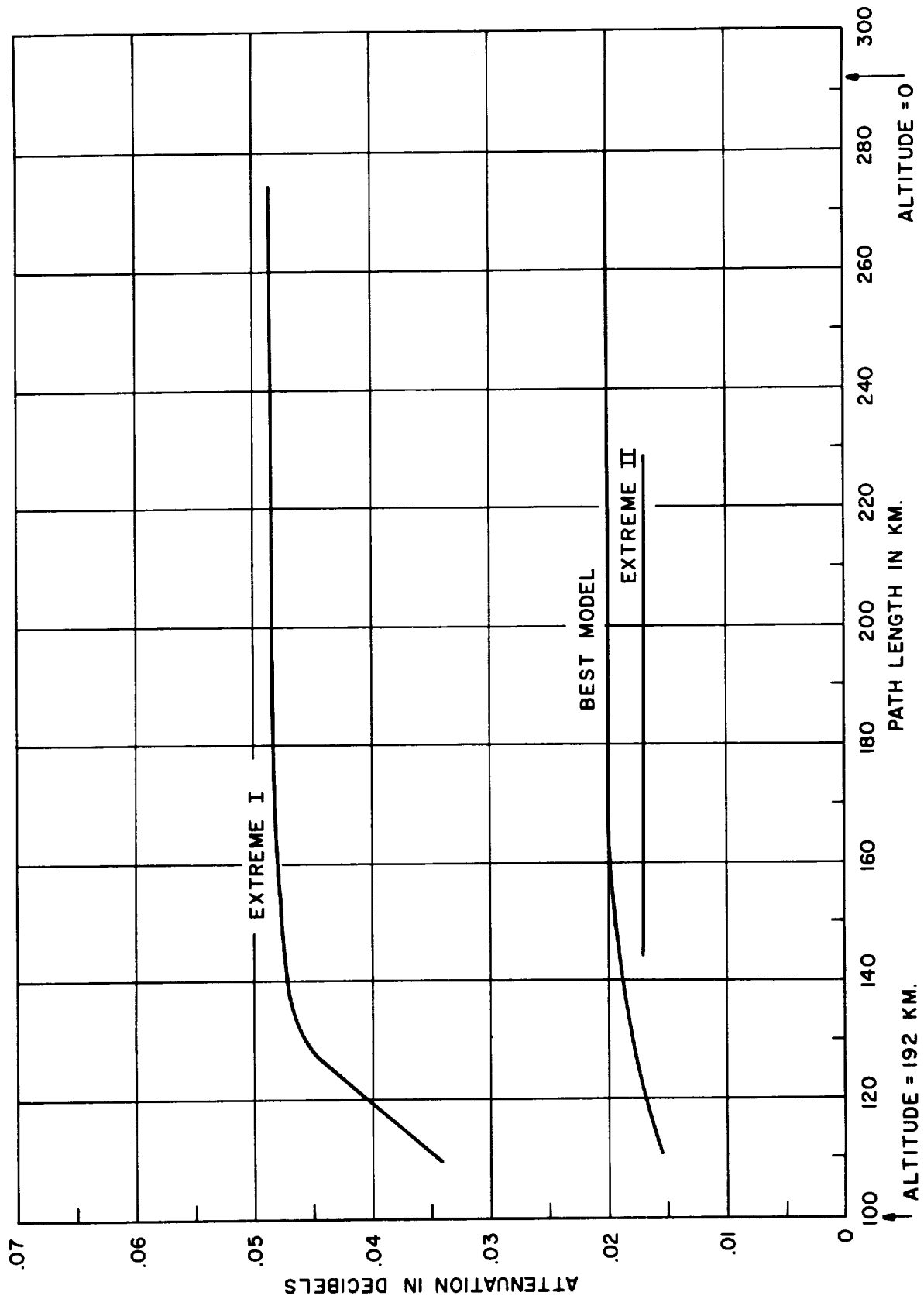


Figure 3.6.2. Venus Ionospheric Attenuation vs. Path Length at $f = 500$ mc.

3.7 MULTIPATH CONSIDERATIONS

3.7.1 Introduction

This section presents a brief discussion of the multipath problem in the transmission of a radio signal from the Venus entry capsule to the Mariner spacecraft (fly-by vehicle). The magnitude of the problem depends on the (unknown) reflection loss at the surface of Venus. It is shown that adequate suppression of the antenna radiation pattern in the forward direction of the capsule will circumvent the problem.

3.7.2 Cause of the Multipath Problem

Multipath effects can occur in radio links in which the signals can follow two or more different paths in traveling between the transmitting point and the receiving point. The signals received over these paths may interfere with each other at the receiver and decrease the system performance.

Consider the geometry shown in Figure 3.7.1.

$$d_2 \sim 0 \text{ to } 76 \text{ km}$$

$$d_3 \sim 10,000 \text{ km}$$

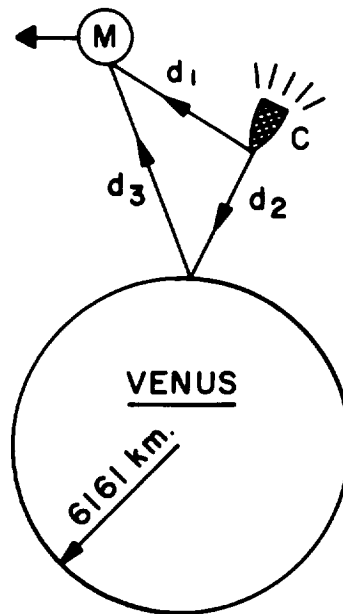


Figure 3.7.1. Multipath Geometry

The miss distance d_3 of the Mariner spacecraft (M) is in the order of 10,000 km, while the capsule (C) altitude d_2 varies from 0 to 250,000 ft. (76 km). The signal can be received at M over both the direct path d_1 and the reflected path d_3 . Since $d_1 \approx d_3$, the strength of a signal received over d_3 which was radiated from an isotropic antenna at C will depend on the reflection loss at the surface of Venus. If 100% reflection occurs, then the two paths will cause destructive interference effects whenever

$$\begin{aligned}(d_2 + d_3) - d_1 &= n \frac{\lambda}{2} - \frac{\theta}{2\pi} \lambda \\ &= \left(\frac{n}{2} - \frac{\theta}{2\pi} \right) \lambda\end{aligned}\tag{3.7-1}$$

(for $n = 1, 3, 5, \dots$)

where λ is the wavelength, and θ is the phase shift due to the reflection ($\theta = \pi$ for a perfect conductor). For radio frequencies between 100 and 500 mc, the wavelength λ lies between two and ten feet.

The reflection coefficient of the surface of Venus is not known. If the surface is comparable to a smooth sea, the reflection coefficient could be 1.0 at vertical incidence, dropping off to about 0.9 when incidence is ten degrees away from the vertical.*

3.7.3 Solution to the Problem

To eliminate the multipath interference problem, the signal received over path d_3 must be made considerably weaker than that received over the direct path d_1 . The extra losses over the reflected path are three:

- (1) Longer path length
- (2) Reflection loss at surface.
- (3) Antenna pattern suppression.

*Reintjes, J. F. and Coate, G. T., Principles of Radar, McGraw-Hill Book Co., 1952.

Since $d_2 \ll d_1$, the length of the reflected path is not appreciably greater than that of the direct path, so item (1) is not significant. Therefore, the sum of items (2) and (3) should be made greater than the design margin over the direct path for adequate elimination of multipath fades.

Since there will be no situation after atmospheric entry in which the capsule will be required to transmit directly forward to the spacecraft, the capsule antenna radiation pattern can be suppressed in the forward direction, giving essentially a hemispherical coverage aft. In fact, if the forward gain of the pattern is made at least eight to ten db less than the aft pattern gain minus the margin, the multipath problem should be obviated, even if 100% reflection from Venus occurs.

3.8 VENUS ENTRY COMMUNICATION

3.8.1 Introduction

As a body passes through a gas at sufficiently high velocity, dynamic heating of the gas causes the formation of an ionized plasma in the vicinity of the body. The presence of this plasma can cause interference with the transmission of electromagnetic signals to and from the body. The primary parameters affecting the nature and degree of the interference are frequency, electron density distribution, collision frequency distribution, static electric or magnetic fields, and the geometry of the situation. In situations where a vehicle is entering the Earth's atmosphere, the interference is sufficiently severe that the system margin is exceeded and a "black out" occurs. Corrective techniques are aimed at maintaining the total attenuation within limits imposed by the communication system.

This portion of the report presents the Venus entry communication calculations made for the following conditions:

- a. "Extreme I" atmosphere (See Section I)
- b. Ballistic coefficient of $61 \text{ lb/ft}^2 (W/C_D A)$
- c. Entry angle of -30° (enters atmosphere at 30° from the tangent)

The calculations have been performed for both a blunt body and a sharp-nosed body. Final results are in terms of critical signal frequency (below which the signal is "black out"), and estimated signal attenuation. The critical frequency is given as a function of altitude, while the attenuation is presented as a function of altitude and frequency.

In order to pose an alternate solution to the communication problem, the effects of a d.c. magnetic field have been investigated. This solution would be applied to the blunt body to allow transmission throughout the entry period. The pertinent question here is concerned with what magnitude of magnetic field is required for transmission through entry.

3.8.2 Summary

1. Blunt Body Flow Field and Attenuation Analysis

The flow in the vicinity of the 10° conical portion of a nominal Discoverer type sphere-cone body was analyzed for surface electron concentration, pressure, and temperature. These results were used to derive plasma frequency and collision frequency, and an approximate inviscid flow field (Section 7.1.3) was used to estimate the plasma thickness.

Figure 3.8.1 gives the temperature and pressure of the gas at the vehicle surface versus altitude. Figure 3.8.2 gives electron concentration versus altitude, which reaches a peak of more than 10^{15} cm^{-3} at 300 K feet. Figure 3.8.3 gives the critical signal frequency, above which communication is possible, as a function of altitude, illustrating the result that communication throughout entry is virtually impossible at all but the very highest frequencies. Figure 3.8.4, the approximate total signal attenuation versus altitude, includes effects of reflection and absorption. Figure 3.8.5 gives a plot of approximate attenuation versus frequency at 300 K feet altitude. Necessary data was not available for calculations above 450 K feet altitude; however, it is safe to extrapolate Figure 3.8.3 to obtain an estimate of the extent of blackout.

2. Conical Body Flow Field and Attenuation Analysis

In Section 7.1.3, are shown calculations of the inviscid flow surrounding a 10° flared-cone using the "Extreme Model I" atmosphere, a 30° re-entry angle and $W/C_D A$ of 61. In the calculations are postulated two extreme conditions of flow "complete separation" and "no separation." The antenna location was taken as $1/4$ wavelength from the tip of the 10° cone. Figure 3.8.6 gives the electron concentration versus altitude in the vicinity of the antenna and Figure 3.8.7 gives the temperature and pressure. Figure 3.8.8 is a plot of critical

frequency against altitude for the two types of flow. Figures 3.8.9 and 3.8.10 give estimated total attenuation, the former versus altitude and the latter versus frequency at 300K feet altitude. These sets of curves show that "no separation" will be no problem, while "complete separation" will be disastrous to entry communications.

3. Effects of a D.C. Magnetic Field

Based on the results of Ratcliffe*, signal attenuation versus the ratio of cyclotron frequency to signal frequency ω_H/ω has been calculated and the results are plotted in Figure 3.8.11. Here we note that the results are highly non-linear, and that ω_H/ω must approach a critical value before any reduction of attenuation is realized. Figure 3.4.12 gives a plot of magnetic field required for transmission versus altitude for two frequencies, which shows the penalty to be paid in order to keep the fade less than 10 db (a practical margin) during the entry period by means of a d.c. magnetic field.

3.8.3 Conclusions

It is obvious that if communication is required throughout a Venus entry, the flared cone configuration will most likely be required, provided the "no separation" condition exists at least in the neighborhood of the antenna. For the blunt body, blackout will last from above 500 K feet to about 225 K feet. The altitude at which blackout begins depends on signal frequency and may be estimated by an extrapolation in Figure 3.8.3.

The reliability of the conclusions concerning the effectiveness of the flared cone appears to be largely dependent on whether the actual flow would approach the low ionization level of the idealized "no separation" case. Unfortunately it is not known with any certainty whether the flow will be of the "complete" or the "no separation" type. It is therefore necessary to assume that complete separation

*Ratcliffe, J. A. "The Magneto-Ionic Theory and Its Applications to the Ionosphere," Cambridge, 1959

will obtain for some part of the entry trajectory. This situation is of some concern because of the sharp difference in the results for "complete" and "no separation," a factor of 10^6 in electron concentration and in plasma frequency. Further study of the flow situation is indicated.

A d.c. magnetic field of 1700 gauss with a signal frequency of 100 mc or a field of 1700 gauss with a frequency of 10 kmc would enable the blunt body to transmit throughout entry. The magnetic field must be transverse to the electric field of the electromagnetic wave. Compromise magnetic fields will reduce extent of blackout over the no-magnetic field case as shown in Figure 3.8.12. In view of the problems associated with producing a magnetic field with such a strong component* transverse to the electric field, it does not appear practical to use this solution to the Venus entry communications problem.

3.8.4 Discussion of Methods Used to Estimate the Signal Attenuation During a Venus Entry

Methods of arriving at flow field information are adequately described elsewhere in this report with the possible exception of the simplification consisting of a Prandtl-Meyer expansion from stagnation conditions to obtain local gas properties. The high temperature thermodynamic properties of the Venusian atmosphere are described in Section 5.1.

*An indication of the problem may be obtained by noting that a magnetomotive force of some 130,000 ampere-turns per meter is required to establish the 1700 gauss at the center of an air core solenoid. Although some judicious use of material with a permeability greater than that of free space might improve this situation, it does appear that the generation of this field throughout an appropriate volume just outside the vehicle surface would require an objectionable weight and power.

First, we consider the calculation of critical signal frequency. An inspection of the curves of the attenuation constant (imaginary part of refractive index multiplied by the wave number) and refractive index of plasmas* shows that a sudden change occurs at some particular electron concentration. (This is most striking for the case when signal angular frequency ω exceeds collision frequency ν .) We, therefore, use the criterion that the critical signal frequency be that above which the real part of the refractive index approaches unity asymptotically (and the imaginary part is less than unity). From the expressions derived in Appendix A, we find that the critical frequency is given by

$$\omega_c = \omega_p \quad \text{when} \quad \omega > \nu \quad (3.8-1)$$

$$\omega_c = \omega_p^2 / \nu \quad \text{when} \quad \nu > \omega \quad (3.8-2)$$

(Plasma frequency $\omega_p \approx 5.6 \times 10^4 \sqrt{n_e}$, where electron concentration n_e is in cm^{-3}). Note that the reflection coefficient for a semi-infinite medium approaches unity asymptotically at frequencies below the critical, giving additional credence to these choices for critical frequency.

We proceed now to the calculation of estimated attenuation. According to the conclusions of Appendix C, we use the equations derived in Appendix C for plasma sheaths having a thickness less than a reciprocal wave number (free-space wave-length divided by 2π). When we have a thick sheath we use the equations of Appendix B, shown in Appendix C to be accurate for attenuation calculations in thick sheaths.

*Sonett, C. P., "Graphs of Electrical Properties of Ionized Media," GM-TM-190, Guided Missile Research Division, the Ramo Wooldridge Corporation, August 30, 1957.

In the case of the blunt body, it is shown in Section 7.1.3 that the plasma will be thick for frequencies above 1000 mc. We therefore use the analysis of Appendix B, i.e.

$$A = 20 \log 1/(1-R_o) + 8.7 \omega/c \int \beta dx \quad (3.8-3)$$

where A is total db attenuation, R_o is reflection coefficient for a semi-infinite medium, c is the speed of light in free-space, and β is the imaginary part of the index of refraction. The integration is carried out perpendicular to the sheath. By the approximations of Appendix A

$$A = B + \int D dx \quad (3.8-4)$$

where the integration is again carried out through the sheath. The functions B and D have various forms according to the following table (use maximum value of ω_p in electron concentration profile for the function B).

	B (db)	D (db/meter)
$\omega_p < \omega < \nu$	$.54 \left(\frac{\omega_p}{\omega} \right)^4$	$1.45 \times 10^{-8} \sqrt{\left(\frac{\omega_p}{\omega} \right)^2}$
$\nu > \omega > \frac{\omega_p^2}{\nu}$	$.54 \left(\frac{\omega_p^2}{\nu \omega} \right)^2$	$1.45 \times 10^{-8} \frac{\omega_p^2}{\nu}$
$\omega_p > \omega > \nu$	$20 \log \left(\frac{\omega_p}{2 \nu} \right)$	$2.9 \times 10^{-8} \omega_p$
$\omega_p > \nu > \omega$ or $\nu > \frac{\omega_p^2}{\nu} > \omega$	$20 \log \left(\frac{\omega_p}{2 \sqrt{2 \nu \omega}} \right)$	$2.05 \times 10^{-8} \sqrt{\frac{\omega}{\nu}} \omega_p$

The last two rows in the table are of interest during blackout. When $\omega_p > \omega > \nu$, attenuation is independent of ω . This is why Figure 4 shows a single line for the range $10^9 - 10^{10}$ cps. In the last row of the table, the reflective term in attenuation decreases with ω while the absorptive term D increases with ω . The 10^8 cps curve in Figure 4 is below the $10^9 - 10^{10}$ curve because the absorptive term

happens to be dominant. However, if we went lower in frequency, the attenuation would not continue to decrease, because the reflective term would soon become dominant. (To be rigorous, we should also change our analysis at low frequencies from that of Appendix B to that of Appendix C. In the analysis of Appendix C, as we shall see below, attenuation increases without limit as signal frequency is reduced.)

When we analyze the conical body, we take the shock layer thickness as an indication of plasma sheath thickness, lacking information on electron concentration profiles. From Section 7.1.3 find that for "complete separation"

$$d = 0.3 z \quad (3.8-5)$$

where d is shock layer thickness and z is distance along the 10° portion of the cone. For "no separation,"

$$d = 0.019 z \quad (3.8-6)$$

Combining these results with an antenna position $z = \lambda/4$ gives

$$d = 0.075 \lambda, \text{ "complete separation"} \quad (3.8-7)$$

$$d = 0.0048 \lambda, \text{ "no separation"} \quad (3.8-8)$$

In both cases $2 \pi d/\lambda$ is less than unity, so that we should use the thin sheath analysis for all frequencies. (From experience we expect the sheath to be even thinner than d , giving added safety in using the thin sheath analysis.) The equation for total attenuation comes from the transmission coefficient T of Appendix C.

$$A = 10 \log 1/T$$

$$10 \log \left[\left(1 + \frac{\frac{2 \pi d}{\lambda} \sqrt{\omega_p^2}}{\omega (\sqrt{\nu^2 + \omega^2})} + \left(\frac{\frac{2 \pi d}{\lambda}}{4 \omega^2} \right)^2 \frac{\omega_p^4}{(\sqrt{\nu^2 + \omega^2})^2} \right) \right] \quad (3.8-9)$$

We find in the "complete separation" case that in the 200 mc to 2 kmc range the last term in brackets in equation (3.8-9) is dominant, giving rise to relatively little frequency dependence of attenuation. In the "no separation" case the last two terms in equation (3.8-9) are much less than unity, so that

$$A = \frac{8.7 \pi d \left(\frac{\omega_p}{\omega} \right)^2}{\lambda (1 + \nu^2 / \omega^2)} \left[\frac{\nu}{\omega} + \frac{\pi d}{2 \lambda} \left(\frac{\omega_p}{\omega} \right)^2 \right] \quad (3.8-10)$$

This results in the approximately inverse cube frequency dependence of attenuation shown in Figure 10 at frequencies above 100 mc.

3.8.5 Transmission Through the Entry-Induced Plasma by Means of a Magnetic Field

Equation (2.6.10) of Ratcliffe's volume* gives the general equation for the index of refraction in the presence of a steady magnetic field. Besides depending on plasma frequency ω_p and collision frequency ν , we have a dependence on cyclotron frequency ω_H , where

$$\begin{aligned} \omega_H &= e H / m \\ &= 1.76 \times 10^7 \text{ H sec}^{-1} \end{aligned} \quad (3.8-11)$$

in emu units, where

e = electron charge

m = electron mass

H = magnetic field in Gauss

Where H is small, we have the usual dependence of attenuation on ω_p and ν . When ω_H exceeds ω , there are two possible modes of propagation. One

*Ratcliffe, J. A., op. cit.

mode remains relatively unchanged from the no-magnetic-field case. The other mode has decreasing attenuation as $\frac{\omega H}{\omega}$ increases beyond unity, the rate of decrease depending on $\frac{\omega p}{\omega}$.

A good physical description of the effects of the magnetic field is as follows. Imposition of the magnetic field causes the free electrons to follow helical paths surrounding the flux lines, "binding" the electrons to flux lines. As with electrons bound to an atom, this effectively removes the electrons from the medium, provided the cyclotron frequency is high enough.

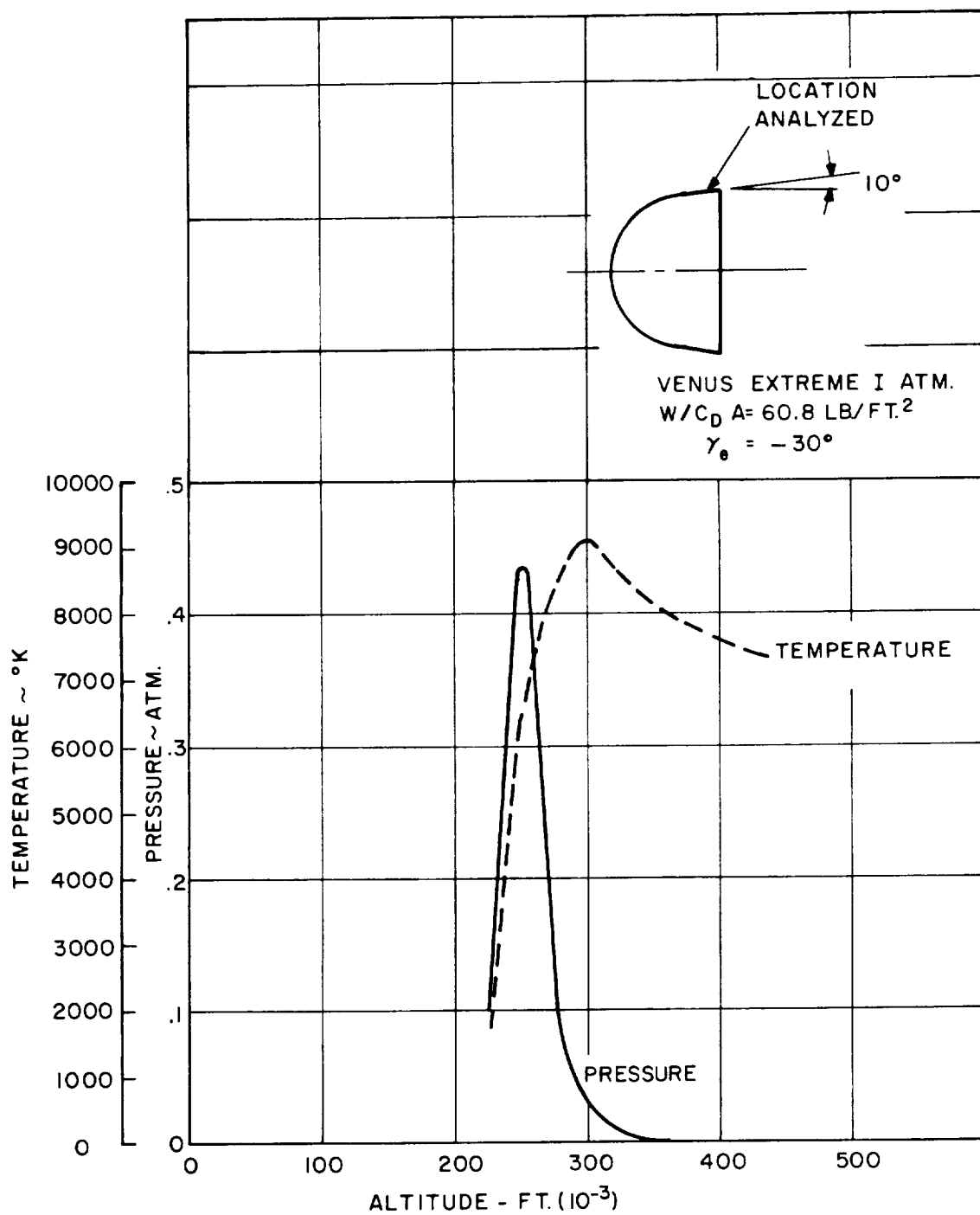


Figure 3.8.1 Temperature and Pressure vs. Altitude

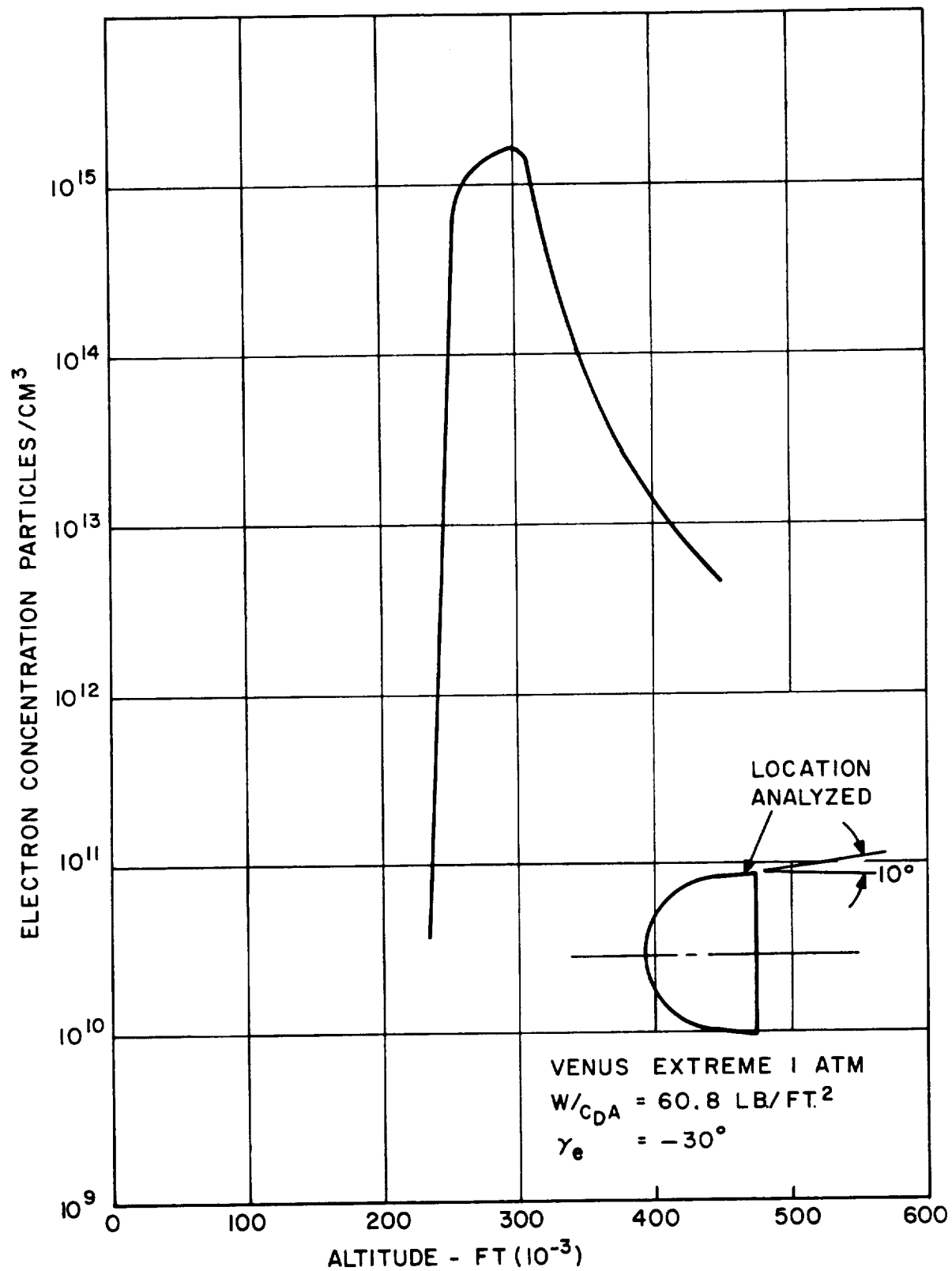


Figure 3.8.2 Electron Concentration vs. Altitude

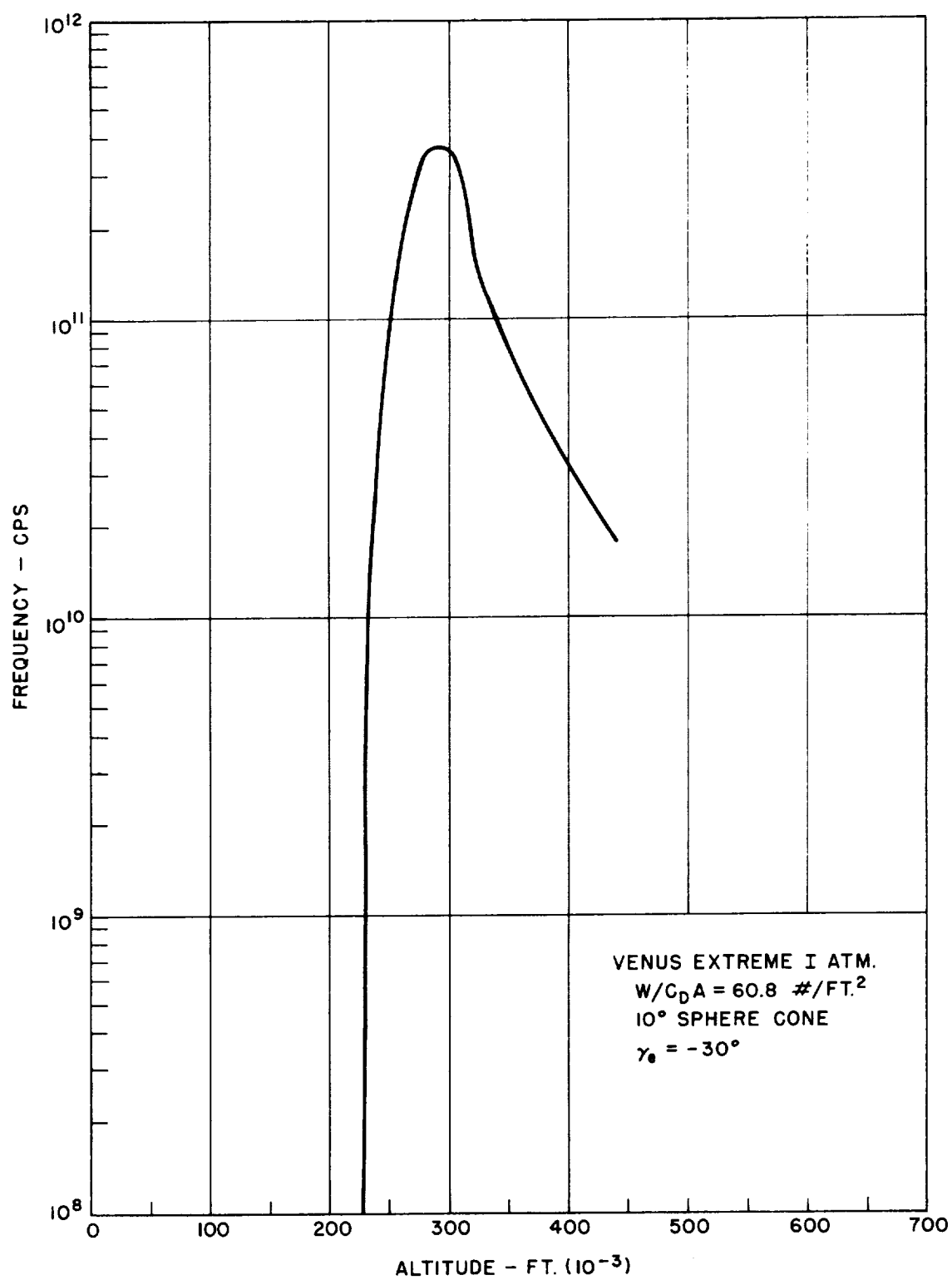


Figure 3.8.3. Critical Frequency vs. Altitude
III-3-198

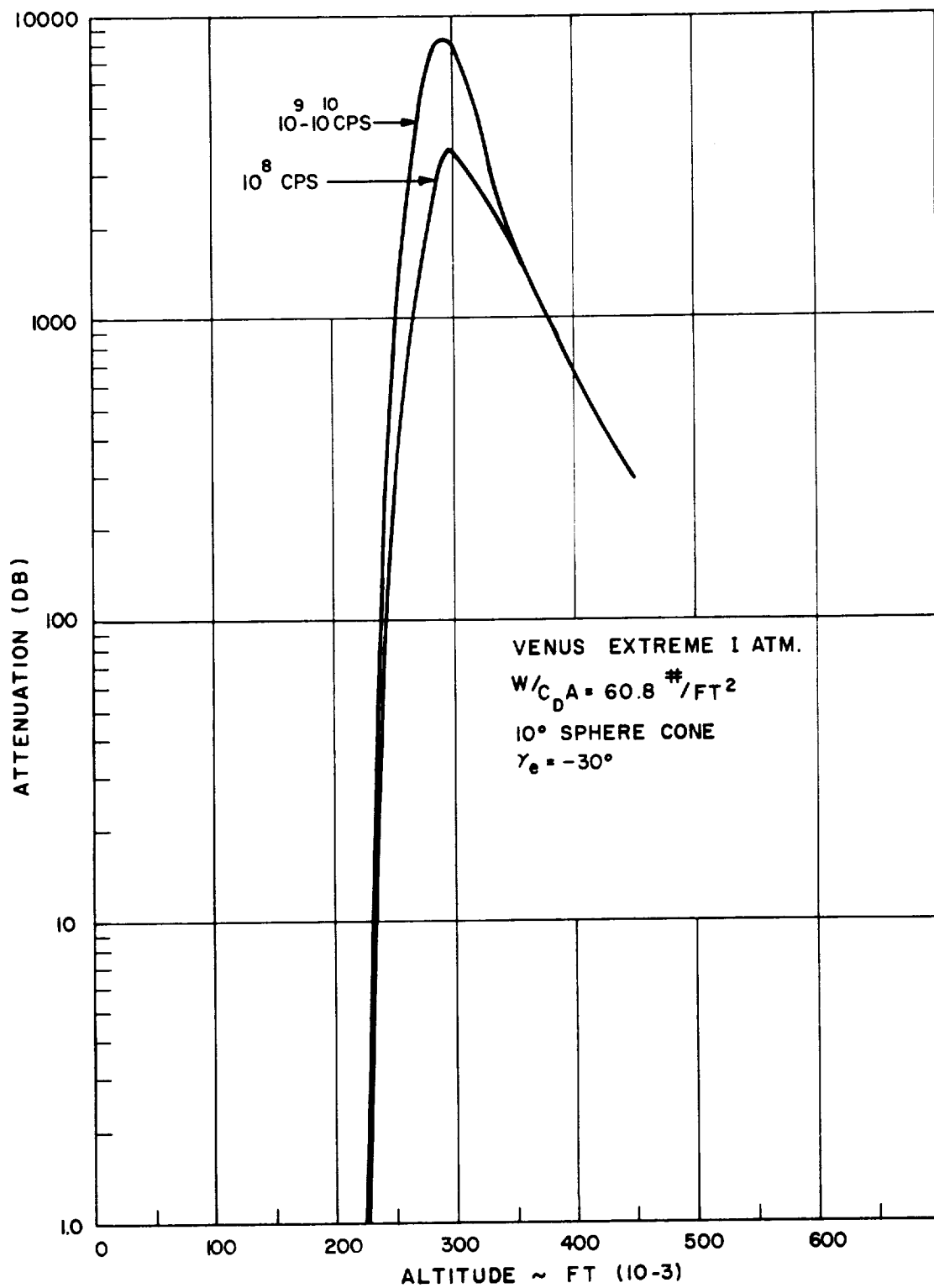


Figure 3.8.4 Total Attenuation vs. Altitude

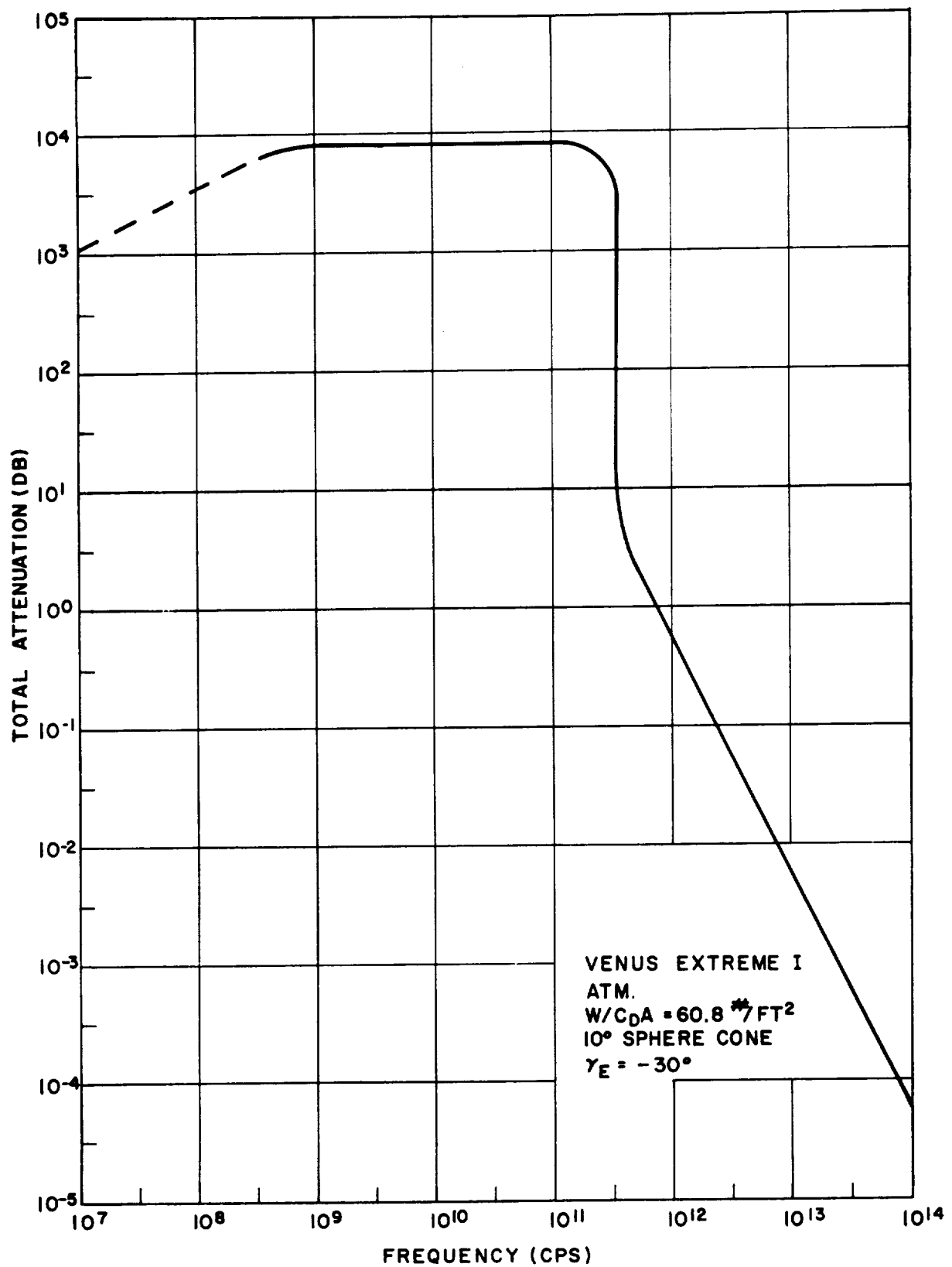


Figure 3.8.5 Total Attenuation vs. Frequency at 300K Ft. Altitude

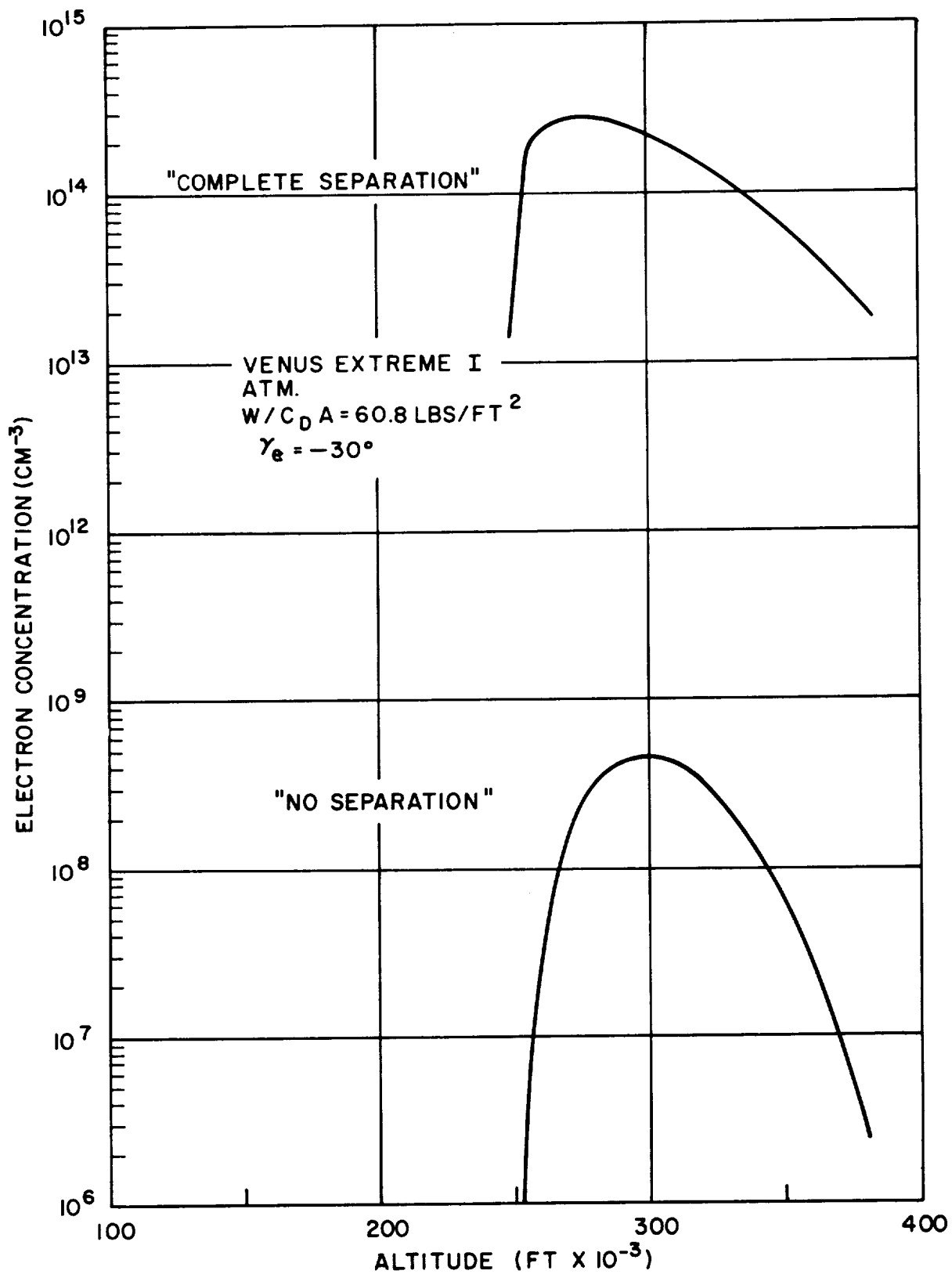


Figure 3.8.6 Electron Concentration vs. Altitude
(10° Cone Portion of Flared Cone)

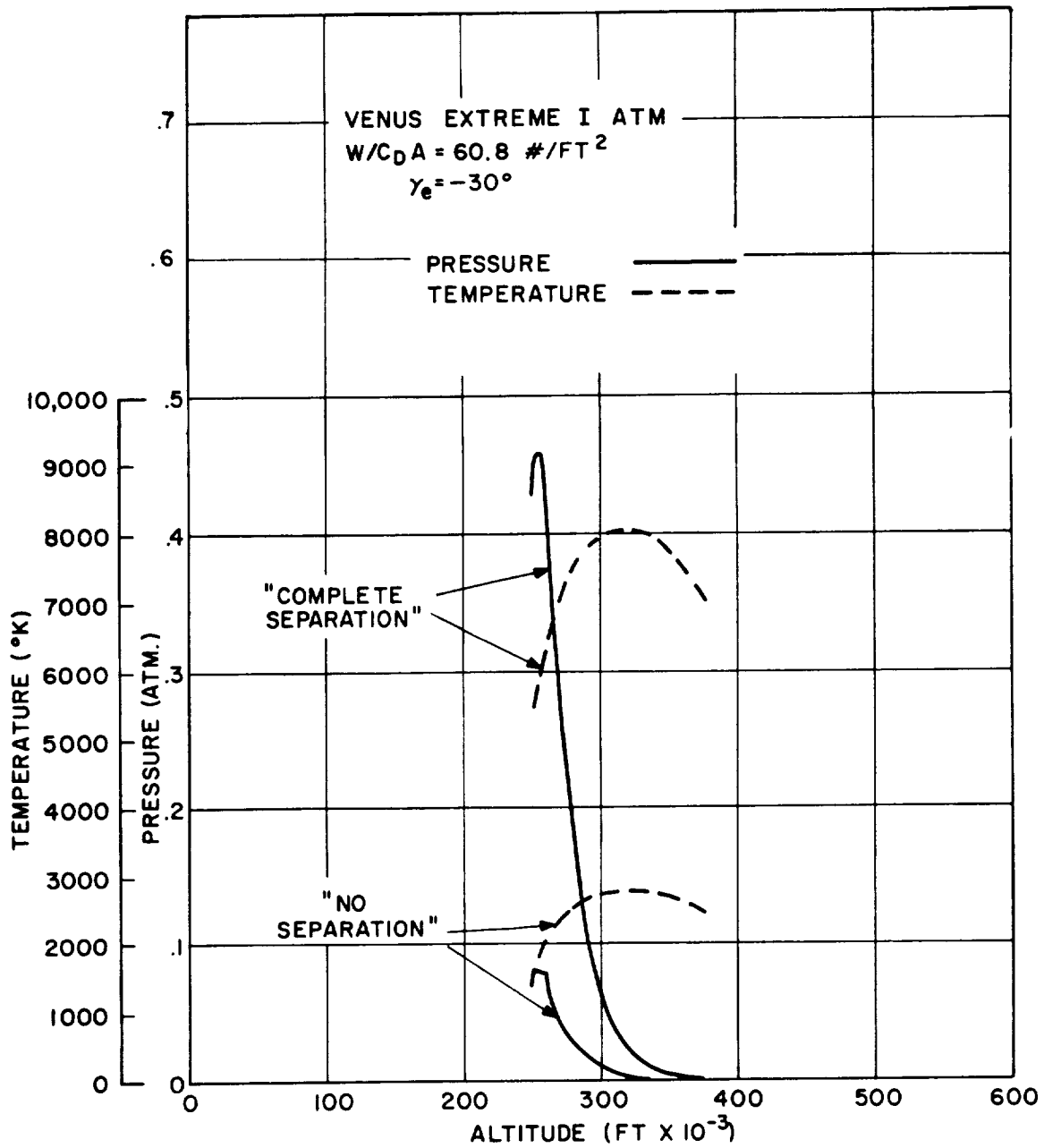


Figure 3.8.7 Temperature and Pressure vs. Altitude
 (10° Cone Portion of Flared Cone)

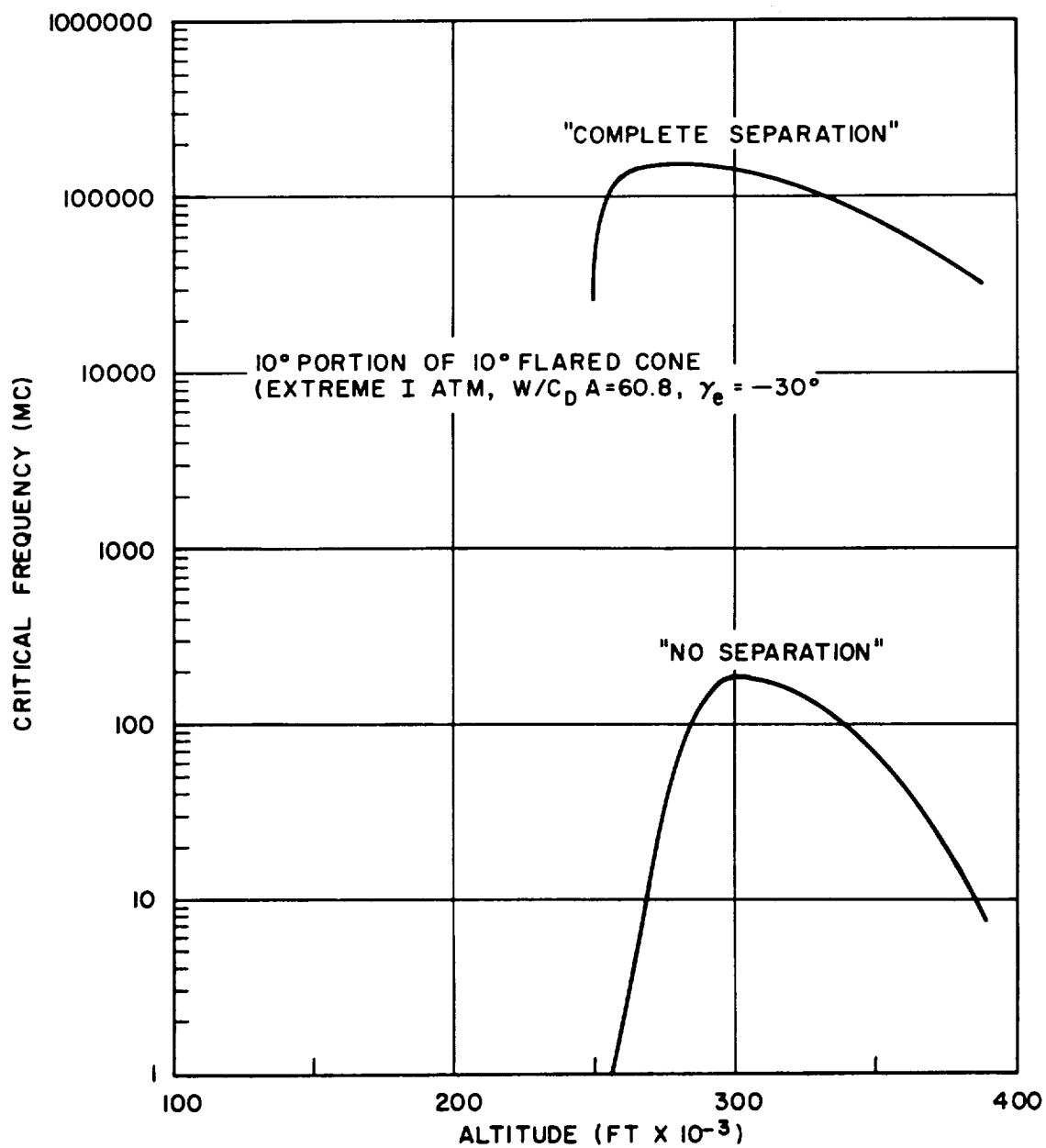


Figure 3.8.8 Critical Frequency vs. Altitude (10° Cone Portion of Flared Cone) (Extreme I Atm., $W/C_D A = 60.8$, $\gamma_E = -30^\circ$)

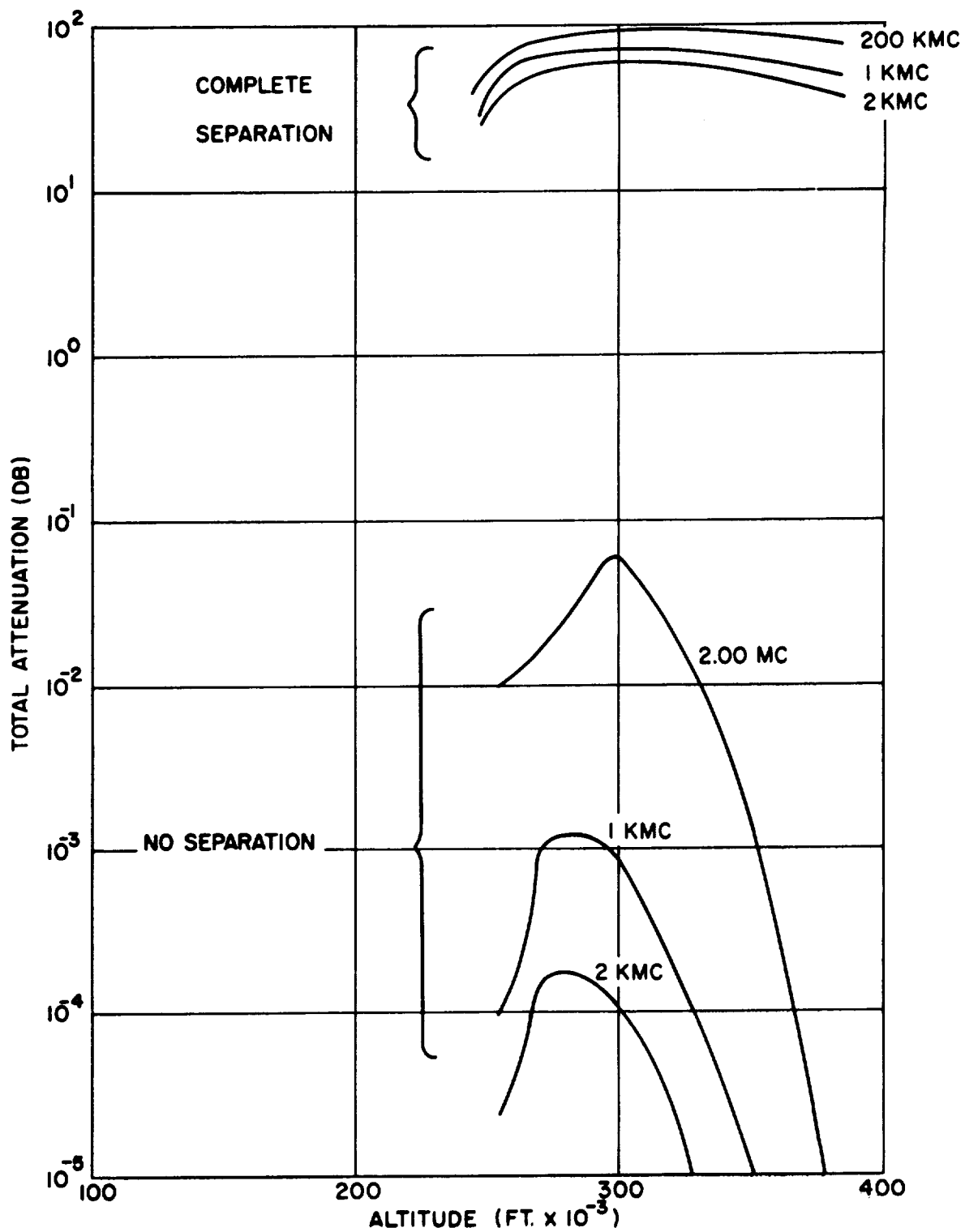


Figure 3.8.9. Estimated Total Attenuation vs. Altitude
(Extreme I, $W/C_{DA} = 60.8$, $\gamma_E = -30^\circ$)

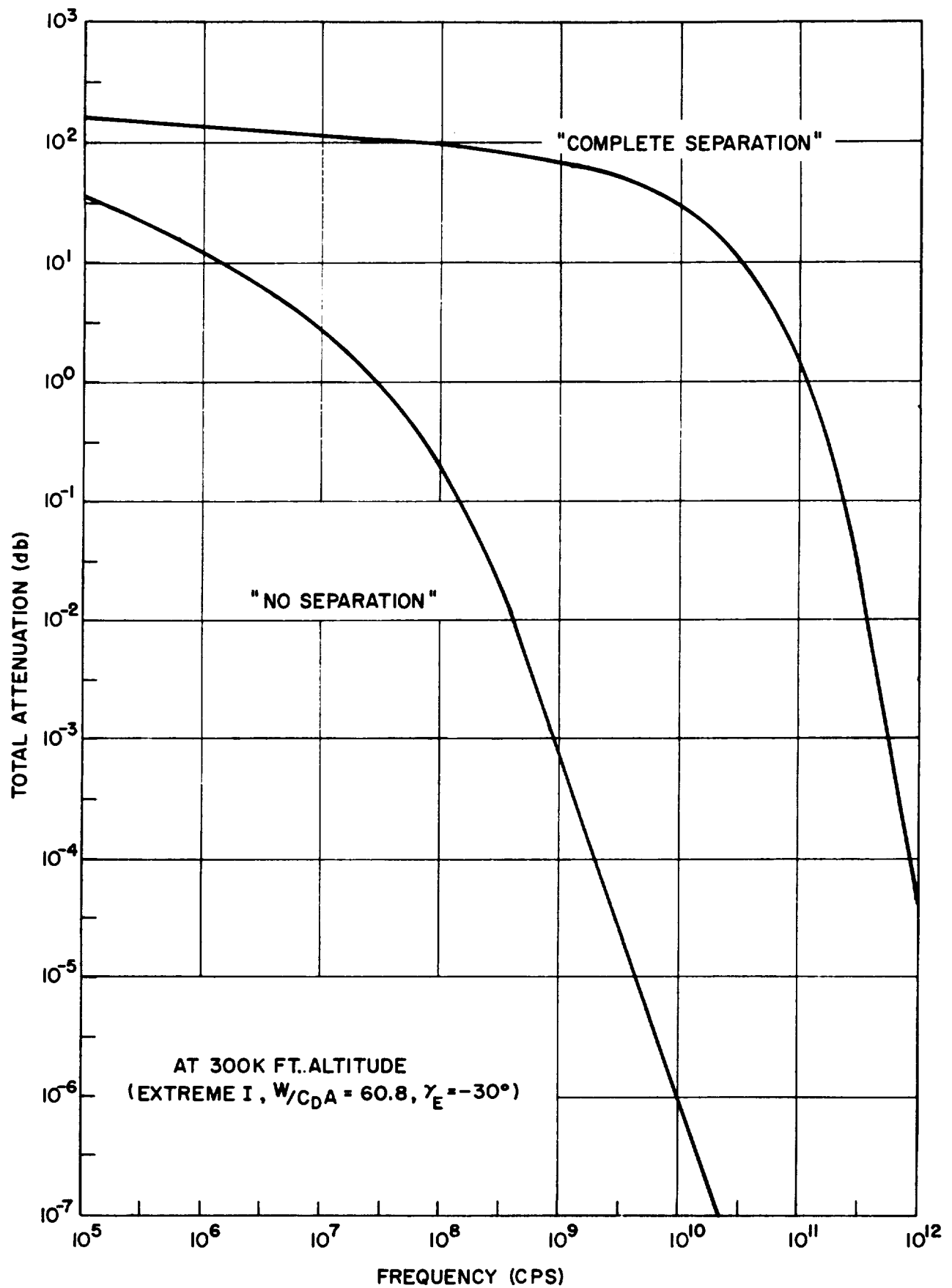


Figure 3.8.10 Estimated Total Attenuation vs. Frequency at 300K Ft. Altitude
(Extreme I, $W/C_D A = 60.8$, $\gamma_E = -30^\circ$)

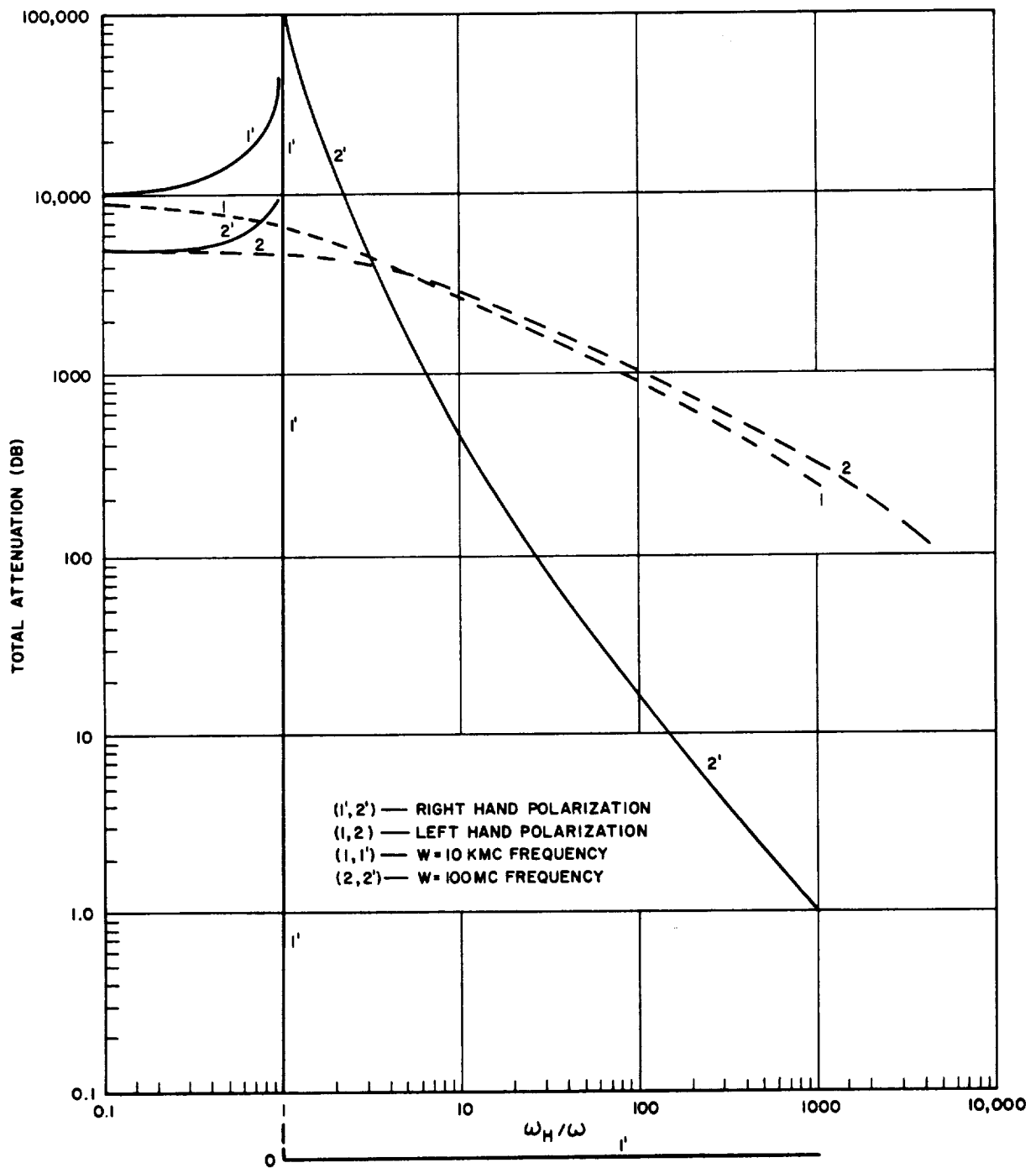


Figure 3.8.11 Total Attenuation vs. $\frac{\omega_H}{\omega}$ at 275 K Ft. Altitude (10° Sphere Cone)

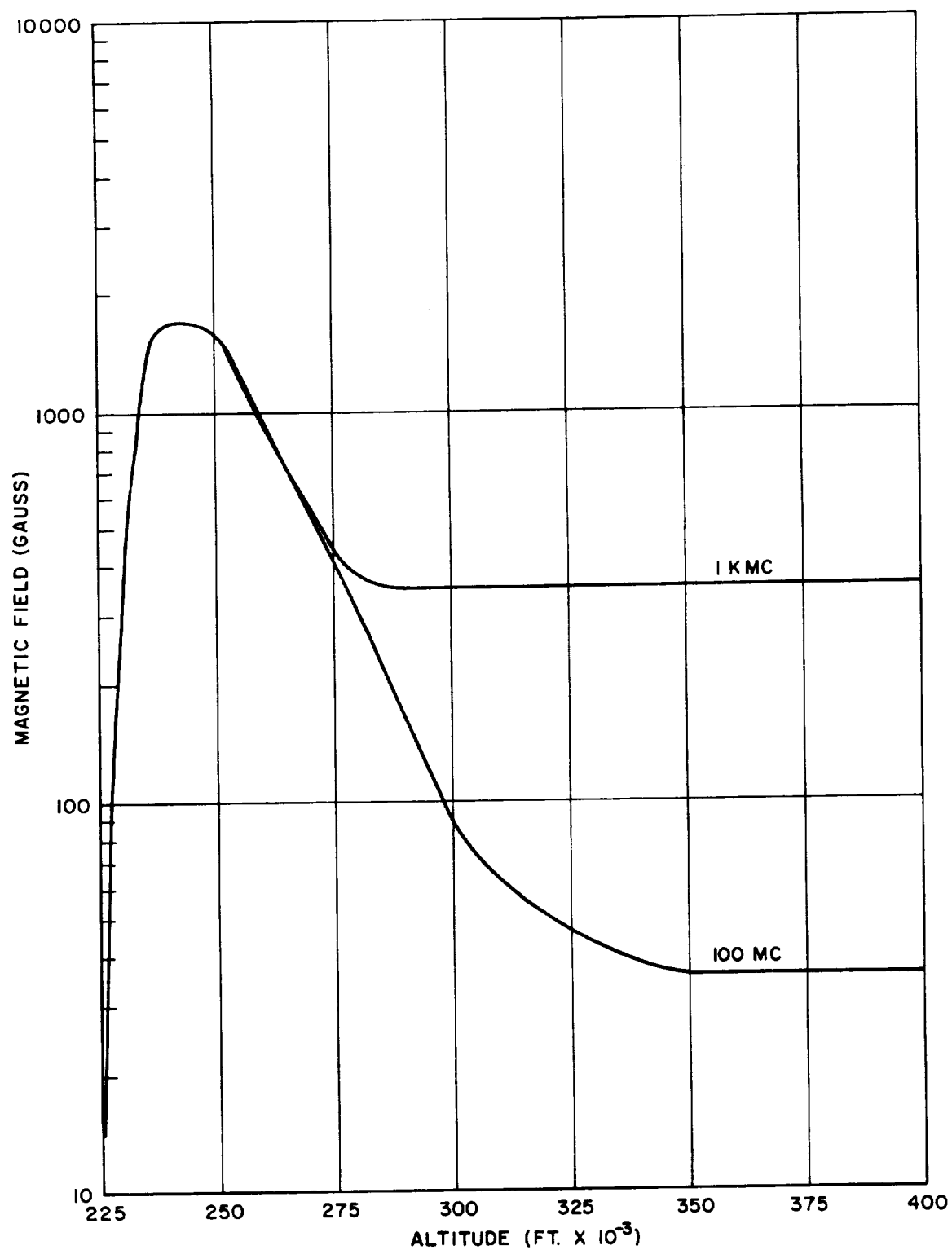


Figure 3.8.12 Magnetic Field vs. Altitude for 10 D B Attenuation (10⁰ Sphere Cone)

APPENDIX A

DERIVATION OF EQUATIONS (3.8-1) and 3.8-2)

The index of refraction $(\alpha + i\beta)$ of a weakly ionized medium is a well known function of plasma frequency, ω_p , collision frequency ν , and signal angular frequency ω ,

$$(\alpha + i\beta)^2 = 1 - \frac{\left(\frac{\omega_p}{\omega}\right)^2 (1 - i\frac{\nu}{\omega})}{1 + \left(\frac{\nu}{\omega}\right)^2} \quad (\text{A-1})$$

Carrying out the algebra associated with the left-hand side of equation (A-1), and solving the two equations formed by taking real and imaginary parts separately, gives

$$\alpha = \sqrt{\frac{\sqrt{V^2 + W^2} + V}{2}} \quad (\text{A-2})$$

$$\beta = \sqrt{\frac{\sqrt{V^2 + W^2} - V}{2}} \quad (\text{A-3})$$

where V and W are the real and imaginary parts of $(\alpha + i\beta)^2$.

$$V = 1 - \frac{\left(\frac{\omega_p}{\omega}\right)^2}{1 + \left(\frac{\nu}{\omega}\right)^2} \quad (\text{A-4})$$

$$W = \frac{\left(\frac{\nu}{\omega}\right) \left(\frac{\omega_p}{\omega}\right)^2}{1 + \left(\frac{\nu}{\omega}\right)^2} \quad (\text{A-5})$$

* Ratcliffe, op. cit.

We wish to find at what value of ω the index of refraction starts to approach unity asymptotically, as ω is increased from zero.

CASE I: $\omega_p > \nu$

When ω is less than ω_p but greater than ν , expansion of (A-4) and (A-5) by the binomial theorem shows that

$$V = 1 - \left(\frac{\omega_p}{\omega}\right)^2 \left[1 - \left(\frac{\nu}{\omega}\right)^2 + \left(\frac{\nu}{\omega}\right)^4 - \dots \right] \quad (\text{A-6})$$

$$W = \frac{\nu}{\omega} \left(\frac{\omega_p}{\omega}\right)^2 \left[1 - \left(\frac{\nu}{\omega}\right)^2 + \left(\frac{\nu}{\omega}\right)^4 - \dots \right] \quad (\text{A-7})$$

$$V = - \left(\frac{\omega_p}{\omega}\right)^2 \left[1 - \left(\frac{\omega'}{\omega_p}\right)^2 - \left(\frac{\nu}{\omega}\right)^2 + \dots \right] \quad (\text{A-8})$$

Hence $|V| > W \quad (\text{A-9})$

$$\sqrt{V^2 + W^2} = |V| \left(1 + \frac{W^2}{2V^2} - \frac{W^4}{8V^4} + \dots \right) \quad (\text{A-10})$$

Therefore, the asymptotic forms for $(\alpha + i \beta)$ are given by

$$\alpha \approx \frac{W}{2\sqrt{|V|}} \approx \frac{\nu \omega_p}{2 \omega^2} \quad (\text{A-11})$$

$$\beta \approx \sqrt{|V|} \approx \frac{\omega_p}{\omega} \quad (\text{A-12})$$

α is decreasing as the inverse square of ω and may be greater than or less than unity. β is decreasing inversely with ω , and is greater than one.

Now suppose ω is greater than ω_p .

$$V = 1 - \left(\frac{\omega_p}{\omega} \right)^2 + \left(\frac{\nu \omega_p}{\omega^2} \right)^2 - \left(\frac{\nu^2 \omega_p}{\omega^3} \right)^2 + \dots \quad (\text{A-13})$$

$$W = \frac{\nu}{\omega} \left(\frac{\omega_p}{\omega} \right)^2 \left[1 - \left(\frac{\nu}{\omega} \right)^2 + \left(\frac{\nu}{\omega} \right)^4 - \dots \right] \quad (\text{A-14})$$

V approaches unity and W is less than unity. Hence,

$$\sqrt{V^2 + W^2} \approx V \left(1 + \frac{W^2}{2V^2} \right) \quad (\text{A-15})$$

$$\alpha \approx \sqrt{1 - \left(\frac{\omega_p}{\omega} \right)^2} \approx 1 - \frac{\omega_p^2}{2\omega^2} \quad (\text{A-16})$$

$$\beta \approx \frac{W}{2\sqrt{V}} \approx \frac{\nu \omega_p^2}{2\omega^3} \left(1 + \frac{\omega_p^2}{2\omega^2} \right) \quad (\text{A-17})$$

Here we find that β is rapidly decreasing and is less than unity, while α is asymptotically approaching unity. The critical value for ω is, therefore, $\omega = \omega_p$, when $\omega_p > \nu$.

CASE II: $\nu > \omega_p$

When ω is less than ω_p

$$V = 1 - \left(\frac{\omega_p}{\nu} \right)^2 \left(1 - \frac{\omega^2}{\nu^2} + \dots \right) \quad (\text{A-18})$$

$$W = \frac{\omega_p}{\nu \omega} \left(1 - \frac{\omega^2}{\nu^2} + \dots \right) \quad (\text{A-19})$$

V approaches unity, however, W may be greater or less than unity, depending on $\frac{\omega_p^2}{\nu \omega}$. When $\omega_p > \sqrt{\nu \omega}$, $W > V$.

$$\sqrt{V^2 + W^2} \approx W \left(1 + \frac{V^2}{2W^2} \right) \quad (\text{A-20})$$

$$\alpha \approx \beta \approx \sqrt{\frac{W}{2}} \approx \frac{\omega_p}{\sqrt{2\nu\omega}} \quad (\text{A-21})$$

When $\omega_p < \sqrt{\nu \omega}$, $V > W$.

$$\sqrt{V^2 + W^2} \approx V \left(1 + \frac{W^2}{2V^2} \right) \quad (\text{A-22})$$

$$2\alpha^2 \approx 2V + \frac{W^2}{2V} \quad (\text{A-23})$$

$$\alpha \approx \sqrt{V} \left(1 + \frac{W^2}{8V^2} \right) \quad (\text{A-24})$$

$$\begin{aligned} &\approx \left(1 - \frac{\omega_p^2}{2\nu^2} \right) \left(1 + \frac{\omega_p^4}{8\nu^2\omega^2} \right) \\ &\approx \left(1 - \frac{\omega_p^2}{2\nu^2} \right) \left(1 - \frac{\omega_p^2}{4\omega^2} \right) \end{aligned} \quad (\text{A-25})$$

$$\beta \approx \frac{W}{2\sqrt{V}} \left(1 - \frac{W^2}{4V^2} \right) \quad (\text{A-26})$$

$$\approx \frac{\omega_p^2}{2\nu\omega} \left(1 + \frac{\omega_p^2}{2\nu^2} \right) \left(1 - \frac{\omega_p^2}{\nu^2} \right) \left(1 - \frac{\omega_p^4}{4\nu^2\omega^2} \right)$$

$$\approx \frac{\omega_p^2}{2\nu\omega} \left[1 + \frac{\omega_p^2}{2\nu^2} \left(1 - \frac{\omega_p^2}{4\omega^2} \right) - \frac{\omega^2}{\nu^2} \right] \quad (\text{A-27})$$

Thus, when $\nu > \omega > \frac{\omega_p}{\nu}$, α approaches unity asymptotically and β is less than unity. Therefore, the critical frequency when $\nu > \omega_p$ is given by $\omega = \frac{\omega_p}{\nu}$.

APPENDIX B

DERIVATION OF EQUATIONS (3.8-3) and (3.8-4)

Following the reasoning on which the analysis is based, assume that the attenuation of an electromagnetic wave through an entry induced plasma can be attributed separately to the following:

- a. a double reflection, once at each surface of the plasma, and
- b. internal absorption on traveling through the plasma.

The reflection is estimated on the basis of the reflection coefficient of a semi-infinite medium at normal incidence and the absorption is estimated from the approximate plane wave solution which makes use of the index of refraction as for a uniform medium.

The reflection coefficient R_o for a semi-infinite uniform medium is (See, for example, Stratton, ELECTROMAGNETIC THEORY, McGraw-Hill, 1941.)

$$R_o = 1 - \frac{4\alpha}{(\alpha + 1)^2 + \beta^2} = \frac{(\alpha - 1)^2 + \beta^2}{(\alpha + 1)^2 + \beta^2} \quad (B-1)$$

where $(\alpha + i\beta)$ is the index of refraction within the medium.

The wave equation for plane wave propagation in a medium of refractive index $(\alpha + i\beta)$ is (See Stratton)

$$\frac{d^2 E}{dx^2} + \frac{\omega^2}{c^2} (\alpha + i\beta)^2 E = 0 \quad (B-2)$$

E is the electric field strength, x is the direction of propagation, ω is the signal angular frequency, and c is the speed of light in free space. A solution of this equation when $(\alpha + i\beta)$ is constant is

$$E = E_o \exp \left[\frac{\omega}{c} (i\alpha x - \beta x) \right] \quad (B-3)$$

By the same token when $(\alpha + i \beta)$ varies with x at a slow enough rate, relative to a wave length, the solution may be written as

$$E = E_o \exp \left[\frac{\omega}{c} (i \alpha x - \int \beta dx) \right] \quad (B-4)$$

(B-3) and (B-4) can be shown to be solutions of equation (B-2) by differentiation and substitution, treating α and β as constants. The transmitted power is proportional to EE^* , where $*$ refers to complex conjugate. Thus, the relative amount of power transmitted is $\exp(-\frac{2\omega}{c} \int \beta dx)$. The power transmitted after each reflection is $(1-R_o)$. Assuming the second reflection also reduces the transmission by $(1-R_o)$, the total reflective contribution to transmission coefficient is $(1-R_o)^2$. Combining reflective and absorptive components in simple manner gives the transmission coefficient T as:

$$T = (1 - R_o)^2 \exp \left(- \frac{2\omega}{c} \int \beta dx \right) \quad (B-5)$$

Attenuation A in db is given by $10 \log (\neq)$, so that

$$\begin{aligned} A &= 10 \log \left(\frac{1}{1 - R_o} \right)^2 + 10 \log \left(e^{-\frac{2\omega}{c} \int \beta dx} \right) \\ &= 20 \log \frac{1}{1 - R_o} + 8.7 \frac{\omega}{c} \int \beta dx \end{aligned} \quad (B-6)$$

Asymptotic forms for β and R_o simplify the calculation of A and give insight into the behavior of A with ω , ω_p (plasma frequency) and ν (collision frequency).

$$\text{Let} \quad 20 \log \frac{1}{1 - R_o} = \beta \quad (B-7)$$

and $8.7 \frac{\omega^2}{c} = D$ (B-8)

CASE I: $\omega > \omega_p$; $\omega > \nu$

Refer to Appendix A for asymptotic forms for α and β when $\omega_p > \nu$.

$$\alpha \approx 1 - \frac{\omega_p^2}{2\omega^2} \quad (B-9)$$

$$\beta \approx \frac{\nu \omega_p^2}{2\omega^3} \left(1 + \frac{\omega_p^2}{2\omega^2} \right) \quad (B-10)$$

$$R \approx \frac{\frac{\omega_p^4}{4\omega^4} + \frac{\nu^2 \omega_p^4}{4\omega^6}}{4 - \frac{2\omega_p^2}{\omega^2} + \frac{\omega_p^4}{4\omega^4} + \frac{\nu^2 \omega_p^4}{4\omega^6}} \quad (B-11)$$

$$R \approx \frac{\omega_p^4}{16\omega^4} \quad (B-12)$$

When we consider the case $\omega > \nu > \omega_p$, equation (A-22) of Appendix A applies and

$$\alpha \approx 1 - \frac{\omega_p^2}{2\omega^2} \quad (B-13)$$

$$\beta \approx \frac{\nu \omega_p^2}{2\omega^3} \left(1 - \frac{\nu^2}{\omega^2} \right) \quad (B-14)$$

$$R_o \cong \frac{\omega_p^4}{16 \omega^4} \quad (\text{B-15})$$

Therefore, when $\omega_p < \omega < \nu$

$$B = 20 \log \frac{1}{1 - \frac{\omega_p^4}{16 \omega^4}} \quad (\text{B-16})$$

$$= -8.7 \ln \left(1 - \frac{\omega_p^4}{16 \omega^4} \right)$$

$$= -8.7 \left[-\frac{\omega_p^4}{16 \omega^4} - \frac{\omega_p^8}{32 \omega^8} - \dots \right]$$

$$\cong \frac{8.7 \omega_p^4}{16 \omega^4}$$

$$= .54 \left(\frac{\omega_p}{\omega} \right)^4 \quad (\text{B-17})$$

$$D \cong \frac{8.7 \omega}{c} \left(\frac{\nu \omega_p}{2 \omega^3} \right)^2 = 1.45 \text{ db/meter} \quad (\text{B-18})$$

CASE II: $\nu > \omega > \frac{\omega_p^2}{\nu}$

This is covered by equations (A-25) and (A-27)

$$R_o \cong \frac{\left(\frac{\omega_p^4}{8 \nu^2 \omega^2} \right)^2 + \frac{\omega_p^4}{4 \nu^2 \omega^2} \left(1 - \frac{2 \omega^2}{\nu^2} - \frac{\omega_p^4}{4 \nu^2 \omega^2} \right)}{4 + \frac{\omega_p^4}{2 \nu^2 \omega^2} + \frac{\omega_p^4}{4 \nu^2 \omega^2}} \quad (B-19)$$

$$\cong \frac{\omega_p^4}{16 \nu^2 \omega^2}$$

$$B \cong .54 \left(\frac{\omega_p^2}{2 \omega} \right)^2 \quad (B-20)$$

$$D \cong 1.45 \times 10^{-8} \frac{\omega_p^2}{\nu} \text{ db/meter} \quad (B-21)$$

CASE III: $\omega_p > \omega > \nu$

Equations (A-11) and (A-12) apply here.

$$R_o \cong 1 - \frac{\frac{2 \nu \omega_p}{\omega^2}}{\frac{\nu^2 \omega_p^2}{4 \omega^4} + \frac{\nu \omega_p}{\omega^2} + 1 + \frac{\omega_p^2}{\omega^2}} \quad (B-22)$$

$$\cong 1 - \frac{2 \nu}{\omega_p}$$

$$B \cong 20 \log \left(\frac{\omega_p}{2\nu} \right) \quad (\text{B-23})$$

$$D \cong 2.9 \times 10^{-8} \omega_p \text{ db/meter} \quad (\text{B-24})$$

CASE IV: $\omega_p > \nu > \omega; \nu > \frac{\omega_p^2}{\nu} > \omega$

When $\omega_p > \nu > \omega$

$$V = 1 - \frac{\omega_p^2}{\nu^2} + \frac{\omega^2 \omega_p^2}{\nu^4} - \dots \quad (\text{B-25})$$

$$W = \frac{\omega_p^2}{\nu \omega} \left(1 - \frac{\omega^2}{\nu^2} + \dots \right) \quad (\text{B-26})$$

$$\sqrt{V^2 + W^2} = W \left(1 + \frac{V^2}{2W^2} - \dots \right) \quad (\text{B-27})$$

$$\alpha \cong \beta \cong \sqrt{\frac{W}{2}} \cong \frac{\omega_p}{\sqrt{2\nu\omega}} \quad (\text{B-28})$$

This is the same result (Equation (A-21)) as when $\nu > \frac{\omega_p^2}{\nu} > \omega$

$$R_o \cong 1 - \frac{2}{\alpha} \cong 1 - \frac{2\sqrt{2\nu\omega}}{\omega_p} \quad (\text{B-29})$$

$$B \approx 20 \log \frac{\omega_p}{2\sqrt{2\nu\omega}} \quad (\text{B-30})$$

$$D \approx \frac{8.7 \omega \omega_p}{c \sqrt{2\nu\omega}} \quad (\text{B-31})$$

$$= 2.05 \times 10^{-8} \sqrt{\frac{\omega}{\nu}} \omega_p \text{ db/meter}$$

APPENDIX C

TRANSMISSION THROUGH A THIN PLASMA SHEATH

Consider a plane electromagnetic wave incident normally from free space on a plasma sheath, as illustrated in figure (C-1). The sheath is non-uniform in the direction of incidence but is thin compared to a wavelength of the incident wave. We wish to calculate the reflection and transmission coefficients in this situation.

The differential wave equation for a plane wave at normal incidence to a medium with a complex conductivity σ is:

$$\frac{d^2 E}{dx^2} + (k^2 + i \omega \mu_0 \sigma) E = 0 \quad (C-1)$$

where $k (= \frac{\omega}{c})$ is the wave number, μ_0 is the permeability of free-space, and σ is the complex conductivity (mks units and equations are used throughout except where noted otherwise). The integral wave equation is thus (Morse, P.M. and H. Feshbach, Methods of Theoretical Physics, McGraw - Hill, 1953, page 1071.)

$$E = e^{ikx} - \frac{1}{2} \mu_0 c e^{ikx} \int_0^x \sigma E e^{-ikx} dx - \frac{1}{2} \mu_0 c e^{-ikx} \int_x^d \sigma E e^{ikx} dx \quad (C-2)$$

where d is the sheath thickness.

$$E = e^{ikx} - e^{ikx} \int_0^x g E e^{-ikx} dx - e^{-ikx} \int_x^d g E e^{ikx} dx \quad (C-3)$$

where we have let:

$$g = 1/2 \mu_o c \sigma = \frac{k}{2} \frac{\left(\frac{\omega_p}{\omega}\right)^2}{\left(\frac{\nu}{\omega} - i\right)} \quad (C-4)$$

Let us solve Equation (C-3) by iteration:

$$E_{(n+1)} = -e^{ikx} \int_0^x g E_n e^{-ikx} dx - e^{-ikx} \int_x^d g E_n e^{ikx} dx \quad (C-5)$$

where the solution E is given by:

$$E = \sum_{n=0}^{\infty} E_n \quad (C-6)$$

provided the series converges. In the case of a unit amplitude incident plane wave:

$$E_o = e^{ikx} \quad (C-7)$$

$$E_1 = \left[-e^{ikx} \int_0^x g dx - e^{-ikx} \int_x^d g e^{2ikx} dx \right] e^{-i\omega t} \quad (C-8)$$

We could carry out the integrations in equation (C-8) for a known function g of x and iterate using equation (C-7). Each approximation for E_n will involve functions of $e^{\pm ikx}$ which would become increasingly complicated as the iteration is continued. Let us apply the assumption of a thin sheath compared to a free-space wavelength, for which the factor $e^{\pm ikx}$ will not contribute to the definite integrals. The wave functions and exponentials in the integrands of equation (C-7) may then be dropped. We may also rewrite equation (C-7) in terms of complex amplitudes only as:

$$E_{(n+1)} = -E_n \int_0^d g \, dx \quad (C-9)$$

Here we have lumped together the contributions of both integrals in equations (C-7). We note by substitution of $x = d$ in equation (C-8) that equation (C-9) defines the transmitted field amplitudes as well as the internal field amplitudes. Denoting the reflected complex amplitude as E_n^- , we obtain, by analogy with the value of equation (C-8) at $x = 0$,

$$E_{(n+1)}^- = -E_n \int_0^d g e^{2ikx} \, dx \quad (C-10)$$

The exponential factor in the integrand of equation (C-10) does not now introduce complications, and it has been retained to allow for cases in which the condition of small thickness is borderline.

It is now obvious from equation (C-9) that the fields in the sheath are approximately:

$$E_n = E_0 (-1)^n, \quad (C-11)$$

where
$$I = \int_0^d g \, dx \quad (C-12)$$

Since E_0 is of unit amplitude and is the phase reference.

$$E_n = (-I)^n \quad (C-13)$$

Performing the summation of equation (C-6) readily gives the complex power series for the transmitted field E_T

$$E_T = \sum_{n=0}^{\infty} (-I)^n \quad (C-14)$$

This is a well known series which converges to

$$E_T = \frac{1}{1 + I} \quad (C-15)$$

with radius of convergence

$$|I| < 1 \quad (C-16)$$

Similarly equation (C-10) gives:

$$E_n = -I_2 (-I)^{n-1} \quad (C-17)$$

where

$$I_2 = \int_0^d g \exp(2ikx) \, dx \quad (C-18)$$

The reflected complex amplitude is thus:

$$E_R = -I_2 E_T \quad (C-19)$$

From equations (C-15) and (C-19) the reflection and transmission coefficients take very simple form.

$$T = \frac{1}{1 + I + I^* + \Pi^*} \quad (C-20)$$

$$R = T (I_2 I_2^*) \quad (C-21)$$

The range of validity of these equations may be predicted from inequality (C-16). Using equation (C-4) for g , when ν is constant,

$$\frac{\left[\int_0^d \omega_p^2 dx \right]^2}{4 c^2 (\nu^2 + \omega^2)} < 1 \quad (C-22)$$

This can be written as:

$$\frac{\omega_p^2}{\omega^2} < \frac{2 \sqrt{1 + \frac{\nu^2}{\omega^2}}}{\frac{\omega d}{c}} \quad (C-23)$$

Thus the average value of the square of the plasma frequency divided by the signal frequency is limited inversely as the sheath thickness relative to a wavelength.

Therefore when the sheath is thin we may apply this method even to cases in which ω_p exceeds ω .

Another feature worthy of comment in our results is that they have the right qualitative form. R increases and T decreases with plasma frequency. (R + T) approaches unity (absorption is negligible) when collision frequency is negligible, and is less than unity when collision frequency is important. (Absorption coefficient = 1 - (R + T).) Thus we find that conservation of energy is maintained.

Although the above results are general and do not require the sheath to be uniform, in order to compare them with other methods we write equations (C-20) and (C-21) for the case when ω_p and ν are both constant in the sheath.

$$T = \frac{1}{1 + \frac{\frac{\nu}{\omega'} \left(\frac{\omega_p}{\omega'}\right)^2 \frac{\omega_d}{c}}{\left(\frac{\nu^2}{\omega'^2} + 1\right)} + \frac{\left(\frac{\omega_p}{\omega'}\right)^4 \left(\frac{\omega_d}{c}\right)^2}{4 \left(\frac{\nu^2}{\omega'^2} + 1\right)}} \quad (C-24)$$

$$R = \frac{T \left(\frac{\omega_p}{\omega}\right)^4 \sin^2 \left(\frac{\omega_d}{c}\right)^2}{4 \left(\frac{\nu^2}{\omega'^2} + 1\right)} \quad (C-25)$$

The exact solution for the uniform case is (Stratton, page 515).

$$R = \frac{\left(\sin \frac{\omega_d}{c} \alpha\right)^2 + \sinh^2 \left(\frac{\omega_d}{c} \beta\right)}{\left\{ \left[\sin \left(\frac{\omega_d}{c} \alpha + \tan^{-1} \frac{2\beta}{\alpha^2 + \beta^2 - 1} \right) \right]^2 + \left[\sinh \left(\frac{\omega_d}{c} \beta - \frac{1}{2} \ln R_0 \right) \right]^2 \right\}} \quad (C-26)$$

$$T = \frac{1 + \left(\frac{\alpha^2 + \beta^2 - 1}{4\beta^2} \right)^2 + \left[\sinh \left(\frac{1}{2} \ln R_o \right) \right]^2}{\left\{ \left[\sin \left(\frac{\omega d}{c} \alpha + \tan^{-1} \frac{2\beta}{\alpha^2 + \beta^2 - 1} \right) \right]^2 + \left[\sinh \left(\frac{\omega d}{c} \beta - \frac{1}{2} \ln R_o \right) \right]^2 \right\}} \quad (C-27)$$

α and β are the real and imaginary parts of the index of refraction and R_o is the reflection coefficient of a semi-infinite medium.

The equations are as follows:

$$R = R_o + R_o (1 - R_o) = 1 - (1 - R_o)^2 \quad (C-28)$$

$$T = (1 - R_o)^2 \exp \left(\frac{-2\omega}{c} \int_0^d \beta \, dx \right) \\ = (1 - R_o)^2 \exp \left(\frac{-2\omega \beta d}{c} \right) \quad (C-29)$$

Calculations of R and T versus $\frac{\omega_p}{\omega}$ were made by equations (C-24), (C-25), (C-26), (C-27), (C-28), and (C-29) for values of $\frac{\nu}{\omega}$ of 0.1, 1, and 10, using the value 0.1 for $\frac{\omega_d}{c}$. These results are plotted in figures 2 through 7. Equations (C-26) and (C-27) are plotted in solid line as a reference. Equations (C-24) and (C-25) are plotted in dashed line while equations (C-28) and (C-29) are plotted in dotted line.

In figures (C-2) through (C-4) we have reflection coefficient for each value of $\frac{\nu}{\omega}$. Here we note the excellent agreement between equations (C-25) and (C-26), and the very poor agreement between equations (C-28) and (C-26). Figures (C-5) through (C-7) illustrate the transmission coefficient. Here the agreement of equation (C-24) with equation (C-27) is good only when $\frac{\omega_p}{\omega}$ is below a certain range of values. Above a certain value of $\frac{\omega_p}{\omega}$ equation (C-24) predicts more signal attenuation than does the exact solution. However, note that equation (C-29) is generally in even greater error than equation (C-24) and over a much wider range of the parameter $\frac{\omega_p}{\omega}$.

The limited range of validity of equation (C-24) is not unexpected, because the analysis predicts an upper limit on $\frac{\omega_p}{\omega}$ for which it is applicable.

$$I I^* < 1 \quad (C-30)$$

In the case we have studied numerically, this condition implies that the upper limit on $\frac{\omega_p}{\omega}$ must be

$$\left(\frac{\omega_p}{\omega} \right)^2 < \frac{2 \sqrt{1 + \frac{\nu^2}{\omega^2}}}{\frac{\omega d}{c}} \quad (C-31)$$

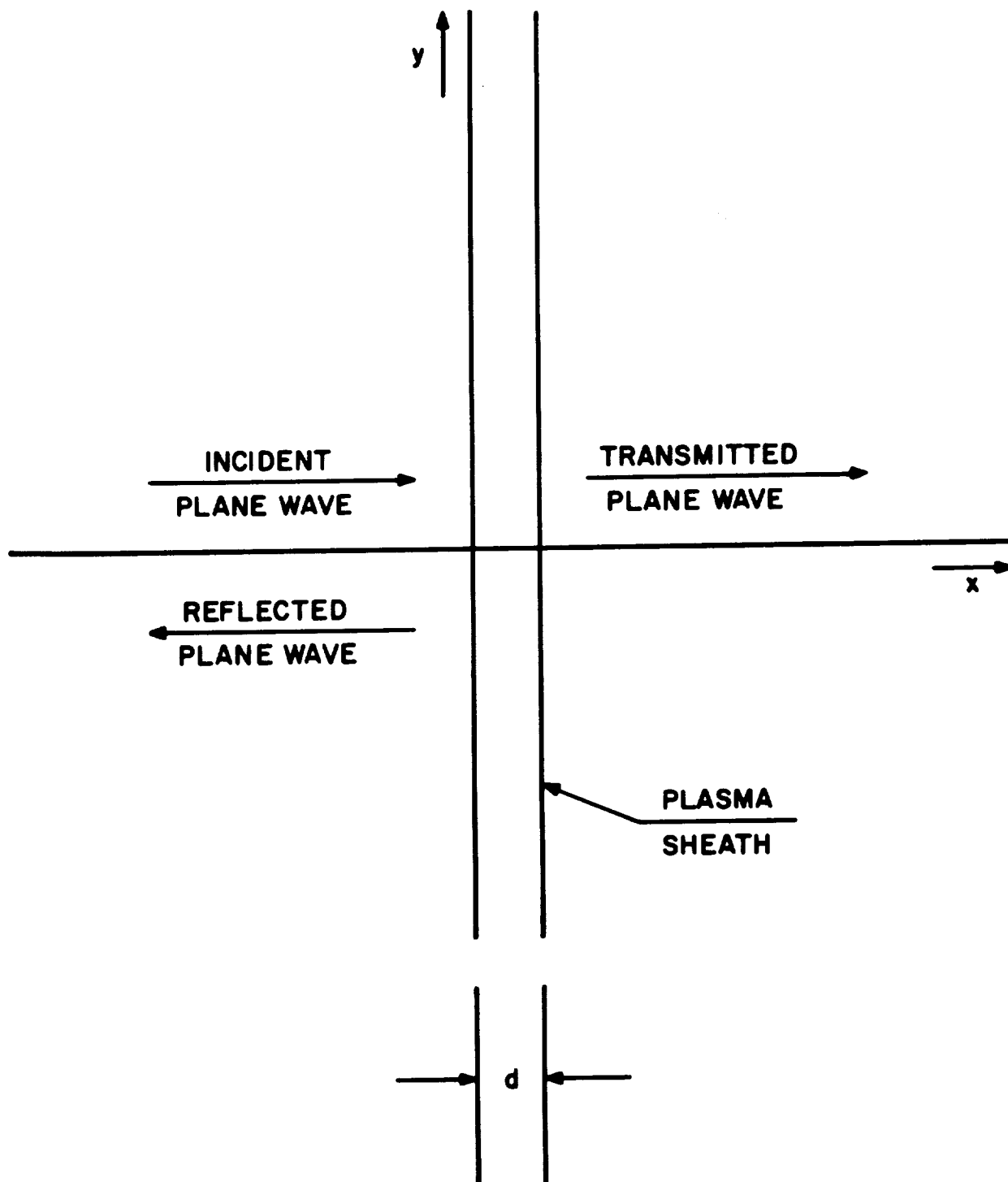
The limitation on the product of electron concentration and sheath thickness expressed by (C-31) suggests that, although the results are derived by assuming the sheath is thin compared to a wavelength, it may be possible to stretch their applicability to thickness greater than a wavelength, when the electron concentration is small. We tested this proposition by calculations of R and T for $\frac{\omega_d}{c} = 10$, as shown in figures (C-8) and (C-9). This was done for only one value of $\frac{\nu}{\omega}$ because, as shown by the previous results, this parameter has little effect on the comparative differences in results.

In figure (C-8) equation (C-25) is not in agreement with equation (C-26). The fact that equation (C-25) approaches a value of R less than unity when $\frac{\omega p}{\omega}$ becomes large may be expected because equations (C-24) and (C-25) yield, in the limit of large $\frac{p}{\omega}$, a reflection coefficient equal to

$$\left[\frac{\frac{\omega d}{\sin c}}{\frac{\omega d}{c}} \right]^2 .$$

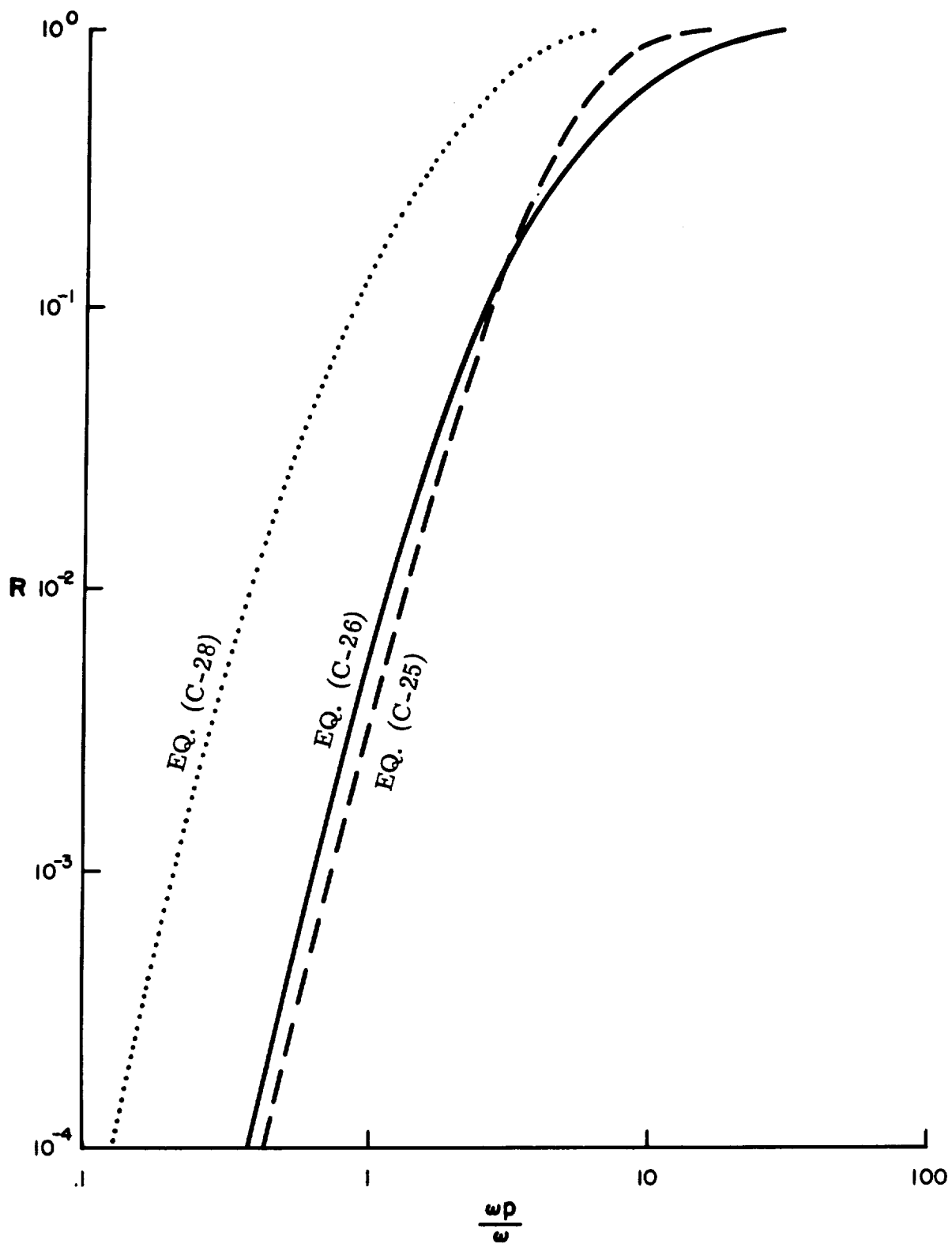
Since we know that every sheath must at some time become a perfect reflector as its conductivity increases, we should reject the use of equation (C-25) for other than small values of $\frac{\omega d}{c}$.

Reference to figure (C-9) shows that for the thick sheath, equations (C-27) and (C-29) are in excellent agreement, while equation (C-24) is not. It appears that the calculation of transmission through sheaths which are greater than a free-space wavelength thick is best accomplished by the methods of Appendix B. Although these methods seem suspect to some degree in their estimation of reflection, as shown by the relatively poor agreement evidenced by figure (C-9) indicates high reliability of prediction of signal attenuation for thick sheaths.



PLANE WAVE INTERACTION WITH A
NON-UNIFORM PLASMA SHEATH

Figure C-1



REFLECTION COEFFICIENT VS. $\frac{\omega_p}{\omega}$
 $\frac{\nu}{\omega} = .1, \frac{\omega_d}{c} = .1$

Figure C-2

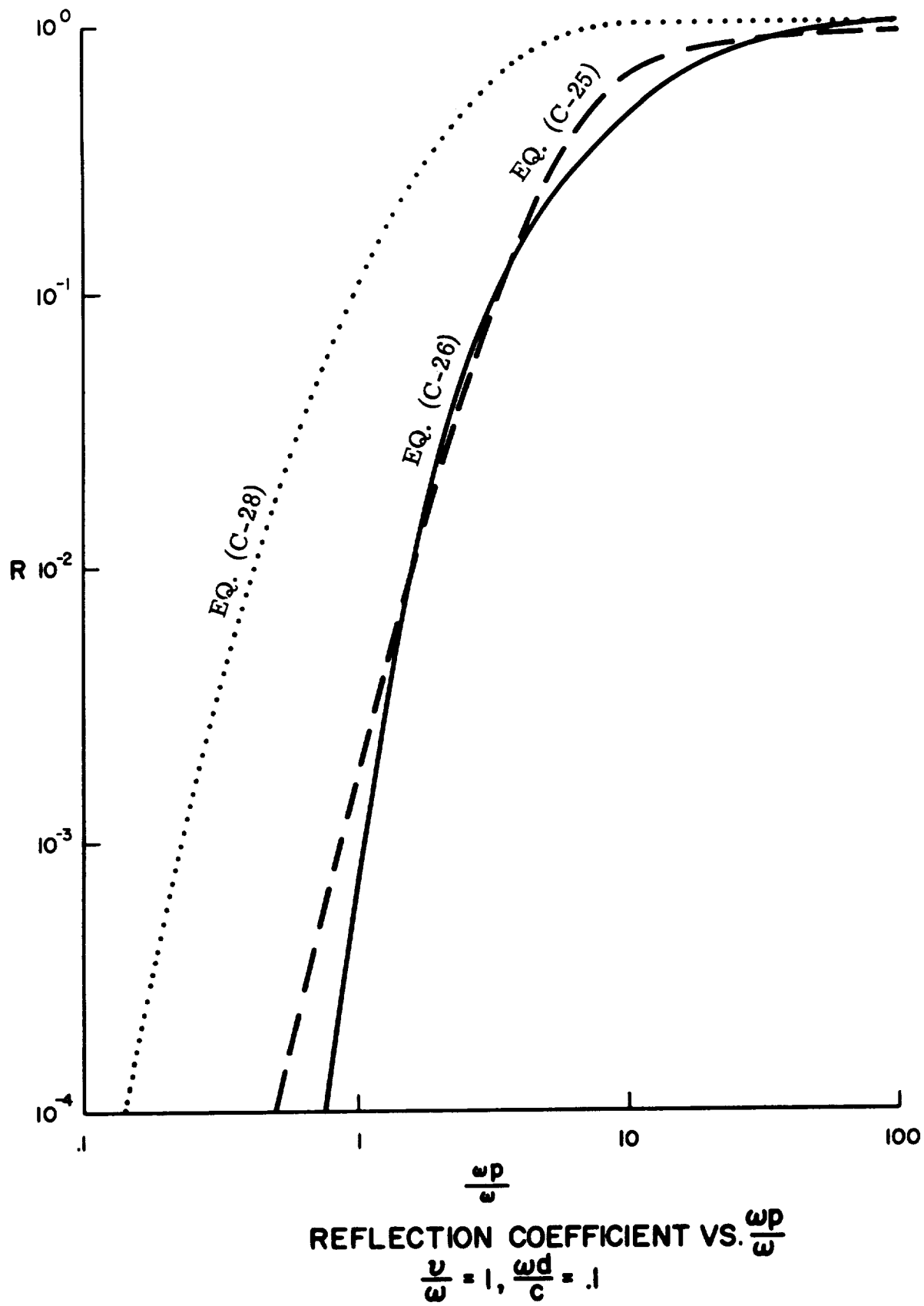
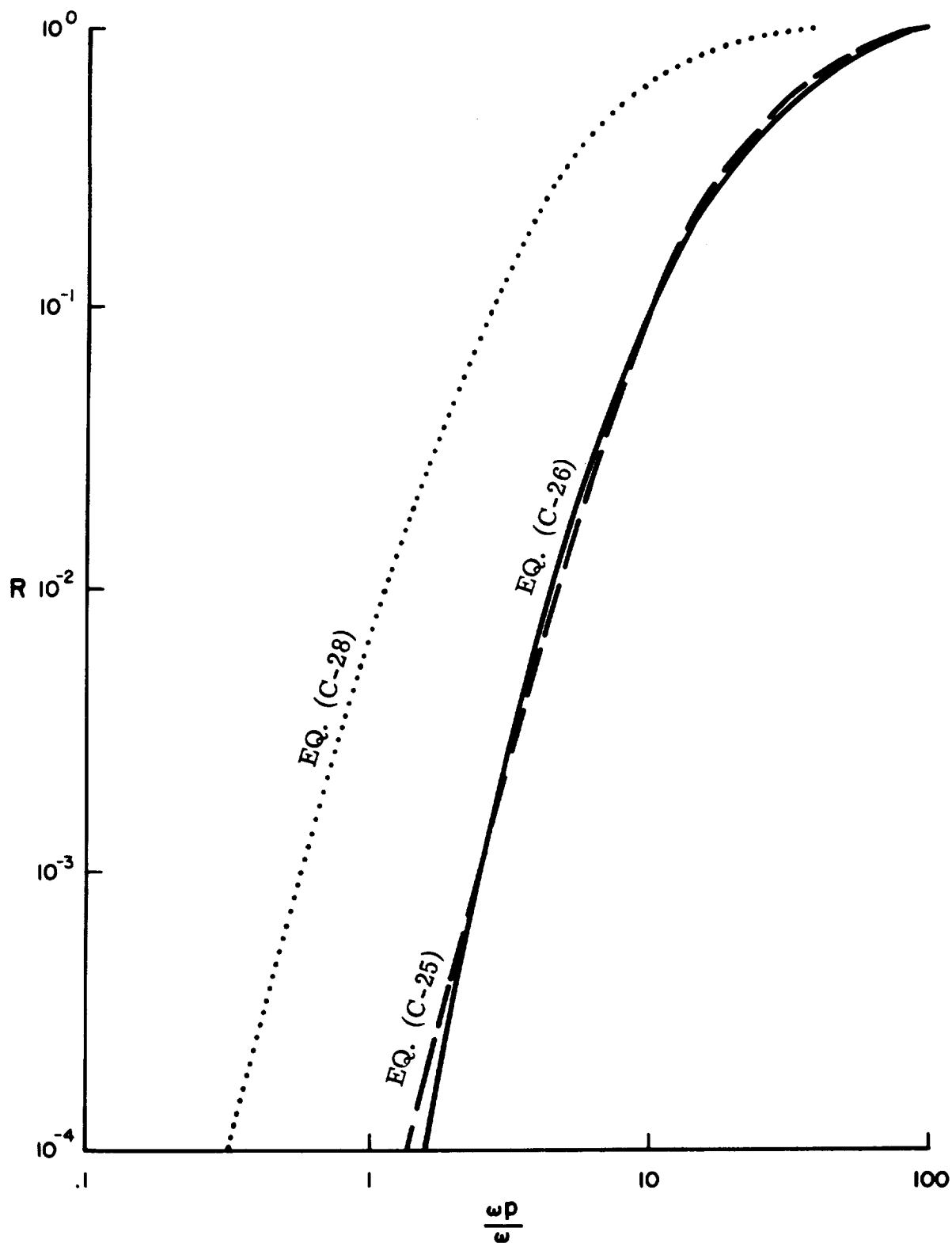


Figure C-3



REFLECTION COEFFICIENT VS. $\frac{\omega_p}{\epsilon}$
 $\frac{\omega}{c} = 10, \frac{\omega_d}{c} = .1$

Figure C-4

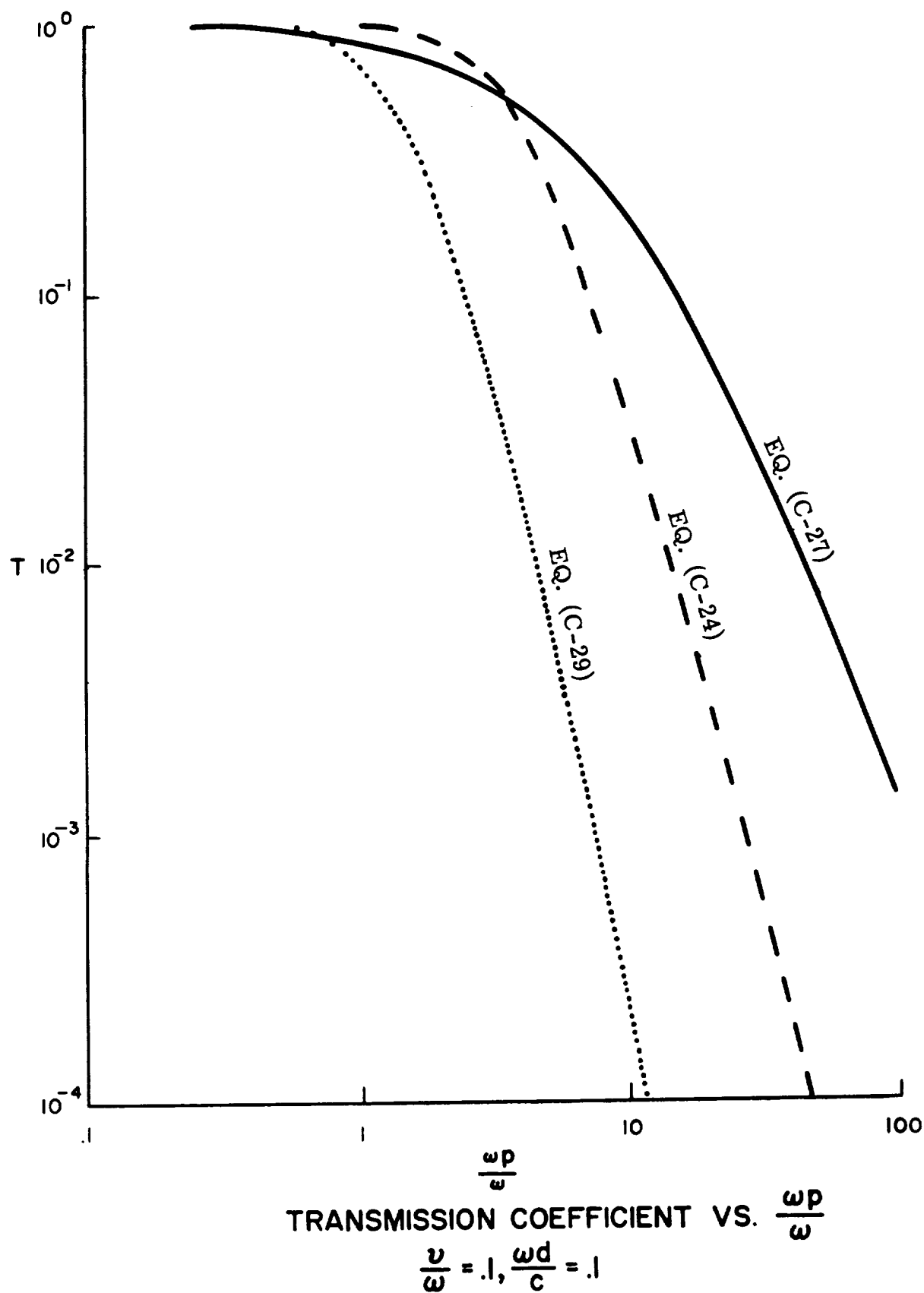


Figure C-5

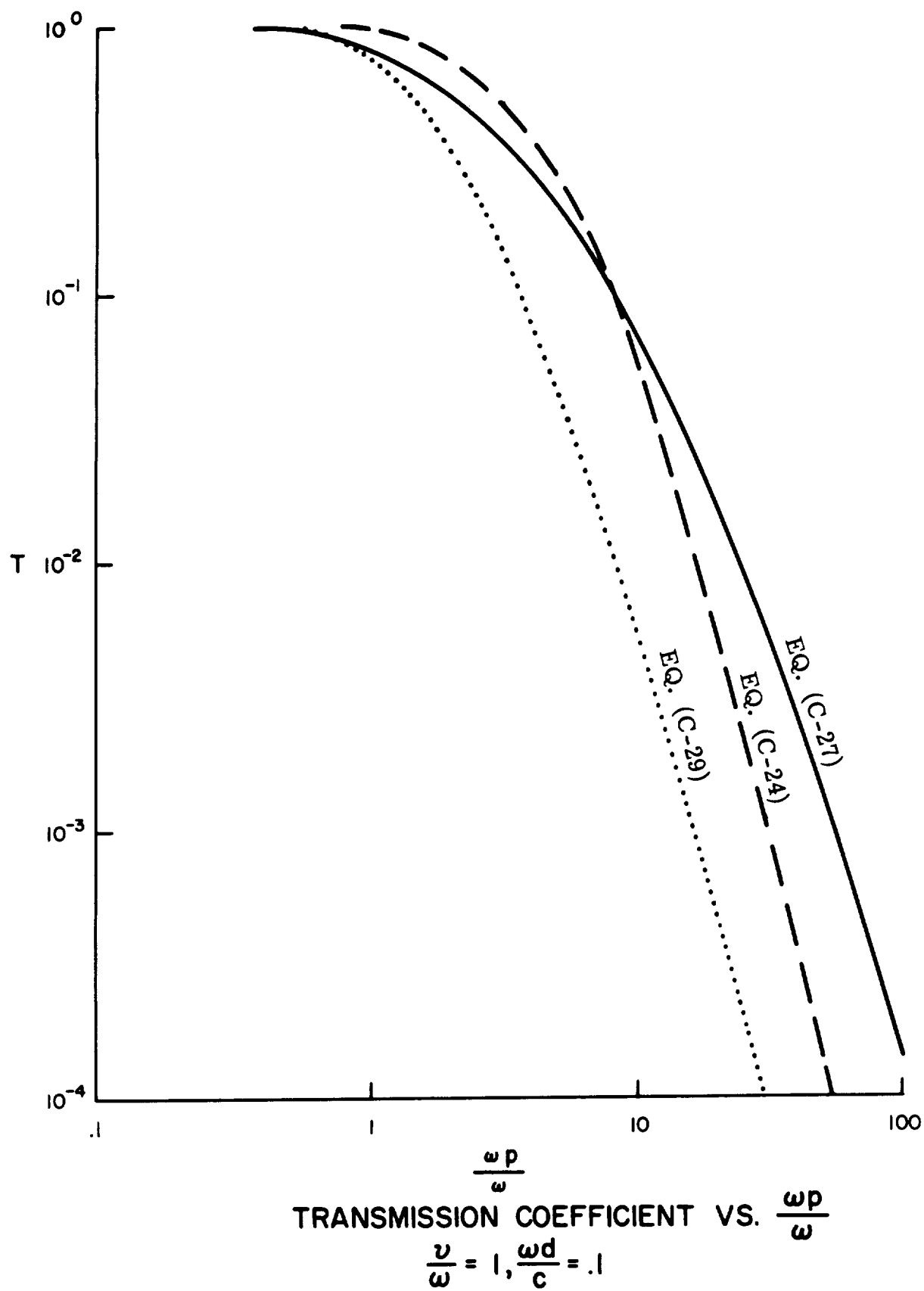
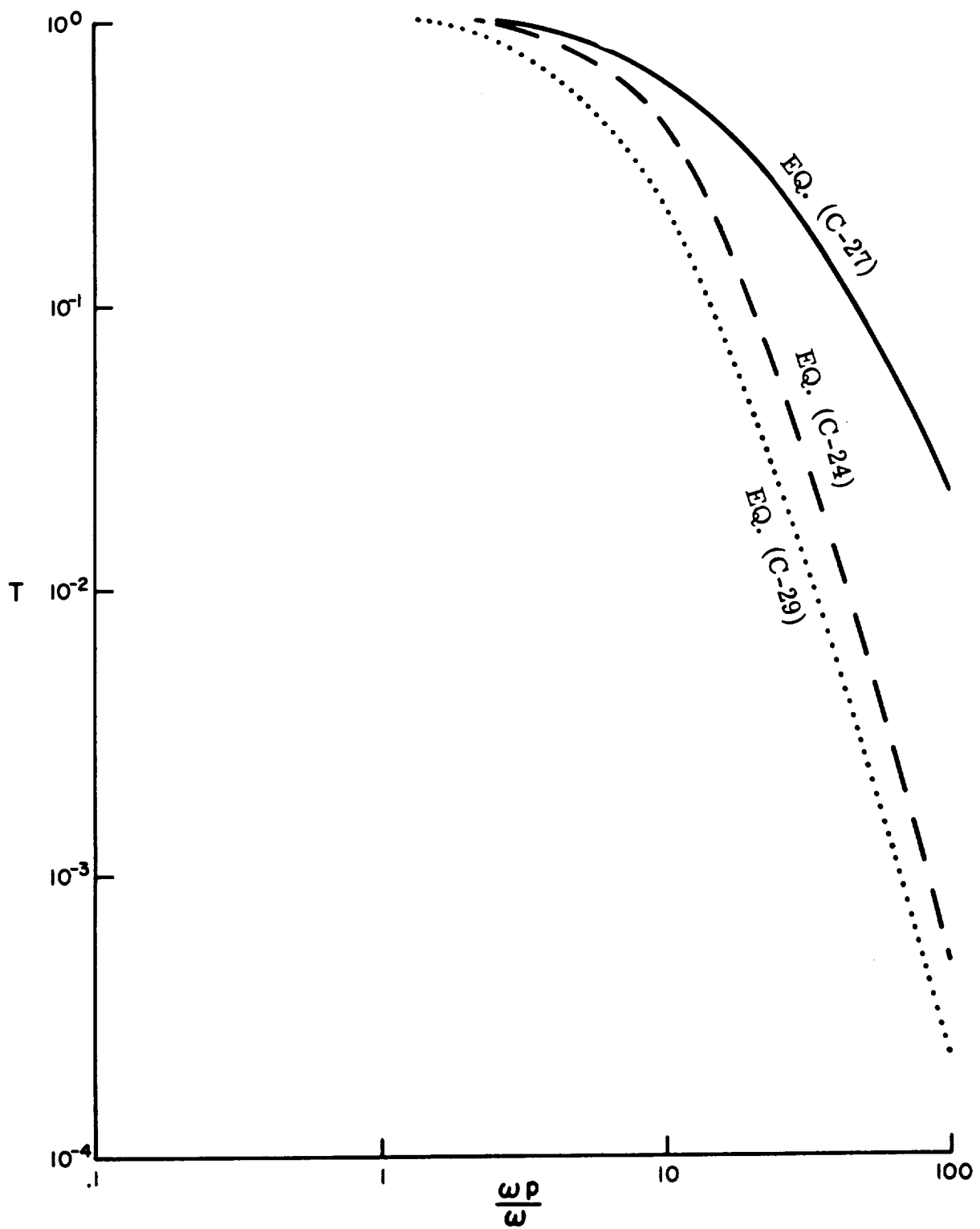
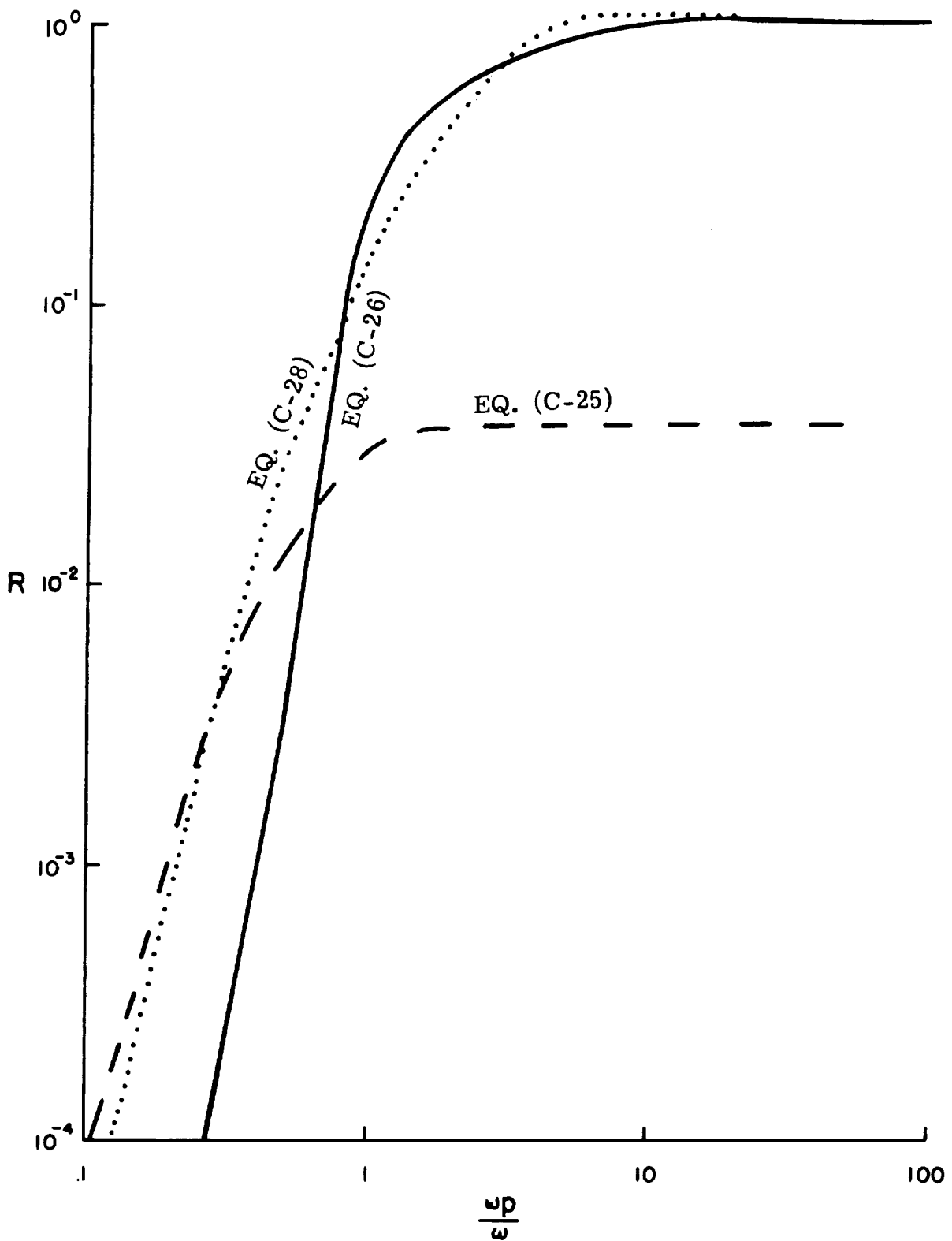


Figure C-6



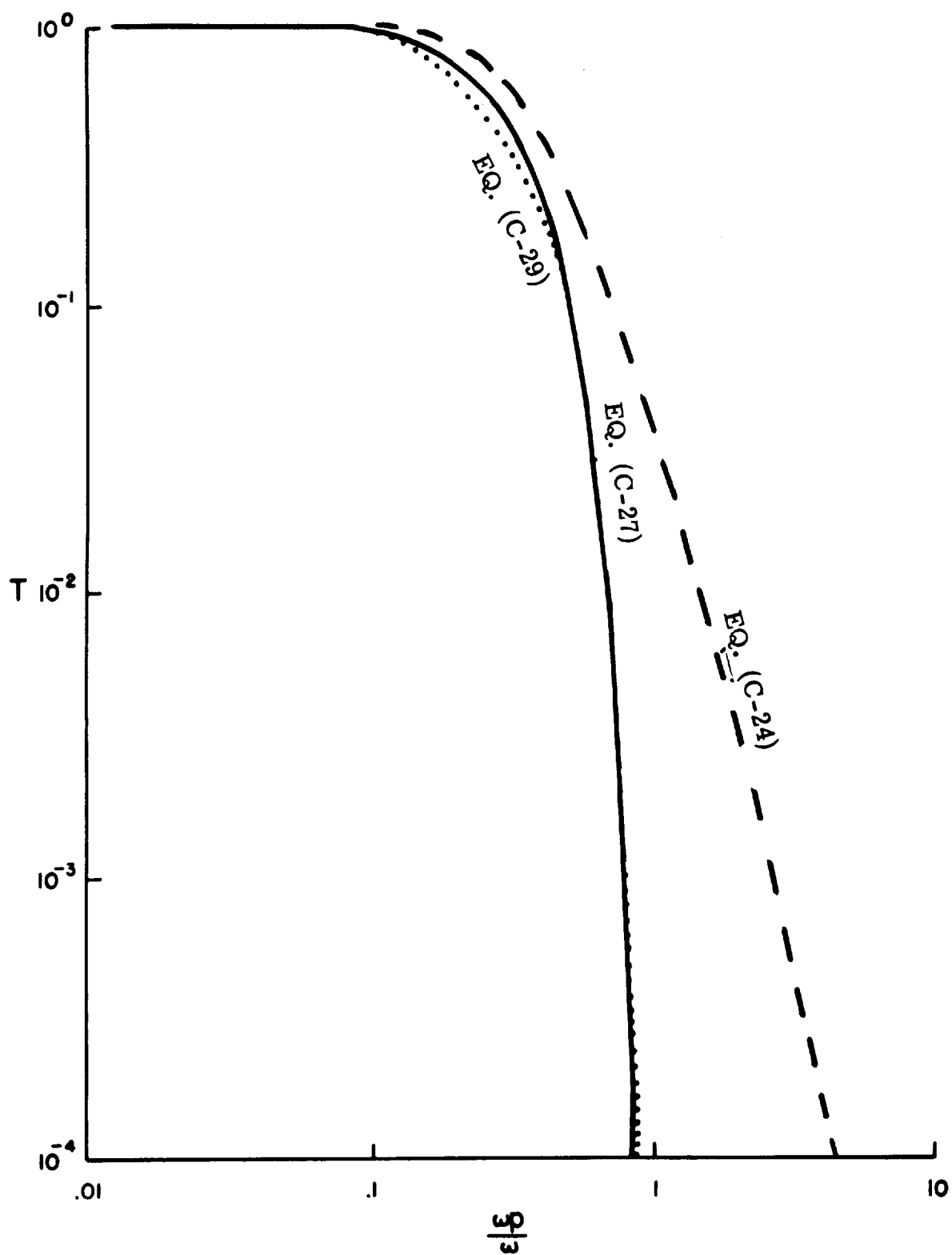
TRANSMISSION COEFFICIENT VS. $\frac{\omega_p}{\omega}$
 $\frac{\nu}{\omega} = 0, \frac{\omega_d}{c} = .1$

Figure C-7



REFLECTION COEFFICIENT VS. $\frac{\omega_p}{\omega}$
 $\frac{v}{\omega} = .1, \frac{\omega d}{c} = 10$

Figure C-8



TRANSMISSION COEFFICIENT VS. $\frac{\omega d}{c}$
 $\frac{v}{\omega} = .1, \frac{\omega d}{c} = 10$

Figure C-9

3.9 ERROR-CORRECTION CODING

3.9.1 Introduction

It is well-known that the signal-to-noise ratio requirements at the receiving terminal of a digital communication link can be favorably reduced by slightly widening the signal bandwidth through the insertion of redundant digits. This permits operation at the same (decoded) error rate while requiring less transmitter power than an equivalent uncoded system would require. The object of this investigation was to determine the reduction possible in transmitter power as well as to estimate the weight and power requirements of the required encoding and decoding equipment.

Examples of single-error correcting, single-error detecting (with probable correction), and double-error correcting codes were considered. The notation used is as follows:

n	= total number of bits in coded word
k	= number of message bits in coded word
p	= bit error probability for received coded word
p_r	= required bit error probability for decoded message
p_w	= word error probability
t	= number of errors corrected by the code

3.9.2 Procedure

The S/N necessary to obtain a given p_r was computed for various codes and for uncoded transmission, and the saving in required S/N for each code was determined. The saving in $ST/(N/B)$ realized by coding was then computed on a word error rate basis.

3.9.2.1 In Terms of Bit Error Probability

For a given p_r , the S/N necessary to transmit the uncoded message in the presence of white Gaussian noise was computed. Then, for the particular code,

the value of p necessary to yield p_r was determined. This p was expressed in terms of required S/N . The difference in required S/N between the uncoded and the coded cases represents a saving; however, there is an increase in bandwidth necessary to enable transmission of the longer coded words at the same data rate. The ratio of the coded transmission bandwidth to the uncoded is n/k , and there is a proportional increase in noise power for the coded case necessitating a compensating increase in signal power to maintain p (and p_r). Subtracting this additional required signal power (expressed as decibels of S/N) from the saving in S/N resulting from the coding yielded the net power saved by use of the code.

3.9.2.2 In Terms of Word Error Probability

The required p_w was expressed in terms of p_r , and p for the particular code. The required S/N was found, and the additional S/N required to compensate for the increased bandwidth was added. This total S/N required for the coded case was expressed in terms of $ST/(N/B)$, and was then subtracted from the required $ST/(N/B)$ for the uncoded case, yielding the saving from use of the code.

3.9.3 Computation of p

Given a code (n, k, t) and a value of p_r , the decoded word error rate may be given as kp_r^* . This may be expressed by

$$1 - \sum_{j=0}^t \binom{n}{j} q^{n-j} p^j = kp_r \quad (3.9-1)$$

where $q = 1 - p$

Ignoring terms of order $t + 2$ and higher in p , equation (3.9-1) reduced to

$$\binom{n}{t+1} p^{t+1} = kp_r \quad (3.9-2)$$

Equation (3.9-2) was solved for p .

*For small p_r and small n , where kp_r was a poor approximation to the decoded word error rate, $1 - q_r^k$ was used, ($q_r = 1 - p_r$). Independence of error probability between bits was assumed.

3.9.4 Computation of Power Saved

A binary symmetric channel perturbed by white Gaussian noise was assumed.
Then,

$$P(1/0) = P(0/1) = 1/2 - \int_0^x f(x) dx$$

$$P(0) = P(1) = 1/2$$

where $P(1/0)$ = probability that "1" is received when "0" is transmitted,

$P(0/1)$ = probability that "0" is received when "1" is transmitted,

$P(0)$ = probability that "0" is transmitted,

$P(1)$ = probability that "1" is transmitted,

$f(x)$ = normal probability density function.

Now,

$$p = P(0) P(1/0) + P(1) P(0/1)$$

Therefore,

$$1 - p = \int_{-\infty}^x f(x) dx, \text{ and} \quad (3.9-3)$$

$$S/N(\text{db}) = 20 \log_{10} x \quad (3.9-4)$$

Having computed p from equation (3.9-2), its value was substituted into equation (3.9-3) to find x . Then $S/N(\text{db})$ corresponding to p was found from equation (3.9-4).

The increase in power necessary to compensate for the increased bandwidth was computed by transforming the ratio n/k into db.

3.9.5 Choice of a Code

3.9.5.1 Hamming Code

A (7, 4, 1) Hamming Code was shown to yield a net power saving of only 0.6 db.

3.9.5.2 Wagner Code

Proceeding to a Wagner code, which detects and with high probability corrects a single error, analysis based on required bit error rate summarized in Tables 3.9.1 and 3.9.2 indicates a net gain of approximately 2.5db for $p_r = 0.001$ and $p_r = 0.0001$. In the tables no account is taken of the (small) probability of not correcting a detected error. Tables 3.9.3, 3.9.4, and 3.9.5 show the reduction in required $ST/(N/B)$ from using the Wagner Code rather than uncoded transmission, as a function of p_w , for $n = 8, 7$ and 6 respectively. Figure 3.9.1 shows the required $ST/(N/B)$ vs. p_w for $n = 8, 7$ and 6 . Figures 3.9.2, 3.9.3 and 3.9.4 compare $ST/(N/B)$ for the Wagner coded and uncoded cases, for $n = 8, 7$ and 6 respectively.

3.9.5.3 Bose-Chaudhuri Code

A single example of a Bose-Chaudhuri double-error correcting code (21, 12, 2) was analyzed, for $p_r = 0.0001$. A saving of 2.5 db is attainable from this code. Since this analysis predicted no improvement over the Wagner code, and the Bose-Chaudhuri is even more difficult to implement, no further consideration was given to double error-correcting codes for this application.

Table 3.9.1 Gain in S/N Using Single Parity Bit, $p_r = 0.001$

n	k	p	S/N (db)	S/N Gain due to coding (db)	n/k	S/N Loss due to increased bandwidth (db)	Net Gain in S/N (db)
2	1	.032	5.4	4.4	2.00	3.0	1.4
3	2	.026	5.8	4.0	1.50	1.8	2.2
4	3	.022	6.1	3.7	1.333	1.2	2.5
5	4	.020	6.3	3.5	1.25	1.0	2.5
6	5	.018	6.4	3.4	1.20	.8	2.6
7	6	.017	6.5	3.3	1.667	.7	2.6
8	7	.016	6.6	3.2	1.143	.6	2.6
9	8	.015	6.7	3.1	1.125	.5	2.6
10	9	.014	6.8	3.0	1.111	.5	2.5
11	10	.0135	6.9	2.9	1.10	.4	2.5

Uncoded message S/N = 9.8

Table 3.9.2 Gain in S/N Using Single Parity Bit, $P_r = 0.0001$

n	k	P	S/N (db)	S/N Gain due to coding (db)	n/k	S/N Loss due to increased bandwidth (db)	Net Gain in S/N (db)
2	1	.01	7.3	4.2	2.00	3.0	1.2
3	2	.0081	7.6	3.9	1.50	1.8	2.1
4	3	.0071	7.8	3.7	1.333	1.2	2.5
5	4	.0063	7.9	3.6	1.25	1.0	2.6
6	5	.0058	8.0	3.5	1.20	.8	2.7
7	6	.0056	8.1	3.4	1.667	.7	2.7
8	7	.0050	8.2	3.3	1.143	.6	2.7
9	8	.0047	8.3	3.2	1.125	.5	2.7
10	9	.0045	8.3	3.2	1.111	.5	2.7
11	10	.0043	8.4	3.1	1.10	.4	2.7

Uncoded message S/N = 11.5 db

Table 3.9.3 Gain in Required ST/(N/B) Using Wagner Code,
for $n = 8$, $k = 7$ (based on word error rate)

P_w	P	S/N (db)	Additional S/N due to Increased BW (db)	ST/(N/B) Required for Wagner Code (db)	ST/(N/B) Required for Uncoded transmission (db)	Savings in ST/(N/B) using Wagner Code (db)
10^{-1}	.0611	3.8	.6	1.4	3.7	2.3
10^{-2}	.0189	6.4	.6	4.0	6.5	2.5
10^{-3}	.0060	8.0	.6	5.6	8.2	2.6
10^{-4}	.0019	9.2	.6	6.8	9.7	2.9
10^{-5}	.0006	10.2	.6	7.8	10.7	2.9
10^{-6}	.0002	11.0	.6	8.6	11.6	3.0

Table 3.9.4 Gain in Required ST/(N/B) Using Wagner Code,
for $n = 7$, $k = 6$ (based on word error rate)

P_w	P	S/N (db)	Additional S/N due to Increased BW (db)	ST/(N/B) Required for Wagner Code (db)	ST/(N/B) Required for Uncoded Transmission (db)	Savings in ST/(N/B) Using Wagner Code (db)
10^{-1}	.0660	3.6	.7	1.3	3.5	2.2
10^{-2}	.0218	6.1	.7	3.8	6.3	2.5
10^{-3}	.0069	7.8	.7	5.5	8.1	2.6
10^{-4}	.0022	9.1	.7	6.8	9.6	2.8
10^{-5}	.0007	10.1	.7	7.8	10.6	2.8
10^{-6}	.0002	10.9	.7	8.6	11.4	2.8

Table 3.9.5 Gain in Required ST/(N/B) Using Wagner Code,
for n = 6, k = 5 (based on word error rate)

p_w	P	S/N (db)	Additional S/N due to Increased BW (db)	ST/(N B) Required for Wagner Code (db)	ST/(N/B) Required for Uncoded Transmission (db)	Savings in ST/(N/B) Using Wagner Code (db)
10^{-1}	.0722	3.3	.8	1.1	3.2	2.1
10^{-2}	.0258	5.8	.8	3.6	6.2	2.6
10^{-3}	.0082	7.6	.8	5.4	8.0	2.6
10^{-4}	.0026	8.9	.8	6.7	9.5	2.8
10^{-5}	.0008	9.9	.8	7.7	10.6	2.9
10^{-6}	.0003	10.8	.8	8.6	11.4	2.8

3.9.6 Implementation of the Wagner Code

A preliminary study was made to estimate the additional power and weight required to add a single-bit parity error correction to a seven-bit code. Results are given separately for the primary (capsule) transmitter at which the parity bit is added and for a receiver feeding a recorder or secondary transmitter at which the received code must be checked and corrected if required. The results have been calculated on the basis of the equivalent number of flip-flops required, where each flip-flop is rated as 0.1 watts and 0.1 pounds.

3.9.6.1 Encoding

Figure 3.9.5 shows a system for adding the parity bit at the primary transmitter. The power and weight requirements of such an encoder are as follows:

Strobe - Delay	1
Complementing Flip-Flop	1
Reset Delay	1.5
Delay Multivibrator	1
Output Gate	0.5
	<hr/>
TOTAL	5.0 = 0.5 watts and 0.5 pounds

3.9.6.2 Decoding and Error Correction

Figure 3.9.6 shows a decoding system for error detection and correction. The added power and weight requirements are as follows:

Parity Check	2
Sync Generator	8
Signal Memory Drive	1
Error Decision	58
Shift Register	12
Memory Register (2)	16
	<hr/>
TOTAL	97 = 9.7 watts and 9.7 pounds

3.9.6.3 Error Decision Sub-system

Upon receipt of a coded word with noise, it is proposed that the dumping integrator be used to reconstruct the noise-free word. If this word fails the parity check, then that bit is changed which had the smallest integrated value during reconstruction. The error-decision circuitry decides which bit this is and routes a signal to change the bit in the decoded word. If no bit can be found of significantly greater error probability than the others, the error decision signal changes the parity bit of the decoded word, on the theory that this choice is as good as any under these circumstances (and is easily arranged).

Figure 3.9.7 gives a logical organization of an error decision sub-system. The analog distributor routes each integrated bit to a set of flip-flops of varying thresholds which are or are not energized according to the amplitude of the analog bit measure. The outputs are sent through a gate array to assign them digital values. The bit value distributor searches all least value digits first, proceeding in order through higher value digits. The first true value digit reached by the distributor is gated out through the bit router mixers to change the proper code-word bit, and to generate a stop signal for the distributor to prevent the changing of higher valued bits. If all bits are high valued, the counter will continue to the final position and generate a change parity signal. (This may be omitted if it is considered more desirable to record or re-transmit the coded word with the non-checking parity to indicate an uncorrectable word.)

The equipment estimate of 58 equivalent flip-flops for the error-decision function is based on known reliable circuits. The acceptance of microelectronic techniques would reduce this considerably.

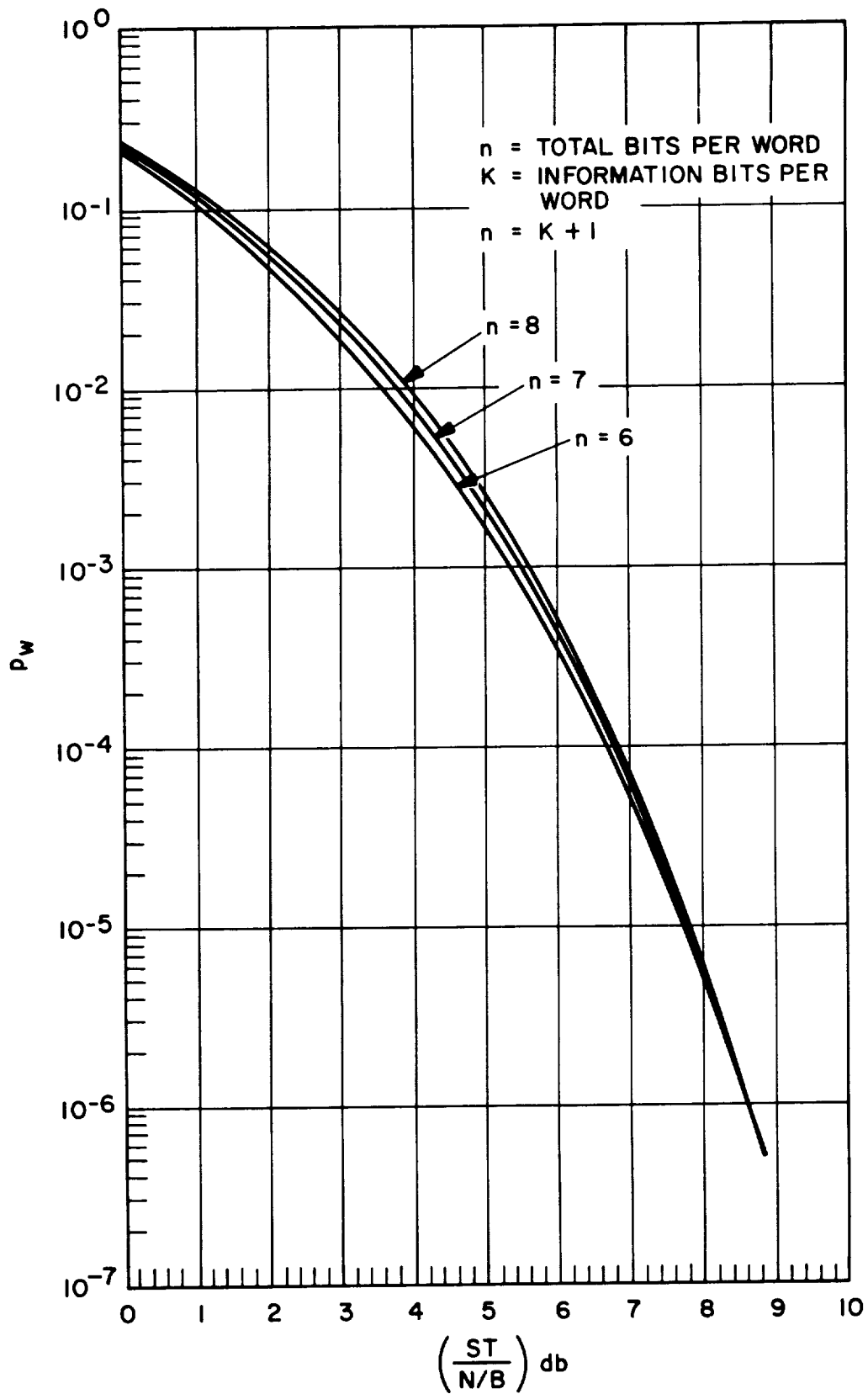


Figure 3.9.1. Word Error Probability - Wagner Codes

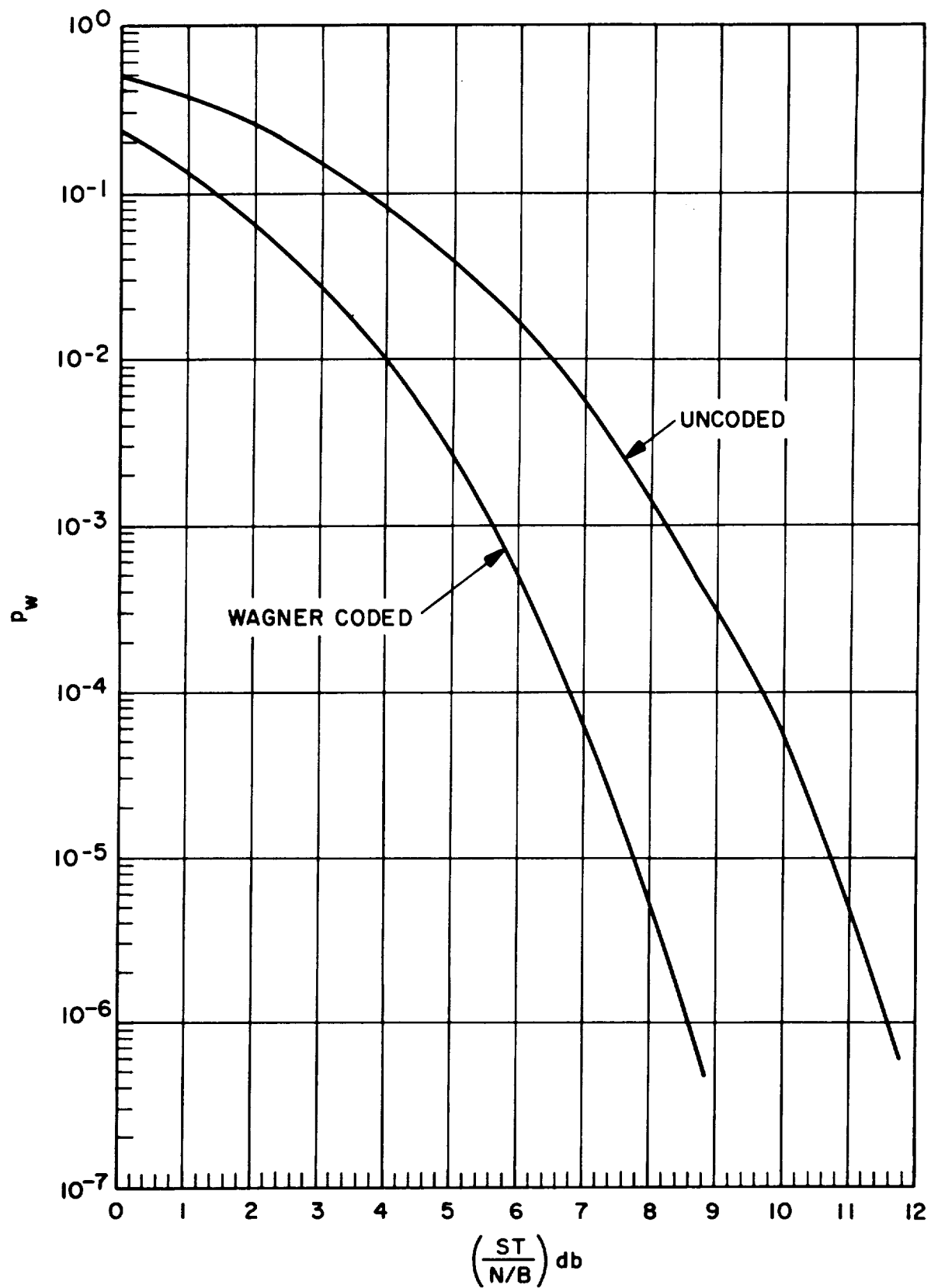


Figure 3.9.2. Coded and Uncoded Word Error Probabilities ($N = 8$)

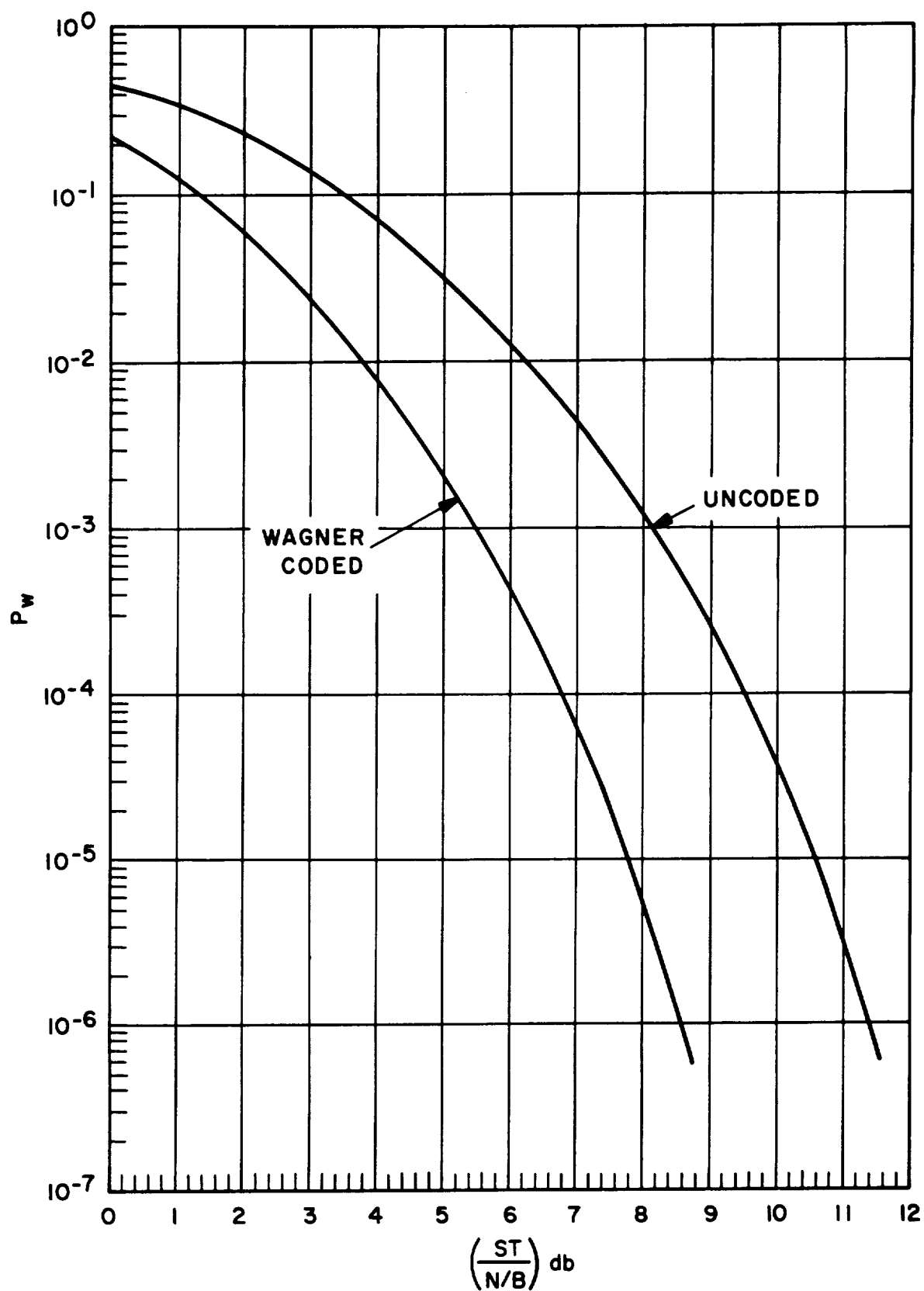


Figure 3.9.3. Coded and Uncoded Word Error Probabilities ($N = 7$)

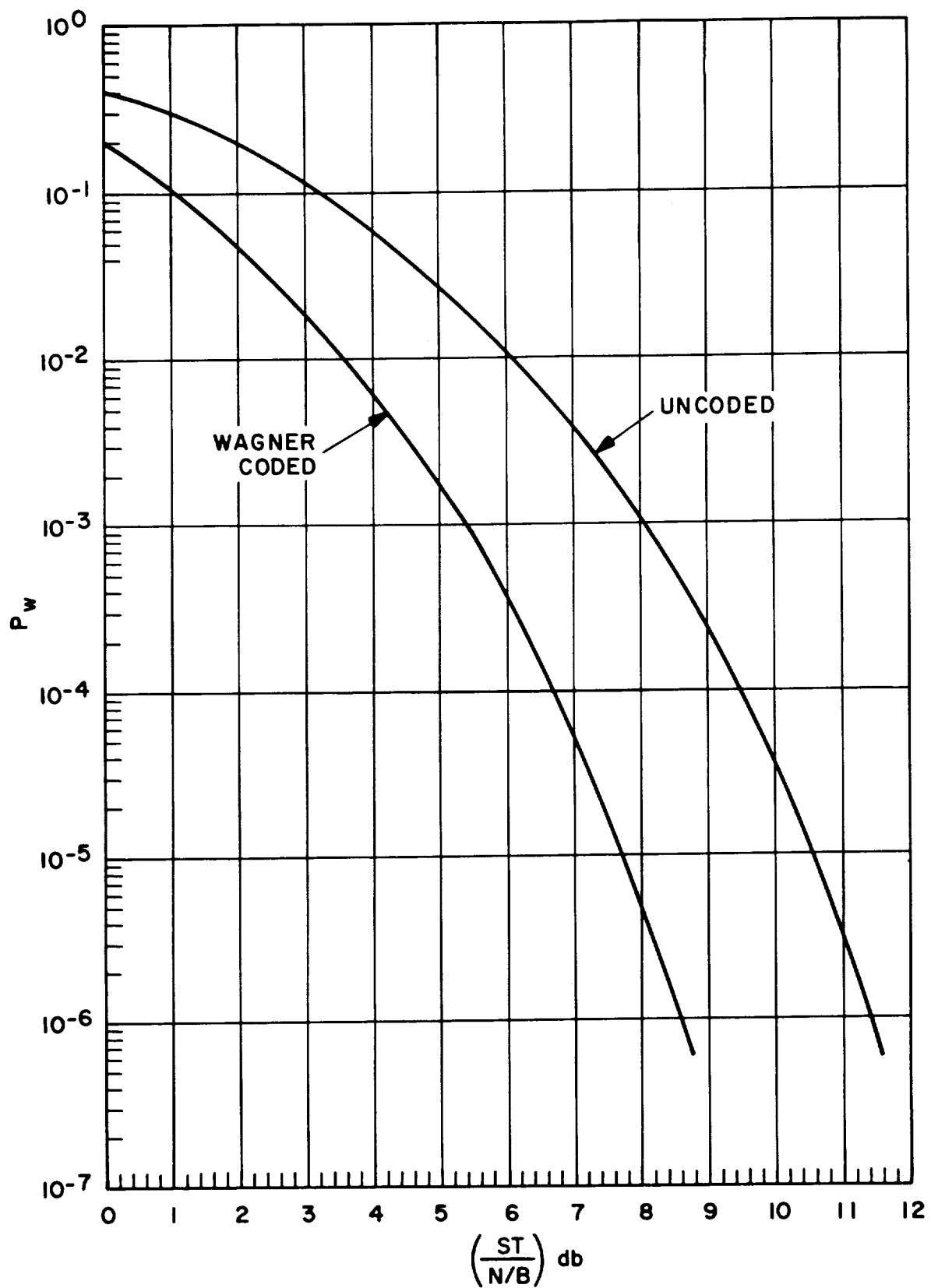


Figure 3.9.4. Coded and Uncoded Word Error Probabilities ($N = 6$)

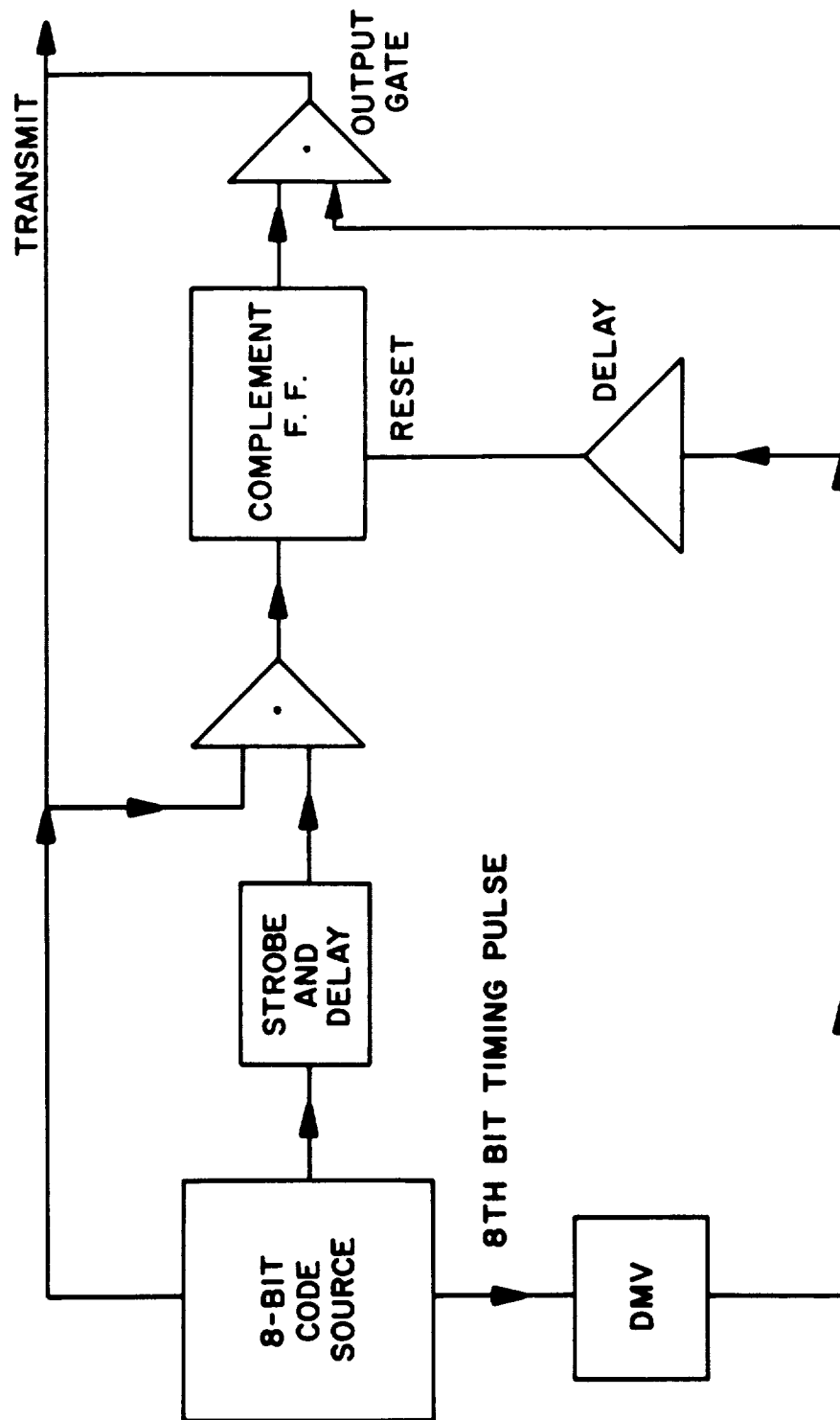


Figure 3.9.5. Addition of Parity Bit

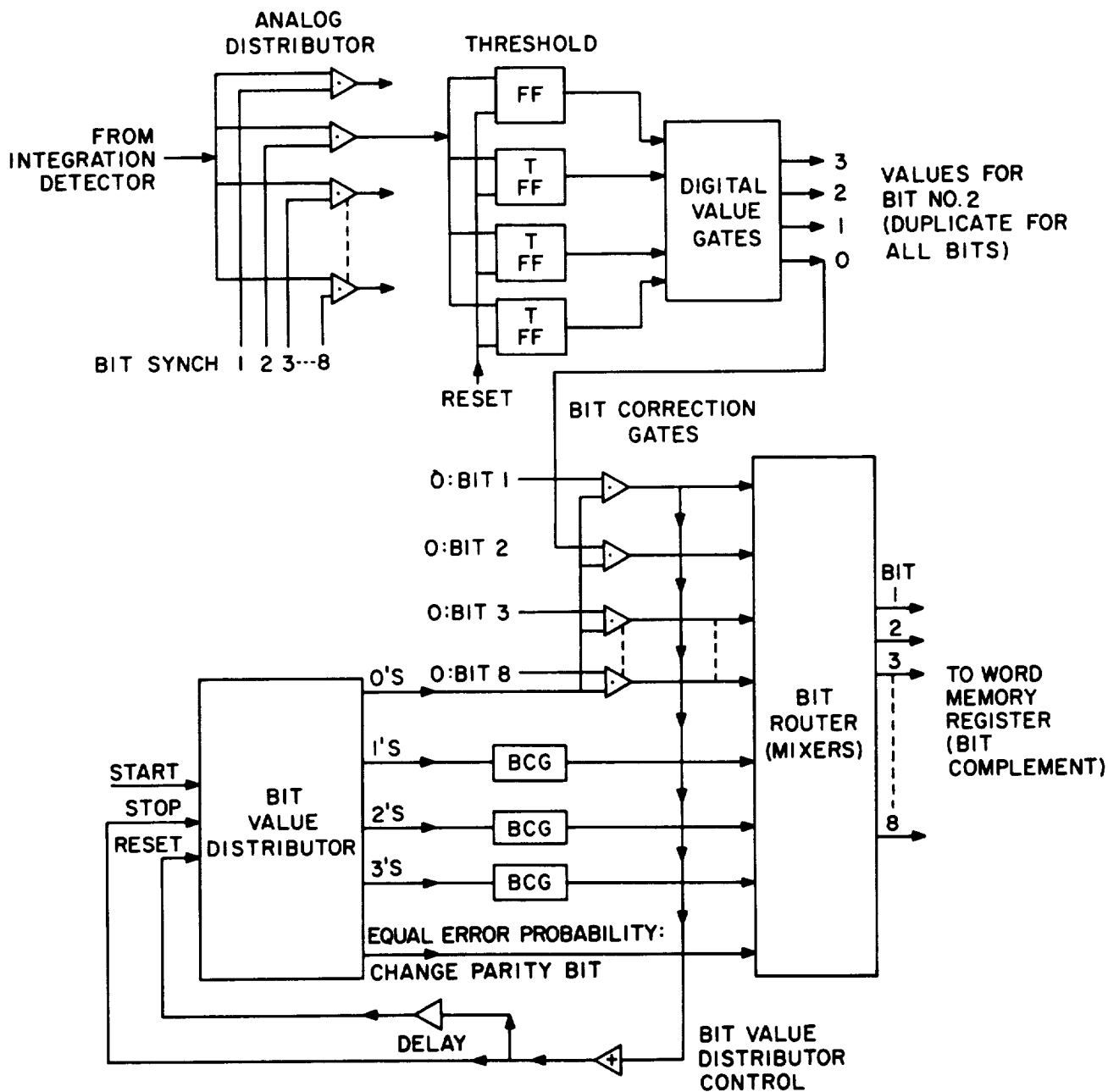


Figure 3.9.7. Error Decision Subsystem

3.10 CAPSULE TRANSMITTING EQUIPMENT

3.10.1 Introduction

Size, weight and power estimates for conservatively designed equipment to operate in a 1965 Venus entry capsule are summarized in Tables 3.10.1 and 3.10.2.

Appropriate block diagrams are given in the figures in this section.

A discussion of the stress environment the electronic components will encounter is included.

3.10.2 Comparison of Vehicle Stress Environment and Present Military Specifications for Electronic Components

As the capsule enters the Venusian atmosphere, extreme forces will be applied to the electronic components inside. Since the vehicle angle of attack oscillates in a damped sinusoidal manner about 0^0 , the direction of the force with respect to the orientation of an electronic component changes with time. The forces applied to a vehicle with three degrees of freedom can be broken down into four components which add vectorially.

These are:

- (1) Axial force due to vehicle deceleration parallel to the vehicle roll axis.
- (2) Normal force due to vehicle deceleration normal to the vehicle roll axis.
- (3) Radial force due to pitch angular velocity of vehicle acting radially from the vehicle pitch axis.
- (4) Tangential force due to pitch angular acceleration of vehicle acting normal to the radial force and in a plane perpendicular to the pitch axis.

The vector sum of the first two is the total deceleration of the vehicle. The magnitude of the last two depends on the magnitude and frequency of vehicle

TABLE 3.10.1. CAPSULE CW TRANSMITTING EQUIPMENT

Frequency and Output Power	Component	Weight* (lbs.)	Input Power (watts)	Size (in.)	Antenna Weight
100 mc 25 w (Solid-State)	Transmitter	2.5	66	4 X 6 X 2	
	Power Amp.	---	---	---	
100 mc 25 w (Ceramic Tube)	Sec. Power Supply	3.0	9	4 X 6 X 2	
	Transmitter	2.5	25	4 X 6 X 2	13.2 lbs at 100 mc
	Power Amp.	3.5	56	3 X 3 X 3.5	
100 mc 50 w	Sec. Power Supply	4.0	9	3 X 3 X 3.5	
	Transmitter	2.5	42	4 X 6 X 2	
	Power Amp.	3.5	110	3 X 6 X 4	
200 mc 25 w	Sec. Power Supply	4.0	25	4 X 4 X 6	
	Transmitter	2.5	32	4 X 6 X 2	
	Power Amp.	3.5	56	3 X 3 X 3.5	8.7 lbs at 200 mc
200 mc 50 w	Sec. Power Supply	4.0	15	4 X 4 X 4	
	Transmitter	2.5	42	4 X 6 X 2	
	Power Amp.	5.0	110	4 X 6 X 4	
500 mc 25 w	Sec. Power Supply	4.0	25	4 X 4 X 4	
	Transmitter	3.0	45	4 X 6 X 2.5	
	Power Amp.	5.0	60	3 X 3 X 3.5	
500 mc 50 w	Sec. Power Supply	4.0	15	4 X 4 X 4	
	Transmitter	4.0	55	4 X 6 X 2.5	1.3 lbs at 500 mc
	Power Amp.	5.0	120	3 X 3 X 3.5	
2295 mc 20 w	Sec. Power Supply	4.5	30	4 X 4 X 4	
	Amplifon	1.0	50% efficiency + 5w. filament	1.3 X 3 diam.	1.5 lbs at 2295 mc
	Driver	1.0		4 X 6 X 4	
2295 mc 50 w	Sec. Power Supply	4.0			
	Amplifon	1.5			
	Driver	2.0			
*Additional weights which are independent of frequency: are assumed to be:	Sec. Power Supply	4.0			
	Multiplexing Equip.	2.0			
	Clock	6.0			
	Misc. Signal Proc.	5.0			
	Equipment				

TABLE 3.10.2. CAPSULE PULSE* TRANSMITTING EQUIPMENT

<u>Frequency & Peak Envelope Power</u>	<u>Component</u>	<u>Weight (lbs)</u>	<u>Average Input Power</u>	<u>Size (in.)</u>	<u>Antenna Weight</u>
100 mc 100 w.(peak)	Transmitter	2.5	3	2.5 X 4 X 3	
	Power Amp.	4.0	26	3 X 4 X 3.5	
	Sec. Power Supply	4.5	7	4 X 4 X 4	
100 mc 1000 w.(peak)	Transmitter	3.0	5.5	2.5 X 4 X 3	13.2 lbs at 100 mc
	Power Amp.	5.5	150	4 X 5 X 4	
	Sec. Power Supply	6.5	40	5 X 6 X 5	
200 mc 100 w.(peak)	Transmitter	2.5	4	2.5 X 4 X 3	
	Power Amp.	4.0	26	3 X 4 X 3.5	
	Sec. Power Supply	4.5	7	4 X 4 X 4	
200 mc 1000 w.(peak)	Transmitter	3.0	6	3.5 X 4 X 3	8.7 lbs at 200 mc
	Power Amp.	5.5	155	4 X 5 X 4	
	Sec. Power Supply	6.5	45	5 X 6 X 5	
500 mc 100 w.(peak)	Transmitter	3.0	5	2.5 X 4 X 3	
	Power Amp.	4.0	30	3 X 4 X 3.5	
	Sec. Power Supply	4.5	8	4 X 4 X 4	
500 mc 1000 w.(peak)	Transmitter	4.0	8	4 X 6 X 2.5	1.3 lbs at 500 mc
	Power Amp.	5.5	165	4 X 5 X 4	
	Sec. Power Supply	6.5	50	5 X 6 X 5	

*Assumed 20 ms. pulses with 200 ms. between pulses.

oscillation and the distance of the electrical component from the vehicle pitch axis. The first two forces can certainly not be considered negligible. Neither can the last two if the electronic component is farther than a few inches from the pitch axis. However, in order to indicate the possible magnitude of the problem, only the normal force due to vehicle deceleration will be considered in the following discussion. The numbers to be determined can therefore be considered optimistic.

The maximum anticipated normal load for a Discoverer type vehicle ($W/C_D A = 60$, Weight = 250 lbs., base diameter = 33 in.) is shown in Section 1 to be ± 465 earth g's. This was determined in a three-degree-of-freedom analysis for a vehicle which enters toward the center of the planet (90° entry) at 12 km/sec. The Extreme I atmosphere was used, and the vehicle was oriented backward ($\alpha_o = 179^\circ$) prior to entry. During entry the vehicle stabilized in the forward direction but oscillated about its pitch axis. When maximum g loading occurred, the frequency of the oscillation was 11.5 cps. Since the maximum load was ± 465 g's and changed direction twice per cycle, this is a change of 930 g's in $1/2 \times 11.5$ seconds. This is a change of approximately 11 g's/0.5 ms or 236 g's/11 ms.

To see how this would affect typical electronic components, applicable military specifications, to which components are presently manufactured, are tabulated below:

TABLE 3.10.3

<u>Device</u>	<u>Mil Spec.</u>	<u>Shock</u>	<u>Accel.</u>	<u>Vib.</u>
Transistors	19500 B	1500 g./0.5 ms	20,000 g.	20 g @
and				40-100 cps
Diodes				
Quartz	C-3098 C	30 g./11 ms.	100 g.	10 g. @
Crystals				10-2000 cps

From these figures it appears that only transistors and diodes have been tested to withstand the predicted stress and only on the basis of shock and constant acceleration. It is questionable whether shock or vibration is a more applicable standard, considering the damped, oscillatory form of the applied stress.

In a fairly extensive literature search and industry and vendor survey, the consensus of opinion was that no testing with such high amplitude stresses has been conducted, or if so, no results have been published.

This indicates that additional testing will be necessary in order to determine the possibility of using presently available components. One possible method of simulating both the axial and normal oscillatory loading environment is by means of a centrifuge and an oscillating component mount. The centrifuge would simulate the total vehicle deceleration along its flight path, while the oscillating mount would simulate the vehicle pitch oscillation about the flight path. Although the total g-loading due to the centrifuge would be relatively constant, rather than transient as would be experienced by a vehicle during entry, this should not invalidate the results since the nature of the total g-loading is not presently considered as important as the effect of the oscillation in the presence of the load. The oscillation itself should be limited to that period of time expected under entry conditions.

3.10.3 Effect of Mechanical Stress on Crystal Oscillator Stability

The ability of a frequency generation circuit to survive atmospheric entry stresses and continue to operate at its original frequency and within its specified phase-jitter tolerance depends mainly on the frequency-determining element. This is generally a quartz crystal machined to exact tolerances in three planes and suspended within its holder by electrical lead wires soldered to it. In some cases, support and electrical contact are made by means of pressure plates.

Since the resonant frequency is determined by the three dimensions of the crystal, deformation in any plane is bound to cause a frequency shift. However, since the elastic limit and ultimate strength of quartz are so close, if the crystal

does not break, it might return to its original frequency within its specified tolerances. Data to confirm this are not available, and, even though the crystal might meet the tolerances allowable in the relay link, it might not meet the more stringent requirements of the direct link (See Section 3.4).

It has been indicated by crystal manufacturers that present mounting jigs (leads, pressure plates) are more likely to fail under high stress than the crystal elements. The U. S. Army Signal Corps at Ft. Monmouth, N.J., has indicated that there is a good possibility that a crystal and mounting can be produced which will meet the environmental and electrical specifications; however, this would require a suitable development program.

XMTR		XTAL	
MC		MC	
100		100	
200		100	
500		125	

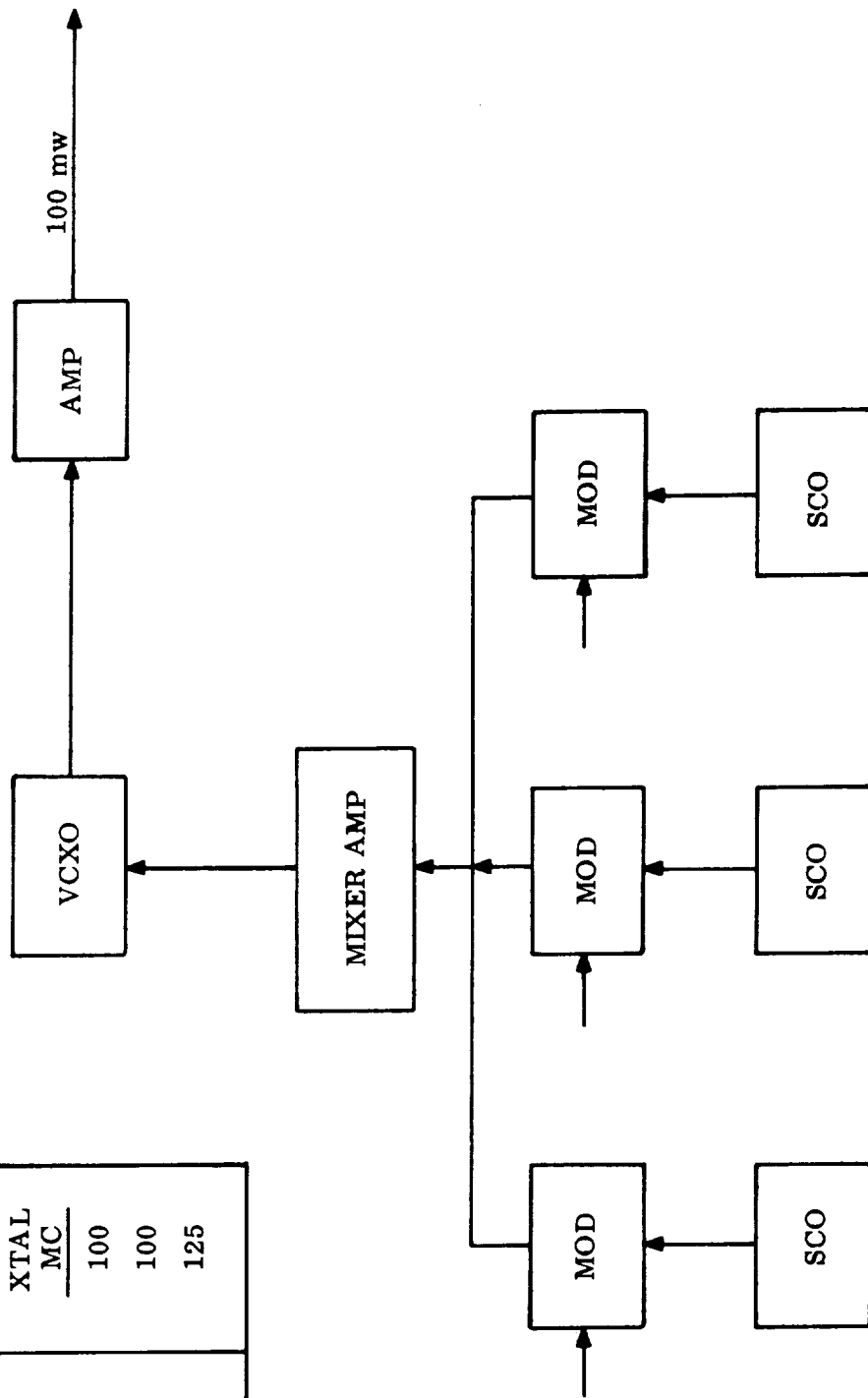


Figure 3.10.1. Am/FM Transmitter

XMTR MC	XTAL MC
100	100
200	100
500	500

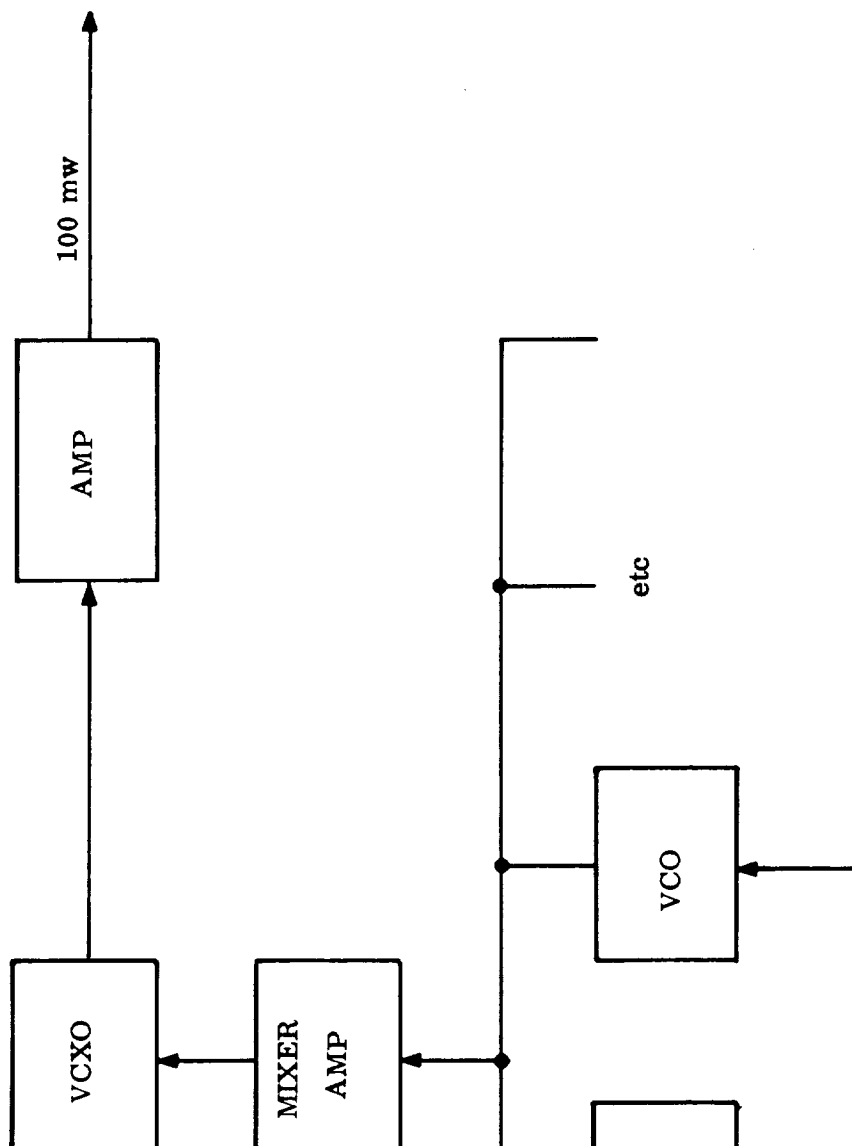


Figure 3.10.2. FM/FM Transmitter

XMTR MC	XTAL MC
100	100
200	66
500	56

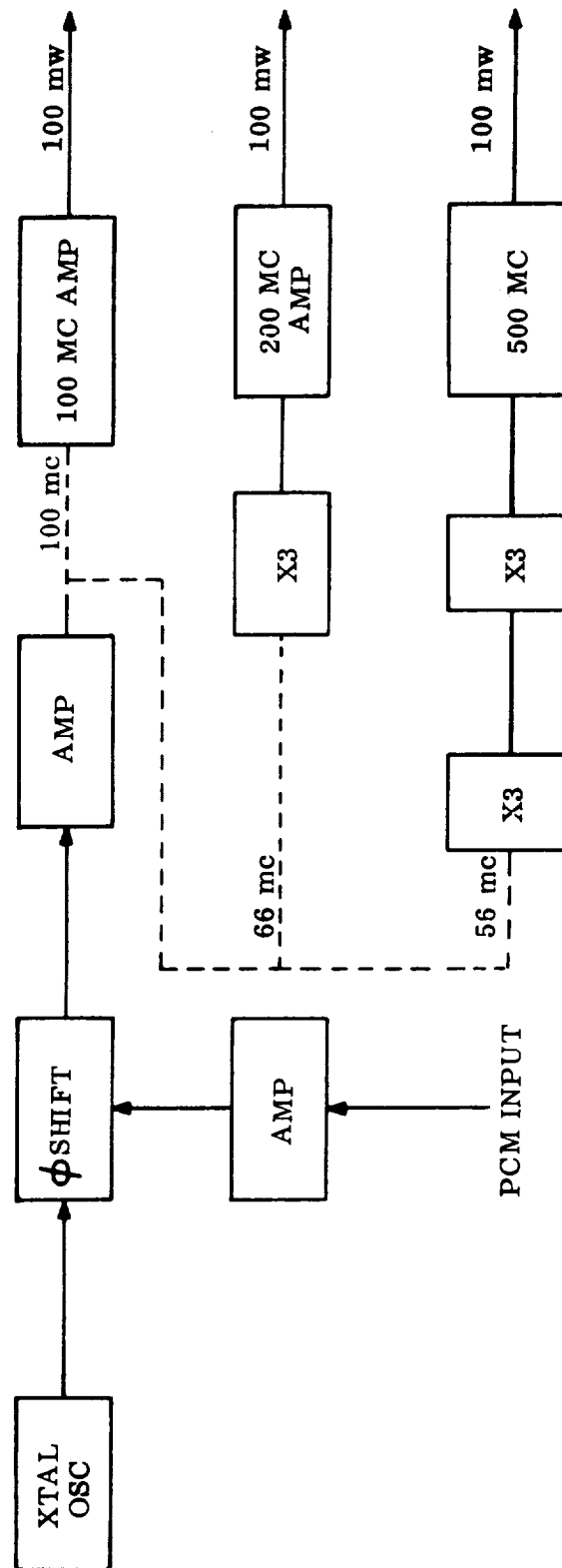


Figure 3.10.3. PCM/PS Transmitter

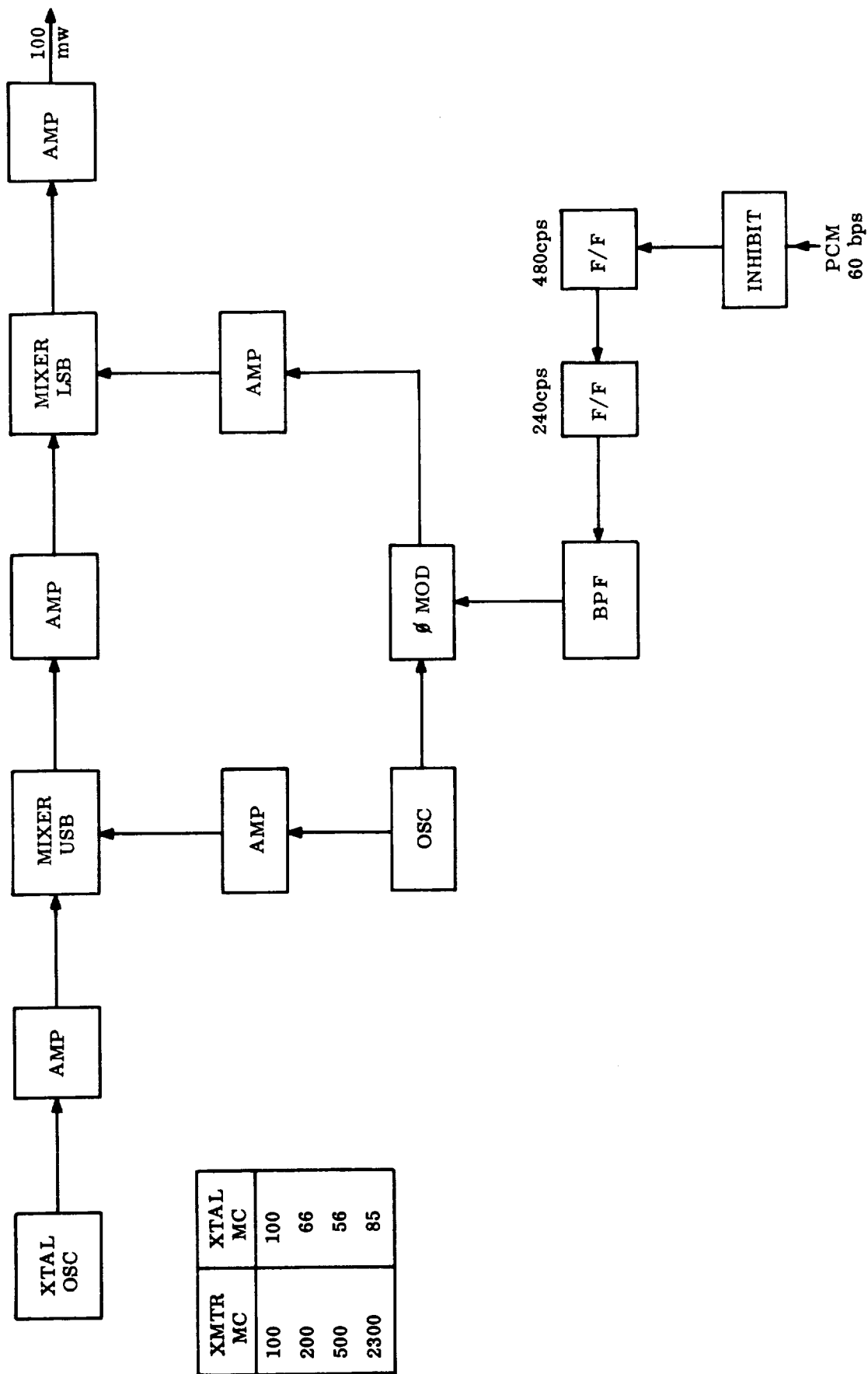


Figure 3.10.4. PCM/PS/PM Transmitter

XMTR MC	XTAL MC
100	100
200	100
500	125

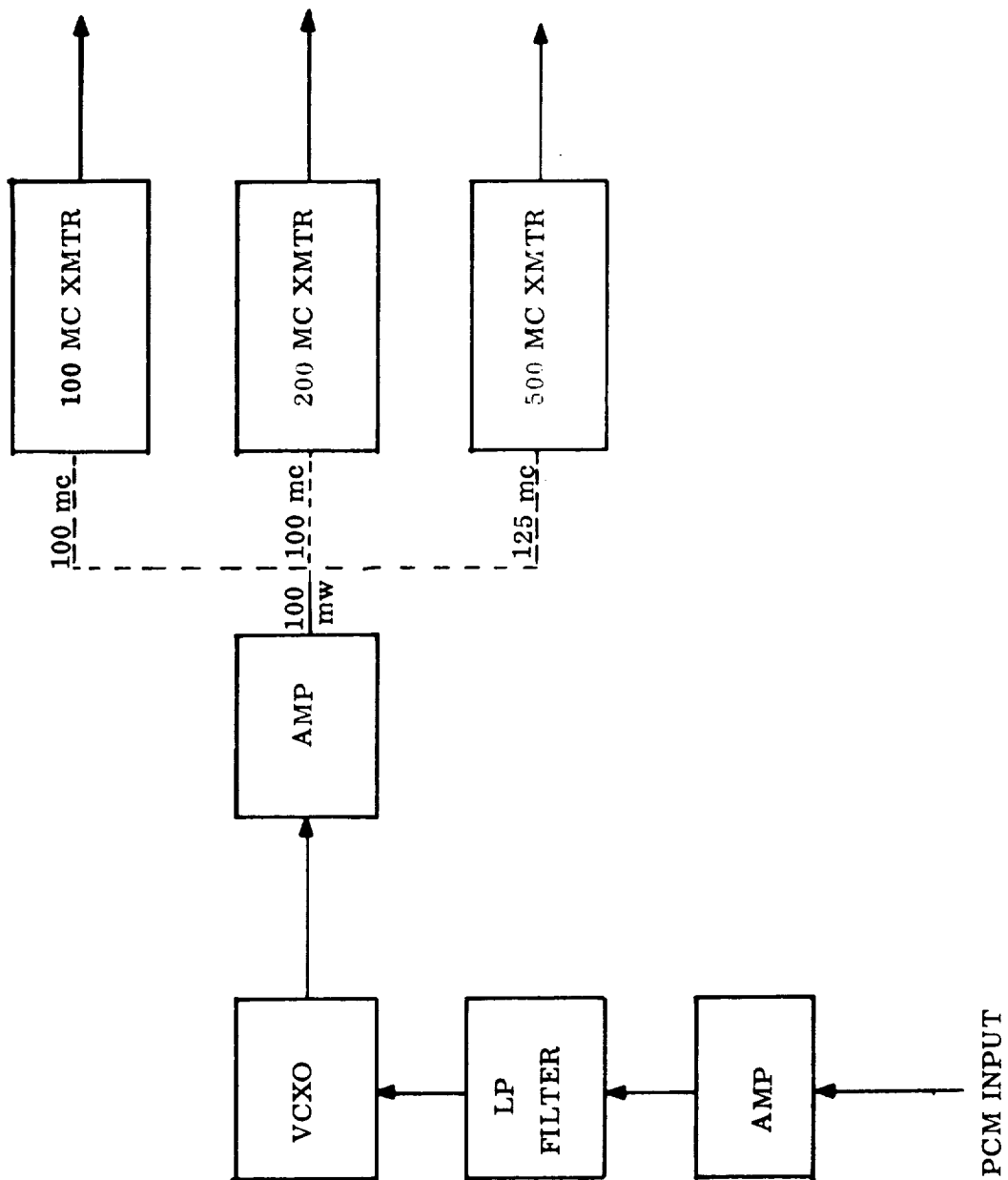


Figure 3.10.5. PCM/FM Transmitter

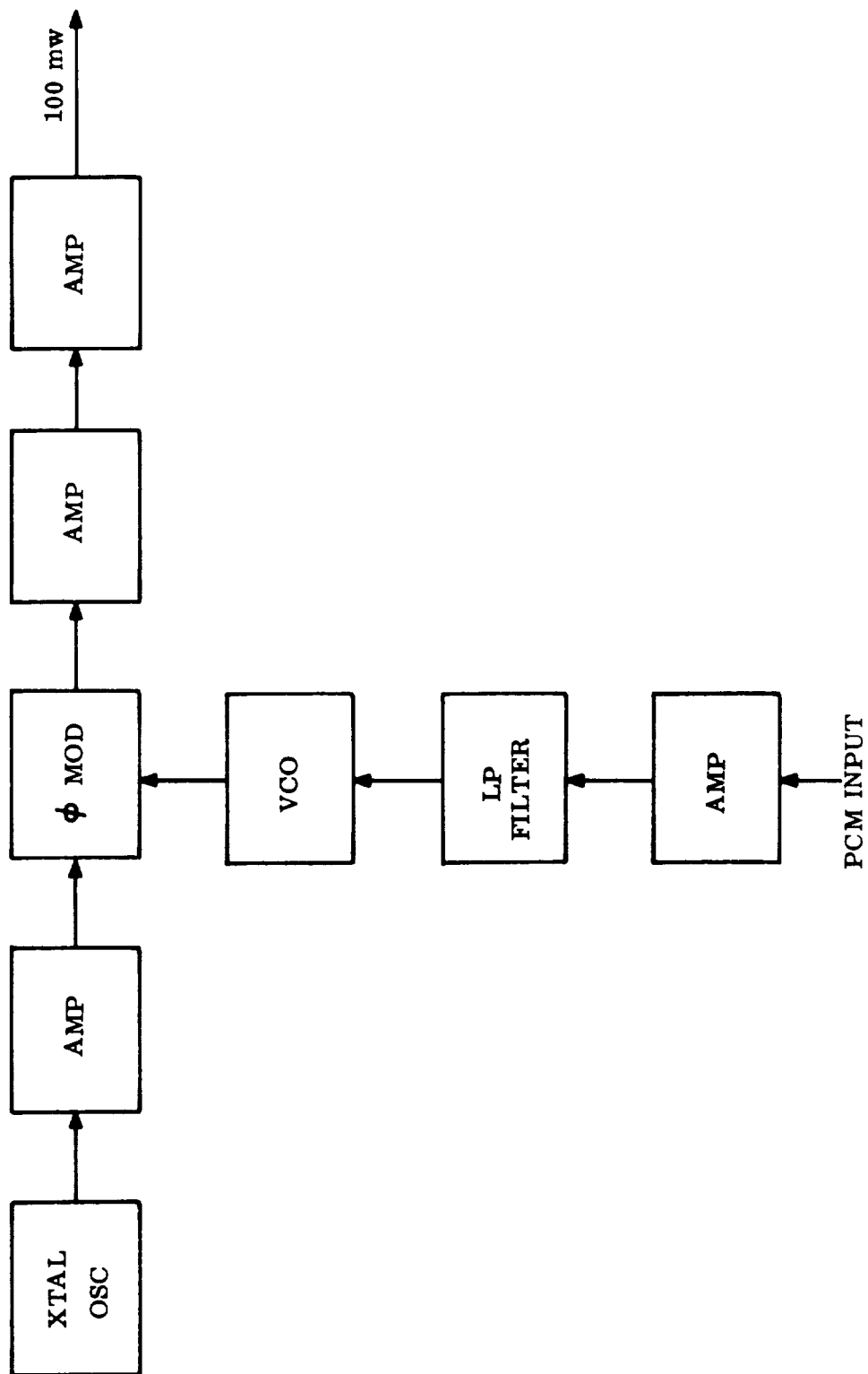


Figure 3.10.6. PCM/FM/PM Transmitter

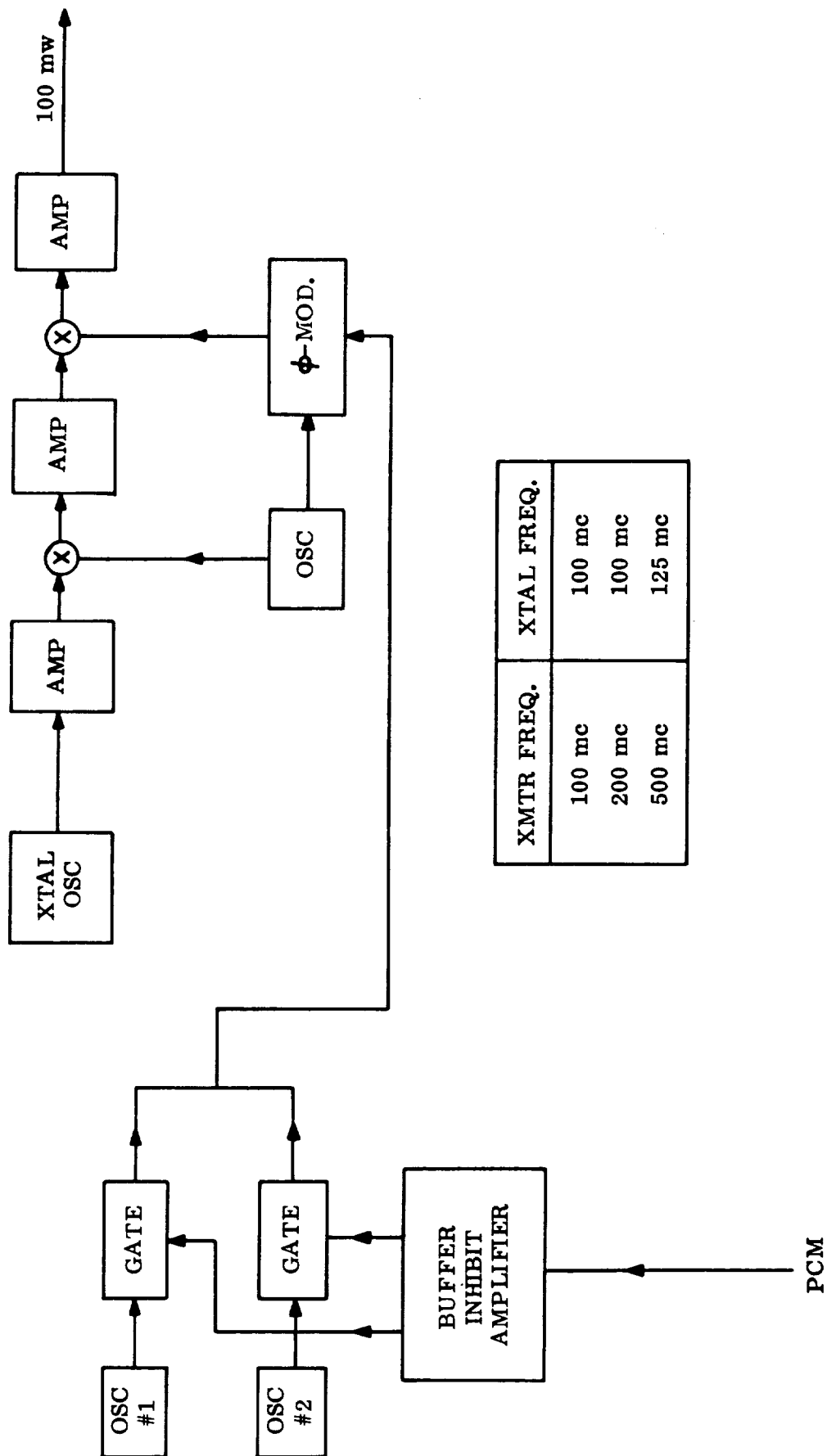


Figure 3.10.7. PCM/FSK/PM Transmitter

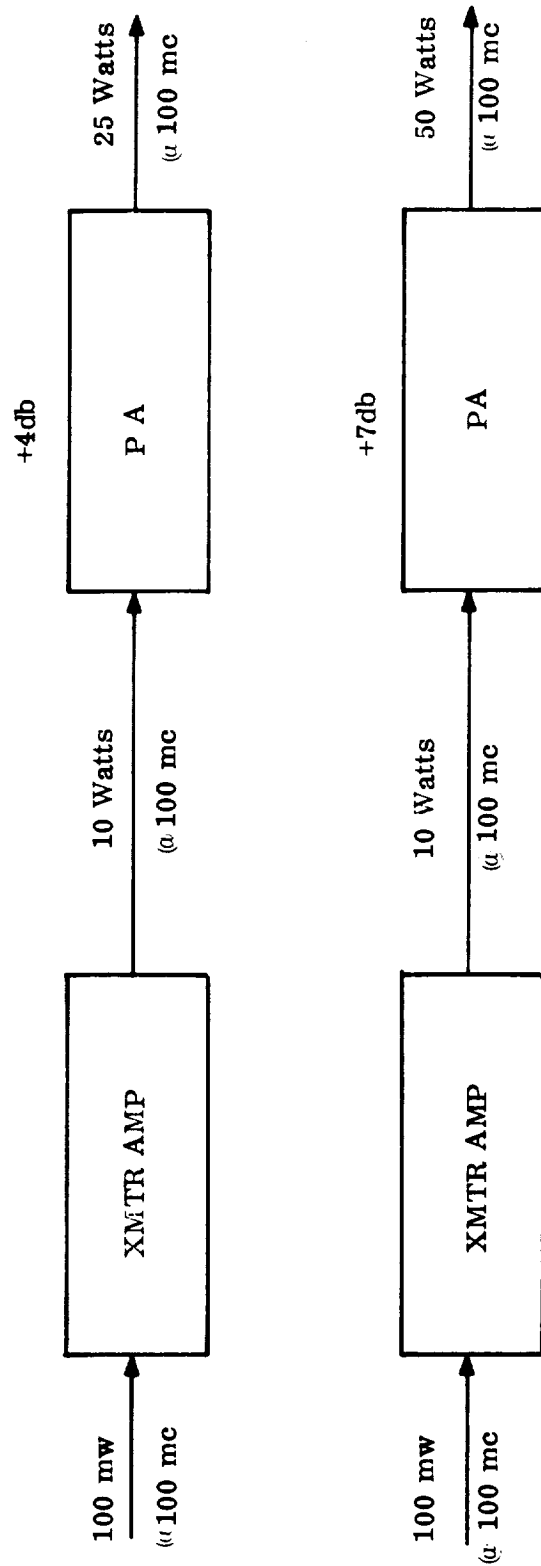


Figure 3.10.8. 100-mc Power Amplifiers

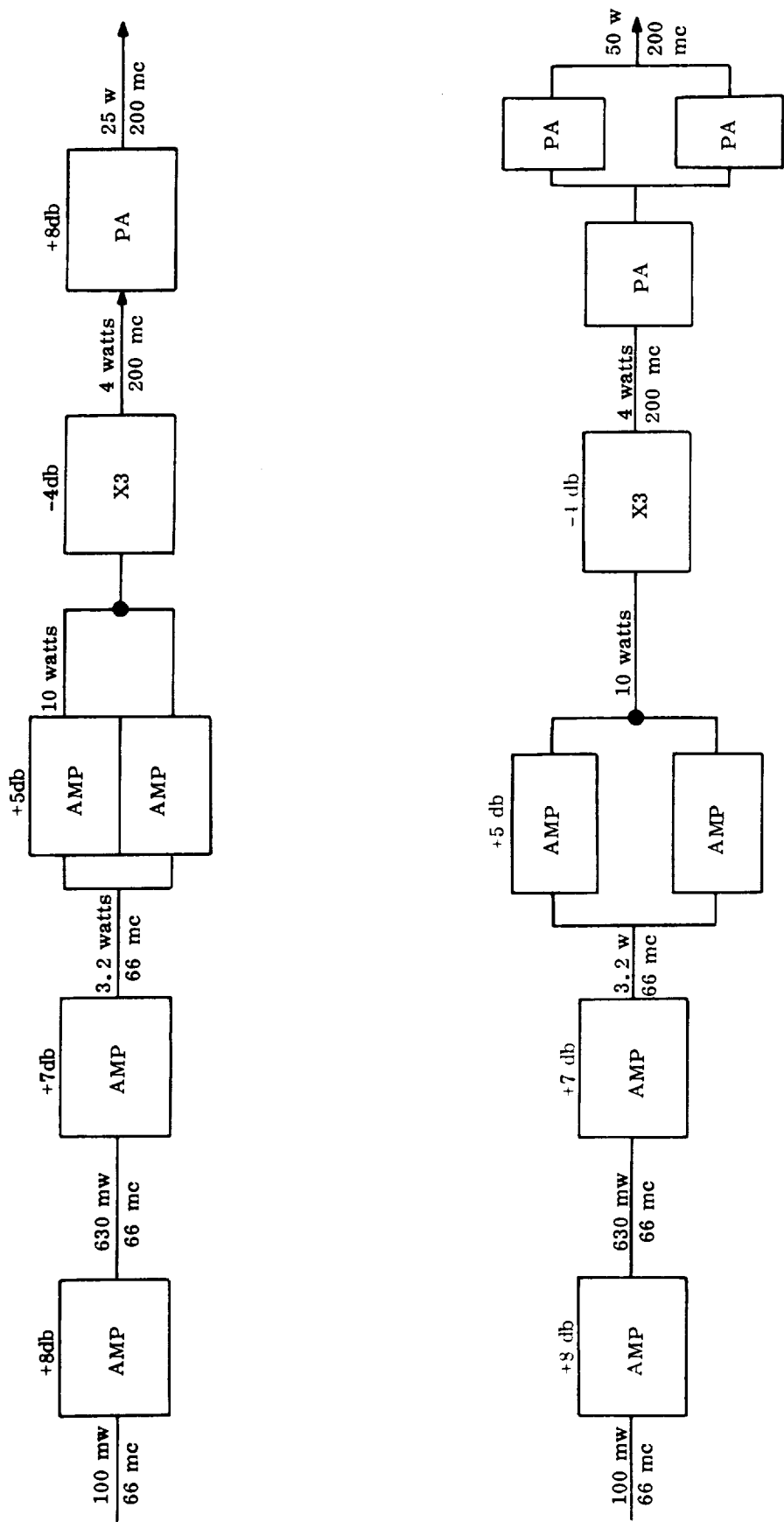


Figure 3.10.9. 200-mc Transmitters for PM or PS

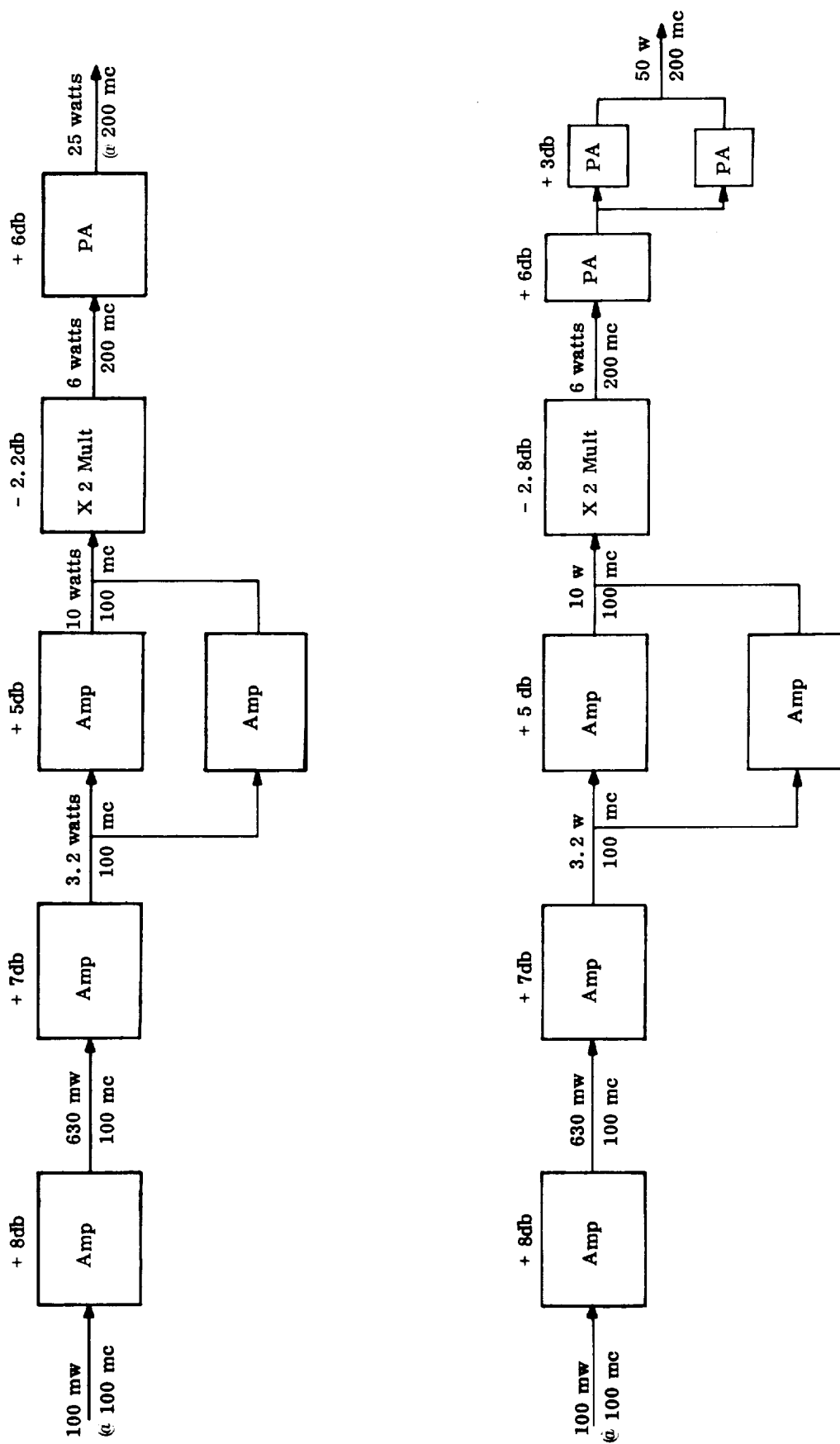


Figure 3.10.10. 200-mc Transmitters for FM

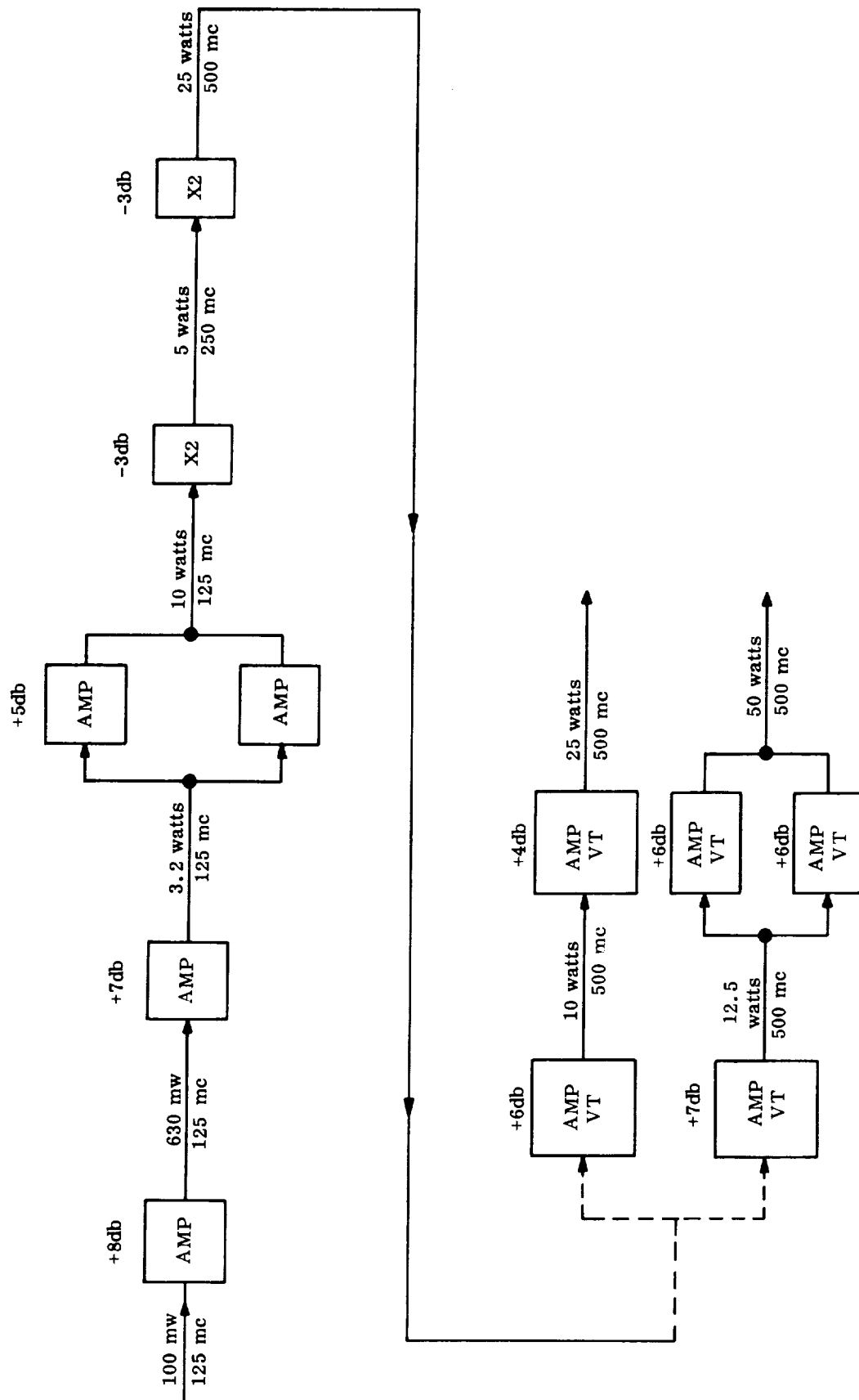


Figure 3.10.11. 500-mc Transmitters for FM

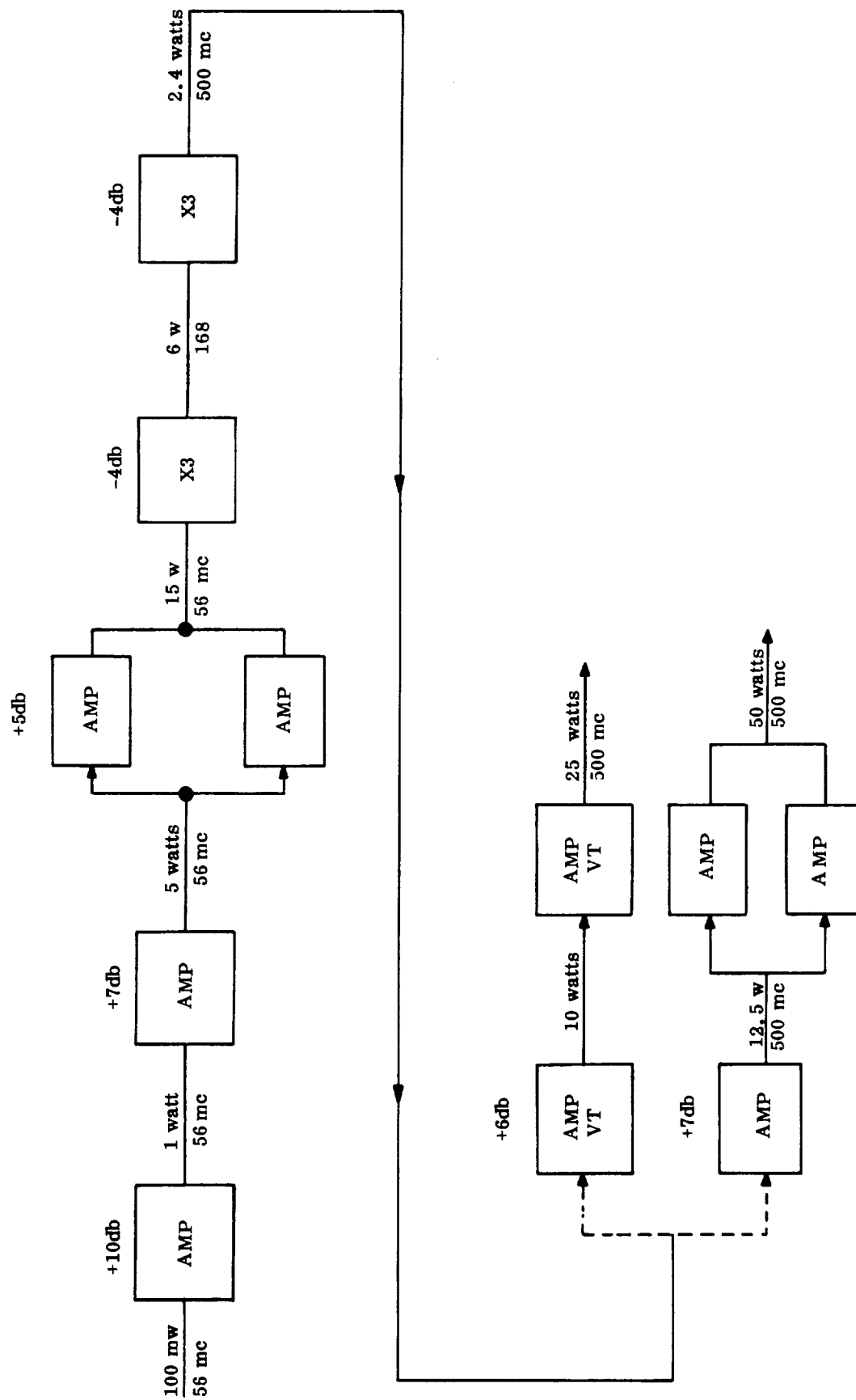


Figure 3.10.12. 500-mc Transmitters for PM

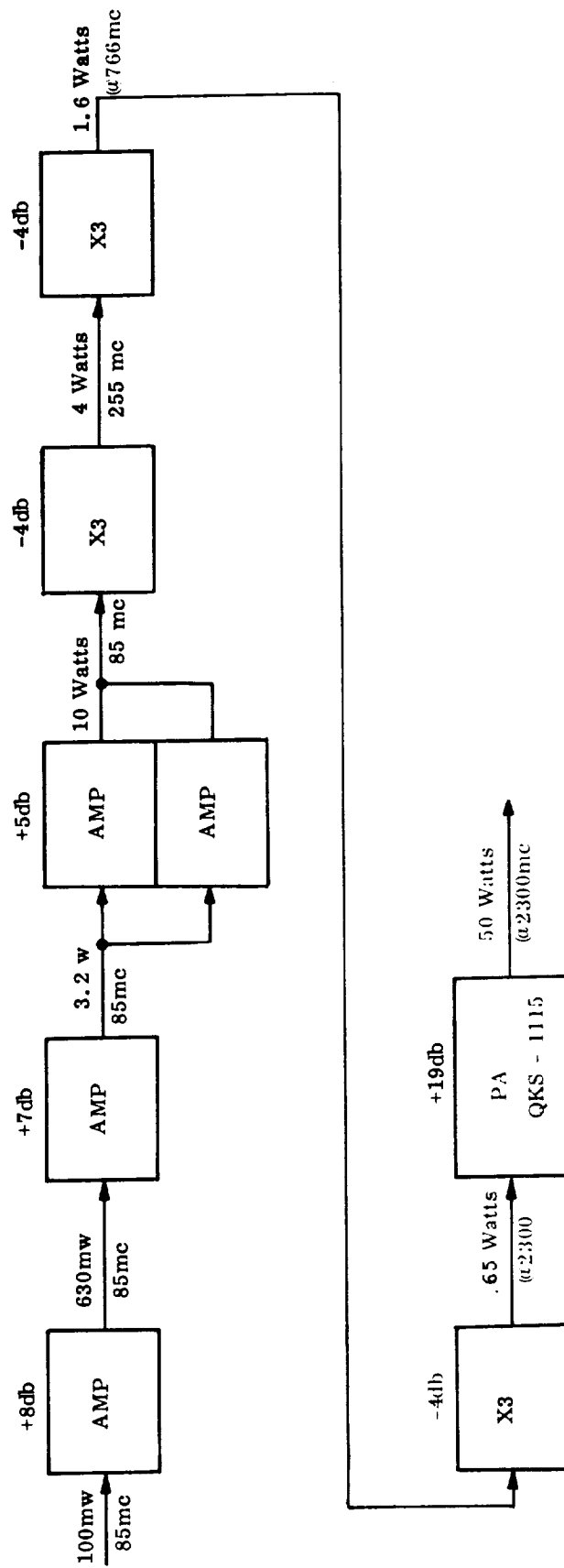


Figure 3.10.13. 2300-mc - 500 w. Transmitter

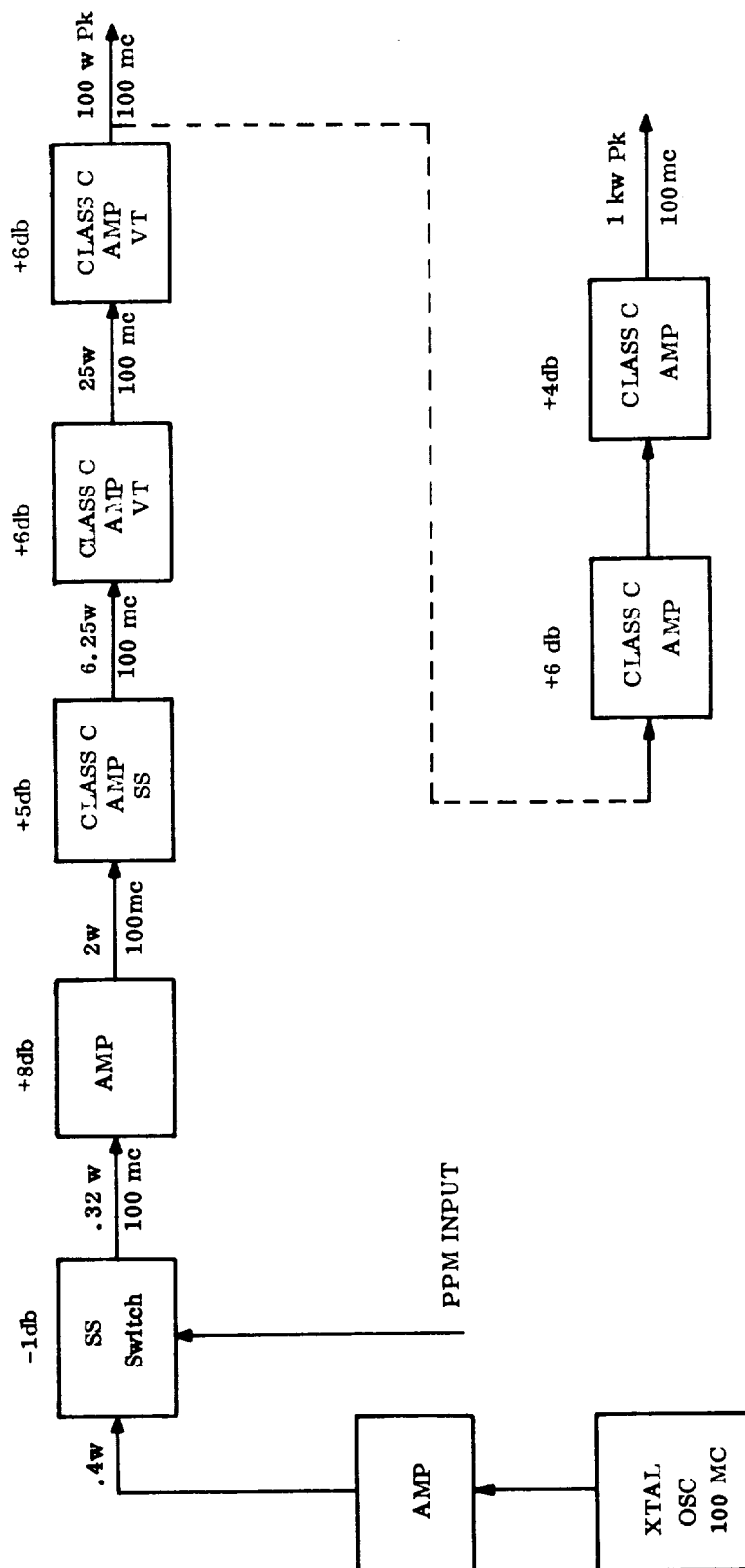


Figure 3.10.14. 100-mc - 100 w. & 1000 w. PPM/AM Transmitters

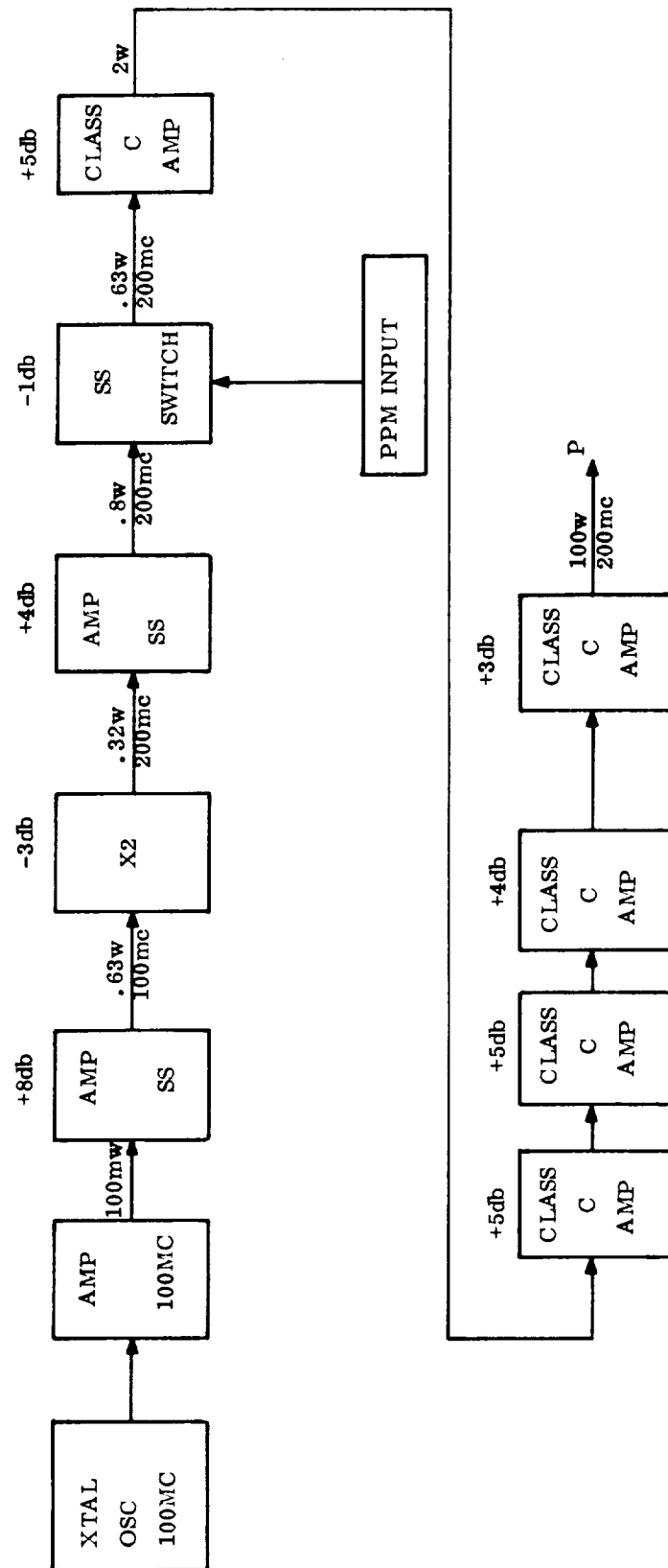
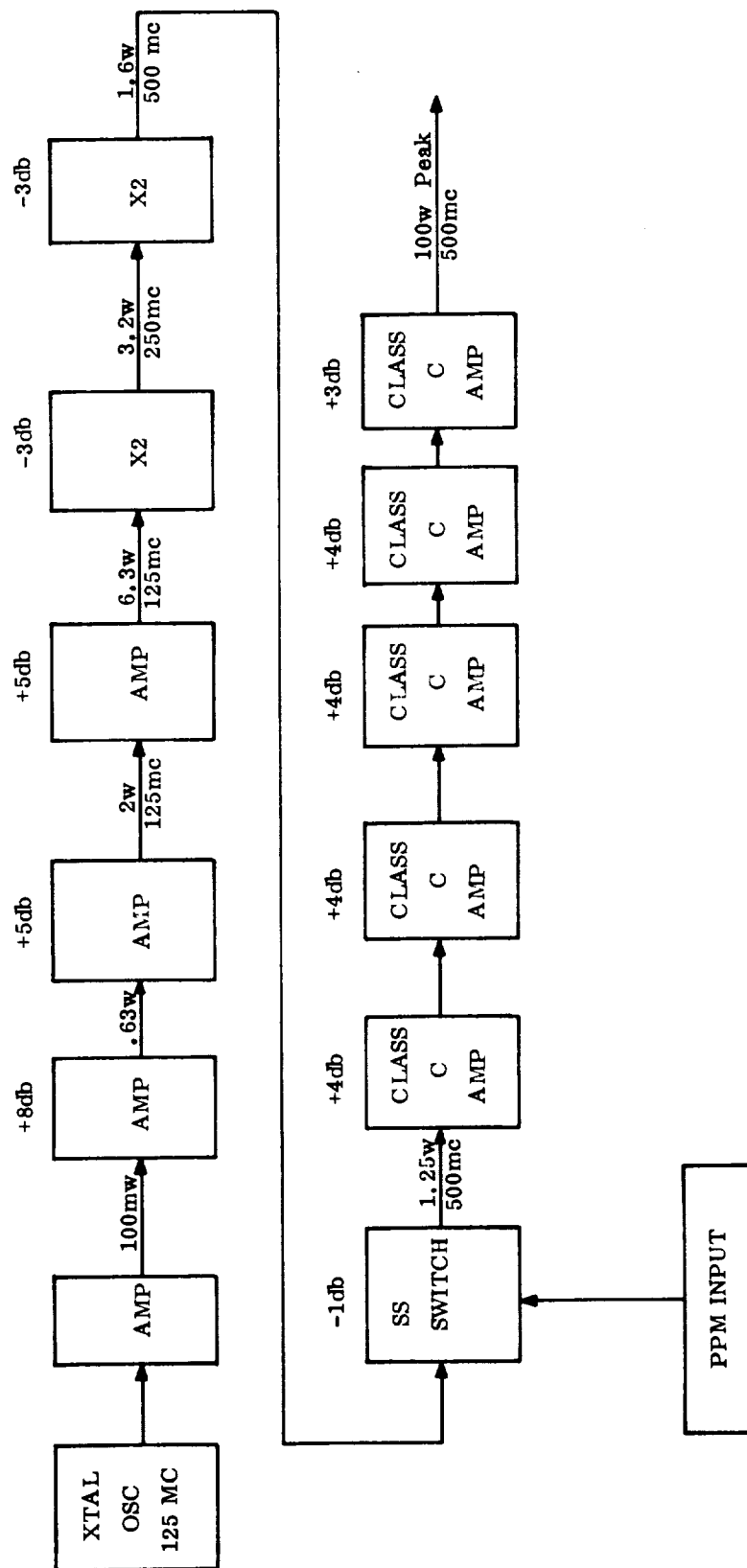


Figure 3.10.15. 200-mc - 100 w. Peak PPM/AM Transmitter



Figures 3.10.16. 500-mc - 100 w. PPM/AM Transmitter

3.11 CAPSULE ANTENNA

3.11.1 Introduction

This section of the report shows the approach taken to appropriate antenna designs for the Venus-Mars capsule.

The discussion of antenna configurations includes both "relay" and "direct" link capabilities for use during post-entry and transit periods. The final choice of whether to use a relay link or a direct link must be the result of a detailed system trade-off, in which one of the factors will be the antenna capabilities.

A general constraint on the communication system is the operating frequency. The direct link, from capsule to Earth, will transmit at 2295 mc. The relay link, from capsule to spacecraft, will operate at a frequency between 100 - 500 mc.

3.11.2 Post-Entry Antennas (Direct and Relay)

3.11.2.1 Design Parameters

3.11.2.1.1 Radiation Pattern Coverage

For the post-entry (aerodynamically stabilized) regime, both the direct and relay systems require a rearward-looking antenna pattern. Assuming that the planetary atmospheric encounter geometry is as presently anticipated, the radiation pattern required is an aft hemisphere of coverage. Forward radiation (toward the planet) must be suppressed to avoid multipath difficulties.

3.11.2.1.2 Polarization

Both the direct and relay link antennas should be circularly polarized.

3.11.2.1.3 Power-Handling Requirements

Both the direct and relay antennas should be capable of accepting and radiating up to 50 watts of power at the appropriate operating frequency.

3.11.2.1.4 Bandwidth and Input Impedance

Both the direct and relay antennas should present a characteristic input impedance of 50 ohms at the operating frequency. The bandwidth requirements are minimal due to the low information rate. The design objective should be a bandwidth of ± 0.5 mc about the operating frequency at a VSWR of 2.0 or less.

3.11.2.1.5 Frequencies

The direct link will operate at 2295 mc. The relay link will operate within 100-500 mc. For the purposes of this study, 100 mc, 200 mc, 300 mc, 400 mc and 500 mc operating frequencies have been investigated.

3.11.2.2 Antenna Configurations

3.11.2.2.1 Location

The basic design of an antenna system depends to a large extent on the vehicle configuration. The determination of the effectiveness of a radiating component can only be accomplished by considering the total structure as part of the radiating device. For the case of the Venus-Mars capsule, the basic Discoverer shape, with appropriate scaling factors, has been used.

During certain phases of this study program, other shapes were considered, such as Nike-Zeus target-vehicle adaptations, and blunted re-entrants, each shape being considered because of an apparent specific advantage. For example, the stinger-type vehicles are useful as RF plasma penetration vehicles.

The portion of the capsule of interest to the antenna designer, considering pattern requirements and available ablation-free area, is the aft surface. Using the Discoverer scaled shape with an afterbody diameter of approximately 28", the vehicle size is appreciable (with respect to a wavelength) at all frequencies except those in the 100 mc region.

The aft portion of the vehicle is advantageous for several reasons. Primarily, much of the radiation pattern may be directed rearward by geometry; secondly, the aft cover mounting will not require an ablation-free RF window as

would any other mounting area; and finally, the environmental problems at the aft cover will be considerably less severe than in other areas.

3.11.2.2.2 Type of Antenna

The choice of a general type of antenna for the Venus-Mars Capsule is considerably narrowed by the expected environmental conditions to be encountered. An external antenna would not suit this mission, since the many structural and material problems involved would require a significant advance in the antenna and vehicle state-of-the art. Therefore, a flush-mounted radiating device appears to be in order. At the relay-link frequencies, a flush-mounted, cavity-backed slot presents an adequate approach. The direct-link frequency and physical parameters indicate that a circular wave-guide antenna would offer a promising means of fulfilling the system requirements.

3.11.2.3 Antenna Design-Relay Link

Figure 3.11.1 shows the structural details of the 100-500 mc antenna. The electrical and mechanical characteristics are given in Table 3.11.1 for the various frequencies within the 100-500 mc range.

TABLE 3.11.1

Physical and Electrical Characteristics - Relay Antenna

FREQUENCY	L	W	H	WEIGHT	EST. LOSS
100 MC	24"	6"	5"	13.2 lbs	3.0 db
200 MC	16"	6"	5"	8.7 lbs	2.0 db
300 MC	12"	5"	4"	4.0 lbs	1.5 db
400 MC	10"	4"	3"	2.2 lbs	1.0 db
500 MC	8"	3"	2"	1.3 lbs	0.5 db

The proposed design, a crossed-slot antenna, is capable of meeting all design requirements and is well within the state-of-the-art. Circular polarization will be developed by feeding equal power to each arm of the cross and delaying

one leg by 90° . The radiation patterns will vary slightly through the 100-500 mc frequency range, as the ratio of wavelength-to-vehicle size varies. Figures 3.11.2 and 3.11.3 show estimated radiation patterns at 100 and 500 mc, respectively. It can be expected that circularity will hold up well for $\pm 60^\circ$ about the boresight axis and that the full aft hemisphere of coverage can be provided. Tuning of each slot to resonance will be accomplished by means of a dielectric-filled variable capacitor. The volumes indicated in Table 3.11.1 are adequate for the bandwidth requirements.

3.11.2.4 Antenna Design-Direct Link

The direct link antenna is similar to the relay link antenna in that the necessity for flush mounting is still apparent. The basic radiating element best suited for the direct link appears to be a cavity-backed helix. The helix would be firmly held in place by a potting substance of low dielectric constant and low loss tangent. The dielectric will provide mechanical rigidity, thermal insulation, and breakdown inhibition. The diameter of the circular aperture is 3.5 inches, and the total depth of the element is 4.9 inches, with a weight of 1.5 pounds. Figure 3.11.4 defines the structure involved. The impedance and bandwidth requirements are readily achieved by variation of physical parameters within the cavity. The radiation pattern may be considered as approximately one-half a dipole pattern whose axis is the roll axis, as shown in Figure 3.11.5.

3.11.2.5 RF Breakdown

A major difficulty encountered in the design of an entry vehicle antenna is the determination of a safe power handling limit. Although the field of RF breakdown at reduced earth atmospheres has been studied considerably and much data has been compiled for specific programs, little has been accomplished concerning atmospheres other than Earth's. However, from the data on the Earth's atmosphere we may be able to reach a few predictable breakdown theories on other atmospheres. The only active gas comprising the Earth's atmosphere is

oxygen, which exists in the free state. The molecular structure of oxygen is such that electron transfer or ionization may occur at significantly lower collision energies than it would in an inert gas.

The Venusian atmosphere is comprised of nitrogen, carbon dioxide, and argon. The presence of free oxygen is not predicted, and the percentage of combined oxygen is at worst similar to Earth's atmosphere. From these few generalizations it may be assumed that RF breakdown levels will be in the same order of magnitude for the two atmospheres. The verification of these assumptions can be accomplished in a laboratory test series utilizing standard apertures and selected gases and combinations of gases.

The margin of safety regarding power handling capability can, of course, be increased if necessary by widening the aperture width, or simply facing the antenna with a dielectric material, with a slight increase in antenna weight.

3.11.2.6 Ablation By-Products

During atmospheric entry it can be expected that ablation by-products will spill over the aft cover. This has been experienced on previous programs, where the recovered vehicles displayed a fine aft covering of what appeared to be carbonized particles. The effect of this layer can be simulated during an antenna design program, and the detuning and attenuation levels predicted. The anticipation in this case is that the by-products are conductive and will cause a slight degradation in the antenna performance.

3.11.3 Auxiliary Antenna System

3.11.3.1 Possibilities

During the transit time between capsule separation and entry, periodic telemetry link tests might be desired to check the operation of the communication equipment. The primary crossed-slot antenna patterns have been discussed, and their coverage may be described as hemispheric, oriented to the rear of the capsule. During the transit phase, the vehicle might well be unstabilized.

At separation from the bus, the vehicle would then assume a random orientation and motion along the impact trajectory. During such an unstabilized period of flight, it may be expected that both direct or relay link radiation pattern coverage will cause signal fades as the capsule tumbles. The depth and width of the forward nulls will be as depicted by the Figures 3.11.2, 3.11.3 and 3.11.5.

The overall trade-off in this instance appears to involve three possibilities:

- (a) provide capsule roll axis stabilization
- (b) utilize an auxiliary system of antennas to approach the desired isotropic radiation pattern, and
- (c) accept the existing radiation patterns because no atmospheric data would be lost in this period of flight, and full-time operation is not mandatory, but only serves as a confidence check.

Possibilities (a) and (c) must be decided at the overall system level. Possibility (b) the auxiliary antenna system, will be covered here.

The primary function of the suggested auxiliary antenna system will be to provide isotropic radiation pattern coverage during capsule unstabilized flight. Since this time period is associated with minimal environmental levels, it may be expected that a simplified external antenna design may be implemented. The general approach to this particular problem will be to provide an auxiliary antenna and coaxial switch, transferring the transmitter output to the primary slot antenna when the level of expected entry "g" loading is reached.

From an overall standpoint, the best choice of auxiliary antenna for the relay link appears to be an aft-mounted quarter-wave stub. This choice is justified below.

3.11.3.2 Radiation Patterns

Within the 100-500 mc region, using the Discoverer capsule previously discussed, the stub will present a smooth radiation pattern with two on-axis nulls to the circular receiving antenna. This is shown in Figure 3.11.6 for two possible stub locations. The resultant radiation pattern may be considered as quite adequate, and has been used successfully on previous programs.

3.11.3.3 System Integration

The use of an external antenna of this nature does not present a difficult structural problem. The stub is not required to survive entry, and the mounting arrangements will be designed to protect the capsule. The method of mounting is shown in Figure 3.11.7.

3.11.3.4 Coaxial Switch

Possibly the greatest problem in such an auxiliary system will be insuring an adequate reliability in the coaxial switch. This switch will be required to transfer the RF power from the auxiliary antenna to the primary antenna upon entry. Switching of this nature requires electromechanical devices which, although manufactured and utilized on many missile programs, will lower the total reliability figure of merit.

3.11.3.5 Direct Link Auxiliary Antenna

The 2295 mc direct link auxiliary antenna presents its own unique problem in that an isotropic radiation pattern with a large-size capsule (i. e., large with respect to λ at 2295 mc) is not so easy to approach. To fill in the forward null of the primary circular antenna, an auxiliary element would best be placed in the vehicle. Another element similar to that proposed for use as a primary antenna could be placed at the stagnation point. Depending on the ablation material used in this area, the antenna may not need an RF window. The combined array pattern is as shown in Figure 3.11.9, and the mounting is shown in 3.11.10. In this case, the RF coaxial switch would merely remove the auxiliary antenna from the circuit when entry deceleration is reached.

3.11.4 Entry Communication Antenna

The electrical design of an antenna to permit propagation through the entry plasma causes many structural problems in the vehicle.

As shown in Figure 3.11.11, the vehicle is divided into two parts by a dielectric collar, and RF energy is fed across the slot. The appearance of the total vehicle is then simplified into a dipole. The radiation patterns are similar to a long dipole with the exact pattern depending on the slot location with respect to the total vehicle length. The dielectric ring is normally located at the area of predicted minimum plasma density.

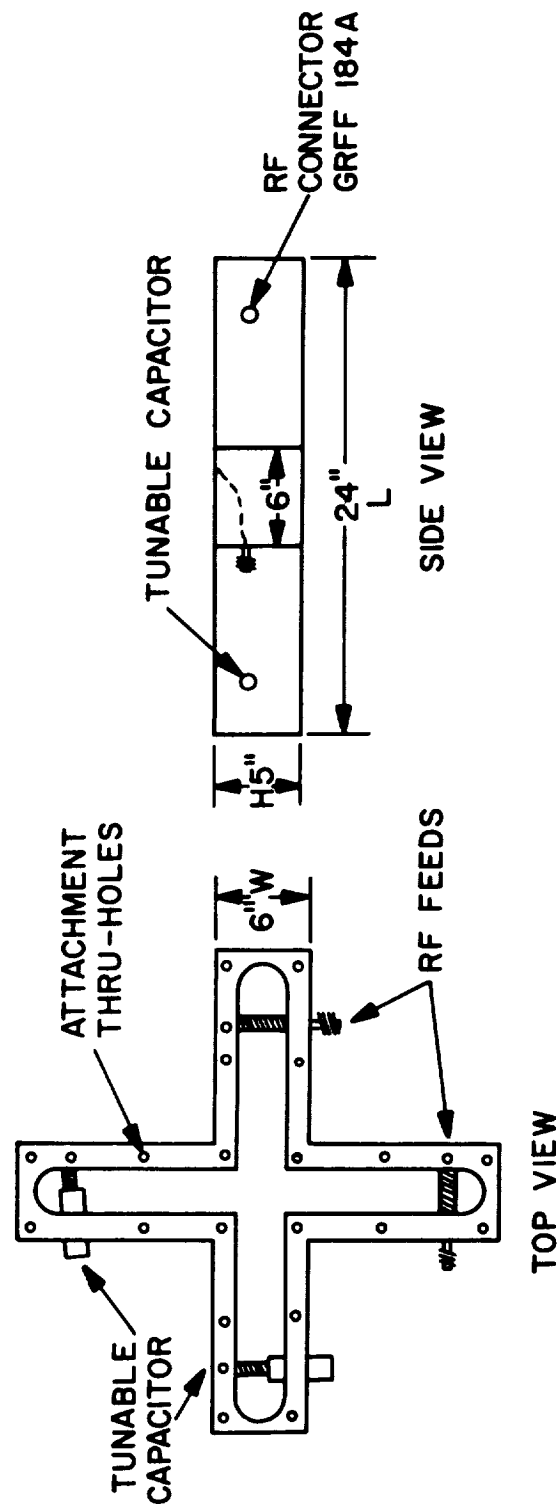


Figure 3.11.1. Relay Antenna

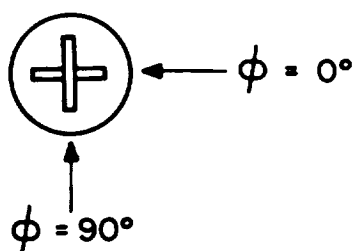
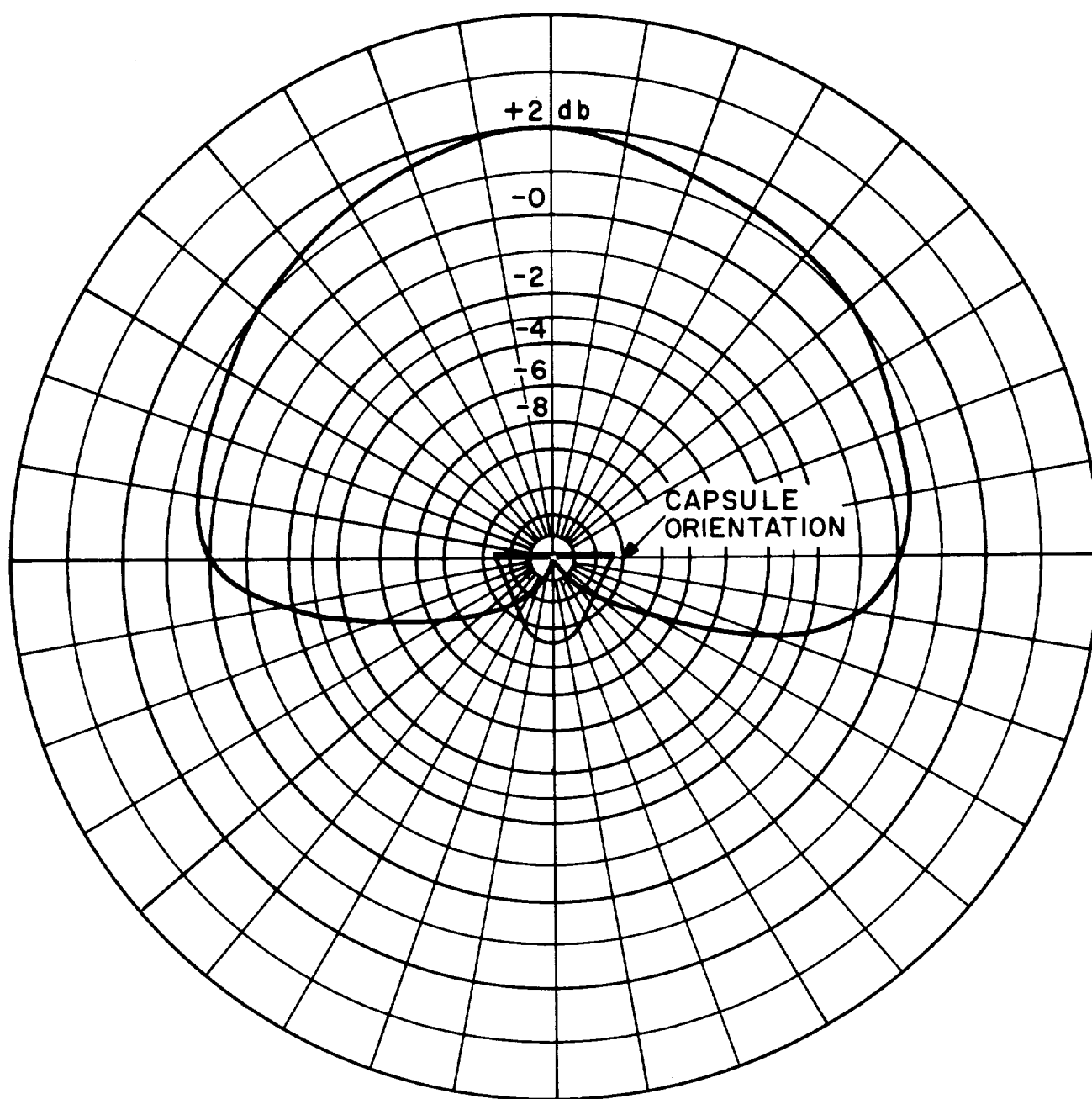


Figure 3.11.2. Estimated Radiation Pattern Crossed-Slot Antenna at 100 mc.

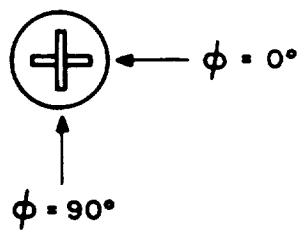
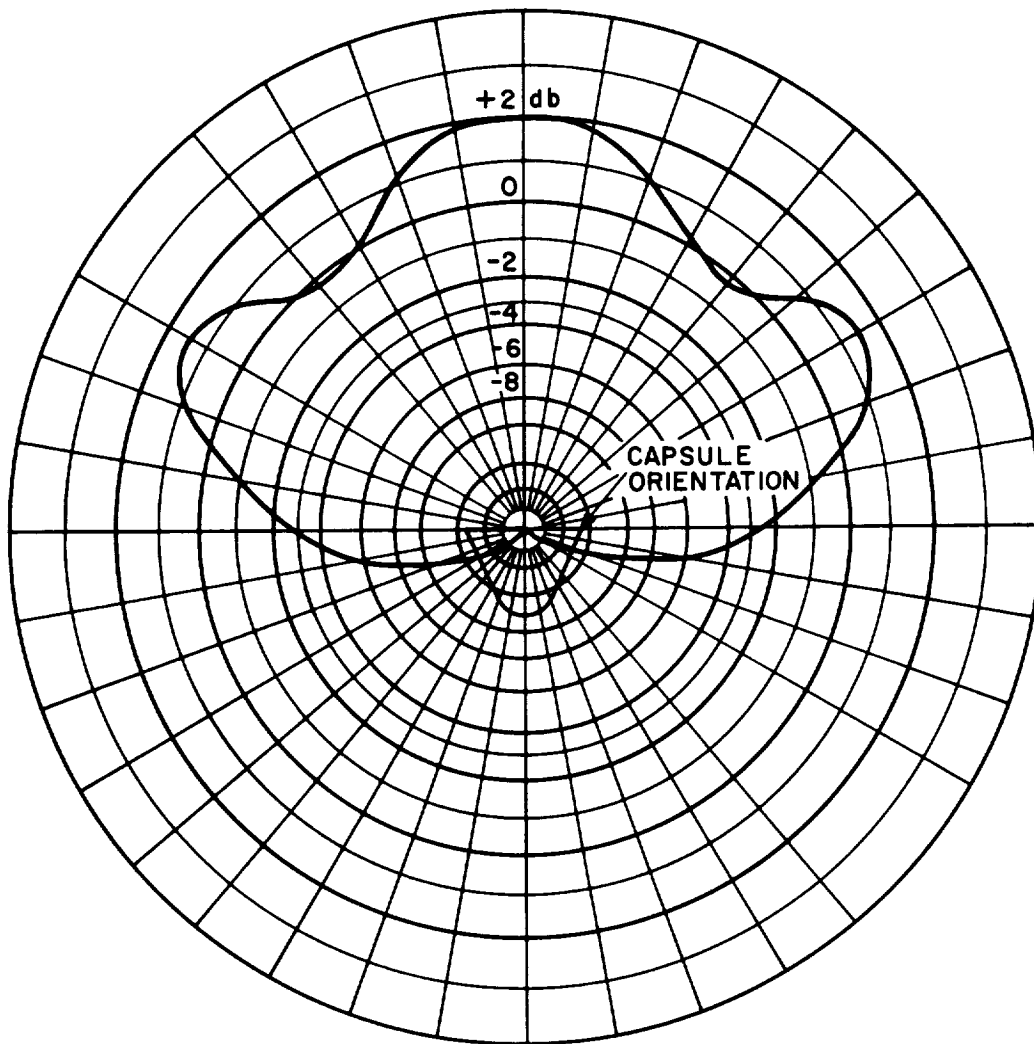


Figure 3.11.3. Estimated Radiation Pattern
Crossed-Slot Antenna at 500 mc.

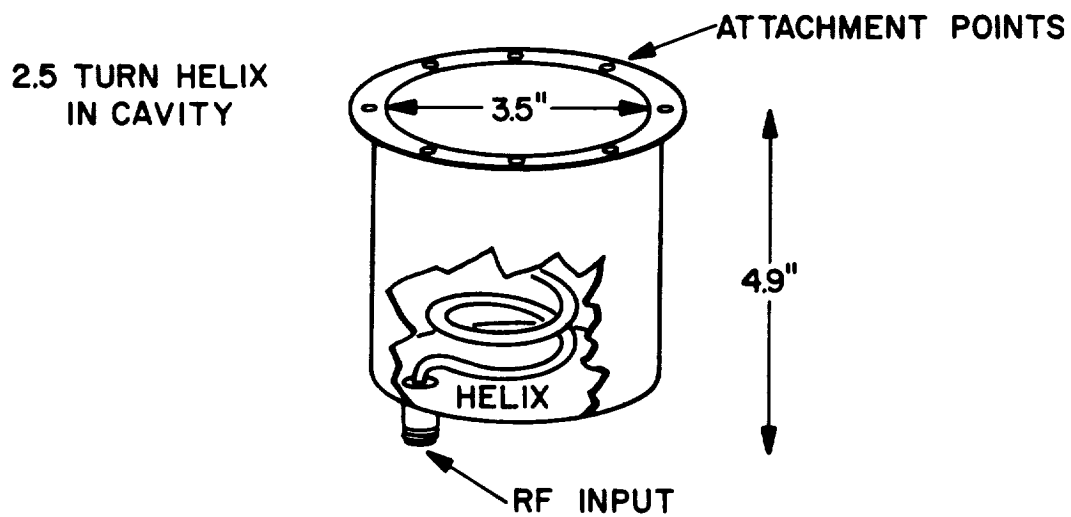


Figure 3.11.4. Antenna Configuration - Direct Link

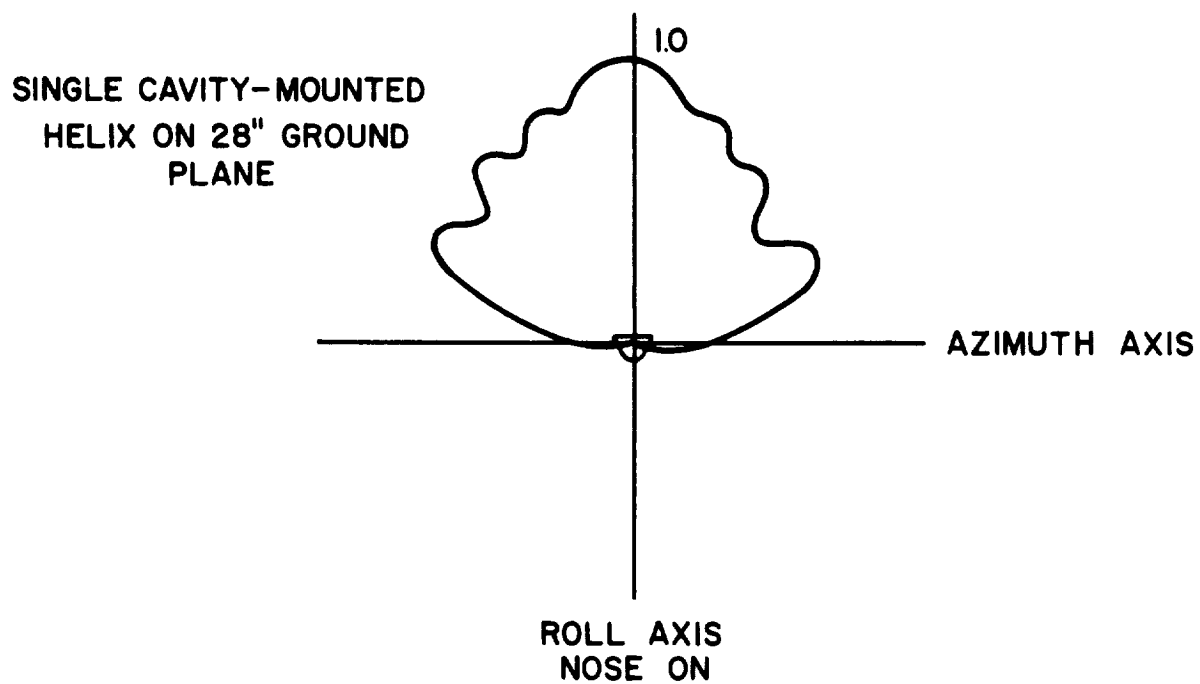
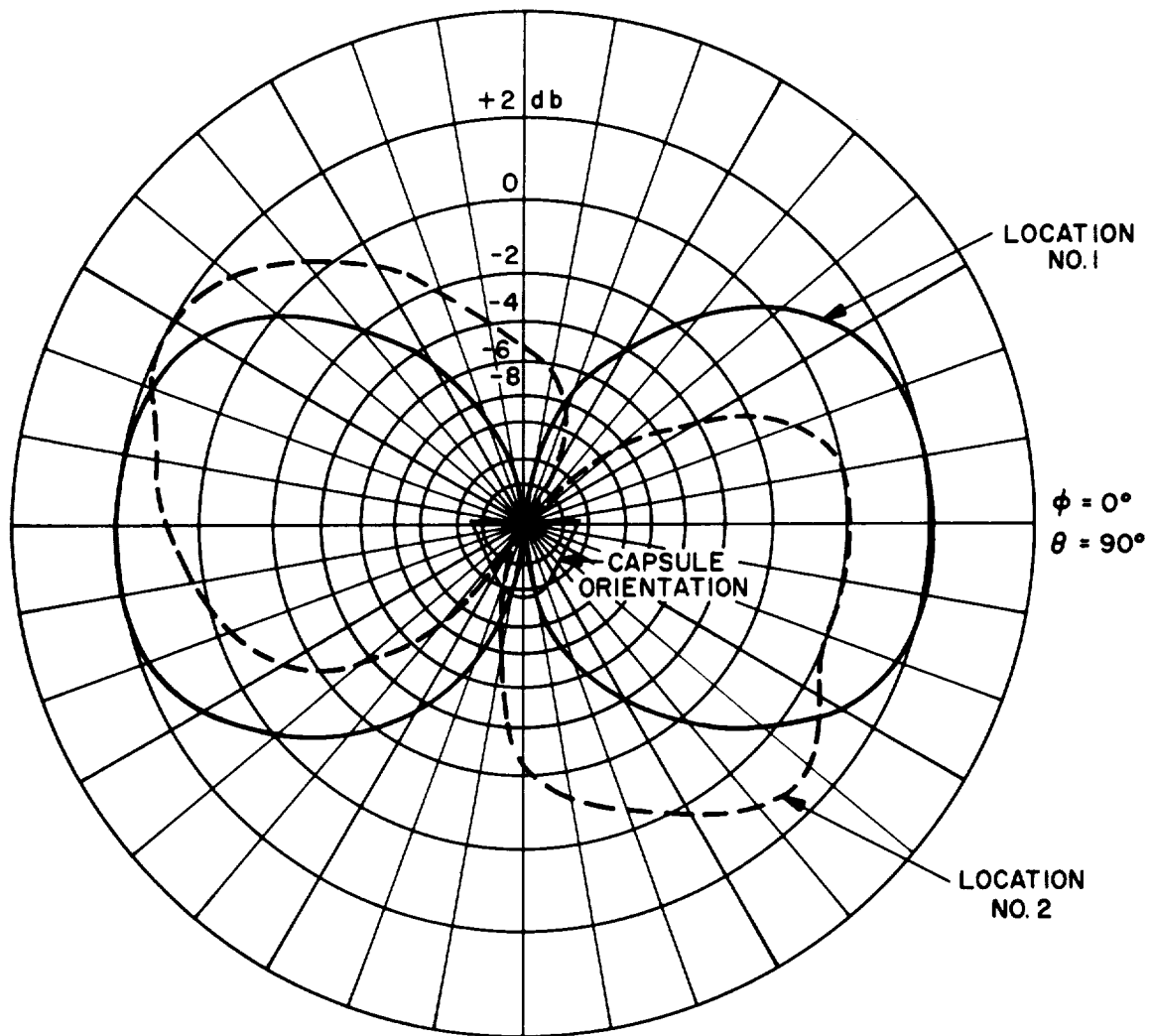


Figure 3.11.5. Estimated Radiation Pattern





- 
STUB LOCATION 1
 $\phi = 0^\circ$
 (CENTERED ON AFT SHIELD)
- 
STUB LOCATION 2
 $\phi = 0^\circ$
 (ON RING OF AFT COVER)

Figure 3.11.6. Estimated Auxiliary Antenna Radiation Patterns
at 100 mc

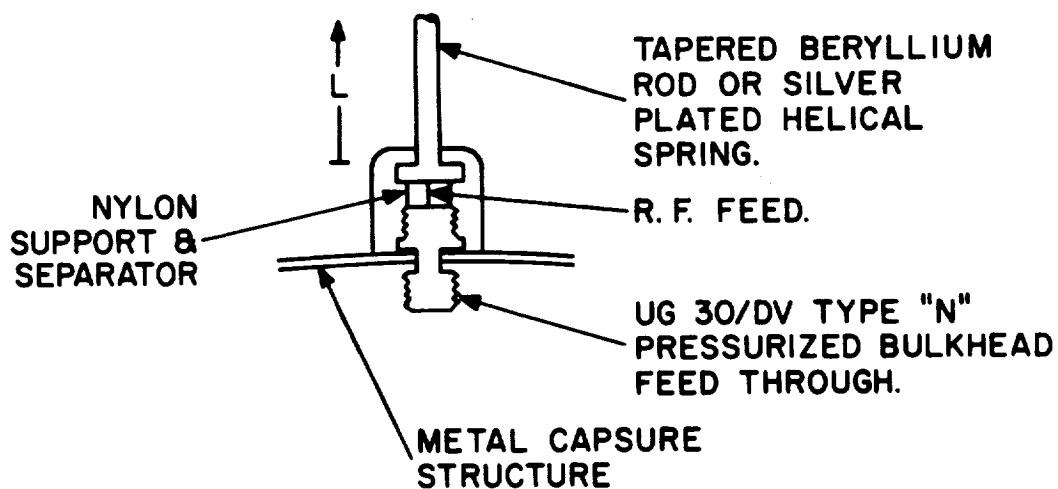


Figure 3.11.7. Mounting the Auxiliary Antenna

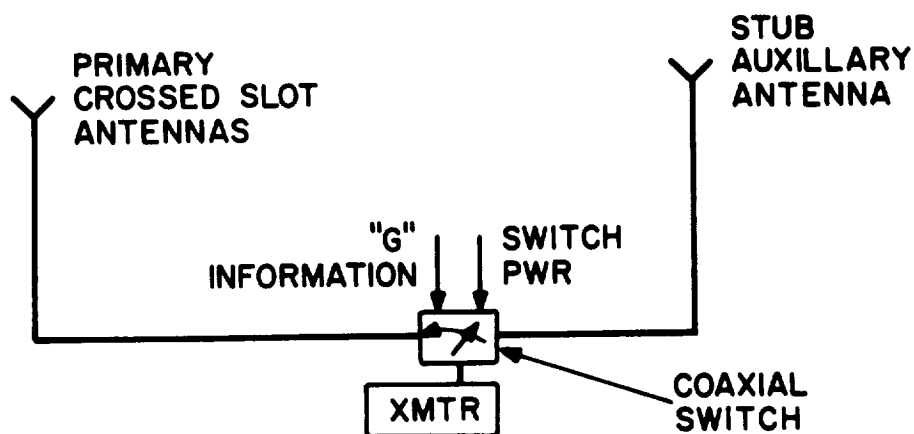


Figure 3.11.8. Possible Antenna Switching Scheme

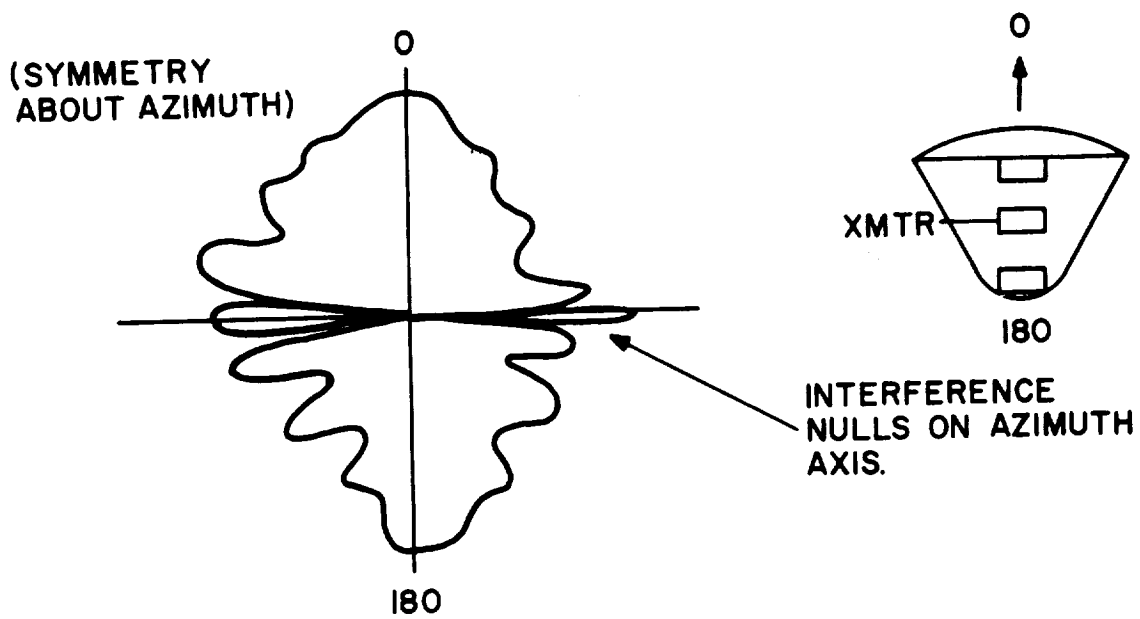


Figure 3.11.9. Direct Link Auxiliary Antenna

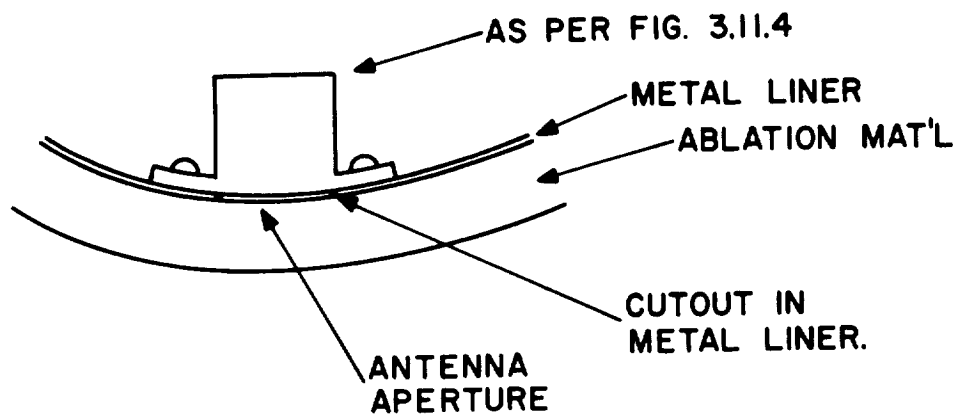


Figure 3.11.10. Mounting the Direct Link Antenna

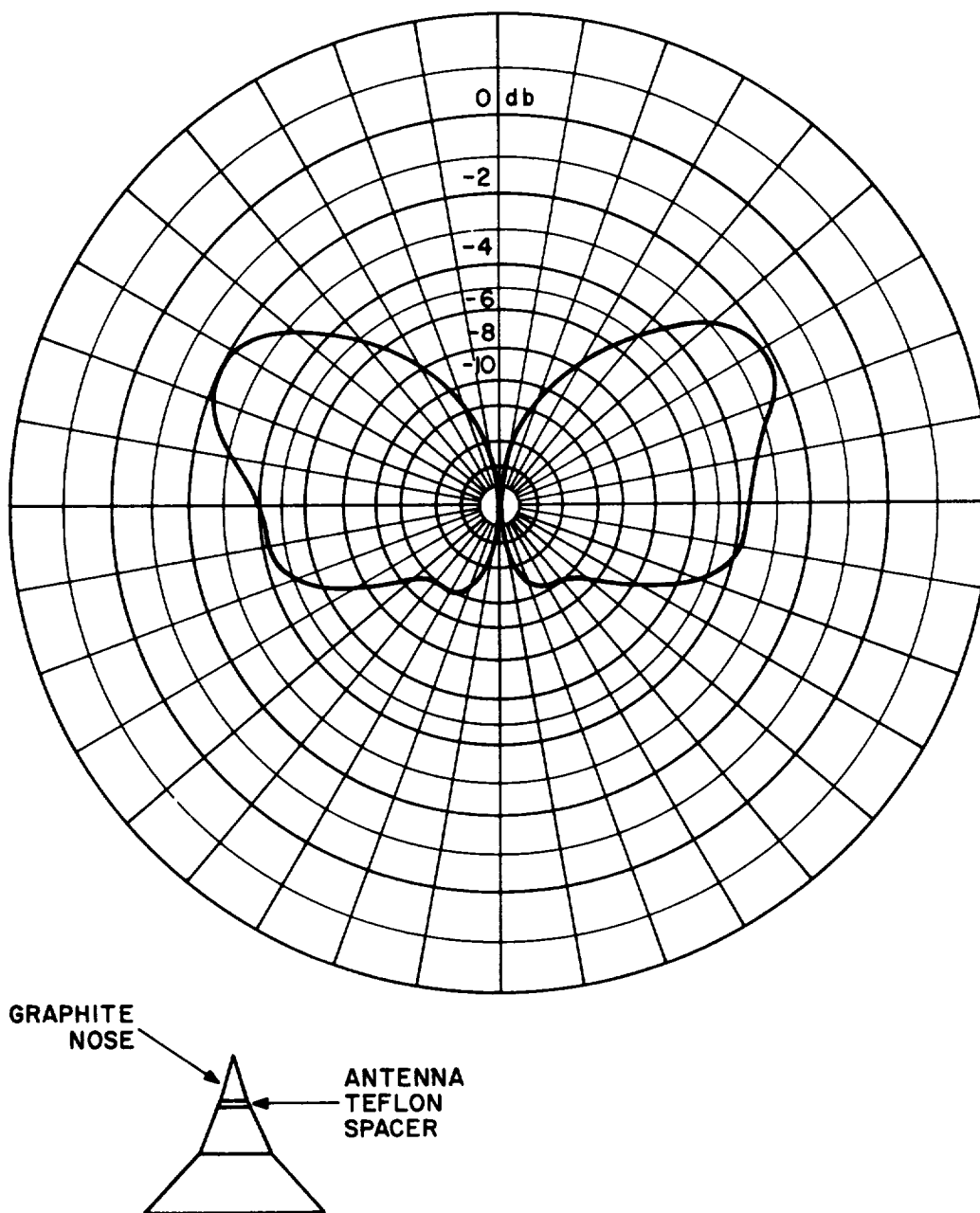


Figure 3.11.11. Estimated Antenna Radiation Pattern for Pointed Vehicle at 260 mc

3.12 RELAY EQUIPMENT REQUIRED FOR MARINER SPACECRAFT

3.12.1 Introduction

This section contains estimates of appropriate radio receiving equipment to be used in the Mariner spacecraft for receiving the signal transmitted from the capsule over a relay link.

Size, weight, and power estimates for conservatively designed equipment for such a 1965 space mission are summarized in Tables 3.12.1. The accompanying figures show appropriate receiver block diagrams.

A discussion of suitable receiving antennas for the spacecraft is also included.

3.12.2 Receiver Size, Weight, and Power Estimates

Table 3.12.1 shows size, weight, and power requirements of appropriate present-day receiving equipment for the 100-500 mc band.

Since this equipment is not required to undergo the sterilization heat treatment, a low-noise Germanium transistor front end (having a noise figure of 4-5 db) can be used. Silicon transistors will be used for the other stages.

TABLE 3.12.1

Spacecraft Receivers

Type of Receiver

AM/FMFB	4.2 X 4 X 7	5.6	15*
FM/FMFB	4.8 X 4 X 7	6.4	15*
PCM/FM	3.6 X 4 X 7	4.8	15*
PCM/FSK/PM	3.5 X 4 X 7	4.4	15*
PCM/PS	3.6 X 4 X 7	4.8	15*
PCM/PS/PM	3.5 X 4 X 7	4.4	15*
PCM/FM/PM	3.5 X 4 X 7	4.4	15*
PPM/AM	3 X 4 X 7	4.0	15*

*Includes 2 watts for receiver and 13 watts for oven.

3.12.3 Spacecraft Antenna Recommendations

3.12.3.1 Requirements

The general requirements of the spacecraft relay link receiving antenna are as follows:

- (a) Radiation Pattern Coverage - Provide generally hemispheric coverage directed toward the capsule.
- (b) Polarization - Provide polarization compatible with the capsule antenna at sensitive look angles. For both linear and RHCP capsule antennas, the spacecraft antenna should be RHCP.
- (c) Frequency - The antenna will operate at a selected frequency within the 100 to 500 mc band. The impedance at the operating frequency should be compatible with a 50-ohm system.
- (d) Mechanical - The antenna should be designed to provide a minimal spacecraft interface condition and to be compatible with the spacecraft environment.
- (e) Power Handling Capabilities - None required. The antenna will function solely as a receiving antenna.

3.12.3.2 General Design Philosophy

- (a) Radiation Pattern Coverage - For this application there are two general possibilities, an "isotropic" radiator or a directive device.

The isotropic radiator is advantageous due to the freedom it allows the geometric variables. The successful operation of the relay link would depend primarily on only the capsule's attitude. If an efficient isotropic radiating device were feasible, the overall telemetry link would achieve a very high reliability. However, RHCP isotropic coverage can only be approached, and even then not very efficiently. Therefore, a directive antenna appears more desirable here.

The directive radiator, either fixed or steerable, has the advantage of utilizing energy more efficiently in selected directions. Many RHCP designs exist that will perform this function quite adequately. However, several disadvantages in the use of directive elements are apparent. The variation in predicted look angles for the desired communication periods is quite large, approaching the possibility of a hemisphere of coverage for a fixed element, while a steerable system suffers from a generally lower reliability figure due to the required electromechanical drives and sensing equipment.

3.12.3.3 Recommended Spacecraft Antennas

The Mariner spacecraft configuration offers the possibility of utilizing either a steerable array or a fixed array with a hemispheric pattern. The planet-seeking device on the planet horizontal platform (PHP) can be utilized as a pointing mechanism for a simple RHCP antenna, or a fixed hemispherical antenna may be located on the favored side of the vehicle (i. e., the side predicted to be toward Venus, based on ephemeris data of the Sun and Canopus). Either type of antenna would weigh about one to two pounds, including cabling.

3.12.3.3.1 Steerable Antenna

Since the capsule will always appear in a position between the spacecraft and the planet of impact, the planet-seeking device on the Mariner could accomplish satisfactory antenna pointing. The antenna would consist of two crossed dipoles fed in phase quadrature, thus forming a turnstile antenna as shown in Figure 3.12.8. The antenna could be made of spring material for ease of stowage.

The size of an element, from base to tip, would vary from 8" to 25" depending on the frequency of operation. At the higher end of the frequency range it might be possible to employ a two-or three-turn helix on the planet seeker.

3.12.3.3.2 Fixed Pointed Antenna

The fixed pointed antenna would necessarily be a broad-beam device, mounted on the side which will be facing the capsule at the appropriate time. The exact design of this antenna would require rather extensive model radiation pattern studies. The basic radiating device would be similar to a turnstile or helix, depending on the simplicity of achieving the desired coverage on the Mariner structure.

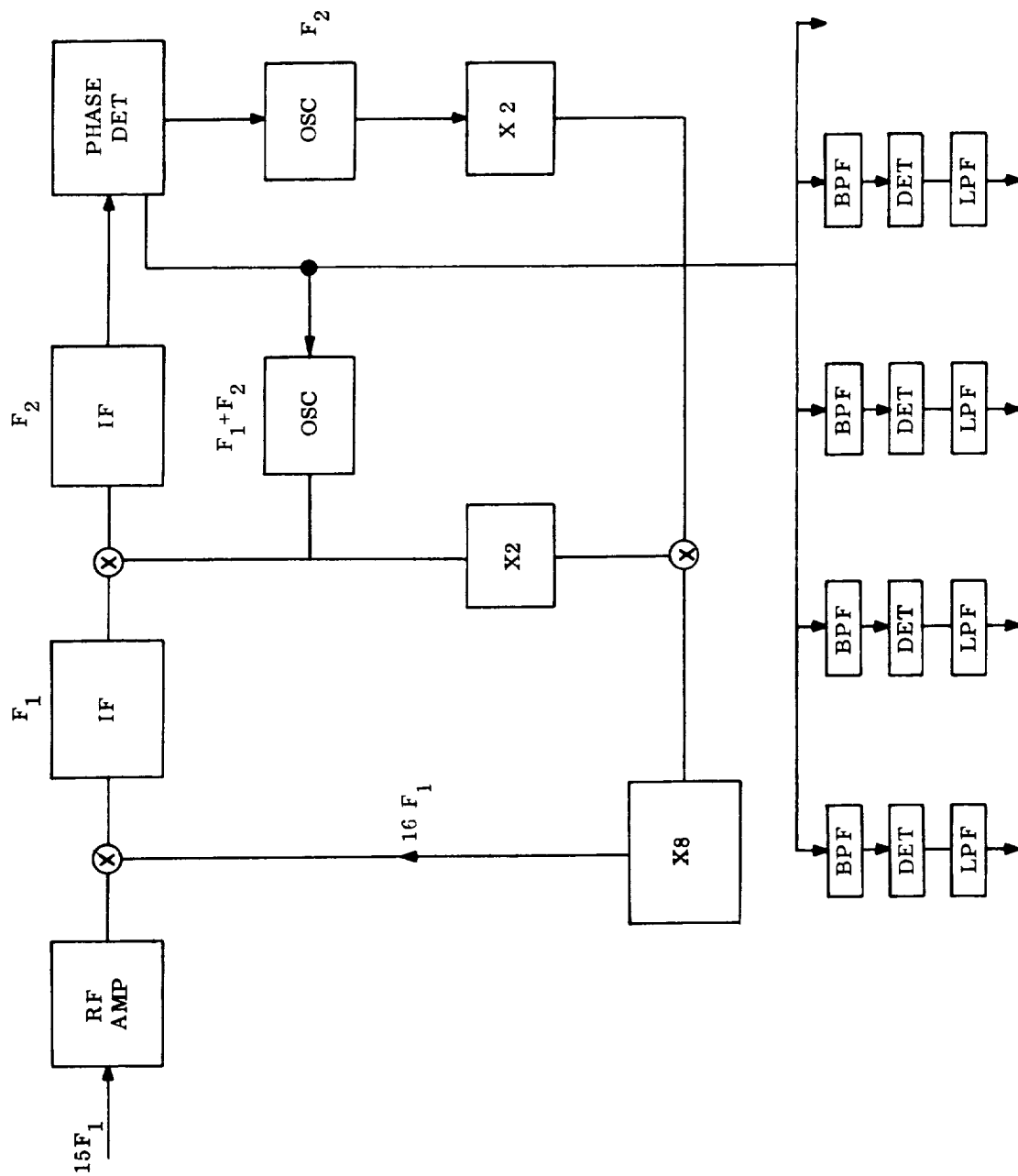


Figure 3.12.1. AM/FMFB Receiver

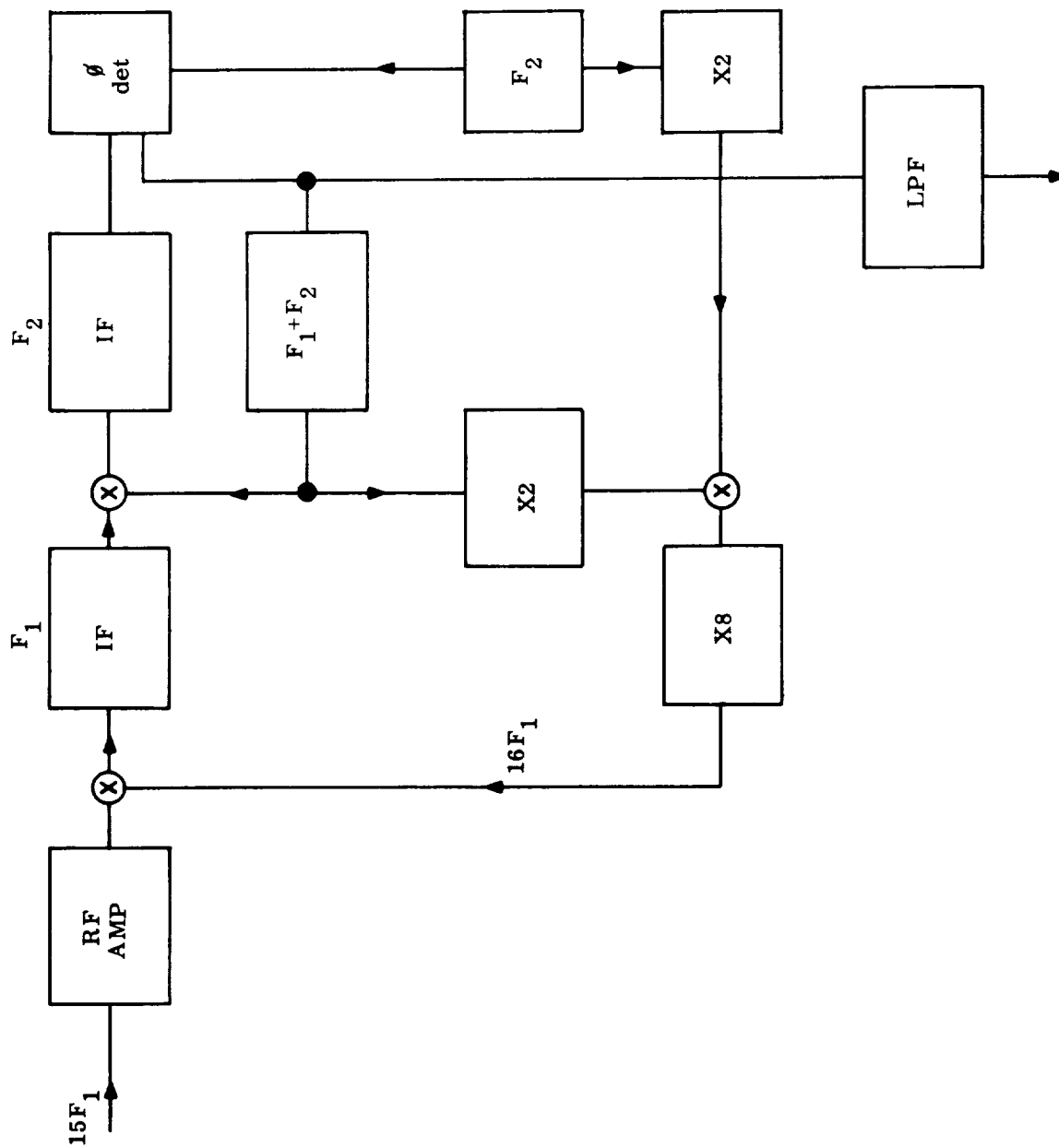
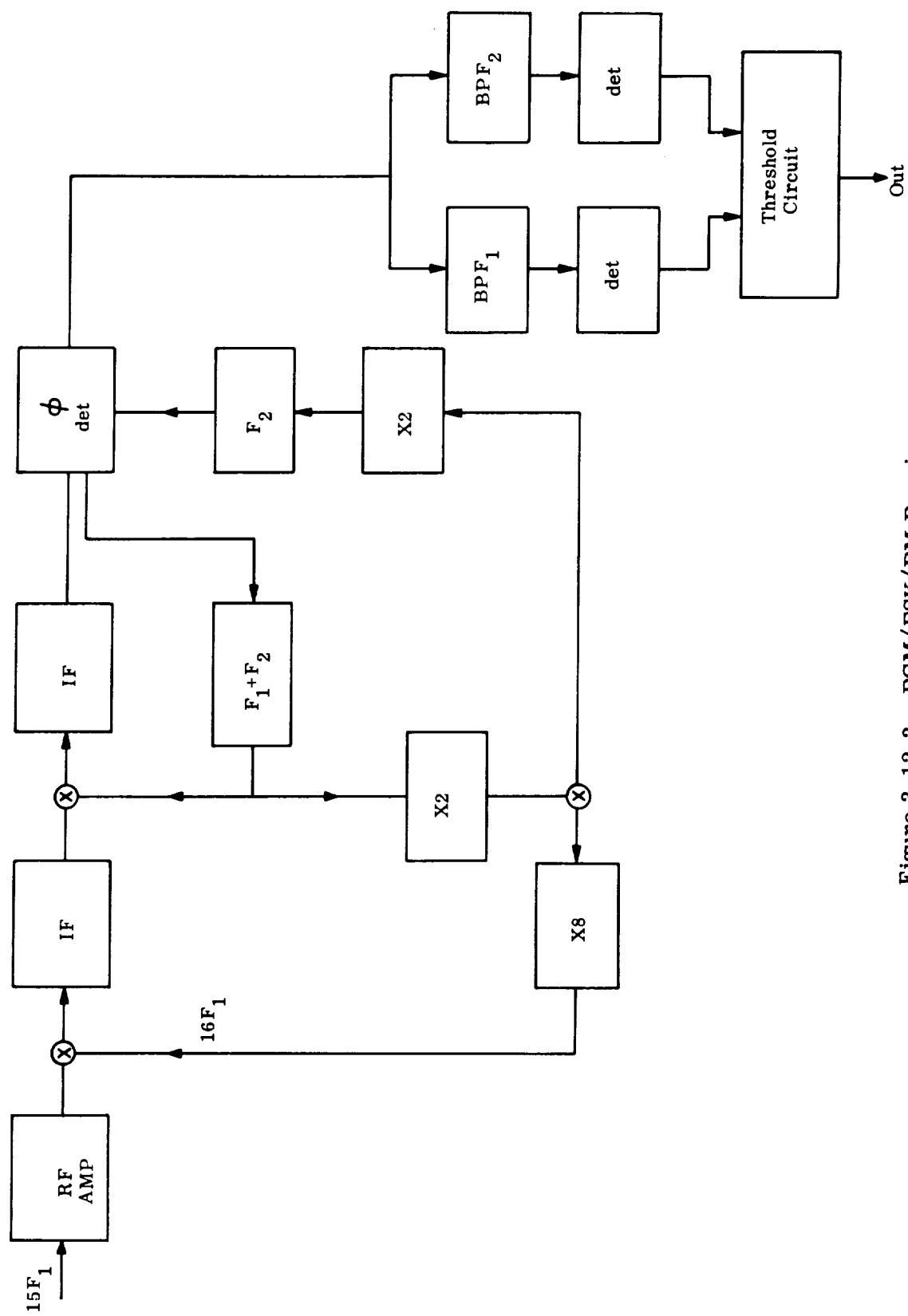


Figure 3.12.2. PCM/FM Receiver



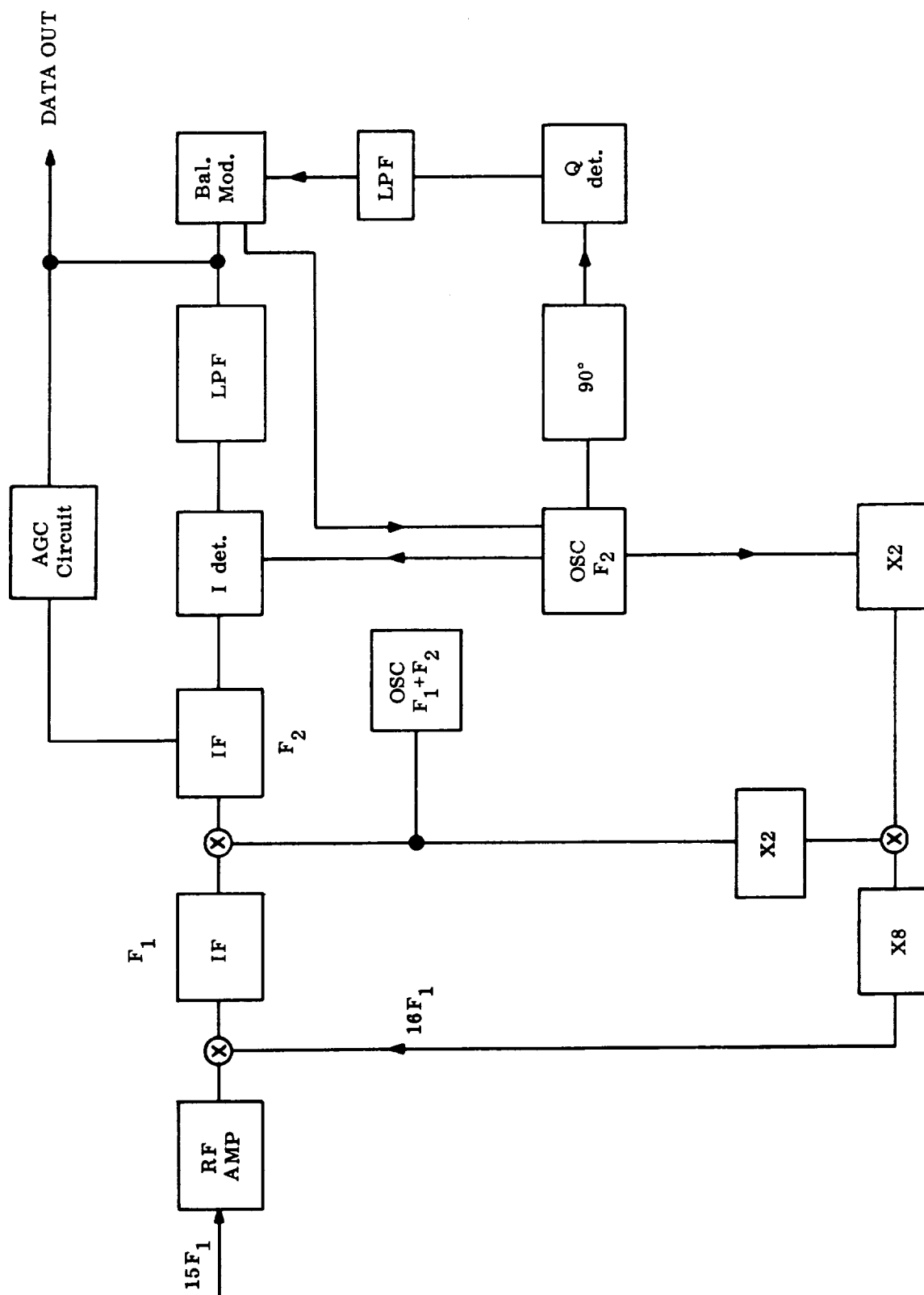


Figure 3.12.4. PCM/PS Receiver

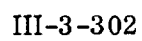


Figure 3.12.5. PCM/PS/PM Receiver

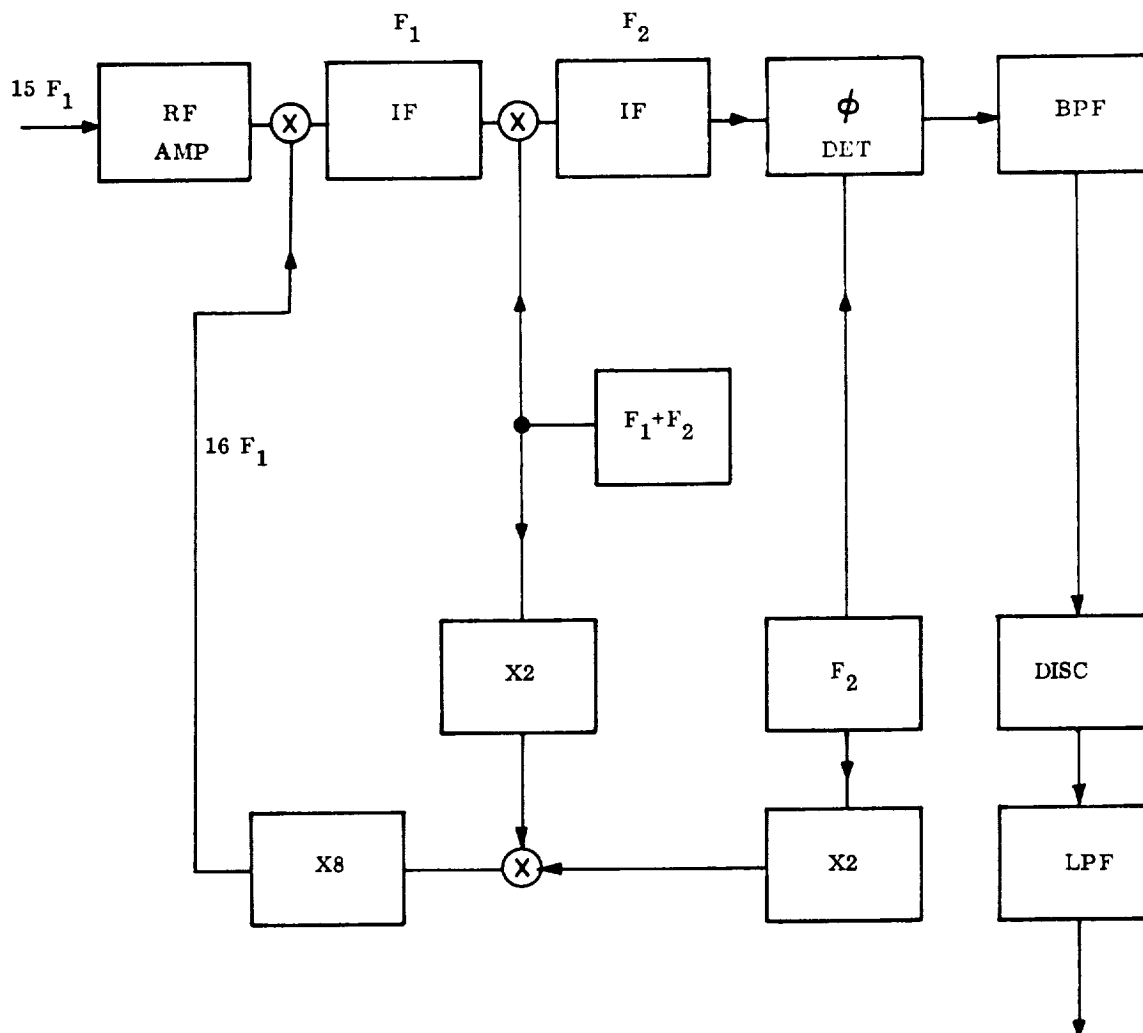


Figure 3.12.6. PCM/FM/PM Receiver

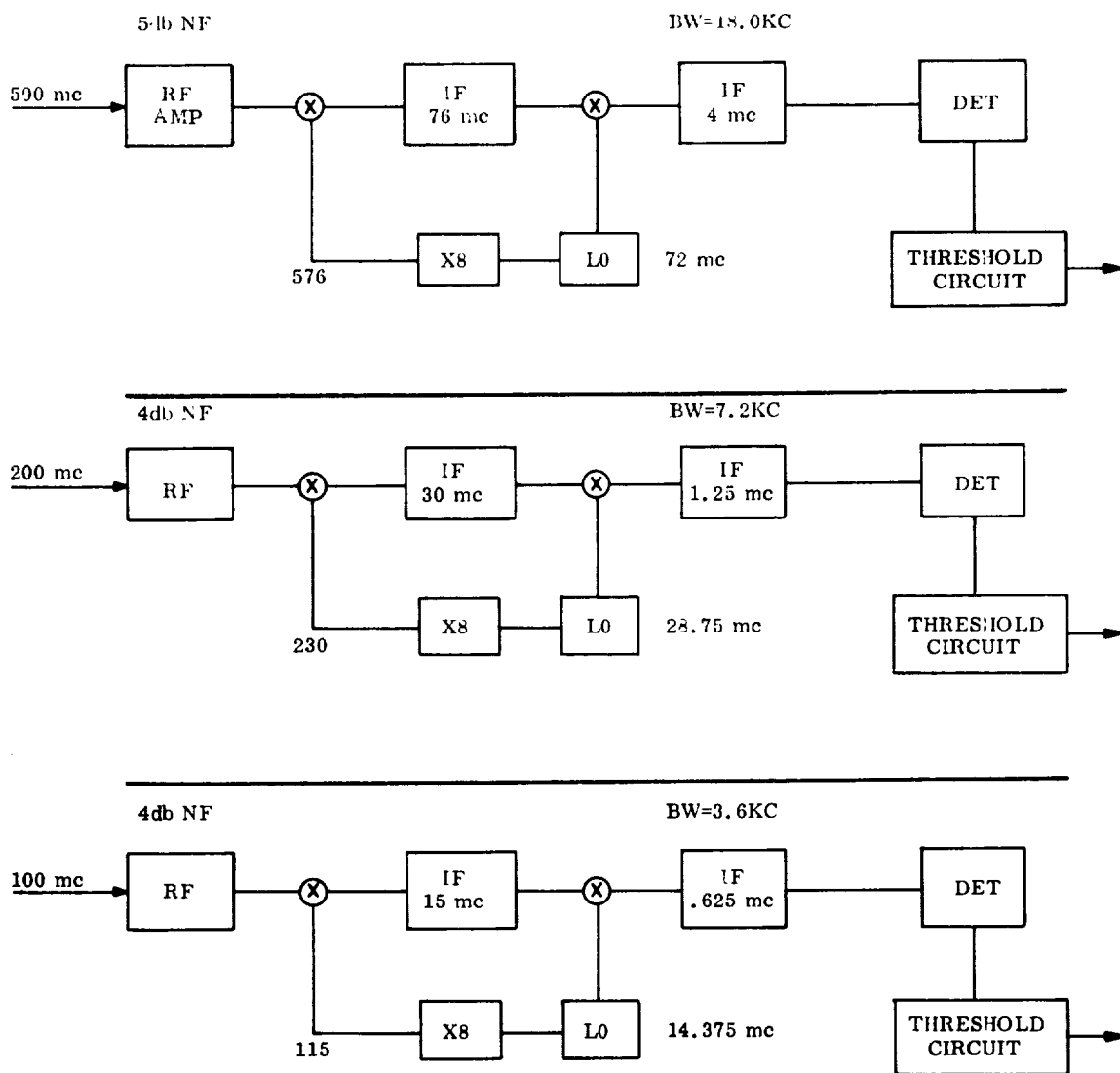


Figure 3.12.7. PPM/AM Receivers

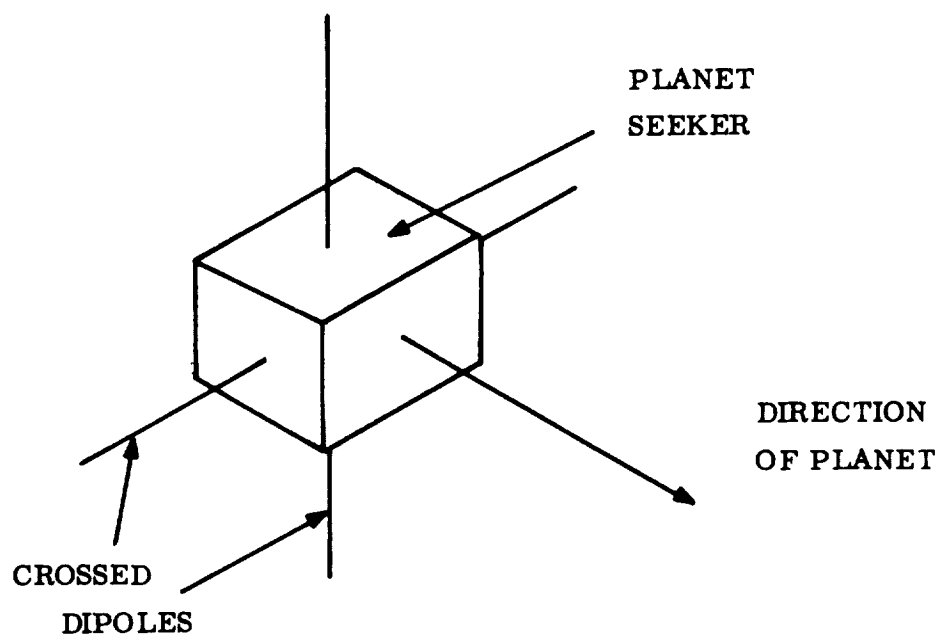


Figure 3.12.8. Spacecraft Antenna

3.13 APPLICATION TO MARS

3.13.1 General Considerations

In order to determine the applicability of the communication systems described for the Venus capsule to a Mars capsule, a comparison of typical values of significant parameters which affect communications will first be made.

These are as follows:

<u>Parameter</u>	<u>Venus</u>	<u>Mars</u>
Capsule Approach Velocity (ft/sec)	40,000	25,000*
Period of Communication (min.)	5---30	8----40*
Axial (g's)	550	120*
Deceleration Loading		
Normal (g's)	450	90*
Frequency of Pitch Oscillation (cps)	11.5	7.*
Closest Approach of Spacecraft to Planet		
(10^3 km)	20--30	15--20**
Flight Time (days)	96-131	178-243**
Communication Distance from Earth to		
Planet for Direct Link (10^6 km)	55-70	150-220**

From the comparison it is apparent that all factors which affect the relay communication capability, with the exception of flight time, are more favorable for Mars than for Venus. Since the communication distance will be only slightly less for a Mars relay link, the power requirement for a similar data rate will be approximately the same. However, if the Venus capsule equipment is used for the Mars link, it will be overdesigned with respect to the Mars entry environment.

*"Suitability of the Discoverer and Nerv Entry Vehicle and Mars Atmospheric Entry-Volume I" MSVD Final Report under JPL Contract 950226, 30 April 1962.

**"Requirements for a Venus-Mars Capsule Study," JPL, EPD-33 Revision 1, 20 April 1962.

One problem which will be more significant in a Mars capsule is antenna packaging. This results from the requirement for a parachute in the aft part of the capsule which is used to slow the capsule descent in the relatively thin atmosphere. The antennas presented for the Venus capsule, therefore, could not be utilized in a Mars capsule.

In a direct link the problem is more significant. Because of the increase in communication range by a factor of three or four, an additional loss of approximately 10 db in communication capability will result. Since the feasibility of direct communication from Venus utilizing an 85-foot dish (51.8 db gain) is questionable due to oscillator stability and acquisition problems, the possibility of communication from Mars with the small dish appears to be nil. With the 210-foot dish (61 db gain) the communication capability from Mars would be approximately equal to that from Venus using the small dish.

3.13.2 Mars Entry Transmission Attenuation

Studies have been made to determine attenuation effects resulting from entry induced plasma for the Mars atmosphere A given in Reference 3. Two physical configurations were used in the analysis; namely, the truncated Discoverer capsule (Reference 1) Figure 3.13.1 with a 22° conical section and a "standard" Discoverer capsule with a 10° conical section. The flight trajectory used for both capsules in this study was a vertical entry ($\gamma_e = 90^\circ$) from an altitude of 800,000 feet, an initial entry velocity of 25,000 feet per second, and a ballistic coefficient of 30 lb/ft.².

Stagnation pressures were computed by application of Earth atmosphere aerodynamic relationships, since the pertinent thermodynamic characteristics of the Mars A atmosphere are quite similar to the Earth's. Static pressures on the conical sections of the capsules were determined by the Prandtl-Meyer expansion techniques, and an isentropic flow expansion was assumed aft of the stagnation point. Local thermodynamic properties at the edge of the boundary layer on the conical sections were then evaluated by using the recently calculated thermodynamic properties data for Mars II environment (consistent with Mars A)

of Reference 4. The resulting computed values for electron concentration at the conical section are given in Figure 3.13.2.

Using the techniques described in Section 3.8, the effects of these electron concentrations on signal attenuation were evaluated by calculating reflection coefficient and attenuation in db/meter, and are shown in Figures 3.13.3 and 3.13.4, respectively. As expected this predicts blackout for frequencies below the plasma frequency, which varies as the square root of the electron concentration. As a result, it becomes apparent that the transmission frequency should be on the order of tens of kmc for communication throughout the entry period. The critical frequency as a function of altitude is presented in Figure 3.13.5.

A more accurate analysis of attenuation which accounts for the sheath thickness and contour might yield more favorable results, if the sheath proved to be effectively thinner than a wavelength. However, since the vehicle is a blunt body, this is definitely not the case as can be seen from the shock standoff distance shown in Figure 3.13.6. Therefore, the frequencies predicted on the simple basis outlined above should give a fairly realistic indication of those required.

The total attenuation at any given frequency and altitude can be determined by multiplying the attenuation in db/meter (Figure 3.13.4) by the shock standoff distance in meters (Figure 3.13.6) and adding that portion due to the reflection coefficient R (Figure 3.13.3) which will be equal to $20 \log (1/1-R)$ as indicated in Section 3.8.

To facilitate further evaluation and reduction of the given information, calculations have been made for both shock separation distance and boundary layer thickness at the conical section location. Figure 3.13.6 shows this data as a function of altitude. It should be noted that the higher altitude portions of these curves are dashed lines which serves to indicate that the basic continuum relationships used in the computations are not completely valid in the rarefied atmosphere prevalent at these altitudes.

REFERENCES

1. DiCristina, V. "Family of Planetary Capsules -- Shape Optimization Study," PIR 7250-25, April 5, 1962.
2. Mundy, A. "Status of Mariner C Trajectories," PIR 8153-106, March 12, 1962.
3. JPL Work Statement SW-2736, December 26, 1961.
4. Browne, W. G., "Equilibrium Thermodynamic Properties of the Environment of Mars," GE-MSVD, Advanced AeroSpace Physics Technical Memorandum #2, March 26, 1962.

Diagram of a quarter-circle structure. The radius is 18.4. The horizontal distance from the center to the right edge is 15.7. The vertical distance from the bottom edge to the top edge is 37.5. The angle between the horizontal line and the top edge is 22° .

Figure 3.13.1. Configurations Diagram

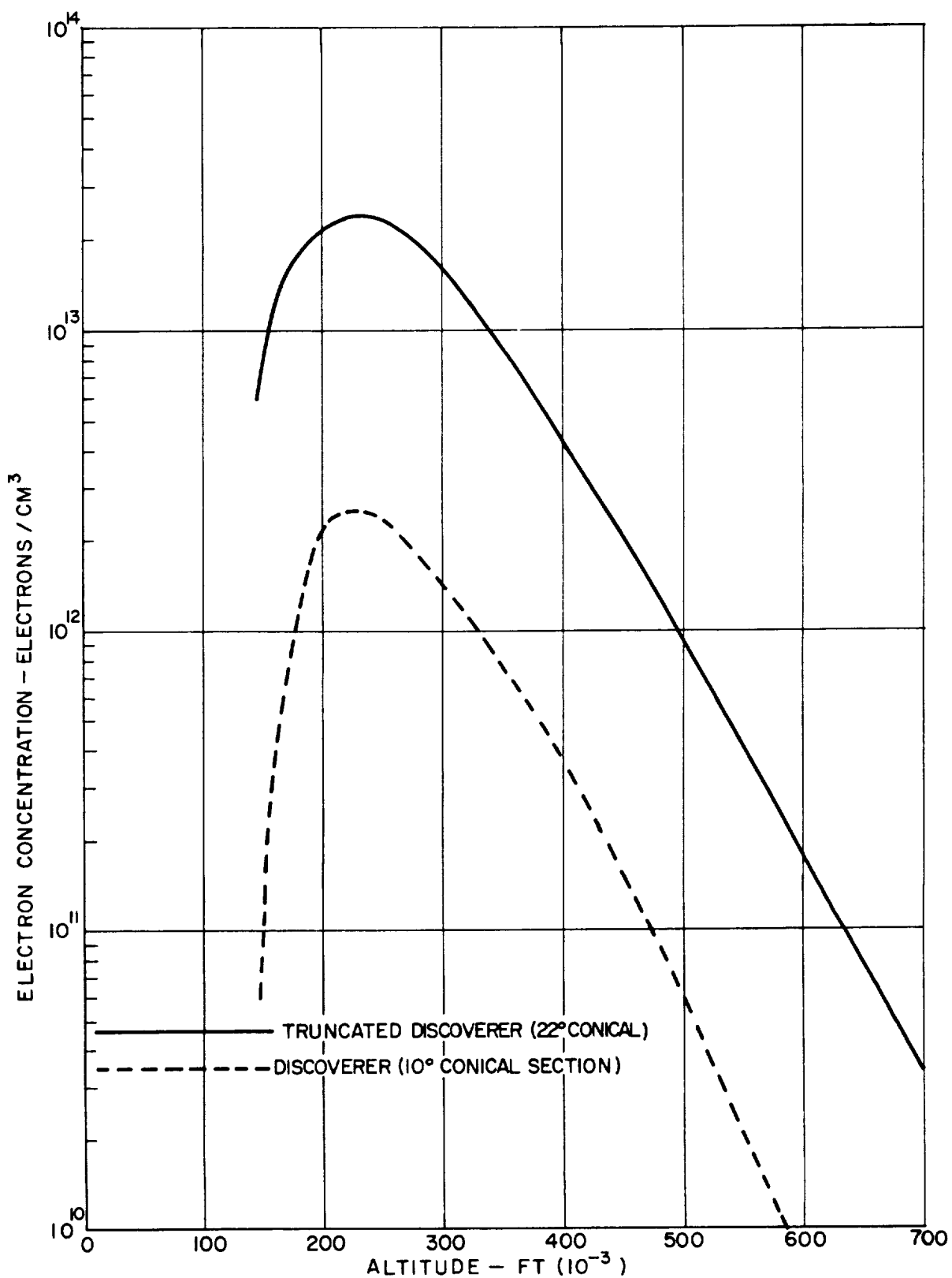


Figure 3.13.2. Electron Concentration vs. Altitude

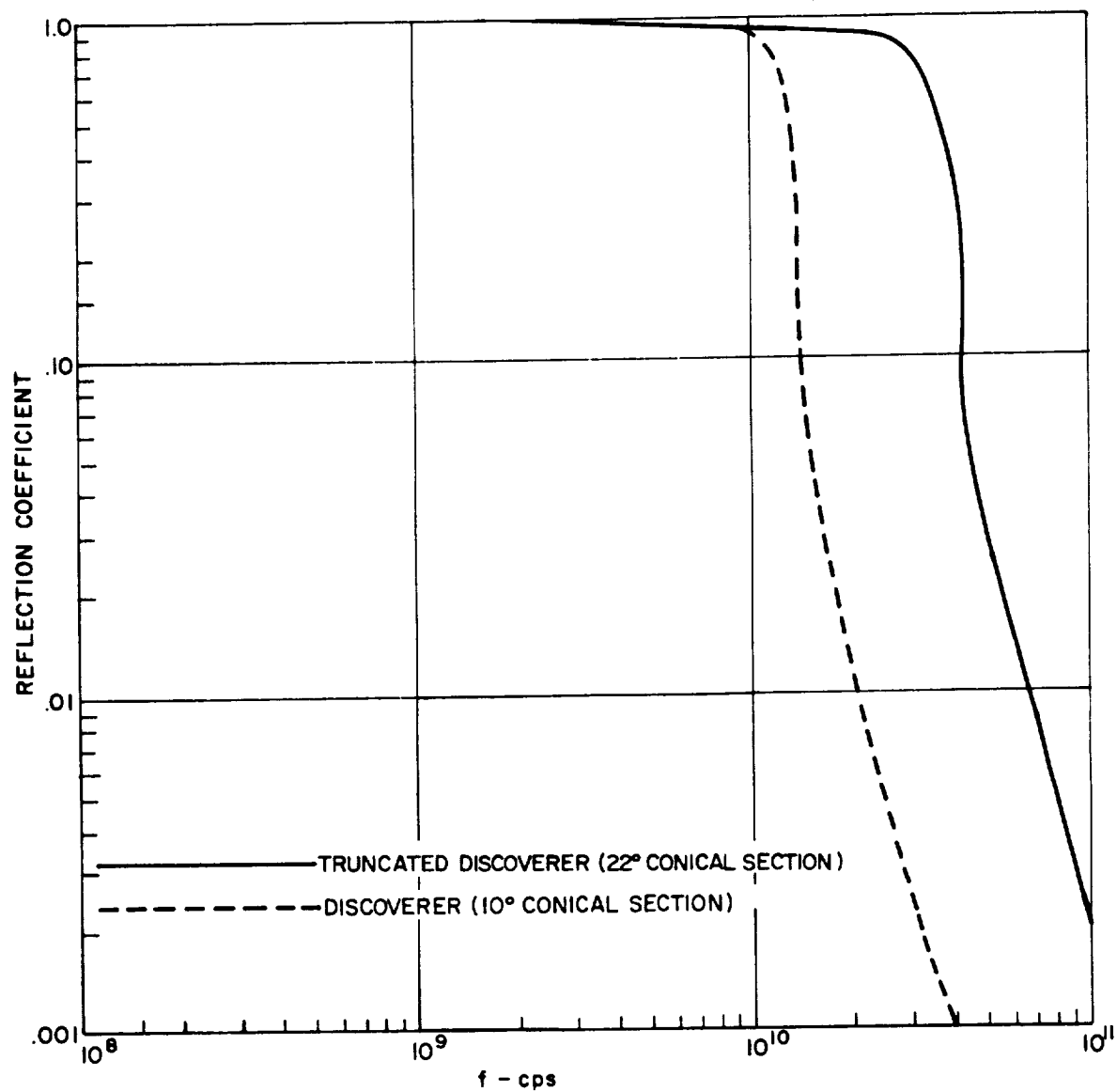


Figure 3.13.3. Reflection Coefficient vs. Frequency

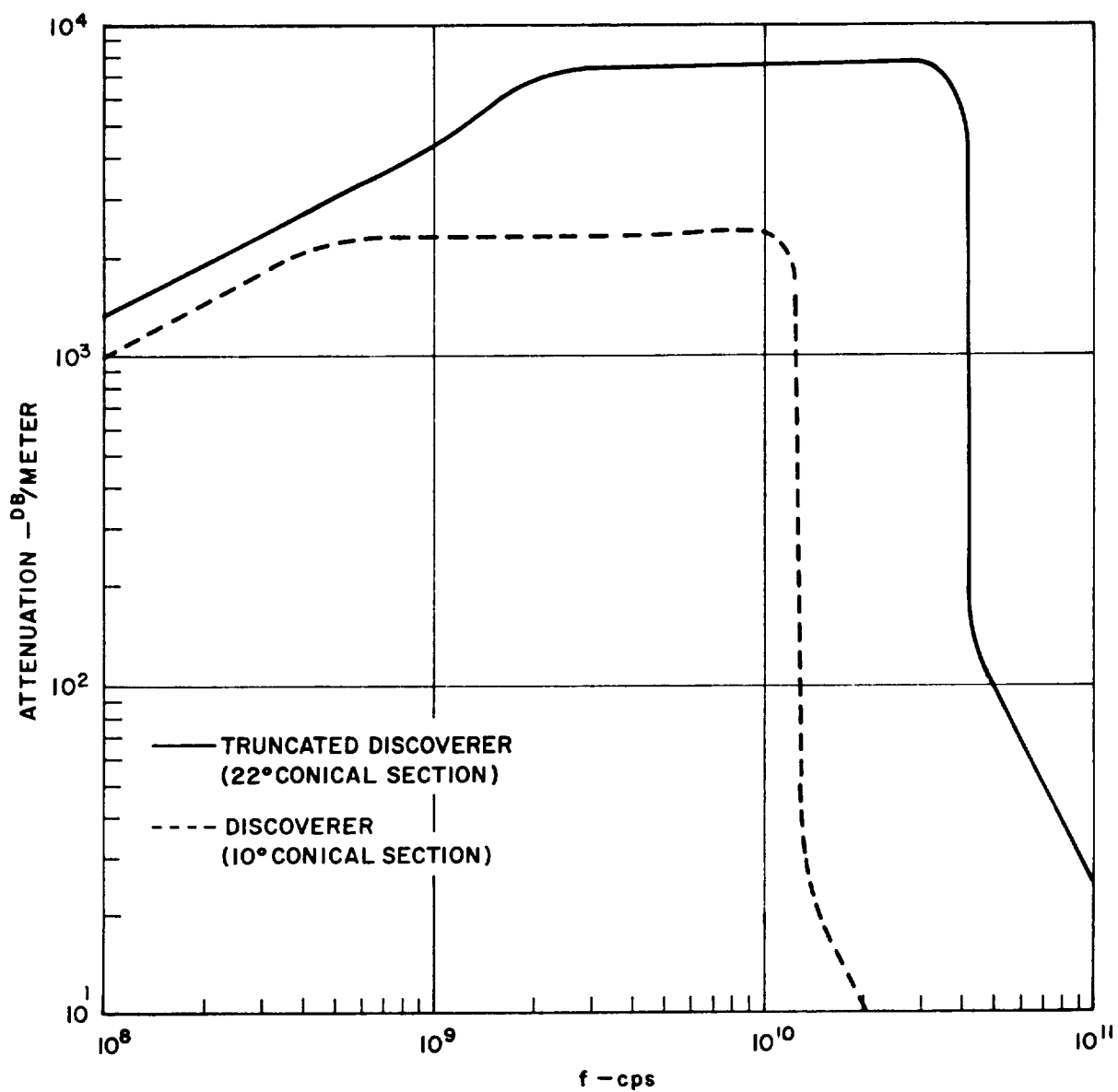


Figure 3.13.4. Attenuation vs. Frequency

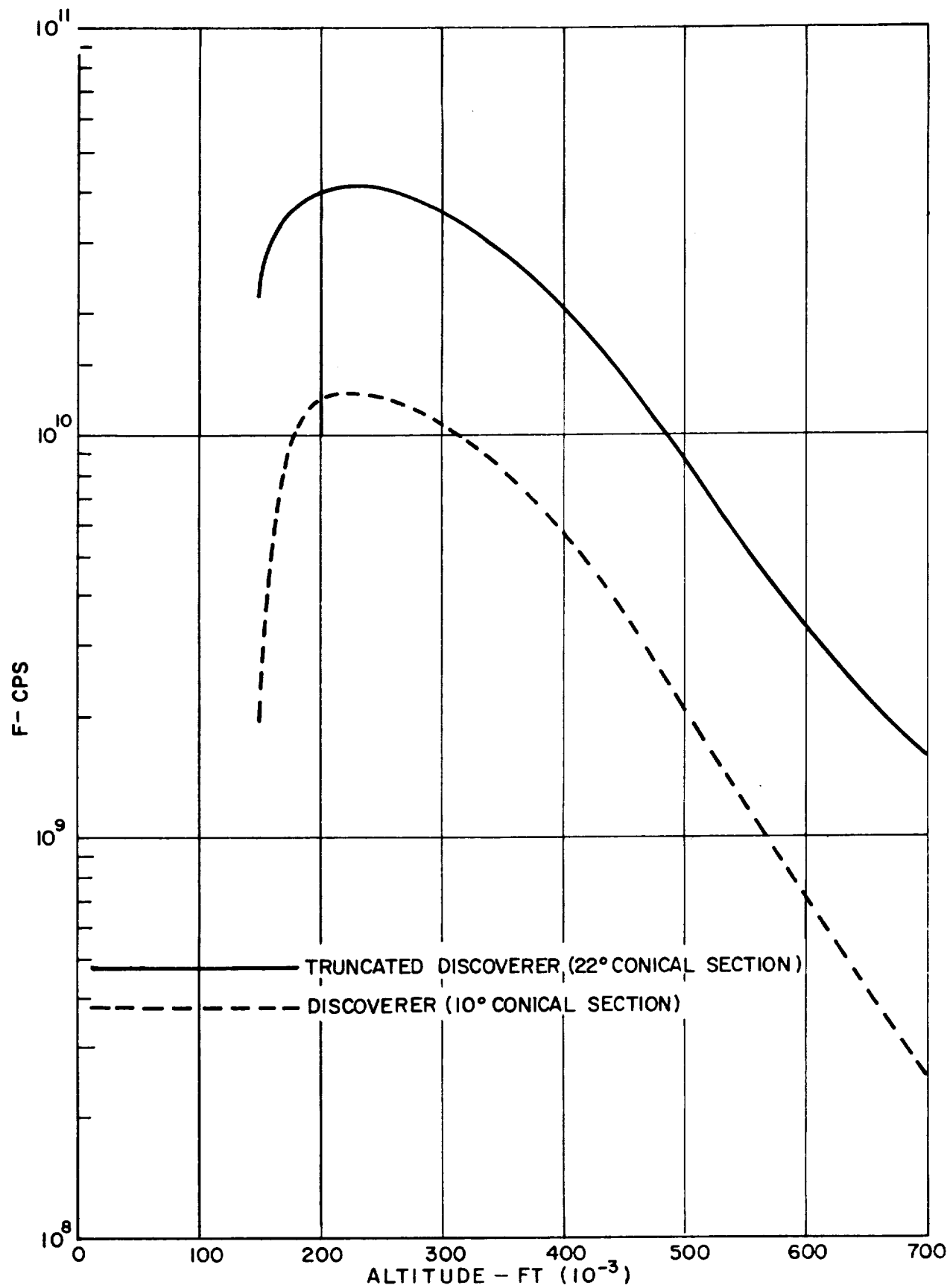


Figure 3.13.5. Critical Frequency vs. Altitude

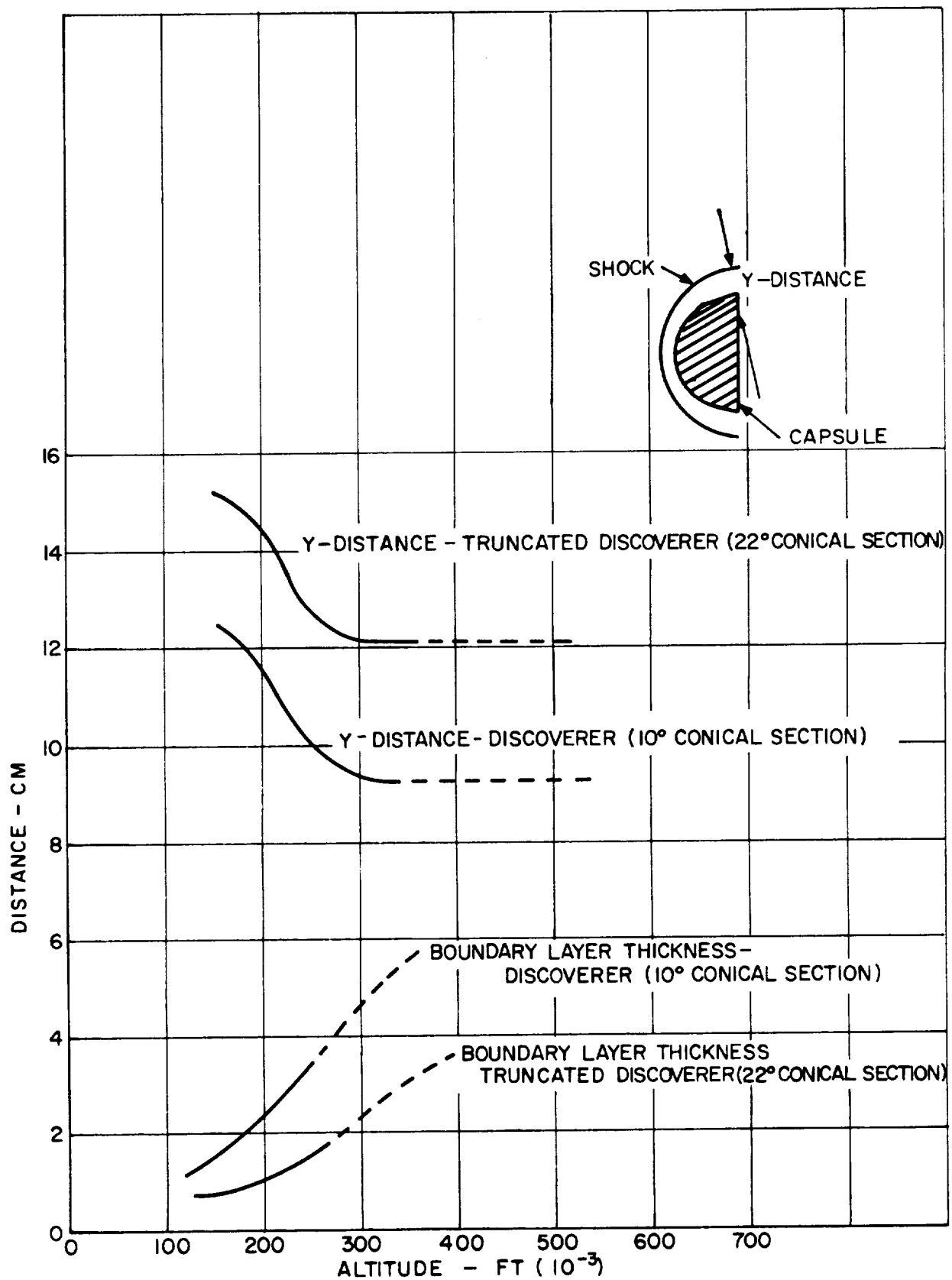


Figure 3.13.6. Shock Separation Distance (Y) and Boundary Layer Thickness vs. Altitude

4. POWER SUPPLY

4.1 SUMMARY OF RESULTS

The capsule power supply is required to provide all electrical power (at $28 \text{ VDC} \pm 10\%$) for the operation of the instrumentation and communication equipment. It must withstand the prelaunch sterilization procedure and must operate under the severe environment to be encountered after entering the Venusian atmosphere.

For this mission two separate power supplies are recommended, due to the differing requirements and environmental conditions to be encountered in the two phases of the mission. The primary power supply will provide all electrical power after atmospheric entry. The auxiliary power supply will be used for equipment check-outs and/or for providing filament-heating power prior to entry, if either of these is required.

Based on the results of the power supply studies presented in this section, the following paragraphs summarize the most promising method found for meeting the probable requirements of this mission.

For the primary power supply, sealed silver-zinc batteries are recommended. They can be designed with additional capacity to allow for losses during inactive transportation and still be relatively light-weight, as shown in Figure 4.1. For instance, a battery capsule of delivering 235 watts for 30 minutes would weigh only about 4-1/2 pounds. This assumes that the capsule will have attained an internal temperature of $+80^{\circ}\text{F}$ just prior to entry into the Venus atmosphere. The temperature must always be maintained above -65°F to prevent the electrolyte from freezing.

For the auxiliary power supply, a small nickel-cadmium battery with a recharging solar array is recommended. Silver-cadmium batteries are not recommended, since the slight weight saving attributed to sil-cads would be more than off-set by the higher reliability of the nickel-cadmium batteries. A nickel-cadmium battery-solar cell system capable of providing 200 watts of

power for 1-1/2 minutes once every 24 to 48 hours would weigh only about five pounds, as shown in Figure 4.2. At the 100-watt level the system would weigh about three pounds.

One of the most difficult problems with a mission of this nature is that of initiating the operation of the electronic equipment at a precise time (i.e., just prior to entry) after a long shut-down period. Data transmission immediately upon entry into the Venusian atmosphere can be initiated with a low-level "g" switch only if the transmitter filaments have been adequately warmed-up. It is understood that the development of a suitable timer for such a purpose, having an accuracy of ± 0.1 per cent, is presently being started by JPL.

4.2 PRIMARY POWER SUPPLY

The primary power requirements during subsonic flight have been estimated to be as follows:

Communication equipment - 70 to 180 watts

Radar altimeter - 25 watts

Other instrumentation - 20 watts

Power supply trade-offs have been based on a requirement of from 100 to 235 watts. Since the transmission of atmospheric data is expected to require a nominal 30 minutes, operating periods ranging between 10 and 50 minutes have been considered. Several possible power supply systems were considered for this mission but the specific mission requirements made it possible to discard most of them with only a preliminary analysis.

Fuel cells appeared attractive, since they are recognized for long-term medium-rate service. However, only hydrogen and oxygen fuel cells (specifically the Pratt-and-Whitney and G.E. systems) are in a state of development which permits consideration at this time. Best estimates available at the present time indicate that the most advanced fuel-cell modules have a minimum weight in the order of ten pounds per 100 watts. This weight must be considered regardless of mission duration, whether it is for minutes or years. The weight of fuel required, on the other hand, is directly a function of mission duration and this weight would be included in addition to the module weight. It will be shown that the fuel-cell module weight is prohibitive when compared with silver-zinc batteries for this mission.

Mercury cells have good stand properties, but are designed for very low-rate discharges over long periods of time. The high discharge rates required in this mission (3-1/2 to 7 amps) rule these batteries out.

Thermal batteries are recommended for certain high-rate, short-duration applications. In addition, they are not sensitive to environmental temperature conditions. However, they become extremely heavy and unreliable if designed for over five-minutes discharge. In addition, a great amount of heat is released during discharge.

Radioisotope thermoelectric generators, similar to the SNAP series, are attractive for long duration missions, but not so for the mission of the Venus capsule. Estimated specific energies for the power supply range from about 2 watts per pound for units of 1 KW power, down to 1.0 to 1.5 watts per pound for units delivering 100 to 200 watts. Considering the type of fuel being used, this power is available, only slightly diminished, for periods of from six months to several years. It can be seen that this would be attractive for long missions demanding a large number of watt-hours of power, but when the time element is short the specific power (watt-hours per pound) is low. For instance, to provide 235 watts for 30 minutes (i.e., 118 watt-hours) at 1-1/2 watts per pound specific energy, the RTG system would weigh about 155 pounds. The specific power would be 0.76 watt-hours per pound.

One of the trade-offs made in the internal environment studies pertained to the temperature-control requirements of the capsule. For silver-zinc batteries to function properly, the temperature must never be allowed to drop below -65°F . If this does happen, the electrolyte freezes and one cannot be sure that adequate thawing time would be available to permit satisfactory battery operation. Silver-zinc batteries can be activated at temperatures as low as $+40^{\circ}\text{F}$, without external heat being required. Below that temperature, heating of the battery would be required prior to - or simultaneously with - activation. If electrical power is not available, the battery would have to be heated chemically. This can be done by igniting a chemical heat powder at the same time the gas cartridge is fired. Activation can be accomplished in one or two seconds, but a weight penalty of 20 to 25 per cent must be added to the estimated weights for unheated automatically activated batteries.

Silver-zinc battery systems appear to be the most promising because of the high specific energies over the time period considered for this mission. It is estimated that the capsule temperature will be maintained at a minimum of $+14^{\circ}\text{F}$ before separation from the main vehicle. Following separation the capsule is expected to heat up slowly and stabilize at about 80°F . Under these conditions the battery would not require heating before being used.

4.2.1 Sealed Silver-Zinc Cells

Sealed cells are manufactured with the electrolyte in the cell and assembled with formed plates. However, if storage is required it is recommended that the cells be discharged at a very low rate and stored in the discharged state. They can then be charged from ground power just before launch. If power in the form of solar cells is available on the capsule, it is recommended that the sealed cells be given a topping charge just before they are required to deliver power to instrumentation.

Sealed cells containing the electrolyte suffer a capacity loss on stand which is very much temperature-related. It is estimated that a three per cent loss in capacity per month will be experienced at a temperature of 80°F . If the temperature is lowered to 60°F , the losses amount to 0.2 per cent per month, and if the storage temperature is lowered to 30°F , capacity losses drop to 0.1 per cent per month. A maximum temperature limit of 90°F is established for sealed cells on stand.

Assuming an 80°F environment during the probe flight, it is estimated that a sealed silver-zinc battery capable of delivering 235 watts for 30 minutes after nine-months storage and transport will weigh about 4-1/2 pounds. Capacity is incorporated in the battery to allow for stand losses and an additional safety factor, e.g., a battery designed to deliver 118 watt-hours after nine months would be constructed with 180 watt-hours of original capacity. The volume of this battery is estimated to be 90 in^3 .

By providing a method for a topping charge prior to separation from the spacecraft, the battery capacity losses on stand could be largely eliminated. It is estimated that under these conditions a battery designed to provide the necessary 118 watt-hours of power, plus 20 per cent, would weigh about 3-1/2 pounds. This is based on an energy density of 40 watt-hours per pound which is representative of present equipment. In Table 4.1 are noted estimates for weights and volumes of sealed-cell batteries for various services. No allowances have been made for a topping charge. The data is plotted in Figure 4.1.

Table 4.1. Sealed Silver-Zinc Batteries, 28 Volts DC
±10% 9 Months Storage at 80°F

Power Req. Watts	Discharge Time, Min	Deliv. Capacity Watt-Hours	Design Capacity Watt-Hours	Est. Wt. Lb.	Est. Vol. In. ³ *
100	10	17	26	1	20
	30	51	77	2 1/2	50
	50	85	128	3 1/2	70
235	10	39	59	2	40
	30	118	180	4 1/2	90
	50	196	295	6 1/2	130

*Based on a density of 20 in³/lb.

4.2.2 Automatically Activated Batteries

An alternate method for supplying power during the entry phase would employ automatically activated silver-zinc batteries. This system has the advantage of being unaffected by inactive storage for periods of several years. The electrolyte is stored in a separate container and is charged into the battery upon signal with the ignition of a gas cartridge. The battery comes up to operating voltage in one to two seconds. Unfortunately a weight penalty must be paid for this system which includes hardware necessary for storage of the electrolyte and activation, in addition to the battery itself.

In Table 4.2 and Figure 4.1 are shown weight and volume estimates for automatically activated silver-zinc batteries, including an additional 25 per cent added capacity as a safety factor.

Table 4.2. Automatically Activated Silver-Zinc Batteries
28 Volts DC $\pm 10\%$

Power Req. Watts	Discharge Time, Min	Deliv. Capacity Watt-Hours	Design Capacity Watt-Hours	Est. Wt. Lb.	Est. Vol. In. ³ *
100	10	17	21	3	24
	30	51	64	4 1/2	63
	50	85	106	5 1/2	77
235	10	39	49	4	56
	30	118	148	6 1/2	91
	50	196	245	8 1/2	119

*Based on 14 in³/lb.

4.2.3 Temperature Increase During Battery Discharge

In order to estimate the temperature increase for the battery during discharge, 235 watts for 30 minutes was used as the basis for the calculations. Battery temperature was assumed to be 80°F at initiation and the battery specific heat was estimated to be 0.25 BTU/lb-°F. Heat generated in the battery is due to internal resistance and may be calculated as the difference between open-circuit voltage (1.60) and operating voltage (1.37), times the current (8.4 amps), times the number of cells (20) times the time (30 min.). Thus:

$$\begin{aligned}
 H_{\text{loss}} &= NI T (V_o - V_d) \\
 &= 20 (8.4) (30) (1.60 - 1.37) \\
 &= 20 (8.4) (30) (.23) \\
 &= 1160 \text{ watt-min} = \frac{1160}{17.6} = 66 \text{ BTU} \\
 &\quad (17.6 \text{ watt-min per BTU})
 \end{aligned}
 \tag{4-1}$$

Designating T_2 as the final temperature after 30 minutes and T_1 as the initial temperature, we have:

$$\begin{aligned}
 T_2 &= T_1 + \frac{66 \text{ BTU}}{\frac{.25 \text{ BTU}}{\text{lb-}^\circ\text{F}} \times (4.5 \text{ lb})} \\
 T_2 &= 80^\circ\text{F} + 60^\circ\text{F} = 140^\circ\text{F at 30 min.}
 \end{aligned}
 \tag{4-2}$$

After 15 minutes the temperature of the battery would be about 110°F. This would be the temperature of the outside of the battery jar, providing no heat were allowed to escape to the surroundings. It is recommended that the battery be insulated to minimize heat losses to its environment since a maximum temperature of 140°F is not detrimental to battery operation.

4.3 AUXILIARY POWER SUPPLY

Present estimates are that from 100 to 200 watts of power might be required periodically for a duration of about 1 1/2 minutes to check out the instrumentation and communication equipment, as well as the thermal control system. These checkouts may be required as frequently as once every other day following separation of the probe from the main vehicle.

4.3.1 Sealed Silver-Zinc Battery

One method considered for providing power is the use of a sealed primary silver-zinc battery. However, this method appears to have quite a weight penalty associated with it. A sealed battery capable of delivering 60 pulses at the 200-watt level would weigh about ten pounds. A battery capable of delivering 60 pulses at the 100-watt level would weigh about six pounds.

4.3.2 Rechargeable Battery with Solar Cells

One promising auxiliary power system is the use of a small nickel-cadmium or silver-cadmium battery capable of being recharged between every checkout by solar cells. The rate of charge would be quite small, since only 1 1/2 minutes are required from the battery during discharge every 48 hours. Silver-zinc batteries cannot be used for this service since they do not possess satisfactory cycling capabilities.

4.3.2.1 Solar-Cell Array

Solar cells mounted on the skin of the capsule could be used with rechargeable nickel-cadmium or silver cadmium batteries for the checkout function. If the cells were mounted directly on the capsule, the temperature of the cells would run about 250°F. At this high temperature the current is increased, but the voltage drops to about 0.28 volts/cell. In order to obtain the 35 volts required for charging the battery, 125 one-centimeter square cells in series would be required. Six such panels spaced around the capsule aft of the heat shield would

be required to insure that one was always facing the sun, each panel being about 6.3" x 4.35" in size (0.19 ft.²). With 10 mils of blue-red filter glass over the cells, a 40 per cent degradation in current output could be expected over six months. However, because of the low power level required for charging the battery, this poses no problem. At 0.6 pounds per square foot, the six panels would weigh about 0.7 pounds.

It might be possible to mount the cells on metal patches inserted in the skin of the probe. This would enable the cells to be spread out such as to radiate much of the waste heat. Allowing 1/2 open-space on the patches, it is estimated the cells would be operating at 200^oF, thereby increasing the voltage to 0.34 volts per cell and decreasing the number of cells to 105. The area of each panel would be 5.9" x 5.5" (0.225 ft.²). Again using 10 mils of red-blue filter, it is estimated that six of these panels of 105 cells each would weigh about 0.5 pounds. Allowing 0.2 pounds for the patches of 20-mil aluminum would bring the total panel weights to 0.7 pounds. In either case about 1/2 pound should be allowed for harnessing, diodes, etc.

By operating at the lower temperature, reliability would be increased, since fewer cells would be required to obtain the desired voltage for charging. In addition, the materials problem would be lessened at the lower temperature.

4.3.2.2 Nickel Cadmium-Solar Cell System

At 200 watts for 1 1/2 minutes, the battery would be delivering 4 watt-hours per cycle. For a 28-volt system, 7.15 amps would be needed, and the battery would be delivering 0.18 ampere-hours. In order to sustain the high rate of discharge, it would be necessary to overdesign the battery probably by as much as a factor of 5. We would then have a one-ampere-hour battery (28 watt-hours for a 28-volt system). At a power density of 8 watt-hours per pound, about 3 1/2 pounds of nickel-cadmium batteries would be required for 200-watt service.

A reasonable charge voltage for a nickel cadmium battery would be about 35 volts, allowing for losses in circuitry. Assuming 100 per cent overcharge, the current for the 24-hour charge would be:

$$\frac{0.18 \text{ ampere hours}}{24 \text{ hours}} \times 2 = 15 \text{ milliamperes} \quad (4-3)$$

4.3.2.3 Silver Cadmium-Solar Cell System

Although silver-cadmium batteries are not in the advanced state of development that nickel cadmium's are, it is reasonable to assume that the state-of-the-art will be advanced in the near future to the point that a 28 watt-hour sil-cad battery will be satisfactory for the 200-watt instrumentation checkout service. If this is accomplished, a sil-cad battery for the above service would weigh about 2.5 pounds, based on a power density of 12 watt-hours per pound. No overcharge is required for silver-cadmium batteries. However, since charging voltage requirements are about the same, it is expected that there would be no saving in solar-cell weights over that required for the nickel-cadmium system.

4.3.2.4 Overall Battery-Solar Cell System Weights

The weights of the nickel-cadmium and silver-cadmium battery-solar cell systems are shown in Table 4.3 and Figure 4.2.

Table 4.3. Auxiliary Power Weights, Batteries with Solar Cells

Battery	Power Watts	Battery Size Watt-hrs.	Battery Wt. lbs.	Solar Cell Wt. lbs.	System Wt. lbs.
Ni-Cad	200	28	3 1/2	1 1/2	5
	100	14	2	1	3
Sil-Cad	200	28	2 1/2	1 1/2	4
	100	14	2	1	3

4.3.3 Radioisotope Power Supply

One method which is being considered for heating the capsule would utilize a radioisotope generator similar to that of the Transit IV-A. Although not an efficient electrical power generator in this case, the electrical output could be used for recharging the auxiliary batteries if the generator is to be included for thermal-control purposes anyway. This would eliminate the need for solar cells.

The Transit IV-A generator develops 52 thermal watts and about 2.7 electrical watts. It weighs approximately four pounds and is 5 1/2 inches long by 4 3/4 inches in diameter. Because of the high voltage required for charging the auxiliary batteries (approximately 35 volts), a DC-DC converter would be required. This converter would weigh about one-half pound and operate at 80-85 per cent efficiency. Since only 0.6 watt is required for the recharging operation, this radioisotope generator would provide ample electrical power. Care must be taken in selecting the fuel, however. One must be selected which has sufficient half-life to provide power throughout the mission, but runs a minimum risk of contaminating the planet, if a malfunction occurs during entry.

4.4 INITIATION OF PRIMARY POWER

If data is required immediately upon entry into the Venus atmosphere, a low-level "g" switch could be used to turn on the equipment. However, the transmitter filaments, requiring perhaps 6 to 12 watts, would be required to be at operating temperature at this time to insure that data transmission could begin instantaneously.

The initiation of the filament heating - soon enough to insure that the equipment is warm, and precisely enough to insure that too much power is not wasted in the "ready" state - demands a very accurate timing device. The timer would have to operate for a period of up to 100 days and consume a very small amount of power.

It is understood that JPL is developing a timer accurate to ± 0.1 per cent. For a 100-day flight period, this would mean 6 to 12 watts would have to be provided for five hours to the filaments prior to entry to insure that they were at operating temperature when the Venus atmosphere is encountered. The additional 30 to 60 watt-hours of power could be built into the primary silver-zinc battery at a weight penalty of one to two pounds. According to a JPL source, the timer would weigh two pounds, occupy 30 to 40 cu. in. and require about one watt of power. This power could be obtained either from the radioisotope generator or by slightly enlarging the secondary battery.

If pre-entry signal acquisition is desired, then the same timing device could be used to turn on full power to the communication equipment before entry.

4.5 PROBLEM AREAS AND RECOMMENDATIONS FOR FURTHER EFFORT

Listed below are some of the more important factors which must be considered before designing the power supply for the Venus capsule.

4.5.1 Primary Battery

- a. Finalize power requirements.
- b. Decide on type of battery based on performance under simulated environment conditions including determination of stand losses. Finalize size.
- c. Perform thermal studies, simulating the environment during transport to Venus and temperature increase during discharge. (Necessary to calculate insulation requirements and determine need for battery heating.)

4.5.2 Auxiliary Power Supply

- a. Determine method of mounting solar cells and expected method of operation of cells.
- b. Investigate Ni-Cad storage battery performance under conditions necessary for checkout duty.
- c. Determine if Sil-Cads warrant further investigation for the above duty.
- d. Finalize battery size.
- e. Determine advisability of using solar cells to provide a topping charge for the primary battery.

4.5.3 Radioisotope Power Supply

- a. Determine advisability of using RTG for recharging auxiliary power, considering weight disadvantage against difficulties of mounting solar cells.
- b. Determine "safe" fuel and specific power (watts per pound) as a function of the type of fuel.

4.5.4 Sterilization

- a. Develop a battery capable of withstanding heat sterilization.
(Developments presently underway will be followed closely.)
- b. Finalize battery sterilization procedures.

4.5.5 Timing Device

- a. Accurate timing is required to turn on equipment when needed at entry into the Venus atmosphere. A thorough investigation or, if necessary, a development program should be undertaken to solve this critical problem. A timer accurate to ± 0.1 per cent over 100 days is required.

4.5.6 Regulation and Control Requirements

- a. The requirements for regulation of the primary and auxiliary power supplies should be determined.
- b. The desirability of overload and short-circuit protection for individual equipments should be determined.